INAUGURAL – DISSERTATION

zur

Erlangung der Doktorwürde

der

Naturwissenschaftlichen – Mathematischen

Gesamtfakultät

der

Ruprecht-Karls-Universität

Heidelberg

vorgelegt von

Dipl.-Phys. Patrick Jöckel

aus Bad Kreuznach

Tag der mündlichen Prüfung: 21. Dezember 2000

Cosmogenic ^{14}CO as tracer for atmospheric chemistry and transport

Gutachter: Prof. Dr. Ulrich Platt

Prof. Dr. Paul J. Crutzen

Dissertation
submitted to the
Combined Faculties for the Natural Sciences and for Mathematics
of the Rupertus Carola University of
Heidelberg, Germany
for the degree of
Doctor of Natural Sciences

Cosmogenic ^{14}CO as tracer for atmospheric chemistry and transport

presented by

Diplom-Physicist: Patrick Jöckel

born in: Bad Kreuznach

Heidelberg, 21. December 2000

Referees: Prof. Dr. Ulrich Platt

Prof. Dr. Paul J. Crutzen

^{14}CO als Indikator für atmosphärische Chemie- und Transportprozesse
Fortschritte in der Atmosphärenchemieforschung hängen in zunehmendem Maße von der Anwendung dreidimensionaler (3-D) Atmosphärenchemiemodelle ab. In der vorliegenden Arbeit wird systematisch die Anwendung von atmosphärischen ^{14}CO Messungen zur Evaluierung solcher Modelle entwickelt. Der Schwerpunkt liegt dabei auf der simulierten globalen Hydroxylradikalverteilung (OH) und ihrer jahreszeitlichen Schwankung, sowie auf den Austauschprozessen zwischen Stratosphäre und Troposphäre. Modellstudien mit zwei unterschiedlichen 3-D-Modellen in verschiedenen Konfigurationen werden vorgestellt. Ein Modell wird mit Hilfe von Standardmethoden, die Simulationen von SF_6, CH_3CCl_3 und $CFCl_3$ umfassen, evaluiert. Dann werden Unsicherheiten bezüglich der kosmogenen ^{14}C-Quellverteilung und die Auswirkungen auf die ^{14}CO Anwendung studiert. Der Einfluß der variablen Sonnenaktivität auf die kosmogene ^{14}C Produktion und auf ^{14}CO in der Atmosphäre wird untersucht, ebenso wie der Effekt der ^{14}C-Produktion, hervorgerufen durch Sonnenprotonenereignisse, auf ^{14}CO in der Atmosphäre. Hinweise auf diesen geophysikalischen Effekt werden in Meßdaten nachgewiesen. Weiterhin wird ein klimatologischer, zonal gemittelter ^{14}CO Jahreszyklus an der Erdoberfläche aus Beobachtungsdaten abgeleitet. Der quantitative Vergleich mit Modellsimulationen führt zu wichtigen Folgerungen in Bezug auf den simulierten Stratosphären - Troposphären Austausch und OH. Daraus ergibt sich eine mögliche Erklärung für die beobachtete ^{14}CO Asymmetrie zwischen beiden Hemisphären.

^{14}CO as tracer for atmospheric chemistry and transport
Advances in atmospheric chemistry research depend increasingly on the use of three-dimensional (3-D) atmospheric transport and chemistry models. In this thesis the application of atmospheric ^{14}CO measurements for evaluation of such models is systematically developed. Emphasis is on the simulated global distribution and seasonality of the hydroxyl radical (OH) and the stratosphere - troposphere exchange (STE). Modeling studies with two different 3-D models in various configurations are presented. One model is evaluated with standard methods, i.e., with simulations of SF_6, CH_3CCl_3 and $CFCl_3$. Next, uncertainties in the cosmogenic ^{14}C source distribution and their implications for the ^{14}CO application are studied. The influence of the variable solar activity on cosmogenic ^{14}C production and atmospheric ^{14}CO is investigated, as is the effect of solar proton event induced ^{14}C production on atmospheric ^{14}CO. Indications for this geophysical effect are derived from observations. Furthermore, a climatological zonally averaged seasonal cycle of ^{14}CO at surface level is constructed from observations. Quantitative comparison with model simulations reveals important implications for the simulated STE and OH. This provides a possible explanation for the observed interhemispheric asymmetry of ^{14}CO.

Für Anikó, Waltraud und Wolfgang.

NON EST AD ASTRA MOLLIS E TERRIS VIA.
Seneca

Contents

1 Introduction

1.1 The ^{14}CO methodology

1.1.1 Motivation

Present knowledge about the atmospheric distribution and seasonal cycle of the OH radical, the most important oxidant in the atmosphere, is mainly based on complex model calculations, since measurements of OH on the global scale are hampered by its high reactivity. Its resulting short lifetime and low concentration not only make detection difficult, but render obtaining a global picture nearly impossible. Although chemistry-transport models are continuously being improved by implementing refined transport schemes, more complete chemistry parameterizations, cloud effects, etc., there is still a considerable degree of uncertainty about OH seasonality and distribution. Because of the great importance of OH in the chemistry of the atmosphere [*Levy*, 1971; *Singh*, 1977; *Logan et al.*, 1981; *Crutzen*, 1995a] independent verification of the calculated OH distribution is therefore necessary.

The most frequently used tracer for this purpose is methylchloroform (CH_3CCl_3, MCF), because its known rate of anthropogenic release into the atmosphere has to be balanced by its removal by mainly OH and the change in atmospheric burden. How difficult it is to constrain the amount of global OH and its distribution is witnessed by discussions in the literature [*Prinn et al.*, 1983b,a, 1987; *Spivakovsky et al.*, 1990; *Hartley and Prinn*, 1991; *Spivakovsky et al.*, 1991; *Cunnold and Prinn*, 1991; *Spivakovsky*, 1991; *Prinn et al.*, 1992, 1995; *Krol et al.*, 1998]. Moreover, the methylchloroform approach suffers from principal limitations on scales smaller than the global scale. The comparably long lifetime of approximately 5 years impedes evaluation of three-dimensional (3-D) model calculated OH distributions and seasonalities. (This is further discussed in chapter 4 in this thesis.) Other reactive gases released into the atmosphere, like HCFC-22 (hydrochlorofluorocarbon), may offer alternatives to CH_3CCl_3 in assessing OH. However, none of the substances available meets all the requirements for optimal testing the OH distribution and seasonality. For HCFC-22 for instance, the results are similar to those for CH_3CCl_3 but less accurate [*Miller et al.*, 1998].

As a consequence it is worthwhile to investigate the possibilities of other tracers for testing model generated distributions and seasonalities of OH. One particularly promising candidate is ^{14}CO. Most ^{14}CO present in the atmosphere is the direct result of the nuclear reaction

$$^{14}\mathrm{N(n,p)}^{14}\mathrm{C} \tag{1.1}$$

[*Libby*, 1946], followed by

$$^{14}C^{*} + O_2 \rightarrow ^{14}CO + O \tag{1.2}$$

in which the excited radiocarbon atom reacts quickly with oxygen and produces preferentially (∼95%) ^{14}CO [*MacKay et al.*, 1963; *Pandow et al.*, 1960]. Therefore the ^{14}CO production rate is directly determined by the atmospheric neutron flux, which strongly depends on the flux and energy spectrum of primary cosmic radiation which initiates the particle cascades terminating in neutron production [*Light et al.*, 1973]. The relevant primary particles (nucleons) are charged particles (about 90% protons, and to a lesser extent alpha-particles and heavier nuclei) from galactic cosmic rays (GCR) with energies up to several GeV. Due to their electric charge the particle trajectories are affected by magnetic fields, in particular by the geomagnetic field and the varying solar wind plasma. Additionally, primary protons of solar origin occasionally contribute to the primary radiation and therefore to the ^{14}CO formation during solar proton events (SPEs). At the same time, a smaller fraction of ^{14}CO (secondary ^{14}CO) is continuously produced in the atmosphere from precursors of biogenic origin, for instance from the oxidation of atmospheric methane and natural non-methane hydrocarbons (NMHCs) [*Volz et al.*, 1981].

Atmospheric ^{14}CO, like CO itself, has two sinks, the smaller one of which is the uptake in soils. This biological sink of CO is estimated to be only about 4-8% of the total [*Sanhueza et al.*, 1998]. The dominant sink process is oxidation with the OH radical, i.e.,

$$^{14}CO + OH \rightarrow ^{14}CO_2 + H\ . \tag{1.3}$$

The reaction rate coefficient (in cm^{-3} s^{-1}) of CO and OH is pressure dependent (p in Pa), i.e.,

$$k_{CO+OH} = 1.5 \cdot 10^{-13} \cdot (1 + 0.6 \cdot \frac{p}{101325}) \tag{1.4}$$

[*DeMore et al.*, 1997]. For ^{14}CO the reaction rate is slightly lower. Based on the reaction rate for ^{13}CO, which has been measured, ^{14}CO reacts about 1% slower than ^{12}CO [*Brenninkmeijer et al.*, 1999]. Assuming a global average OH concentration of 10^6cm^{-3} the lifetime of ^{14}CO can be estimated to

$$\tau_l = (k_{OH+CO}[\bar{OH}])^{-1} \approx 2 \text{ months}, \tag{1.5}$$

with an average atmospheric pressure of 500 hPa. This very rough estimate does not, however take into account the non-homogeneous distribution of OH and ^{14}CO in the vertical and horizontal directions.

Figure 1.1 summarizes in a schematic overview the relevant processes determining atmospheric ^{14}CO. The basic processes determining the local atmospheric ^{14}CO mixing ratio are

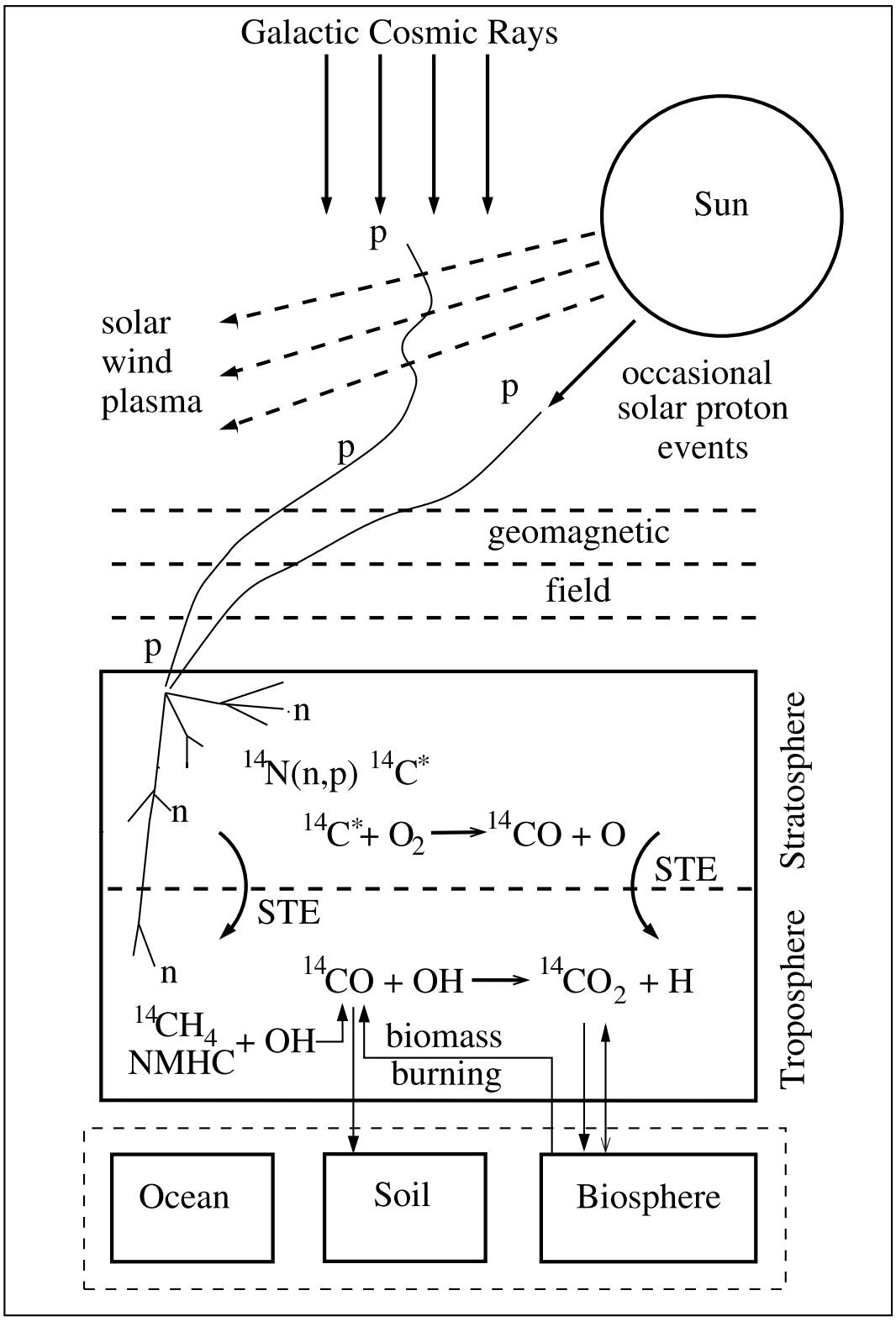

Figure 1.1: Schematic overview of the processes determining the atmospheric ^{14}CO mixing ratio (p: protons, n: neutrons, STE: stratosphere - troposphere exchange, NMHC: non-methane hydrocarbons).

- the global source distribution and strength of ^{14}CO,
- the OH distribution and seasonality,
- atmospheric transport.

Assuming that two of these three processes are well known, the third one can in principle be derived using ^{14}CO measurements. This defines the "^{14}CO methodology". That this statement holds and ^{14}CO indeed is a useful tracer has yet to be proven. Nonetheless some properties of ^{14}CO seem favorable:

1. The source of ^{14}CO is mainly cosmogenic and therefore independent of climate, atmospheric chemistry, and human activity. At any time in the future, measurements of ^{14}CO can be repeated for testing the understanding of the atmosphere and to track changes.
2. The chemical lifetime of ^{14}CO of about 2 to 3 months is shorter than the time constant of globally important atmospheric transport processes, specifically stratosphere - troposphere exchange and interhemispheric transport.
3. The chemical lifetime of ^{14}CO is comparable to the seasonal changes in OH, yet sufficiently long to reconstruct its distribution from a realistic number of atmospheric observations.
4. The cosmogenic component of ^{14}CO can be estimated from measurements by correcting these for the biogenic (secondary) ^{14}C contribution. This correction can be derived from the CO content of the air and its specific activity (number of disintegrations per unit of mass and time), knowing the specific activities of the different sources. In this way, cosmogenic ^{14}CO can be treated as an independent tracer.

The main problem with the ^{14}CO methodology is that roughly 50% of all cosmogenic ^{14}CO is produced in the stratosphere, and furthermore some uncertainty in the vertical distribution of the ^{14}CO source remains. This implies that transport from the stratosphere into the troposphere is important, and in particular this process presents great challenges for all presently available models. Imperfections in the cross-tropopause transport realization in models will therefore lead to severe difficulties in tropospheric OH validation. This may have been part of the problems encountered in the past (see below). However, a detailed understanding of transport from the stratosphere into the troposphere is of great importance [*Rosinski and Williamson*, 1997; *Holton et al.*, 1995], and for instance, the question about the amount of ozone imported from the stratosphere is still an issue for research [*Roelofs*

and Lelieveld, 1997; *Lawrence et al.*, 1999a]. What may be seen as a problem in applying ^{14}CO may eventually be useful in its own right.

1.1.2 The history

Already before the discovery of the important role of OH in the troposphere [*Levy*, 1971], *Weinstock* [1969] estimated the residence time of CO, using ^{14}CO measurements, or more precisely the specific activity of CO measured by *MacKay et al.* [1963]. The implicit assumptions of the approach of *Weinstock* [1969] and the implications for CO budget calculations are discussed by *Junge et al.* [1971]. *Volz et al.* [1981] applied the ^{14}CO concept in a systematic manner and concluded that the abundance and seasonality of ^{14}CO is in accordance with that of OH used in a two-dimensional (2-D) atmospheric chemistry model. ^{14}CO measurements had been exclusively performed using proportional gas counters requiring large amounts of air (≈ 200 m^3) to be processed.

Routine measurements of ^{14}CO in smaller air samples (≤ 1 m^3) with increased precision became possible with the arising technique of the accelerator mass spectrometry (AMS). Air sampling techniques suitable for isotopic analysis and extraction procedures for isolating CO from the air samples are described for instance by *Brenninkmeijer and Roberts* [1994], *Mak and Brenninkmeijer* [1994], and *Brenninkmeijer* [1993]. Aspects of the AMS measurements are discussed in *Rom et al.* [1999b]. *Brenninkmeijer et al.* [1992] observed lower ^{14}CO levels in the southern hemisphere, which were attributed to higher southern hemisphere (SH) OH levels, in contradiction to ideas about higher northern hemisphere (NH) OH values due to the importance of NO in recycling OH [*Crutzen and Zimmermann*, 1991]. *Mak et al.* [1992, 1994] measured ^{14}CO in air sampled in the free troposphere, applied two different 2-D models and concluded that apart from the NH-SH asymmetry, generally atmospheric levels seemed lower than inferred by the models employed. *Quay et al.* [2000] investigated various ^{14}CO measurements with a 2-D model and concluded that either a higher horizontal mixing or a higher OH concentration in the SH is responsible for the observed interhemispheric asymmetry of ^{14}CO. The discrepancies between 2-D model predictions and observations of ^{14}CO, especially the issue of the interhemispheric asymmetry, have remained unresolved up to date, and in fact more problems than solutions have occurred since Weinstock's insight. An overview of the present knowledge is presented in *Brenninkmeijer et al.* [1999]. In the meantime, more and more ^{14}CO measurements at surface level and in the free troposphere have become available [*Röckmann and Brenninkmeijer*, 1997; *Mak and Southon*, 1998; *Röckmann et al.*, 1999; *Rom et al.*, 2000; *Kato et al.*, 2000; *Quay et al.*, 2000; *Tyler et al.*, 1999]. The first ^{14}CO analysis of lower stratospheric air

samples is reported by *Brenninkmeijer et al.* [1995].

1.1.3 Units

"The internationally accepted radiocarbon dating reference value is 95% of the activity, in AD 1950, of the NBS oxalic acid normalized to δ^{13}C = -19$^{o}/_{oo}$ with respect to PDB" [*Stuiver and Polach*, 1977]. $\delta^{13}C$ is the deviation of the ^{13}C/^{12}C ratio from the standard. For geochemical samples, usually the ^{14}C activity is expressed in units of pMC (per-cent modern carbon) [*Stuiver and Polach*, 1977]. This unit is related to the ^{14}C/^{12}C ratio by

$$\frac{^{14}\mathrm{C}}{^{12}\mathrm{C}} = \frac{\mathrm{pMC}}{100} \cdot (\frac{1000(1+\delta^{13}\mathrm{C})}{975})^2 \cdot 1.189 \cdot 10^{-12} \tag{1.6}$$

[*Brenninkmeijer*, 1993; *Rom et al.*, 1999b].

Atmospheric ^{14}CO observations are conveniently reported in molecules per cubic-centimeter of air at standard temperature and pressure (1013.25 hPa, 273.15 K), denoted as molec cm^{-3} STP. The relation to the mass mixing ratio χ in kg ^{14}CO per kg air is

$$\chi = \frac{\mathrm{molec}}{\mathrm{cm^3\ STP}} \cdot \frac{m_m(^{14}\mathrm{CO})}{m_m(\mathrm{air})} \frac{V_{\mathrm{STP}}}{N_a}\ , \tag{1.7}$$

where m_m is the mole weight (air: 28.97 g mol^{-1}, ^{14}CO: 30 g mol^{-1}), $N_a = 6.022{\cdot}10^{23}$ mol^{-1} is the Avogadro-constant, and $V_{\mathrm{STP}} = 22.4 \cdot 10^3$ cm^3 the volume of one mole of air at STP. Inserting the numbers, the conversion constant is $2.59609 \cdot 10^{19}$ molec cm^{-3} STP, i.e., 1 molec cm^{-3} STP corresponds to $3.85195 \cdot 10^{-20}$ kg kg^{-1}, respectively. Furthermore, for ^{14}CO the mass mixing ratio is close to the volume mixing ratio (mole fraction), since the mole weight of ^{14}CO is close to that of dry air. As a consequence, 1 molec cm^{-3} STP corresponds to $3.71969 \cdot 10^{-20}$ mol mol^{-1}.

The vertical coordinate of the cosmogenic ^{14}CO source distribution is mostly reported as atmospheric depth in g cm^{-2} (mass area density) increasing from the "top of the atmosphere" to the surface level. The atmospheric depth d is related to atmospheric pressure p by

$$p = d \cdot \frac{g}{10}\ , \tag{1.8}$$

where p is in hPa, and $g = 9.81$ m s^{-2} is the gravity acceleration at the surface.

1.1.4 Source estimates of ^{14}CO

The average cosmogenic production rate of ^{14}CO is roughly 1.6 - 2 molecules per second and per square-centimeter of the Earth's surface (for references see chapters 5

and 8), corresponding to a total production of approximately 13 kg - 16 kg ^{14}CO per year.

The global emission of CO from biomass burning is estimated to be $750 \cdot 10^{12}$ g CO per year [*Galanter et al.*, 2000]. The average specific ^{14}C activity of biomass corresponds to 120 pMC, i.e., the $^{14}C/^{12}C$ ratio (Eq. (1.6)) is $1.43 \cdot 10^{-12}$ (for $\delta^{13}C = -25^{o}/_{oo}$). The resulting annual global average source strength of ^{14}CO from biomass burning is therefore 1.15 kg ^{14}CO per year ($m_m(CO) = 28$ g mol^{-1}, $m_m(^{14}CO) = 30$ g mol^{-1}), which is about 7% - 9% of the primary cosmogenic ^{14}CO source contribution.

The approximate global average source of ^{14}CO from methane (CH_4) oxidation can be estimated in the same way. Assuming a turnover of about $600 \cdot 10^{12}$ g methane per year by OH oxidation [*Crutzen*, 1995b; *Lelieveld and v. Dorland*, 1995], the resulting ^{14}CO production is approximately 1.6 kg per year (120 pMC, $\delta^{13}C = -25^{o}/_{oo}$, $m_m(CH_4) = 16$ g mol^{-1}), i.e. roughly 10% - 12% of the annual cosmogenic production. Approximately a similar amount of ^{14}CO originates from NMHC oxidation. Estimates of global CO from NMHC oxidation, however, exhibit a considerable uncertainty [e.g., *Kanakidou and Crutzen*, 1999].

Compared to this the ^{14}CO release from the ocean is small. *Bates et al.* [1995] provide a maximum estimate of the CO flux from the oceans of 10^{12} g CO per year. With a natural ^{14}C activity of 120 pMC, ($\delta^{13}C = -25^{o}/_{oo}$, Eq. (1.6)), the resulting flux of ^{14}CO is 1.53 g ^{14}CO per year, i.e., less than 0.2% of the primary cosmogenic production of ^{14}CO.

A possible additional "anthropogenic" source of ^{14}CO, e.g., the emission of ^{14}CO by nuclear power plants, is at this stage purely speculative. If this contribution were significant, occasionally high mixing ratios of ^{14}CO would have been detected at locations downwind of these potential point-like sources, e.g., at central European sampling sites. This has, however, up to now not been observed.

In summary, from the numbers above the primary cosmogenic production of ^{14}CO can be estimated to amount for 75% to 80% of the total ^{14}CO production. The minor contribution of 20% to 25% is secondary ("biogenic") ^{14}CO from methane and NMHC oxidation and biomass burning.

1.2 Scope of this thesis

1.2.1 Objective and route

The objective of the present thesis is to develop a framework for the application of the "^{14}CO methodology" as a standard test for 3-dimensional (3-D) global atmospheric transport and chemistry models. It is the first time a global 3-D atmospheric model is

applied systematically to investigate and improve the understanding of the processes determining the atmospheric ^{14}CO mixing ratio. Although all studies are performed with a chemical tracer model (CTM, i.e, an "offline model" driven by prescribed meteorological data), the methods to be described are also applicable to general circulation models (GCM) without changes.

In order to estimate the uncertainty arising from imperfections in the model realization different model configurations are used. These and the overall model setup are described below in section 1.3. Moreover, three different estimates of tropospheric OH distributions and seasonalities are tested in order to assess the influence of tropospheric OH on the simulated ^{14}CO mixing ratio. These are introduced in section 1.4.

Before the application of the ^{14}CO methodology is systematically developed, in chapter 2 a fundamental and to date unresolved problem related to recently developed mass flux form advection schemes for 3-D global models is unraveled and discussed. This is necessary, since in one of the model configurations employed in this study such an advection algorithm is implemented. The resulting limitations are further used to track uncertainties arising from inaccuracies of the model realization.

The next step comprising two chapters is the evaluation of the model setup with already established methods. In chapter 3 the simulated atmospheric transport is tested by simulations of the tracer SF_6. For this purpose a test-setup (taken from a published model inter-comparison study) is reproduced with the chosen model configurations. The model configurations are classified in comparison to other "state-of-the-art" 3-D models, and, even more important, in comparison to observations of SF_6. Furthermore, the oxidation capacity of the model atmosphere, i.e., the prescribed OH distribution, is tested in chapter 4 by simulations of methylchloroform (MCF) and trichlorofluoromethane (F11). On the global scale, the average OH abundance is tested. On a smaller scale, in contrast, the method is limited. These limitations are discussed.

For a reasonable application of the ^{14}CO methodology, the source distribution of cosmogenic ^{14}CO has to be known sufficiently well. However, uncertainties about this distribution, especially about the ^{14}CO production distribution in the vertical direction are not yet fully clarified. Moreover, the source distribution also varies with solar activity with a nominal period of 11 years. These issues are investigated and discussed in chapter 5. A minor influence on the atmospheric ^{14}CO mixing ratio is exerted by soils which represent an additional sink. The resulting effects are estimated in chapter 6. Not only the source distribution of cosmogenic ^{14}CO varies with solar activity, but also the global source strength, i.e., the global average production rate of ^{14}CO. In chapter 7 the response of the atmospheric ^{14}CO mixing ratio to this

variation is assessed. The applied concept indicates far reaching consequences of the methodological aspect and is generally applicable to other meteorological or climatological parameters depending on a global scaling. In chapter 8 the time-varying global source strength of ^{14}CO itself is discussed. Together with the previous results a basis is provided for the comparison of ^{14}CO measurements of different periods with respect to the solar activity. This is used in later chapters.

The influence of occasionally occurring solar proton events on the atmospheric ^{14}CO mixing ratio is investigated in chapter 9, and further it is shown how this effect can potentially be used to extend the present knowledge about the stratosphere - troposphere exchange. From observations of ^{14}CO several indications are derived that the model predicted geophysical effect of this solar phenomenon is indeed observable.

Chapter 10 provides an example of how the ^{14}CO methodology can be applied to 3-D models. By means of a model inter-comparison study several aspects of the simulated stratosphere - troposphere exchange of ^{14}CO are discussed. This is finally rounded up in chapter 11. All available ^{14}CO observations are collected; the contribution of the secondary source (biogenic ^{14}CO) is estimated and subtracted. Based on the observations, and by means of the previous results with respect to the solar cycle dependence, a climatological zonally averaged seasonal cycle of cosmogenic ^{14}CO at surface level is constructed. This is quantitatively compared to model simulations. Furthermore, ^{14}CO observations collected during aircraft campaigns in the free troposphere and the lower stratosphere are compared to the model simulations. Implications for the assessment of the OH distribution and stratosphere - troposphere exchange are discussed. Especially the issue of the observed interhemispheric asymmetry of ^{14}CO is revisited.

Throughout this thesis, ^{14}CO of primary cosmogenic origin is regarded as an independent tracer. The smaller secondary "biogenic" contribution is, however, taken into account, when model results are compared with observations. Atmospheric ^{14}CO values, either model results or observations, are exclusively reported in units of molec cm^{-3} STP. The unit "months" for time intervals is defined as 1/12 of one year of exactly 365 days, i.e., 1 month corresponds to 2628000 seconds.

1.2.2 A note on the style

Each chapter is written to form its own entity introduced by a separate abstract which, however, does not contain a summary of all conclusions. The chapters describing particular modeling studies are all structured similarly. After introductory remarks about the motivation and the purpose of each particular study, the model setup is presented. This includes at some stages technical descriptions necessary to keep all steps comprehensible and reproducible. For compactness, and since those

details are not too numerous, special appendices are omitted on purpose. Ideally, it should be possible to reproduce all studies of this thesis with similar 3-D atmospheric models without further information.

For the sake of clarity, unalterable model results (section "Model results") are as strictly as possible segregated from their interpretation and discussion (section "Discussion"). This implies that the presentation of the model results tends to be purely descriptive without explanations, however in the discussion the results are resumed and sometimes restructured in a more coherent context. The resulting possibly longer text is taken in favor of the purity. Results from other chapters are briefly repeated (mostly with cross-references to figures), where they are needed for the discussion, but not discussed again.

Finally, the figure and table captions include ideally as much information as needed for understanding the presented results without re-reading the whole text (e.g., following a cross-reference back to a previous chapter). This further aims again at making results reproducible. On the other hand, as much information as needed to understand the figures and tables without necessarily reading the captions is contained in the text in order to allow a fluent reading. As a consequence, necessarily some descriptions occur twice, once in the caption and once in the text.

In summary, this thesis strives to meet the demands of scientific reproducibility and clarity, which together form an important prerequisite for the acceptance of scientific results. This characteristic is unfortunately not self-evident in the field of atmospheric chemistry modeling; especially many publications about 3-D modeling studies, due to the limited space, lack sufficient important information needed to give a complete picture. As a consequence, some years after publication, the results may be believed or not; they are, however, in most cases not reproducible anymore. The second important demand of scientific results is a discussion of the uncertainty range (i.e., the "error-bars") of the results. This is, due to the difficulties and lacking definitions of "uncertainty", generally omitted in most publications of 3-D modeling studies. Official criticism of the way these problems are addressed (or ignored) by the majority of the atmospheric modeling community has already found its way into the literature [*Heymann*, 1998].

In this thesis a discussion of uncertainties inherent to the modeling approach is included wherever possible. At least the lower limit of uncertainty ranges are estimated. Mostly, this is achieved by the comparison of results obtained with differing model configurations under the same boundary conditions.

1.3 Model description

One of the two 3-D models used for the studies in this thesis is the meteorological component of the "Model of atmospheric chemistry and transport" (MATCH, *Rasch et al.* [1997]) in the Max-Planck-Institute for Chemistry (MPICH) versions 1.2 [*Lawrence*, 1996] and 2.0 [*Lawrence et al.*, 1999a]. MATCH is an "offline" model; the basic meteorological parameters such as temperature, pressure, meridional and zonal wind speeds, surface wind stresses, latent and sensible heat fluxes, and optionally water vapor are read from data archives at regular time intervals during the simulation. All other meteorological parameters, such as vertical velocities, and convective mass fluxes, are either computed online based on these basic meteorological fields ("diagnosed mode"), or the respective values are read in from archived previous calculations ("archived mode"). Throughout this thesis the model is used in archived mode, whereby the basic meteorological data are 6-hour averages from the NCEP/NCAR (National Centers for Environmental Prediction / National Center for Atmospheric Research) 40-year reanalysis project [*Kalnay et al.*, 1996], further denoted as NCEP reanalysis data. The horizontal resolution employed consists of 32 latitude times 64 longitude intervals, the vertical grid structure comprises 28 terrain-following sigma coordinates ($\sigma = p/p_s$, where p_s is surface pressure) from surface level up to 0.0027 times the surface pressure (upper layer mid-level pressure). The chosen model time step is 30 minutes. For this the meteorological data is linearly interpolated from the 6 hour averages to the 30 minute time intervals. Three basic components of tracer transport are simulated by MATCH: advection, dry turbulent mixing (vertical diffusion), and moist convection. Different realizations of the particular components are used in three model configurations:

- 1.2-SLT: In this configuration the shape-preserving semi-Lagrangian (SLT) transport scheme [*Rasch and Williamson*, 1990; *Williamson and Rasch*, 1989] is used to calculate the advective component. The moist convection parameterization is implemented according to *Pan and Wu* [1995].

- 2.0-SLT: This configuration also includes the SLT advection scheme, however moist convection is calculated in a combination of the two individual schemes proposed by *Zhang and McFarlane* [1995] and *Hack* [1994].

- 2.0-SPF: This configuration uses the same convection parameterization as 2.0-SLT, however the SLT advection scheme is replaced by the SPITFIRE (Split implementation of transport using flux integral representation) advection scheme [*Rasch and Lawrence*, 1998], which is a mass flux form advection scheme.

Common to all model configurations is the parameterization of the vertical diffusion (dry turbulent mixing) according to *Holtslag and Boville* [1993]. The two SLT configurations further include the "mass-fixer" of *Rasch et al.* [1995] used to force global tracer mass conservation. The SPITFIRE advection scheme in 2.0-SPF is itself inherently mass conserving; however, in its implementation in MATCH it is not. This is discussed further in chapter 2.

The second 3-D model used additionally for some of the studies in comparison to the MATCH model is the Royal Netherlands Meteorological Institute (KNMI) Version of the global atmospheric tracer model TM3 [*Dentener et al.*, 1999; *Jeuken*, 2000], which is a further development of TM2 [*Heimann*, 1995]. TM3 is also an offline model; the meteorological parameters (wind, surface pressure, temperature, and humidity) are taken from the European Center for Medium-range Weather Forecasts (ECMWF) (re)analysis data. Those fields are updated every 6 hours [*van Velthoven and Kelder*, 1996] and interpolated to the TM3 model grid. The advection of the tracers in the model is calculated with the "slopes-scheme" of *Russell and Lerner* [1981]. Convective fluxes are calculated using the scheme of *Tiedtke* [1989]. And finally, vertical diffusion is parameterized according to *Louis* [1979] for stable conditions and according to *Holtslag and Boville* [1993] for unstable conditions [*Jeuken*, 2000]. The TM3 model is used with three different grid resolutions:

- TM3-L-L19: 48 latitude intervals, 72 longitude intervals, 19 vertical levels on hybrid coordinates from surface level up to 10 hPa, 80 minutes time step
- TM3-H-L19: 72 latitude intervals, 144 longitude intervals, 19 vertical levels on hybrid coordinates from surface level up to 10 hPa, 40 minutes time step
- TM3-L-L31: 48 latitude intervals, 72 longitude intervals, 31 vertical levels on hybrid coordinates from surface level up to 10 hPa, 60 minutes time step

All TM3 simulations presented in this thesis have been performed at KNMI (Ad Jeuken, Peter F.J. van Velthoven , personal communication 1998-2000).

1.4 OH distribution and seasonality

In the model simulations, the known chemical processes of the atmosphere are not calculated online, the OH distribution is rather prescribed offline from previously performed model calculations including complex chemistry parameterizations. This approach is possible due to the short lifetime ($\approx$ 1s) of OH. As a consequence, the OH concentration is a "local" quantity and OH does not have to be transported as a tracer in the model, in contrast to its precursors. This further implies that

OH distributions and seasonalities predicted by other models can be independently tested as well.

The source of cosmogenic ^{14}CO is quasi constant throughout the year with respect to its distribution and global strength. Furthermore, the OH concentration is not affected by ^{14}CO in contrast to CO which has a 12 orders of magnitude larger abundance. The atmospheric lifetime of ^{14}CO before oxidation by OH is approximately 2 - 3 months. Therefore, the OH seasonality can be probed by means of ^{14}CO down to a time scale of approximately one month. As a consequence, monthly average OH distributions are prescribed for the oxidation of ^{14}CO in the model atmosphere.

Since global tropospheric OH distributions generated by atmospheric models are to be evaluated, and yet roughly 50% of the ^{14}CO is produced in the stratosphere, the stratospheric OH distribution also has to be taken into account. Most modeling approaches focus either on tropospheric or on stratospheric chemistry. Therefore independent estimates of stratospheric and tropospheric OH distributions are combined in order to derive a best estimate for the entire model atmosphere domain.

In order to estimate the influence of the tropospheric OH distribution on the atmospheric ^{14}CO mixing ratio, three different model predicted tropospheric OH distributions are used for the model simulations. The tropospheric OH distributions calculated by *Lawrence* [1996] and *Lawrence et al.* [1999a] are in the following denoted as OH-1 and OH-2. For comparison, the tropospheric OH climatology of *Spivakovsky et al.* [2000], further denoted as OH-S, is used in addition. The latter has been tested with various reactive tracers [*Spivakovsky et al.*, 2000]. Since OH-1 and OH-2 have been calculated with the MATCH model which is also used for most studies presented in this thesis, no grid transformation is needed. The OH-S distribution however, is provided on 9 pressure levels between 100 hPa and 1000 hPa, 24 latitude, and 36 longitude intervals. From this grid the OH distribution is redistributed offline onto the MATCH model grid in the horizontal direction, and onto 10 equidistant pressure levels (100 hPa to 1000 hPa), keeping the global average. Finally, linear interpolation in vertical direction onto the varying pressure levels of the MATCH model sigma grid is performed online. The transformation of OH-1 onto the TM3 model grid is described in more detail in chapter 10.

The monthly zonal average distributions of the three tropospheric OH distribution estimates as they appear in the MATCH model atmosphere are shown in Figures 1.2 (OH-1), 1.3 (OH-2), and 1.4 (OH-S) respectively.

The stratospheric OH distribution is taken from 2-dimensional (2-D) stratospheric chemistry model simulations (Ch. Brühl, unpublished data, personal communication 1998-2000). This distribution is further denoted as OH-2D. For the use in the 3-D model, zonal symmetry is assumed. The original 2-D model output is provided on

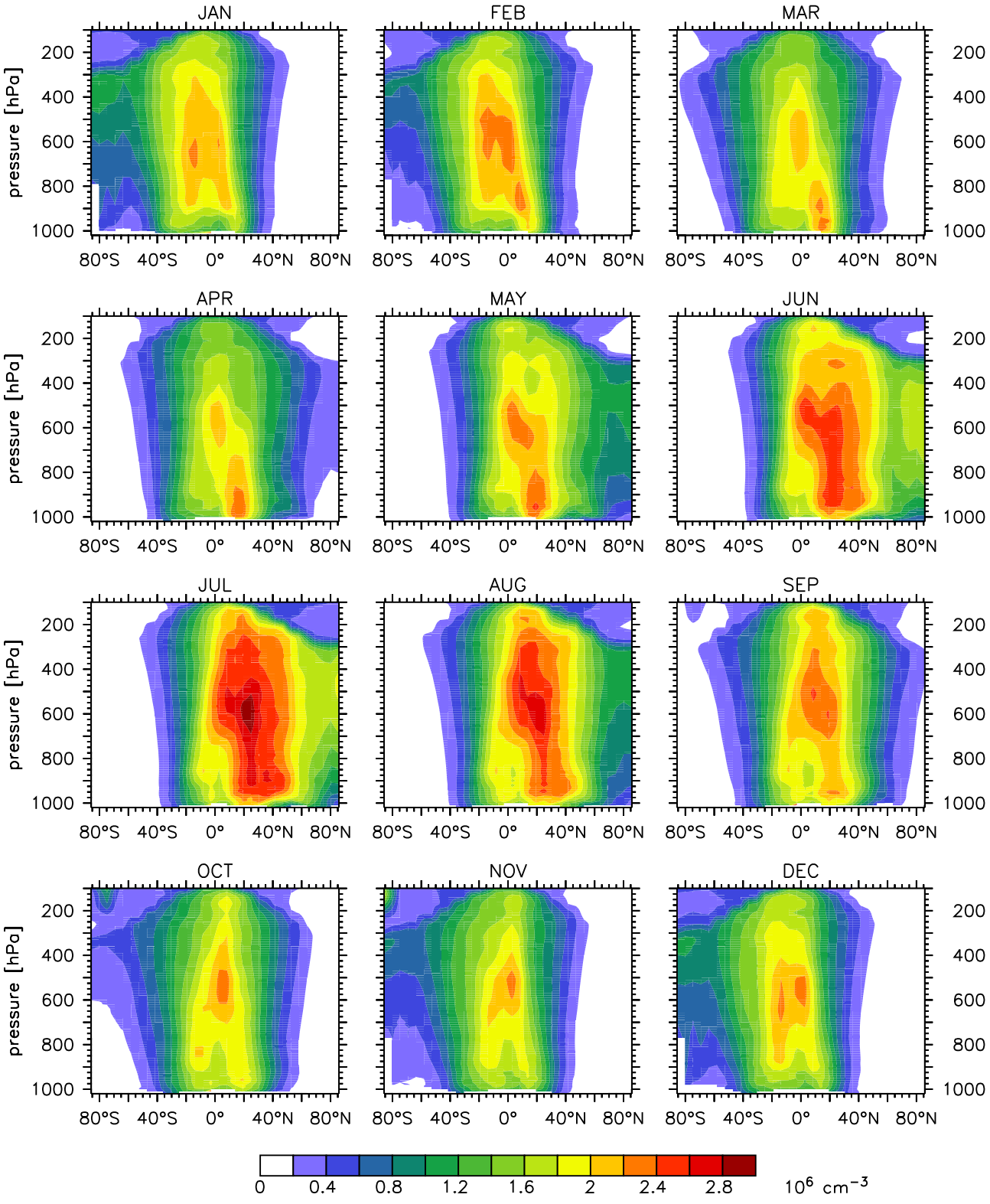

Figure 1.2: Monthly zonal mean OH concentration (OH-1).

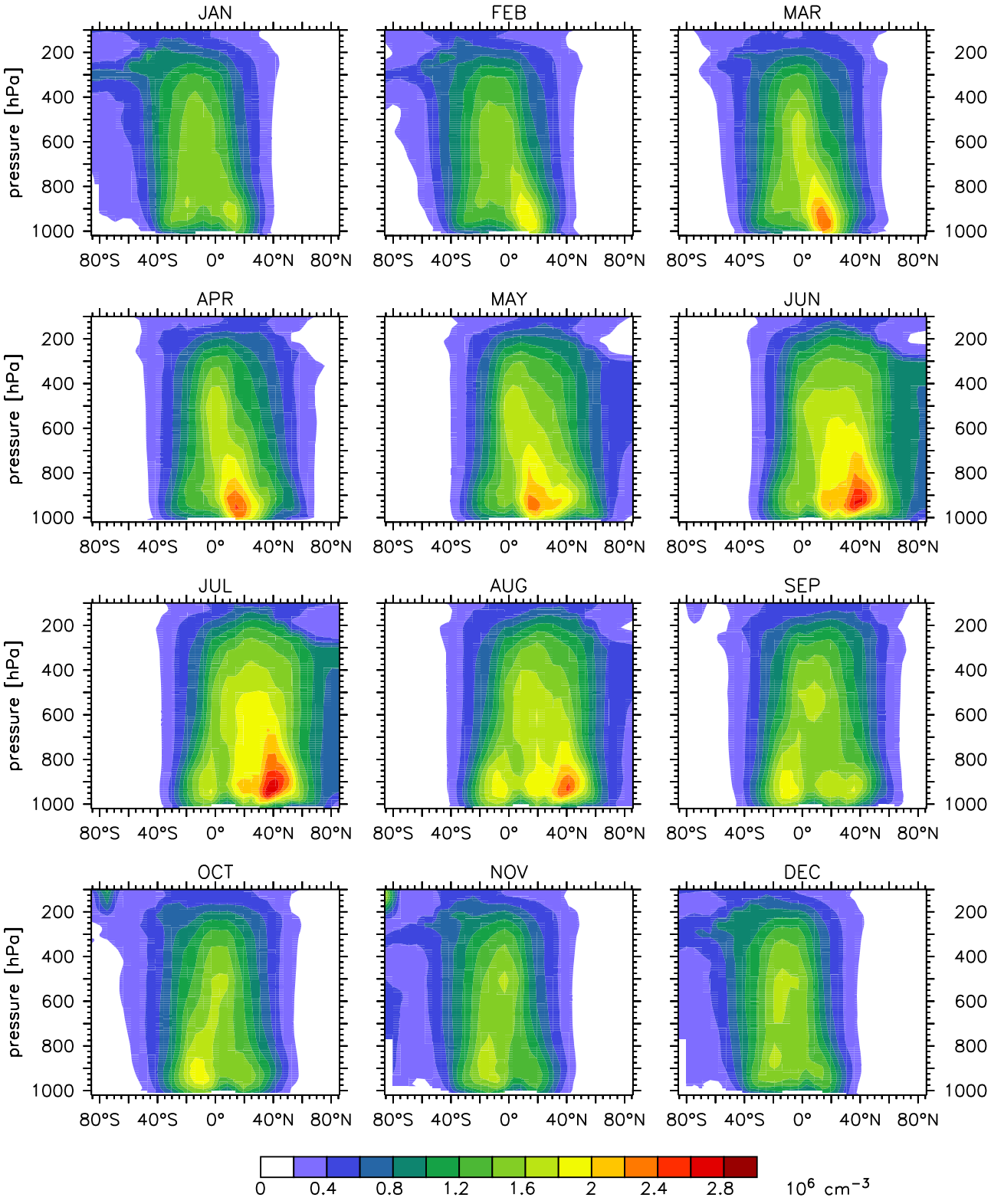

Figure 1.3: Monthly zonal mean OH concentration (OH-2).

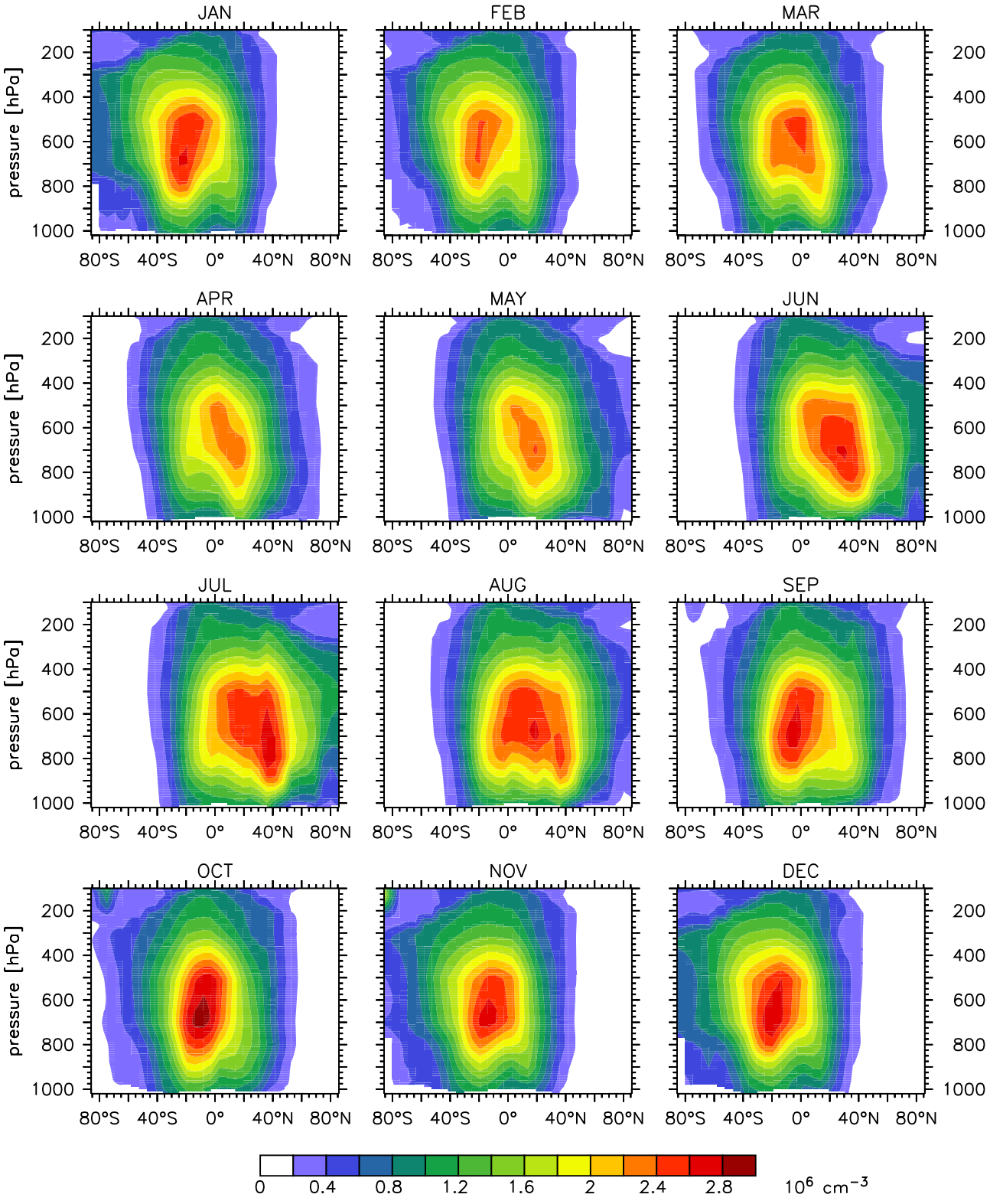

Figure 1.4: Monthly zonal mean OH concentration (OH-S).

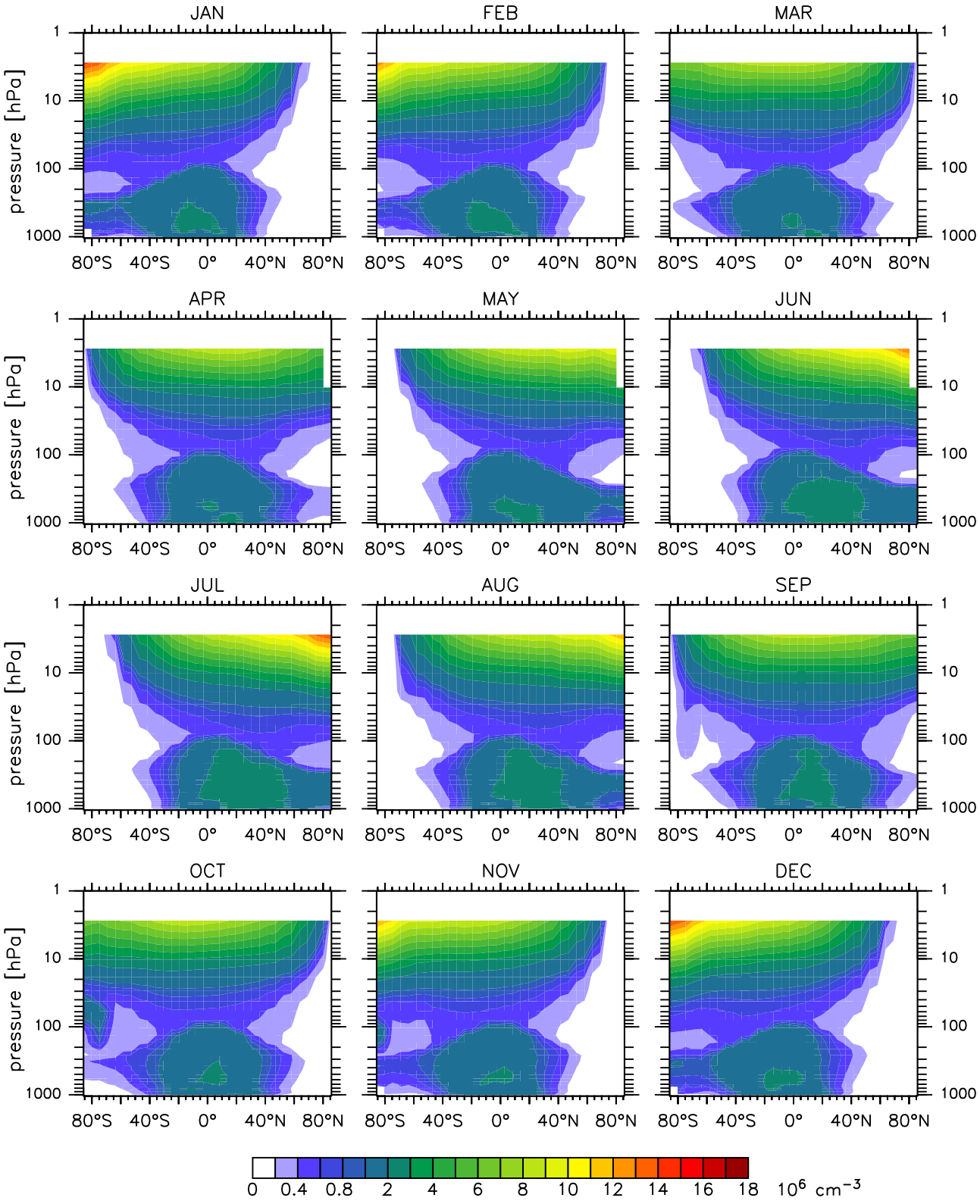

Figure 1.5: Monthly zonal mean stratospheric OH-2D distribution combined with the tropospheric OH-1 distribution.

34 pressure levels and a 10^o interval latitude grid. Keeping the pressure levels, the OH distribution is redistributed offline onto the 3-D model grid in the latitudinal direction (MATCH or TM3). Finally, linear interpolation onto the actual pressure levels of the 3-D model vertical sigma (MATCH) or hybrid (TM3) grid is performed online. The resulting zonal monthly average OH distribution in the 3-D model atmosphere of MATCH is depicted in Figure 1.5, in combination with the OH-1 distribution in the troposphere. The definition of the tropopause as the interface between stratospheric and tropospheric OH is discussed in section 1.5 below. The 2-D model used by Ch. Brühl predicts enhanced OH concentrations at high southern latitudes, due to increased ClOH in the ozone hole region. This effect might be overestimated in the model; however, it is not of relevance for the present study (chapter 7, chapter 11).

For convention, the different global OH distributions are further denoted as OH-1, OH-2, and OH-S, whereby the respective tropospheric distributions are combined with the OH-2D distribution in the stratosphere, unless indicated otherwise. Knowing the differences between the particular OH distributions, the effect on atmospheric ^{14}CO can be discussed. Figure 1.6 therefore summarizes the average OH abundance and seasonality of the different OH distributions. The air mass weighted average OH concentration is defined as

$$[\bar{OH}] = \frac{\sum_{i=1}^{N}(m_i \cdot [OH]_i)}{\sum_{i=1}^{N} m_i} \ , \tag{1.9}$$

where the summation is over the model grid boxes (index i) of the particular atmospheric domain, $[OH]$ denotes the OH concentration, and m_i the air mass in grid box i. Finally, Table 1.1 lists the air mass weighted average OH concentration used for quantitative comparisons.

1.5 Tropopause definitions

1.5.1 The thermal tropopause

As indicated above, the stratosphere - troposphere exchange is an important atmospheric process determining the tropospheric ^{14}CO mixing ratio. As a consequence, an analysis of the tropopause is required in the model simulations. Daily averages of the tropopause pressure of the year 1993 are provided by NCEP. These data can be used offline in the model. Since the NCEP reanalysis data used for driving the advection in MATCH do not include the analyzed tropopause pressure, it must be diagnosed online, i.e. during the model simulation, at least for years other than 1993. The World Meteorological Organization (WMO) provides a definition of the

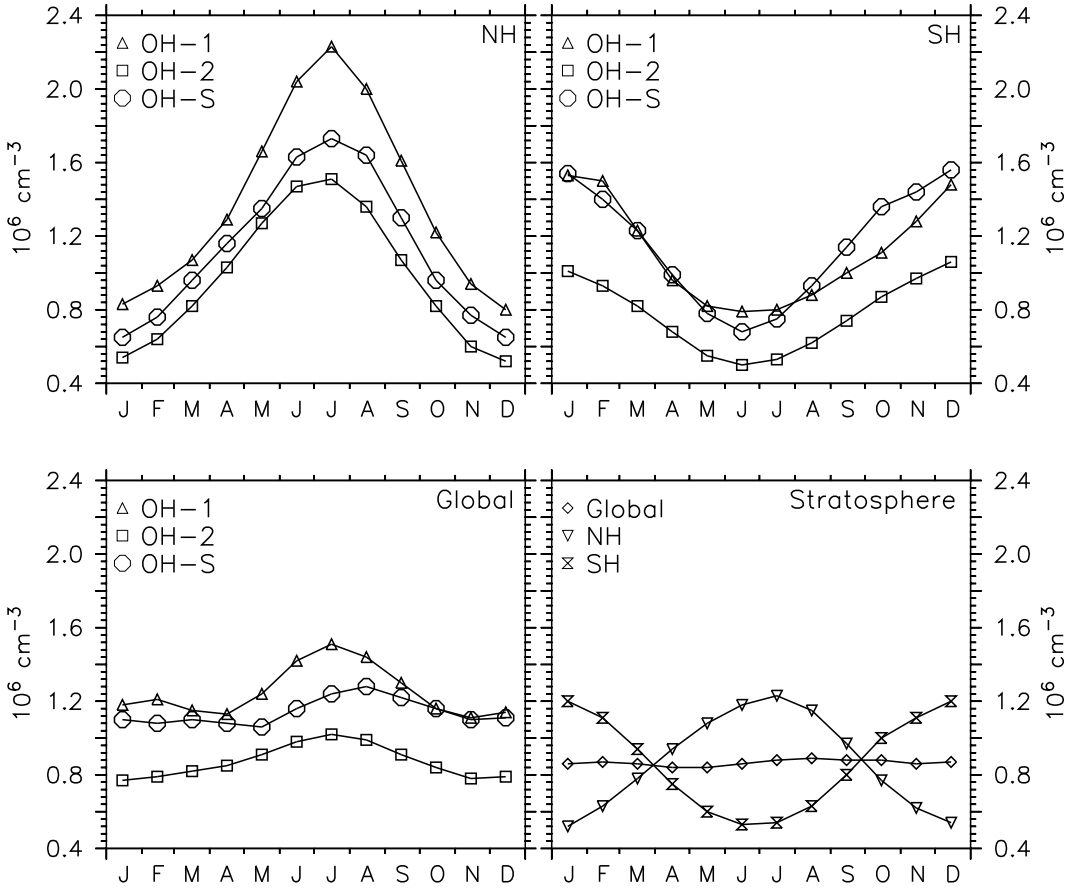

Figure 1.6: Air mass weighted monthly mean OH concentration for the northern hemisphere troposphere (NH), the southern hemisphere troposphere (SH), the entire globe (Global), and the stratosphere. The tropospheric averages are shown for the OH distributions from *Lawrence* [1996]; *Lawrence et al.* [1999a] (OH-1, OH-2) and for the OH distribution from *Spivakovsky et al.* [2000] (OH-S). The stratospheric averages (OH-2D) are shown for the 2-dimensional model results of Ch. Brühl (unpublished data, personal communication 1998-2000). The tropopause-interface between stratospheric and tropospheric OH is defined as the climatological mean (section 1.5), i.e., $(300 - 215 \cdot cos^2(\phi))$ hPa, where ϕ is latitude.

tropopause [*WMO*, 1992]: *"The first tropopause is defined as the lowest level at which the lapse rate decreases to 2°C per kilometer or less, provided also the average lapse rate between this level and all higher levels within 2 kilometers does not exceed 2°C per kilometer."* On the basis of this definition *Dameris et al.* [1995] and *Reichler* [1995] developed a tropopause diagnostic algorithm. This is adapted for use in the MATCH model configurations.

The implementation can be tested by comparison of the model diagnosed tropopause pressure simulated with the NCEP reanalysis data of the year 1993 with the respective tropopause pressure directly provided by NCEP. The result is shown in Fig-

	OH-1			OH-2			OH-S			OH-2D		
month	NH	SH	G	NH	SH	G	NH	SH	G	NH	SH	G
JAN	0.83	1.53	1.18	0.54	1.01	0.77	0.65	1.54	1.10	0.52	1.20	0.86
FEB	0.93	1.50	1.21	0.64	0.93	0.79	0.76	1.40	1.08	0.63	1.11	0.87
MAR	1.07	1.23	1.15	0.82	0.82	0.82	0.96	1.23	1.10	0.78	0.94	0.86
APR	1.29	0.96	1.13	1.03	0.68	0.85	1.16	0.99	1.08	0.94	0.75	0.84
MAY	1.66	0.82	1.24	1.27	0.55	0.91	1.35	0.78	1.06	1.08	0.60	0.84
JUN	2.04	0.79	1.42	1.47	0.50	0.98	1.63	0.68	1.16	1.18	0.53	0.86
JUL	2.23	0.80	1.51	1.51	0.53	1.02	1.73	0.75	1.24	1.23	0.54	0.88
AUG	2.00	0.88	1.44	1.36	0.62	0.99	1.64	0.93	1.28	1.15	0.63	0.89
SEP	1.61	1.00	1.30	1.07	0.74	0.91	1.30	1.14	1.22	0.97	0.80	0.88
OCT	1.22	1.11	1.16	0.82	0.87	0.84	0.96	1.36	1.16	0.77	1.00	0.88
NOV	0.94	1.28	1.11	0.60	0.97	0.78	0.77	1.44	1.10	0.62	1.11	0.86
DEC	0.80	1.48	1.14	0.52	1.06	0.79	0.65	1.56	1.11	0.54	1.20	0.87
	1.39	1.11	1.25	0.98	0.77	0.87	1.14	1.15	1.14	0.87	0.86	0.87

Table 1.1: Air mass weighted monthly average OH concentration (10^6 cm^{-3}). The last line lists the annual average. Tropospheric averages are shown for the OH distributions from *Lawrence* [1996] and *Lawrence et al.* [1999a] (OH-1, OH-2) and for the OH distribution from *Spivakovsky et al.* [2000] (OH-S). Stratospheric averages are shown for the 2-dimensional model results of Ch. Brühl (OH-2D, unpublished data, personal communication 1998-2000). The tropopause pressure is defined as climatological mean (section 1.5), i.e., $(300 - 215 \cdot cos^2(\phi))$ hPa, where ϕ is latitude.

ure 1.7. In the left panel the reanalyzed tropopause pressure $p_{\rm tp}^{\rm NCEP}$ is plotted versus the online diagnosed tropopause pressure $p_{\rm tp}^{\rm diag}$ at the same time and the same grid point. The correlation analysis shown in the right panel is performed with 5-day average values and results in a slope close to one and a squared correlation coefficient R^2 larger than 0.99 throughout the year. Conclusively, the implemented algorithm is consistent with the NCEP reanalysis data.

1.5.2 The climatological chemical tropopause

As introduced above, stratospheric and tropospheric OH distributions and seasonalities are taken into account separately and from different sources. The assembly of stratospheric and tropospheric OH in the model atmosphere also requires a definition of the tropopause separating the stratosphere from the troposphere. For the modeling approach, also the thermal tropopause could in principle be used, however this implies some disadvantages. Since the investigated OH distributions in this study are used in a climatological approach, i.e., without inter-annual variations, the tropopause suited for separating stratospheric OH from tropospheric OH should also

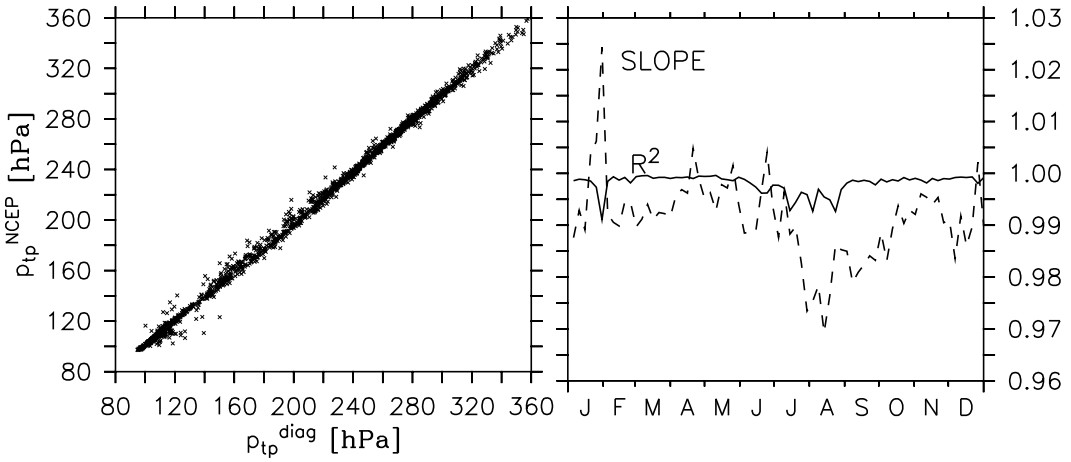

Figure 1.7: Comparison of reanalyzed and online diagnosed tropopause pressure. $p_{\mathrm{tp}}^{\mathrm{NCEP}}$ is the reanalyzed tropopause pressure from the NCEP reanalysis data [*Kalnay et al.*, 1996], $p_{\mathrm{tp}}^{\mathrm{diag}}$ is the model calculated tropopause pressure derived online in accordance with the WMO-definition [*WMO*, 1992]. In the left figure 5-day averages are plotted, the right figure shows the square of Pearson's correlation coefficient (R^2) of the linear regression analysis.

not exhibit inter-annual variations. Furthermore, it is advantageous for an easier interpretation if this tropopause also does not vary on smaller time scales. Moreover, the focus is on evaluating tropospheric OH, and therefore the tropopause for this purpose should be consistent with the chemistry model the tropospheric OH distribution was obtained with. Finally, when different tropospheric OH distributions calculated by different atmospheric models with alternative chemistry implementations are to be compared by means of the effect on ^{14}CO, the stratospheric OH distribution should be identical in all cases, in order to enable an interpretation independent of the stratospheric OH.

Therefore a different approach is taken as an optimal compromise addressing these requirements with respect to the OH distribution in the model atmosphere. From the tropospheric chemistry simulations of *Lawrence* [1996], also performed with the MATCH model, the monthly average chemical tropopause defined by an ozone mixing ratio of 150 nmol mol^{-1} is approximated by an annual average tropopause. The resulting annual zonal average tropopause pressure (in hPa) is

$$p_{\mathrm{tp}}^{\mathrm{clim}} = 300 - 215 \cdot cos^2(\phi) \ , \tag{1.10}$$

where ϕ is the latitude. This tropopause is further denoted as "climatological tropopause", and used as the interface between the tropospheric and the stratospheric OH distribution. It is further used in some studies as standard "control surface" (tropopause), which is easy to handle and to interpret from the modeling point of view.

1.6 Some technical remarks

The program code of the MATCH configurations employed and the newly developed extensions are written in Fortran 77. The MATCH model simulations presented in this study were performed at the German Climate Computing Centre (Deutsches Klimarechenzentrum, Hamburg) on a CRAY C916/16-256 (64-bit, IP-Name: sea). In October 1999 the operating system was updated from UNICOS Release 9 to Release 10.0.0.5, with the implication that the Fortran 77 V6.0.4.28 compiler was no longer available. For the calculations performed later the Fortran 90 compiler V3.2.0.1 was used. Consistency has been checked by repeating a previously performed simulation in the new system environment. No deviations in the results were detected.

The MATCH calculations with reduced horizontal grid resolution presented in chapter 2 were performed at the Max-Planck-Institute for Chemistry (MPICH) in Mainz (Germany) on a DEC-Alpha (32-bit), using the Digital Fortran 90 compiler V5.2 under the operating system OSF1 V4.0. These simulations were performed in double precision. Previous tests showed that calculations in single precision suffer severely from the rapid growth of numerical round-off errors [*Lawrence et al.*, 1999b].

The program code of TM3 is implemented in Fortran 90. The TM3 simulations have been performed at KNMI on a CRAY-C90 (Ad Jeuken, personal communication, 1989-2000).

All Figures, except for Figures 1.1, 2.1, and 2.2 have been created with the freely available software tool "Ferret" (Version 5.0b1.1), which has been developed at the National Oceanic and Atmospheric Administration - Pacific Marine Environmental Laboratory (NOAA-PMEL, U.S.A.). The model data has been archived in "Network Common Data Form" (NetCDF), an architecture-independent data format especially developed for 4-dimensional geophysical data-sets (Unidata Program Center, Boulder, Colorado).

Finally, sampling of model simulations at a given location (latitude, longitude) is performed via bi-linear interpolation of the model results at the surrounding grid points, in order to account for the horizontal gradients.

2 On a fundamental problem in implementing flux-form advection schemes for tracer transport in 3-dimensional general circulation and chemical transport models

Abstract. The use of sigma or hybrid coordinates in Eulerian tracer transport models allows representation of surface features such as orography and changes in surface pressure due to weather systems. However, because the pressure levels of such vertical grids are not fixed, but rather change with time, difficulties are often encountered with their use. One particular aspect of these difficulties which commonly results from inconsistencies between the advection scheme and model winds is addressed. The focus is on mass flux-form advection schemes which readily allow a mathematical formulation and quantification of the problem; however, in principle the discussion applies to nearly any situation in which the pressure levels change in a model. Flux-form schemes advect air mass densities; this results in a change in the air mass density in each cell, which in turn implies a change in the pressure levels at the interfaces between each layer. The interface pressure levels on this "implied" grid following the advection step are not necessarily the same as the interface pressure levels on the "standard" grid (i.e., based on the sigma or hybrid coordinates and the current surface pressure); this applies although the surface pressure of a given column is the same for the implied and standard grid. Tracers must then be transferred in some fashion from this implied grid back to the standard grid. If the simplest transfer is applied, that is, the tracer mixing ratios in each cell are kept the same (i.e., an index-to-index transfer), then the global tracer mass will generally not be conserved. If instead the absolute masses of each tracer are transferred from each cell of the implied grid to the standard grid, which yields new mixing ratios in each cell, then a homogeneous tracer will not remain homogeneous. Neither of these results are acceptable for applications such as photochemical modeling. A mass conserving grid to grid transformation scheme is constructed which only uses the current tracer mass mixing ratio distribution. It is shown that only one solution exists that is comprehensively valid for any arbitrary tracer distribution. Using a CTM with a set of idealized tracers it is shown that this type of correction introduces an additional undesired artificial vertical diffusion component into the model transport, which increases with increasing tracer mass mixing ratio gradients and may exceed the physical vertical transport itself. It is found that the results of any supplementary fix, either mass fixer or grid-to-grid transformation, are generally unacceptable for global modeling applications. Finally, it is concluded that the only alternative which can produce reliable results for any arbitrary tracer is to maintain a consistent grid throughout the entire model time step, where all changes in pressure levels exactly match the changes implied by the surface pressure at the next time step. This would require significant changes in the structure of several general circulation and chemistry-transport models, in particular in the advection scheme employed or its input wind fields.

2.1 Introduction

Progress in atmospheric sciences depends increasingly on sophisticated 3-dimensional (3-D) atmospheric models [*IPCC*, 1994]. One of the most important processes simulated in these models is large scale (advective) atmospheric transport, the change with time of the spatial tracer distribution as a function of wind velocities. Numerical treatment of advection can present a special challenge in computational physics due to the large number of gases and aerosols (with widely varying spatial gradients and time scales) to be transported. Several different approaches have been developed for computing advective transport [e.g., *Russell and Lerner*, 1981; *Prather*, 1986; *Bott*, 1989; *Rasch and Williamson*, 1990; *Bott*, 1992; *Machenhauer et al.*, 1998; *Hourdin and Armengaud*, 1999]. For an extensive overview see *Rood* [1987].

One can consider at least three fundamental physical properties of atmospheric flow which one would expect from a reliable advection scheme [*Rasch and Williamson*, 1990]:

1. Global tracer mass conservation. An inert tracer is transported without change in its total mass. The global mass of reactive tracers changes only by explicitely described sources, sinks and chemical transformations.

2. Monotonicity (for which the second law of thermodynamics, i.e. entropy, is the underlying physical principle). Spatial gradients are not artificially increased; the atmosphere tends to a more mixed state. Thus, a homogeneously distributed inert tracer remains homogeneous. This is especially important because many non-transport processes in the models (such as chemistry, radiation) are nonlinearly dependent on the tracer mixing ratio. Small deviations can easily lead to completely different results, implying the risk of unstable behavior of the model system.

3. Transport. The transport calculated by the model is purely physical, as described by the basic equations. The approximation of actual atmospheric transport is in principle possible at any desired precision. This includes that artifacts of "non-physical diffusion" do not occur.

In addition to these requirements, schemes are also designed to meet other conditions, such as providing positive-definite results (no negative mixing ratios), and stable solutions when the initial conditions vary only slightly. The various advection schemes noted above each have their strengths and weaknesses within this framework. In this study we focus on one particular type of advection scheme, the mass flux-form algorithms [e.g., *Bott*, 1989, 1992; *Lin and Rood*, 1996; *Rasch and Lawrence*, 1998] which have been implemented in a variety of 3-D chemical tracer models (CTMs) and general circulation models (GCMs) [*Brasseur et al.*, 1998; *Lawrence et al.*, 1999a; *Steil et al.*, 2000]. These schemes have several strong points,

for instance: Within their own internal grid they are mass conserving, they allow the fluxes of trace gases in various directions to readily be tracked, they can very effectively limit numerical diffusion, and they are able to handle tracers with extremely noisy spatial distributions (e.g., cloud water), etc. However, these schemes have the problem that they implicitly change the vertical grid every time step; as discussed below, this can lead to undesired results, such as violating mass conservation, unless very special precautions are taken. Mass flux-form advection schemes readily allow a rigorous mathematical formulation and quantification of the problem; however, the problem to be discussed may in principle apply to other types of advection schemes as well.

Furthermore, the problem discussed as well as the mathematical formulation presented generally applies any time that pressure levels are changed inconsistently in models with sigma or hybrid coordinates. A typical situation of changing pressure coordinates in models (also in models that do not use flux-form advection schemes) is, for instance, when the surface pressure is updated to the next time step in an offline model (based on the surface pressures archived by a weather center). Or similarly, when the surface pressure is updated to the values from a spectral advection scheme in a GCM which uses separate advection schemes for air mass density and for trace gases (e.g., spectral for air masses, and semi-Lagrangian for trace gases and water vapor, as is implemented in CCM2 [*Hack et al.*, 1993] and ECHAM3 [*DKRZ*, 1992]). Re-mapping tracer distributions from any modified vertical grid onto the "standard" hybrid or sigma coordinates grid used in the model results in a loss of information; in section 2.1 below it is shown that this in turn leads to a failure to fulfill at least one of the three fundamental transport criteria listed above. This issue has been touched on in the literature [*Heimann and Keeling*, 1989], however, a careful treatment of its implications is not generally available. The goal of this chapter is to address this problem and its implications carefully for the specific case of flux-form schemes, to develop a framework which can be applied to the more general problem in future studies, and to suggest steps towards remedying the situation for flux-form schemes.

The difficulty to focus on with using flux-form schemes for tracer advection arises because the schemes advect air mass densities, where the mass fluxes across each grid box boundary are calculated from given wind velocities. Since the model "standard" grid pressure levels are completely specified by the constant sigma or hybrid coefficients and the current surface pressure, the change of air mass in each grid box within a given time step is solely determined by the change of the surface pressure. If the wind velocities are not consistent with the mass change in each grid box the flux-form advection scheme produces an "implied" grid which differs from the "standard" grid. This applies even when the surface pressure of a given column

is the same for the implied and standard grids; for instance, the advection scheme could increase the implied thickness of one layer (in Pa) while decreasing the implied thickness of the layer above by the same amount, changing the pressure interface level but leaving the surface pressure unaffected.

Frequently the wind velocities used as input to advection schemes are not absolutely consistent with the change of mass in each grid box ("mass/wind inconsistency"). A mass/wind inconsistency can occur for various reasons, for example the winds and surface pressure are derived by algorithms that are independent of the advection scheme used for tracer transport. In the case of GCMs, the wind velocities are often calculated by solving the basic equations in spectral space and then transformed back to the Eulerian standard grid. In the case of CTMs, the "offline" wind velocities are usually derived from data assimilation procedures of meteorological data into 3-D models. In many cases, these results are subsequently interpolated (spatially and temporally) onto the desired model grid for tracer transport.

As a consequence of the mass/wind inconsistency, tracers must be transferred in some fashion from the implied grid following the advection step to the standard grid. If the simplest transfer is applied, that is, the tracer mixing ratios in each cell are kept the same (index-to-index transfer), then the global tracer mass will generally not be conserved, violating the first desired property listed above. If instead the absolute masses of each tracer are transferred from each cell of the implied grid to the standard grid, which yields new mixing ratios in each cell, then a homogeneous tracer will not remain homogeneous, which violates the second desired property above. A common alternative, a supplementary fix which maintains both mass conservation and homogeneity, results in artificial global diffusion of the tracers, which then violates the third property above.

These conceptual points are more precisely mathematically formulated in this work as follows. In section 2.2 it is derived, how a simple index-to-index transfer of tracer mixing ratios from the implied grid (following the mass flux-form advection scheme) back to the standard model vertical grid generally leads to a violation of global tracer mass conservation, unless the implied and standard grid are identical, that is, unless there is no mass/wind inconsistency. The discussion in section 2.3 is about ways in which the global mass-mismatch can in principle be corrected, and what problems are associated with these methods. In section 2.4 a new mass conserving, grid-to-grid transfer procedure is constructed, which uses only the current tracer mass mixing ratio distribution. It is shown that due to the loss of information when a grid is changed, any mass-conserving re-gridding procedure such as this introduces a non-physical diffusion. Section 2.5 describes the problems that are associated with the lower model boundary; this class of problems is independent of the previous and can generally be avoided. Finally, in section 2.6 a modeling study

considers the quantitative implications of the problems associated with changes in the vertical grid during a time step (both due to the flux-form advection scheme, and due to the surface pressure updates). Section 2.7 gives recommendations for generally improving global 3-D models in view of the problems discussed here.

2.2 Inherent mass-mismatch due to grid inconsistency

Often model grid-box levels are defined by constant hybrid-coordinates h_a and h_b of unit one, such that the pressure levels at the box interfaces (p_I) can be written as

$$p_I(p_s^{i,j}, k) = h_a(k) \cdot p_s^{i,j} + h_b(k) \cdot p_0 \tag{2.1}$$

with $k\epsilon\{1, ..., n+1\}$, where n is the number of model layers, and k is the level index. Here k is counted in "top-to-bottom-order", i.e. towards increasing pressure. i is the longitude index, j the latitude index, p_0 a constant pressure, and p_s the surface pressure of the column with indices i and j. Consistency requires that the lowest interface corresponds to the surface pressure:

$$h_a(n+1) = 1 \quad \text{and} \quad h_b(n+1) = 0 \quad . \tag{2.2}$$

If $h_b(k) = 0$ for all k the vertical coordinate is a pure sigma-coordinate with $\sigma(k) = h_a(k)$. Often the $h_a(k)$ values for the upper layers are zero; the vertical coordinates in this region are then constant pressure levels.

For a given latitude and longitude (index-pair $\{i, j\}$), the pressure differences across the grid-boxes are defined as

$$\Delta p_k = p_I(p_s^{i,j}, k+1) - p_I(p_s^{i,j}, k) \tag{2.3}$$

for $k\epsilon\{1, ..., n\}$.

With the specific humidity $s_{i,j,k}$ of the air in grid-box $\{i, j, k\}$

$$s_{i,j,k} = \frac{m_{i,j,k}^{H_2O}}{m_{i,j,k}^{air} + m_{i,j,k}^{H_2O}} \tag{2.4}$$

(m are the masses of water-vapor (index H_2O) and dry air (index air)), the respective pressure difference $\Delta\bar{p}_k$ of the dry air can be written as

$$\Delta\bar{p}_k = \Delta p_k \cdot (1 - s_k) \tag{2.5}$$

Although in reality moist air is physically advected, the advection of dry air is needed in the model, because the tracer mixing ratios are based on dry air.

A flux-form advection scheme can be regarded as an operator Γ acting on the whole set $\{\Delta\bar{p}^{t_0}_{i,j,k}\}$ at time t_0 and performing a mapping onto a new set $\{\Delta\bar{p}^{t_1}_{i,j,k}\}$ at time t_1:

$$\Gamma(\{\Delta\bar{p}^{t_0}_{i,j,k}\}, t_0, t_1) = \{\Delta\bar{p}^{t_1}_{i,j,k}\} \quad . \tag{2.6}$$

Γ depends on the horizontal wind field at time t_0 which for chemical tracer models (CTMs) is provided offline. For general circulation models (GCMs) the wind field results from solving the basic equations, e.g., in the spectral part of the model.

The advection operator acts similarly on the specific humidity (s) and on a tracer distribution (c, given as mass mixing ratio in units of kg tracer per kg of dry air). Both are implicitly converted to and from units of kg m^{-2} for the advection step. Thus for s

$$\Gamma(\{s^{t_0}_{i,j,k}\}, t_0, t_1) = \{s^{t_1}_{i,j,k}\} \quad , \tag{2.7}$$

and for c

$$\Gamma(\{c^{t_0}_{i,j,k}\}, t_0, t_1) = \{c^{t_1}_{i,j,k}\} \quad . \tag{2.8}$$

At time t_1 the moisture induced pressure level differences across box k in a certain column $\{i, j\}$ are then

$$\Delta p^{t_1}_k = \Delta\bar{p}^{t_1}_k/(1 - s^{t_1}_k) \quad . \tag{2.9}$$

If the advection scheme is inherently mass conserving, then

$$M^{t_1} = M^{t_0} \tag{2.10}$$

where M is either the global mass of dry air

$$M_{\text{air}} = \frac{1}{g}\sum_{i,j}\Delta A_{i,j}\sum_{k=1}^{n}\Delta\bar{p}_{i,j,k} \quad , \tag{2.11}$$

or the global mass of water vapor

$$M_{\text{H}_2\text{O}} = \frac{1}{g}\sum_{i,j}\Delta A_{i,j}\sum_{k=1}^{n}\Delta p_{i,j,k}s_{i,j,k} \quad , \tag{2.12}$$

or the global mass of tracer c

$$M_{\text{c}} = \frac{1}{g}\sum_{i,j}\Delta A_{i,j}\sum_{k=1}^{n}\Delta\bar{p}_{i,j,k}c_{i,j,k} \quad . \tag{2.13}$$

g is the gravity-acceleration which is approximately constant within the atmosphere, and $\Delta A_{i,j}$ is the surface area of the model grid column.

Usually the post-advection variable sets ($\{s^{t_1}_{i,j,k}\}$, $\{c^{t_1}_{i,j,k}\}$), which are on the advected vertical grid, are re-associated with the model hybrid grid. Subsequently other

processes such as chemistry- and sub-grid scale parameterizations acting on s and c may follow, which are not considered in this discussion. However, since the "re-association"

$$s^{t'_1} \Leftarrow s^{t_1} \quad \text{and} \quad c^{t'_1} \Leftarrow c^{t_1} \tag{2.14}$$

is commonly on an index-to-index basis, violation of the tracer mass conservation occurs, as shown below.

After the advection step, generally the surface pressure in any model column will have changed because the advection scheme changes the pressure level differences Δp^{t_0} into Δp^{t_1} (Eq. (2.6)). For a certain model column $\{i, j\}$ the surface pressure can be calculated by

$$p_s^{i,j,t_1} = \sum_{k=1}^{n} \Delta p_k^{t_1} + p_I(p_s^{i,j,t_0}, 1) \quad . \tag{2.15}$$

Here the second term is explicitely needed if the upper model boundary is not at pressure level zero. In the discussion here it will be assumed that

$$p_I(p_s^{i,j,t}, 1) = 0 \quad . \tag{2.16}$$

However, the following discussion is also valid for the more general case of a constant upper model boundary pressure $p_I(p_s^{i,j,t}, 1)$.

The post-advection surface pressure derived in this way implicitly defines the model grid levels at time t_1 by Eq. (2.1) and (2.2), and also the respective pressure differences along the grid-boxes (Eq. (2.3)). These grid-levels, which are indexed t'_1 for further analysis are in general not the same as the grid levels that the advection scheme produced (index t_1, see Fig. 2.1). Note that t_1 and t'_1 refer to the same time step interval, but indicate different internal states of the model.

Thus, the "re-associated" (index-to-index) global tracer mass (Eq. (2.14)), calculated according to Eq. (2.13) becomes

$$M_{\mathrm{c}}^{t'_1} = \frac{1}{g} \sum_{i,j} \Delta A_{i,j} \sum_{k=1}^{n} \Delta \overline{p}_{i,j,k}^{\,t'_1} c_{i,j,k}^{t_1} \quad . \tag{2.17}$$

The "true" post-advection tracer mass is, however,

$$M_{\mathrm{c}}^{t_1} = \frac{1}{g} \sum_{i,j} \Delta A_{i,j} \sum_{k=1}^{n} \Delta \overline{p}_{i,j,k}^{\,t_1} c_{i,j,k}^{t_1} \quad . \tag{2.18}$$

The mismatch in the global tracer mass therefore is

$$\Delta M_c = M_c^{t'_1} - M_c^{t_1} = \frac{1}{g} \sum_{i,j} \Delta A_{i,j} \sum_{k=1}^{n} c_{i,j,k}^{t_1} (\Delta \overline{p}_{i,j,k}^{\,t'_1} - \Delta \overline{p}_{i,j,k}^{\,t_1}) \quad . \tag{2.19}$$

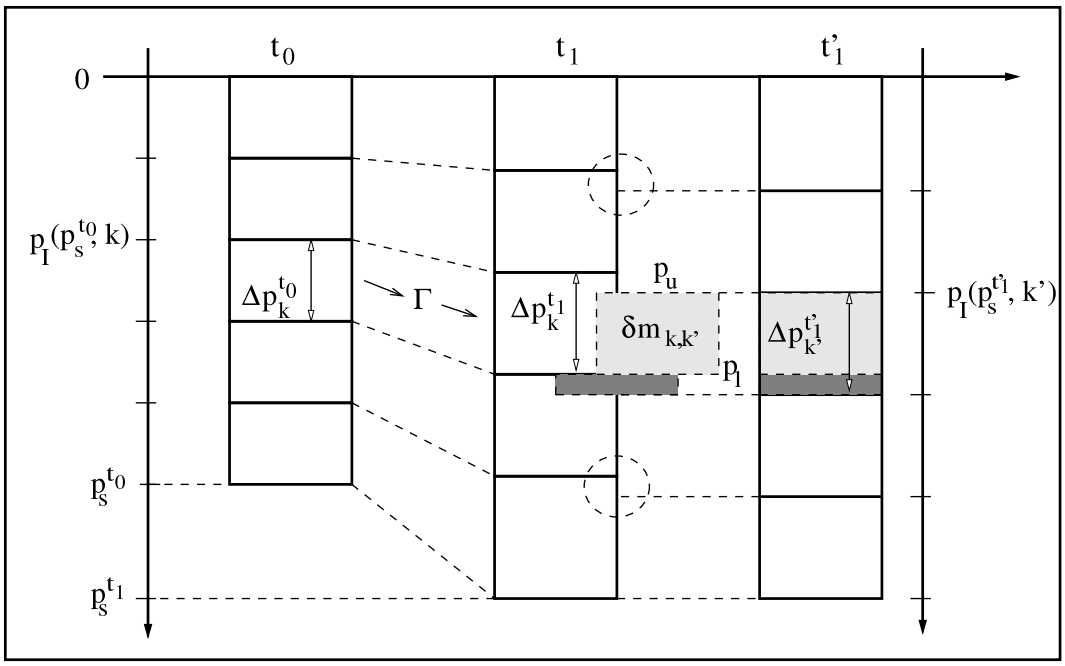

Figure 2.1: Schematic diagram of the grid-level mismatch between implicit grid after the flux-form advection calculation (t_1) and model hybrid grid (t'_1) at the same time step for one model column. The advection operator Γ acts on the model hybrid grid of the previous time step (t_0).

Both the tracer mass mixing ratio c and the pressure differences $\Delta\bar{p}$ depend on all 3 indices (latitude, longitude, and pressure level). Since the global air mass ($c_{\mathrm{air}} = 1$, regarding air itself as a tracer) is not changed by the advection algorithm (Eq. (2.10) and (2.11)), and further

$$\frac{1}{g}\sum_{i,j}\Delta A_{i,j}\sum_{k=1}^{n}(\Delta\bar{p}^{t'_1}_{i,j,k} - \Delta\bar{p}^{t_1}_{i,j,k}) = 0 \quad , \tag{2.20}$$

ΔM_c in general only vanishes if

$$c_{i,j,k} = \text{const.} \quad \text{for all } \{i,j,k\} \quad , \tag{2.21}$$

i.e., for a homogeneously distributed tracer. Consequently, in Eq. (2.19), the tracer mass mixing ratio c can be interpreted as a local weight function of the pressure difference mismatch between the grid levels after advection (t_1) and the standard hybrid grid levels (t'_1).

From this discussion, it is clear that a tracer distribution with non-zero spatial gradients (along latitude, longitude and/or height (pressure)) leads inevitably to violation of the global tracer mass conservation. This violation increases with increasing spatial gradients of the species. The problem is inherent to the discretization, i.e., the

use of finite grid levels, that are required for the computational treatment of the advection in an Eulerian framework.

The question which immediately arises is whether this problem of global tracer mass mismatch can somehow be solved. This is discussed in the next section.

2.3 Principle "mass fixers"

A way to correct for the mass discrepancy ΔM_c is to rescale the tracer mass mixing ratio in each grid-box at every time step, which forces global mass conservation, according to

$$c_{i,j,k}^{t_1} \leftarrow c_{i,j,k}^{t_1} \cdot \frac{M_c^{t_0}}{M_c^{t_0} + \Delta M_c} \quad . \tag{2.22}$$

This correction is simple to implement and it re-distributes the artificially generated/destroyed mass ΔM_c globally, preserving the relative spatial gradients of the tracer. This technique introduces the same relative change of the tracer mass mixing ratio at any point. However it has a fundamental flaw, namely that requirement No. 3 is strongly violated. The mass mismatch error is replaced by a non-physical, far-reaching transport component that "spreads" tracer mass all over the globe on an arbitrarily short time scale.

An alternative approach to getting rid of the mismatched mass locally (e.g., by performing a columnwise re-scaling) immediately leads to violation of the monotonicity requirement (No. 2). The respective re-scaling procedure for one model column (index-pair $\{i, j\}$) is then given by

$$c_{i,j,k}^{t_1} \leftarrow c_{i,j,k}^{t_1} \cdot \frac{m_{i,j}^{t_0}}{m_{i,j}^{t_0} + \Delta m_{i,j}} \tag{2.23}$$

with the mass mismatch of column $\{i, j\}$ (cf. Eq. (2.19))

$$\Delta m_{i,j} = \frac{1}{g} \Delta A_{i,j} \sum_{k=1}^{n} c_{i,j,k}^{t_1} (\Delta \bar{p}_{i,j,k}^{t_1'} - \Delta \bar{p}_{i,j,k}^{t_1}) \quad . \tag{2.24}$$

Since the rescaling factor for each column is in general independent of all other columns, and $\Delta m_{i,j}$ can even differ in sign between neighboring columns, this correction leads to violation of requirement No. 2. The distribution of an initially homogeneously distributed tracer will eventually develop artificial horizontal structures, which also lead to vertical structures because of tracer transport. Consequently, both ways to correct for the mass-mismatch by re-scaling do not fulfill all 3 fundamental requirements at the same time.

2.4 A mass conserving grid-to-grid transformation

Since both methods described in the previous section lead to unsatisfactory effects, one has to go one step back: not to correct for the mass mismatch, but to avoid it. This can possibly be achieved by replacing the simple index-to-index re-association (Eq. (2.14)) by a more elaborate method to calculate $c^{t'_1}$, the tracer mass mixing ratio on the model hybrid grid, that replaces c^{t_1} in Eq. (2.17). The idea is to re-distribute the tracer from grid t_1 after the advection in a mass-conserving way to grid t'_1, which is the model hybrid grid. As indicated in Fig. 2.1, the tracer masses are "re-gridded" according to the overlap between the boxes of the two grids. This will now be shown for one model column, i.e., for a given $\{i, j\}$. The latitude and longitude indices are in the following occasionally omitted for the sake of readability.

Box k' on grid t'_1 contains a certain fraction of the tracer mass of box k on grid t_1 it overlaps with. This mass contribution is

$$\delta m^{t_1}_{k,k'} = \frac{1}{g} A_{i,j} \frac{p_l(k,k') - p_u(k,k')}{\Delta p^{t_1}_k} \Delta \bar{p}^{t_1}_k c^{t_1}_k \tag{2.25}$$

where p_l and p_u are the lower and upper boundaries of the overlap region (Fig. 2.1). These can be calculated by

$$p_l(k,k') = min(p_I(p^{i,j}_s, k+1), p_I(p^{i,j}_s, k'+1)) \tag{2.26}$$

and

$$p_u(k,k') = max(p_I(p^{i,j}_s, k), p_I(p^{i,j}_s, k')) \quad . \tag{2.27}$$

Mass conservation requires

$$\delta m^{t_1}_{k,k'} = \delta m^{t'_1}_{k,k'} = \frac{1}{g} A_{i,j} \Delta \bar{p}^{t'_1}_k \delta c^{t'_1}_{k,k'} \quad , \tag{2.28}$$

where $\delta c^{t'_1}_{k,k'}$ is the fractional contribution of tracer c in box k to the mass mixing ratio in box k'. Using the relationship for the dry pressure differences (Eq. (2.5)), this becomes

$$\delta c^{t'_1}_{k,k'} = \frac{p_l(k,k') - p_u(k,k')}{\Delta p^{t'_1}_{k'}} \cdot \frac{1 - s^{t_1}_k}{1 - s^{t'_1}_{k'}} \cdot c^{t_1}_k \quad . \tag{2.29}$$

Summation over k gives the total mass mixing ratio $c_{k'}$ in box k'.

Consequently, an $n \times n$ matrix, describing the overlap of grid t'_1 (k') with grid t_1 (k) in one model column $\{i, j\}$ can be defined by

$$o_{k,k'} = f_{k,k'} \cdot \frac{p_l(k,k') - p_u(k,k')}{\Delta p^{t'_1}_{k'}} \cdot \frac{1 - s^{t_1}_k}{1 - s^{t'_1}_{k'}} \tag{2.30}$$

with

$$f_{k,k'} = 1 \quad \text{for} \quad p_l > p_u \quad ; \quad f_{k,k'} = 0 \quad \text{for} \quad p_l \leq p_u \quad . \tag{2.31}$$

$f_{k,k'}$ ensures that only these matrix elements of the overlap-matrix are non-zero for which the respective boxes do overlap. As long as the grid mismatch between t_1 and t'_1 is not extremely large, the overlap-matrix $o_{k,k'}$ is sparse (values close to 1 on the diagonal, small values close to the diagonal, and zero elsewhere). Furthermore, if the upper model boundary is at zero, or non-zero constant pressure (Eq. (2.16)), and since the surface pressure $p_s^{i,j}$ is the same on both grids, the total column overlap of both grids t_1 and t'_1 is 100%:

$$\sum_{k=1}^{n} o_{k,k'} = 1 \quad \text{and} \quad \sum_{k'=1}^{n} o_{k,k'} = 1 \quad . \tag{2.32}$$

With the above definition of the overlap-matrix (Eq. (2.30)) the transformed tracer mass mixing ratio in box $\{i, j, k'\}$ on grid t'_1 can be written as

$$c_{i,j,k'}^{t'_1} = \sum_{k=1}^{n} o_{k,k'} \cdot c_{i,j,k}^{t_1} \cdot w_k(p_u(k,k'), p_l(k,k'), \frac{\delta c_k^{t_1}}{\delta p}) \quad . \tag{2.33}$$

Here w_k is a vertical tracer gradient $(\delta c_k^{t_1}/\delta p)$ dependent weight function that contains sub-grid scale information such as the assigned distribution of the tracer within the box. Usually the assumption is made, e.g., when calculating chemical interactions, that all tracers are homogeneously distributed within a grid box, i.e. $w_k = 1$.

Thus, a linear transformation for "re-gridding" the mass from the post-advection grid t_1 to the model hybrid grid t'_1 is found. It still has to be shown that this transformation is mass conserving. This will especially restrict the choice of possible weight functions w_k.

After transformation, the tracer mass mismatch between post-advection grid t_1 and model hybrid grid t'_1 at a given model column $\{i, j\}$ becomes (Eq. (2.24))

$$\Delta m_{i,j} = \frac{1}{g} \Delta A_{i,j} \sum_{k=1}^{n} (c_k^{t'_1} \Delta \bar{p}_k^{t'_1} - c_k^{t_1} \Delta \bar{p}_k^{t_1}) \quad . \tag{2.34}$$

Substituting $c_k^{t'_1}$ in Eq. (2.34) by Eq. (2.33) and using Eq. (2.5), (2.30), and the relationship

$$\sum_{k=1}^{n} f_{k,k'}(p_l(k,k') - p_u(k,k')) = \Delta p_{k'} \tag{2.35}$$

it turns out that

$$\Delta m_{i,j} = 0 \quad , \tag{2.36}$$

if the condition

$$\sum_{k=1}^{n} c_k^{t_1} \Delta\bar{p}_k^{t_1} (w_k - 1) = 0 \tag{2.37}$$

is fulfilled. Therefore, $w_k = 1$ is the only solution for a mass conserving transformation, that holds for any arbitrary tracer distribution $c_k^{t_1}$.

As a consequence, it is shown that the suggested grid transformation is indeed mass conserving, even within each column of given latitude/longitude. However, one further aspect has to be addressed. The overlap-matrix (Eq. (2.30)) depends on the specific humidity on both grids, but it is not clear yet, how to derive the specific humidity on the model hybrid grid ($s^{t'_1}$). In a first approach one could argue that the ratio of specific humidities in Eq. (2.30) is close to one

$$\frac{1 - s_k^{t_1}}{1 - s_{k'}^{t'_1}} \approx 1 \quad . \tag{2.38}$$

This assumption will introduce a second order violation (proportional to mass mixing ratio times specific humidity) of the mass conservation, as can be derived from Eq. (2.34). Since in general

$$s \ll 1 \quad \text{and} \quad c \ll 1 \tag{2.39}$$

this error is much smaller than the error introduced by the simple index-to-index mapping discussed above.

However, this smaller error is also correctable. The fraction of water-vapor mass in box k' on grid t'_1 that originates from box k on grid t_1 can be calculated similar to Eq. (2.25). $c_k^{t_1}$ has to be replaced by $s_k^{t_1}$, and $\Delta\bar{p}$ by Δp, since the specific humidity usually relates the water-vapor mass to the total mass and not to the mass of the dry air (Eq. 2.4). Summation over k taking into account the overlap leads to the total water-vapor mass in box k'

$$m_{k'}^{H_2O} = \sum_k f_{k,k'} \cdot \delta m_{k,k'}^{H_2O} \quad . \tag{2.40}$$

The water-vapor mass defines the specific humidity (Eq. (2.4)), and since the dry air mass in the box is (cf. Eq. (2.11))

$$m_{k'}^{air} = \Delta p_{k'}^{t'_1} (1 - s_{k'}) \frac{A_{i,j}}{g} \tag{2.41}$$

it follows

$$m_{k'}^{H_2O} = \Delta p_{k'}^{t'_1} s_{k'}^{t'_1} \frac{A_{i,j}}{g} \quad . \tag{2.42}$$

The solution for s can be written as

$$s_{k'}^{t'_1} = f[s_k^{t_1}, 0, 0, 1] \quad , \tag{2.43}$$

where $f[c, s^{t_1}, s^{t'_1}, w]$ is defined by the mass mixing ratio overlap transformation (Eq. (2.30) and (2.33)).

The algorithm derived above couples mass flux-form advection schemes to 3-D Eulerian atmospheric models avoiding the mass mismatch caused by inherent grid inconsistencies. Independent of this coupling, other problems associated with the model grid can occur and are described in the next section.

2.5 Lower model boundary and surface pressure mismatch

The coupling problem described so far is in many cases convoluted with another problem which is related to the lower model boundary. The lower model boundary is at the same pressure level on both the advection grid (t_1) and the hybrid grid (t'_1), since the post-advection surface pressure defines the pressure levels of the hybrid-grid (Eq. (2.1) and (2.2)). So far no boundary problem occurs at the lower boundary. However, in many 3-D global atmospheric models the surface pressure is changed in an additional step.

GCMs often calculate the basic variables (wind vectors, pressure etc.) in a separate module (e.g. in spectral space) and use these to "drive" the advection. Afterwards, the tracer mass mixing ratios are kept, whereas other quantities that are consistently calculated by the advection scheme, in particular the surface pressure, are overwritten by the independently calculated variables (e.g. spectral module) of the next time step.

The advection of CTMs is driven "offline", e.g., by re-analyzed data such as wind vectors, pressure, etc. These variables are usually derived by data assimilation techniques involving various 3-D global weather prediction models and presumably are inherently consistent concerning the basic equations. Often a grid-to-grid interpolation follows in order to adapt the data to the CTM grid, and usually a subset of this data is used to drive the advection of the CTM. The output calculated by the advection scheme is, due to differing algorithms, in most cases no longer consistent with the offline-data of the next time step. In order to force the CTM to "follow" the offline-data, only the tracer mass mixing ratios calculated by the advection scheme are kept, whereas, similar to the case of GCMs, in particular the surface pressure is overwritten by the offline surface pressure.

Consequently, in either case a third grid is introduced into the model, namely the pressure levels on the hybrid coordinates defined by the "new" surface pressure.

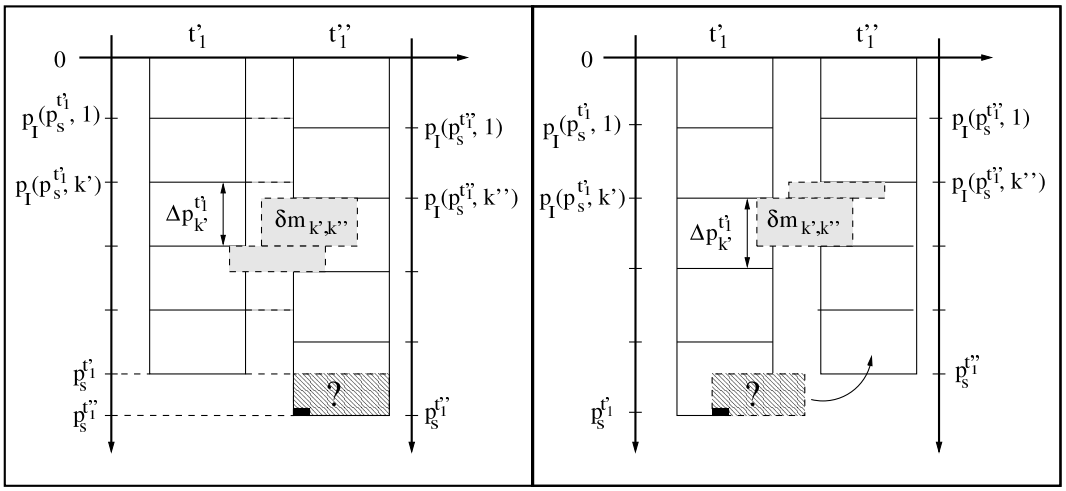

Figure 2.2: Schematic diagram of the grid mismatch after the advected surface pressure (on grid t'_1) is replaced by the non-consistent surface pressure of the offline-data (CTMs) or the spectral surface pressure (GCMs) that defines the grid t''_1. On the left side the new surface pressure is larger, on the right side it is smaller then the advected surface pressure. The hatched boxes indicate where a lack of information occurs.

This grid is denoted with t''_1, since it still happens within the same time-step. Simply maintaining the tracer mass mixing ratios calculated by the advection scheme ("re-associating" them on an index-to-index basis from grid t'_1 to the changed grid t''_1) leads to a violation of mass conservation in the same way as described for the respective transfer from the advection grid (t_1) to the hybrid-grid (t'_1) (both with the same lower boundary). This occurs at least at those levels where $h_a \neq 0$. However, in addition the lower boundary between t'_1 and t''_1 differs (and if $h_a(1) \neq 0$ the upper boundary does as well). In this case, the overlap between a column of grid t''_1 with the respective column on grid t'_1 is no longer 100% and a simple overlap transformation is no longer mass conserving or violates the monotonicity requirement, as outlined in Fig. 2.2. The left part of Figure 2.2 shows the situation when the new surface pressure is larger than the advected surface pressure. In this case, the overlap transformation is mass conserving, since the lowermost box of grid t'_1 is fully overlapped by the respective column of grid t''_1. However, the monotonicity requirement is violated, since the mass mixing ratio in the lower grid box of grid t''_1 is artificially reduced, because the lower box of grid t'_1 extends to a higher pressure level than that of grid t''_1. The information about what mass to put into that column extension does not exist.

The opposite case, when the overwritten surface pressure is smaller than the advected surface pressure is outlined in the right part of Figure 2.2. Now, the overlap transformation as described above is no longer mass conserving since the mass fraction of the non-overlapping area (indicated by the question-mark in Figure 2.2) at

the lower model boundary is lost. The possibilities of correcting (rescaling) for that mismatch are the same as discussed previously - with all their disadvantages. One additional method is to put the missing mass into the lowermost grid-box of grid t_1''. Although this fulfills the mass conservation requirement, it violates the monotonicity requirement in the lower layer, since the mass mixing ratio there is artificially increased.

Consequently, a consistent surface pressure (implying that $t_1' = t_1''$) is required to avoid mass mismatch at the lower model boundary.

2.6 A modeling study

2.6.1 Model setup

In order to demonstrate and to quantify the effects described so far model simulations with the 2.0-SPF configuration of MATCH were performed. The model is used in two horizontal resolutions, once in the standard resolution of 32 latitudes × 64 longitudes (section 1.3), and second in a reduced resolution of 16 latitudes × 32 longitudes. Model simulations with the reduced horizontal resolution were performed on a DEC-Alpha in 32-bit precision (MPICH, Mainz), the standard resolution simulations on a Cray-C916 (DKRZ, Hamburg). The offline-data to drive the advection for all simulations is the NCEP-reanalysis meteorology of the year 1993 [*Kalnay et al.*, 1996]. The time step is 1/2 hour, and the meteorological data is interpolated from its 6 hourly average to the model time-step. The surface pressure calculated by the advection scheme is overwritten by the surface pressure of the offline-data (interpolated in time) at every time-step. Since the vertical coordinates of the version used are pure sigma-coordinates of the form $\sigma = p/p_s$, an additional mismatch at the upper boundary occurs. This problem is similar to the mass-mismatch at the lower boundary (see the previous section) and therefore not discussed separately. Note, however, that the upper boundary mismatch occurs in both steps, from grid t_1 to t_1' and again from grid t_1' to t_1''.

The model was initialized for Jan 1, 1993 with 7 (6 in the standard resolution) inert tracer distributions. Five of them were homogeneously distributed in the troposphere (TROP), in the stratosphere (STRAT), in the lowest model layer (BL) extending to 0.99 times the surface pressure, in the entire model atmosphere (HM), and in the grid boxes that comprise the tropopause (TP). The tropopause was diagnosed according to the World Meteorological Organization definition [*WMO*, 1992], as described in section 1.5. The sixth tracer was initialized with a typical ^{14}CO distribution (14C-INI), the seventh with a typical atmospheric ozone distribution (O3-INI). The latter, however was only calculated with the reduced horizontal res-

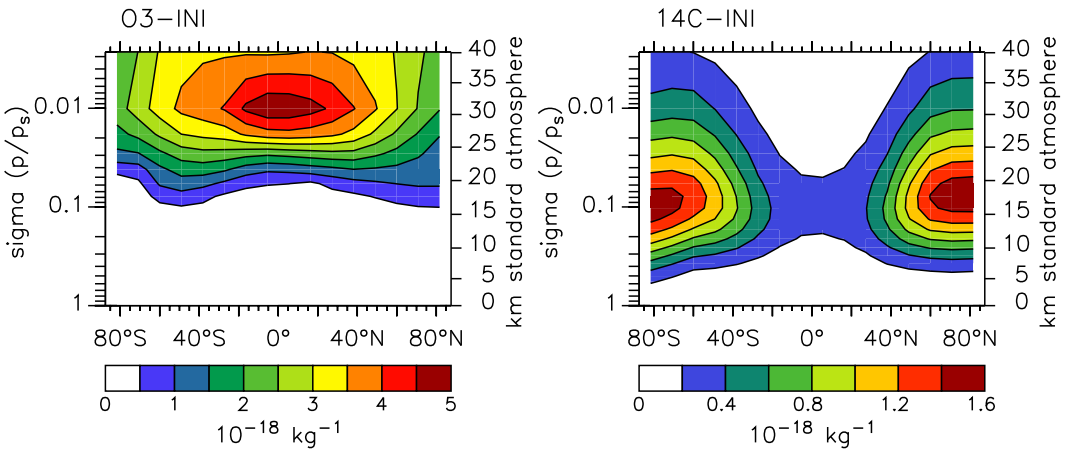

Figure 2.3: Initial zonal mean tracer distribution (mass mixing ratio normalized to a global abundance of 1 kg tracer in the model atmosphere) for O3-INI (left) and 14C-INI (right) in reduced horizontal resolution.

olution. The initial relative zonal mean distributions for 14C-INI and O3-INI are shown in Figure 2.3 (reduced resolution). All these tracers were transported without invoking any sources or sinks.

Additionally, ^{14}CO was simulated with the source distribution of *Lingenfelter* [1963] (LF), i.e., a constant atmospheric source distribution complying with its cosmogenic production (normalized to a global average production rate of 1 molecule cm^{-2} s^{-1}). The source distribution of ^{14}CO shows a considerable vertical gradient with the maximum production rate in the lower stratosphere. Further details concerning the source of ^{14}CO are described in chapter 5 and are not of special relevance at this point. The standard OH-1 distribution (monthly averages) was prescribed as the atmospheric sink of ^{14}CO (see section 1.4). The mass mixing ratio of ^{14}CO was initially set to zero.

Model calculations (one year) in 5 different setups were performed:

1. The basic model configuration (2.0-SPF) without any corrections is applied, i.e., employing an index-to-index transformation between t_1 and t_1' and t_1' and t_1'' respectively. This setup is further denoted as "B".

2. An overlap transformation between t_1 and t_1' as described in section 2.4 is implemented. The index-to-index transformation between t_1' and t_1'' is kept, however masses of non-overlapping areas at the upper boundary are put into the uppermost grid box, to force mass conservation. This setup is further denoted as "OV-1".

3. An additional overlap transformation between t_1' and t_1'' after the new pressure is read from the offline data is included. In the upper and lower box, in case

of incomplete overlap, the tracer mass mixing ratio of the same index-set of grid t_1' is assumed. The resulting mass-mismatch is not corrected. This setup is further denoted as "OV-1-2".

4. The mass calculated on grid t_1'' is globally rescaled to the mass on grid t_1 at every time-step (denoted as "RSC").

5. An overlap transformation between t_1 and t_1', and rescaling the mass on grid t_1'' globally to that on grid t_1' at every time-step, is applied (denoted as "OV-1-RSC").

All model output was archived as 5-day-averages. An additional setup of the model in which the offline-surface pressure is ignored and the advection-consistent surface pressure is kept was also tested (reduced resolution only). This was done in order to eliminate the $t_1' \rightarrow t_1''$ mass mismatch due to the surface pressure discrepancy between advection scheme and offline-data. However, it turned out that maintaining the advection consistent surface pressure and ignoring the offline surface pressure, leads to surface pressure values between 500 hPa and 1700 hPa already after a few time-steps. The reason is most probably that the horizontal wind-fields of the offline-data, that are used to drive the advection, are not consistent with the advection scheme calculated surface pressure.

2.6.2 Model results

2.6.2.1 Global tracer mass of "conserved" tracers The evolution of the global mass for the various initial tracer distributions is shown in Figure 2.4. The results are only shown for the model configurations (B, OV-1, OV-1-2) that do not include a global re-scaling, since for the latter mass conservation is forced. Figure 2.4 shows the relative mass, i.e. the ratio between global mass and initial global mass. Without any correction, only the mass of the homogeneously distributed tracer distribution is kept constant (Figure 2.4, upper), as can be expected from Eq. (2.19) and (2.20). The global masses of tracers with larger abundances in the stratosphere (STRAT, 14C-INI, and O3-INI) are artificially increased by a considerable amount after one year simulation time (40-70%, reduced resolution). The effect is smaller if calculated in standard horizontal resolution (24-46%). The increase of mass is larger for larger initial vertical gradients of the tracer distribution. The mass of the tracer that was initialized in the tropopause region (TP) also increases by about 40% in reduced, and by about 24% in standard resolution in one year. In contrast to that, the global masses of tracers with larger abundances in the troposphere (TROP and BL) decrease in time by up to 15% within one year, with a moderate

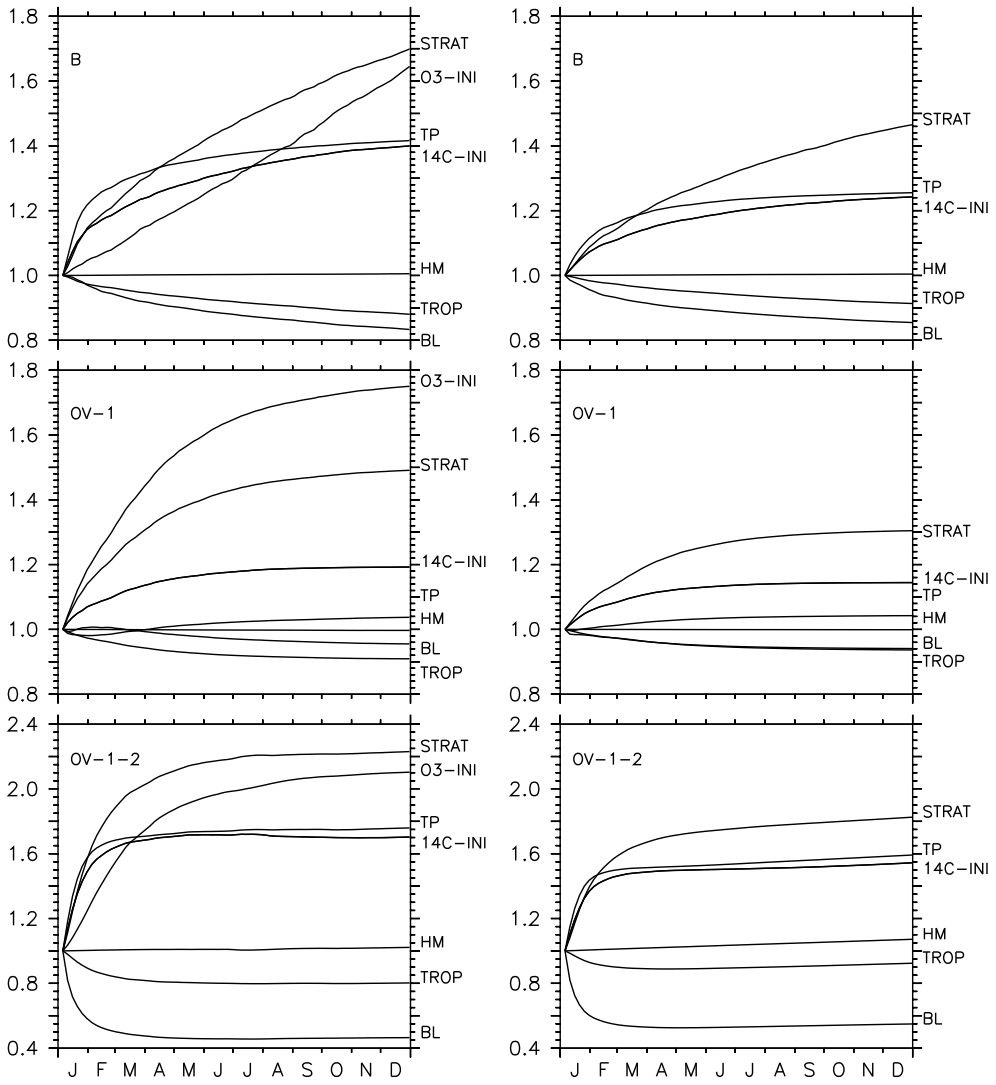

Figure 2.4: Evolution of the global tracer mass relative to the initial mass for the 7 tracers described in the text. The results of 3 model configurations are shown: the model without correction (B, upper), the model including an overlap transformation from the advection output grid (t_1) to the model hybrid grid (t_1') (OV-1, middle), and including a second overlap transformation from the hybrid grid (t_1') to the hybrid grid (t_1'') after the surface pressure has changed as described in the text (OV-1-2, lower). The left column shows the results obtained with the reduced resolution, the right column those obtained with the standard resolution, respectively.

difference between the resolutions. This artificial relative loss increases again with an increasing initial vertical gradient. Furthermore, all tracer masses (except STRAT and O3-INI) tend towards a constant value in the long-term limit. This can be expected, since the model transport transforms any initial tracer distribution into a homogeneous distribution after long enough time, presuming that there are neither sources nor sinks. The mass of a homogeneously distributed tracer, as shown by

the results, is kept constant. If, however, the mass-mismatch, which can also be interpreted as additional artificial source or sink, is "faster" than the atmospheric transport, this equilibrium state is never reached. This is possibly the case for STRAT and O3-INI in the reduced resolution.

The effect of the overlap transformation from the advection grid t_1 to the hybrid-grid t_1' (OV-1) is shown in Figure 2.4 (middle). The mass of the homogeneously distributed tracer is conserved, which shows that this transformation is indeed mass conserving. The mass mismatch of all tracers, except O3-INI, is reduced. All masses, including those of STRAT and O3-INI, now tend towards saturation. The sign of the remaining mass mismatch is still positive (artificial source) for the "stratospheric" tracers (O3-INI, STRAT, and 14C-INI) and negative (artificial sink) for the "tropospheric" tracers (TROP and BL). Interestingly, the reduction of the mass mismatch is largest for TP; from 40% (26%) without correction to less than 5% using the overlap transformation. Obviously, the mass conservation violation due to the lower boundary mismatch (the upper one was corrected) does not play a significant role for this tracer, because there the tracer mass mixing ratio is initially zero and increases only slowly. Furthermore, this possibly indicates that the mass mismatch occurring after advection, during the transformation (index-to-index) to the model hybrid grid is largest in the tropopause region.

The overlap transformation (OV-1) was also considered with the slight modification of not shuffling the mass at the upper boundary into the uppermost box when the surface pressure increased (reduced horizontal resolution only). The result (not shown) does not differ significantly from the result shown in Figure 2.4 (mid left). The maximum increase of tracer mass within one year was then 80% for O3-INI, compared to 75% for the case when the upper boundary correction is included. The upper boundary mass mismatch for this tracer is therefore negative. For the "tropospheric" tracers the change is negligible, since the mixing ratios of these tracers at the upper boundary are small.

By including a second overlap transformation between grid t_1' and t_1'' without correction for the upper and lower boundary problem (OV-1-2) the situation changes drastically (Figure 2.4, lower). In this case, the mass conservation violation for all tracers is even larger than for the model configuration without any correction (B, cf. Figure 2.4, upper). However, still all tracer masses tend towards saturation. Thus apparently, the correction step between t_1' and t_1'' increases the mass mismatch at the upper and lower boundary where the columns of t_1' and t_1'' do not fully overlap. This is the only uncorrected mismatch in this configuration. Since the pressure levels themselves are not affected by the overlap transformation, the only explanation is that the overlap transformation artificially shifts tracer mass to the boundaries and increases the mismatch there.

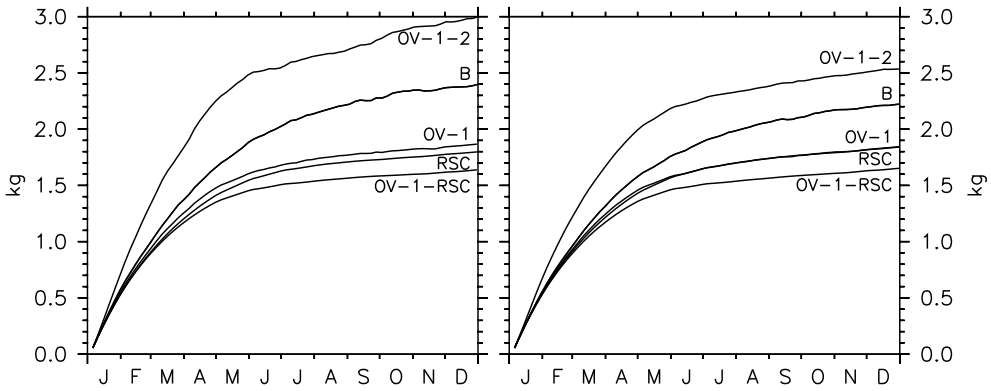

Figure 2.5: Evolution of global atmospheric ^{14}CO mass for the 5 different model configurations as described in the text. Results obtained with the reduced horizontal resolution are on the left, those obtained with the standard resolution on the right.

2.6.2.2 Global tracer mass of non-conserved tracers The situation is further complicated when sources and sinks are involved, as is the case for ^{14}CO. Figure 2.5 shows the evolution of the global tracer mass of ^{14}CO for the various model setups and horizontal resolutions over a 1 year period. The constant source in conjunction with tracer transport and the concentration dependent loss rate (reaction with OH) leads to an equilibrium global tracer mass after roughly one year. However, the level of this equilibrium global tracer mass differs strongly between the different model configurations. Compared to the uncorrected model calculation (B), the equilibrium global mass decreases if tracer mass conservation violation during the advection is partly (OV-1) or fully (RSC, OV-1-RSC) corrected in every time step. For the two-fold overlap correction configuration (OV-1-2) the equilibrium mass is largest, consistent with the results for the inert tracers. Again, the mass mismatch at the upper and lower boundary is increased by the second correction step, since mass is shifted towards the boundary. It is interesting to note that even the two configurations with full mass mismatch correction (RSC and OV-1-RSC) show different results (Figure 2.5). In the RSC case the total mass mismatch is globally rescaled in every time step, whereas in the OV-1-RSC case it is partly corrected by the overlap transformation and the rest is globally rescaled. The overlap transformation, however, implies an artificial vertical transport of the tracer between overlying grid boxes and therefore changes the local tracer mass mixing ratio. The sink distribution (OH) is prescribed, and the reaction rate of ^{14}CO with OH is pressure dependent (Eq. (1.4)). Since the OV-1-RSC equilibrium mass is lower than the RSC equilibrium mass, on average the overlap transformation tends to transport the tracer artificially to regions with higher OH and/or a faster reaction rate, i.e. down towards increasing pressure.

2.6.2.3 Vertical tracer distribution As already noted, the overlap transformation implies an additional artificial vertical transport, which of course changes the tracer distribution. To show the effect, the mass mixing ratio (model output) of every tracer is globally re-normalized at each archived time step to the same global integral mass. This gives the relative distribution of a tracer per unit mass. The zonal mean ratio between the model result (OV-1) including the overlap transformation between the advection grid (t_1) and the model hybrid grid (t_1'), and the model result without any correction (B) is shown in Figure 2.6 for 3 tracers on the two different horizontal resolutions. The figure shows the 5-day averages at the end of the indicated time intervals. Values below 1 indicate regions where the tracer mass mixing ratio is lowered by the overlap transformation compared to the uncorrected result, and values above 1 indicate regions where the tracer mass mixing ratio is increased. Since the overlap transformation is mass conserving the global average (surface-area- and mass weighted) of this ratio is one, and the respective global integral of the re-normalized mass mixing ratio gives one unit of mass. The tracer which is initially homogeneously distributed in the stratosphere (STRAT) is effectively transported down into the troposphere by the overlap transformation (Figure 2.6, upper). Thus, the additional artificial vertical transport component notably increases the stratosphere - troposphere exchange. The upward transport of the tropospheric tracer (TROP) in the model is generally slower than the downward transport of STRAT. Therefore it was necessary to choose a longer integration time for TROP (1 year instead of 60 days) for comparison. The upward transport is also increased by the overlap transformation (Figure 2.6, middle). The mass mixing ratio of 14C-INI (Figure 2.6, lower) is lowered in the tropopause region, where it is at its maximum at initialization (cf. Figure 2.3), and increased in the higher stratosphere and in the lower troposphere. Obviously, the overlap transformation causes a vertical transport that follows the gradients of the tracer. This is confirmed by the respective ratio (including overlap transformation to without) of the O3-INI tracer distribution shown in Figure 2.7 in comparison to the initial O3-INI distribution (cf. Fig. 2.3). Furthermore, it turns out that the additional vertical transport is the more effective, the larger the tracer gradient is. Finally, all effects are larger for the reduced horizontal resolution.

Consequently, the theoretical calculations (section 2.2, Eq. (2.19)) and the model results (Figure 2.4) show that the mass mismatch of an uncorrected model configuration (index-to-index-re-association) increases with increasing tracer gradients. This mass mismatch can be corrected by the overlap transformation described above, but then the mass mismatch is replaced by an artificial transport component (vertical diffusion), which again increases in strength with increasing tracer gradients.

The model simulations indicate further (not shown) that for the inert tracers (no

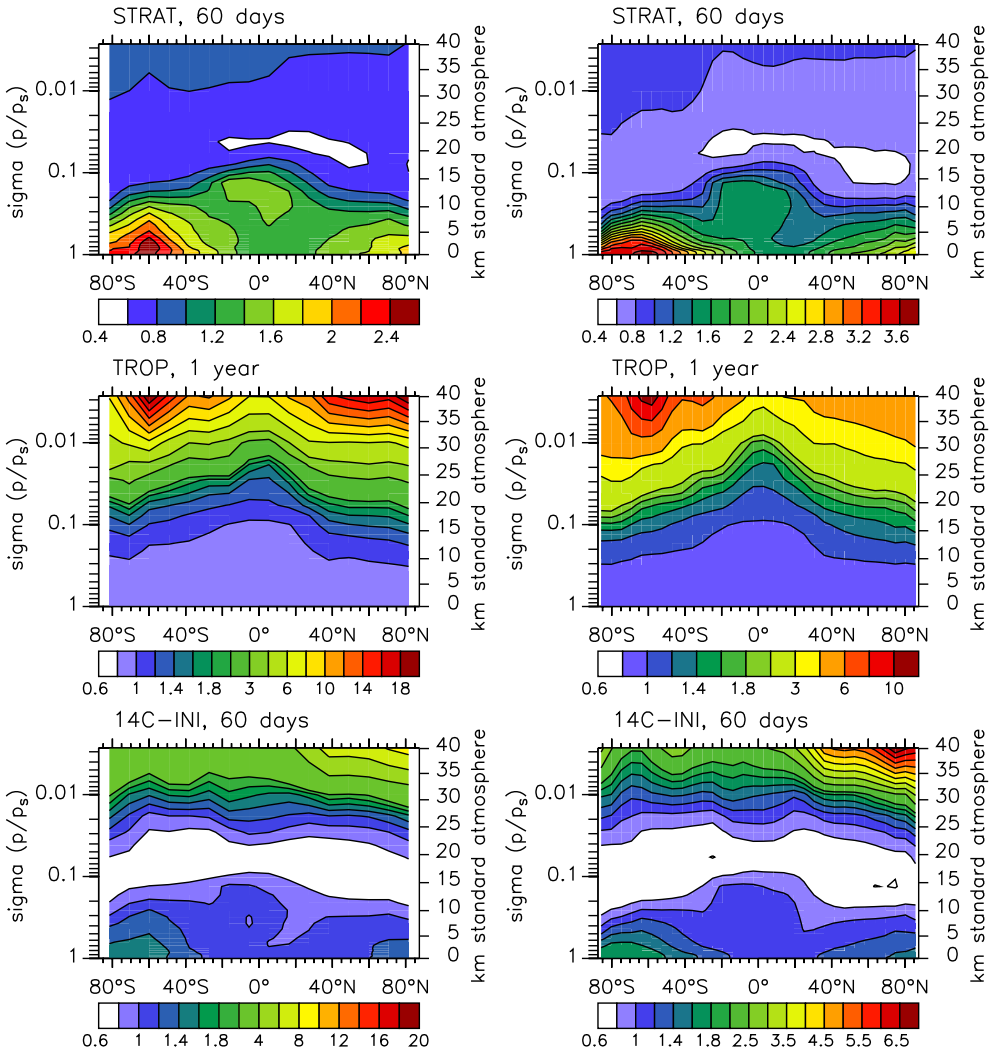

Figure 2.6: Zonal mean ratio of the re-normalized tracer distribution (mass mixing ratio per unit tracer mass) calculated with the OV-1 model configuration (overlap transformation from the advection grid to the model hybrid grid) versus the result of the uncorrected, re-normalized tracer distribution. The integration time is 60 days for STRAT (upper) and 14C-INI (lower), and 1 year for TROP (middle). The values are 5-day averages at the end of the indicated time intervals. The left column shows the result calculated with the reduced horizontal resolution, the right column that with the standard horizontal resolution.

sources and sinks) a global rescaling of the mass mismatch in every time step (RSC) does not significantly change the relative tracer distribution obtained with the uncorrected model configuration. However, this relative tracer distribution still suffers from the fact that the mass mismatch does not occur homogeneously distributed, but is globally corrected.

Figure 2.8 presents the change of the tracer distribution of ^{14}CO for three correction configurations. Shown is the annual zonal mean ratio of the re-normalized tracer

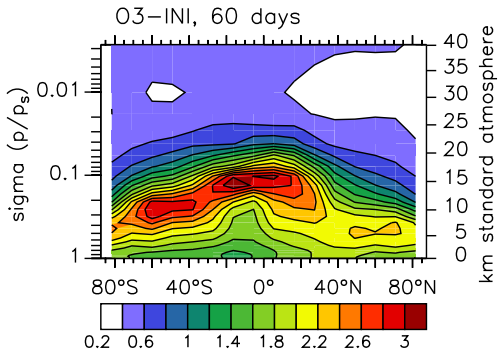

Figure 2.7: Zonal mean ratio of re-normalized O3-INI distribution (mass mixing ratio per unit tracer mass) calculated with the OV-1 model configuration (overlap transformation from the advection grid t_1 to the model hybrid grid t_1') versus the result of the uncorrected, re-normalized tracer distribution. The integration time is 60 days. Shown is the 5-day average at the end of this time interval. The result was obtained with the reduced horizontal resolution.

distribution "corrected to uncorrected". The variation with time is rather small. The result for the overlap correction from the advection grid to the model hybrid grid (OV-1, Figure 2.8, upper) is comparable to the respective result for the inert tracer 14C-INI (Figure 2.6). This is understandable because of the constant source distribution which tends to keep the relative tracer distribution as it is. Implementing the second, non-mass conserving overlap transformation (between the hybrid grid immediately after advection and the hybrid grid with the new offline surface pressure, OV-1-2) increases, as already shown, not only the global mass mismatch (Figure 2.5), but also the vertical diffusion (see Figure 2.8). In effect the second error is increased by correcting the first error, or in other words, in the uncorrected version (B), the effects of two errors partly cancel out.

Finally, it turns out that for ^{14}CO, global rescaling of the mass mismatch at every time step (RSC) changes the relative tracer distribution (Figure 2.8, lower), in contrast to what is found for the inert tracers (see above).

2.7 Conclusions

A simple coupling (index-to-index) of a mass flux-form advection scheme to a 3-D global atmospheric model (GCM or CTM) with a fixed hybrid-grid can readily lead to a violation of global tracer mass conservation, even if the advection scheme itself is perfectly mass conserving (as is the case for the SPITFIRE advection scheme used in the modeling study presented above). The impact of this increases with increasing vertical tracer gradients, and the resulting mass mismatch can be of either sign. The problem is fundamental and independent of the boundary-problems many GCMs and

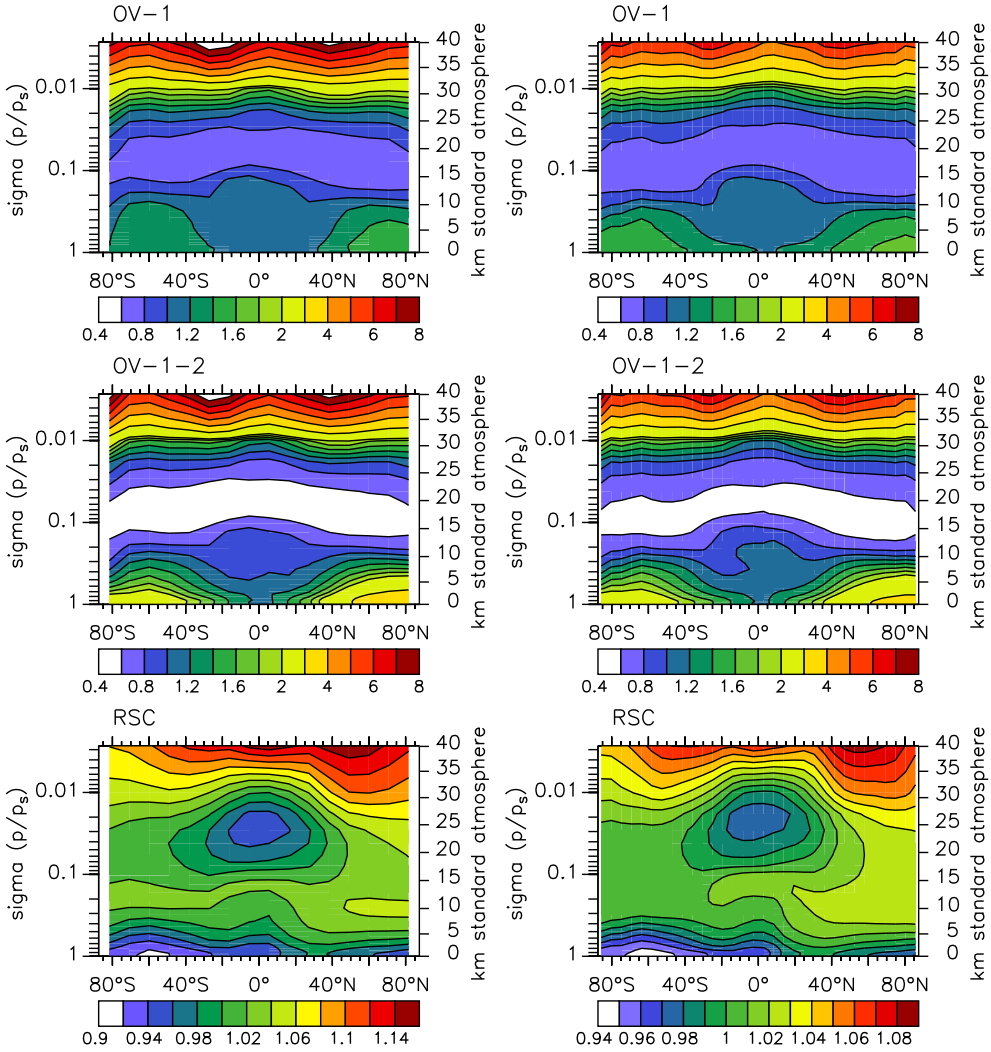

Figure 2.8: Annual zonal mean ratio of the re-normalized ^{14}CO distribution (mass mixing ratio per unit tracer mass) of 3 model configurations versus the result of the uncorrected model setup. The left column shows the result calculated with the reduced horizontal resolution, the right column that with the standard horizontal resolution.

CTMs intrinsically have in addition, such as the use of a surface pressure that is not consistent with the surface pressure derived from the advection scheme. The latter kind of problems can principally be avoided by using a constant pressure upper boundary and forcing the advection scheme to follow a given surface pressure (e.g., re-analyzed data in case of CTMs, spectral surface pressure in case of GCMs). But even if these "boundary conditions" are fulfilled, the fundamental mass mismatch does not necessarily vanish, because the advection scheme can change the underlying grid at every time step, as long as the input parameters (wind velocities) are not consistent with the advection procedure and the mass change in each grid box arising

from the surface pressure change (mass/wind inconsistency).

Simple mass fixer constructions have severe disadvantages since they either violate the monotonicity requirement or introduce "non-physical" transport components. In order to illustrate the severity of the mass mismatch, a mass conserving transformation that calculates the mean mass mixing ratio on a destination grid due to the overlap (in pressure coordinates) with the source grid is constructed. The algorithm is only applicable if the upper and lower boundaries of source and destination grids are the same. Otherwise, a lack of information occurs where the two grids do not fully overlap. The overlap transformation uses only the information that is implied in the model's state, i.e., the current tracer mass mixing ratio distribution. Trying to construct a more advanced re-distribution (including more information, e.g. sub-grid-scale information) from one grid to another is not possible in a comprehensive way that is valid for any arbitrary tracer distribution (cf. Eq. (2.37)).

This kind of mass conserving transformation introduces an additional vertical diffusion. The artificial diffusion is of comparable magnitude to or even larger than the physical transport components of the model. The strength of this vertical diffusion increases with increasing vertical tracer gradients.

In general the same problem occurs nearly any time the model grid is changed and tracer mass mixing ratios have to be transferred from one grid to another. The reason is that due to the averaging over discrete, finite grid intervals, information is lost (diffusion).

From this it can be deduced that within the framework of mass flux-form advection schemes a mass/wind consistency is a basic requirement in order to fulfill simultaneously (1) global tracer mass conservation, (2) monotonicity (i.e. no artificial spatial gradients), and (3) "physical-transport only" (i.e. no artificial diffusion). This mass/wind consistency constraint can neither be ignored for long lived tracers, nor for short lived tracers when (non-linear) chemistry is involved.

Since the mass/wind consistency must be defined in terms of the numerical method used for advection, an additional step is required in CTMs and GCMs, namely a preprocessing of the advection scheme input winds so that they will result in an implied grid (after advection) which exactly agrees with the standard grid at the next time step. Such preprocessing has been done for other advection schemes [*Prather*, 1986; *Heimann and Keeling*, 1989; *Heimann*, 1995]. However, such a preprocessing algorithm for general application to mass flux-form advection schemes, which would probably need to be iterative to be accurate, has yet to be published.

In particular, the surface pressure that is calculated by the advection scheme has to match the independently calculated surface pressure (in case of CTMs from the offline data; in case of GCMs the surface pressure that is consistent with the cal-

culated wind fields). In the notation used here, this means that $p_s^{i,j}$ for all $\{i, j\}$ is prescribed at any time. This determines at any time step the air mass change of each model column. Moreover, within every model column the pressure difference across each box calculated by the advection scheme has to match the respective model grid pressure difference of the next time step ($\Delta\bar{p}^{t'_1} = \Delta\bar{p}^{t''_1}$ for all $\{i, j, k\}$, cf. Eq. (2.19) applied to the $t'_1 \rightarrow t''_1$ transition). This determines the air mass change of every model grid box. The only free parameters left then are the mass-flux directions. It has yet to be shown that this modification of the input fields is possible without being forced to introduce an unrealistic vertical flux, which is treated in many models as a diagnosed variable.

The achievement of mass/wind consistency can therefore be regarded as the basis for the definition of a consistent grid throughout the model. The use of such a consistent grid throughout the model is thus an important requirement and also encompasses model grids which do not explicitely occur in the model code, but which instead have to be implicitly assumed in order to couple different model operators sequentially together.

The problem discussed in this chapter, the fundamentally inherent mass-mismatch (section 2.2), may easily lead to a misinterpretation of model results. This is demonstrated here by considering 3-D CTM results for ^{14}CO and several artificial tracers. In more complex setups the intrinsic model error might become completely convoluted and obscured and therefore overlooked. This risk increases with increasing complexity of the treatment of atmospheric chemistry in a model. Furthermore, it turns out that the mass-mismatch is worse at reduced horizontal resolution, which can be attributed to an enhanced mass/wind inconsistency due to a separate degradation of the meridional and zonal wind components for the reduced resolution setup.

It is important to point out that this does not imply that flux-form advection schemes should be rejected, because the same problem can apply in principle with other schemes (e.g., whenever the surface pressure is changed). On the contrary, the problem discussed could potentially be remedied in a GCM setting in which density and tracers are both advected flux-form, or in a CTM/reanalysis setting, where the reanalysis model provides air mass fluxes (instead of wind velocities) that are used directly by the CTM on the same consistent grid.

Throughout this study two configurations of MATCH with the SPITFIRE advection scheme are employed: the uncorrected standard version 2.0-SPF (section 1.3, in this chapter denoted as "B"), and the configuration with global rescaling ("RSC" in this chapter), hereafter denoted as 2.0-SPFR. This choice was made, since both the mass conservation violation of 2.0-SPF and the artificial diffusion introduced by the

overlap transformation are unacceptable, and furthermore the effect of the global rescaling correction (Eq. (2.22)) seems to have a comparably moderate effect on the ^{14}CO distribution (cf. Figure 2.8). Comparison of the results of these two configurations in the following chapters sheds light on the importance of the fundamental problems discussed here, on the one hand. On the other hand, differences between these configurations are used to assess the uncertainties of model predictions arising from inaccuracies of the realization of the tracer transport in 3-D models.

3 Evaluation of the simulated tropospheric transport with SF_6

Abstract. Following a published model inter-comparison study based on SF_6 simulations and observations, different MATCH configurations are tested and compared. Several aspects of tropospheric transport are addressed. The meridional and zonal transport components are evaluated by means of SF_6 observations at the surface level collected at various locations and during diverse campaigns. The simulated vertical mixing is compared to results of other models and assessed with respect to the influence of vertical mixing on the simulated SF_6 mixing ratio at the surface level. Finally the simulated interhemispheric exchange time based on the SF_6 simulations is calculated. In comparison to the models involved in the inter-comparison study, the MATCH configurations tested can be regarded as an ensemble with small deviations between the particular configurations. Differences in the SF_6 simulations can be used to estimate the uncertainty of model simulations arising from uncertainties of the simulated transport. Overall, the vertical mixing simulated by MATCH is rather weak, and the interhemispheric exchange rather long compared to other models involved in the inter-comparison study. The observations of SF_6 at the surface level are reasonably well reproduced (within the uncertainties) by all of the MATCH configurations tested.

3.1 Introduction

Sulfur hexafluoride (SF_6) can be used to characterize certain aspects of tracer transport in 3-D global atmospheric models [*Denning et al.*, 1999]. Since it has no relevant chemical or biological interactions it is a long lived trace gas with an atmospheric lifetime of more than 3000 years [*Ravishankara et al.*, 1993]. It is primarily emitted into the atmosphere by leakage out of electric equipment and therefore shows steady (anthropogenic) emissions with no known seasonal variations [*Maiss and Brenninkmeijer*, 1998].

Denning et al. [1999] compared the transport characteristics of various 3-D global atmospheric models by simulating the atmospheric SF_6 distribution under prescribed boundary conditions (model inter-comparison) and compared the results to existing observations (model evaluation).

In this chapter the results of simulations with various MATCH configurations under these TransCom-2 [*Denning et al.*, 1999] conditions are discussed. The purpose is not only to classify the model in terms of some general transport properties compared to a number of other "state-of-the-art" models, but in particular to evaluate the model's tracer transport properties, as far as possible with the limited number of observations, that were only available at ground level.

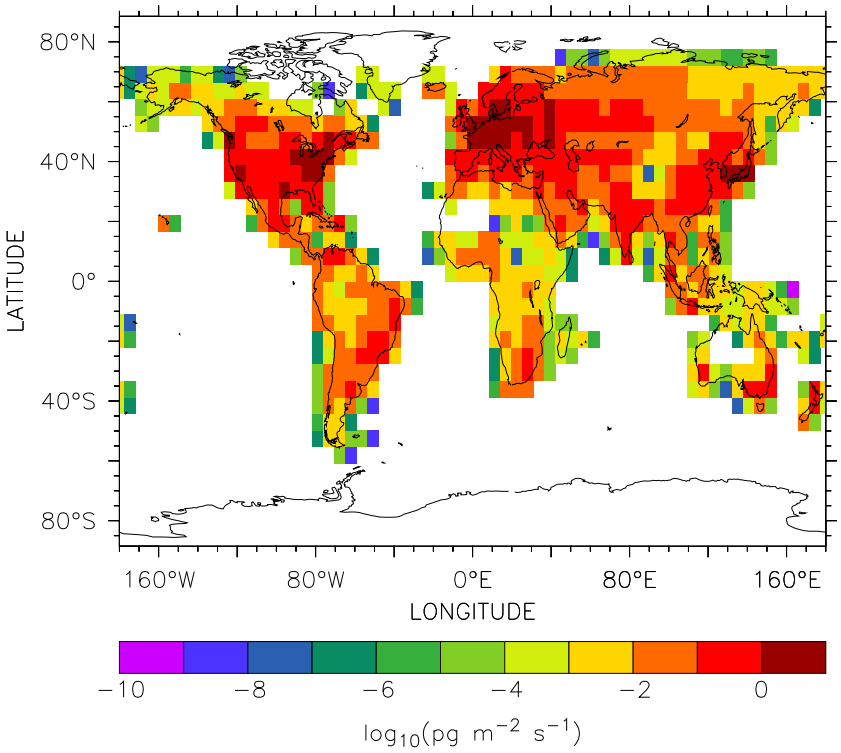

Figure 3.1: SF_6 emission map averaged onto the MATCH grid (32 latitudes × 64 longitudes)

3.2 Model setup

The model was initialized with a uniform SF_6 mole fraction of 2.06 pmol mol^{-1} for January 1, 1989 and integrated 5 years with the NCEP reanalysis meteorology of 1993 [*Kalnay et al.*, 1996]. The total emissions of SF_6 during this period are prescribed according to the global estimates of *Levin and Hesshaimer* [1996], linearly interpolated to daily values. The global emissions are geographically distributed by country in accordance with the electrical power usage [*United Nations*, 1994] and within each country according to the population density [*Tobler*, 1995]. From the original $0.5^o \times 0.5^o$ distribution an area-weighted average emission map on the coarser model grid is calculated. The result is shown in Figure 3.1.

The model-predicted global SF_6 mole fraction distribution of the last year of integration (1993) is archived as monthly average values for further analysis. This simulated mole fraction (χ in pmol mol^{-1}) is adjusted by scaling the mole fraction difference from the initial condition of 2.06 pmol mol^{-1}

$$\chi_{\text{adj}} = 2.06 + 0.936(\chi - 2.06) \tag{3.1}$$

in order to correct for a known overestimate of the chosen global SF_6 emission rate [*Denning et al.*, 1999].

3.3 Model results

The model results are subdivided into two categories: First, predictions for the ground level mixing ratio of SF_6, where observational data exist. And second, predictions of the vertical profile, for which at the time of the TransCom-2 study only a model inter-comparison was possible. Furthermore an SF_6 based analysis of the interhemispheric exchange time predicted by the model is provided.

3.3.1 Ground level data

The simulated SF_6 mole fraction in the lowest model layer at various locations is compared to observational data at ground level in Table 3.1. The observations were extrapolated in time using a linear trend of 0.202 pmol mol^{-1} yr^{-1} derived from the data for the mid-1990s. This value reflects the average growth rate at the measurement stations [*Denning et al.*, 1999]. In remote areas (far from the source regions) the SF_6 mole fraction is purely determined by the long range atmospheric transport, whereas in the vicinity of source areas, the SF_6 mole fraction is determined by the nearby source strength and the small scale short range transport. These two model transport properties can be tested separately when measurements in remote areas and source regions are considered. Figure 3.2 shows maps of the simulated annual mean SF_6 mole fraction in the lowest model layer and its deviation from the observed values at ground level. All 4 model configurations tend to overestimate the surface SF_6 mole fraction in source areas, and likewise underestimate it far from source regions. The global average surface SF_6 mole fraction is (2.97 ± 0.02) pmol mol^{-1} for all configurations in agreement with the results of *Denning et al.* [1999], which range from 2.94 to 3.01 pmol mol^{-1}.

3.3.1.1 Latitudinal gradient The latitudinal profile of the observations and model results at locations in the marine boundary layer (MBL, Table 3.1) is shown in Figure 3.3. It shows a pole-to-pole difference of about 0.3 pmol mol^{-1}, i.e. a latitudinal gradient of about 10% at these sites, which is captured by all model configurations, however slightly overestimated by the 2.0-SLT configuration. *Denning et al.* [1999] found a relation between the surface mean mole fraction and the mean latitudinal gradient, which is confirmed, since the largest mean latitudinal gradient coincides with the largest global mean surface mole fraction (2.0-SLT, see Figures 3.2 and 3.3).

Table 3.2 lists the RMS-deviation between model results (mod) and observations (obs), providing a quantitative assessment of the model performance concerning transport away from the source regions into remote areas. The RMS-deviation is

Station	LAT	LON	Obs.	1.2-SLT	2.0-SLT	2.0-SPF	2.0-SPFR
Neumayer	-71.0	-8.0	2.78	2.75	2.76	2.76	2.78
Tierra del Fuego	-54.9	-68.5	2.78	2.77	2.77	2.77	2.79
Cape Grim	-40.7	144.7	2.79	2.79	2.80	2.79	2.81
Barbados	13.2	-59.4	3.14	3.05	3.06	3.01	3.03
Guam	13.4	144.8	3.03	3.03	3.04	2.99	3.01
Kumukahi	19.5	-154.8	3.12	3.09	3.10	3.04	3.06
Izaña	28.0	-16.0	3.10	3.16	3.20	3.13	3.15
Bermuda	32.4	-64.7	3.20	3.17	3.22	3.15	3.17
N. Carolina Tower*	35.4	-77.4	3.41	3.35	3.53	3.42	3.44
Tae Ahn Peninsula*	36.7	126.1	3.25	3.30	3.42	3.31	3.33
Azores	38.8	-27.1	3.21	3.18	3.23	3.15	3.17
Utah*	39.9	-113.7	3.21	3.30	3.25	3.18	3.20
Wisconsin Tower*	45.9	-90.3	3.31	3.34	3.43	3.34	3.37
Hungary*	47.0	16.4	3.42	3.66	3.74	3.63	3.65
Fraserdale*	50.0	-82.0	3.25	3.28	3.35	3.27	3.29
Mace Head	53.3	-9.9	3.25	3.26	3.35	3.26	3.28
Cold Bay	55.2	-162.7	3.20	3.17	3.22	3.14	3.16
Alert	82.5	-62.5	3.17	3.20	3.26	3.19	3.21
Atlantic transect 1	39.5	-14.3	3.18	3.21	3.29	3.19	3.22
Atlantic transect 2	29.2	-17.1	3.17	3.16	3.21	3.14	3.16
Atlantic transect 3	20.1	-21.2	3.15	3.12	3.16	3.09	3.11
Atlantic transect 4	9.4	-23.7	2.97	3.06	3.07	3.01	3.04
Atlantic transect 5	-0.2	-18.5	2.91	2.88	2.87	2.85	2.87
Atlantic transect 6	-11.7	-7.3	2.82	2.80	2.81	2.80	2.82
Atlantic transect 7	-18.8	8.0	2.86	2.80	2.81	2.80	2.82
Atlantic transect 8	-25.9	10.1	2.84	2.79	2.79	2.78	2.80
Atlantic transect 9	-32.7	8.6	2.83	2.78	2.79	2.78	2.80
Atlantic transect 10	-39.5	7.9	2.81	2.78	2.78	2.78	2.80
Atlantic transect 11	-48.1	9.1	2.81	2.77	2.78	2.77	2.79
Atlantic transect 12	-56.6	9.1	2.82	2.76	2.77	2.77	2.79

Table 3.1: Observed (Obs., see *Denning et al.* [1999]) and simulated SF_6 mole fraction (pmol mol^{-1}). Locations (LATitude, LONgitude) marked with * are not considered to be in the marine boundary layer (MBL).

calculated according to

$$\Delta\chi_{\mathrm{RMS}} = \left(\frac{1}{n}\sum_{i=1}^{n}(\chi_{\mathrm{mod},i} - \chi_{\mathrm{obs},i})^2\right)^{\frac{1}{2}} \quad , \tag{3.2}$$

where χ is the mole fraction, for all observations ($n = 30$) and for observations within the MBL only ($n = 24$, see Table 3.1). Compared to the results obtained

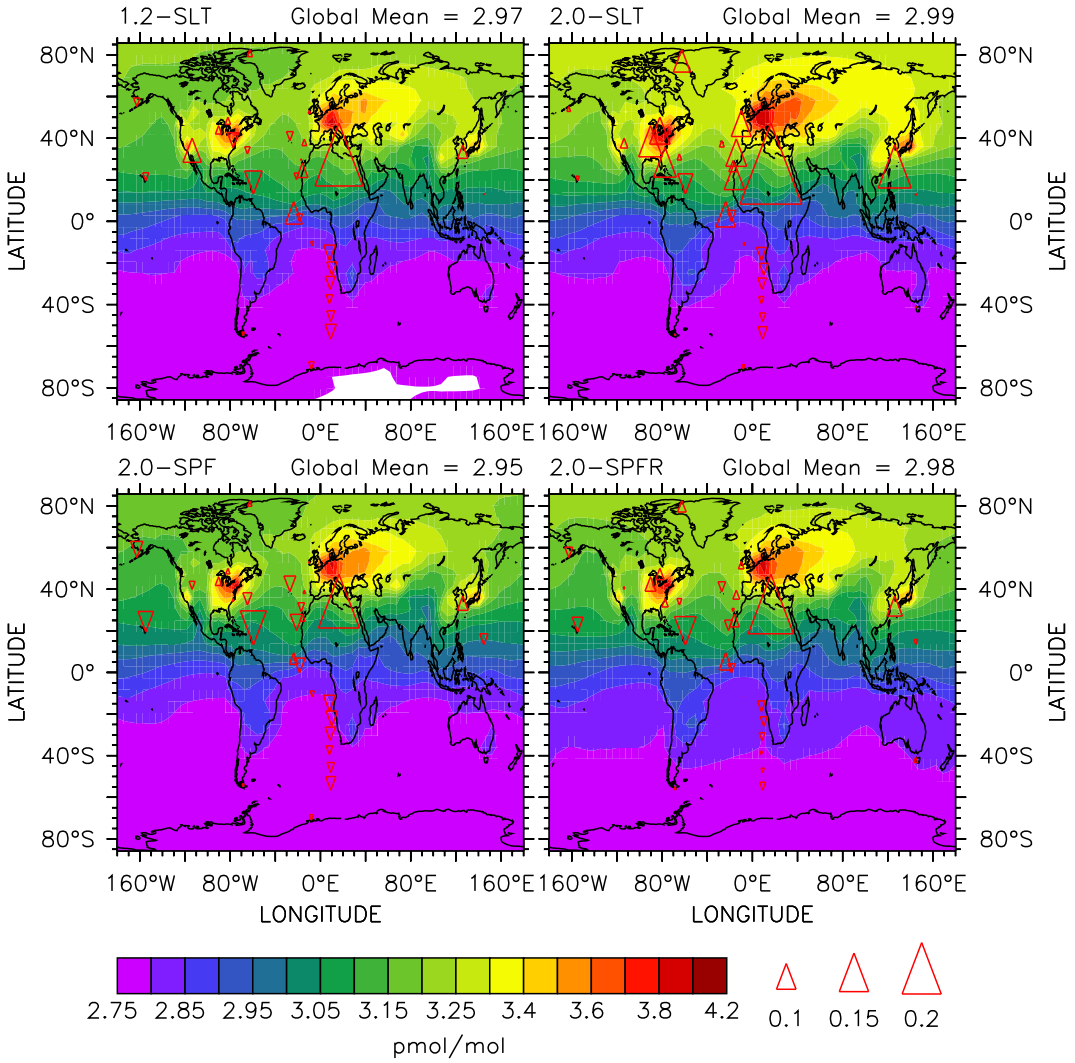

Figure 3.2: Simulated annual mean surface mole fraction of SF_6 (1993) resulting from various model configurations. The results are emission adjusted as described in the text. The indicated global mean values are area-weighted annual means for the surface layer. The triangles represent the deviation (simulated minus observed) for the station locations and Atlantic transect measurements (time adjusted as described in the text). Upward-pointing triangles indicate model overestimates, downward-pointing triangles indicate model underestimates with the magnitude defined in the legend.

with the 11 models in *Denning et al.* [1999], in which $\Delta\chi_{\mathrm{RMS}}$ ranged from 0.0489 to 0.1312 pmol mol^{-1}, the MATCH configurations 1.2-SLT, 2.0-SLT, 2.0-SPF, and 2.0-SPFR would take the ranks 6, 10, 5, and 4 (of 15), respectively, when all stations are considered. For the MBL locations only (Figure 3.3), $\Delta\chi_{\mathrm{RMS}}$ ranges from 0.0402 to 0.1101 pmol mol^{-1}, and the MATCH configurations would take the ranks 5, 9, 7, and 2, respectively. It is interesting to note that the 1.2-SLT configuration predicts SF_6 mole fractions closer to the observed values than the 2.0-SLT configuration

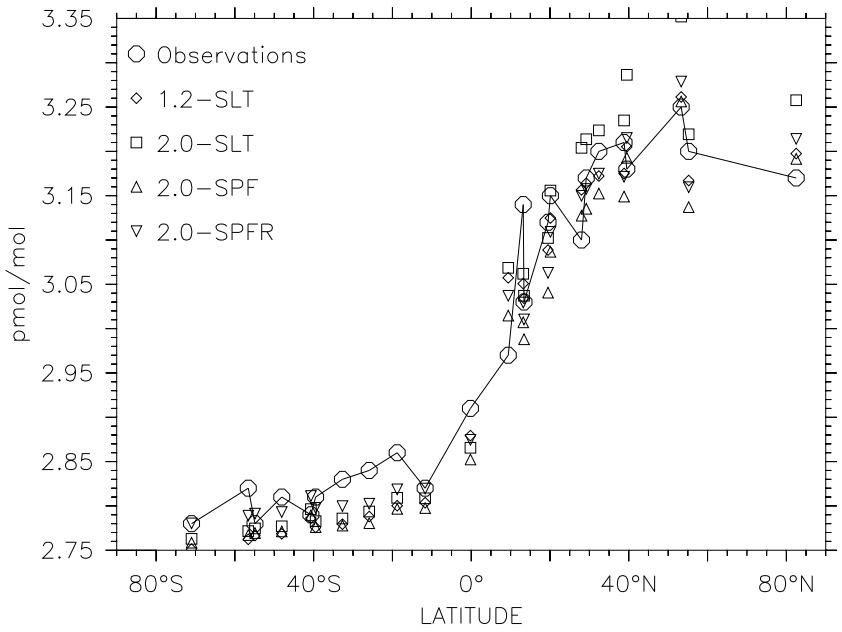

Figure 3.3: Latitudinal profiles of simulated and observed (see *Denning et al.* [1999]) 1993 annual mean surface mole fraction of SF_6. The observations have been time adjusted as described in the text. The figure includes all October/November 1993 Atlantic transect measurements, station locations considered within the marine boundary layer (cf. Table 3.1), and Izaña, which is in the mid-troposphere.

Model	ALL	MBL
1.2-SLT	0.0624	0.0425
2.0-SLT	0.0904	0.0552
2.0-SPF	0.0609	0.0506
2.0-SPFR	0.0569	0.0413

Table 3.2: RMS-deviation (in pmol mol^{-1}) of various model results from observed SF_6 station data considering all locations listed in Table 3.1 (ALL), and considering only locations within the marine boundary layer (MBL, including Izaña)

with the same semi-Lagrangian advection scheme. Furthermore, compared to the other 3-D models [*Denning et al.*, 1999, cf.], MATCH (with the exception of the uncorrected 2.0-SPF configuration) performs better for the MBL observations than for the entire set of observations.

Among the various MATCH configurations the 2.0-SPFR configuration predicts SF_6 mole fractions that are closest to the observations. Figure 3.4 shows the comparison to the semi-Lagrangian configurations. The 2.0-SLT configuration predicts higher SF_6 surface mole fractions throughout the NH than the 2.0-SPFR configuration, in particular within the source regions; obviously the transport out of the source regions is less effective than that calculated with the 2.0-SPFR configuration. The

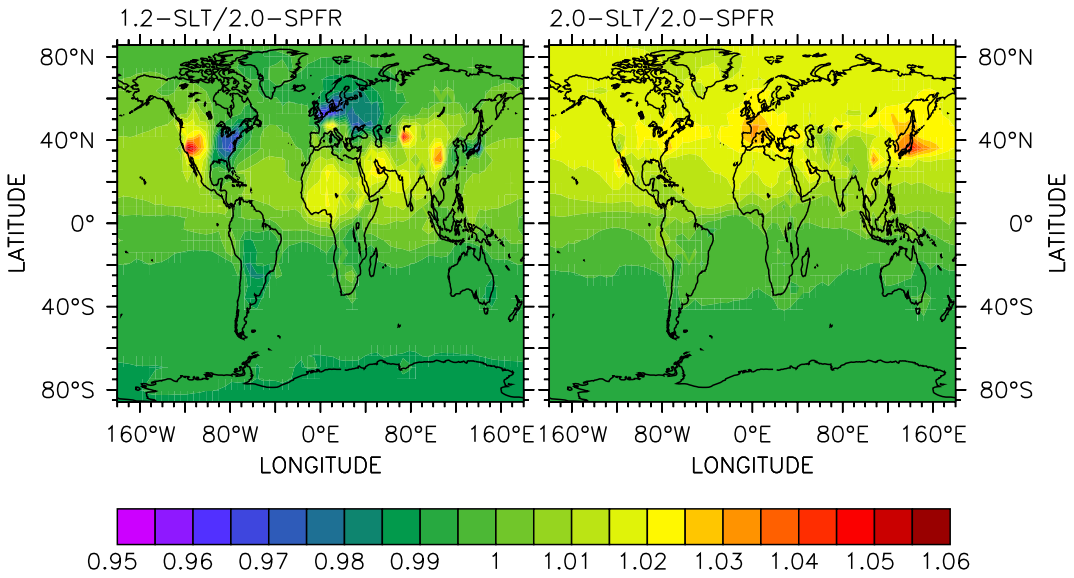

Figure 3.4: Ratio of simulated SF_6 surface mole fractions between two Semi-Lagrangian model configurations and the rescaled SPITFIRE (SPFR) configuration.

situation is more complicated for the 1.2-SLT configuration. Compared to the 2.0-SPFR configuration, the 1.2-SLT configuration predicts higher values of the SF_6 surface mole fraction in the northern hemisphere tropics and mid-latitudes except around the source regions of eastern North America and Europe, where the 1.2-SLT calculated SF_6 mole fraction is lower. In other source regions, such as western North America and China, the surface mole fraction is higher (in the same way as calculated with the 2.0-SLT configuration compared to the 2.0-SPFR configuration). In the source region of Japan, however, there is no significant difference between the 1.2-SLT and 2.0-SPFR configuration.

3.3.1.2 Longitudinal transect Measurements of SF_6 during the TROICA-2 (**Tr**ans-Siberian **O**bservations **I**nto the **C**hemistry of the **A**tmosphere) campaign (July 25 – August 12, 1996) on board a Trans-Siberian Railroad wagon [*Crutzen et al.*, 1998] provide a longitudinal transect of the surface SF_6 mixing ratio. Since these measurements extend eastward from the European source region across Eurasia, the observed west-east gradient provides a means to evaluate the model's zonal transport properties. The simulated mole fractions are linearly extrapolated for 3 years, using the model's average growth rate along the transect in 1993. This is necessary, because the observations are from 1996, the simulations, however, for the year 1993. The trend is averaged along the transect, because the simulated growth rate itself shows a longitudinal gradient, with the maximum near the western source region. Using a longitude dependent growth rate for the time extrapolation would

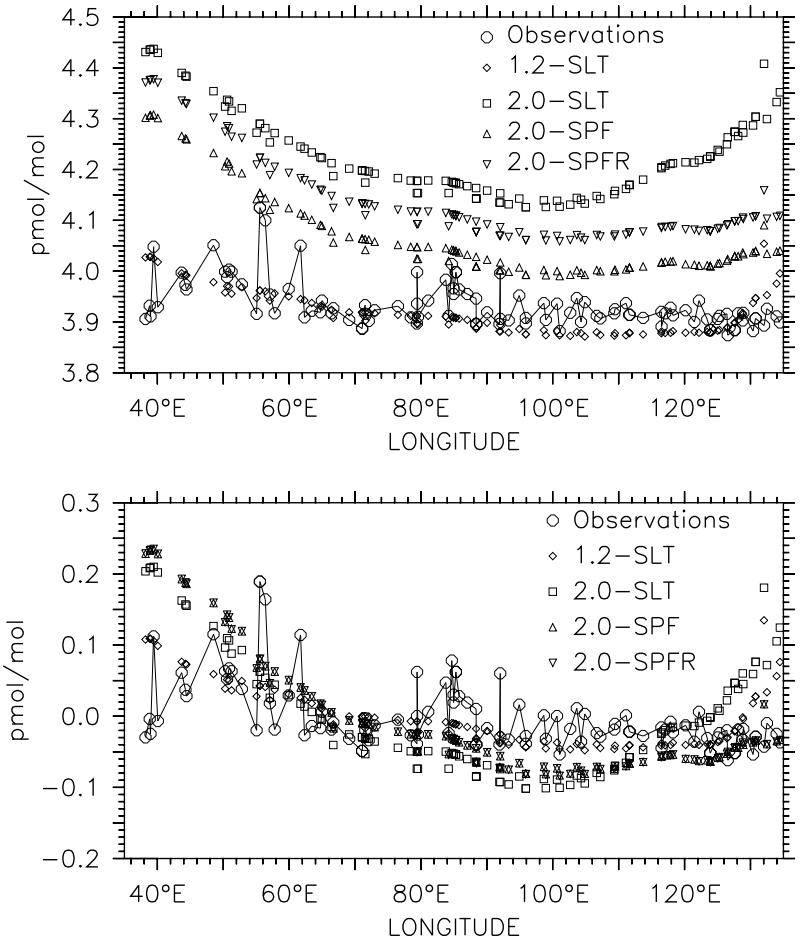

Figure 3.5: Simulated and observed longitudinal gradient of SF_6 mole fraction across Eurasia (upper), and deviation of SF_6 mole fractions from the respective simulated and observed across-transect averages (lower). Measurements were taken during the TROICA-2 campaign (July 25 through August 12, 1996). The simulated mixing ratios have been obtained by temporal and spatial interpolation of the monthly mean model output to the measurement dates and coordinates of the observations. The model results were further extrapolated from 1993 to 1996, using each configuration's transect-average linear trend of 1993, derived from 12 monthly mean values.

therefore result in an artificially steepened west-east gradient [*Denning et al.*, 1999]. Figure 3.5 shows the result obtained with the MATCH configurations compared to the observations. The absolute level along the transect is best reproduced by the 1.2-SLT configuration and overestimated by all others. This may be due to an overestimate of the growth rate along the transect that is used for the time extrapolation. None of the configurations capture the local extrema of the observational data, which may be attributed to local sources and/or different origins of the air mass sampled [*Crutzen et al.*, 1998] that are not resolved by the model. Furthermore, short term variations are averaged out in the monthly mean model output. The deviation from

the longitudinal mean (Figure 3.5, lower) shows a surprisingly low west-east gradient of the observations, which can possibly be explained by significant Siberian SF_6 emissions, e.g. along the railroad itself [*Denning et al.*, 1999]. Since these (small scale) local emissions are not prescribed in the model emission map (Figure 3.1), the model tends to overestimate the west-east gradient. The 2.0-SLT configuration, and to a lesser extend also the 1.2-SLT configuration show a steep positive SF_6 gradient from 110^{o}E eastward, which results most probably from a too strong zonal transport of SF_6 out of the eastern source regions. The overall model performance concerning the prediction of the east-west gradient can be quantified again by the RMS-deviation of the model results from the observations ($n = 113$). To account for the uncertainty in the absolute values, the RMS-deviation is, however, calculated from the longitudinal mean reduced quantities (i.e., χ in Eq. (3.2) is replaced by $\Delta\chi = \chi - \bar{\chi}$, where $\bar{\chi}$ denotes the longitudinal mean, cf. Figure 3.5). The results for the 1.2-SLT, 2.0-SLT, 2.0-SPF, and 2.0-SPFR configurations are 0.0510, 0.0835, 0.0735, and 0.0736 pmol mol^{-1} respectively.

3.3.1.3 Seasonal cycle Since SF_6 can be regarded as inert and its source is rather steady (continuously increasing, however without a seasonal cycle, see section 3.1), temporal variations of the mole fraction on top of the long-term positive trend can only be attributed to variations in transport. *Denning et al.* [1999] reported the detrended seasonal cycle of SF_6 measurements at Izaña (20^{o}N, 16^{o}W, 2367 m msl (mean sea level)) and the Antarctic coastal station Neumayer (71^{o}S, 8^{o}W, 42 m msl). These measurements can be used to evaluate the model's transport seasonality at the two locations. Figure 3.6 shows the detrended observed seasonal cycle at these two stations and the respective model predictions of various MATCH configurations. The original model results are detrended by first subtracting a linear trend of 0.201 pmol mol^{-1} yr^{-1} and then subtracting the resulting annual mean. The seasonal cycle at Izaña shows two maxima in spring and autumn with minima in summer and winter. Trajectory analyses showed that both maxima coincide with periods of elevated westerly air mass transport from latitudes higher than 40^{o}N, while the minima reflect transport of air from Africa [*Denning et al.*, 1999]. The SF_6 seasonality at Neumayer is somewhat weaker with a well-defined maximum in the SH spring and minimum values in SH autumn (February through April). *Denning et al.* [1999] explain this seasonality with the periodicity of SF_6 input into the SH and an additional phase lag determined by the transport time from the equator to the high latitude station. All MATCH configurations capture the fact that the absolute seasonal amplitude is higher at Izaña than at Neumayer, however the phase is incorrectly predicted in all cases. Table 3.3 lists the RMS-deviation of the model predictions from the observations (Eq. (3.2), $n = 12$). The 1.2-SLT predictions show

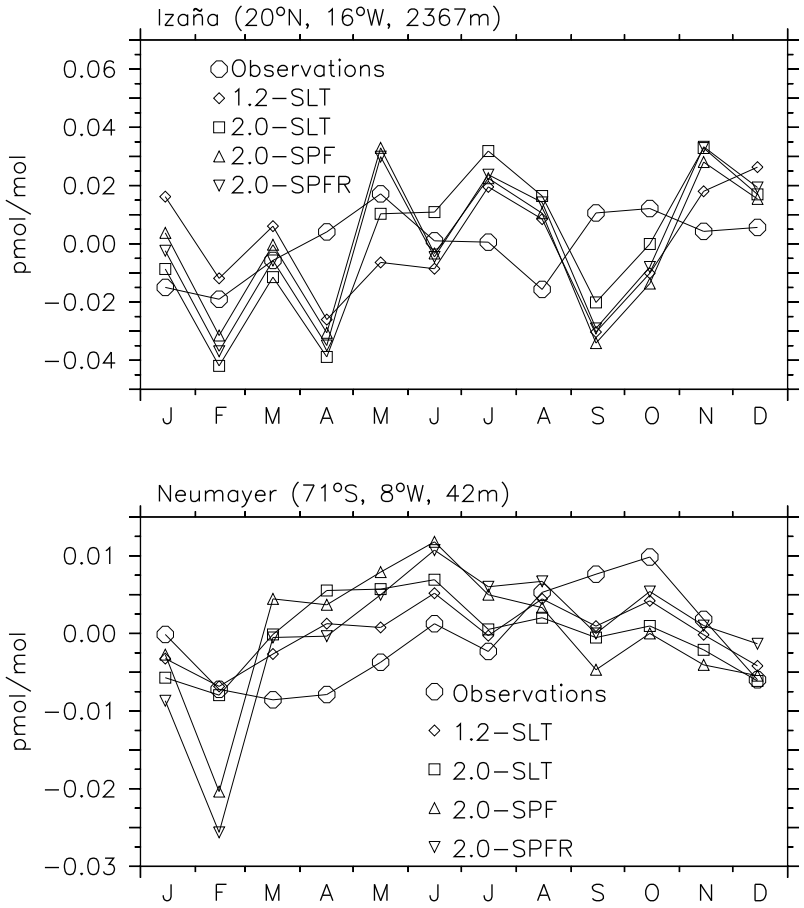

Figure 3.6: Observed and simulated detrended seasonal cycle of SF_6 at Izaña (upper) and the Antarctic station Neumayer (lower). The model simulations have been detrended as described in the text.

Model	Izaña	Neumayer
1.2-SLT	0.0232	0.00458
2.0-SLT	0.0235	0.00697
2.0-SPF	0.0233	0.00944
2.0-SPFR	0.0235	0.00851

Table 3.3: RMS-deviation (in pmol mol^{-1}) of various model simulations from detrended observed seasonal cycle of SF_6 at Izaña (20°N, 16°W, 2367 m msl) and Neumayer (71°S, 8°W, 42 m msl). Model results have been detrended as described in the text.

the smallest deviation from the observations at both locations, although at Izaña the variation between the configurations is small. At Neumayer the predictions of the two semi-Lagrangian configurations are closer to the observations than those of the SPITFIRE configurations.

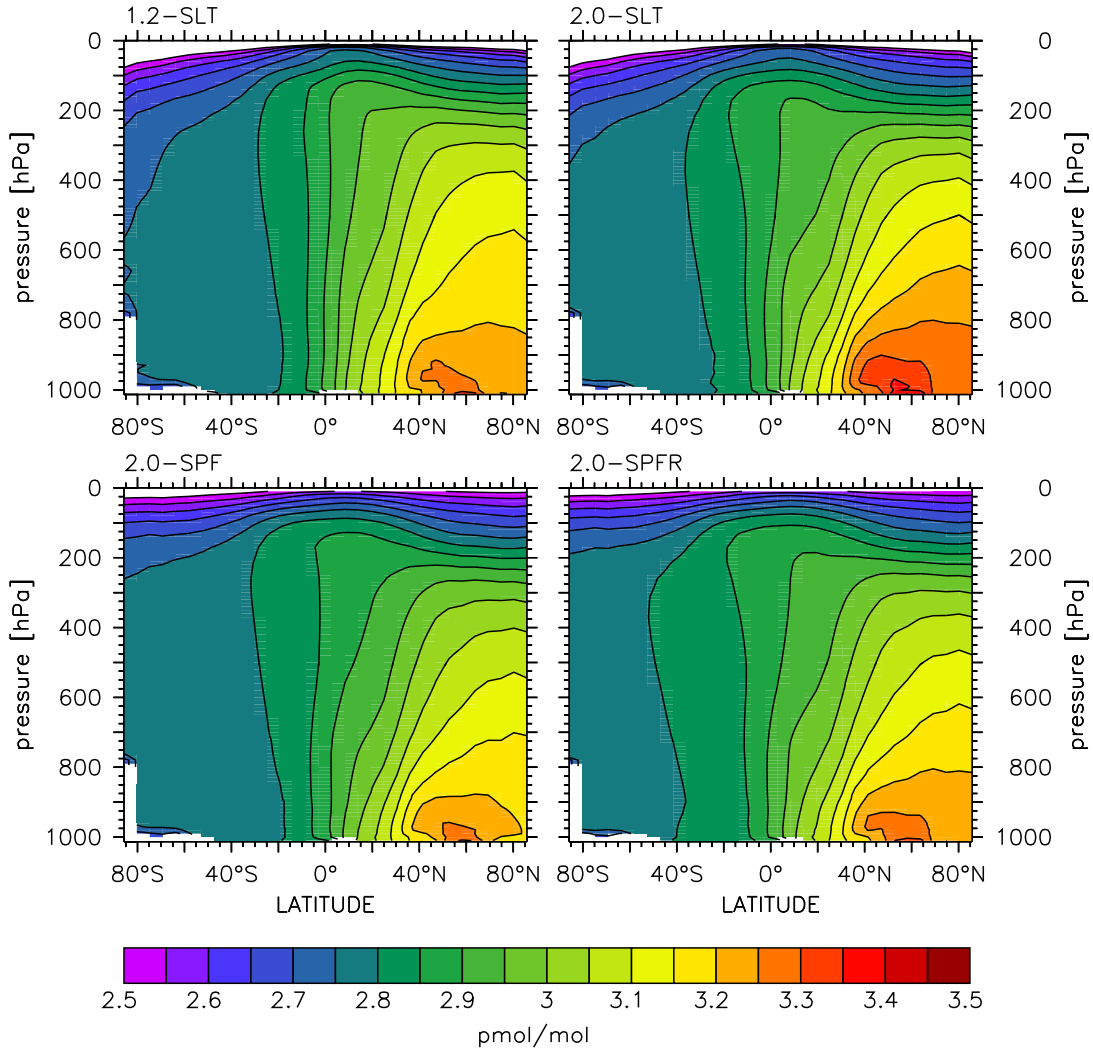

Figure 3.7: Simulated annual zonal mean latitude-pressure cross-section of SF_6 (1993) for various model configurations.

3.3.2 Vertical distribution of simulated SF_6

Model predictions of the annual zonal mean vertical distribution of SF_6 are depicted in Figure 3.7. The strongest vertical gradient over the NH source region is predicted by the 2.0-SLT configuration, however, the difference among the MATCH configurations is rather small compared to the difference between other models [cf. *Denning et al.*, 1999]. The simulated pole-to-pole difference in the mid-troposphere (around 600 hPa) is 0.41, 0.42, 0.36, and 0.36 pmol mol^{-1} for the 1.2-SLT, 2.0-SLT, 2.0-SPF, and 2.0-SPFR configurations, respectively. Predictions by the models tested in *Denning et al.* [1999] range from 0.15 to 0.40 pmol mol^{-1}. Figure 3.8 shows the relative difference between the two advection schemes employed. The semi-

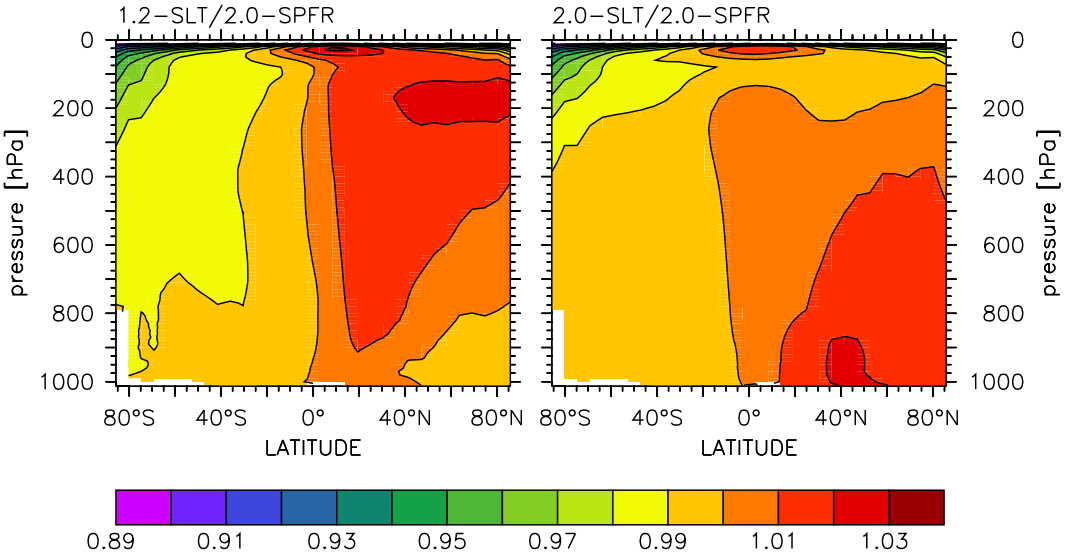

Figure 3.8: Annual zonal mean ratio of SF_6 simulated with two semi-Lagrangian model configurations to SF_6 predicted by the rescaled SPITFIRE (2.0-SPFR) configuration (1993).

Lagrangian transport from the NH to the SH is weaker than that of the SPITFIRE configurations. The vertical mixing, however, is more effective in the SLT configurations, especially in 1.2-SLT. To be consistent with the above result, namely that the SLT configurations tend to predict higher SF_6 mixing ratios in the NH source regions, the "weaker" interhemispheric mixing of the SLT configurations obviously asserts more influence on the NH SF_6 surface mole fraction than the "stronger" vertical mixing. This is the case in the entire NH of the 2.0-SLT configuration, however in the 1.2-SLT configuration it only applies south of 40^oN. At higher latitudes the stronger vertical mixing reduces the surface mixing ratio of SF_6 more than the reduced interhemispheric exchange (compared to the 2.0-SPFR configuration) enhances it. This explains the more complicated structure of the surface mixing ratio difference between 1.2-SLT and 2.0-SPFR (Figure 3.4).

In the context of the models tested in *Denning et al.* [1999] all MATCH configurations belong to the category of models with a rather weak vertical mixing. However the generalized thesis of *Denning et al.* [1999] that models with weaker vertical mixing generally accumulate more SF_6 in the NH lower stratosphere and therefore predict a stronger surface latitudinal gradient, which is in the remote MBL closer to the observed gradient than models with a stronger vertical mixing, only holds in comparison of the MATCH ensemble to all other tested models. On a closer look, however, this thesis has to be partly extended, and the combination of interhemispheric exchange and vertical mixing has to be taken into account, rather than only vertical mixing. This can be seen from the results obtained with the various

MATCH configurations. The 2.0-SPFR configuration shows a weaker vertical mixing than the SLT configurations (Figure 3.8) and best predicts the remote MBL latitudinal gradient (Table 3.2). However the remote MBL latitudinal gradient is steepest (and overestimated) in the 2.0-SLT version (Figure 3.3), which simulates a more intense vertical mixing.

Denning et al. [1999] further found that models with weaker vertical mixing overestimate systematically SF_6 at continental sites in general, which is also true for the MATCH ensemble (Table 3.1, Figure 3.2). However, among the individual MATCH configurations this simplification does not hold. The 2.0-SPFR configuration predicts the SF_6 mole fraction at the continental sites better than the SLT configurations, although its vertical mixing is weaker (Figure 3.8).

The annual mean SF_6 mole fraction in the NH (averaged over 0^o to 90^oN) decreases from 1000 hPa to 200 hPa by 0.16, 0.24, 0.20, and 0.20 pmol mol^{-1} in the 1.2-SLT, 2.0-SLT, 2.0-SPF, and 2.0-SPFR configuration respectively. The SH mean differences are 0.018, 0.007, 0.002, and 0.002 pmol mol^{-1}, respectively. Thus in contrast to 10 of 11 models tested in *Denning et al.* [1999], the MATCH configurations do not predict a reversed vertical gradient (SF_6 increasing with height) in the SH. Therefore, the interhemispheric exchange cannot directly be attributed to a definite altitude band, as can also be seen from Figure 3.7.

3.3.3 Interhemispheric exchange times

As indicated by Figure 3.8 and the above results there are differences in the interhemispheric exchange among the various MATCH configurations. A suitable parameter to characterize this exchange is the interhemispheric exchange time τ_{ex}, which is the time scale for the equilibration of tracer mass differences between two connected boxes representing the hemispheres.

Following *Denning et al.* [1999], the annual mean interhemispheric exchange time can be calculated under assumption of the two boxes being in steady state

$$\tau_{ex}^{(s)} = \frac{2\Delta M}{\Delta S} \quad , \tag{3.3}$$

or on an instantaneous basis as

$$\tau_{ex}^{(i)} = \frac{2\Delta M}{\Delta S - d(\Delta M)/dt)} \quad , \tag{3.4}$$

where $\Delta M = M_N - M_S$ is the SF_6 mass difference between NH and SH, and ΔS the respective difference of the emitted SF_6 masses. ΔM is calculated by integrating the

Model	$\tau_{ex}^{(s)}$	$\tau_{ex}^{(i)}$
1.2-SLT	1.17 ± 0.07	1.34 ± 0.23
2.0-SLT	1.04 ± 0.08	1.22 ± 0.26
2.0-SPF	0.85 ± 0.06	0.97 ± 0.18
2.0-SPFR	0.86 ± 0.06	0.97 ± 0.18

Table 3.4: SF_6 based interhemispheric exchange times (years) estimated with various model configurations. The standard deviation of 12 monthly average values from the annual mean is given as error estimate.

uncorrected (cf. Eq. (3.1)) local SF_6 mixing ratio χ predicted by the model times the air mass of the grid box

$$M = \frac{1}{g} \sum_{i,j,k} \chi_{i,j,k} \Delta p_{i,j,k} \quad , \tag{3.5}$$

where the indices i, j, k count the grid boxes along longitude, latitude, and altitude respectively. The uncorrected mixing ratio χ is used, since only then the prescribed SF_6 emissions and the model predicted mole fractions are consistent. The results are listed in Table 3.4. For all configurations, the steady state assumption ($\tau_{ex}^{(s)}$, Eq. (3.3)) results in a 12% to 15% lower exchange time compared to the exchange time based on instantaneous values ($\tau_{ex}^{(i)}$, Eq. (3.4)). The 1.2-SLT configuration calculates the slowest interhemispheric exchange. This is in agreement with Figure 3.8. However, in contrast to the results of *Denning et al.* [1999] the configuration with the strongest vertical mixing (1.2-SLT) does not show the lowest interhemispheric exchange time. τ_{ex} of the SPITFIRE configurations are even lower, although the vertical mixing is weaker than in the SLT configurations. Finally, it should be noted that the interhemispheric exchange time of the SPITFIRE configuration is not significantly changed by the global tracer mass rescaling correction.

3.4 Discussion

The model evaluation part of the analysis depends on a limited number of observations that have to be assumed to be representative of a certain atmospheric domain, e.g. as latitudinal average, in order to provide global estimates. Therefore, the gradient derived from the MBL locations can only be regarded as a rough estimate of the overall interhemispheric gradient, because longitudinal variations (cf. Figure 3.2) are not taken into account by this approach, and the result may depend on the choice of sampling locations. Therefore, the model output at the sampling locations of the observations was used for consistency.

A further problem is that observations are included, which do not fall within the simulated time interval, as is the case for the Trans-Siberian Railroad observations.

In this case, either model results or measurements have to be extrapolated in time before comparison. The extrapolation used here depends on the model predicted growth rate averaged along the transect, implying the assumption that this growth rate is constant for 3 years. Furthermore, this simulated trend is only derived from 12 monthly mean values at each location in 1993 and therefore may be not well defined. *Denning et al.* [1999] already noted that for these reasons, a comparison of the extrapolated model results with the TROICA-2 observational data should be made with caution. The simulated data along the Trans-Siberian transect suffer further from possible unresolved local SF_6 sources along the rail track, that are indicated by the variability of the observations, and are not present in the model results, due to the coarse time-resolution (1 month) of the model output.

The lack of measured altitude profiles of SF_6 complicates a complete identification of the relevant processes. For instance, the combination of a too strong vertical mixing combined with a likewise too strong zonal mixing can probably explain the good agreement between the 1.2-SLT predictions and the observations along the Trans-Siberian Railroad. SF_6 is effectively transported from the eastern and western source regions to central Siberia, and lifted there to higher altitudes. The reputedly good model performance results then from compensating shortcomings.

Because of the long lifetime and the inert character of SF_6 only a moderate seasonal cycle can be detected in the SF_6 mixing ratio. Furthermore, the monthly mean observations presented here are estimated to be accurate to within 0.01 pmol mol^{-1} [*Denning et al.*, 1999]. Therefore, the comparison of seasonality between model and observations (Figure 3.6) should not be over-interpreted.

As discussed in *Denning et al.* [1999] and references therein, the interhemispheric exchange time (τ_{ex}) is a useful quantity because it collapses all transport mechanisms into a single parameter for comparison of models among each other as well as with observations. However, its value depends on the method of calculation, and is sensitive to the latitudinal distribution of the tracer emission [*Denning et al.*, 1999, and references therein]. Nevertheless, it is still useful for model inter-comparison, provided that the tracer related boundary conditions are the same in all models. Here only the 3-D mass based exchange time was calculated for model inter-comparison, because *Denning et al.* [1999] showed that an interhemispheric exchange time based on ground observations / model results is a rather poor measure of true interhemispheric mixing.

The global tracer mass rescaling correction implemented in the 2.0-SPFR configuration does not alter the interhemispheric exchange time based on SF_6 compared to the uncorrected 2.0-SPF configuration. Furthermore, the relative quantities, such as the deviation from the across-transect average along the Trans-Siberian Railroad

(Figure 3.5, lower), and the detrended seasonal cycle at two selected locations (Figure 3.6) are hardly changed by the rescaling. This is in agreement with the result for inert tracers obtained in chapter 2.

3.5 Conclusions

SF_6 is a suitable tracer for testing various tropospheric transport properties of 3-D global atmospheric models, because it is quasi inert and is steadily emitted into the atmosphere.

In comparison to the models tested by *Denning et al.* [1999], the MATCH configurations employed here can be regarded as an ensemble with a rather weak vertical mixing and a long interhemispheric exchange time. The semi-Lagrangian configurations show a stronger vertical mixing and a longer interhemispheric exchange time than the SPITFIRE configurations. The interhemispheric exchange time of the uncorrected SPITFIRE configuration (2.0-SPF) is not changed when a global mass mismatch rescaling correction is included (2.0-SPFR).

All configurations tend to overestimate the SF_6 mixing ratio at continental sites within or near the source areas, however the latitudinal gradient in the marine boundary layer defined by a set of observations is reasonably well reproduced. Among the MATCH configurations, the 2.0-SPFR predictions are closest to the observations at the continental and MBL locations.

The simplified relation from *Denning et al.* [1999] that models with a weaker vertical mixing in general predict stronger surface latitudinal gradients, which are in the MBL closer to the observations does not hold in detail. The relation is not strict because it does not take into account differences in interhemispheric exchange, which cannot be attributed to differences in vertical mixing. Similarly, the overestimation of the SF_6 mixing ratio at continental sites within or near the source areas cannot solely be explained by a weaker vertical mixing.

The longitudinal gradient along the Trans-Siberian Railroad is, within its uncertainties, also reasonably well reproduced by all MATCH configurations tested. The closest agreement with the observations is obtained with the 1.2-SLT configuration, but this is possibly due to an enhanced zonal transport of SF_6 from the western and eastern source regions to central Siberia where SF_6 is moved upwards by strong vertical transport.

The small amplitude of the seasonal cycle at two selected stations is slightly overestimated by the model; all configurations fail to reproduce its phase. Since the results are similar for all configurations, this may be caused by the offline wind data that are used to calculate the advection.

In summary, the four MATCH configurations used in this thesis have been classified in the framework of a number of other "state-of-the-art" 3-D atmospheric models. None of the configurations predicts results that are fundamentally different from results of the other configurations. All results agree reasonably well with the observations so far. A decision on which configuration reproduces the observations "best" is hard to make, but the deviation between the configurations can be used to estimate the model uncertainty in further studies.

4 Assessment of global OH using CH_3CCl_3 and $CFCl_3$

Abstract. Methylchloroform (MCF, CH_3CCl_3) and tri-chloro-fluoro-methane ($CFCl_3$, F11) are atmospheric tracers of anthropogenic origin. MCF is mainly removed from the atmosphere through oxidation by OH. F11 being less reactive is primarily photolytically dissociated in the stratosphere. Long term simulations (40 years) with prescribed emission fields, OH distributions, and photolysis rates are performed with various configurations of the 3-dimensional model MATCH. The results are compared to time series of MCF and F11 observations at 5 locations. The atmospheric lifetime of MCF is calculated and compared with previously published results in order to evaluate the prescribed OH abundance. The simulated F11 mixing ratio is used to estimate the uncertainty of the method arising from uncertainties in the simulated transport. The global average OH concentration can be constrained by the available MCF observations. However, evaluation of the OH distribution on smaller scales, e.g., on a hemispheric scale, is limited, since the lifetime of MCF is long compared to the interhemispheric exchange time, and latitudinal gradients are therefore dominated by the interhemispheric exchange.

4.1 Introduction

CH_3CCl_3 (1,1,1-trichloroethane or methylchloroform, MCF) is an atmospheric compound of anthropogenic origin. Its global emission history is claimed to be known with high accuracy [*Midgley*, 1989; *Midgley and McCulloch*, 1995]. Emissions started around 1950 and declined after 1990, because MCF was restricted under the Montreal Protocol for the protection of the ozone layer. MCF is mainly removed from the atmosphere via oxidation by the OH radical [*Singh*, 1977] and by photolytic destruction. A small fraction (5-11%, *Butler et al.* [1991]) is dissolved in the oceans. The tropospheric lifetime of MCF was first estimated by *Singh* [1977] to be 7.2 ± 1.2 years.

Long term measurements (from 1978 on) of the MCF mixing ratio at 5 locations have been carried out within the Atmospheric Lifetime Experiment / Global Atmospheric Gases Experiment (ALE/GAGE) [*Prinn et al.*, 1983b,a]. "Polluted" events, i.e. measurements taken downwind of the continental source areas are filtered out by a screening procedure. This procedure should ensure the "remote" character of the time-series provided. *Prinn et al.* [1987] estimated from these measurements an average tropospheric lifetime of MCF (1000 hPa to 200 hPa) of 6.3 $(+1.2, -0.9)$ years. This was later revised [*Prinn et al.*, 1995] and constrained to be 4.6 ± 0.3 years. *Prinn et al.* [1995] also deduced a trend in OH of $0.0 \pm 0.2\%$ yr^{-1} based on the ALE/GAGE MCF measurements using an inversion technique. A dispute about

calibration issues and several aspects of the method used by *Prinn et al.* [1987] and *Prinn et al.* [1995] to constrain atmospheric OH and its global trend can be found in literature [*Spivakovsky et al.*, 1990; *Hartley and Prinn*, 1991; *Spivakovsky et al.*, 1991; *Cunnold and Prinn*, 1991; *Spivakovsky*, 1991]. *Krol et al.* [1998] performed an independent modeling study, using a Monte Carlo technique involving a 3-D global atmospheric model. They found that the tropospheric (1000 hPa - 100 hPa) lifetime of MCF has changed from 4.7 ± 0.1 years in 1978 to 4.5 ± 0.1 years in 1993, and deduced a positive OH trend of $0.46 \pm 0.6\%$ yr^{-1} between 1978 and 1993. These results are also based on the ALE/GAGE measurements.

Since the estimated lifetime of MCF is long compared to global tropospheric mixing times, its distribution can be expected to be almost homogeneous within a hemisphere, with low variability. Indeed, the measurements of *Prinn et al.* [1983b] and *Prinn et al.* [1983a] show a rather small seasonal cycle. A possible asymmetry between the NH and SH MCF abundance can be attributed to an asymmetry of the sources (most sources are located in the NH), and possibly also to a speculative asymmetry in the OH abundance between NH and SH. *Montzka et al.* [2000] used the dramatic decline of MCF emissions after 1990 and used a simple 2-box model to estimate a global MCF lifetime of 5.2 $(+0.2, -0.3)$ years, a SH MCF lifetime of 4.9 $(+0.2, -0.3)$ years, and deduced that OH is $15 \pm 10\%$ higher south of the intertropical convergence zone (ITCZ). The latter finding is very similar to earlier results of *Brenninkmeijer et al.* [1992] based on ^{14}CO measurements.

Another industrial gas closely related to MCF is $CFCl_3$ (F11). A spatial distribution of its emission into the atmosphere is given by *McCulloch et al.* [1994], the global emission history by *Fisher et al.* [1994]. The oxidation of F11 by OH is much less effective than that of MCF, and photodissociation in the stratosphere is relatively more important for its removal from the atmosphere than for MCF. Consequently, its atmospheric lifetime is longer. Estimates of the lifetime of F11 (and further references) are given, e.g., in *Singh* [1977] and *Cunnold et al.* [1983, 1994], and range from 36 to 78 years with a large uncertainty. It is important to note, however, that the values given in these studies are not necessarily comparable, since different definitions of "atmospheric lifetime" have been used [*Cunnold et al.*, 1983].

Both MCF and F11, along with other HCFCs, can be used in standard tests for evaluation of model predicted atmospheric OH [e.g., *Spivakovsky et al.*, 1990; *Krol et al.*, 1998; *Spivakovsky et al.*, 2000]. Incorporating the known emission and reaction rates into the model, the model predictions of the species distribution can be compared with measurements to provide information about the modeled atmospheric oxidation capacity. In this chapter this test for various MATCH configurations is discussed. The focus is on the sensitivity of model predictions of F11 and MCF to variations in the realization of the model's tracer transport dynamics. OH distributions and

Year		Year		Year	
1951	0.1	1971	170.0	1991	636.0
1952	0.2	1972	214.0	1992	592.0
1953	0.9	1973	266.0	1993	387.0
1954	0.6	1974	305.0		
1955	7.5	1975	309.0		
1956	13.0	1976	382.0		
1957	19.0	1977	462.0		
1958	20.0	1978	513.0		
1959	29.0	1979	511.0		
1960	35.0	1980	537.0		
1961	37.0	1981	548.0		
1962	54.0	1982	522.0		
1963	55.0	1983	536.0		
1964	57.0	1984	585.0		
1965	75.0	1985	594.0		
1966	105.0	1986	603.0		
1967	133.0	1987	623.0		
1968	147.0	1988	666.0		
1969	156.0	1989	690.0		
1970	149.0	1990	719.0		

Table 4.1: Global CH_3CCl_3 emissions in 10^6g from 1951 to 1993 (1951-1969: *Prinn et al.* [1987], 1970-1993: *Midgley and McCulloch* [1995]).

photolysis rates are prescribed. The aim is to estimate to what extent global OH can be constrained with MCF and F11, when an uncertainty is assigned to the modeled transport. This will provide a minimum error estimate of the modeled OH distribution due to uncertainties in the model's dynamics.

4.2 Model setup

As in *Krol et al.* [1998], the global emissions of MCF are taken from the estimates of *Prinn et al.* [1987] (1951-1969) and *Midgley and McCulloch* [1995] (1970-1993), and are listed in Table 4.1. MCF emissions are distributed globally as in *Krol et al.* [1998], according to *Midgley and McCulloch* [1995] among the countries and within the countries according to the population density used by *Fung et al.* [1991]. The resulting emission map averaged onto the model grid is depicted in Figure 4.1 (left). From 1980 on, the global emissions are subdivided into six distinct regions as reported by [*Midgley and McCulloch*, 1995], and listed in Table 4.2. The implementation of these regions on the model grid is shown in Figure 4.2. Within

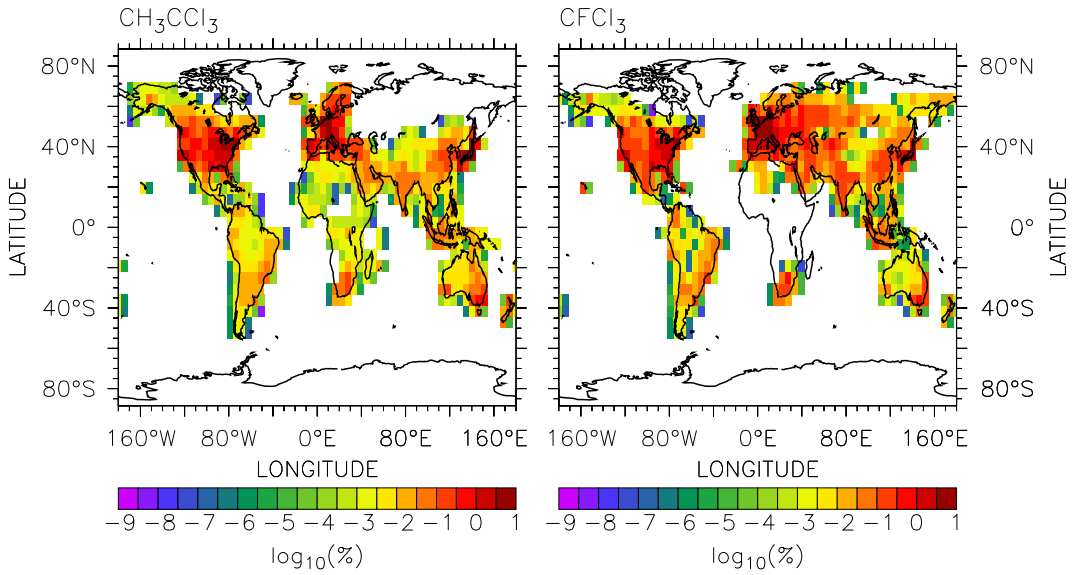

Figure 4.1: Relative distribution of CH_3CCl_3 (left) and $CFCl_3$ (right) emissions averaged on the MATCH grid (32 latitudes $\times$ 64 longitudes).

Year	NA	EU	FE	NM	NT	SH
1980	270	152	86	2	4	23
1981	262	161	96	2	6	21
1982	233	163	98	1	6	21
1983	233	162	112	2	7	20
1984	260	162	129	4	9	21
1985	249	169	143	3	8	22
1986	247	164	147	3	16	26
1987	249	162	166	5	16	25
1988	266	157	190	9	18	26
1989	259	164	210	11	20	26
1990	271	153	242	8	25	20
1991	215	143	211	8	37	22
1992	204	116	191	8	54	19
1993	126	106	94	9	29	23

Table 4.2: Regional CH_3CCl_3 emissions in 10^6g from 1980 to 1993. (*Midgley and McCulloch* [1995], NA: North America, EU: Europe, FE: Far East, NM: Northern Mid-latitudes (30^oN-90^oN), NT: Northern Tropics (0-30^oN), SH: Southern Hemisphere)

each of the six regions the respective total emissions are distributed according to the relative emission distribution among countries and according to the population density (Figure 4.1).

Global emissions of F11 are taken from *Fisher et al.* [1994] and are listed in Ta-

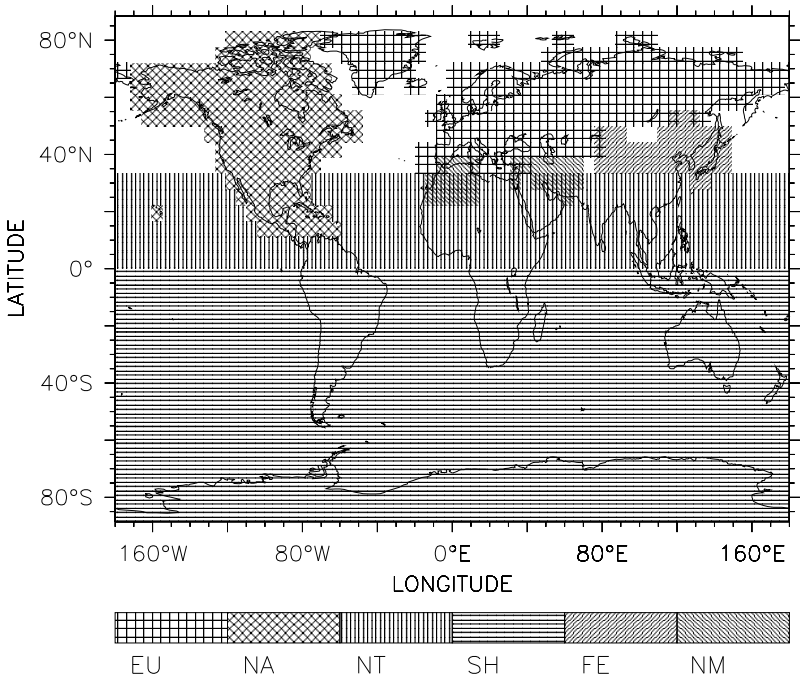

Figure 4.2: Regions of CH_3CCl_3 emissions after 1980 as they appear on the model grid (*Midgley and McCulloch* [1995], NA: North America, EU: Europe, FE: Far East, NM: Northern Mid-latitudes (30^{o}N-90^{o}N), NT: Northern Tropics (0-30^{o}N), SH: Southern Hemisphere).

ble 4.3. The emission distribution of F11 is obtained from a Global Emission Inventory Activity (GEIA) compilation [*Cunnold*, 1995] based on emissions provided by *McCulloch et al.* [1994]. An area-weighted average distribution computed for the model grid is shown in Figure 4.1 (right).

OH fields are prescribed as monthly averages (see section 1.4). The oxidation of MCF and F11 are parameterized as

$$CH_3CCl_3 + OH \rightarrow \text{products} \tag{4.1}$$

$$k_{\text{MCF}} = 1.8 \times 10^{-12} exp(\frac{-1550}{T}), \tag{4.2}$$

and

$$CFCl_3 + OH \rightarrow \text{products} \tag{4.3}$$

$$k_{\text{F11}} = 1.0 \times 10^{-12} exp(\frac{-3700}{T}) \tag{4.4}$$

respectively, where T is the temperature in Kelvin. The rate coefficients are taken from *DeMore et al.* [1997].

Photolysis rates of MCF and F11 are taken from calculations with a 2-D model (Ch. Brühl, unpublished data, personal communication, 1998-2000) and are also

Year		Year		Year		Year	
		1951	7.7	1971	229.7	1991	233.0
		1952	11.1	1972	259.1		
		1953	15.1	1973	296.6		
		1954	18.7	1974	327.1		
		1955	23.1	1975	318.4		
		1956	28.9	1976	325.4		
		1957	32.4	1977	313.8		
1938	0.1	1958	30.4	1978	294.7		
1939	0.1	1959	31.2	1979	275.9		
1940	0.1	1960	40.9	1980	264.5		
1941	0.1	1961	52.6	1981	263.7		
1942	0.1	1962	65.9	1982	257.1		
1943	0.2	1963	80.6	1983	273.4		
1944	0.2	1964	95.7	1984	295.1		
1945	0.3	1965	109.1	1985	308.3		
1946	0.6	1966	122.3	1986	326.8		
1947	1.3	1967	138.8	1987	345.8		
1948	2.3	1968	158.1	1988	353.6		
1949	3.8	1969	183.8	1989	304.7		
1950	5.5	1970	209.0	1990	255.2		

Table 4.3: Global CCl_3F emissions in 10^6g from 1938 to 1991 [*Fisher et al.*, 1994].

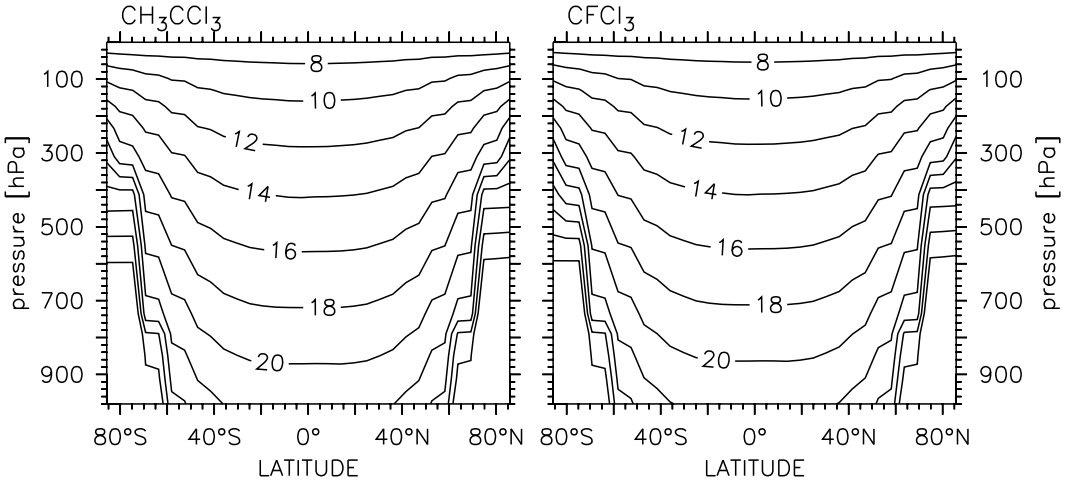

Figure 4.3: Negative decadal logarithm of the photolysis rates (in units s^{-1}) of CH_3CCl_3 (left) and $CFCl_3$ (right).

prescribed as monthly averages. Zonal symmetry is assumed. Annual averaged values of the (almost identical) photolysis rates are shown in Figure 4.3.

The uptake of MCF in ocean water is parameterized following *Krol et al.* [1998], who in turn, followed *Kanakidou et al.* [1995]. The oceanic loss term is

$$L_o = \epsilon \frac{HRT_o}{\Delta Z_1}(\Delta Z_2 k_H + (D_2 k_H)^{\frac{1}{2}}) \tag{4.5}$$

accounting for the height of the atmospheric mixed layer (ΔZ_1), the height of the oceanic mixed layer (ΔZ_2), and the ocean temperature (T_o). ϵ is a flag (0 or 1) for land/ocean on the model grid, "H is Henry's law coefficient (mol atm^{-1}), R is the gas constant (0.083 atm mol^{-1}), k_H is the hydrolysis rate (s^{-1}), and D_2 is the diffusion coefficient in the deep (non-mixed layer) ocean (1.7 cm^{-2} s^1). The temperature dependent hydrolysis rate k_H and Henry's law coefficient H of MCF are calculated through [*McLinden*, 1989; *Gerkens and Franklin*, 1989]:

$$H = \frac{1013}{133.5} exp(-20.29 + \frac{4655}{T_o}) \tag{4.6}$$

$$k_H = 3.1 \times 10^{-8} exp(-10000(\frac{1}{T_o} - \frac{1}{298})). \tag{4.7}$$

T_o is given in Kelvin, and the value for H is corrected for the effect of sea salt by multiplying with a factor of 0.8 [*McLinden*, 1989] " [*Krol et al.*, 1998].

Ocean mixed-layer depth, ocean temperatures, and the height of the atmospheric mixed layer are prescribed as time varying fields (monthly averages). The ocean mixed-layer depth was obtained from the Max-Planck-Institute (MPI) Hamburg ocean model (data provided by M. Krol, IMAU, Utrecht, see *Krol et al.* [1998]). The ocean temperatures were taken from the Integrated Global Ocean Series System (IGOSS) Products Bulletin for the year 1993 [*Reynolds and Smith*, 1994]. Finally, the height of the atmospheric mixed layer was pre-calculated with MATCH, according to *Holtslag and Boville* [1993], using the NCEP-reanalysis data for 1993 [*Kalnay et al.*, 1996], archived as monthly averages, and used offline afterwards.

All model simulations discussed in this chapter are performed with the NCEP reanalysis meteorology of 1993 [*Kalnay et al.*, 1996]. The first simulation was with the 1.2-SLT configuration for the years 1950 to 1991 for F11 and to 1993 for MCF. Emissions of F11 prior to 1950 ($14.7 \cdot 10^6$g, Table 4.3) were emitted in 1950. This introduces an offset, but due to the long atmospheric lifetime of F11 and increasing emissions, the resulting error for atmospheric inventories later than 1978 (when the ALE/GAGE measurements begin) is less than the uncertainty in the emission estimates and therefore negligible. Further simulations with the 2.0-SLT, 2.0-SPF, and 2.0-SPFR configuration for the years 1970 to 1991/1993 were initialized with the tracer distribution of the 1.2-SLT simulation for Dec 1969 (monthly average). A second 2.0-SLT simulation was performed with the same initialization and for the

same time interval, but using the OH-2 distribution instead of the standard OH-1 distribution (see section 1.4).

Although the available ALE/GAGE measurement time series extends until 1997, the model simulations are only performed until 1991 for F11 and 1993 for MCF respectively because global emission data of the two species were not available thereafter.

4.3 Model results

The model simulations provide overall estimates of global atmospheric timescales for the tracer species, such as the global atmospheric lifetime. Furthermore, the model predictions are compared to the time series of the ALE/GAGE measurements.

4.3.1 Atmospheric lifetime of CH_3CCl_3 and $CFCl_3$

The change of mass M of a first order decaying tracer in the atmosphere can be described by

$$\frac{dM}{dt} = S - \frac{M}{\tau_l} \ , \tag{4.8}$$

where S is the source strength (in g yr^{-1}) and τ_l the atmospheric lifetime (in years). If the atmosphere is represented by two hemispheric boxes, the change of tracer mass in each hemisphere can be formulated respectively:

$$\frac{dM_{N,S}}{dt} = -\frac{M_{N,S}}{\tau_{N,S}} \mp \frac{(M_N - M_S)}{\tau_{ex}} + S_{N,S} \ , \tag{4.9}$$

where the indices N and S denote the NH and SH respectively. In case of a NH-SH asymmetry of the tracer distribution, the interhemispheric exchange time τ_{ex} has to be taken into account. The negative sign is assigned to the second term of the NH equation, and the positive sign to the second term in the SH equation respectively. $\tau_{N,S}$ are the hemispheric lifetimes of the tracer. For a totally inert tracer $(\tau_{N,S})^{-1} = 0$. This assumption was made in section 3.3.3 to deduce the model predicted interhemispheric exchange time from SF_6 simulations (cf. Eq. (3.3), $dM_{N,S}/dt = 0$ (steady state), and Eq. (3.4) (instantaneous)). Solving Eq. (4.9) for $\tau_{N,S}$ results in

$$\tau_{N,S} = \frac{M_{N,S}}{S_{N,S} - \frac{dM_{N,S}}{dt} \mp \frac{\Delta M}{\tau_{ex}}} \ , \tag{4.10}$$

with $\Delta M = M_N - M_S$ being the tracer mass difference between NH and SH. Adding Eq. (4.9) for the NH and the SH, and inserting Eq. (4.8), the relation between the global atmospheric lifetime τ_l and the hemispheric lifetimes $\tau_{N,S}$ becomes

$$\frac{1}{\tau_l} = \frac{M_N}{M} \cdot \frac{1}{\tau_N} + \frac{M_S}{M} \cdot \frac{1}{\tau_S} \ . \tag{4.11}$$

Model	CH_3CCl_3 τ_l	τ_N	τ_S	$CFCl_3$ τ_l
1.2-SLT	4.44 ± 0.10	4.74 (4.16, 5.93)	4.08 (4.90, 3.30)	43.85 ± 2.15
2.0-SLT	4.44 ± 0.10	4.54 (3.92, 6.04)	4.31 (5.40, 3.29)	45.69 ± 2.31
2.0-SPF	3.70 ± 0.09	3.37 (3.03, 4.02)	4.24 (5.14, 3.38)	14.39 ± 0.42
2.0-SPFR	4.32 ± 0.09	3.83 (3.45, 4.59)	5.11 (6.26, 4.04)	30.59 ± 1.14
2.0-SLT (OH-2)	5.61 ± 0.14	5.37 (4.76, 6.58)	5.97 (7.34, 4.73)	45.71 ± 2.31

Table 4.4: Global atmospheric lifetime (τ_l, in years) of CH_3CCl_3 and $CFCl_3$, and hemispheric lifetimes (τ_N: NH; τ_S: SH) of CH_3CCl_3. The standard deviation of annual mean values from the long-term mean (1978-1990) is given as error estimate for τ_l. The range of hemispheric lifetimes (in parentheses) is calculated by varying the interhemispheric exchange time according to the error estimate in Table 3.4 ($\tau_{ex} + \Delta\tau_{ex}, \tau_{ex} - \Delta\tau_{ex}$).

Thus, the sum of the tracer mass weighted inverse hemispheric lifetimes is the inverse of the global lifetime.

The model predicted atmospheric lifetimes (τ_l) of MCF and F11 are listed in Table 4.4 for various MATCH configurations. The range of τ_l is estimated by the standard deviation of annual averages from the long term average (1978 to 1990). The interhemispheric exchange $\tau_{ex}^{(i)}(SF_6)$ of the respective model configuration (see Table 3.4) is used for the calculation of the hemispheric lifetimes ($\tau_{N,S}$) from Eq. (4.10). Results for $\tau_{N,S}$ for MCF are also listed in Table 4.4. The range (given in parentheses) is derived by varying the interhemispheric exchange time ($\tau_{ex}^{(i)}(SF_6) \pm \Delta\tau_{ex}^{(i)}$) within the range given in Table 3.4. It is important to note that the derived lifetime predictions are based on the total tracer loss (oxidation by OH, photodissociation, and, in the case of MCF, additionally oceanic uptake).

The model predicted MCF lifetime calculated with the OH-1 distribution is, within the uncertainty range, in agreement among all configurations (4.4±0.2 years), except for the 2.0-SPF configuration, which predicts a roughly 16% shorter lifetime. Calculation with the 2.0-SLT configuration and the OH-2 distribution results in a 26% longer MCF lifetime compared to the result obtained with OH-1. This is because the annual global mass weighted average concentration of OH in the troposphere is 30% lower for OH-2 than for OH-1 (cf. Table 1.1).

The lifetime of F11 is estimated to be 44.8 ± 2.3 years with the semi-Lagrangian configurations, and 30.6±1.1 years with the 2.0-SPFR configuration. The prediction of the 2.0-SPF configuration is only 14.4 ± 0.4 years, and therefore significantly lower. The sensitivity of the F11 lifetime to the global average OH concentration is negligible. This is to be expected, since F11 is mainly destroyed photolytically.

An estimate of the hemispheric lifetimes in terms of the above noted 2-box model is difficult, if not impossible. The results for MCF deduced from the model output

(listed in Table 4.4) show a very high sensitivity to the interhemispheric exchange time. This is understandable, because in the mass balance equation (Eq. (4.9)) the exchange term $(M_N - M_S)$ is weighted by τ_{ex}^{-1}, whereas the loss term is proportional to $\tau_{N,S}^{-1}$. If the atmospheric lifetime of a tracer $(\tau_{N,M})$ is longer than the interhemispheric exchange time (τ_{ex}), the hemispheric mass balance is dominated by the interhemispheric exchange. This is the case for MCF, where $\tau_{ex}/\tau_{N,S} \approx 1/5$, and even more for F11, where $\tau_{ex}/\tau_{N,S} \approx 1/45$. As a consequence, no reliable interhemispheric asymmetry of the lifetime of MCF and F11 can be derived with this method.

4.3.2 Simulations and measurements

The time series of MCF and F11 at five ALE/GAGE stations [*Prinn et al.*, 1983b; *Cunnold et al.*, 1983; *Prinn et al.*, 1992, 1995] are shown in Figures 4.4 and 4.5. Observational data is presented as monthly averages, error bars denote the standard deviation derived from single measurements, respectively. The dotted lines indicate the result of a functional approximation that is described below. Comparison of the model simulations with measurements is, however, not straightforward. First, the ALE/GAGE observations are filtered ("polluted events" are rejected) in order to achieve data that are representative for the remote atmosphere (see section 4.1). Second, the simulated data are based on one and the same meteorological dataset driving the model's advection over many years (NCEP reanalysis 1993 [*Kalnay et al.*, 1996]), whereas the meteorological conditions in the real atmosphere vary from year to year. The first requirement is especially important for the stations Ireland and Oregon, which are located within model grid boxes that cover source regions of F11 and MCF. Sampling the model results in those grid boxes would result in a bias due to the local sources. In order to improve comparability with the "remote" observations, the modeled measurement locations are shifted westward into the neighboring grid boxes, which are free of emissions. Simulations for Ireland are therefore sampled at 11.3°W instead of 10°W, and for Oregon at 129.4°W instead of 124°W.

To address the second difference, observational data and simulation results are post-processed following an approach of *Prinn et al.* [1995]. The observed and simulated mixing ratio χ of MCF and F11 is approximated by the function

$$\chi'(t) = \sum_{k=0}^{n} c_k \cdot P_k\left(\frac{t}{N} - 1\right) , \tag{4.12}$$

where P_k is the Legendre-polynomial of order k $(P_0 = 1)$. N is half the length of the time series of the particular station counted in months. The time t then runs from 0 to $2N$ months. The argument of the Legendre-polynomials is therefore

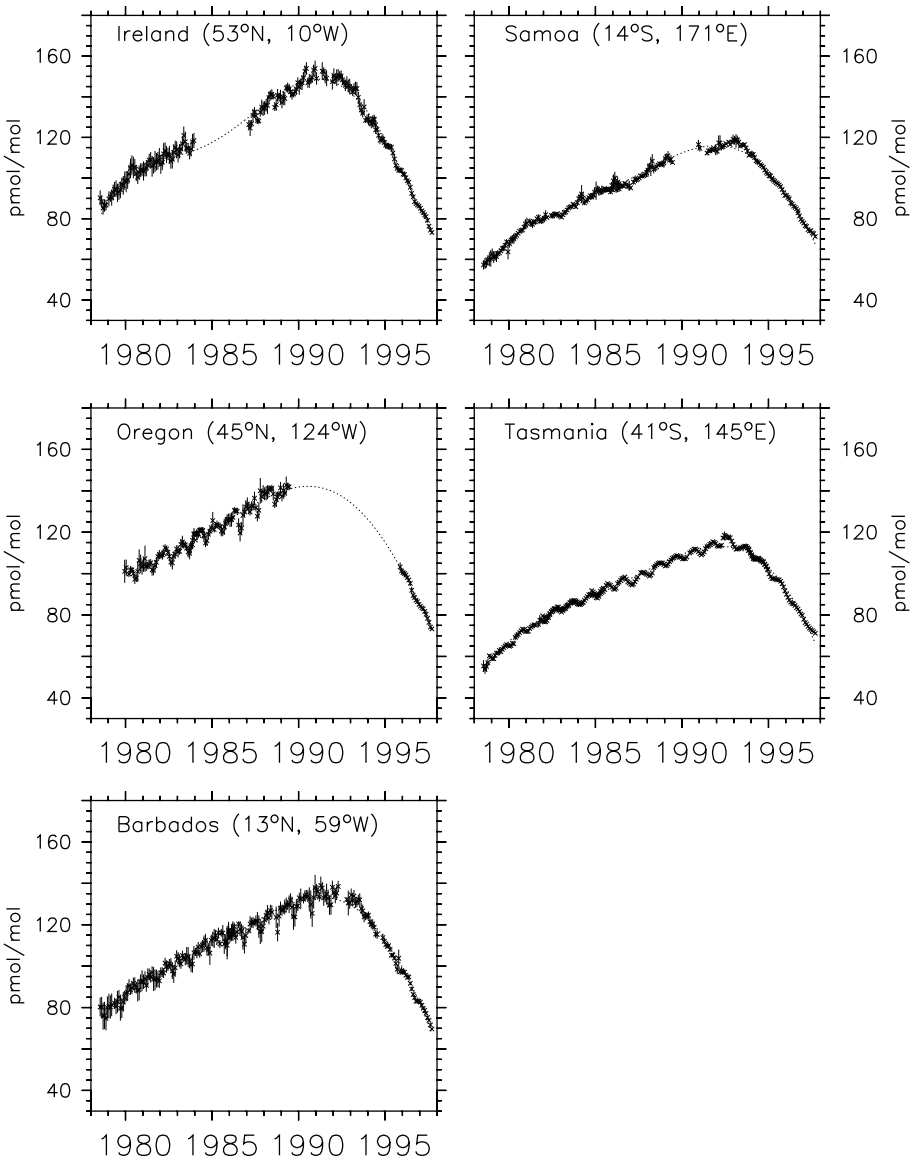

Figure 4.4: Observed CH_3CCl_3 time series and Legendre polynomial representation. Error bars denote the standard deviation of measurements during 1 month.

always between -1 and 1. The maximum order is chosen to be $n = 5$. By this form of approximation the long term trend of measurements / simulations is described, whereas the seasonal cycle is filtered out. The coefficients c_k are determined by minimizing the deviation

$$f_\chi = \sum_{t=0}^{2N} (\chi'(t) - \chi(t))^2 \ . \tag{4.13}$$

Krol et al. [1998] already applied this method, also omitting the terms that describe the seasonality [*Prinn et al.*, 1995], however varying the order n among the different

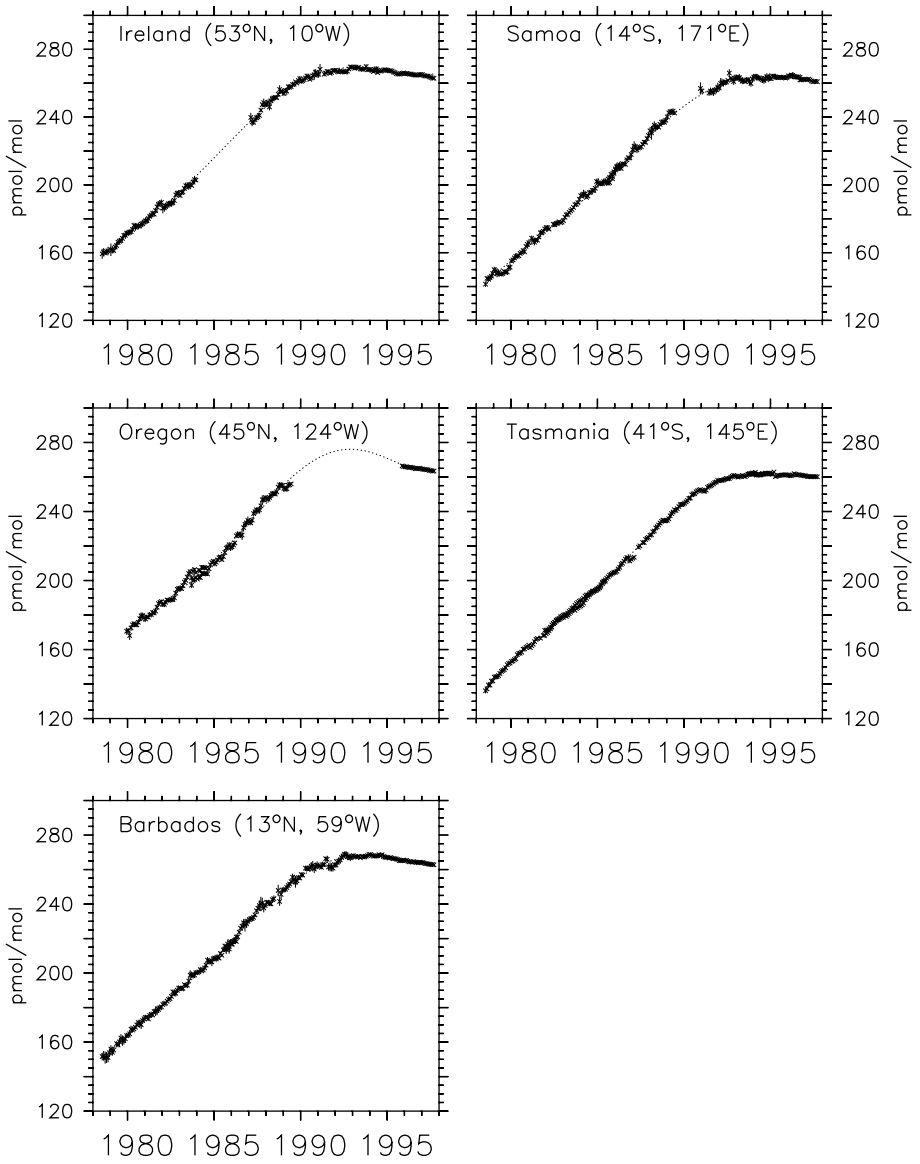

Figure 4.5: Observed $CFCl_3$ time series and Legendre polynomial representation. Error bars denote the standard deviation of measurements during 1 month.

stations. The resulting functions $\chi'(t)$ (Eq. (4.12)) of the observational data are plotted in Figure 4.4 (MCF) and in Figure 4.5 (F11). The time interval taken into account for the fit of the observational data is 231 ($2N = 230$) months (Jul 1978 to Sep 1997) for Ireland, Barbados, Samoa, and Tasmania, and 213 ($2N = 212$) months (Dec 1979 to Sep 1997) for Oregon.

In Figure 4.6 the functional approximations of the observational MCF data are plotted together with the likewise approximated model simulations. At all stations 192 ($2N = 191$) months (Jan 1978 to Dec 1993) are taken into account for the functional

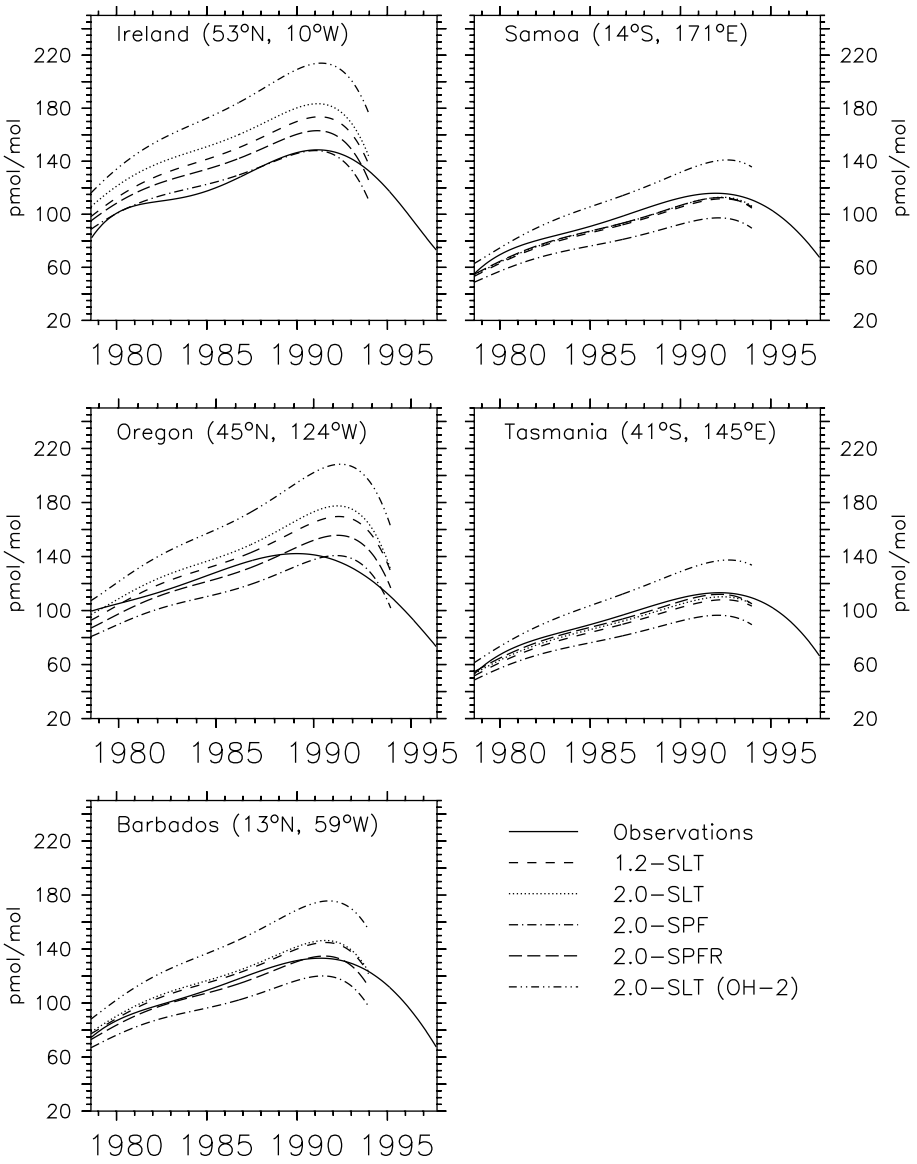

Figure 4.6: Functional representations of observed and simulated CH_3CCl_3 time series.

representation of the model simulations. The appropriate coefficients c_k of observational and simulated data are listed in Table 4.5. Figure 4.7 presents the result of the same approximation procedure applied to the observed and simulated F11 mixing ratios. The time interval taken into account for the functional representation of the F11 simulations is 168 ($2N = 167$) months from Jan 1978 to Dec 1991. Table 4.6 lists the respective coefficients c_k of the Legendre-polynomial approximation. For the Oregon station, the Legendre-polynomial representation of the observations does not provide a reasonable interpolation between 1989 and 1995 because during this period no observations exist. This time interval, however, comprises the period of

	Station	c_0	c_1	c_2	c_3	c_4	c_5
Observations	Ireland	120.61	8.90	-37.09	-22.83	-6.66	10.20
	Oregon	120.94	0.36	-35.63	-15.87	0.98	2.55
	Barbados	110.14	11.41	-33.31	-17.70	-6.14	3.13
	Samoa	94.44	17.29	-26.11	-13.84	-7.32	3.03
	Tasmania	92.62	17.69	-25.15	-12.54	-8.05	1.77
1.2-SLT	Ireland	143.14	35.98	-15.41	-8.43	-12.49	-4.81
	Oregon	136.35	37.56	-14.10	-11.19	-13.32	-6.51
	Barbados	117.02	34.13	-10.51	-5.30	-9.09	-4.51
	Samoa	87.91	30.80	-6.03	-0.34	-4.32	-2.43
	Tasmania	85.41	29.81	-6.15	-0.23	-3.83	-1.74
2.0-SLT	Ireland	152.36	36.32	-17.15	-9.15	-13.63	-4.63
	Oregon	141.99	38.88	-15.24	-13.36	-15.04	-7.21
	Barbados	118.69	34.08	-10.83	-5.24	-9.26	-4.19
	Samoa	88.99	30.88	-6.19	-0.54	-4.36	-2.61
	Tasmania	87.53	30.05	-6.52	-0.47	-4.04	-1.76
2.0-SPF	Ireland	123.73	26.62	-14.30	-8.82	-12.23	-4.06
	Oregon	114.22	28.22	-12.30	-10.58	-12.15	-5.60
	Barbados	98.08	26.06	-9.18	-5.25	-8.52	-3.73
	Samoa	77.65	25.24	-5.60	-0.88	-4.44	-2.47
	Tasmania	77.50	24.96	-6.01	-0.85	-4.28	-1.83
2.0-SPFR	Ireland	135.44	31.54	-15.20	-8.91	-12.65	-4.32
	Oregon	125.88	33.14	-13.19	-10.66	-12.56	-5.86
	Barbados	109.41	30.89	-10.03	-5.30	-8.89	-3.97
	Samoa	89.16	30.29	-6.46	-0.85	-4.76	-2.70
	Tasmania	89.19	30.11	-6.88	-0.81	-4.60	-2.05
2.0-SLT (OH-2)	Ireland	174.85	48.44	-18.38	-9.49	-13.93	-4.90
	Oregon	164.39	51.14	-16.44	-13.94	-15.52	-7.61
	Barbados	139.81	45.67	-11.84	-5.43	-9.45	-4.41
	Samoa	108.43	41.93	-6.94	-0.56	-4.33	-2.87
	Tasmania	106.20	40.86	-7.19	-0.42	-3.93	-1.93

Table 4.5: Coefficients of 5^{th}-order Legendre polynomial representations of observed and simulated CH_3CCl_3 time series. The unit is pmol mol^{-1}.

maximum abundance of MCF in the atmosphere around 1991/92, and the time when the F11 growth rate starts to decline (cf. Figures 4.4 and 4.5). This certainly affects the functional approximation.

Except for the 2.0-SPF configuration, the model employing the OH-1 distribution tends to overestimate the NH-SH gradient of MCF. The deviation of the simulated MCF mixing ratio from the observations is larger in the NH than in the SH. Fur-

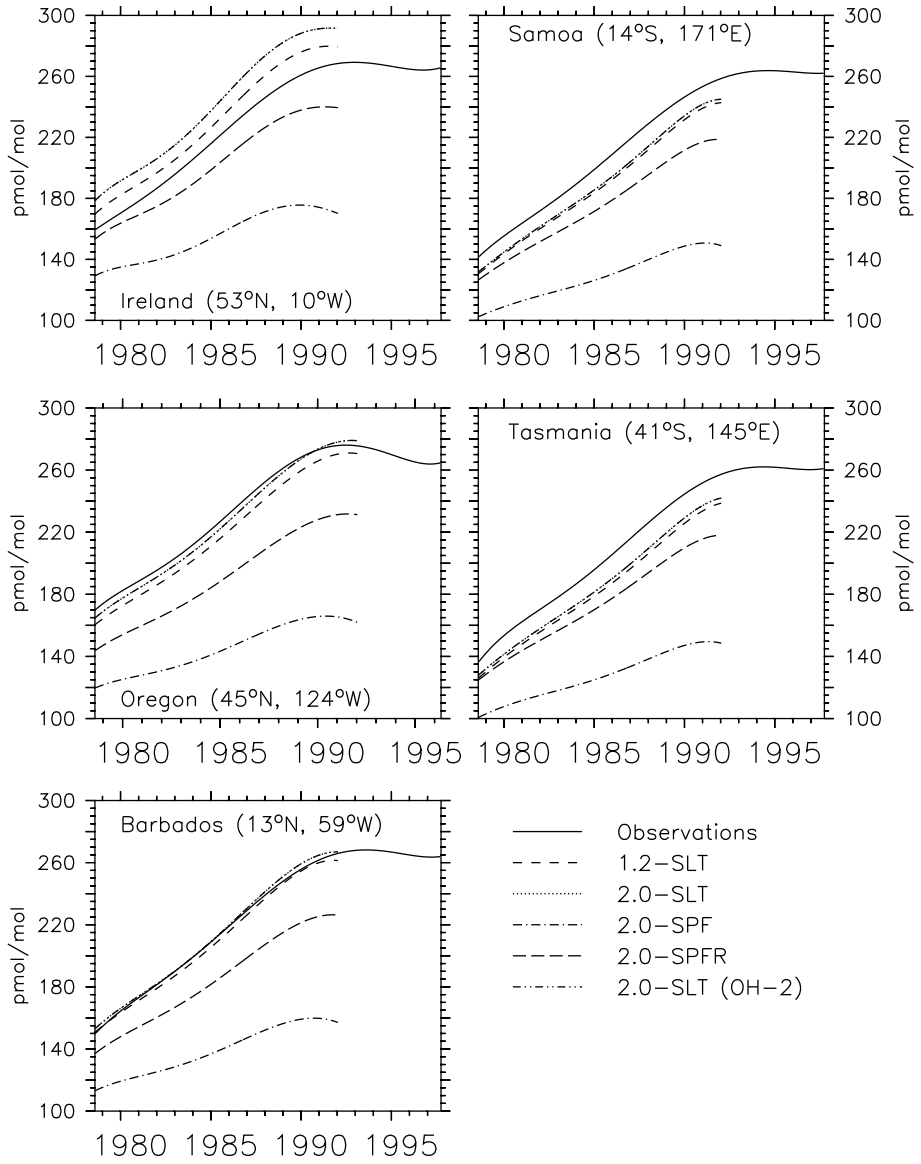

Figure 4.7: Functional representations of observed and simulated $CFCl_3$ time series.

thermore, the scatter among the various configurations is higher at the NH stations than at the SH stations. The 2.0-SLT configuration in combination with the OH-2 distribution overestimates the MCF mixing ratio at all stations, while the 2.0-SPFR configuration with OH-1 underestimates it, except at Ireland. Finally, the declining phase of the atmospheric MCF mixing ratio (after 1990/91) is predicted by the model to be steeper than observed, at least in the NH.

All model configurations underestimate the F11 mixing ratio in the SH. Both SPITFIRE configurations underestimate the F11 mixing ratio at all stations, the (uncorrected) 2.0-SPF configuration by 30-35%. As expected, a change in OH does not

	Station	c_0	c_1	c_2	c_3	c_4	c_5
Observations	Ireland	232.40	60.13	-25.42	-10.84	5.30	4.02
	Oregon	238.82	56.00	-26.08	-14.70	4.24	6.35
	Barbados	227.93	64.07	-23.16	-11.40	1.74	4.71
	Samoa	220.21	67.99	-19.32	-11.16	0.58	3.78
	Tasmania	218.01	68.53	-19.13	-11.26	-0.69	5.50
1.2-SLT	Ireland	1078.22	306.11	-6.43	-39.07	-23.27	8.79
	Oregon	1030.72	302.32	-1.43	-29.72	-21.75	3.06
	Barbados	981.81	296.72	1.79	-20.81	-20.58	0.03
	Samoa	880.40	286.23	7.74	-1.47	-16.35	-6.40
	Tasmania	856.87	282.25	8.18	2.60	-14.90	-4.93
2.0-SLT	Ireland	1129.58	317.25	-9.26	-45.10	-24.77	13.79
	Oregon	1060.13	312.15	-1.79	-31.10	-22.31	5.13
	Barbados	999.20	303.80	1.65	-21.00	-20.82	2.09
	Samoa	889.09	290.26	7.95	-2.87	-16.28	-7.39
	Tasmania	869.61	287.14	8.14	1.16	-15.28	-4.95
2.0-SPF	Ireland	730.71	132.62	-10.37	-34.98	-20.24	10.46
	Oregon	683.61	130.35	-5.02	-24.69	-18.24	3.62
	Barbados	653.49	128.99	-2.93	-17.36	-17.71	1.63
	Samoa	604.26	127.58	0.62	-4.83	-15.26	-4.68
	Tasmania	597.70	127.50	0.43	-2.45	-14.90	-3.33
2.0-SPFR	Ireland	945.27	243.30	-7.68	-34.50	-21.41	10.50
	Oregon	898.10	241.03	-2.36	-24.19	-19.45	3.66
	Barbados	867.47	239.53	-0.30	-16.83	-18.89	1.64
	Samoa	820.35	239.40	3.08	-4.62	-16.74	-5.45
	Tasmania	813.43	239.25	2.89	-2.15	-16.35	-4.01
2.0-SLT (OH-2)	Ireland	1129.66	317.30	-9.26	-45.10	-24.77	13.79
	Oregon	1060.21	312.21	-1.78	-31.10	-22.31	5.13
	Barbados	999.28	303.85	1.65	-21.00	-20.82	2.09
	Samoa	889.17	290.31	7.96	-2.87	-16.28	-7.39
	Tasmania	869.69	287.19	8.14	1.16	-15.28	-4.95

Table 4.6: Coefficients of 5^{th}-order Legendre polynomial representations of observed and simulated CCl_3F time series. The unit is pmol mol^{-1}.

significantly affect the 2.0-SLT predicted F11 mixing ratio evolution: the respective lines (2.0-SLT and 2.0-SLT (OH-2)) in Figure 4.7 are not distinguishable. The difference of F11 mixing ratio predictions among the semi-Lagrangian configurations (1.2-SLT and 2.0-SLT) is also rather small, implying that F11 is not notably affected by convection, which differs between 1.2-SLT and 2.0-SLT (cf. section 1.3).

To further quantify the differences between the model simulations and the observa-

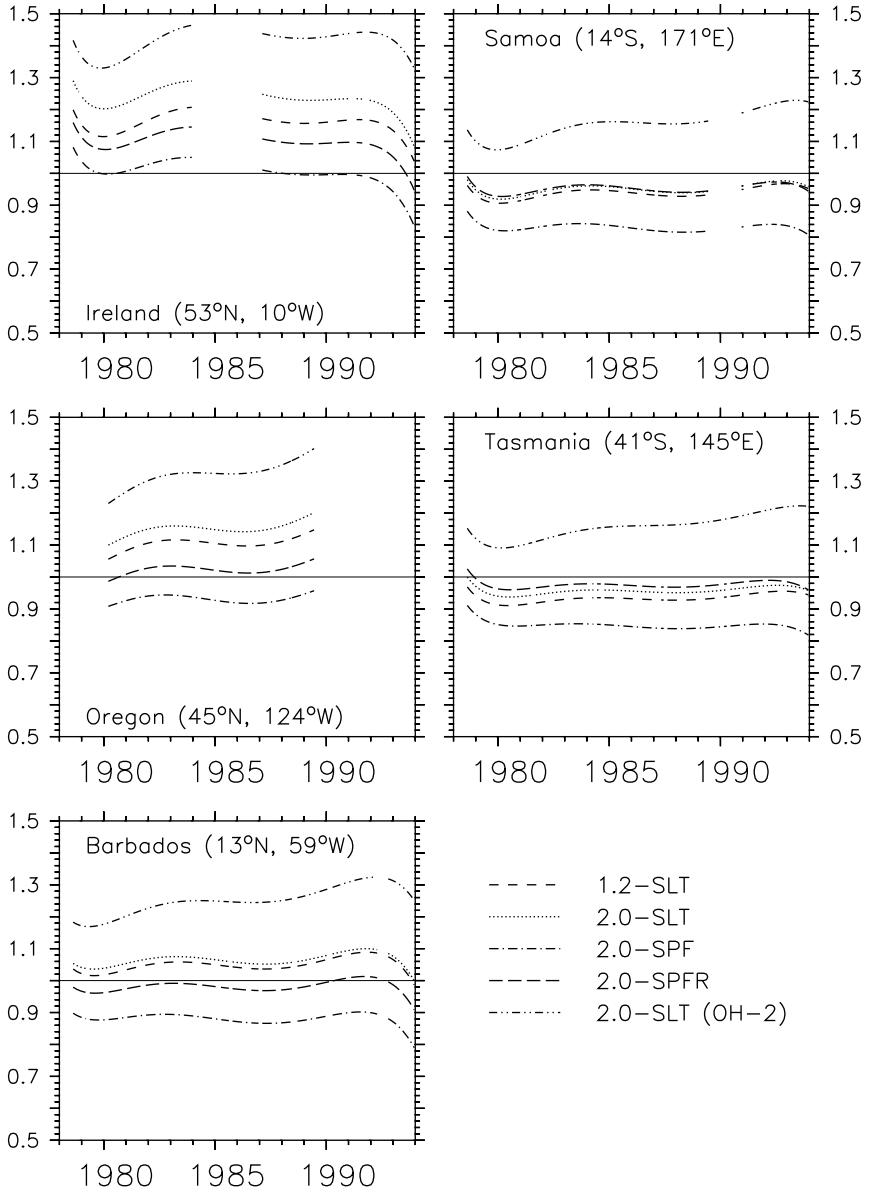

Figure 4.8: Ratio of approximated simulated to approximated observed CH_3CCl_3 time series for various model configurations. The ratio is only plotted at points in time (months), where observational and simulated data are available.

tions, Figure 4.8 shows the ratio r of the (approximated) simulated MCF mixing ratio to the (approximated) observed MCF mixing ratio at the 5 ALE/GAGE stations. Only points in time where observational data exists are taken into account. Figure 4.9 shows the respective ratios calculated from the F11 observations and simulations, both represented by the functional approximations.

In the case of MCF (Figure 4.8), the overall deviation of the model predictions from the measurements is smallest for the 2.0-SPFR configuration, followed by the

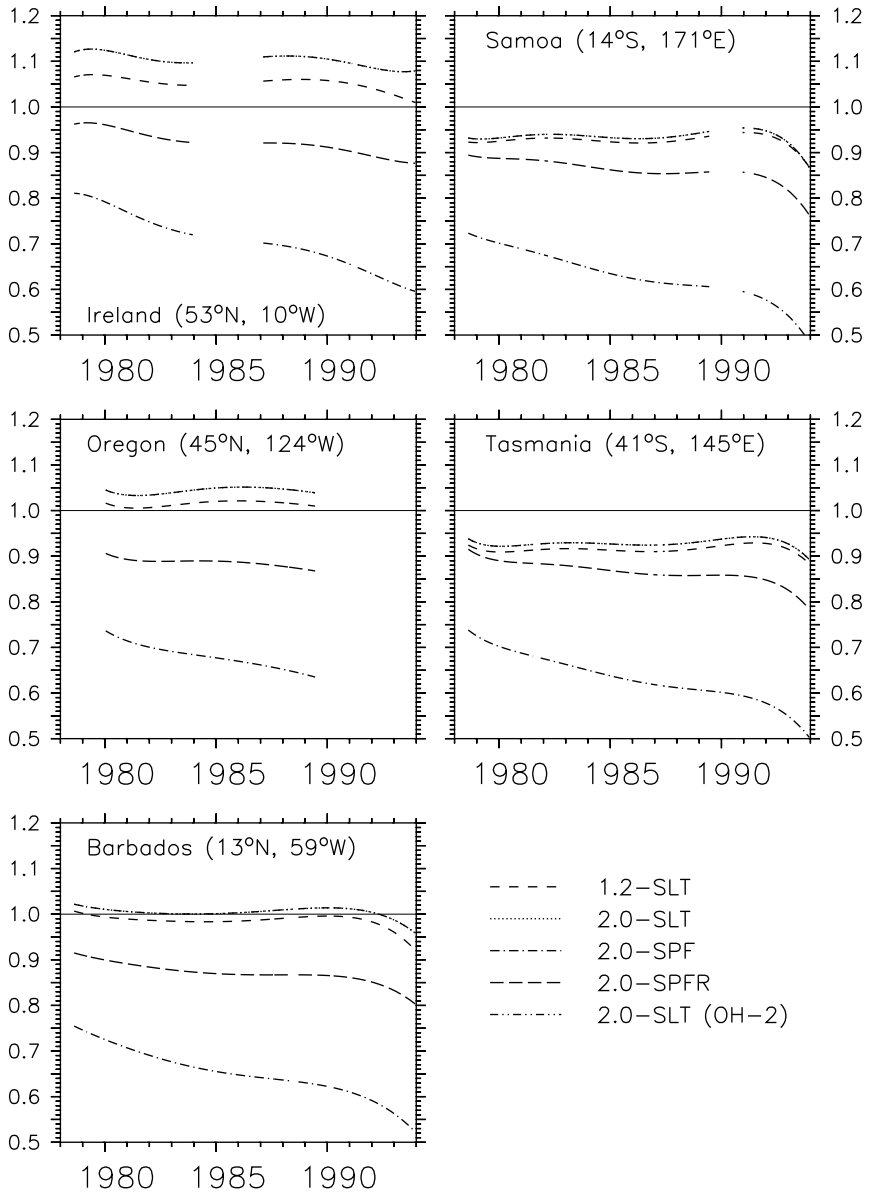

Figure 4.9: Ratio of approximated simulated to approximated observed $CFCl_3$ time series for various model configurations. The ratio is only plotted at points in time (months), where observational and simulated data are available.

1.2-SLT configuration and the 2.0-SLT configuration. The 1.2-SLT predictions are closer to the observations than the 2.0-SLT predictions in the NH, whereas in the SH the opposite is found. The lowest MCF mixing ratios are predicted by the 2.0-SPF configuration, the highest by the 2.0-SLT configuration with the OH-2 distribution. The results are similar for F11 (Figure 4.9). In the NH (except for Barbados) the 1.2-SLT based predictions and in the SH the 2.0-SLT based predictions are closest to the observed F11 mixing ratios. The ratio between model simulations

and observations varies for both species with time at all stations. In particular the F11 results (Figure 4.9) suggest a long term trend in the difference between model simulations and observations.

In order to collapse the model results into as few parameters as possible, the ratios shown in Figures 4.8 and 4.9 are approximated further by a least-squares approximation of the form

$$r'(t) = r_0 + s \cdot t \ , \tag{4.14}$$

where r' is the approximated ratio at time t, and s the slope. Only points in time, where observational data is available are taken into account. This determines the total number K of months for each station. The analysis is performed within the time interval Jan 1980 to Dec 1990, with the limitation to 1990 chosen for 2 reasons. First, the rapid decline of the MCF mixing ratio after 1990/91 is predicted by the model to be steeper than observed (cf. Figure 4.6). This period is excluded. And second, the data gap at the Oregon station between 1989 and 1995 (cf. Figure 4.4) affects the functional approximation of the measured time series, as already discussed above. Since the particular results are to be compared, the same time interval for all stations and species is chosen.

The resulting parameters are listed in Table 4.7 for MCF and in Table 4.8 for F11, including the standard deviation of the original ratios r from the linear approximation (Eq. (4.14)), i.e.,

$$\sigma = (\frac{1}{K} \sum_{t=1}^{K} (r(t) - r'(t))^2)^{\frac{1}{2}} \ , \tag{4.15}$$

and the average ratio ($\bar{r}$) during the period 1980 to 1990. The standard deviation σ (Eq. (4.15)) is a measure for the quality of the linear approximation. In case of MCF, the linear approximation for all configurations is best justified (lowest σ) at Tasmania, and poorest at Ireland. The latter also holds for the F11 approximation.

For both species, a NH-SH gradient of the average ratio $\bar{r}$ is common to the results of all model configurations. This means the model tends to overestimate MCF and F11 mixing ratios in the NH, and likewise underestimates MCF and F11 mixing ratios in the SH. This effect is smaller for F11 than for MCF. For MCF, this gradient is biased in the 2.0-SPF configuration which predicts too low MCF mixing ratios also in the NH (except for Ireland). Vice versa, the 2.0-SLT/OH-2 configuration overestimates the MCF mixing ratio at all stations. The latter is in agreement with the lower global average OH concentration of OH-2 (see Table 1.1). The average ratios $\bar{r}$ based on F11 simulations of the SPITFIRE configurations are similarly biased. Both, 2.0-SPF and 2.0-SPFR underestimate the F11 mixing ratio at all stations. Generally, the model predictions of F11 are closer to the observations than the MCF predictions (except for 2.0-SPF).

	Station	r_0	s	$10^3\sigma$	$\bar{r}$
1.2-SLT	Ireland	1.16	0.09	2.28	1.16
	Oregon	1.09	0.40	1.28	1.10
	Barbados	1.04	0.21	1.03	1.05
	Samoa	0.93	0.14	1.06	0.93
	Tasmania	0.92	0.18	0.49	0.93
2.0-SLT	Ireland	1.25	-0.08	2.34	1.24
	Oregon	1.13	0.48	1.32	1.15
	Barbados	1.06	0.14	0.99	1.06
	Samoa	0.94	0.12	1.09	0.95
	Tasmania	0.94	0.14	0.47	0.95
2.0-SPF	Ireland	1.03	-0.28	1.67	1.01
	Oregon	0.93	0.04	1.05	0.93
	Barbados	0.89	-0.07	0.87	0.88
	Samoa	0.84	-0.14	0.82	0.83
	Tasmania	0.85	-0.09	0.36	0.85
2.0-SPFR	Ireland	1.11	-0.11	1.95	1.10
	Oregon	1.01	0.22	1.15	1.02
	Barbados	0.98	0.10	0.92	0.98
	Samoa	0.95	0.04	1.03	0.95
	Tasmania	0.97	0.09	0.46	0.97
2.0-SLT (OH-2)	Ireland	1.38	0.55	2.88	1.41
	Oregon	1.26	1.18	1.48	1.32
	Barbados	1.20	0.78	1.12	1.25
	Samoa	1.10	0.82	1.52	1.14
	Tasmania	1.10	0.81	0.78	1.15

Table 4.7: Linear approximation of simulated to observed CH_3CCl_3 time series ratio (1980-1990) for different model configurations. Only the points in time when observational data exists have been considered for the regression analysis. r_0 is the y-axis (ratio) intercept at the first time-step, s is the slope in %/year. The respective standard deviation (σ) is also included. $\bar{r}$ is the ratio averaged over all points in time, for which observational data is available.

For an interpretation of the slope s, the initial ratio r_0 also has to be considered. A divergence (with time) of the model predictions from the observations is indicated by a positive slope s in combination with an initial ratio $r_0 \geq 1$ between simulations and observations (increasing overestimate), or a negative slope s and an initial ratio $r_0 \leq 1$ (increasing underestimate). Other combinations of r_0 and s indicate that the model simulations tend to converge towards the observations within the considered time interval.

For MCF (Table 4.7) the picture is only clear for the 2.0-SLT/OH-2 configuration,

	Station	r_0	s	$10^3\sigma$	$\bar{r}$
1.2-SLT	Ireland	1.06	-0.01	0.56	1.06
	Oregon	1.01	0.11	0.41	1.01
	Barbados	0.98	0.07	0.32	0.99
	Samoa	0.93	-0.01	0.43	0.93
	Tasmania	0.91	0.09	0.35	0.91
2.0-SLT	Ireland	1.11	-0.04	0.73	1.11
	Oregon	1.04	0.14	0.46	1.04
	Barbados	1.00	0.10	0.31	1.01
	Samoa	0.93	0.03	0.43	0.94
	Tasmania	0.92	0.11	0.32	0.93
2.0-SPF	Ireland	0.77	-1.01	0.81	0.72
	Oregon	0.72	-0.90	0.33	0.68
	Barbados	0.71	-0.92	0.53	0.66
	Samoa	0.69	-1.05	0.55	0.64
	Tasmania	0.69	-0.97	0.46	0.64
2.0-SPFR	Ireland	0.95	-0.37	0.62	0.93
	Oregon	0.90	-0.25	0.31	0.89
	Barbados	0.89	-0.28	0.37	0.87
	Samoa	0.89	-0.40	0.41	0.87
	Tasmania	0.89	-0.33	0.27	0.87
2.0-SLT (OH-2)	Ireland	1.11	-0.04	0.73	1.11
	Oregon	1.04	0.15	0.46	1.04
	Barbados	1.00	0.10	0.31	1.01
	Samoa	0.93	0.03	0.43	0.94
	Tasmania	0.92	0.11	0.32	0.93

Table 4.8: Linear approximation of simulated to observed CCl_3F time series ratio (1980-1990) for different model configurations. Only the points in time when observational data exists have been considered for the regression analysis. r_0 is the y-axis (ratio) intercept at the first time-step, s is the slope in %/year. The respective standard deviation (σ) is also included. $\bar{r}$ is the ratio averaged over all points in time, for which observational data is available.

which diverges from the observations at all stations. MCF predictions of the semi-Lagrangian configurations using OH-1 converge towards the SH observations and tend to diverge from the observations in the NH (except for Ireland in 2.0-SLT). The opposite is found for the 2.0-SPF configuration. The 2.0-SPFR MCF predictions tend to converge at all stations except for Oregon.

The SPITFIRE configuration based F11 predictions diverge from the observations at all stations (Table 4.8). The F11 predictions of 2.0-SLT do not change if a different OH distribution (OH-2) is used. Therefore the resulting parameters of

the linear approximation are identical for 2.0-SLT (OH-1) and 2.0-SLT (OH-2). As for MCF, the 2.0-SLT configuration generally predicts F11 mixing ratios that tend increasingly closer to the SH observations, but diverge from the NH observations (except for Ireland). For the 1.2-SLT configuration no generalized pattern can be derived.

The rate of divergence / convergence ($|s|$ in % yr^{-1}) of the model simulated MCF mixing ratio from / towards the observations is higher for all configurations in the NH than in the SH (except for Ireland). This does not hold for the simulated F11 mixing ratio. Furthermore, the MCF rate of divergence / convergence ($|s|$) increases (except for 2.0-SPF) in both hemispheres from the tropics to the mid-latitudes, i.e., with increasing latitude (Ireland excluded). A similar pattern is found for the F11 simulations, except for the SPITFIRE configurations. Finally, the rate of divergence / convergence for both species is generally small compared to the averaged relative deviation ($|1 - \bar{r}| \cdot 100$, in %) of model simulations from the observations.

4.4 Discussion

4.4.1 Effects of the global mass mismatch rescaling

The results for F11 clearly show that the 2.0-SPF based predictions are fundamentally different from those of other configurations tested. The 2.0-SPF predicted global atmospheric lifetime of F11 is 14.4 ± 0.4 years and therefore significantly (62%) lower than that predicted by other configurations (30 - 45 years). Moreover, the 2.0-SPF configuration underestimates the F11 observations at all ALE/GAGE stations by roughly 30%. As discussed in chapter 2, the global tracer mass is not conserved in the 2.0-SPF configuration. Obviously, F11 is a tracer that is significantly influenced by this mismatch. F11 has a long atmospheric lifetime (of the order of 50 years), it is quasi-inert in the troposphere, and almost purely destroyed by photodissociation in the stratosphere. Its main source is anthropogenic emissions at ground level. Therefore a strong vertical gradient can be expected, with the F11 mixing ratio decreasing with height. Since the mass mismatch in the uncorrected SPITFIRE configuration (2.0-SPF) is sensitive to certain tracer characteristics, especially to the vertical gradient of the tracer (cf. chapter 2), the model error introduces an additional effective loss term for F11.

For MCF this effect is still present, although less pronounced. The predicted global atmospheric lifetime of MCF is 16% lower than in the other configurations. The relative deviation of the 2.0-SPF predictions from the ALE/GAGE measurements is similar to that of the other configurations. Consequently, from the MCF based results alone, the additional loss term due to the mass mismatch could easily be

misinterpreted and attributed to an overestimation of the prescribed sinks (OH, photolysis, hydrolysis in ocean water).

It has to be noted at this point that for SF_6 the mole fractions (remote latitudinal gradient at ground level, Figure 3.3) predicted by the uncorrected SPITFIRE configuration (2.0-SPF) are still in reasonable agreement with the observations, and the mass mismatch error seems to be negligible. Furthermore, the global rescaling to force tracer mass conservation has hardly any effect on the latitudinal gradient at ground level. In contrast to that, the 2.0-SPF configuration totally fails to reproduce the F11 mixing ratios at the ALE/GAGE stations. Moreover, the global rescaling to force global tracer mass conservation (2.0-SPFR) does hardly improve the results. The F11 mixing ratio is still underestimated by 7-13% at the NH stations and by 13% at the SH stations (cf. Table 4.8). This can be interpreted as a negatively biased, overestimated relative latitudinal gradient. The negative bias indicates a too strong tracer loss, provided that the emissions are not underestimated. Assuming a larger emission rate, however, would in turn increase the semi-Lagrangian results. Global tracer mass conservation is forced in the 2.0-SPFR configuration, therefore an artificial sink can be excluded. However, the mass conservation is enforced by a global rescaling of the tracer mass after each advection step. Such a rescaling procedure keeps all relative gradients, and assigns the same relative change to the tracer mixing ratio everywhere (see chapter 2).

SF_6 can be regarded as quasi-inert and is continuously accumulated in the atmosphere (see chapter 3). The vertical gradient of SF_6 is steepest near the surface where the species is emitted into the atmosphere. Since the local mass mismatch (2.0-SPF) increases with the tracer gradients, SF_6 in the model is mainly lost near the surface (see chapter 2). Compared to the global mass of SF_6 in the atmosphere, the integrated mass mismatch is therefore small. Consequently the scaling factor to enforce mass conservation is small. In 2.0-SPFR, this small amount of lost mass is rescaled globally, i.e., the mixing ratio is also increased at higher levels where no tracer loss occurred. Thus, mass is artificially lifted to higher levels.

Basically the same happens in the case of F11, which has some similar characteristics to SF_6. Both tracers are mainly emitted in the NH at ground level by anthropogenic activity, therefore the emissions distributions follow similar patterns. The basic difference, however, is the global atmospheric lifetime of the tracers. Whereas SF_6 can be regarded as quasi-inert and is continously accumulated in the atmosphere, F11 is destroyed by photodissociation. The efficiency of this loss process increases in the atmosphere exponentially with height (i.e., with decreasing pressure, cf. Figure 4.3), due to the increasing intensity of short wave radiation. Therefore the removal of F11 from the atmosphere takes place mainly in the stratosphere. This enhances the vertical tracer gradient of F11 in the troposphere compared to that

of SF_6. As a consequence, the vertical gradient dependent mass mismatch in the model occurs throughout the troposphere, and is relatively larger than in the case of SF_6. The global rescaling of the integrated mass mismatch in 2.0-SPFR then enhances the stratospheric mixing ratios artificially. Thus, tracer mass is continuously and effectively shifted to higher levels, where the photolytic destruction is increasingly effective. Integration over time results in a reduced global tracer mass due to an enhanced tracer loss. This mechanism explains the reduced F11 mixing ratios predicted by the 2.0-SPFR configuration.

Furthermore, from the discussion so far it follows why both configurations (2.0-SPF and 2.0-SPFR) predict mass mixing ratios that are not only biased but further diverge from the observations, whereas such a generalized pattern cannot be derived for the semi-Lagrangian configurations. In the case of the 2.0-SPF configuration the artificial loss due to the mass mismatch is responsible, in the case of the 2.0-SPFR configuration, it is the continuous shift of tracer mass towards the major sink region.

The same mechanisms apply to MCF, although attenuated, because MCF is effectively oxidized by OH in the troposphere. This weakens the vertical gradient compared to F11, resulting in a reduced mass mismatch compared to the global tracer mass. Furthermore, the fraction of artificial loss compared to the total tracer loss is smaller for MCF than for F11, because the lifetime of MCF is much shorter. The removal of MCF by oxidation with OH is more effective than the artificial loss, which itself is more effective than the photodissociation in the stratosphere.

As a consequence, the results obtained with the SPITFIRE configurations are not further taken into consideration for the evaluation of OH in the discussion below.

4.4.2 The interhemispheric gradient of $CFCl_3$

For SF_6, the remote interhemispheric gradient at ground level is reproduced by the model within ±3% (cf. Figure 3.3 and Table 3.1). The mixing ratios of F11 are overestimated by the semi-Lagrangian configurations (Table 4.8) by 6-11% at Ireland (53^oN), 1-4% at Oregon (45^oN), are reproduced within ±1% at Barbados (13^oN), and are underestimated by 6-7% at Samoa (14^oS), and by 7-9% at Tasmania (41^oS). Thus the deviation from the observed F11 NH-SH gradient seems higher than that for SF_6. This difference is, however, not significant for various reasons. First, the ALE/GAGE stations are not necessarily representative for the respective latitude, just as the SF_6 observations listed in Table 3.1 do not necessarily represent the zonal average. Second, "polluted" events are filtered out of the F11 measurements at the ALE/GAGE stations, which especially affects the time series at Ireland and Oregon. Although mixing ratios for these stations in the model are sampled westward of their geographical position in source-free grid boxes, the sampled mixing ratios are not

filtered for the wind direction. Therefore, the simulations at Ireland and Oregon are possibly still biased compared to observations, due to the influence of neighboring sources.

4.4.3 Evaluation of global OH

The estimated lifetime of MCF is 4.4 ± 0.1 years for the OH-1 distribution, and 5.6 ± 0.1 years for the OH-2 distribution which has a 30% reduced annual global mass weighted average concentration in the troposphere (Table 1.1) compared to OH-1. Obviously, OH-2 underestimates the tropospheric oxidation capacity, in accordance with the long methane lifetime found by *Lawrence et al.* [1999a] for OH-2. MCF is more accumulated in the model atmosphere than in the real atmosphere, and therefore its mixing ratios are overestimated. This also explains the divergence of the model results (2.0-SLT (OH-2)) from the observations at all stations (Table 4.7).

The simulated interhemispheric gradient of MCF is overestimated by the model (Figures 4.6 and 4.8, Table 4.7), and the question arises to what extent this is to be attributed to the interhemispheric exchange and/or to the NH-SH asymmetry of the sink. A comparison of the latitudinal gradients of F11 (or SF_6) and MCF possibly provides this information.

In order to compare the relative NH-SH gradients of MCF and F11 based on OH-2 with that based on OH-1, the different global average OH concentration has to be taken into account, because F11 is not affected by OH like MCF. Because OH oxidation is not the only sink for MCF (photodissociation in the stratosphere and hydrolysis in the ocean provide minor contributions to the total loss of MCF), a global scaling of OH by an arbitrary factor, will not necessarily result in a likewise scaled mass mixing ratio everywhere.

The MCF mass mixing ratio gradients, however, do not change if the global lifetime is scaled, which implies also a scaling of the minor sink processes. The more the tracer loss is dominated by OH compared to the other loss processes, the more the global atmospheric lifetime is representative for the global average OH concentration, however. In this case the scaling of the global atmospheric lifetime is possible in good approximation by solely scaling the global average OH concentration. In the present case, the mass weighted global average concentration of OH in the troposphere in OH-2 is 30% lower than in OH-1 (Table 1.1). The predicted lifetime of MCF is, however, 27% longer. The influence of the minor sink processes can therefore be regarded as small.

For a normalization to the model predicted global atmospheric lifetime of MCF, the ratio $\bar{r}$ (2.0-SLT (OH-2), Table 4.7) is scaled with 0.79, which is the ratio of the

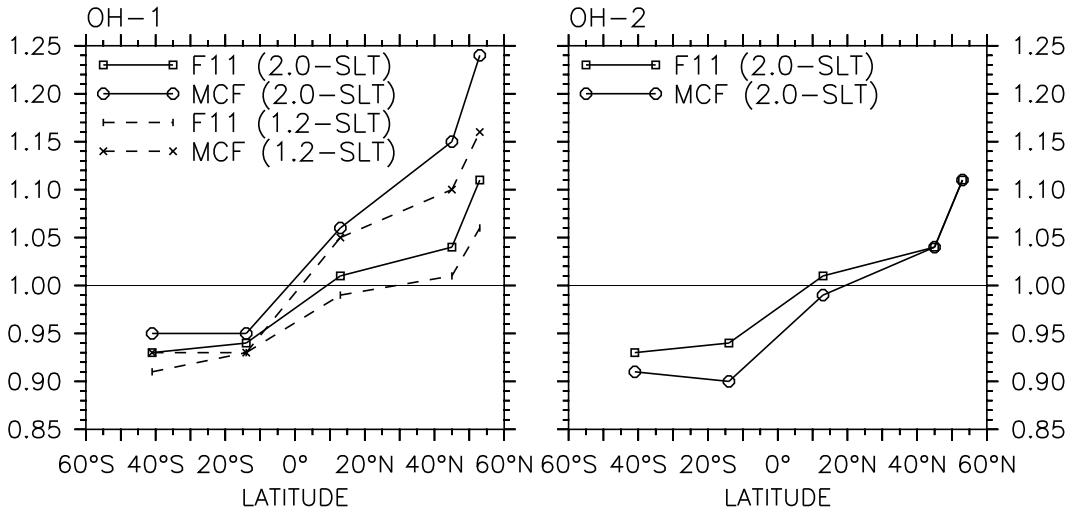

Figure 4.10: Latitudinal gradient of the deviation between simulated and observed levels of CH_3CCl_3 (MCF) and $CFCl_3$ (F11) for different OH distributions. Shown is the ratio $\bar{r}$ of simulated to observed quantities averaged in the time interval 1970-1980 (cf. Tables 4.7 and 4.8). The values for OH-2 (right) are lifetime adjusted as described in the text.

global lifetimes predicted with the two OH distributions (2.0-SLT, Table 4.4). The results are 1.11, 1.04, 0.99, 0.90, and 0.91 for Ireland, Oregon, Barbados, Samoa, and Tasmania, respectively. In Figure 4.10 the relative deviations from the observations (plotted as ratio $\bar{r}$, Tables 4.7 and 4.8) are compared. For 2.0-SLT (OH-2) the respective lifetime adjusted ratios are included.

In case of OH-1, the F11 and MCF observations are almost equally underestimated by the model in the SH, whereas in the NH MCF is more overestimated than F11. In case of OH-2, the SH deviation of the simulations from observations is somewhat larger for MCF than for F11, whereas the relative deviation in the NH is almost exactly the same for MCF and F11. For both OH distributions, the relative NH-SH gradient of MCF is therefore more overestimated than that of F11. The interhemispheric gradients of F11 and MCF predicted by 1.2-SLT are closer to the observations than those of 2.0-SLT. This must be attributed to differences in the interhemispheric exchange / vertical mixing (mainly convection, cf. section 1.3) between these specific model configurations, and is further in accordance with the results derived from the SF_6 simulations (chapter 3).

The 2.0-SLT configuration with OH-2 predicts a reduced interhemispheric gradient of MCF compared to OH-1. The deviations of the F11 and MCF gradient from the respective observations are not significantly different when OH-2 is involved. Since the NH-SH asymmetry of the tropospheric OH distribution of OH-2 is somewhat higher (OH(NH)/OH(SH)=1.27, see Table 1.1) than that of the OH-1 distribution (1.25), this result suggests that a higher OH asymmetry between NH and SH is in

favor of model results that are closer to observations. A higher NH-SH asymmetry, however, implies a higher OH concentration in the NH and/or a lower OH concentration in the SH. The opposite has been suggested by *Brenninkmeijer et al.* [1992] based on ^{14}CO measurements, who even predicted a reversed hemispheric asymmetry of OH with a higher average concentration in the SH, which was also found by *Montzka et al.* [2000].

From the analysis presented here, a larger interhemispheric asymmetry can, however, only be concluded with caution. First, the lifetime normalization on which this result is based, not only scales the OH concentration, but also the minor sink processes of MCF. Therefore, reducing the global lifetime by scaling also increases the loss by hydrolysis in ocean water. Due to the global land / sea distribution, the absolute sink by hydrolysis is then more enhanced in the SH than in the NH, which also affects the interhemispheric tracer gradient. However, this effect is possibly small, because the overall loss of MCF through hydrolysis in ocean water is small compared to the loss of MCF by oxidation with OH. Second, the more important restriction is the uncertainty that has to be assigned to the model transport. The differences "caused" by the change of OH are of similar magnitude as the general deviation of model predictions from observations that do not involve OH. For instance, exchanging OH-1 by OH-2 causes a decrease of the model deviation from the MCF observation at Oregon from 15% to 4% (Table 4.7). The respective deviation of F11 is also 4% (Table 4.8). This is solely attributed to transport, because F11 is not influenced by OH. Consequently, the "effect" of predictions coming closer to observations with an increased OH asymmetry cannot definitely be attributed to the change in OH alone. This is further supported by the fact that differences between the model configurations that use OH-1 and therefore only differ in the realization of tracer transport are likewise of the same magnitude (see Figure 4.10).

4.5 Conclusions

Due to the mass mismatch occurring in the SPITFIRE configurations of the model (see chapter 2) the simulations of MCF and F11 of those configurations cannot be used. The total amount of F11 that is artificially lost in the uncorrected configuration (2.0-SPF) is larger than the amount that is destroyed by photodissociation. Although the artificial loss of MCF is smaller than the loss by oxidation through OH, it is still large. In the configuration with forced mass conservation by global rescaling of the tracer mass (2.0-SPFR), the artificial loss is replaced by an unphysical transport of tracer mass to higher levels, i.e., towards the stratospheric sink region. This effect is much larger for F11 than for MCF, since the mass mismatch is dependent on the vertical tracer gradient, which is steeper for F11 than for MCF.

From the semi-Lagrangian configurations the global atmospheric lifetime of F11 is estimated to be 44.8 ± 2.3 years. Measurements of F11 at the ALE/GAGE stations between 1980 and 1990 are reproduced within (+11%, -9%) by the model.

The estimated global atmospheric lifetime of MCF involving the OH-1 distribution is 4.4 ± 0.1 years, which is in good agreement with estimates of *Prinn et al.* [1995] (4.6 ± 0.3 years), and *Krol et al.* [1998] (4.5 ± 0.1 to 4.7 ± 0.1 years). The respective mass weighted global average concentration of OH is $1.25 \cdot 10^6$ cm^{-3}. Calculations with the OH-2 distribution with a 30% reduced tropospheric average concentration of OH result in a 27% prolonged atmospheric lifetime of MCF. Measurements of MCF at the ALE/GAGE stations between 1980 and 1990 are reproduced within (+24%, -7%) by the model involving OH-1. The observations are overestimated by 15% to 41%, if the calculations are performed with the OH-2 distribution.

An estimate of hemispheric lifetimes for F11 and MCF from a simple 2-box model is not possible, because the dominating time scale is the interhemispheric exchange time, which is small compared to the global atmospheric lifetimes of the species.

The interhemispheric gradient of the deviation between model predictions and observations of F11 at the ALE/GAGE stations is, within the uncertainties, in agreement with the results obtained from the SF_6 simulations. Observed interhemispheric gradients (defined at particular locations) of both tracers are slightly overestimated by the model. The measurements are reproduced within ± 3 to ± 10% (SF_6 and F11). This is the uncertainty, which has to be assigned to the modeled interhemispheric exchange process.

The comparison of the relative latitudinal gradients of F11 and MCF (simulated versus observed) with respect to the model configuration and the OH distribution indicate a relation between the interhemispheric gradient of MCF and the interhemispheric OH asymmetry. An increased NH-SH OH asymmetry seems to reduce the predicted NH-SH gradient of MCF, implying improved model simulations. A quantification of this effect is, however, hardly possible, since the sensitivity of the simulated interhemispheric MCF gradient (at the ALE/GAGE stations) is of similar magnitude to the uncertainty in the modeled dynamics, especially the interhemispheric exchange.

Finally, it can be concluded that the evaluation of 3-D modeled OH by MCF measurements at the 5 ALE/GAGE stations is limited to the global scale. Only the global average concentration of OH can be constrained, always based on the assumption that the history of emissions is accurately known. Further details, such as an interhemispheric asymmetry in OH, are convoluted by inaccuracies in the modeled transport. In particular uncertainties in the interhemispheric exchange of tracer mass in 3-D models limit the usefulness of further investigations which aim

at improving the quality of OH predictions. The reason is that the timescale of interhemispheric exchange is roughly 1/5 of the lifetime and therefore dominates the evolution of the interhemispheric gradient. As a consequence the minimum error that has to be attributed to MCF based OH evaluations is the uncertainty that has to be attributed to the interhemispheric exchange. This error estimate is independent of other systematic errors and solely caused by inaccuracies of the model transport. For the model tested here, the mass weighted global average OH concentration of $1.25 \cdot 10^6$ cm^{-3} reproduces the MCF observations at the ALE/GAGE stations between 1980 and 1990 within +24 to -7% (full range). The latitudinal gradient of MCF is higher than observed; however this cannot definitely be attributed to the NH-SH asymmetry of the OH distribution, since the deviation from the observed gradient is of the same order as the model's inaccuracy in predicting the interhemispheric exchange, derived from SF_6 and F11 simulations.

5 Uncertainty and variability in the distribution of the cosmogenic ^{14}C production rate: Effects on the atmospheric ^{14}CO distribution

Abstract. Most atmospheric ^{14}CO is produced by cosmic rays in the lowermost stratosphere and upper troposphere. The main removal process for ^{14}CO is oxidation by OH radicals. Assuming that the spatial distribution of OH is well known, ^{14}CO can be useful as a tracer for the transport properties of a three-dimensional model. Conversely, if the transport schemes of the model are sufficiently realistic, in particular with respect to stratosphere - troposphere exchange, the OH distribution can be evaluated. In either case, it has to be assumed that the source of ^{14}CO is known in sufficient detail. Three presently available distributions of cosmogenic ^{14}C production in the atmosphere are implemented into the MATCH model and tested with two different advection schemes (2.0-SLT and 2.0-SPF). The uncertainty in the simulated tropospheric ^{14}CO mixing ratios resulting from the uncertainty in the atmospheric ^{14}CO source distribution is rather small compared to other uncertainties implied in the modeling approach. The spatial distribution of ^{14}C production in the atmosphere is further expected to vary with changes of the solar activity. The effect of this variation on the atmospheric distribution of ^{14}CO is estimated. Calculations for solar minimum and solar maximum conditions are performed. The spatial distribution of tropospheric ^{14}CO is almost unaffected by the solar activity, and the absolute mixing ratio of ^{14}CO scales with the global average production rate of ^{14}CO.

5.1 Introduction

Before the ^{14}CO methodology can be applied for evaluation of model predicted OH fields and/or stratosphere - troposphere exchange (STE) rates, a fundamental issue has to be resolved. That is, the ^{14}CO production distribution has to be known sufficiently well. In particular the cosmogenic source component is of concern, since it contributes the largest fraction to atmospheric ^{14}CO, whereas other source contributions are comparatively small (see chapter 1). Knowledge of the spatial and temporal distribution of cosmogenic ^{14}CO production is therefore of special importance and the following questions are relevant:

1. What is the distribution of the cosmogenic ^{14}CO production in the atmosphere?
2. Is the precise source distribution a very critical parameter?
3. How does the ^{14}CO distribution vary with the solar cycle?

In this chapter the sensitivity of model predicted ^{14}CO to uncertainties and temporal variations in the spatial cosmogenic ^{14}C production rate distribution is calculated, disregarding other source contributions. This aims at taking a first systematic step towards resolving the various problems affecting the application of ^{14}CO for the evaluation of modeled OH distribution and seasonality and/or the simulated STE by means of ^{14}CO measurements.

Three independently published ^{14}C production distributions are compared (see question 1) and implemented into the 3-D model in order to test the sensitivity of model predicted ^{14}CO to the differences in the production rate distribution pattern (question 2). This provides an estimate to what extent uncertainties of the present knowledge about ^{14}C production limit the desired application of atmospheric ^{14}CO measurements for model evaluation. The last issue (question 3) is closely related, at least from the modeling point of view, and can be addressed with similar methods. The spatial distribution pattern of ^{14}C production is influenced by the solar activity, due to the effect of the solar wind plasma on the charged primary particles (cosmic rays). The solar activity, and with it the solar wind plasma density, varies quasi periodically with a cycle period of 11 years (solar cycle). This influence of solar activity on the atmospheric ^{14}CO distribution is also tested. The sensitivity test is again based on the three independently published source distributions of ^{14}C.

At this point, the focus is on the relative spatial distribution of atmospheric ^{14}CO only; the absolute scale and its temporal variation are discussed as separate issues in chapters 7 and 8. Furthermore, an equilibrium between atmospheric ^{14}CO distribution and the ^{14}C production rate distribution at solar minimum and maximum conditions is assumed. This assumption is reasonable, since the timescales of the relevant atmospheric processes (such as the lifetime of ^{14}CO, and tropospheric mixing) are short compared to the period of the solar cycle.

Two model configurations (2.0-SLT and 2.0-SPF) are considered that differ only in the realization of advective tracer transport. The purpose is to estimate the uncertainty of the results in terms of the uncertainties that have to be attributed to the tracer transport. The mass conservation violation inherent to the 2.0-SPF configuration can be ignored at this stage, since only the relative spatial tracer distribution is investigated and the focus is on the source distribution. However, the influence of the mass mismatch rescaling correction (2.0-SPFR, chapter 2) is also discussed.

5.2 The cosmogenic ^{14}CO production rate

5.2.1 The cosmogenic source of ^{14}CO

The cosmogenic component of atmospheric ^{14}CO is formed by the nuclear reaction

$$^{14}\mathrm{N(n,p)}^{14}\mathrm{C} \tag{5.1}$$

[*Libby*, 1946], followed by rapid oxidation of the recoil radiocarbon atom to ^{14}CO

$$^{14}\mathrm{C}^{*} + \mathrm{O}_2 \rightarrow ^{14}\mathrm{CO} + \mathrm{O}\ . \tag{5.2}$$

The yield of the oxidation reaction is about 95% [*MacKay et al.*, 1963; *Pandow et al.*, 1960]. Therefore the ^{14}CO production rate is directly related to the atmospheric neutron flux. The atmospheric neutrons, in turn, originate from galactic cosmic rays (GCRs), i.e., about 90% protons, 9% alpha-particles, and the rest heavier nuclei, with energies up to 10^{20} GeV [*Gaisser*, 1990]. Those particles interact with atmospheric nuclei, and initiate intensive particle cascades [*Smart and Shea*, 1985], terminating in neutron production [*Light et al.*, 1973]. Therefore, the atmospheric neutron flux and consequently the ^{14}C(O) (i.e., ^{14}C and ^{14}CO) formation strongly depends on the flux and energy spectrum of the primary cosmic radiation.

The flux of the GCRs is constant, homogeneous and isotropic on time-scales of up to 10^4 to 10^5 years [*Reedy et al.*, 1983]. However, within the solar system, the GCR flux interacts with the solar wind plasma. The solar wind is "an expanding fully ionized and highly conducting plasma, which contains frozen-in irregular magnetic fields. Cosmic rays undergo many scatterings from these irregularities and execute a random walk in the solar wind. The cosmic ray population outside the heliosphere diffuses inward, and during this diffusive process it undergoes deceleration by the adiabatic cooling associated with the expansion of the solar wind" [*Smart and Shea*, 1985] (see also *Jokipii* [1991]). This deceleration effect increases with increasing density of the plasma, which itself increases with increasing solar activity. Therefore the flux of primary GCR particles reaching the Earth is anti-correlated to the solar cycle with a nominal period of 11 years [*Damon and Sonett*, 1991]. This results in a modulation of the total ^{14}C(O) source strength with a peak to mean amplitude of 20-25% and a period of 11 years [*Lingenfelter*, 1963; *Damon and Sonett*, 1991; *Reedy et al.*, 1983]. The modulation of the GCR particle flux reaching the Earth is usually described in terms of a modulation potential Φ (in MV). Φ is the heliocentric potential, i.e., the energy per unit charge a particle loses while penetrating the solar wind from the heliopause to the Earth's orbit [*Ehmert*, 1959; *Smart and Shea*, 1985]. It is observed that the level of mean solar activity (e.g. expressed in terms of Φ) varies from solar cycle to solar cycle and on average gradually increased during the

last century (Keran O'Brien, personal communication, 1999). Typical values of the shielding potential range from 300 MV to 500 MV for solar minimum conditions, and from 800 MV to 1200 MV for solar maximum conditions.

The Earth's magnetic field disturbs the isotropy of the incident GCR particles, because of the Lorentz force that the magnetic field exerts on the moving charged particles. Since the magnitude of this force depends on the angle between the path of the particle and the magnetic field line, a particle approaching the earth normal to its surface at low geomagnetic latitudes, where this angle is around 90^o, requires a higher momentum over charge ratio to be able to reach the atmosphere than a respective particle near the geomagnetic poles, where the angle is close to zero. The momentum over charge ratio, the so-called rigidity, is therefore a measure of the resistance of a charged particle to a magnetic force that deflects the particle from a straight-line trajectory. The minimum rigidity that an incident charged particle needs to reach a certain point within the atmosphere is the "cut-off rigidity" of this specific location. Particles with rigidity lower than the cut-off rigidity are effectively shielded. This shielding effect increases with the strength of the magnetic field. As a consequence, the flux of incident primary particles is anti-correlated to the long-term variation (of the order of 10^3-10^4 years) of the Earth's magnetic field [*Damon et al.*, 1978; *Damon and Sonett*, 1991]. For the application of ^{14}CO (with an atmospheric lifetime of about 3 months) the long-term variation of the magnetic field can be neglected, but the solar modulation has to be taken into account when ^{14}CO time series are to be compared.

The interaction of GCR particles with the solar wind plasma also depends on the particle rigidity [*Lal*, 1988]. As a consequence, the shape of the GCR particle rigidity spectrum reaching the atmosphere also changes with solar activity, which affects the relative distribution of neutron production and ^{14}C(O) production within the atmosphere. Only primary particles with high enough rigidity (above the respective cut-off rigidity) reach the lower-latitudes, and can penetrate into the atmosphere, because the low-rigidity particles are effectively shielded by the Earth's magnetic field. Furthermore, the particles with a high rigidity are less affected by changes of the solar wind during the solar cycle than the particles with lower rigidity. Therefore, the flux of low-rigidity particles varies with a larger amplitude during the solar cycle than that of particles with high rigidity. As a consequence, the ^{14}C production rate over a solar cycle changes more at high latitudes and high in the atmosphere (it decreases with increasing solar activity) than in equatorial regions and deep in the atmosphere. This results in a relative shift of the production rate towards lower latitudes and altitudes (larger depth) during solar maximum compared to solar minimum and vice versa.

Finally, one further effect has to be mentioned. Besides modulating the GCR flux,

the sun itself produces low to medium energy protons (up to 10^{10}eV) during solar proton events (SPEs), which also initiate particle cascades in the atmosphere [*Smart and Shea*, 1985]. Because of the generally lower energy of the SPE protons compared to GCR protons, this additional production of ^{14}CO has a spatial distribution that differs from that of galactic cosmic rays [*Lingenfelter and Flamm*, 1964; *Masarik and Reedy*, 1995]. The solar proton contribution to the ^{14}C production averaged over a whole solar cycle for current solar activity is of the order of 10% of the total cosmogenic production [*Lingenfelter and Flamm*, 1964; *Lingenfelter and Ramaty*, 1970]. This is neglected in the present analysis, which focuses on the effect of the source distribution and not on the absolute scale. However, it should be mentioned that the temporal variation of the solar proton component plays a significant role for short-term fluctuations, because a large fraction of the additional ^{14}C production can originate from a few single solar proton events on the time scale of hours to days [*Lal*, 1988; *Lingenfelter and Ramaty*, 1970; *Lal and Peters*, 1967]. The influence of such solar proton events (SPEs) on atmospheric ^{14}CO is as separate issue discussed in chapter 9.

The rather complex interactions of the GCR particles with the solar wind plasma and the magnetic field of the Earth lead to a characteristic spatial distribution and energy spectrum of neutrons in the atmosphere [*Hess et al.*, 1961, 1959; *Armstrong et al.*, 1973; *Merker et al.*, 1973; *Light et al.*, 1973; *Miles*, 1964]. The reaction cross section of the ^{14}C formation (Eq. (5.1)), however, depends on the neutron energy, as shown in Figure 5.1 (left). The atmospheric neutron spectrum also shown in Figure 5.1 (right) is taken from *Hess et al.* [1959]. Since the cross section is largest at low neutron energies, neutron thermalization within the atmosphere has to be taken into account in order to derive the ^{14}CO production rate from the neutron production rate.

5.2.2 The spatial distribution of ^{14}CO production in the atmosphere

The rather complex relations described so far clearly show that an accurate determination of the 3-dimensional ^{14}C(O) production rate distribution in the atmosphere and its temporal variation is not straightforward. Only three independent estimates of this production rate distribution (with high enough spatial resolution for application in atmospheric chemistry modeling) are currently available.

1. *Lingenfelter* [1963] used measurement data on neutron count rates and star (nuclear disintegrations) production rates to derive a 3-D neutron production rate for solar minimum and solar maximum conditions. Compiling this with a neutron-diffusion code, *Lingenfelter* [1963] derived the atmospheric equilibrium neutron flux and, using the cross section for radiocarbon formation (Eq. (5.1)), was able to deduce

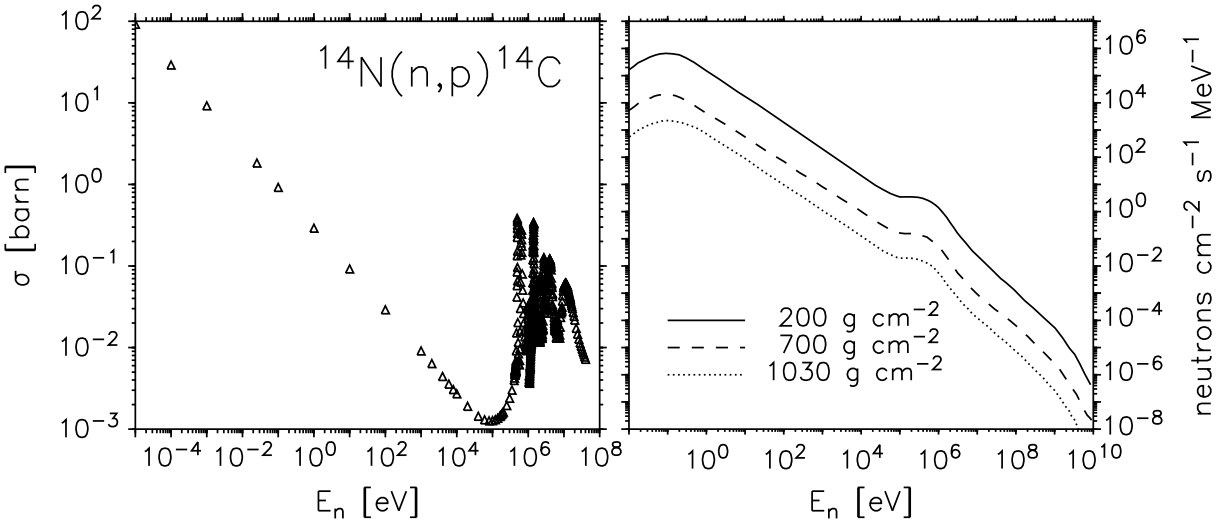

Figure 5.1: Cross section σ of the ^{14}N(n,p)^{14}C reaction versus neutron energy E_n (*Young et al.* [1994], left) and atmospheric neutron spectrum (*Hess et al.* [1959], right). The spectrum is shown for 44^o geomagnetic latitude at three atmospheric depths.

a 3-D distribution of the ^{14}C production rate. For time dependence, *Lingenfelter* [1963] interpolated linearly between the production rates for solar minimum and solar maximum conditions. This source distribution of ^{14}C(O) is further denoted as LF.

2. The approach of *O'Brien et al.* [1991] (based on *O'Brien* [1971] and *O'Brien* [1979]) differs. *O'Brien et al.* [1991] carried out "detailed calculations of the physical processes involved in cosmogenesis, taking into account the structure of the geomagnetic field, the interaction of galactic cosmic rays with it and with the solar wind, and the subsequent hadronic cascade in the atmosphere" [*O'Brien et al.*, 1991], yielding estimates of the cosmic ray particle spectrum at a given location in the Earth's atmosphere for a given solar modulation. From this the radiocarbon production rate is derived for 5 solar modulation potentials (Φ = 0, 300, 600, 900, and 1200 MV). This ^{14}CO source distribution is further denoted as OB.

3. *Masarik and Beer* [1999] (and earlier *Masarik and Reedy* [1995]) developed a "purely physical" model for the simulation of cosmic ray particle induced atmospheric cascades, including the transport of secondary particles. From the calculated neutron fluxes and the cross sections for the ^{14}C production, the ^{14}C production rate distribution is calculated. Data for the solar modulation potential Φ ranging from Φ = 0 MV to Φ = 1000 MV in steps of 50 MV is provided (J. Masarik, personal communication, 1999). This ^{14}CO source distribution is further denoted as MA.

All three source distributions are given in geomagnetic coordinates, taking into account the electromagnetic properties of the primary particles, and are considered

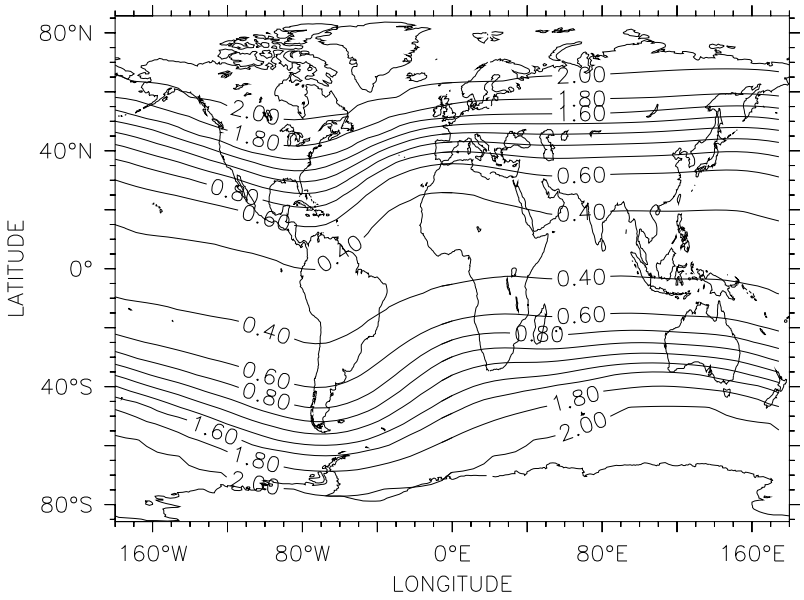

Figure 5.2: Depth integrated annual mean cosmogenic production rate of ^{14}CO. The data is taken from *Lingenfelter* [1963] (solar minimum) and transformed from geomagnetic to geographic coordinates, using the AACGM-algorithm of *Bhavnani and Hein* [1994]. The unit is ^{14}CO-molecules cm^{-2} s^{-1} normalized to a global average production rate of 1 ^{14}CO-molecule cm^{-2} s^{-1} in an idealized static atmosphere of constant depth (1033 g cm^{-2}).

symmetric with respect to the geomagnetic equator. The vertical dimension is provided as atmospheric depth in g cm^{-2}. To calculate the global atmospheric ^{14}CO mixing ratio with a 3-D atmospheric model, the provided coordinates (geomagnetic coordinates and atmospheric depth) have to be transformed to the respective model coordinates (geographic coordinates and atmospheric pressure). To a first-order approximation, the Earth's magnetic field is a dipole. The intercept points of the dipole axis with the Earth's surface are the geomagnetic poles, and in principle the transformation can be accomplished by a simple coordinate rotation. At a closer look, the dipole approximation turns out to be deficient because it does not account for important deviations from dipole symmetry (multi-pole moments of higher order) which also affect the primary particle trajectories and hence the production rate distribution of cosmogenic isotopes. Therefore a more accurate coordinate conversion, in the form of a code for calculating 'altitude adjusted corrected geomagnetic coordinates" (AACGM) [*Bhavnani and Hein*, 1994] is applied. This code is essentially based on a 4$^{\text{th}}$ order spherical harmonics expansion of the geomagnetic field, however implies further corrections.

The transformed depth integrated source distribution (annual average, LF, solar minimum) is depicted in figure 5.2. The distribution is normalized to a global average production rate of 1 molec cm^{-2} s^{-1} in an idealized static atmosphere of

constant depth (1033 g cm^{-2}). The effect of the geomagnetic field is clearly visible, since the axis of the dipole component of the field does not coincide with the rotation axis. The use of AACGM-coordinates introduces a slight asymmetry between NH and SH, caused by the asymmetry of the magnetic field. The lines of constant production rate in Figure 5.2 mirror directly the lines of constant cut-off rigidity for the cosmic ray particles that are given by *Smart and Shea* [1985] and can, e.g., be obtained from the " National Geophysical Data Center - Space Physics Interactive Data Resource" (NGDC-SPIDR). Because the AACGM transformation is identically applied to all three source distributions, and the sources hardly differ concerning the relative horizontal distribution (as shown below), Figure 5.2 looks almost identical for the MA and OB source distribution.

The vertical distribution of the ^{14}CO production rate under solar minimum conditions (zonal average) is shown in the left part of Figure 5.3. The right part shows the relative change (plotted as ratio r to the respective solar minimum distribution) of the production rate, when the solar activity is at its maximum. All source distributions are normalized to a global average production rate of 1 molec cm^{-2} s^{-1} in an idealized static atmosphere of constant depth (1033 g cm^{-2}), in order to compare for the relative distribution only, and to be independent of the change of the actual global average production rate of ^{14}CO with the solar activity. The actual ratio δ of the absolute local production rate between solar maximum and solar minimum can then be calculated by

$$\delta = r \cdot w \ , \tag{5.3}$$

where r is the normalized ratio and w the ratio between the global average production rate at solar maximum and solar minimum.

The same normalization is chosen for the comparison of the different source distributions (solar minimum conditions) depicted in Figure 5.4. The upper panel of Figure 5.4 shows again the annual zonal average production rate of *Lingenfelter* [1963] (LF) under solar minimum conditions, below are the relative differences of the MA, and the OB source respectively, plotted as ratio to the LF distribution.

The ^{14}CO production rate is largest in polar regions at 70 to 100 g cm^{-2}, which corresponds to an altitude of roughly 15-20 km in a standard atmosphere. Below this level (at larger depth), the production rate at all latitudes drops down exponentially. This property is common to all three distributions, however with different attenuation "lengths" (in units of atmospheric depth). The LF distribution implies the longest attenuation length, i.e., the "slowest" decline of production rate with increasing atmospheric depth. In contrast to this, the attenuation length below the production rate maximum is shorter in the MA and OB distribution, with little difference between the two. Compared to the LF source distribution, in the MA

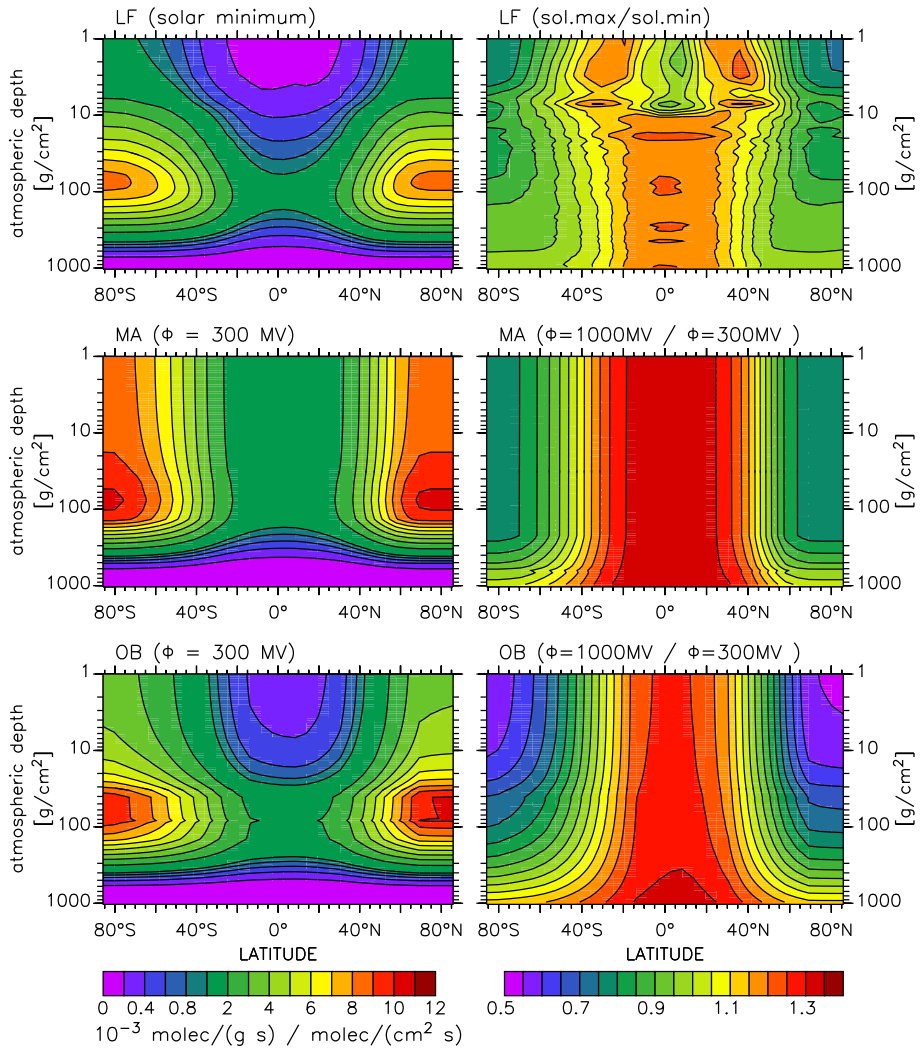

Figure 5.3: Annual zonal mean cosmogenic ^{14}CO production rate for solar minimum conditions (Φ=300 MV) taken from *Lingenfelter* [1963] (LF), *Masarik and Beer* [1999] (MA), and *O'Brien et al.* [1991] (OB) (left column), and relative deviation of the respective distribution for solar maximum conditions (Φ = 1000 MV, right column). The unit of the production rate (left) is 10^{-3} molec g^{-1} s^{-1} normalized to a global average production rate of 1 molec cm^{-2} s^{-1} in an idealized atmosphere of constant depth (1033 g cm^{-2}). The dependence of the solar activity (right) is plotted as ratio of the solar maximum distribution to the solar minimum distribution. All original distributions are transformed from geomagnetic to geographic coordinates using the AACGM-algorithm of *Bhavnani and Hein* [1994].

and OB source the production rate at the surface level is more than 90% reduced.

Above the production rate maximum (at smaller atmospheric depth) the production rate decreases steepest in the LF distribution, less pronounced in the OB distribution, and is almost constant towards the top of the atmosphere in the MA distribution.

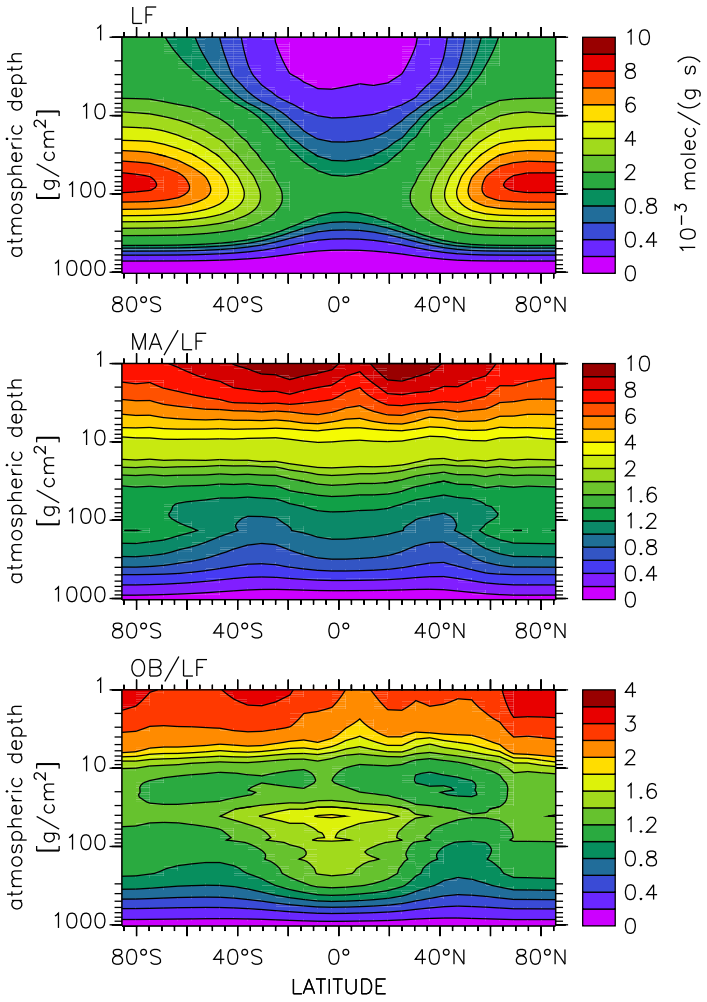

Figure 5.4: Annual zonal mean cosmogenic production rate of ^{14}CO taken from *Lingenfelter* [1963] (LF), and the relative deviations (plotted as ratio to the LF-estimate) of the respective estimates of *Masarik and Beer* [1999] (MA/LF) and *O'Brien et al.* [1991] (OB/LF). The distributions are for solar minimum conditions (Φ=300 MV). All original distributions are transformed from geomagnetic to geographic coordinates using the AACGM-algorithm [*Bhavnani and Hein*, 1994], and are normalized to a global average production rate of 1 molec cm^{-2} s^{-1} in an idealized atmosphere of constant depth (1033 g cm^{-2}). The unit of the LF distribution is 10^{-3} molec g^{-1} s^{-1} per molec cm^{-2} s^{-1} global average production rate.

The horizontal variation among the three source distributions is rather small; the lines of constant ratio in Figure 5.4 are nearly horizontal. This is completely different for the variation of the source pattern with the solar cycle (Figure 5.3, right). During the transition from solar minimum to solar maximum, all three source distributions exhibit a relative shift of production rate mainly in the horizontal direction from high to low latitudes, according to the rigidity dependence of the GCR - solar wind interaction. Due to the same effect, a relative shift of the production rate from

	LF		MA		OB	
	sol. min	sol. max	Φ= 300 MV	Φ= 1000 MV	Φ= 300 MV	Φ= 1000 MV
NH	48.26	48.42	48.43	48.60	47.47	47.95
STRAT	53.08	50.98	66.32	62.09	59.62	54.08
NH-STRAT	25.90	24.91	32.37	30.37	28.55	26.07
SH-STRAT	27.18	26.08	33.95	31.73	31.08	28.01

Table 5.1: Fraction (in %) of global cosmogenic ^{14}CO production in the northern hemisphere (NH), the stratosphere (STRAT), the northern hemisphere stratosphere (NH-STRAT), and the southern hemisphere stratosphere (SH-STRAT). The cosmogenic ^{14}CO distributions are taken from *Lingenfelter* [1963] (LF), *Masarik and Beer* [1999] (MA), and *O'Brien et al.* [1991] (OB), and have been transformed from geomagnetic to geographic coordinates according to *Bhavnani and Hein* [1994]. The integrations are performed assuming an idealized atmosphere of constant depth (1033 g cm^{-2}) with a climatological mean tropopause pressure of $(300 - 215 \cdot cos^2(\phi))$ hPa, where ϕ is the geographic latitude (see section 1.5). Distributions for solar minimum (sol.min, Φ=300 MV) and solar maximum conditions (sol.max, Φ=1000 MV), where Φ is the solar modulation potential, are taken into account.

higher to lower altitudes is visible, mostly at high latitudes. The solar modulation effect on the production rate distribution is most pronounced in the MA source distribution, and least in the LF distribution.

For a more quantitative comparison of the different source distribution estimates, and further to quantify the influence of the solar cycle on the production rate distribution, Table 5.1 lists the relative distribution of the ^{14}CO production rate in various atmospheric domains. Common to all three source distribution estimates is a slight asymmetry of the total ^{14}CO production between the two hemispheres, with a 5-6% larger production in the SH than in the NH. This asymmetry results from the asymmetric structure of the geomagnetic field (cf. Figure 5.2) and does therefore not vary significantly with the solar cycle.

The most important difference between the production rate estimates is, as already shown above, the relative distribution in vertical direction. More than half of the ^{14}CO production takes place in the stratosphere in any case. The calculations of *Masarik and Beer* [1999] (MA) predict the largest fraction (62-66%) of ^{14}CO production in the stratosphere, followed by *O'Brien et al.* [1991] (OB) with 54-59%, and by *Lingenfelter* [1963] (LF) with the smallest fraction in the stratosphere (51-53%). These ranges are due to changes in solar activity with the larger stratospheric fraction during solar minimum, and the smaller during solar maximum conditions respectively.

The rather small NH-SH asymmetry of the ^{14}CO production, and the likewise small

variation of the partitioning between stratosphere and troposphere during a solar cycle, combine to result in a SH stratospheric fraction that is larger than the NH stratospheric fraction; however, both decrease with increasing solar activity, in favor of the (generally lower) tropospheric fractions of the respective hemispheres.

Finally, in this context, it is interesting to note that the ^{14}CO source distribution and its sink distribution (OH) have nearly opposite structures in horizontal and vertical direction (cf. Figures 1.5 and 5.3). The ^{14}CO production rate is largest in the lower polar stratosphere, i.e., in the "lowermost stratosphere" [*Holton et al.*, 1995], where the OH concentration is very low, and it is smallest in the tropics of the troposphere, where the OH concentration is high.

5.3 Model Setup

The model is initialized with an atmospheric ^{14}CO mixing ratio equal to zero at simulation time Jan 1, 1993. The original source distribution is projected offline onto the horizontal model grid using the AACGM algorithm of *Bhavnani and Hein* [1994], for transformation from geomagnetic to geographic coordinates. At this stage, the atmospheric depth is kept as vertical coordinate. During the model integration, the production rate data is converted from atmospheric depth levels to the pressure levels defined by the model's hybrid coordinates and the temporally varying surface pressure (see chapter 2). This conversion is performed by a linear interpolation of the decadal logarithm of the production rate onto the pressure levels. The simulation time is 2 years, driven by the NCEP reanalysis data of the years 1993 and 1994 [*Kalnay et al.*, 1996]. Only the output from the second year (5 day averages of the ^{14}CO mixing ratio) is used for further analysis. The OH-1 distribution (monthly averages) is prescribed for the oxidation of ^{14}CO (see section 1.4).

Identical model simulations are performed with two model configurations (2.0-SLT and 2.0-SPF) for the LF, MA, and OB source distribution, for solar minimum and solar maximum conditions respectively. For solar minimum, $\Phi = 300$ MV, and for solar maximum, $\Phi = 1000$ MV is considered for the MA and OB distributions. All source distributions are normalized to a constant global average production rate of 1 molec cm^{-2} s^{-1} in an idealized static atmosphere of constant depth (1033 g cm^{-2}). This normalization is performed in order to account only for differences in the ^{14}CO production rate distribution and not for the absolute scale. The scaling is possible, because the simulated ^{14}CO mixing ratio is linearly dependent on the constant global average production rate. Finally, one model simulation was performed with the 2.0-SPFR configuration (LF source distribution, solar minimum), in order to estimate the effect of the mass conservation violation on the simulated ^{14}CO distribution.

	LF		MA		OB	
	sol. min	sol. max	Φ= 300 MV	Φ= 1000 MV	Φ= 300 MV	Φ= 1000 MV
NH	48.26	48.42	48.43	48.60	47.47	47.95
STRAT	56.12	54.04	69.17	65.12	62.53	57.17
NH-STRAT	27.79	26.78	34.18	32.21	30.33	27.93
SH-STRAT	28.33	27.26	34.99	32.91	32.20	29.24
$f_{\bar{q}}$	1.000	1.000	1.010	1.010	1.005	1.004

Table 5.2: Annual average fraction (in %) of global cosmogenic ^{14}CO production in the northern hemisphere (NH), the stratosphere (STRAT), the northern hemisphere stratosphere (NH-STRAT), and the southern hemisphere stratosphere (SH-STRAT). The cosmogenic ^{14}CO distributions are taken from *Lingenfelter* [1963] (LF), *Masarik and Beer* [1999] (MA), and *O'Brien et al.* [1991] (OB). Distributions for solar minimum (sol.min, Φ=300 MV) and solar maximum conditions (sol.max, Φ=1000 MV), where Φ is the solar modulation potential, are taken into account. The original source distributions are transformed from geomagnetic to geographic coordinates according to *Bhavnani and Hein* [1994], and normalized to a global average production rate of 1 molec cm^{-2} s^{-1} in an idealized atmosphere of constant depth (1033 g cm^{-2}). The integrations are performed after online interpolation onto the model grid (NCEP meteorology of 1994). The tropopause is online diagnosed according to the WMO-definition [*WMO*, 1992]. Model output is archived as 5-day averages. $f_{\bar{q}}$ is the fraction of the global average production rate in an idealized atmosphere of constant depth (1033 g cm^{-2}) that appears on the model grid.

5.4 Model results

Before the model results are compared with regard to differences between the source distributions and variations with the solar cycle, the online interpolation of the source distribution onto the model grid has to be checked. Table 5.2 lists again the relative distribution of the ^{14}CO production rate integrated for various atmospheric domains (cf. Table 5.1), this time however integrated in the model atmosphere (model output), instead of the idealized static atmosphere. Furthermore the WMO-tropopause definition [*WMO*, 1992] is used instead of the climatological approximation (cf. section 1.5).

The asymmetry between NH and SH is preserved, as expected, since the transformation from geomagnetic to geographic latitudes is calculated offline. However the fraction of ^{14}CO that is produced in the stratosphere is larger in the model atmosphere (Table 5.2) than in the idealized atmosphere (Table 5.1) by a constant offset of roughly +3% (+2% in the NH, +1% in the SH). This is most likely caused by the different tropopause definitions. In the idealized atmosphere, the climatological tropopause is fixed at a given latitude; in the model atmosphere the diagnosed tropopause varies with time. The annual mean tropopause heights of both defini-

tions are not necessarily identical.

As also shown in Table 5.2, the global average production rate of ^{14}CO in the model atmosphere is up to 1% larger than that in the idealized static atmosphere. This small deviation arises from the online interpolation of the source distribution on the temporally varying pressure levels in the model atmosphere, and has to be taken into account later when absolute values of atmospheric ^{14}CO mixing ratios are to be compared. At this stage, however, only relative distributions are of interest.

Moreover, neglecting the production rate above the non-zero upper boundary of the model atmosphere (see section 1.3 and chapter 2) introduces a systematic error, which is small, however. Only 0.7%, 3%, and 1.1% (LF, MA, OB) of the total ^{14}CO production occur at depths lower than 10 g cm^{-2}, with a small variation between solar minimum and maximum.

An issue is the inherent mass mismatch of the 2.0-SPF configuration. Since relative distributions of atmospheric ^{14}CO are to be compared, all simulated mixing ratios of ^{14}CO in the further analysis are normalized at each time step of the model output (5-day averages) to a global average burden of 1 kg ^{14}CO in the model atmosphere.

5.4.1 The effect of uncertainties in the source distribution of ^{14}CO

Figure 5.5 shows the differences in the vertical distribution of atmospheric ^{14}CO when different source distributions (solar minimum) are applied. As in the discussion of the differences between the three source distributions (section 5.2.2), the LF source is again chosen as the "standard", to which the other two are compared.

The simulated distribution of ^{14}CO in the atmosphere resembles the distribution of ^{14}C(O) production (cf. Figure 5.3) with a maximum in the polar lower stratosphere, and a minimum in the lower equatorial troposphere. The predicted mixing ratio maximum in the lowermost stratosphere of both model configurations is larger in the SH than in the NH. Furthermore, both maxima (NH and SH) are smaller in the 2.0-SLT simulation than in the 2.0-SPF simulation.

The effect of different source distributions, which mostly differ in their vertical structure, on the vertical atmospheric ^{14}CO distribution is almost identical for both model configurations. Applying the MA or the OB source instead of the LF source results in lower levels of ^{14}CO in the troposphere below 90 hPa - 100 hPa, and higher ones above. The variation of this effect with latitude is weak, conforming with the fact that the three sources differ primarily in their vertical gradients of ^{14}C(O) production (cf. Figure 5.4).

Within the stratosphere, the differences in the vertical gradients of the ^{14}C(O) production rate (Figure 5.4) are mirrored in the simulated atmospheric ^{14}CO mixing

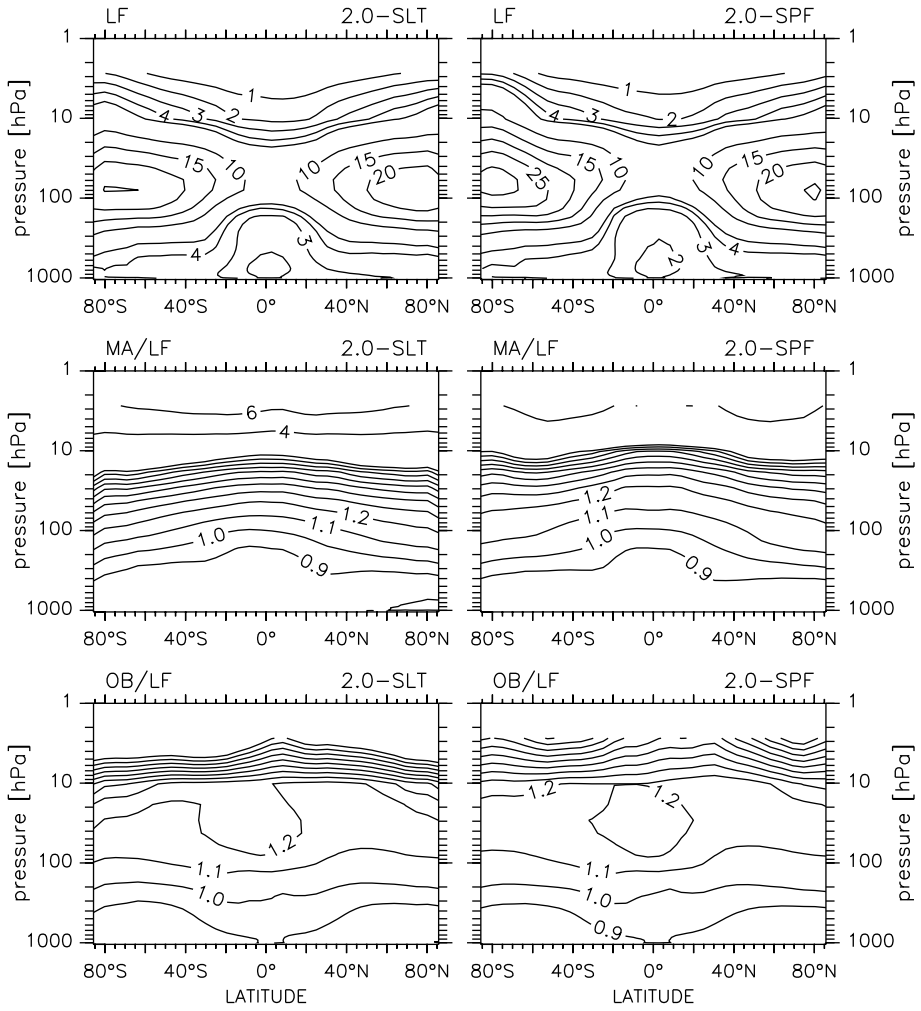

Figure 5.5: Annual zonal mean distribution of cosmogenic ^{14}CO calculated with two model configurations (2.0-SLT and 2.0-SPF). The upper row shows the results (in molec cm^{-3} STP normalized to an annual average atmospheric burden of 1 kg) calculated with the source distribution of *Lingenfelter* [1963] (LF) for solar minimum conditions. Below are the deviations of the respective calculations (plotted as ratio to the LF-result) with the distributions from *Masarik and Beer* [1999] (MA) and *O'Brien et al.* [1991] (OB), both for a solar modulation potential of $\Phi = 300$ MV. Isolines between 1.2 and 2 are in steps of 0.1.

ratios (Figure 5.5). For instance, the MA source distribution implies the largest production rate above 10 hPa among the three distributions. As a consequence, with the MA distribution the largest mixing ratio above this level is simulated. For the OB distribution, even the local maximum of the production rate ratio in the tropics at about 50 hPa (Figure 5.4) is present in the respective ratio of mixing ratios (Figure 5.5), although less distinct.

Within the troposphere, a similar result is observed, but with an important difference compared to the stratosphere. The ^{14}CO mixing ratio is smaller near the surface for

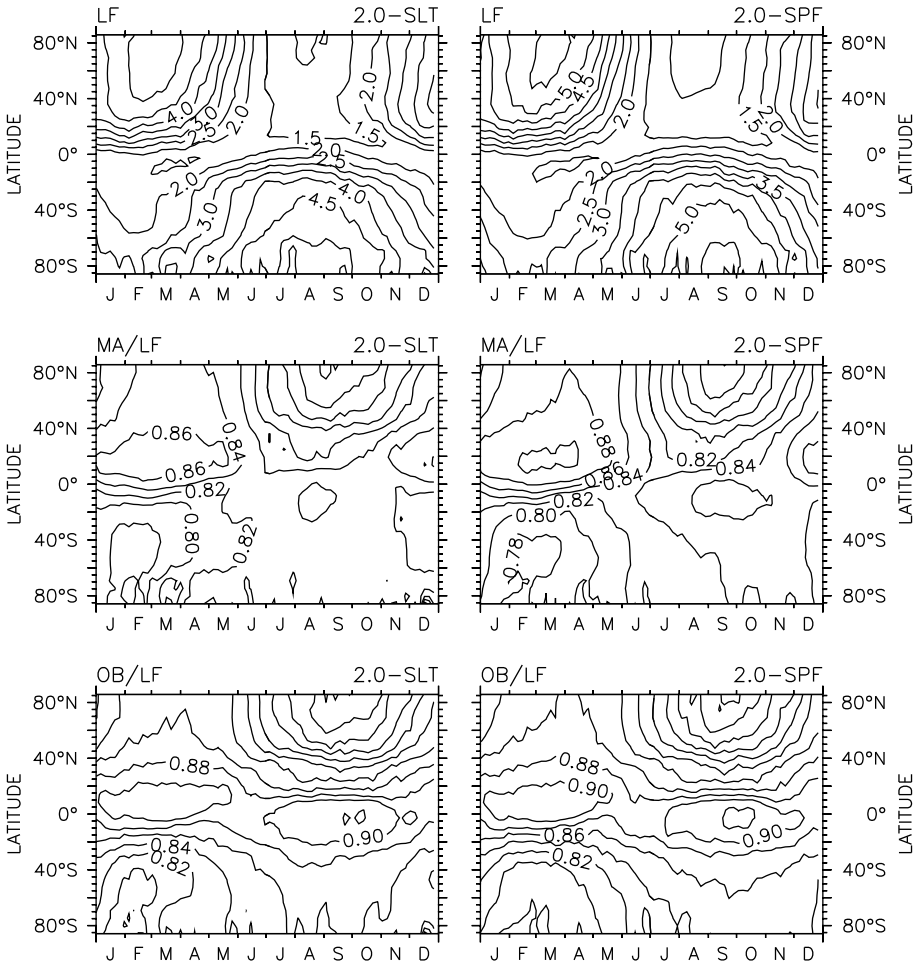

Figure 5.6: Annual cycle of zonal mean ^{14}CO at the surface level resulting from model calculations with different model configurations (2.0-SLT and 2.0-SPF). The upper row shows the results (in molec cm^{-3} STP normalized to an annual average atmospheric burden of 1 kg) calculated with the source distribution of *Lingenfelter* [1963] (LF) for solar minimum conditions. Below are the deviations of the respective calculations (plotted as ratio to the LF-result) with the distributions from *Masarik and Beer* [1999] (MA) and *O'Brien et al.* [1991] (OB), both for a solar modulation potential of $\Phi = 300$ MV, and likewise normalized to an annual average atmospheric burden of 1 kg before comparison.

the two source distributions (MA and OB) with less production near the surface. However, the vertical gradients in the mixing ratios are much smaller than the vertical gradients in the production rates, indicating that the troposphere in the model as in reality is well mixed, in contrast to the stratosphere.

Simulations of the zonal average annual cycle of ^{14}CO at the surface level are depicted in Figure 5.6. The simulated ^{14}CO mixing ratio at the surface shows a maximum in spring and a minimum in autumn. The amplitude of this annual cycle is very low around the equator and increases with latitude.

Applying the OB or MA source distribution instead of the LF distribution, the surface level mixing ratio is reduced (Figure 5.6), in accordance with the reduced tropospheric production rate of OB and MA compared to LF (Figure 5.4). The 2.0-SLT configuration predicts an annual zonal mean reduction of the ^{14}CO mixing ratio at the surface level compared to the LF-"standard" of 18% when the MA source distribution is applied, and of 14% when the OB distribution is applied. The respective values simulated with the 2.0-SPF configuration are 16% (MA) and 14% (OB), respectively.

This reduction however, exhibits a latitude dependent seasonal modulation with values varying from 26% at high NH latitudes around September (shortly after the mixing ratio is at its minimum) to 10%-14% in the tropics. The largest reduction is common to both model configurations for both the MA and OB distributions. The lowest reduction, in contrast, is lower for the OB source distribution, although, it hardly varies between the two model configurations.

The simulations with different source distributions further reveal a general asymmetry between NH and SH in the model. The annual variation of the ^{14}CO mixing ratio reduction at the surface level due to the different vertical source structure is very pronounced in the NH with a striking maximum of 26% in autumn. This characteristic is much less distinct in the SH, where the overall seasonal amplitude of this reduction is lower (Figure 5.6).

Table 5.3 lists the relative distribution of the simulated atmospheric burden (annual average) of ^{14}CO over various atmospheric domains. In general, this distribution mirrors the relative distribution of the ^{14}CO production (Table 5.2), however with small differences. The NH-SH asymmetry of the atmospheric burden is somewhat larger than that of the production rate distribution, i.e. more ^{14}CO is found in the SH of the model.

Furthermore, the fraction of atmospheric ^{14}CO, that on average resides in the stratosphere is smaller than the fraction of ^{14}CO that is produced there. This discrepancy between production and burden is larger in the 2.0-SLT configuration than in the 2.0-SPF configuration, in agreement with the lower maximum mixing ratios around 80 hPa in polar regions predicted by the 2.0-SLT configuration compared to the 2.0-SPF configuration (cf. Figure 5.5). In combination, the NH-SH asymmetry is more enhanced in the 2.0-SPF atmosphere, especially in the stratosphere, and not significantly enhanced in the 2.0-SLT atmosphere.

Finally, the relative distribution of the atmospheric ^{14}CO burden over the four domains hardly varies with solar activity. This is to be expected, since the solar cycle variation of the source distribution in vertical direction is rather small, and the respective variation in horizontal direction is almost hemispherically symmetric

		LF		MA		OB	
		sol. min	sol. max	Φ= 300 MV	Φ= 1000 MV	Φ= 300 MV	Φ= 1000 MV
2.0-SLT	NH	47.49	47.58	47.97	48.10	47.12	47.42
	STRAT	42.76	42.47	50.39	50.12	47.09	45.43
	NH-STRAT	20.59	20.50	24.33	24.30	22.34	21.76
	SH-STRAT	22.17	21.97	26.05	25.82	24.76	23.67
2.0-SPF	NH	45.83	45.96	46.33	46.53	45.50	45.85
	STRAT	45.07	44.69	51.35	50.88	49.38	47.76
	NH-STRAT	20.72	20.62	23.79	23.73	22.43	21.95
	SH-STRAT	24.35	24.07	27.56	27.16	26.95	25.81

Table 5.3: Annual mean fraction of atmospheric ^{14}CO burden (in %) in the northern hemisphere (NH), the stratosphere (STRAT), the northern hemisphere stratosphere (NH-STRAT), and the southern hemisphere stratosphere (SH-STRAT) calculated with the 2.0-SLT and 2.0-SPF model configurations. The cosmogenic ^{14}CO distributions are taken from *Lingenfelter* [1963] (LF), *Masarik and Beer* [1999] (MA), and *O'Brien et al.* [1991] (OB). Distributions are for solar minimum (sol.min, Φ=300 MV) and solar maximum conditions (sol.max, Φ=1000 MV), where Φ is the shielding potential. They have been transformed from geomagnetic to geographic coordinates using the AACGM algorithm of *Bhavnani and Hein* [1994], and normalized to a global average production rate of 1 molec cm^{-2} s^{-1} in an idealized atmosphere of constant depth (1033 g cm^{-2}). The integrations are performed after online interpolation onto the model grid, using the NCEP meteorology of 1994. The tropopause is online diagnosed according to the WMO-definition *WMO* [1992].

(cf. Figure 5.3).

On a shorter timescale, however, the distribution of ^{14}CO burden varies considerably, due to seasonal variations of atmospheric transport and OH. This is shown in Figure 5.7 for the 2.0-SLT configuration, and in Figure 5.8 for the 2.0-SPF configuration. The simulated global atmospheric burden of ^{14}CO is almost constant throughout the year and varies only ±3% around the annual average. However, the partitioning among the hemispheres and atmospheric layers is by far not constant.

In the troposphere the burden is largest in autumn, i.e. in the SH in August, and in the NH in February. Therefore the tropospheric burden of each hemisphere exhibits the same annual cycle as the respective OH concentration, however with a time lag of approximately 2 months (cf. Figure 1.6). The annual average burden fraction is larger in the SH troposphere than in the NH troposphere, reflecting the larger OH abundance in the NH model troposphere (cf. Table 1.1 for OH-1). Furthermore, the tropospheric burden is larger when more ^{14}CO is produced in the troposphere, i.e. lowest for the MA source distribution and largest for the LF source distribution. The difference in the tropospheric burden fraction between the model configurations is small, apart from a slightly lower fraction in the 2.0-SPF NH than in the 2.0-SLT

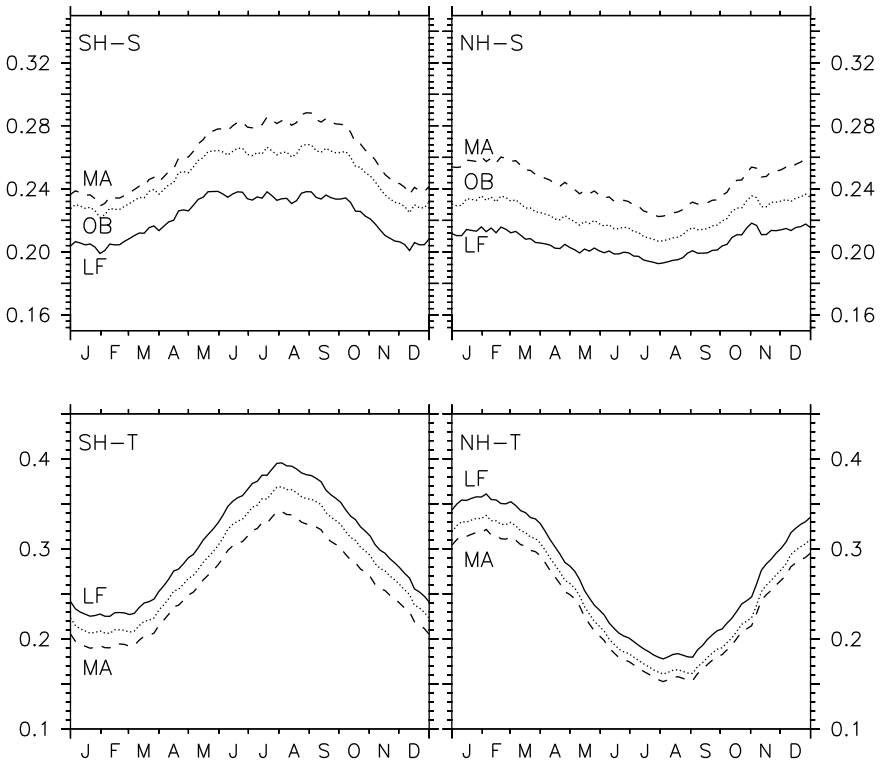

Figure 5.7: Seasonal cycle of the atmospheric ^{14}CO burden fraction in the southern hemisphere stratosphere (SH-S), the northern hemisphere stratosphere (NH-S), the southern hemisphere troposphere (SH-T), and the northern hemisphere troposphere (NH-T), calculated with the 2.0-SLT configuration and the ^{14}CO source distributions from *Lingenfelter* [1963] (LF), *Masarik and Beer* [1999] (MA), and *O'Brien et al.* [1991] (OB) for solar minimum conditions (Φ=300 MV). The tropopause is online diagnosed according to the WMO definition [*WMO*, 1992]. The annual variability of the total atmospheric burden is in all cases less than $\pm$3% around the annual average.

NH, and a somewhat larger fraction in the 2.0-SPF stratosphere, compared to the 2.0-SLT stratospere.

The stratospheric burden fraction is, similar to the troposphere, larger when more ^{14}CO is produced in the stratosphere, i.e. smallest for the LF source distribution and largest for the MA source distribution. In the stratosphere the annual cycle of the relative atmospheric ^{14}CO burden fraction differs, however, in shape between the two hemispheres. In the SH it exhibits a broad maximum extending from June to October and a minimum from December to February. In the NH, in contrast, the amplitude of the seasonal cycle is smaller, with the burden fraction almost linearly decreasing from February to August and increasing again until February. The stratospheric seasonal cycle of the burden fraction is also roughly anti-correlated to the respective seasonal cycle of OH (cf. Figure 1.6). Finally, the amplitudes of the stratospheric burden fractions are larger in the 2.0-SPF atmosphere than in the

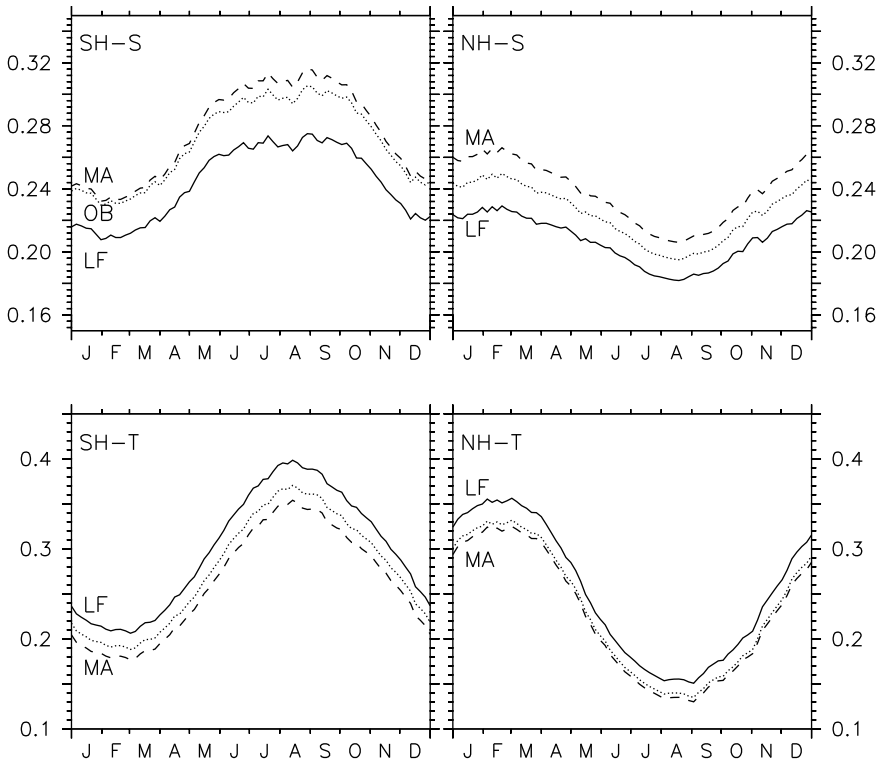

Figure 5.8: Same as Figure 5.7, calculated with the 2.0-SPF configuration.

2.0-SLT atmosphere.

5.4.2 The effect of variations in the source distribution of ^{14}CO with solar activity

The vertical, annually zonally averaged distributions of atmospheric ^{14}CO for solar minimum and solar maximum conditions are compared in Figure 5.9 (2.0-SLT), and in Figure 5.10 (2.0-SPF). The left columns show the annual zonal mean ^{14}CO mixing ratio, normalized to an annual average atmospheric burden of 1 kg, and for solar minimum conditions. The right columns depict the relative change (plotted as ratio to solar minimum conditions) when solar maximum is reached.

The ^{14}CO maximum in the SH polar lower stratosphere (at solar minimum) is larger than the respective NH maximum in both model configurations for all three source distributions. The vertical gradient in the troposphere is very similar for all source distributions and model configurations. Above 10 hPa, however, the vertical gradient differs between the results obtained with different source distributions. It is steepest when the LF source is applied, and flattest in the MA case. This follows the differences in the production rate gradients above 10 hPa (cf. Figure 5.3). It is observed independent of the model configuration.

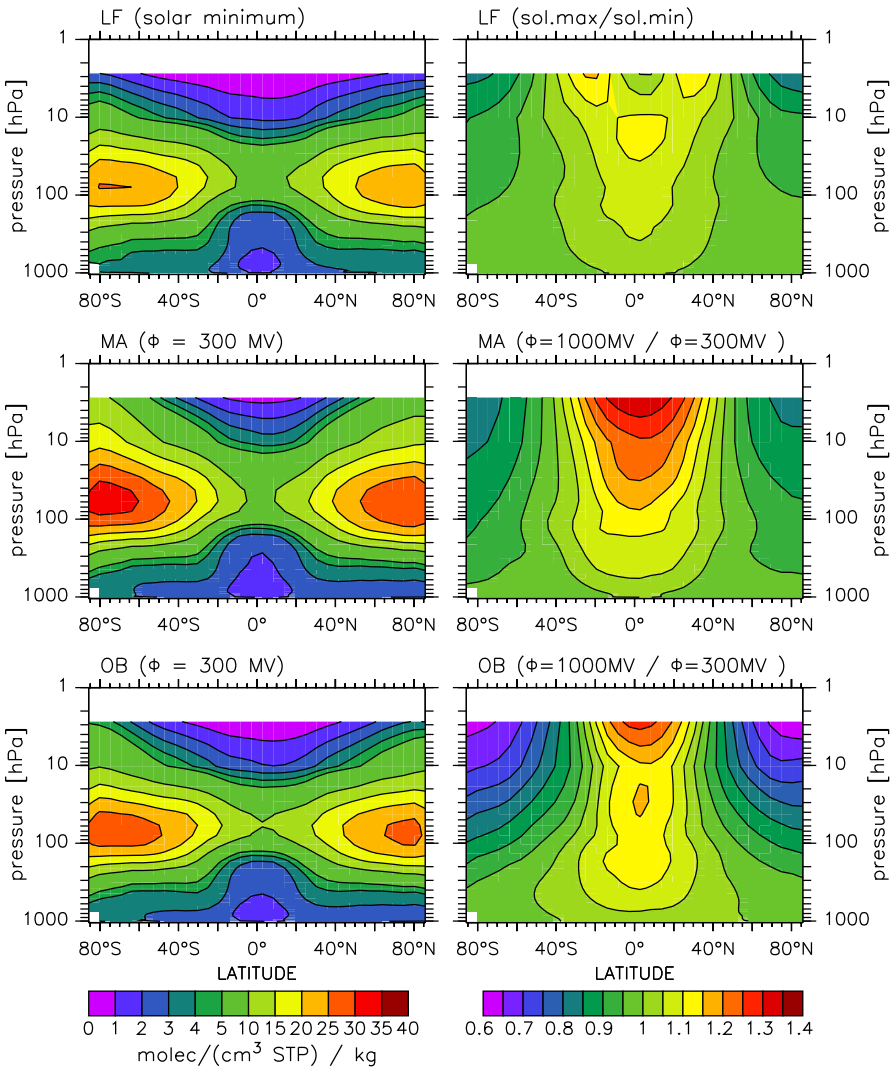

Figure 5.9: Annual zonal mean distribution (in molec cm^{-3} STP per 1 kg annual average atmospheric burden) for solar minimum conditions (Φ=300 MV, left column), and relative shift when solar maximum conditions (Φ=1000 MV) are assumed (right column). Shown is the ratio between the solar maximum result and the solar minimum result, both normalized to an annual average atmospheric burden of 1 kg ^{14}CO. Model calculations are performed with the 2.0-SLT configuration and the source distributions of *Lingenfelter* [1963] (LF), *Masarik and Beer* [1999] (MA), and *O'Brien et al.* [1991] (OB).

For a given source distribution, the relative change in the ^{14}CO mixing ratio due to variations in the solar activity is also largely independent of the model configuration (Figures 5.9 and 5.10). The relative horizontal shift of the mixing ratio during a solar cycle is quasi hemispherically symmetric (from the poles to the equator) as is the relative horizontal re-distribution of the ^{14}CO production rate (cf. Figures 5.3, 5.9, and 5.10).

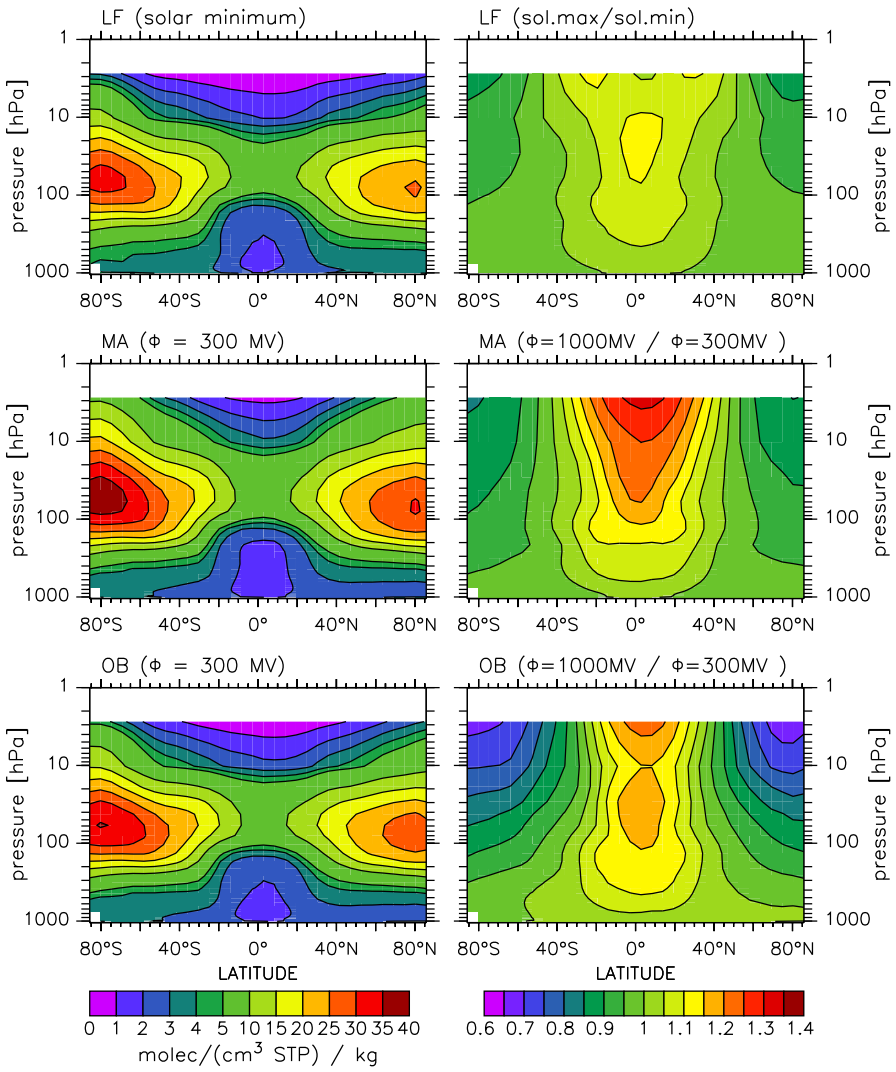

Figure 5.10: Same as Figure 5.9, calculated with the 2.0-SPF configuration.

As discussed above, solar activity primarily affects the relative horizontal distribution of the ^{14}CO production (cf. Figure 5.3). As a consequence the atmospheric distribution of ^{14}CO also changes mainly in horizontal direction during the transition from solar minimum to solar maximum. The effect of horizontally re-distribution of the ^{14}CO source with varying solar activity is visible in the simulated mixing ratios, although less pronounced. For instance, applying the MA source distribution, the relative production rate at about 500 hPa above the equator increases from solar minimum to solar maximum by about 35% and decreases at the poles by 5-10% (Figure 5.3). The resulting changes of the atmospheric mixing ratio are a 5% increase at the equator, and a 5% decrease at the poles respectively (Figures 5.9 and 5.10). Applying the OB source distribution, the result is similar. With the LF source, a relative increase of 15-20% in the production from solar minimum to solar maximum

at the equator and no change at the poles results in a less than 5% reduction in the mixing ratio at the poles and no change at the equator at 500 hPa. The (simulated) atmospheric processes therefore damp the change in the source distribution during a solar cycle, resulting in a weaker latitudinal gradient of the mass mixing ratio amplitude compared to the latitudinal gradient of the production rate amplitude. With increasing height, however, the amplitudes of the production rate variation and of the mixing ratio variation tend to converge.

This implies that the variation in the atmospheric ^{14}CO mixing ratio due to solar activity is smallest at the surface level. This is outlined in Figure 5.11 for the 2.0-SLT configuration and in Figure 5.12 for the 2.0-SPF configuration. The figures show the zonally averaged seasonal cycle of the atmospheric ^{14}CO mixing ratio in the lowest model layer during solar minimum conditions (left column) and the relative change (plotted as ratio to solar minimum conditions) when solar maximum is reached (right column), both normalized to an annual atmospheric burden of 1 kg.

The shape of the seasonal cycle is similar for all three source distributions and the two model configurations. The absolute level is different for the different source distributions according to the vertical structure of the sources. For instance, the surface level ^{14}CO mixing ratio is on average lower when simulated with the MA source distribution compared to OB and LF, because the MA source implies relatively more production at higher levels.

During the transition from solar minimum to solar maximum the surface level mixing ratio of ^{14}CO tends to increase in tropical regions and to decrease at high latitudes. This effect of the solar cycle related re-distribution of ^{14}CO production in the atmosphere on the relative mixing ratio is rather small. The change between solar minimum and solar maximum ranges only from -4% to 4%. The effect is largest when the MA distribution is applied, and smallest for the LF distribution. This is consistent with the ranking among the different source distributions with respect to the relative shift of ^{14}CO production in the horizontal direction (cf. Figure 5.3).

The seasonal variation of the change in surface level ^{14}CO is small. This is to be expected, because each given source distribution and strength is constant throughout the year. Finally, the results calculated with the two model configurations do not differ significantly.

5.4.3 Uncertainty related to model transport

When a global rescaling is applied to ensure global tracer mass conservation (2.0-SPFR), the relative distribution of ^{14}CO in the model atmosphere changes in com-

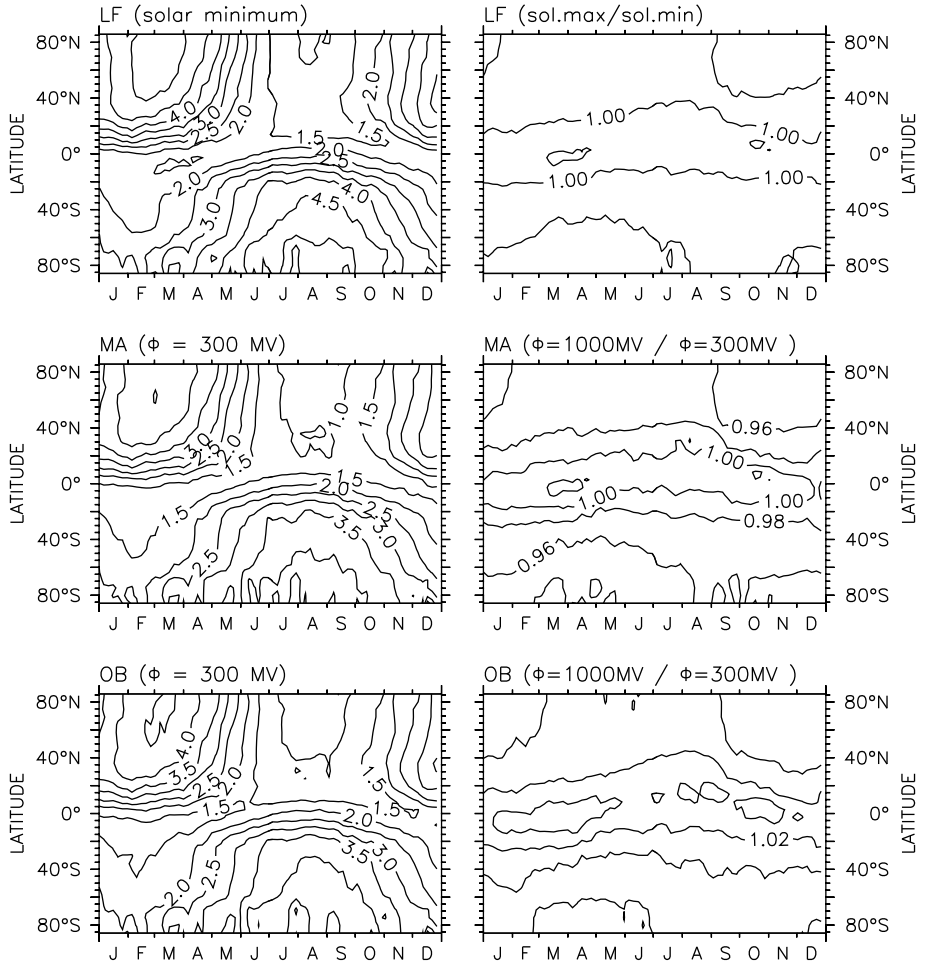

Figure 5.11: Seasonal cycle of surface level ^{14}CO mass mixing ratio (in molec cm^{-3} STP per kg atmospheric burden) under solar minimum conditions (Φ=300 MV, left column), and relative shift when solar maximum conditions (Φ=1000 MV) are assumed (right column). Shown is the ratio between the solar maximum result and the solar minimum result, both normalized to an annual average atmospheric burden of 1 kg ^{14}CO. Model calculations are performed with the 2.0-SLT configuration and the source distributions of *Lingenfelter* [1963] (LF), *Masarik and Beer* [1999] (MA), and *O'Brien et al.* [1991] (OB).

parison to the distribution simulated by the uncorrected model configuration (2.0-SPF, see chapter 2). This undesirable effect can now be used to estimate the (systematic) error of the model results arising from uncertainties in the simulated atmospheric transport. This is achieved by comparing model simulations of the 2.0-SPF and 2.0-SPFR configurations under otherwise identical conditions (see section 5.3). Figure 5.13 shows the effect of the global rescaling correction on the annual average vertical distribution of ^{14}CO in the atmosphere. In the tropical lower stratosphere the relative ^{14}CO mixing ratio is reduced, with a maximum reduction of 4% around 20 hPa. In the lower troposphere the mixing ratio is likewise reduced by 4-6%. In

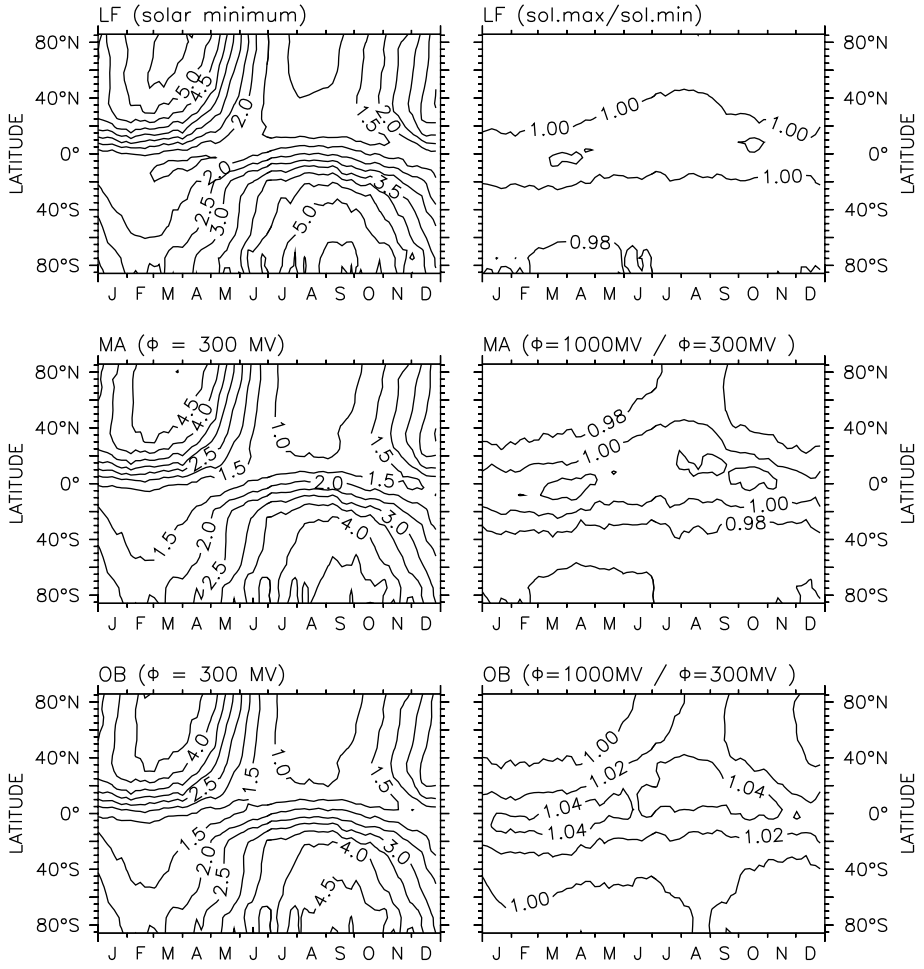

Figure 5.12: Same as Figure 5.11, calculated with the 2.0-SPF configuration.

contrast to that, the relative mixing ratio increases in the tropopause region, in the polar stratosphere, and in the upper stratosphere of the model, when the rescaling is applied.

Especially the change at the surface level is of interest, when model simulations are to be compared to observations at the surface level. The result of further investigation is depicted in Figure 5.14, which shows the effect of the global mass rescaling on the zonal mean annual cycle of the ^{14}CO mixing ratio at the surface level. The change of the zonal mean surface mixing ratio of ^{14}CO is not hemispherically symmetric. The maximum increase of up to 8% occurs in the NH mid-latitudes in September / October, whereas the respective increase in the SH in April / May is only half as large. In both model hemispheres, the mixing ratio is decreased by the rescaling in spring (when the ^{14}CO mixing ratio is large, cf. Figures 5.11 and 5.12) by up to 6%, with the maximum decrease at high latitudes, approximately 2 months after the ^{14}CO maximum. In equatorial regions the surface mass mixing ratio increases

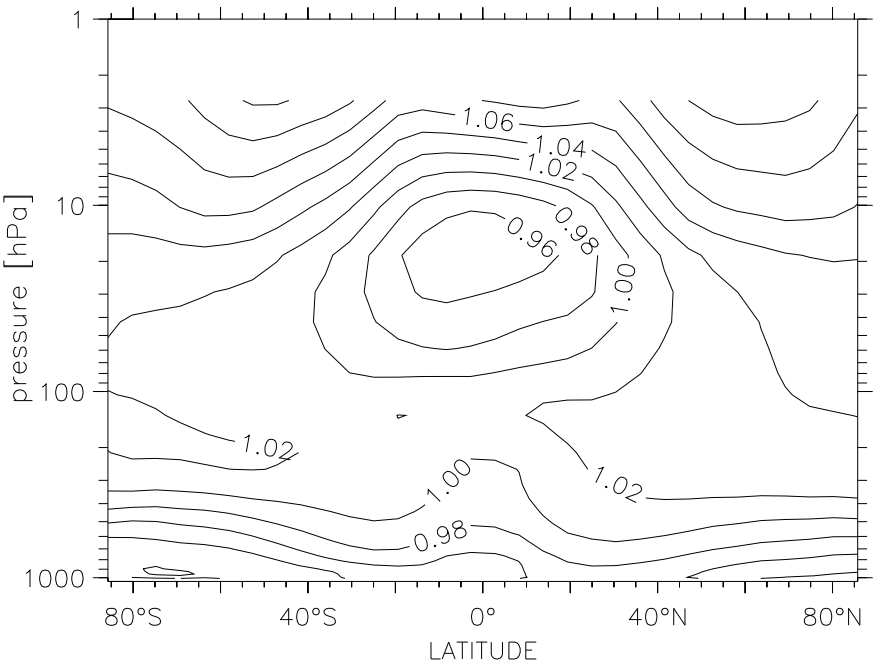

Figure 5.13: Annual zonal mean ratio of ^{14}CO distribution calculated with the 2.0-SPFR configuration versus that calculated with the 2.0-SPF configuration. Both simulations are performed with the source distribution of *Lingenfelter* [1963] for solar minimum conditions. The simulated distributions of ^{14}CO are normalized to an annual average atmospheric burden of 1 kg ^{14}CO before the ratio is averaged over time.

by about 2% throughout the year when the global mass rescaling is applied.

5.5 Discussion

In order to relate the uncertainties in the model predicted ^{14}CO mixing ratios to the uncertainty in the ^{14}CO source distribution, both need to be compared quantitatively. In the model simulations above, the LF source distribution is used as "standard" distribution. The ^{14}CO mixing ratio at the surface level is reduced by 14% and 18% respectively (annual zonal average) when the other two source distributions (OB, MA) are applied. This range is independent of the model configuration; however, it varies with latitude and season (Figure 5.6) up to a maximum reduction of about 26% To obtain an upper limit of the average uncertainty of the ^{14}CO mixing ratio at the surface level arising from uncertainties in the source distribution, only the two extreme estimates are considered, yielding a value of 0.91 ± 0.09 of the LF estimate; thus the relative uncertainty is $\pm 10\%$. Applying the same approach to the maximum deviation (-26% of LF), the uncertainty is likewise $\pm 15\%$ around 0.87 of the LF based estimate. The uncertainty in the source distribution itself has to be defined for comparison. For this, also the extreme estimates are considered only.

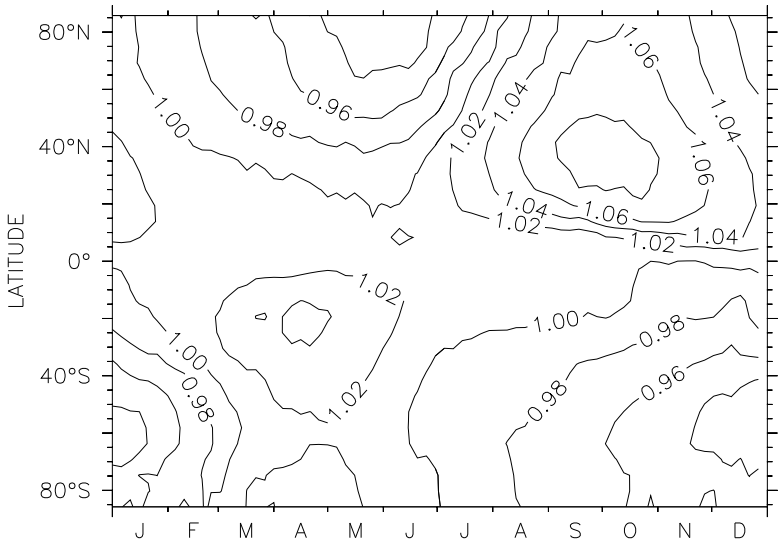

Figure 5.14: Zonal mean ratio of surface ^{14}CO distribution calculated with the 2.0-SPFR configuration versus that calculated with the 2.0-SPF configuration. Both simulations are performed with the source distribution of *Lingenfelter* [1963] for solar minimum conditions. The simulated ^{14}CO distributions are normalized to an annual average atmospheric burden of 1 kg ^{14}CO before the ratio is averaged.

The ^{14}CO production rate at the surface level is more than 90% lower for the OB and MA source distributions than for the LF source distribution. The uncertainty is therefore at least ±81%, the estimate of the production rate at the surface level being 55% of the LF production rate at the surface. For comparison with the resulting mass mixing ratio at the surface, this value is, however, not representative. The troposphere is well mixed and tropospheric levels of ^{14}CO are influenced by stratospheric ^{14}CO as well. At least the production in the troposphere has to be considered for the ^{14}CO mixing ratio at the surface level. A more suitable measure of the uncertainty in the vertical source distribution is therefore based on the fraction of ^{14}CO that is produced in the troposphere. This fraction ranges from 31% to 44% (solar minimum) dependent on the source distribution (Table 5.2). Hence, the relative uncertainty is ±17% around an average fraction of 37.5% of ^{14}CO that is produced in the troposphere. This uncertainty is somewhat larger than the resulting uncertainty in the model simulated ^{14}CO mixing ratio at the surface level derived above.

The relative variation (full range) of the normalized ^{14}CO mixing ratio at the surface level during the transition from solar minimum to solar maximum is ±4% for all employed source distributions and model configurations, and therefore smaller than the uncertainty resulting from the limited knowledge of the vertical production rate distribution pattern. As a consequence, this effect can be neglected until the vertical

source distribution is constrained with higher accuracy.

These uncertainty estimates arising from uncertainties in the source distribution are further to be compared to the uncertainties resulting from model deficiencies, especially concerning the tracer transport dynamics. A minimum estimate of these systematic model uncertainty can be provided by the comparison of two related model configurations. In the present analysis, only relative distributions of tracer mass are investigated. All simulated mixing ratios are normalized to a specific global atmospheric burden. Therefore the 2.0-SPF configuration can also be used for simulation of such relative distributions disregarding the global tracer mass conservation violation, which is inherent to this configuration (see chapter 2). The global rescaling for correction of this tracer mass conservation violation is known to introduce artificial transport components (see chapter 2), which in summary result in a vertical, horizontal, and seasonal re-distribution of ^{14}CO tracer mass (Figures 5.13 and 5.14). The effect of this disturbance of the tracer transport on the simulated mixing ratios is used to estimate a minimum systematic uncertainty introduced by inaccuracies of the model transport. The resulting uncertainty range of 2% to 8% (depending on latitude and season) in the ^{14}CO mixing ratio at the surface level, is similar to, or larger than the predicted variation with the solar cycle. This fortifies the argument for neglecting the solar cycle effect on the ^{14}CO mixing ratio distribution at the surface level.

Comparison of predictions simulated with different model configurations under equal conditions reveals information that can be used to assign the relevant processes to the emerging effects. In the above model results, several insights concerning the simulated stratosphere - troposphere exchange (STE) are revealed. First, predictions of the mass mixing ratio in the region of the lowermost stratosphere production rate maximum (around 80 hPa) are lower when calculated with 2.0-SLT compared to 2.0-SPF. Including the rescaling correction (2.0-SPFR, Figure 5.13), the lowermost stratosphere maximum tends to be even more enhanced compared to the troposphere and the tropical stratosphere. Second, the discrepancy between the fraction of ^{14}CO which is produced in the stratosphere and the fraction of ^{14}CO that resides on average in the stratosphere (burden) is predicted by 2.0-SLT to be larger compared to 2.0-SPF. Consequently, more ^{14}CO disappeared out of the 2.0-SLT stratosphere than out of the 2.0-SPF stratosphere. Because the source distribution and the OH distribution are the same in both configurations, only differences in the simulated STE rate can achieve this. As a consequence, in 2.0-SLT ^{14}CO seems to be more effectively transported downward from the stratosphere into the troposphere than in 2.0-SPF.

In much the same way, interhemispheric differences of the STE can be derived. The annual average and seasonal cycle of the stratospheric burden is different between

NH and SH (Figures 5.7 and 5.8). Since the seasonal cycle of OH in the stratosphere is almost perfectly symmetric between the two hemispheres (equal amplitude, 6 months phase lag, see Figure 1.6), at least in the prescribed OH distribution (OH-1, including OH-2D), and further the source of ^{14}CO is constant throughout the year, interhemispheric differences of the stratospheric burden fraction can only arise from interhemispheric differences in the simulated atmospheric transport, in particular with respect to STE. Hence, the simulated STE is stronger in the NH than in the SH. This is observed in both model configurations, whereby this NH-SH asymmetry of STE is more pronounced in the 2.0-SPF configuration.

5.6 Conclusions

Complex interactions of galactic cosmic ray particles with the solar wind plasma, the geomagnetic field, and the atmosphere, along with neutron diffusion in the atmosphere determine the primary production of ^{14}C and ^{14}CO in the atmosphere. An estimate of the spatial source distribution and its variability with the solar cycle is not straightforward. Three independent estimates with high enough spatial resolution to be applicable for 3-D atmospheric chemistry model investigations are currently available.

The three 3-D source distributions of ^{14}CO were successfully implemented into the 3-D atmospheric transport and chemistry model. Model simulations were performed with the source distributions normalized to an arbitrary global average production rate of ^{14}CO, which is simply a global scaling factor, due to the linearity of the model.

The source distribution of atmospheric ^{14}CO exhibits a small interhemispheric asymmetry because of the shape of the geomagnetic field. The total production of ^{14}CO in the SH is 5-6% larger than in the NH. 51%-66% of the global ^{14}CO production occurs in the stratosphere, depending on the source distribution estimate, and is inversely related to the solar activity with an amplitude of 2%-4% (absolute). The maximum production rate is located in the lower stratosphere in polar regions (above the geomagnetic poles), i.e., in the lowermost stratosphere. The source and sink (OH) distributions of ^{14}CO are quasi mirrored: The OH abundance is large in the equatorial troposphere, where the ^{14}CO production is negligible, and low in the lowermost stratosphere, where the ^{14}CO production rate is largest.

The three source distribution estimates differ mainly in terms of the relative distribution of ^{14}C production in the vertical direction. These differences are used to assess the uncertainty of model predicted atmospheric ^{14}CO arising from uncertainties in the knowledge of the 3-dimensional ^{14}C(O) production rate distribution.

The uncertainty in the ^{14}CO source distribution in the vertical results on average in a ±10% uncertainty in simulated ^{14}CO mixing ratios at the surface level. This uncertainty, however exhibits an annual and latitudinal variation with values up to ±15% (high latitude NH, Sep/Oct). Compared to the difference of the local production rate at the surface level of ±81% between the sources this uncertainty is small. The uncertainty in the vertical source distribution, based on the fraction of tropospheric ^{14}CO production is ±17%, and therefore somewhat larger than the resulting uncertainty in the simulated ^{14}CO mixing ratio at the surface level.

The three source distributions differ further in terms of the time dependence of the relative horizontal distribution of ^{14}C production in the atmosphere due to the solar cycle. This time dependence is used to probe the effect of variations in solar activity on the simulated atmospheric ^{14}CO mixing ratio. For this the assumption is made that during the time of maximum and minimum solar activity, the atmospheric ^{14}CO distribution and seasonality is in equilibrium with the respective production rate distribution. This assumption is justified, since the relevant atmospheric time scales (such as the lifetime of ^{14}CO, and tropospheric mixing) are short compared to the period of the solar cycle. The resulting latitude dependence of the ^{14}CO mixing ratio variation with the solar activity increases with altitude. Tropospheric horizontal mixing attenuates the original steep latitudinal gradient in the production rate. As a consequence, the variation of the normalized surface level ^{14}CO mixing ratio with the solar cycle is less than ±4%.

The simulated global atmospheric burden of ^{14}CO is almost constant throughout the year; however, the partitioning among the hemispheres and the troposphere / stratosphere oscillates with a period of one year. This oscillation is mainly driven by the annual cycle of OH in the respective domains, superimposed by the annual variability of stratosphere - troposphere exchange. The average fraction of the stratospheric burden is 42%-51% (dependent on the source distribution estimate and the solar activity), i.e., lower than the fraction of ^{14}CO that is produced in the stratosphere. The cross tropopause downward transport of ^{14}CO therefore affects tropospheric ^{14}CO levels. This is to be expected, since more than 50% of the ^{14}CO is produced in the stratosphere, but the main sink is located in the troposphere.

Differences of the predicted ^{14}CO mixing ratio distributions between the two model configurations (2.0-SLT and 2.0-SPF) indicate differences in the stratosphere - troposphere exchange (STE) rate. The simulated STE of ^{14}CO is stronger in the 2.0-SLT configuration than in the 2.0-SPF configuration. Both model configurations exhibit a NH-SH asymmetry of the STE, with stronger downward transport in the NH. This effect is, however, less pronounced in the 2.0-SLT configuration. In contrast, no significant differences emerge between the configurations with respect to predictions of the relative horizontal distribution of simulated atmospheric ^{14}CO. The inaccuracy

of the simulated model transport dynamics, estimated by the effect of the global mass mismatch rescaling, yields an uncertainty of -4% to +8% in the simulated ^{14}CO mixing ratio at the surface level, dependent on latitude and season. The annual zonal average uncertainty at higher levels is in the same range, dependent on altitude and latitude.

In conclusion, the effect of the solar activity on horizontal gradients in the surface level ^{14}CO mixing ratio is small compared to the general uncertainties arising from the inaccurate model transport and uncertainties in the vertical structure of the source distribution. This effect can therefore be neglected at first, and the predicted ^{14}CO mixing ratios at the surface level simply scale with the actual global average production rate, which is modulated by the solar activity (see section 5.2.1, further discussed in chapter 7). As a consequence, the solar activity strongly affects the global average ^{14}CO mixing ratio, but hardly affects its distribution in the model. Model simulations of surface level ^{14}CO can therefore be performed with an average production rate distribution that is normalized with respect to the global average production rate. Comparison of these model simulations with measurements obtained at any time during the solar cycle can then in principle be performed after scaling the simulated ^{14}CO mixing ratios with the actual global average production rate at the time of the measurements. This is further investigated in chapter 7. The vertical gradient in the troposphere is fairly flat, due to the effective tropospheric vertical mixing, which is fast compared to the average lifetime of ^{14}CO. The seasonal cycle of ^{14}CO is mainly driven by OH, but is also overlaid by the seasonal cycle of STE.

6 Uptake of ^{14}CO in soil

Abstract. Atmospheric CO is primarily removed from the atmosphere by oxidation with OH. A small fraction, however, is consumed by the soil-vegetation system. The influence of ^{14}CO uptake in soils on the atmospheric ^{14}CO mixing ratio is estimated with the 3-dimensional global model MATCH. The overall effect of soil activity on the simulated atmospheric ^{14}CO mixing ratio is small.

6.1 Introduction

The main removal process of ^{14}CO from the atmosphere is oxidation by OH. Additionally soils are generally recognized to consume atmospheric CO by CO-utilizing microorganisms [*Conrad and Seiler*, 1985]. The interaction between the soil-vegetation system and the atmosphere is therefore expected to likewise affect ^{14}CO. This effect of ^{14}CO uptake and destruction in soils on the atmospheric ^{14}CO mixing ratio is estimated with the 3-D model.

6.2 Model setup

The destruction of ^{14}CO in soils is implemented into MATCH. The soil sink for ^{14}CO is parameterized with an average deposition velocity v_d. *Conrad and Seiler* [1985] and *Sanhueza et al.* [1998] reported average deposition velocities for CO in soil. The maximum estimate of $v_d = 0.04$ cm s^{-1} is chosen for the deposition velocity in order to estimate the maximum possible effect of the soil sink.

The deposition can be described by a piston moving with velocity v_d pushing the tracer of the lowest model layer beyond the lower boundary into the soil. The tracer within a grid box is homogeneously distributed, and the temperature is constant within the box. The length $\Delta z = v_d \cdot \Delta t$ the piston moves in a time interval Δt corresponds, according to the isothermal barometric altitude, to a pressure difference of

$$\Delta p = p_s(e^{-k\Delta z} - 1) \ , \tag{6.1}$$

with the surface pressure p_s and

$$k = \frac{m_m}{T \cdot R_g} g \ . \tag{6.2}$$

$m_m = 28.97 \cdot 10^{-3}$ kg mol^{-1} is the mass of one mole of air, $R_g = 8.314$ J mol^{-1} K^{-1} is the gas constant, $g = 9.81$ m s^{-1} is the gravity acceleration at the surface, and T is the temperature in Kelvin. Since the exponential term in Eq. (6.1) is small compared

to 1 ($\approx 8.5 \cdot 10^{-5}$ for $T = 288.15$K and the model time step of $\Delta t = 1800$s), Eq. (6.1) can be approximated by a first order Taylor expansion, resulting in

$$\Delta p = -p_s k \Delta z \ . \tag{6.3}$$

The fraction f of the grid box that is pushed by the piston into the soil during the time interval Δt is then

$$f = \frac{\Delta p}{p_{top} - p_s} = \frac{-p_s k v_d \Delta t}{p_{top} - p_s} \ , \tag{6.4}$$

where p_{top} is the pressure at the upper boundary of the lowest model grid box. Using sigma-coordinates in the vertical, i.e., $p = \sigma \cdot p_s$ (see chapter 2), the loss rate (in s^{-1}) of ^{14}CO in soil can be written as

$$l_{\text{soil}} = \frac{f}{\Delta t} = \frac{-k v_d}{\Delta \sigma} \ , \tag{6.5}$$

where $\Delta\sigma$ is the difference of sigma levels between top and bottom of the lowest layer ($\Delta\sigma < 0$).

Simulations are performed with the 2.0-SLT and the 2.0-SPFR model configuration. The OH-1 distribution is prescribed for the oxidation of ^{14}CO. The advection is driven by the NCEP-reanalysis meteorology of the year 1993 [*Kalnay et al.*, 1996]. To exclude soil activity in desert and permafrost regions [*Conrad and Seiler*, 1985], the model soil sink is only active when the relative humidity in the lowest model layer is above a threshold of 40% and the temperature is within the interval of 5^o to 35^oC.

The ^{14}CO mixing ratio is initialized with zero. Two years are integrated with the ^{14}C(O) source distribution of *Lingenfelter* [1963] for solar minimum conditions (LF, see chapter 5) normalized to a global average production rate of 1 molec cm^{-2} s^{-1} in an idealized atmosphere of constant depth (1033 g cm^{-2}). The simulations are performed once without the parameterized soil sink, and repeated with the soil sink included. The second year model output is archived as 5 day averages and used for the analysis.

6.3 Model results

It turns out that the predicted effect of the soil sink on the atmospheric mixing ratio of ^{14}CO is very similar for the two configurations (2.0-SLT and 2.0-SPFR) tested. Therefore, only results averaged over both configurations are presented in the subsequent analysis. The effect of soil activity on the ^{14}CO mixing ratio at the surface level is depicted in Figure 6.1. Shown is the ratio of the ^{14}CO mixing ratio

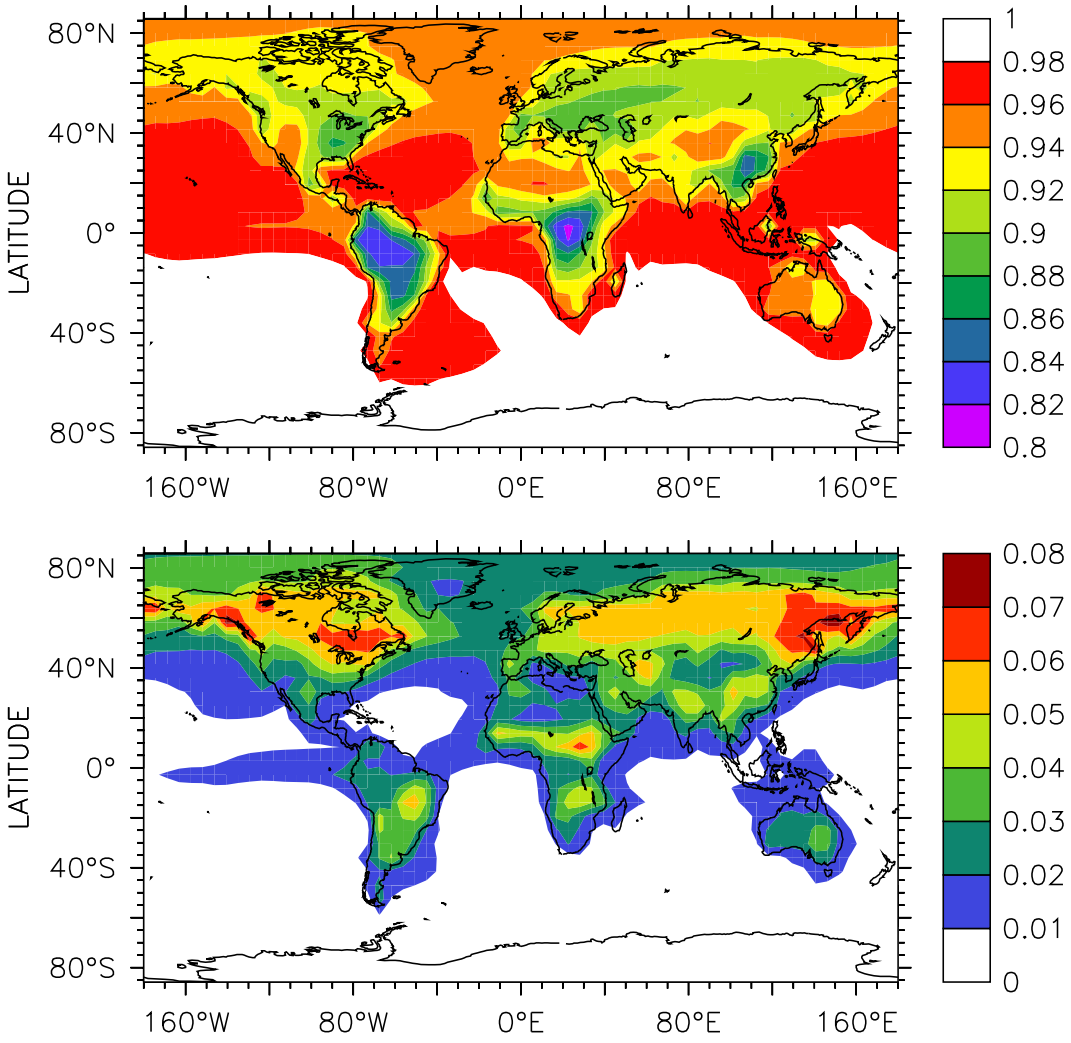

Figure 6.1: Annual mean reduction of ^{14}CO at the surface level by uptake in soils. Shown is the ratio of the ^{14}CO mixing ratio in the lowest model layer when the soil sink is included versus the respective ^{14}CO mixing ratio without the soil sink (upper), and the standard deviation of this ratio with respect to time (lower). The ratios calculated from the 2.0-SLT and the 2.0-SPFR simulations are averaged.

simulated with an active soil to the simulated ^{14}CO mixing ratio without soil sink. The standard deviation with respect to time is a measure for the annual variability.

The overall reduction of the ^{14}CO mixing ratio at the surface level is on average less than 5% except over some continental areas, where the soil sink reduces the atmospheric ^{14}CO mixing ratio by up to 20%. South America and Central Africa are most affected by the chosen soil sink parameterization. The annual variability is largest at high northern latitudes, possibly due to the chosen temperature and relative humidity range for soil activity in the model. Local maxima of the variability are also pronounced over Central Africa and South America.

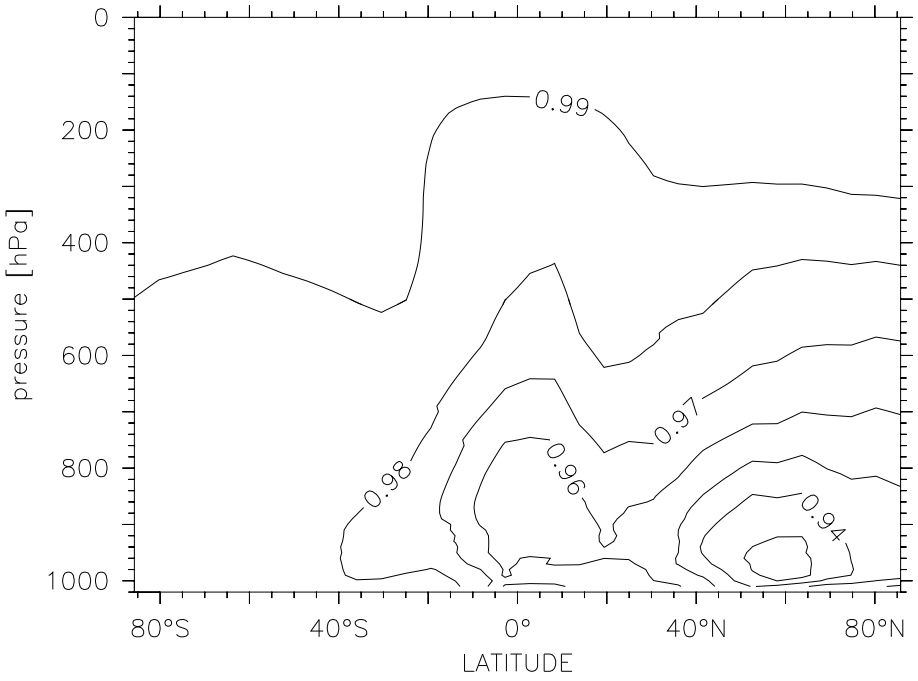

Figure 6.2: Annual zonal mean reduction of ^{14}CO by uptake in soils. Shown is the ratio of the ^{14}CO mixing ratio when the soil sink is included to the respective ^{14}CO mixing ratio without soil sink. The ratios calculated from the 2.0-SLT and the 2.0-SPFR simulations are averaged.

The zonal average reduction of atmospheric ^{14}CO in the troposphere due to the soil activity is shown in Figure 6.2. The soil sink slightly enhances the weak vertical gradient of ^{14}CO in the model troposphere. The zonally averaged reduction is largest around 50^{o}N with a maximum of 7% between 900 hPa and 1000 hPa. The overall effect in the troposphere is small compared to the local effects in the surface layer. Moreover, the effect is larger in the NH than in the SH, due to the sea / land distribution on the globe.

The hemispherically averaged effect of the soil sink on the ^{14}CO mixing ratio and the average effect over the continents in the lowest model layer is shown in Figure 6.3. Throughout the year, the average soil effect is almost constant in the SH where the atmospheric ^{14}CO mixing ratio at the surface level is reduced by 3% on average. In the NH, the effect of the soil is larger (6% on average) and exhibits an annual cycle. The NH maximum reduction of 8% is reached in summer, the minimum reduction in winter is about 4%. Over the continents the average reduction varies between 6% in summer and 10% in winter. The predicted annual average reduction of ^{14}CO due to soil activity over the continents is 8%.

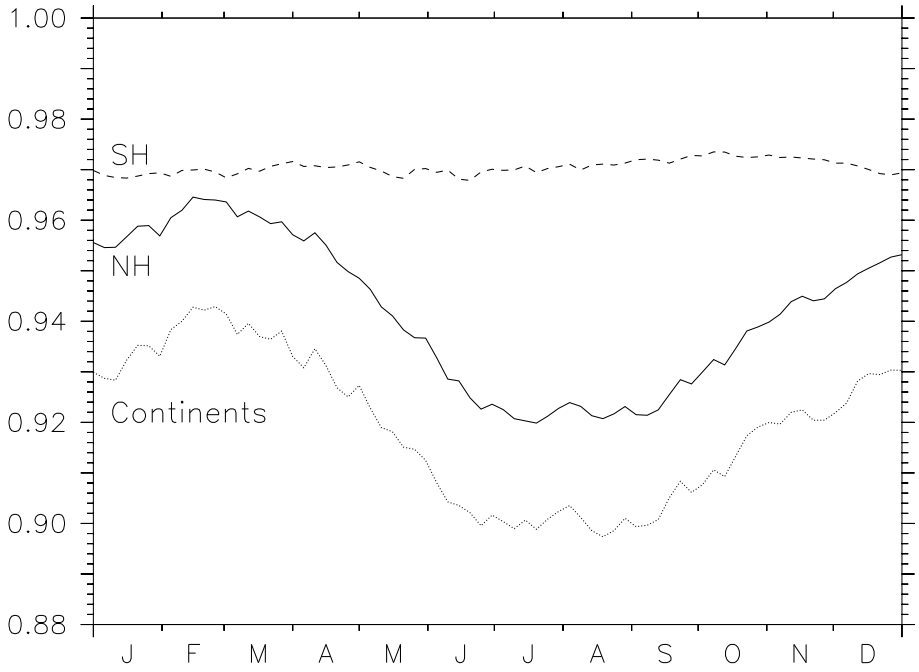

Figure 6.3: Northern (NH, solid line) and southern hemisphere (SH, dashed line) average reduction of ^{14}CO at the surface level by uptake in soils. The average reduction over the continents (dotted line) is also included. Shown is the ratio of the ^{14}CO mixing ratio in the lowest model layer when the soil sink is included to the respective ^{14}CO mixing ratio without soil sink. The ratios calculated from the 2.0-SLT and the 2.0-SPFR simulations are averaged.

6.4 Discussion

The investigation of soil activity here provides only a very rough estimate of its effect on atmospheric ^{14}CO mixing ratios at the surface level. The intervals of temperature and relative humidity chosen as thresholds for the simulated uptake in soils are, although motivated, somewhat arbitrary. The maximum estimate of the deposition velocity is chosen, in order to assess an upper limit of the soil effect. The lower limit is simply provided by the assumption that the effect of soil activity on atmospheric ^{14}CO is negligible.

Furthermore, *Conrad and Seiler* [1985] and *Sanhueza et al.* [1998] found that the uptake of CO in soil depends on the particular soil characteristics, and probably for some soils also on soil temperature and soil moisture. Such effects are not taken into account in the above analysis. However, the simulations indicate that at particular locations soil activity may significantly influence the local atmospheric ^{14}CO mixing ratio near the surface, especially at continental sites. The simulated ^{14}CO mixing ratio at "remote" locations, or in the free troposphere are, in contrast, hardly influenced by uptake of ^{14}CO in soils.

6.5 Conclusions

The simulated uptake of ^{14}CO in soils reduces the atmospheric ^{14}CO mixing ratio at the surface level on average by at most 3% in the SH to 6% in the NH. Whereas the average SH reduction is almost constant throughout the year, the average NH reduction exhibits an annual cycle with an amplitude of 4% to 8%. Over the continents, the simulated effect of soil activity on the atmospheric ^{14}CO mixing ratio is larger, and the ^{14}CO mixing ratio at the surface level is reduced by 6% to 10% on average. However, the model simulations indicate that the effect of ^{14}CO uptake in soils at the surface may be even larger at specific continental locations. At higher altitude the effect of the soil activity is smaller. The maximum annual average ^{14}CO reduction of 7% occurs in the NH mid-latitude free troposphere. The overall effect is small compared to uncertainties arising from uncertainties of the global source strength (as discussed in chapter 8).

Finally, significant uptake of ^{14}CO in soils, if present in the real atmosphere / soil vegetation system is expected to introduce an interhemispheric asymmetry to the ^{14}CO mixing ratio with a lower reduction, i.e., potentially higher levels of ^{14}CO in the SH, resulting from the hemispherically asymmetric distribution of land on the globe. The opposite, i.e. lower ^{14}CO levels in the SH, has been observed [*Brenninkmeijer et al.*, 1992], however.

7 Atmospheric response time of cosmogenic ^{14}CO to variations of the global source strength

Abstract. The atmospheric ^{14}CO mixing ratio scales with the global source strength (global average production rate). The cosmogenic source strength of ^{14}CO itself is inversely correlated to the solar activity. Thus, when ^{14}CO measurements are compared to model results, a time-dependent rescaling is required to account for the solar modulation of the production rate. The same applies when measurements sampled under different solar cycle conditions are to be compared in order to investigate the global distribution and trends of OH and/or the stratosphere - troposphere exchange. For this rescaling, a two-parameter filter is derived from calculations with two 3-dimensional global atmospheric models in various configurations. The model self-consistent filter function defines the atmospheric response time of the ^{14}CO mixing ratio to changes in the total cosmogenic ^{14}CO source strength. The latitude dependence of the response time in addition to the atmospheric lifetime of the tracer provides useful information about the model's transport properties, especially about the role of stratosphere - troposphere exchange. It may serve as a direct indicator to help understand the unresolved issue of the interhemispheric asymmetry of the atmospheric ^{14}CO mixing ratio. The general concept can be applied as a diagnostic test for coupled changes in atmospheric transport and chemistry in models. Time series of ^{14}CO measurements can provide this information about the real atmosphere.

7.1 Introduction

The cosmogenic ^{14}CO production rate is not constant in space and in time, but is modulated by solar activity. This modulation has a substantial amplitude of $\pm 20\%$ to $\pm 25\%$ (see section 5.2.1) with a period of typically 11 years.

If ^{14}CO is to be used to evaluate the OH distribution and/or STE and possible trends, the modulation of the global average production rate has to be taken into account. For instance, ^{14}CO measurements sampled under different solar activity conditions must be corrected for changes in the production rate as accurately as possible before information about OH and/or STE can be obtained.

In the modeling approach the solar modulation effect can principally be taken into account by incorporating the variable $^{14}C(O)$ source into the model. This requires separate model runs for different periods during the solar cycle. This by itself is no limitation for the ^{14}CO methodology. However, the global average production rate is to date not accurately known. This is discussed separately in chapter 8. Thus, including the absolute source strength into the modeling approach would introduce an additional uncertainty. This however, can be prevented using the results from chapter 5. As already shown there, the equilibrium spatial distribution

of tropospheric ^{14}CO is not very sensitive to the degree of modulation by solar activity. Specifically, the variations in the ^{14}CO distribution pattern are small, and the local change of the ^{14}CO mass mixing ratio can very well be accounted for by an overall scaling factor.

Nevertheless, an important question concerns the actual local speed with which the distribution of ^{14}CO adjusts itself to the changing cosmogenic production field. The modulation of solar activity is not a smooth function over the 11 year period, but has considerable month-to-month variations. For instance, for the period from June 1976 to January 1998 (solar cycles 21, 22, and beginning 23) a mean deviation of $\pm 23\%$ is calculated for the monthly mean sunspot number relative to the smoothed sunspot number. In principle it has to be assumed that this variability of solar activity directly affects the global average production rate of ^{14}CO, which, as a consequence, is likewise variable.

In this chapter the delay between solar activity changes and the corresponding change in atmospheric neutron flux, and therefore ^{14}CO formation, is not considered. This important issue is discussed separately in chapter 8. For the investigations at this stage, the assumption is made that the timing of the global average production rate is known.

However, the atmospheric ^{14}CO mixing ratio does not respond instantaneously to ^{14}C(O) production rate changes because atmospheric transport processes are on the same timescale as the production rate variations. Therefore, scaling the atmospheric ^{14}CO mixing ratio simply by the actual monthly mean ^{14}CO production rate would be a very poor approximation because this would imply that the mixing ratio is totally determined by the local production rate. This is certainly not true, in particular not in the troposphere as shown in chapter 5.

The response of the atmospheric ^{14}CO mixing ratio to changes in the global source strength is simulated with two 3-dimensional atmospheric models in various configurations. From this the local scaling factor can be derived. It turns out that the local scaling can be described with sufficient accuracy by a simple two-parameter filter, with the two parameters being independent of the unknown instantaneous global average ^{14}CO production rate.

As a consequence, model simulations with a source distribution which is normalized to a constant, arbitrary global average production rate of ^{14}CO can be efficiently scaled to the actual solar activity conditions. Moreover, measurements of ^{14}CO can be corrected for the solar modulation of the production rate with the same filter function, assuming that the simulated response approximately represents the response of the real atmosphere.

The treatment of the response time of ^{14}CO to variations in its global source strength

is a special case of the response of an atmospheric tracer to changes in sources, precursors or sinks and may serve as an example for far reaching applications of the general concept [*Prather*, 1996; *Tans*, 1997; *Manning*, 1999].

7.2 Model setup

The $^{14}C(O)$ production rate distribution of *Lingenfelter* [1963] (LF) is used to prescribe the cosmogenic source of ^{14}CO. The best estimate of a mean relative source distribution with respect to the solar cycle variation is obtained by local linear interpolation between solar minimum and solar maximum. The global source strength is normalized to a global average production rate of $q_n = 1$ molecule cm^{-2} s^{-1} in an idealized static atmosphere of constant depth (1033 g cm^{-2}). The OH-1 distribution is prescribed for the ^{14}CO oxidation (see section 1.4). Four configurations of the MATCH model are used (1.2-SLT, 2.0-SLT, 2.0-SPF, and 2.0-SPFR) for the analysis in order to estimate the uncertainty of the results in terms of inaccuracies of the tracer transport realization in the model. The ^{14}CO soil sink parameterization (chapter 6) is included in all four MATCH configurations. Tracer advection in the MATCH configurations is driven by the NCEP-reanalysis meteorology of the year 1993 [*Kalnay et al.*, 1996].

With one configuration (2.0-SLT), simulations with three different OH distributions (OH-1, OH-2, and OH-S) are performed to estimate the sensitivity of the response to the tropospheric OH distribution. All distributions include the OH-2D distribution in the stratosphere above the climatological tropopause (see section 1.4).

Furthermore, a simulation with the TM3 (KNMI configuration TM3-L-L31, cf. section 1.3) is performed (Ad Jeuken, KNMI, personal communication 1998-2000), using the OH-1 distribution. No soil sink parameterization is implemented. The advection is based on the ECMWF-reanalysis meteorology of 1993.

With this setup the atmospheric mixing ratio of two different tracers is simulated: the ^{14}CO mixing ratio χ_n resulting from the source with the normalized global average production rate q_n, and the mixing ratio χ_s resulting from a time dependent production rate

$$q_s = c_q(t) \cdot q_n \ , \tag{7.1}$$

where the global source scaling function $c_q(t)$ varies monthly. All model output is archived as monthly average values. The question to answer now is: How does the ratio

$$c_\chi(t) = \frac{\chi_s(t)}{\chi_n(t)} \tag{7.2}$$

depend on the input parameter $c_q(t)$? Or, in other words, how does the system respond to the input signal, in this case the scaling of the source distribution?

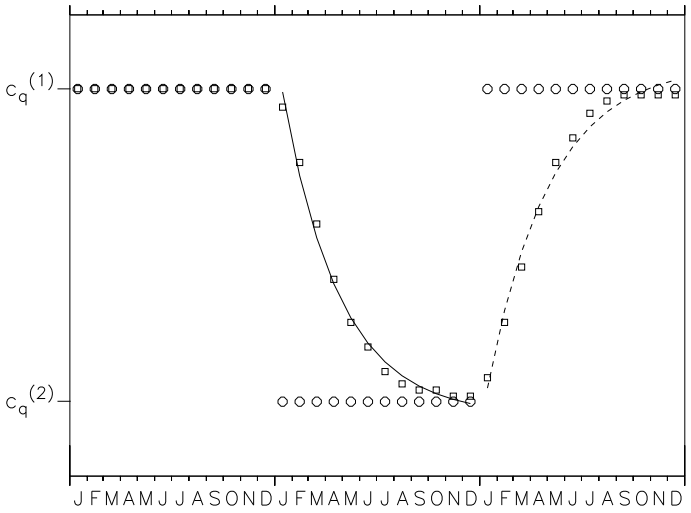

Figure 7.1: Response signal c_χ of the ^{14}CO mixing ratio scale (squares) and rectangular input signal c_q (absolute scale of ^{14}CO source strength, circles) for Mainz (50^oN, 8.2^oE). The lines are exponential approximations of the second and third year response, respectively.

In a first step, the response of the model atmosphere to a rectangular input signal is calculated. The simulation is performed with the 1.2-SLT configuration; the integration time is 3 years. The response to the rectangular input signal provides the basis for a general approach to resolve the relation between $c_\chi(t)$ and $c_q(t)$.

7.3 Response to a rectangular input signal

First, a 3-year simulation (1.2-SLT) with a rectangular input signal is performed; that is, $c_q = c_q^{(1)}$ during the first and last year, and $c_q = c_q^{(2)}$ during the intermediate year. The model is initialized with the result $\chi_n^{(0)}$ of a 2-year integration that started from zero mixing ratio ($\chi_n^{(0)}(0) = 0$). This result is used as initial condition for χ_n, and multiplied by $c_q^{(1)}$ for initialization of χ_s.

The input signal $c_q(t)$ together with the resulting output signal $c_\chi(t)$ for one surface location as an example is shown in Figure 7.1.

From the first month after a step of the source strength scaling c_q onward, the mixing ratio scale c_χ can, to a good approximation, be described by an exponential decay function of the form

$$c_\chi(t) = c_0 \exp(-\frac{(t - t_0)}{\tilde{\tau}}) \ , \tag{7.3}$$

with t_0 being the time of the step. It has to be assumed that the decay constant $\tilde{\tau}$ may depend on latitude and the season because the system parameters responsible for the decay, transport, and OH distribution are time- and latitude-dependent. To calculate a mean, latitude-dependent decay time constant requires rerunning the

model at least 12 times with the step function in different months, because monthly average input data for OH and the source scaling is used. However, a different method is explored in the following, which avoids the need for numerous model simulations.

7.4 A model self-consistent filter

The aim is to find a relationship for scaling ^{14}CO measurements at different times during a solar cycle to standard conditions with respect to solar activity. To better apply the model results to the real atmosphere, this task can also be formulated from a different point of view: Is it possible to calculate the current scaling factor c_χ (Eq. (7.2)) of the atmospheric ^{14}CO mixing ratio directly from the scaling of the ^{14}CO source strength c_q (Eq. (7.1)) without rerunning the model? This would have several advantages. First, it is more economical. The solar cycle effect can completely be excluded from the model simulations, and the results can then be scaled. Second, the same method can be applied with other 3-D atmospheric chemistry models. All the calculations can be performed in a "normalized mode", and the resulting ^{14}CO distributions are directly comparable. Finally, only the ^{14}CO distribution is then relevant for evaluation of the OH distribution, but not the absolute ^{14}CO source strength. The latter then determines the global average OH concentration. As a consequence, distribution and global scale of OH can be completely "decoupled" within the ^{14}CO methodology.

The methodological approach is sketched in Figure 7.2. To find an adequate relationship between c_χ and c_q and to answer the above question, MATCH simulations (8 years simulation time), and a TM3 simulation (6 years simulation time) with a "realistic" input signal are performed. As a realistic input signal, the solar activity dependence of the global average ^{14}C(O) production rate estimated by *Lingenfelter* [1963] is arbitrarily chosen. This parameterization is a simple linear interpolation of the global average production rate of ^{14}C(O) between solar maximum and solar minimum by means of the sunspot number. Although *Stuiver and Quay* [1980] showed that this is only a poor approximation on timescales shorter than the period of the solar cycle, it is sufficient for the analysis here. The input signal is therefore

$$c_q(t) = (2.61 - 0.003 \cdot (s(t) - 9.1)) \cdot 0.95 \tag{7.4}$$

where $s(t)$ is the monthly mean sunspot number and the factor 0.95 accounts for the reaction yield of ^{14}C to ^{14}CO [*Pandow et al.*, 1960; *MacKay et al.*, 1963]. Monthly mean sunspot numbers of solar cycle 21 and 22 are depicted in Figure 7.3. The time interval 1988 to 1995 is chosen for the analysis. In this period the monthly average sunspot number ranged from 9 to 200.3, resulting in a source scaling $c_q(t)$

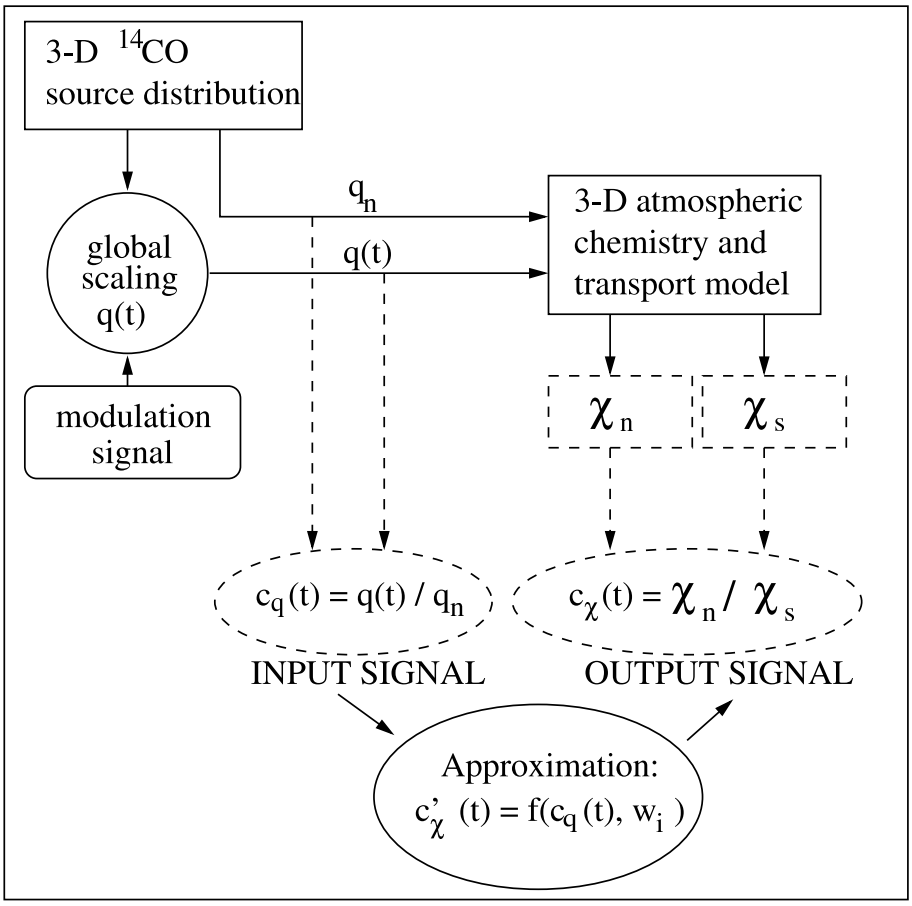

Figure 7.2: Schematic diagram of the atmospheric response time analysis. Two tracer mixing ratios are simulated, χ_n with a constant source strength q_n, and χ_s with a time dependent source strength $q(t)$. The resulting ratio c_χ is then approximated by a function c'_χ of the ratio c_q of the source strengths, whereby the approximation function is optimized by variation of the parameters w_i.

between 1.93 and 2.48. At the beginning of the first year the model was initialized in the same way as for the rectangular input signal calculation. For the tracer with the scaled production rate (χ_s) the initial distribution is multiplied by a factor of 2.42 which is the respective scaling factor c_q for the annual mean sunspot number $s = 29.225$ of 1987 (Eq. (7.4)). The input signal c_q together with the resulting mixing ratio scaling c_χ at a single location is shown in Figure 7.4 (left).

For a direct calculation of c_χ an approach suggested by the results of the model runs with the rectangular input signal is made. A single step in the input signal shows an exponentially relaxing (or decaying) output signal (from the first month after the step on) with a certain time constant, which is a measure of the memory time of the system or the model's response. The approximate ratio of ^{14}CO mixing ratios c'_χ (scaled to normalized, Eq. (7.2)) for a sequence of steps in the input signal can

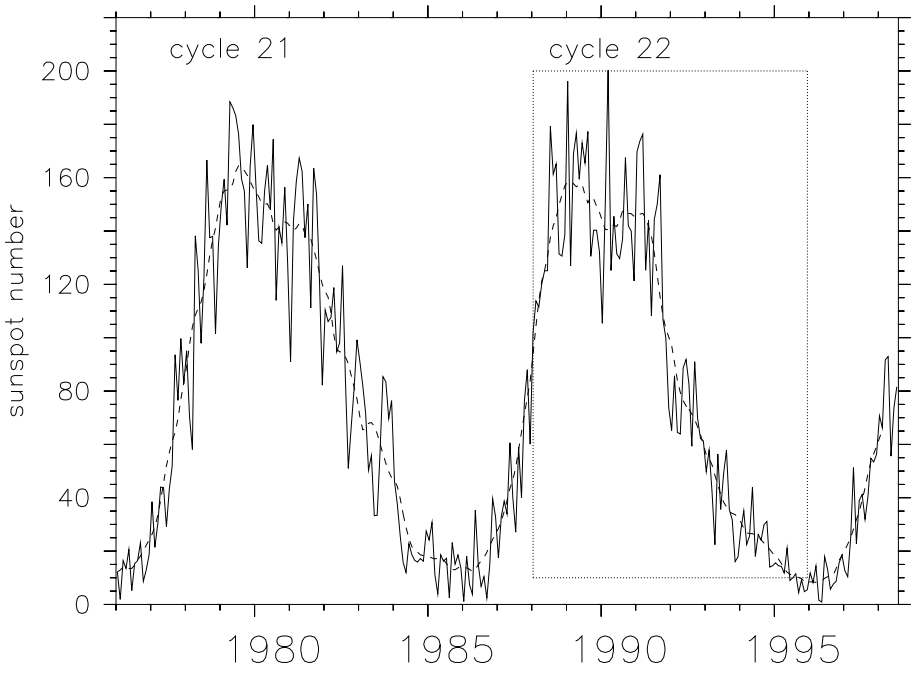

Figure 7.3: Monthly mean sunspot number (solid line) and smoothed sunspot number (dashed line) of solar cycles 21 and 22. The dotted box indicates the time interval that is used to derive the input-signal (see Figure 7.4) for the response time analysis.

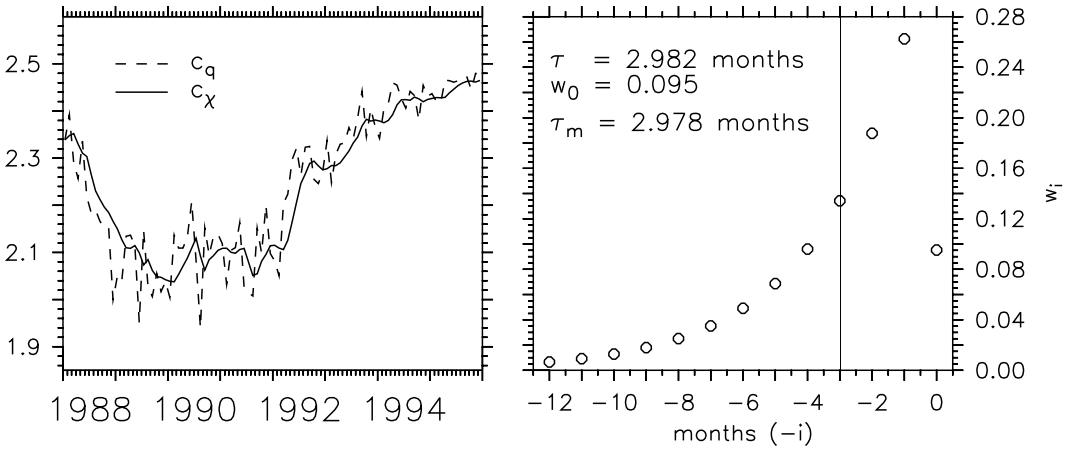

Figure 7.4: Model (1.2-SLT) calculated response signal c_χ (solid line) to arbitrary 8-year input signal c_q (monthly averages of global source scaling, dashed line) for Mainz (50^{o}N, 8.2^{o}E) (left) and appropriate filter (weight distribution) for $n = 12$ months (right). The resulting response time τ and weight w_0 of the current month's production rate scale are also included. The vertical line indicates the respective mean memory time τ_m. The filter based approximate response signal c'_χ is not plotted (left), since it is not distinguishable from the model calculated response within the drawing accuracy.

therefore be assumed to have the form

$$c'_\chi(t) = \sum_{i=0}^{n} w_i \cdot c_q(t - i\Delta t) \tag{7.5}$$

with

$$w_i = \exp(-i\frac{\Delta t}{\tau}) \text{ for } i > 0, \tag{7.6}$$

$\Delta t = 1$ month, and the requirement that

$$\sum_{i=0}^{n} w_i = 1. \tag{7.7}$$

The parameter i counts the months backward from the current (i=0). Using this form of the "filter", i.e., the weight distribution w_i, two independent parameters are introduced, the time parameter τ and the weight of the current month's production rate scale w_0. The number n of months backward that have to be taken into account depends on the maximum allowed deviation of c'_χ from the model calculated c_χ. With this approach the deviation function

$$f_e = \sum_{k=n}^{N} (c'_\chi(k) - c_\chi(k))^2 \tag{7.8}$$

can be defined, with k counting the months from month n to the end of the simulated time interval T divided in N months. Minimizing this deviation function defines the optimal parameters w_0 and τ, the response time. The weight distribution (filter) w_i further defines another time constant,

$$\tau_m = \Delta t \sum_{i=0}^{n} i \cdot w_i \ , \tag{7.9}$$

i.e., the "center of mass" of the weight distribution, which is a measure of the average memory time of the system, i.e., the mean memory time. In the case of the two parameter filter derived here, it combines the two parameters into a single one. The filter resulting from the optimized approximation with $n = 12$ for one specific location is depicted in Figure 7.4 (right). The approximated response signal c'_χ is omitted in Figure 7.4 (left), because it is not distinguishable from the model simulated response c_χ, within the accuracy of the drawing.

7.5 Response time and lifetime

The response time τ, the mean memory time τ_m, and the weight of the current month's production rate scale w_0 are time-averaged quantities which, in principle, depend on latitude, longitude, and height. However, taking the zonal mean (denoted by $< \ldots >$) of the approximated mixing ratio scale as

$$< c_\chi > := \frac{< \chi_s >}{< \chi_n >} \ , \tag{7.10}$$

and neglecting the longitude dependence results in a maximum relative deviation, defined as

$$\frac{\Delta c_\chi}{< c_\chi >} = \frac{c_\chi}{< c_\chi >} - 1 \ , \tag{7.11}$$

ranging from -1.5% to +1.2% taken over all model grid boxes. This is the full range including all used model configurations and OH distributions with only one exception. The full range of the deviation from the zonal mean obtained with the 2.0-SLT - OH-S combination is ±2.5%.

Temporal and spatial mean ratios c_χ can likewise be defined by averaging the mixing ratios χ_n and χ_s over a volume V' and a time interval T', replacing the zonal average $< \ldots >$ (Eq. 7.10). The optimized approximation of an appropriate c'_χ, using the filter approach from above (Eq. (7.5), (7.6), and (7.7)), yields an average response time, mean memory time and weight of the current month's production rate scale, for the volume V' and the time interval T'.

Before results of such average response times are presented and discussed, two further parameters characterizing a tracer species are introduced in order to be compared with the response time. One commonly used parameter is the average lifetime of a tracer species. The (spatially and temporally) averaged lifetime τ_l of a tracer is defined as the ratio of the total tracer mass to the total tracer loss in a volume V' during a time interval T',

$$\tau_l = \frac{\int\int_{V',T'} \chi(\vec{x},t) m(\vec{x},t) d\vec{x} dt}{\int\int_{V',T'} l(\vec{x},t) m(\vec{x},t) d\vec{x} dt} \tag{7.12}$$

where χ is the tracer mass mixing ratio, l is the loss rate in kg kg^{-1} s^{-1}, and m is the air mass in a volume element $d\vec{x}$ around the point $\vec{x}$. In analogy to the lifetime, a "production time" τ_q can be defined by replacing the local loss rate l with the local production rate in Eq. (7.12).

In the following discussion, the processes determining the response time τ of the atmospheric ^{14}CO mixing ratio to changes in the global source strength of cosmogenic ^{14}CO are explored.

7.6 Model results

Figure 7.5 depicts the average response time τ of atmospheric ^{14}CO to changes in the global source strength of ^{14}CO, as simulated by various model configurations, and derived by the analysis presented above. The figure shows average values for the stratosphere, the troposphere, and the lowest model layer respectively, where the averaging was performed according to Eq. (7.10). $< \ldots >$ here denotes not

only the zonal average, but rather the air mass weighted average over the respective atmospheric domain in vertical direction, and the average over the simulation time interval T. $n = 12$ months backward are taken into account for the approximation (Eq. (7.5)). Figure 7.5 further includes the respective weight of the production rate scaling of the current month (w_0), and the lifetime τ_l, according to Eq. (7.12). The loss rate determining the lifetime comprises the oxidation by OH and the uptake in soil, except for TM3, where no soil sink for ^{14}CO is implemented. The climatological mean tropopause (Eq. (1.10), section 1.5) is used for definition of the atmospheric domains.

Figure 7.6 shows the corresponding mean memory time τ_m, and the production time defined by Eq. (7.12) after exchanging the loss rate with the production rate. Furthermore, the full range (i.e. maximum and minimum) of the relative deviation introduced by approximation of the model response with the filter is included in Figure 7.6. This relative deviation is defined as

$$\frac{\Delta c_\chi}{c_\chi} = \frac{c'_\chi}{c_\chi} - 1 \ . \tag{7.13}$$

7.6.1 The simulated atmospheric lifetime of ^{14}CO

By definition the lifetime gives a static picture. It is the time it would take to reduce the amount of tracer to $1/e$ of its current level, under the assumption that there is neither production nor transport, and that the loss frequency (in s^{-1}) remains constant. In the case of ^{14}CO the lifetime in the stratosphere and in the troposphere is shortest in equatorial regions, where the OH concentration is highest. At higher latitudes it increases steeply, due to the fact that there the OH concentration is very low. The definition of an average lifetime is not very useful for polar regions; it may temporarily go to infinity during polar winter.

For a given latitude the tropospheric lifetime in the northern hemisphere (NH) is shorter than in the southern hemisphere (SH), due to the higher OH concentration in the NH (OH-1, Figure 1.2, Table 1.1) of the model. The stratospheric lifetime is almost hemispherically symmetric, except at high latitudes ($> 60^o$). This conforms with the temporal asymmetry of the OH-2D distribution at high latitudes, due to enhanced OH in the SH ozone hole region (see section 1.4).

Concerning the atmospheric lifetime of ^{14}CO, the model configurations can be grouped together into two categories. The first comprises the 1.2-SLT configuration and the TM3 model, which both generally predict shorter lifetimes than the second group, i.e., all 2.0 configurations of MATCH. Within the first group, the

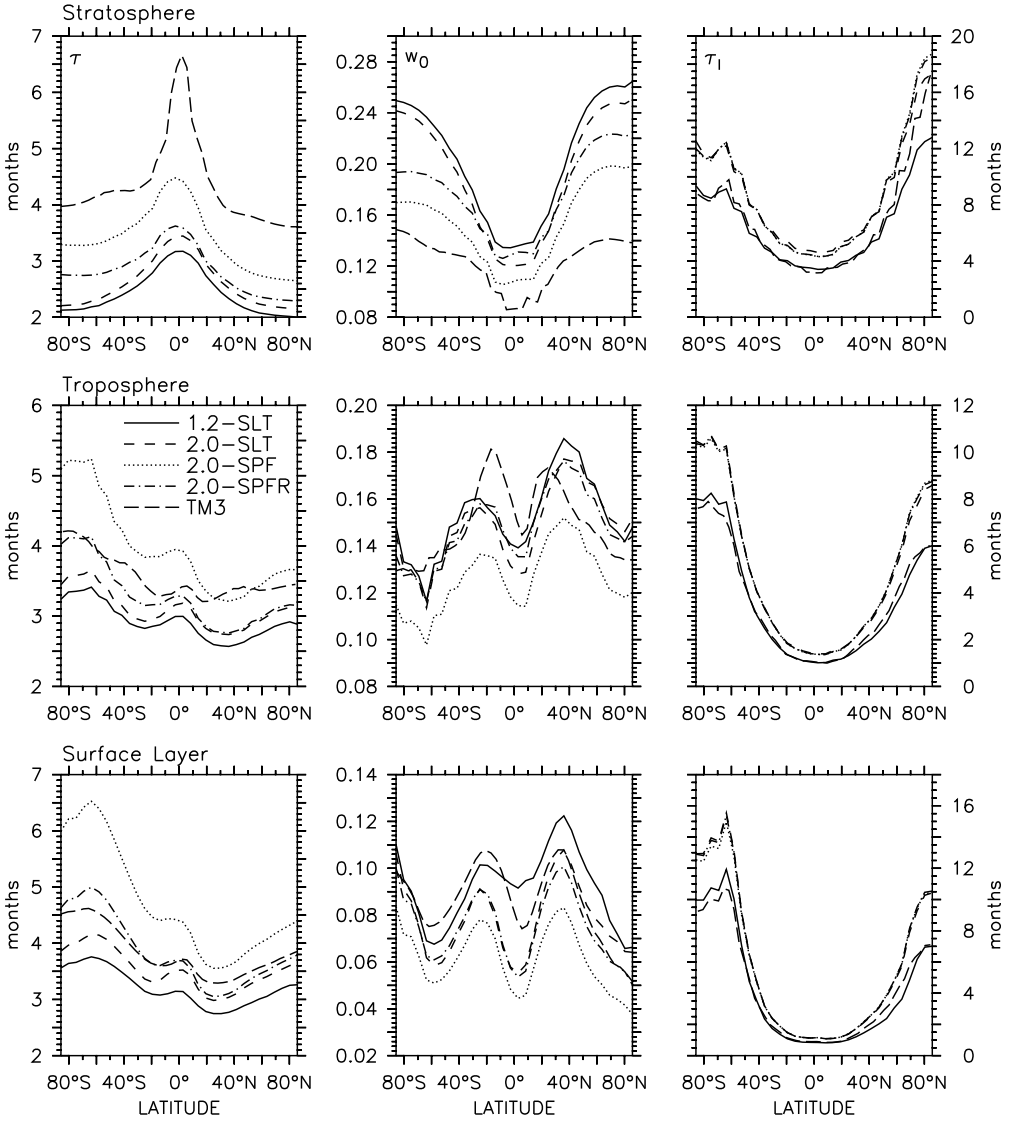

Figure 7.5: Annual zonal mean atmospheric response time (τ, left column) to global source scaling, weight of the current month's production rate scaling (w_0, middle column), and atmospheric lifetime (τ_l, including the soil sink (except for TM3), right column) of ^{14}CO calculated with various model configurations for the stratosphere (upper row), the troposphere (middle row), and the lowest model layer (up to 0.99 times the surface pressure, lower row). A climatological mean tropopause pressure of $(300 - 215 \cdot cos^2(\phi))$ hPa, where ϕ is latitude, is assumed.

predicted lifetime differs only significantly in the NH stratosphere at high latitudes, where TM3 predicts a longer lifetime compared to the 1.2-SLT configuration. North of 60^o the TM3 predicted lifetime is intermediate to the two groups. Interestingly, at most latitudes TM3 predicts lifetimes as short as predicted by the 1.2-SLT configuration, especially for the surface layer, although it does not include a parameterization

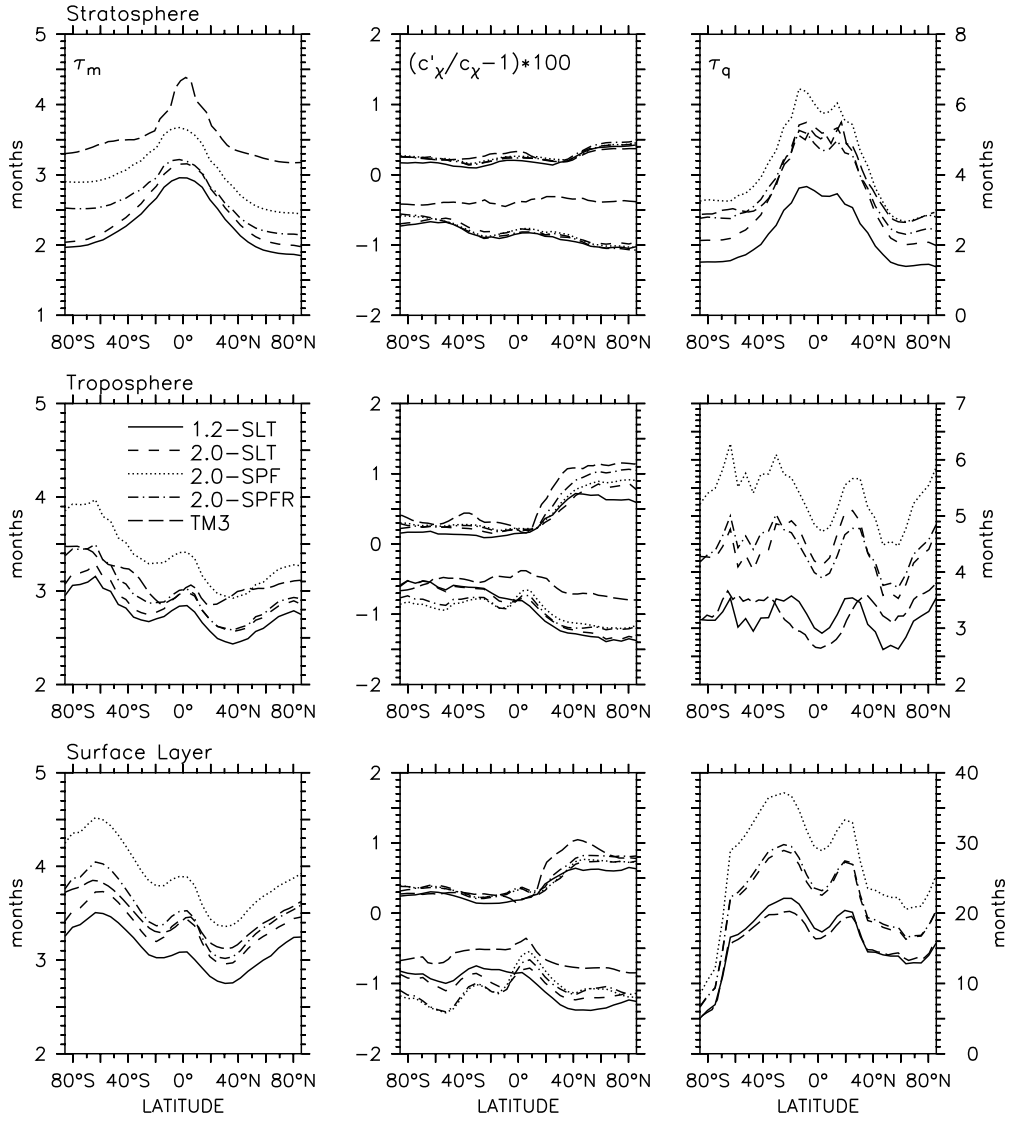

Figure 7.6: Annual zonal mean memory time (τ_m, left column) and production time (τ_q, right column) of atmospheric ^{14}CO calculated with various model configurations for the stratosphere (upper row), the troposphere (middle row), and the lowest model layer (up to 0.99 times the surface pressure, lower row). A climatological mean tropopause pressure of $(300 - 215 \cdot cos^2(\phi))$ hPa, where ϕ is latitude, is assumed. The middle column shows the range of the relative deviation (in %) of the approximated mixing ratio scaling (c'_χ, calculated from c_q with the filter function, Eq. (7.5)) from the respective model calculated signal (c_χ).

of the soil sink. As a consequence, either the TM3 predicted lifetime is generally shorter, or the uptake of ^{14}CO in soil is negligible compared to the oxidation by OH for determining the lifetime in the surface layer. The difference between the lifetimes predicted by the 2.0 configurations of MATCH is not significant, in particular, the

global mass mismatch rescaling (2.0-SPFR compared to 2.0-SPF) does hardly effect the simulated atmospheric lifetime of ^{14}CO.

In Table 7.1 the simulated average lifetime of ^{14}CO based on the OH-1 distribution in different atmospheric domains is summarized for various model configurations. The values in parentheses are the overall standard deviations calculated from the standard deviations

$$\sigma_x = (\frac{1}{N-1}\sum_{i=1}^{N}(x_i - \bar{x}_i))^{\frac{1}{2}} \tag{7.14}$$

of the ^{14}CO mixing ratio ($x = \chi$) and loss ($x = l$) with respect to time (monthly averages, 8 year simulation time), using

$$\sigma_{\tau_l} := (\frac{\sigma_\chi}{\bar{\chi}} + \frac{\sigma_l}{\bar{l}})\tau_l \ , \tag{7.15}$$

where the bar denotes the spatial and temporal average. Thus these standard deviations represent a measure of the temporal variation of the monthly mean values during the 8 year simulation time.

The annual variability of the lifetime in atmospheric sub-domains is high, due to the annual variation of OH. On a global scale, however the respective variation is rather small. This is consistent with the small variation of the simulated global atmospheric burden of ^{14}CO (see chapter 5). The estimates of the global atmospheric lifetime of ^{14}CO range from 2.54 to 3.64 months. The average is 3.09 months with a full range uncertainty of $\pm$0.55 months or $\pm$18%. If only the oxidation by OH is considered, the global atmospheric lifetime is somewhat longer, 3.17 ± 0.56 months. As a consequence, the destruction of ^{14}CO in soil has no significant influence (within the uncertainty range) on the global atmospheric lifetime of ^{14}CO.

In contrast to that, the lifetime at the surface level is reduced in comparison with the tropospheric lifetime by the soil sink. The lifetime is related to the loss rate and to the rate of uptake in soil (Eq. 7.12). Thus a tropospheric lifetime of ^{14}CO that only takes into account the uptake in soil ($\tau_l^{(\mathrm{soil})}$) can be estimated from τ_l and $\tau_l^{(\mathrm{OH})}$ by

$$\frac{1}{\tau_l} = \frac{1}{\tau_l^{(\mathrm{OH})}} + \frac{1}{\tau_l^{(\mathrm{soil})}} \ , \tag{7.16}$$

yielding 4.8, 7.6, and 7.9 years for the 1.2-SLT, the 2.0-SLT and the 2.0-SPF(R) configuration respectively. Finally, the global stratospheric lifetime (6.96 ± 1.07 months) is about a factor of 3 longer than the global tropospheric lifetime (2.19 ± 0.36 months, including the soil sink).

		τ_l			$\tau_l^{(OH)}$		
		SH	NH	GL	SH	NH	GL
1.2-SLT	COL	2.76 (1.09)	2.32 (1.12)	2.54 (0.60)	2.83 (1.14)	2.39 (1.15)	2.61 (0.62)
	STR	5.87 (2.83)	5.89 (2.86)	5.88 (1.27)	5.87 (2.83)	5.89 (2.86)	5.88 (1.27)
	TRO	2.03 (0.85)	1.64 (0.90)	1.83 (0.46)	2.09 (0.89)	1.70 (0.94)	1.89 (0.48)
	SRF	1.85 (0.85)	1.36 (0.83)	1.59 (0.45)	2.00 (0.93)	1.49 (0.92)	1.73 (0.49)
2.0-SLT	COL	3.76 (1.18)	3.22 (1.26)	3.48 (0.15)	3.82 (1.23)	3.31 (1.31)	3.56 (0.15)
	STR	7.81 (3.05)	7.89 (3.00)	7.85 (0.44)	7.81 (3.05)	7.89 (3.00)	7.85 (0.44)
	TRO	2.74 (0.95)	2.25 (1.09)	2.49 (0.17)	2.80 (0.98)	2.32 (1.13)	2.56 (0.17)
	SRF	2.54 (1.05)	1.88 (1.13)	2.19 (0.19)	2.71 (1.15)	2.05 (1.25)	2.36 (0.19)
2.0-SPF	COL	3.90 (1.55)	3.34 (1.47)	3.62 (0.09)	3.97 (1.60)	3.43 (1.52)	3.71 (0.09)
	STR	7.92 (3.60)	8.01 (3.21)	7.96 (0.74)	7.92 (3.60)	8.01 (3.21)	7.96 (0.74)
	TRO	2.79 (1.20)	2.29 (1.26)	2.54 (0.12)	2.85 (1.24)	2.37 (1.31)	2.61 (0.12)
	SRF	2.55 (1.30)	1.90 (1.32)	2.21 (0.18)	2.71 (1.41)	2.07 (1.46)	2.38 (0.19)
2.0-SPFR	COL	3.92 (1.45)	3.36 (1.49)	3.64 (0.19)	3.99 (1.50)	3.45 (1.54)	3.73 (0.19)
	STR	7.95 (3.53)	8.03 (3.32)	7.99 (0.66)	7.95 (3.53)	8.03 (3.32)	7.99 (0.66)
	TRO	2.79 (1.11)	2.30 (1.26)	2.54 (0.20)	2.85 (1.15)	2.37 (1.31)	2.61 (0.20)
	SRF	2.53 (1.20)	1.89 (1.31)	2.19 (0.25)	2.70 (1.31)	2.07 (1.45)	2.37 (0.27)
TM3	COL				3.38 (1.49)	3.02 (1.57)	3.20 (0.15)
	STR				6.25 (3.06)	6.47 (3.06)	6.36 (0.45)
	TRO				2.21 (1.07)	1.83 (1.22)	2.02 (0.19)
	SRF				2.03 (1.07)	1.57 (1.18)	1.78 (0.22)

Table 7.1: Annual mean atmospheric lifetime (τ_l, in months) of ^{14}CO calculated with different model configurations and the standard OH-1 distribution. The lifetime is averaged over the model column (COL), the stratosphere (STR), the troposphere (TRO), and the lowest model layer (SRF) of the southern hemisphere (SH), the northern hemisphere (NH), and the global atmosphere (GL). A climatological mean tropopause pressure of $(300 - 215 \cdot cos^2(\phi))$ hPa where ϕ is latitude, is assumed (see section 1.5). The left side lists the lifetime when the soil sink is included (τ_l); on the right side only the loss through oxidation by OH is accounted for ($\tau_l^{(OH)}$). The values in parentheses are the standard deviations with respect to time (equation 7.15) as a measure of the annual variability of the lifetime.

7.6.2 The simulated response time of atmospheric ^{14}CO to variations in the global source strength

As indicated above, the mean memory time enfolds both the response time and the weight of the current month's production rate scale in one parameter. For the case of the filter form used in this analysis (Eq. (7.5) and (7.6)), $\tau_m < \tau$ (cf. Figures 7.5 and 7.6); however, both τ_m and τ exhibit a very similar latitude dependence in all atmospheric domains considered. Therefore, the following discussion focuses on the response time τ. It should be noted, however, that the conclusions are also valid for

the mean memory time τ_m.

The relative deviation of the approximate ^{14}CO mixing ratio scale c'_χ (which defines the response time) from the model simulated mixing ratio scale c_χ is overall within $\pm 1.5\%$ for all configurations, with little scatter among them. In the SH, the approximation is somewhat better justified than in the NH. This characteristic is most pronounced in the troposphere and common to all configurations (Figure 7.6, middle column).

The response time τ (Figure 7.5, left column) shows a specific latitude dependence in all three atmospheric domains, which is common to all model configurations. In the troposphere the response time (like the lifetime) is longer in the SH than in the NH for the same absolute latitude. The tropospheric response time has local minima at latitudes around 25^o to 30^o in both hemispheres, except for TM3, which predicts local minima of the response time below 20^o in both hemispheres. At middle and high latitudes ($> 40^o$) τ increases with latitude. In the SH the maximum response time is reached at the edge of the polar vortex (around 60^oS), and it decreases again towards the south pole. This characteristic is predicted by all MATCH configurations, however not by the TM3 model, where the maximum response time occurs close to the pole. The highest values attained globally are in the SH high latitudes. In the NH troposphere, in contrast, the response time increases with latitude north of the local minimum and reaches the NH maximum close to the north pole. This characteristic is simulated by all employed MATCH configurations. The TM3 model further predicts a local maximum of the lifetime around 40^oN with a response time as long as at the north pole. The characteristics of the tropospheric response time are basically mirrored in the surface layer. There, the TM3 model exhibits a very similar latitude dependence of the response time compared to the MATCH configurations.

Like in the troposphere, the stratospheric response is also slower in the SH than in the NH at a given latitude. The stratospheric response time increases in both hemispheres gradually from the polar minimum with decreasing latitude to its maximum at the equator. The TM3 model predicts a very distinct, narrow, and large stratospheric maximum in the tropics, compared to the MATCH configurations.

The magnitude of the response time, in contrast to the overall latitude dependence, exhibits a significant scatter when different model configurations are compared. In particular, the 2.0 MATCH configurations predict different response times, though almost identical lifetimes (Figure 7.5).

Table 7.2 gives an overview of the response times τ, averaged over various domains of the model atmosphere for different configurations. The values in parentheses are the weight of the current month's production rate scale (w_0). For complete-

		τ (w_0)			τ_m		
		SH	NH	GL	SH	NH	GL
1.2-SLT	COL	2.76 (0.17)	2.54 (0.19)	2.69 (0.18)	2.60	2.41	2.54
	STR	2.40 (0.21)	2.28 (0.22)	2.35 (0.21)	2.27	2.15	2.21
	TRO	3.01 (0.15)	2.72 (0.16)	2.92 (0.15)	2.82	2.60	2.76
	SRF	3.37 (0.09)	2.93 (0.10)	3.24 (0.09)	3.24	2.93	3.15
2.0-SLT	COL	2.90 (0.16)	2.72 (0.18)	2.84 (0.17)	2.70	2.55	2.65
	STR	2.55 (0.20)	2.46 (0.21)	2.51 (0.20)	2.39	2.31	2.35
	TRO	3.15 (0.14)	2.90 (0.16)	3.08 (0.15)	2.92	2.73	2.87
	SRF	3.69 (0.07)	3.24 (0.08)	3.55 (0.07)	3.45	3.18	3.38
2.0-SPF	COL	3.89 (0.14)	3.24 (0.15)	3.62 (0.14)	3.31	2.94	3.18
	STR	3.51 (0.15)	2.98 (0.17)	3.27 (0.16)	3.07	2.72	2.92
	TRO	4.21 (0.12)	3.45 (0.13)	3.91 (0.12)	3.50	3.11	3.38
	SRF	5.21 (0.06)	3.90 (0.06)	4.63 (0.06)	4.11	3.62	3.93
2.0-SPFR	COL	3.19 (0.16)	2.77 (0.17)	3.03 (0.16)	2.89	2.59	2.78
	STR	2.91 (0.18)	2.55 (0.20)	2.75 (0.18)	2.67	2.39	2.55
	TRO	3.42 (0.14)	2.95 (0.16)	3.26 (0.14)	3.06	2.75	2.97
	SRF	4.15 (0.08)	3.34 (0.07)	3.84 (0.07)	3.66	3.27	3.54
TM3	COL	3.99 (0.14)	3.71 (0.14)	3.88 (0.14)	3.35	3.23	3.31
	STR	4.28 (0.13)	3.94 (0.13)	4.12 (0.13)	3.51	3.37	3.45
	TRO	3.65 (0.15)	3.37 (0.15)	3.60 (0.15)	3.14	3.00	3.15
	SRF	4.02 (0.09)	3.50 (0.08)	3.87 (0.08)	3.54	3.32	3.50

Table 7.2: Annual mean response time (τ, in months), weight of the current month's production rate scale (w_0), and mean memory time (τ_m, in months) of atmospheric ^{14}CO to changes in the global source strength calculated with various model configurations and the standard OH-1 distribution. The values are averages over the model column (COL), the stratosphere (STR), the troposphere (TRO), and the lowest model layer (SRF) of the southern hemisphere (SH), the northern hemisphere (NH), and the global atmosphere (GL). A climatological mean tropopause pressure of $(300 - 215 \cdot cos^2(\phi))$ hPa, where ϕ is latitude, is assumed.

ness, the mean memory time τ_m is also listed. The global average response time of the simulated atmospheric ^{14}CO mixing ratio to changes in the global source strength of ^{14}CO production varies from 2.69 to 3.88 months, depending on the model configuration. This is on average a response time of 3.3 ± 0.6 months, i.e. the relative uncertainty is $\pm 18\%$. The stratospheric response in all MATCH configurations (2.81 ± 0.46 months) tends to be faster than the tropospheric response (3.42 ± 0.5 months). This is, however, reversed in the TM3 model. Common to all model configurations examined, the NH mixing ratio responds faster than the SH mixing ratio.

7.6.3 Sensitivity to the tropospheric OH distribution

To assess the influence of the tropospheric OH distribution on the model simulated response time and lifetime, Figure 7.7 depicts τ, w_0, and τ_l (including the loss by uptake in soil), calculated with the above analysis from 2.0-SLT simulations with three different tropospheric OH distributions, while Figure 7.8 shows τ_m, τ_q, and the quality of the approximative mixing ratio scaling (c'_χ), measured in % relative deviation (full range) from the original model simulated scaling (c_χ), respectively. The quantities are averaged for the stratosphere, the troposphere, and the lowest model layer.

The latitude dependence of the atmospheric lifetime in the stratosphere (Figure 7.7, right column) is unaffected by the tropospheric OH distribution, because in the stratosphere the OH distribution is the same in all cases (OH-2D). In the troposphere and in the surface layer, the average lifetime at high latitudes is considerably different for the different tropospheric OH distributions. It is lowest there for the OH-1 distribution, and highest for the OH-2 distribution. Differences between the lifetime based on OH-2 and OH-S are more pronounced in the SH high latitudes, whereas in the NH both are almost identical, and longer than the lifetime based on OH-1. At lower latitudes ($< 40^o$) the predicted tropospheric lifetimes differ by about 1 month between the involved OH distributions; in the surface layer, they are almost identical.

Table 7.3 lists the simulated average lifetime of ^{14}CO in various domains of the model atmosphere and its annual variability, dependent on the chosen tropospheric OH distribution. The mass weighted global average OH concentration in the troposphere is 30% lower in the OH-2 distribution than in the OH-1 distribution (cf. Table 1.1). The resulting global average lifetime ($\tau_l^{(OH)}$) based on OH-2 is 26% longer compared to the OH-1 based estimate. This is almost exactly the same relative prolongation of the lifetime as calculated for CH_3CCl_3 (MCF, see chapter 4). Moreover, the tropospheric lifetime based on OH-1 is 30% lower than the respective lifetime based on OH-2, and therefore the lifetime is inversely proportional to the average OH concentration on a global scale, as is to be expected. This relationship also holds within $\pm 2\%$ on the hemispheric scale, when different OH distributions are compared. For instance, the mass weighted global average OH concentration in the troposphere is 14% lower in the OH-2 distribution than in the OH-S distribution; the NH lifetime of ^{14}CO based on OH-S in the troposphere is 12% shorter than that based on OH-2. Interestingly, the inverse relation between lifetime and average OH concentration on the hemispheric scale seems to be more violated when the NH-SH asymmetry of a given OH distribution is considered. For example, based on the OH-1 distribution, the tropospheric lifetime is 21% longer in the SH than in the NH, however the

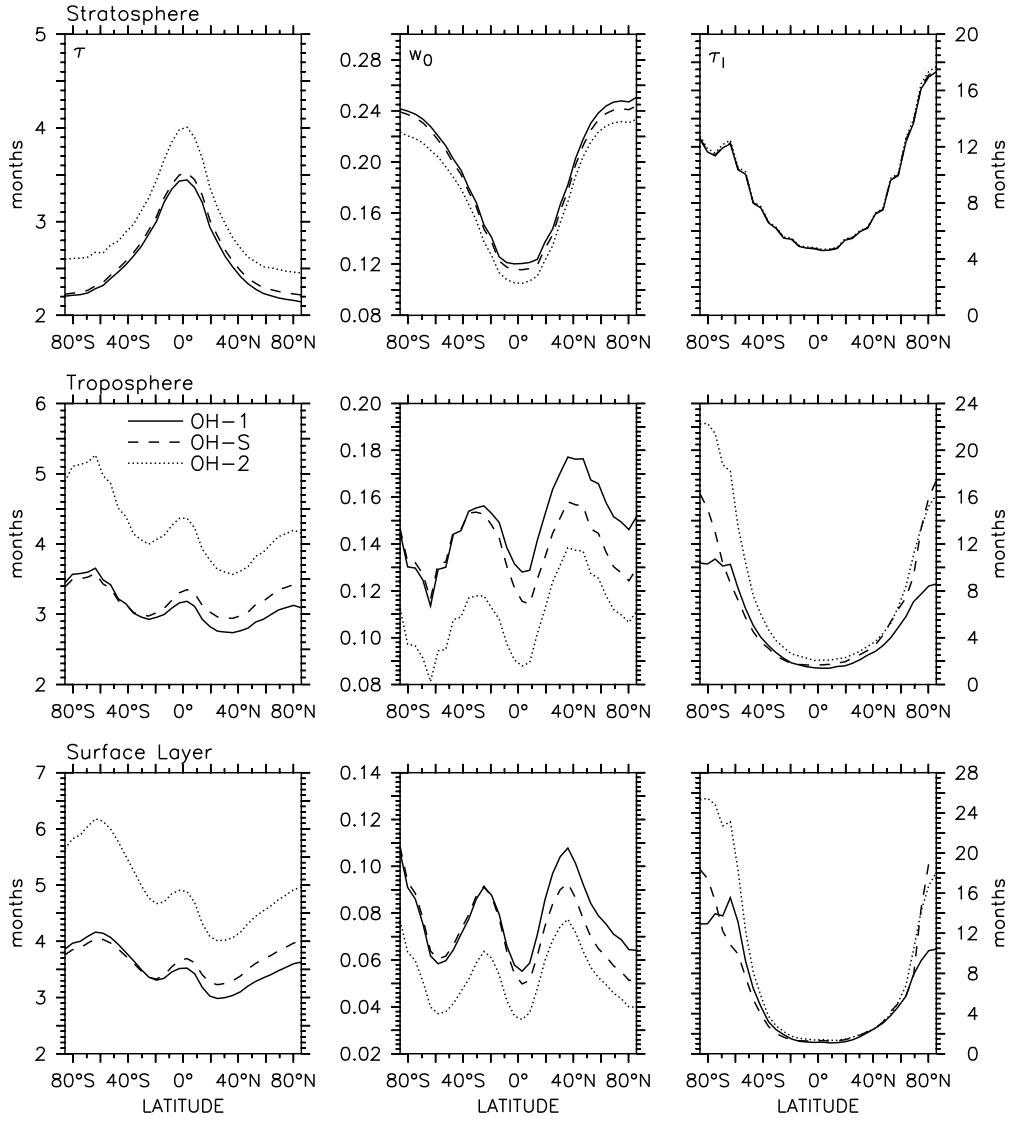

Figure 7.7: Annual zonal mean atmospheric response time (τ, left column) to global source scaling, weight of the current month's production rate scale (w_0, middle column), and atmospheric lifetime (τ_l, including the soil sink, right column) of ^{14}CO calculated with the 2.0-SLT model configuration for the stratosphere (upper row), the troposphere (middle row), and the lowest model layer (up to 0.99 times the surface pressure, lower row). A climatological mean tropopause pressure of $(300 - 215 \cdot cos^2(\phi))$ hPa, where ϕ is latitude, is assumed. Different tropospheric OH distributions are taken into account. The stratospheric OH-distribution in all cases is OH-2D.

average OH concentration in the NH is 25% higher in the NH compared to the SH. Finally, the uptake of ^{14}CO in soil reduces the lifetime of ^{14}CO in the troposphere and in the surface layer ($\tau_l < \tau_l^{(\mathrm{OH})}$).

The quality of the approximate mixing ratio scale c'_χ does not significantly depend

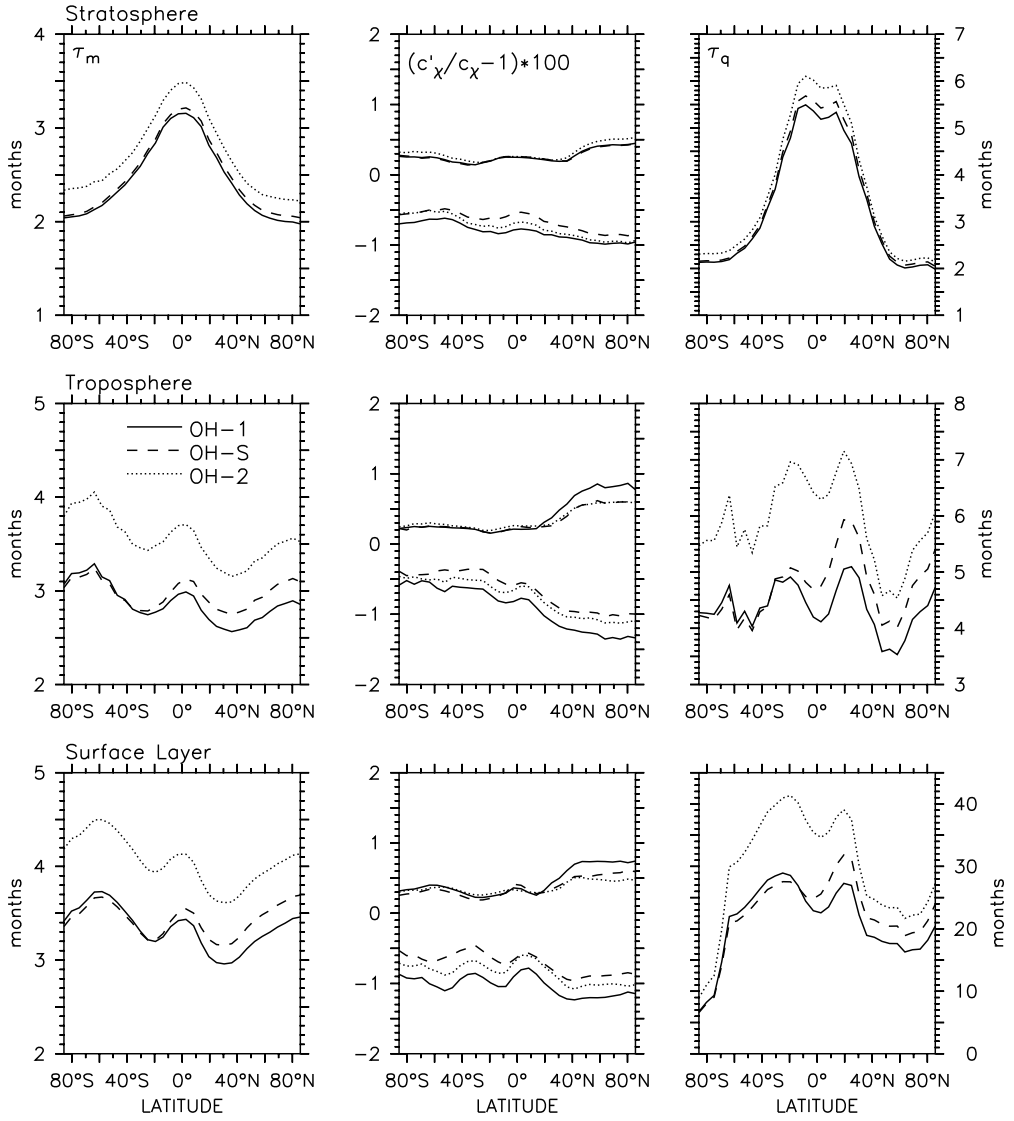

Figure 7.8: Annual zonal mean memory time (τ_m, left column) and production time (τ_q, right column) of atmospheric ^{14}CO calculated with the 2.0-SLT model configuration for the stratosphere (upper row), the troposphere (middle row), and the lowest model layer (up to 0.99 times the surface pressure, lower row). A climatological mean tropopause pressure of $(300 - 215 \cdot cos^2(\phi))$ hPa, where ϕ is latitude, is assumed. The middle column shows the range of the relative deviation (in %) of the approximated mixing ratio scaling (c'_c, calculated from c_q with the filter function, Eq. (7.5)) from the respective model calculated signal (c_c). Different tropospheric OH distributions are taken into account. The stratospheric OH-distribution in all cases is OH-2D.

on the tropospheric OH distribution (Figure 7.8, middle column). The relative deviation from the simulated scaling c_χ is overall in the interval ±1.5%. The interhemispheric asymmetry of this deviation with a larger deviation in the NH is common to all simulations, independent of the OH distribution.

		τ_l			$\tau_l^{(OH)}$		
		SH	NH	GL	SH	NH	GL
OH-1	COL	3.76 (1.18)	3.22 (1.26)	3.48 (0.15)	3.82 (1.23)	3.31 (1.31)	3.56 (0.15)
	STR	7.81 (3.05)	7.89 (3.00)	7.85 (0.44)	7.81 (3.05)	7.89 (3.00)	7.85 (0.44)
	TRO	2.74 (0.95)	2.25 (1.09)	2.49 (0.17)	2.80 (0.98)	2.32 (1.13)	2.56 (0.17)
	SRF	2.54 (1.05)	1.88 (1.13)	2.19 (0.19)	2.71 (1.15)	2.05 (1.25)	2.36 (0.19)
OH-S	COL	3.66 (1.21)	3.70 (1.44)	3.68 (0.20)	3.72 (1.25)	3.83 (1.51)	3.77 (0.21)
	STR	7.83 (3.06)	7.92 (3.02)	7.87 (0.47)	7.83 (3.06)	7.92 (3.02)	7.87 (0.47)
	TRO	2.65 (1.00)	2.75 (1.27)	2.70 (0.19)	2.70 (1.04)	2.86 (1.34)	2.78 (0.19)
	SRF	2.37 (1.20)	2.10 (1.26)	2.23 (0.29)	2.52 (1.32)	2.33 (1.42)	2.42 (0.31)
OH-2	COL	4.76 (1.58)	3.99 (1.65)	4.37 (0.32)	4.88 (1.67)	4.14 (1.74)	4.50 (0.32)
	STR	7.92 (3.11)	7.97 (3.05)	7.94 (0.50)	7.92 (3.11)	7.97 (3.05)	7.94 (0.50)
	TRO	3.89 (1.37)	3.09 (1.50)	3.48 (0.33)	4.02 (1.45)	3.24 (1.58)	3.61 (0.34)
	SRF	3.00 (1.24)	2.13 (1.21)	2.53 (0.33)	3.23 (1.39)	2.36 (1.38)	2.77 (0.36)

Table 7.3: Annual mean atmospheric lifetime (τ_l, in months) of ^{14}CO calculated with the 2.0-SLT model configuration and various tropospheric OH distributions combined with the standard OH-2D stratospheric OH distribution. The lifetime is averaged over the model column (COL), the stratosphere (STR), the troposphere (TRO), and the lowest model layer (SRF) of the southern hemisphere (SH), the northern hemisphere (NH), and the global atmosphere (GL). A climatological mean tropopause pressure of $(300 - 215 \cdot cos^2(\phi))$ hPa, where ϕ is latitude, is assumed. The left side lists the lifetime when the soil sink is included (τ_l); on the right side only the loss through oxidation by OH is accounted for ($\tau_l^{(OH)}$). The values in parentheses are the standard deviations with respect to time (equation 7.15) as a measure for the annual variability of the lifetime.

The overall latitude dependence of the ^{14}CO mixing ratio response time to variations in the global source strength is rather unaffected by the OH distribution; the local extrema are similarly placed and of similar relative magnitude (Figure 7.7). However, calculations with the OH-S distribution result in a much less pronounced, almost vanishing NH-SH asymmetry of the tropospheric and surface layer response time, compared to the calculations with the OH-1 or OH-2 distribution. This effect is also visible in the stratosphere, though less distinct. It is obviously directly related to the NH-SH symmetry of the OH-S distribution, compared to OH-1 and OH-2, which both exhibit an asymmetry between the average tropospheric OH concentration in the NH and SH (cf. Table 1.1). Moreover, the absolute value of the response time at a given latitude increases with decreasing average tropospheric OH concentration. This, however, not only holds for the tropospheric and surface layer response time, but is also observed (less pronounced) for the stratospheric response time, although the stratospheric OH distribution is the same in all cases.

For further quantification, Table 7.4 lists the calculated average response time of the ^{14}CO mixing ratio to variations in the global source strength in various atmospheric

		τ (w_0)			τ_m		
		SH	NH	GL	SH	NH	GL
OH-1	COL	2.90 (0.16)	2.72 (0.18)	2.84 (0.17)	2.70	2.55	2.65
	STR	2.55 (0.20)	2.46 (0.21)	2.51 (0.20)	2.39	2.31	2.35
	TRO	3.15 (0.14)	2.90 (0.16)	3.08 (0.15)	2.92	2.73	2.87
	SRF	3.69 (0.07)	3.24 (0.08)	3.55 (0.07)	3.45	3.18	3.38
OH-S	COL	2.93 (0.16)	2.88 (0.16)	2.93 (0.16)	2.73	2.69	2.73
	STR	2.59 (0.19)	2.53 (0.20)	2.56 (0.20)	2.43	2.36	2.40
	TRO	3.17 (0.14)	3.12 (0.14)	3.19 (0.14)	2.94	2.91	2.96
	SRF	3.66 (0.08)	3.50 (0.07)	3.65 (0.07)	3.44	3.37	3.45
OH-2	COL	3.81 (0.13)	3.44 (0.15)	3.67 (0.14)	3.29	3.07	3.21
	STR	2.93 (0.18)	2.79 (0.19)	2.87 (0.18)	2.67	2.56	2.62
	TRO	4.37 (0.11)	3.86 (0.12)	4.18 (0.11)	3.63	3.37	3.54
	SRF	5.28 (0.05)	4.39 (0.06)	4.92 (0.05)	4.19	3.85	4.07

Table 7.4: Annual mean response time (τ, in months), weight of the current month's production rate scale (w_0), and mean memory time (τ_m, in months) of atmospheric ^{14}CO to changes in global source strength calculated with the 2.0-SLT model configuration and various tropospheric OH distributions combined with the standard OH-2D stratospheric OH distribution. The values are averages over the model column (COL), the stratosphere (STR), the troposphere (TRO), and the lowest model layer (SRF) of the southern hemisphere (SH), the northern hemisphere (NH), and the global atmosphere (GL). A climatological mean tropopause pressure of $(300 - 215 \cdot cos^2(\phi))$ hPa, where ϕ is latitude, is assumed.

domains, dependent on the OH distribution. Calculations are performed with the 2.0-SLT configuration. The respective mean memory time (τ_m) is also listed, as well as the weight of the current month's production rate scale (w_0).

The global average atmospheric response time τ is 29% longer for the OH-2 distribution than for the OH-1 distribution (Table 7.4). This is in agreement with the difference in the tropospheric OH concentrations of 30% (cf. Table 1.1). In the troposphere itself, the effect of a prolonged response with decreasing OH concentration is even more enhanced; the average response is 36% slower for OH-2 compared to OH-1. Moreover, the tropospheric OH concentration seems to affect also the stratospheric response time, which is 14% longer for OH-2 than for OH-1, although the stratospheric OH distribution is identical in both cases. The response times based on OH-1 and OH-S do not differ significantly, consistent with the similar OH abundances (cf. Table 1.1), despite the NH-SH (a)symmetry already mentioned above.

7.7 Discussion

A two parameter filter (w_i) based approximation of the time dependent ^{14}CO mixing ratio scaling (c'_χ), which is a function of the global source strength scaling c_q, is possible with high accuracy. Taking into account a 12-month history of the variable global source strength of ^{14}CO, the approximate mixing ratio scaling function reproduces the model derived scaling function within $\pm 1.5\%$ on the hemispheric scale, as well as averaged over the stratosphere and troposphere. Local deviations from the zonal average are of the same order and range from -1.5% to +1.2%. These relative deviations are the minimum uncertainties that have to be attributed for the optimal filter parameters minimizing the deviations, i.e., for the response time and the weight of the current month's production scale, and further for the mean memory time.

Variations of the atmospheric ^{14}CO mixing ratio arising from variations of the global source strength can therefore effectively be calculated without involving the 3-D model itself. The uncertainty arising from this procedure (which defines the model self-consistent filter) is $\pm 1.5\%$, and therefore far smaller than other uncertainties involved, primarily the uncertainty in the absolute source strength of cosmogenic ^{14}CO (this will be further discussed in chapter 8). Moreover, the simulated response time differs significantly between the employed model configurations compared to this minimum uncertainty. The response time can therefore be used for a quantitative comparison of various model configurations. Together with the simulated lifetime of the tracer, the response time may reveal several other important aspects of the simulated dynamics.

Three mechanisms, each with a characteristic timescale, determine the local (cosmogenic) ^{14}CO mixing ratio:

- the loss by oxidation through OH and uptake in soil,
- the production by cosmic rays,
- atmospheric transport and mixing.

The lifetime is the time scale of the loss; likewise, the production time is the time scale of the local production. Atmospheric transport and mixing processes occur on several time scales, depending on the specific transport component. Calculating semi-hemispheric (i.e., NH-troposphere, etc.) averages, all processes on smaller scales (e.g. tropospheric vertical mixing) cancel out, and in principle only two global transport components are left which potentially influence the semi-hemispheric averages: interhemispheric exchange and stratosphere - troposphere exchange (STE).

For ^{14}CO, the source distribution is quasi hemispherically symmetric. More than half of ^{14}CO is produced in the stratosphere. The temporally varying NH-SH asymmetry of the ^{14}CO burden is mainly driven by the annual variation of OH (see chapter 5). Therefore, averaging over a long enough (> 1 year) time also cancels out the influence of the oscillating interhemispheric exchange, while keeping the unidirectional flow of ^{14}CO from the stratosphere into the troposphere. In the analysis above, the derived response time of the atmospheric ^{14}CO mixing ratio to variations in the global source strength is averaged over several years. As a consequence, it can be expected that this response time is somehow related to the simulated STE. In the following discussion the response time is compared to the lifetime including the soil sink, because the effect of the soil sink cannot be separated from the response time as readily as from the lifetime.

Simulations with the 2.0 MATCH configurations provide a set of predictions of the response time that are derived under equal boundary conditions, with the only exception that the model advective transport is implemented differently. Exchanging 2.0-SLT with 2.0-SPFR, the atmospheric lifetime increases by less than 2.2% in all domains (Table 7.1). The response time increases by about 2% in the NH-troposphere, 4% in the NH stratosphere, 9% in the SH troposphere, and 14% in the SH stratosphere (Table 7.2). The analysis in chapter 5 indicated differences of the STE rate between the 2.0 MATCH configurations. The STE is found to be stronger in the 2.0-SLT configuration than in the 2.0-SPF(R) configuration. Furthermore, the interhemispheric asymmetry of STE is more pronounced in the 2.0-SPF(R) configurations than in 2.0-SLT. Assuming that the response time is directly related to the STE implies that the response time decreases with increasing STE. Taking into account the interhemispheric asymmetry this interpretation is still coherent. Whereas the ratio of NH to SH lifetime remains 1.01 in the stratosphere and 0.82 in the troposphere (Table 7.1), unaffected by the different realization of transport, the ratio between NH and SH response time (Table 7.2) decreases from 0.96 to 0.88 in the stratosphere, and from 0.92 to 0.86 in the troposphere when 2.0-SPFR is used instead of 2.0-SLT, i.e., the NH-SH asymmetry of the response time increases with an increasing interhemispheric asymmetry of the STE. Since especially the SH response time changes between 2.0-SLT and 2.0-SPFR (see numbers above), one further observation is implied. In the NH the response time is only moderately enhanced in 2.0-SPFR compared to 2.0-SLT; the NH STE does not differ too much between the two configurations. In the SH, in contrast, this effect is larger, implying a weaker SH STE in 2.0-SPFR compared to 2.0-SLT. This effect of the interhemispheric asymmetry of STE on the response time can also be seen in Figure 7.5 in all three domains.

In summary, the response time of the ^{14}CO mass mixing ratio to variations in the

global source strength seems to be more sensitive to changes in the realization of atmospheric dynamics in the model than the lifetime of the tracer. This observation is also supported by the effect of the global mass mismatch rescaling correction, which introduces an artificial transport component (see chapters 2 and 5). The lifetime τ_l is almost insensitive to the mass mismatch rescaling correction (2.0-SPFR) in all domains (cf. Table 7.1 and Figure 7.5). In contrast to that, the response time τ decreases considerably when the mass mismatch rescaling correction is used (cf. Table 7.2).

To interpret the processes determining the response time, the sensitivity to OH needs to be tested. From the model simulations involving different OH distributions it is obvious that the response time is not only affected by atmospheric transport, but also by OH. Exchanging OH-1 by OH-2 (Table 7.3) the tropospheric lifetime of ^{14}CO increases by 40%, in the SH by 45%, and in the NH by 37%. The tropospheric response time (Table 7.3) increases similarly, globally by 36%, 39% in the SH, and 33% in the NH. Therefore, the effect of tropospheric OH on the lifetime is only somewhat larger than on the response time in the troposphere. This is different in the model stratosphere. There, the lifetime increases by 1% to 1.5% when OH-2 is used instead of OH-1. The stratospheric response time, however increases by 15% in the SH and by 13% in the NH. Since in both simulations the same model configuration (2.0-SLT) and the same stratospheric OH distribution (OH-2D) is used, the prolonged response time in the stratosphere has to be caused by the differences between the tropospheric OH distributions.

The interhemispheric asymmetry of the average OH concentration is most pronounced in the OH-2 distribution. The ratio of the NH to SH average OH abundance is 1.27, whereas the annual average OH-S distribution almost hemispherically symmetric (ratio of 0.99, cf. Table 1.1). The interhemispheric asymmetry of the OH concentration also affects response time and lifetime. Using OH-2 instead of OH-S, the NH to SH ratio of the response time is almost unchanged in the stratosphere (0.98 to 0.95), whereas in the troposphere the ratio decreases from 0.98 to 0.88 (Table 7.4). At the same time, the NH to SH ratio of the stratospheric lifetime remains 1.01, however the respective ratio in the troposphere decreases from 1.04 to 0.79 (Table 7.3). Thus, the tropospheric lifetime is more sensitive to differences in tropospheric OH than the tropospheric response time. In the stratosphere, the response time in contrast to the lifetime, is also sensitive to changes in tropospheric OH (Figure 7.7).

So far, the origin of interhemispheric differences in the response time and lifetime of ^{14}CO can be traced back to interhemispheric differences of OH and STE. For variations of the response time on increasingly smaller scales, i.e., the latitude dependence, transportation of the tracer becomes increasingly important. This can

clearly be seen in the tropics. There both the stratospheric and the tropospheric response time exhibits a maximum (or a local maximum), although the lifetime is shortest due to the high OH abundance. Furthermore, the stratospheric response time at high latitudes is shortest, whereas the lifetime is longest. The production rate in the equatorial troposphere is lowest. Because of the low mixing ratio, the production time has a local minimum (Figure 7.6). If both production time and lifetime are short, one at first expects a fast response. However, the tropospheric response time has a local maximum near the equator (Figure 7.5). If this maximum in the equatorial troposphere were due to inadvertent partial integration over stratospheric regions caused by the chosen static tropopause approximation, one would not expect a maximum at the surface as well. Therefore atmospheric transport has to be considered. Tropical tropospheric transport is dominated by convergence and upwelling. The convergence imports air masses from higher latitudes; through upwelling, local air masses are lost into the stratosphere. These are the only two effects that can be identified for the prolonged response time. This also implies an explanation for the tropical stratospheric maximum of the response time.

The subtropical local minimum of the tropospheric response time can be explained in a similar way. Here the production time has a local maximum (Figure 7.6, right column), indicating that the local mixing ratio is high in terms of the local production rate. The lifetime is longer than in the tropics (Figure 7.5, right column). However, the response time is at its minimum in both hemispheres (Figure 7.5, left column). The tropospheric mid-latitudes, at least in the model, are the regions most influenced by the stratosphere through downward transport. This accounts for the reduced local response time. Thus even on smaller scales a link between the response time of ^{14}CO to variations of the cosmogenic source strength and the STE can be established.

One minor issue to be discussed is the difference of the chosen simulation time, which for the MATCH configurations is 8 years, for the TM3 model, however only 6 years. This is addressed by an analysis of the MATCH simulations taking into account only the first 6 years of model output. The results (not shown) are nearly identical to the analysis of 8 year model output and, e.g., not distinguishable within the drawing accuracy of the figures presented above. As a consequence, 6 year simulation time suffices for the response time analysis.

Another difference is that of incorporating a soil sink parameterization into the MATCH model, but not into the TM3 model. The effect on the lifetime can very well be separated, as is done in the analysis. In contrast, the potential effect of ^{14}CO uptake in soil on the response time can not directly be assessed.

Finally, the response time as derived here may be time-dependent. The 8 (6 for

TM3), years of simulation time were all performed with the 1993 meteorology (MATCH: NCEP, TM3: ECMWF) driving the offline models. Thus the response time shown here is the typical response time for 1993. Climatological means of the response time could be achieved by model runs with different years of meteorological data. Changes in the response time can then indicate changes in the atmospheric circulation.

7.8 Conclusions: ^{14}CO - An important diagnostic for changes in chemistry and circulation

Generally, the response time concept is a useful tool to derive basic dynamic properties of complicated systems. For atmospheric applications its relevancy has been shown, for example, by *Prather* [1996] and *Tans* [1997]. The filter function used here defines a time parameter which can be interpreted as the response time, or more generally, as the mean memory time of the system. As a system variable, this time parameter contains in particular information about the dynamics of the system, in the case of ^{14}CO information about the model transport. A coherent link between the derived response time and the stratosphere - troposphere exchange (STE) down to the zonal average scale is established. Since the response time is also sensitive to the OH distribution it can serve in combination with the atmospheric lifetime of the tracer, as a semi-quantitative measure of the simulated STE.

The lifetime and the production time of a tracer are both dependent on the local tracer mixing ratio, which in turn is dependent on the production rate, the loss rate, and the transport. The time-dependent absolute scale of the ^{14}CO mixing ratio can be calculated by a two-parameter filter function from the time series of the absolute scale of the ^{14}CO production rate (i.e., the input signal). A model self-consistent approach is accurate within $\pm 1.5\%$. This uncertainty is lower than other uncertainties, in particular than the uncertainty in the global average production rate of cosmogenic ^{14}CO. Further development of the ^{14}CO methodology is therefore possible without knowing the actual absolute source scaling. Measurements and model results can be scaled or standardized to well defined source conditions with respect to the solar activity dependence. Models can trace ^{14}CO in a normalized mode. The resulting distributions are directly comparable.

The global atmospheric lifetime of ^{14}CO is estimated to 3.1 ± 0.55 months, 2.2 ± 0.4 months in the troposphere, and 7 ± 1 months in the stratosphere. These estimates are based on the same OH distribution (OH-1) resulting in a lifetime of CH_3CCl_3 (MCF) of 4.4 ± 0.1 years (chapter 4). The uncertainties arise from uncertainties in the simulated tracer transport. The shorter the lifetime of a species, the more the

lifetime is affected by the tracer transport. Furthermore, the tropospheric lifetime of ^{14}CO against destruction in soil is estimated to 4.8 to 7.9 years, dependent on the model configuration. On the global scale, the response time (also called adjustment time) of ^{14}CO to variations in the global source strength is estimated to be 3.3 ± 0.6 months, and therefore, within the uncertainty range, equal to the atmospheric lifetime of ^{14}CO, as is to be expected [*Seinfeld and Pandis*, 1997].

Interhemispheric asymmetries of the OH distribution and the STE rate must determine the NH-SH asymmetry of tropospheric ^{14}CO mixing ratios observed by *Brenninkmeijer et al.* [1992], since the relative source distribution is hemispherically symmetric in the zonal average. The response time of ^{14}CO to variations of the global source strength, as well as the atmospheric lifetime of ^{14}CO, differ in their sensitivity to tropospheric OH and STE in different atmospheric sub-domains. As a consequence, the response time and the lifetime in combination may provide a direct indicator for the solution of the ^{14}CO interhemispheric asymmetry. Comparison of the lifetime and the latitude dependence of the response time indicates a possible alternative explanation of the observed NH-SH-asymmetry of the ^{14}CO mixing ratio, namely, a weaker stratosphere - troposphere exchange in the SH instead of a possibly higher OH concentration in the SH [cf. *Brenninkmeijer et al.*, 1992; *Spivakovsky et al.*, 2000]. The analysis further suggests that a time series of ^{14}CO measurements could serve as a sensitive diagnostic for (coupled) changes in chemistry and transport as climate and atmospheric composition change.

8 The absolute ^{14}CO production rate and its variation with solar activity

Abstract. Atmospheric ^{14}CO measurements can be applied to trace changes in the OH concentration and/or atmospheric transport after they are standardized to the same conditions with respect to the solar activity, which modulates the global source strength of cosmogenic ^{14}CO. Measurements can be rescaled to an arbitrary "standard" condition, i.e., standard source strength, as long as the relative timing of the global source strength is known. The required temporal resolution of the source strength modulation is of the order of the atmospheric lifetime of ^{14}CO, i.e., about 3 months. Comparison of measurements with model simulations additionally requires the absolute value of the standard source strength. Several published estimates of the absolute source strength are collected for comparison; a considerable uncertainty remains. This uncertainty in the absolute global source strength determines directly the uncertainty that has to be attributed to ^{14}CO measurement based estimates of the global average OH abundance. The relative modulation of the global ^{14}CO source strength on the time scale of the atmospheric lifetime of ^{14}CO is estimated, using three different approaches involving neutron count rates, sunspot numbers, and the calculated heliospheric modulation potential in order to parameterize "solar activity" with respect to the effect on the global average atmospheric ^{14}C production rate. With these approaches and the results of previous chapters, a scaling function is derived which can be applied to separate effects of the solar modulation from measurements of atmospheric ^{14}CO. Uncertainties in this scaling function are discussed. The main uncertainty arises from the lack of a measurable global parameter that quantitatively describes "solar activity" and its effect on the global average atmospheric ^{14}CO production rate as a function of it. Within these uncertainties, the OH distribution and seasonality can in principle be constrained, independent of the uncertainty in the absolute global average production rate.

8.1 Introduction

To extract a signal from ^{14}CO measurements that is caused by changes in atmospheric transport, or by changes in the atmospheric OH concentration, all effects of other known processes have to be assessed. The most important process is the modulation of the global background GCR ^{14}CO production rate during the solar cycle (section 5.2.1). Possible modulations of the OH concentration by changing solar irradiance during the solar cycle, or by year-to-year changes in precursor emissions and atmospheric humidity are not taken into account here.

The relative spatial modulation of the ^{14}C(O) production rate distribution in the atmosphere during a solar cycle only has a small effect on the relative distribution of ^{14}CO in the troposphere, as was shown in chapter 5. Furthermore, the time

dependence of the GCR based global average ^{14}CO production rate is convoluted with atmospheric transport and oxidation, considered as time dependent transformation functions. As discussed in chapter 7, this convolution can be described by an atmospheric filter function with a latitude dependent atmospheric response time.

The application of these results to a time series of measurements would require a complete knowledge of the time dependence of the cosmogenic ^{14}CO production rate scaling ($c_q(t)$, Eq. (7.1)). This determines the relative modulation compared to an arbitrary "standard" (e.g., the average atmospheric production rate during an 11 year solar cycle). For an absolute comparison of model results with measurements of atmospheric ^{14}CO, the "standard" global average production rate of ^{14}CO has to be known in addition.

OH reacts to about 70% with CO, and therefore the OH distribution and global abundance are heavily influenced by the amount of total CO. In contrast to that, the OH distribution and global abundance is essentially unaffected by ^{14}CO, since the abundance of ^{14}CO in the atmosphere is 12 orders of magnitude smaller than of ^{12}CO. The soil sink of ^{14}CO is also independent of the ^{14}CO abundance. More than 90% of the ^{14}CO is removed from the atmosphere through oxidation by OH, i.e., the atmospheric lifetime of ^{14}CO and its local mixing ratio are determined by the OH abundance. The "standard" global average production rate of ^{14}C(O) and the global average OH abundance are therefore simply global scaling factors of the atmospheric ^{14}CO mixing ratio, and of the estimated atmospheric lifetime of ^{14}CO. As a consequence, the relative uncertainty of an estimate of the global average OH abundance based on ^{14}CO measurements is directly related to the uncertainty in the "standard" global ^{14}C(O) source strength.

Many estimates of the total global average production rate of ^{14}C for the current geomagnetic field have been made, following different methodologies. Table 8.1 gives an overview of the development. The numbers are for an average shielding potential (due to solar activity) of 300 MV (solar minimum) and 1000 MV (solar maximum). Certain interest in the global average number arises from the needs to reconcile it with global carbon reservoir turnover and size estimates. Considerable uncertainties are apparent, and improved estimates will be required for future studies.

According to the results in chapters 5 and 7, however, assessments of the global average can be "decoupled" from the relative spatial and temporal distribution, i.e., the spatial distribution and seasonality of predicted OH can still be evaluated by ^{14}CO measurements, independent of the uncertainty in the "standard" global average production rate. For this, however, the relative variations of the global source strength of ^{14}C(O), which occur on time scales similar to the lifetime (or response time to the global source strength variation), of the tracer have to be

Reference	Solar Minimum ($\Phi = 300MV$)	Solar Maximum ($\Phi = 1000MV$)
Lingenfelter [1963]	2.61±0.50	2.08±0.4
Lingenfelter and Ramaty [1970]	2.42±0.48	1.93±0.39
O'Brien [1979]	1.76	1.40
Lal [1988]	3.04	1.99
O'Brien et al. [1991]	2.12	1.52
Masarik and Reedy [1995]	2.40 ±20%	1.40 ±20%
Masarik and Beer [1999]	2.41 ±10%	1.57 ±10%

Table 8.1: Global average production rate of ^{14}C in atoms cm^{-2} s^{-1} for solar minimum and solar maximum for the present day magnetic dipole field from different publications. The original value of *Masarik and Reedy* [1995] for Φ=550 MV is extrapolated with the results of *Blinov* [1988]. The values of *O'Brien* [1979] and *Masarik and Reedy* [1995] for solar maximum are linearly extrapolated.

known,i.e., variations in the order of 3 months. The question therefore arises: How can the time dependence of the global source strength of the ^{14}C(O) production rate $c_q(t)$ be parameterized on this time scale as accurately as possible?

If a measurable parameter $x(t)$ of solar activity exists, on which the global average ^{14}CO production rate is linearly dependent, the relative global source strength scaling "standardized" on solar minimum conditions (cf. Eq. (7.1)) can be written as

$$c_q(t) = \frac{q(t)}{q_{smin}} = 1 + (q_r - 1) \cdot \frac{x(t) - x_{smin}}{x_{smax} - x_{smin}} \tag{8.1}$$

where q_r is the ratio of the global average ^{14}CO production rate at solar maximum (index *smax*) to that at solar minimum (index *smin*). To find an appropriate parameter $x(t)$, one has to consider the physical processes that determine the atmospheric GCR flux reaching the top of the atmosphere.

The density of the solar wind plasma changes with solar activity, which results in a variation in the shielding strength against the GCR protons. The denser the solar wind plasma, the more effectively the protons are decelerated and shielded by the geomagnetic field (section 5.2.1). However, the shielding strength is not in phase with the density of the solar wind plasma released in the immediate solar environment, because the plasma first has to reach a certain distance in space to provide an effective shielding. The magnitude of this distance, and therefore the phase shift between solar activity and the GCR shielding, is still under investigation [*Smart and Shea*, 1985, R. Reedy, personal communication, 1999]. But even if this phase shift was fully understood, the question would remain, how to define "solar activity" and the global ^{14}CO production as a function of it.

In order to obtain a valid analysis of ^{14}CO data sets, i.e., the rescaling of the ^{14}CO measurements to "standardized" solar activity conditions, three different approaches to derive the time dependence of the global ^{14}CO source strength scaling $c_q(t)$ are discussed.

8.2 Variables related to solar activity

8.2.1 Neutron monitor count rates

A useful approach for parameterizing the time dependence of the global average ^{14}CO production rate may start with atmospheric neutrons, the direct precursor of cosmogenic ^{14}C(O). Once the GCRs, mostly energetic protons, reach the top of the atmosphere, they immediately initiate nucleonic cascades that branch off into the atmosphere. Neutrons are produced along the cascade within seconds. Thermalization and diffusion processes of the neutrons determine finally the ^{14}CO production rate distribution; the number of neutrons determine the total ^{14}CO source strength.

O'Brien and de P. Burke [1973] established the relationship between the solar modulation potential Φ and the neutron count rates of four neutron monitoring stations by comparing the measurements with the results of their nucleonic transport code. With the same code the global average ^{14}C production rate as a function of Φ was derived earlier [*O'Brien*, 1971]. Figure 8.1 shows the combination of these results, i.e., the global average ^{14}C production rate as a function of the local neutron count rate. A linear correlation is found with $R^2 > 0.98$ for all stations. R^2 is the square of Pearson's correlation coefficient r

$$r(x,y) = \frac{\sum_{k=1}^{N}(x_k - \bar{x}) \cdot (y_k - \bar{y})}{(\sum_{k=1}^{N}(x_k - \bar{x}))^{\frac{1}{2}} \cdot (\sum_{k=1}^{N}(y_k - \bar{y}))^{\frac{1}{2}}} \ , \tag{8.2}$$

where k counts the $N = 8$ pairs of values, and the bar denotes the average.

As a consequence, the neutron count rate n can directly be used as parameter x in Eq. (8.1). Moreover, assuming that the relative amplitude of the global average GCR ^{14}CO production rate due to the solar cycle is the same as that of atmospheric neutrons, the ratio of solar maximum to solar minimum production rate q_r in Eq. (8.1) can also be derived. Solar maximum conditions are then defined by the minimum neutron count rate, and solar minimum conditions by the maximum neutron count rate.

For an assessment of the absolute global scale of the ^{14}CO abundance beyond its relative temporal variability, neutron count rates are, however, not applicable. Atmospheric neutron count rates only give information about the local ^{14}CO production rate, which only partly determines the local atmospheric ^{14}CO mixing ratio (see

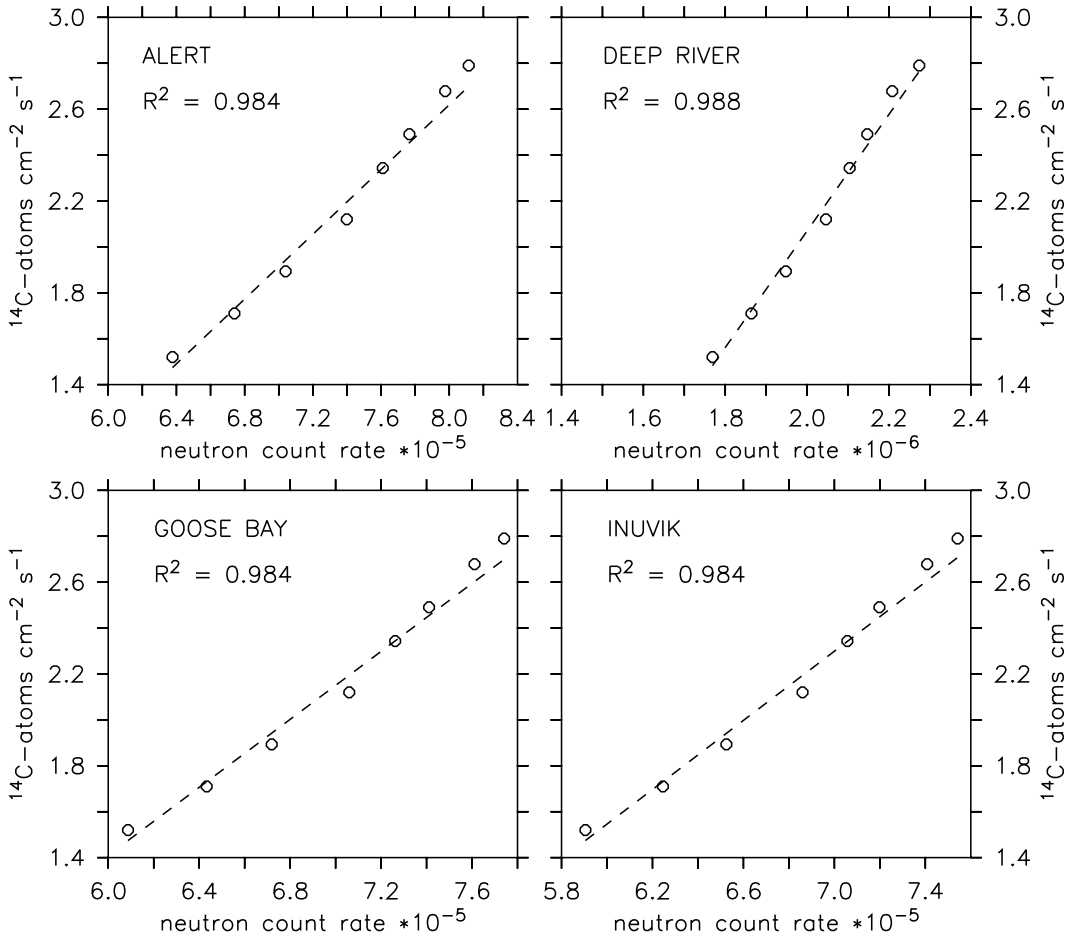

Figure 8.1: Correlation of global average ^{14}CO production rate and neutron monitor count rates derived from *O'Brien* [1971] and *O'Brien and de P. Burke* [1973]. The neutron monitors are located at Alert (82.50^{o}N, 62.33^{o}W), Deep River (46.10^{o}N, 77.50^{o}W), Goose Bay (53.27^{o}N, 60.40^{o}W), and Inuvik (68.35^{o}N, 133.72^{o}W).

chapters 5 and 7). Thus local atmospheric neutron fluxes do not provide a single global parameter for the absolute global ^{14}CO source strength. Furthermore, long term neutron monitor data is available nearly exclusively at ground level, where the lowest ^{14}CO production takes place.

8.2.2 Sunspot numbers

The most popular measure of solar activity is the sunspot number. In 1848 Johann Rudolph Wolf devised a method of estimating solar activity by counting the number of individual spots and groups of spots on the face of the sun for a particular day. His method is basically applied up to the present, i.e., the sunspot number s is

defined as:

$$s = K(10 \cdot G + I) \ , \tag{8.3}$$

where G is the number of sunspot groups visible on the sun, I is the total number of individual spots visible, and K is an instrumental factor to take into account differences between observers and observatories. The sunspot number as an index can be defined on a daily basis but because of the large day-to-day variation is usually averaged over longer periods, the most common being the monthly and the yearly average. The "smoothed sunspot number" (s_s) is defined as the average of 13 monthly sunspot numbers, centered on the month of interest. The 1st and 13th months are given a weight of 0.5, i.e.,

$$s_s(t) = \frac{1}{12} \cdot \sum_{i=t-5}^{t+5} s(i) + \frac{1}{2} \cdot (s(t-6) + s(t+6)) \ , \tag{8.4}$$

where t is the month of interest, and i counts in steps of 1 month.

From its definition, the sunspot number is a single, global, easily measurable observable. A long time series exists. Although the variability in the number of sunspots is "the most obvious manifestation of solar change, it should be noted that sunspots do not directly cause the changes in the solar wind magnetic properties that result in cosmic-ray modulation" [*Stuiver and Quay*, 1980]. The relationship between the modulation potential Φ and s is therefore not necessarily linear and still not known in detail.

Lingenfelter [1963] and *O'Brien* [1979] established an empirical linear relation between the global average ^{14}C production rate and the annual sunspot number, which is also employed for the model simulations in chapter 7, but instead using monthly mean sunspot numbers (Figure 7.3). *Stuiver and Quay* [1980] discussed the applicability of this approach for long term variations of ^{14}C. In those particular applications of calculating the solar cycle average global ^{14}C production, a possible phase shift (of the order of some months) between the change in sunspot number and the change of the ^{14}C production rate (see section 8.1) has not to be considered. For the ^{14}CO methodology, however, shorter time scales are relevant, monthly mean sunspot numbers have to be considered, and therefore this phase shift has to be taken into account.

To estimate the phase shift, the neutron monitor data (monthly averages) that are available from the World Data Center (WDC-C2) are quantitatively compared with the sunspot number. Both the monthly mean and the smoothed sunspot number are considered in order to estimate the influence of short term variations. Only neutron monitor time-series that were measured for at least 100 months under the same experimental conditions are taken into account. For every such neutron monitor the delay time between sunspot number and neutron count rate, which results

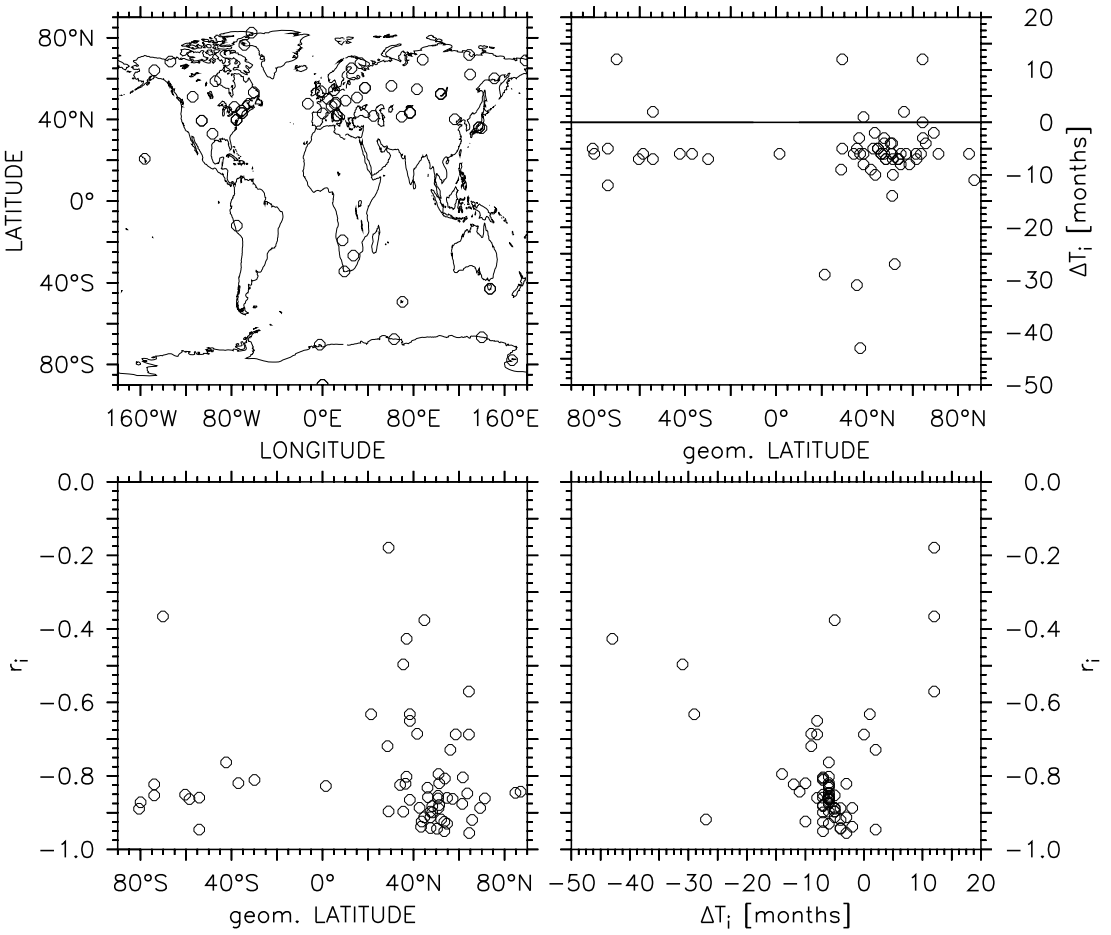

Figure 8.2: Neutron monitor locations (upper left), delay in months between smoothed sunspot number and neutron count rate for optimum (negative) correlation (upper right), correlation coefficient versus geomagnetic latitude (lower left), and correlation coefficient versus delay (lower right). Only neutron monitor data with time series longer than 100 months under the same experimental conditions are taken into account. Geomagnetic latitudes are calculated from the geographic locations with the AACGM algorithm of *Bhavnani and Hein* [1994].

in the optimum (negative) correlation, is calculated by minimizing the (negative) correlation coefficient (Eq. (8.2))

$$r_i(s(t + \Delta T_i), n_i(t)) \rightarrow \text{ min.} \tag{8.5}$$

The index i denotes a particular monitor station, k counts the number N of available monthly average count rates at the particular location, and the bar denotes the average of the considered time interval (Eq. (8.2)). The results are shown in Figure 8.2 (smoothed sunspot number) and Figure 8.3 (monthly mean sunspot number). The time interval ΔT_i between the sunspot number s and the appropriate neutron count rate n at various monitor locations exhibits a large scatter with values from -45

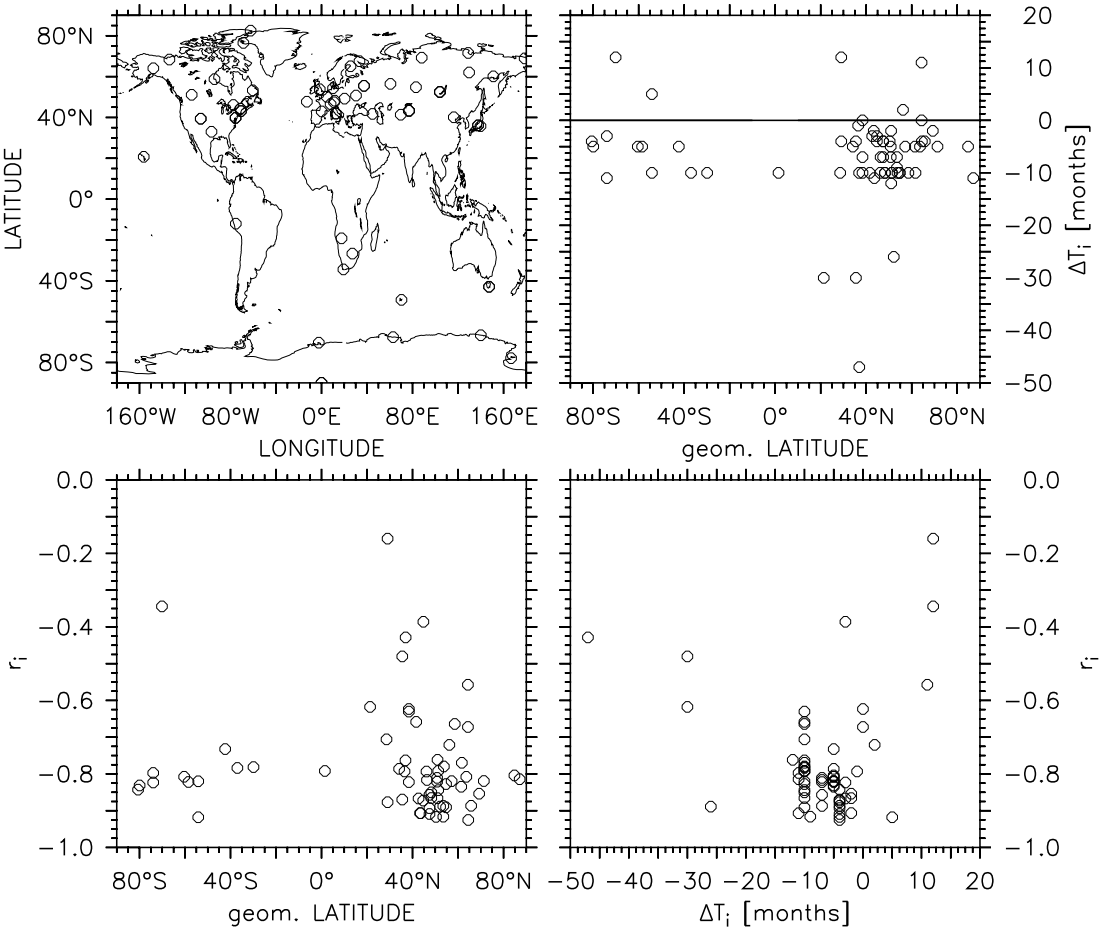

Figure 8.3: Same as Figure 8.2, except calculated with the unsmoothed monthly mean sunspot numbers.

months to +15 months. However, ΔT_i tends to be negative, i.e., variations of the neutron count rate follow after variations of the sunspot number. Beside the large scatter, most ΔT_i values are around -5 to -10 months with a correlation coefficient of -0.75 to -0.95. The results for the monthly mean sunspot numbers do not differ qualitatively from the calculations with the smoothed sunspot numbers. From the individual monitor results an average delay time ΔT is calculated, weighted by the correlation coefficient r_i and the number N_i of available monthly average values of the count rate at each individual monitor:

$$\Delta T = \frac{\sum_{i=1}^{M} \Delta T_i |r_i| N_i}{\sum_{i=1}^{M} |r_i| N_i} \ , \tag{8.6}$$

where M is the total number of neutron monitors that are taken into account. The result is $\Delta T = -6.7$ months for the smoothed sunspot numbers with an average correlation coefficient of $\bar{r} = -0.81$, and $\Delta T = -7.3$ months ($\bar{r} = -0.78$) for the monthly mean sunspot numbers. This delay between solar activity changes and

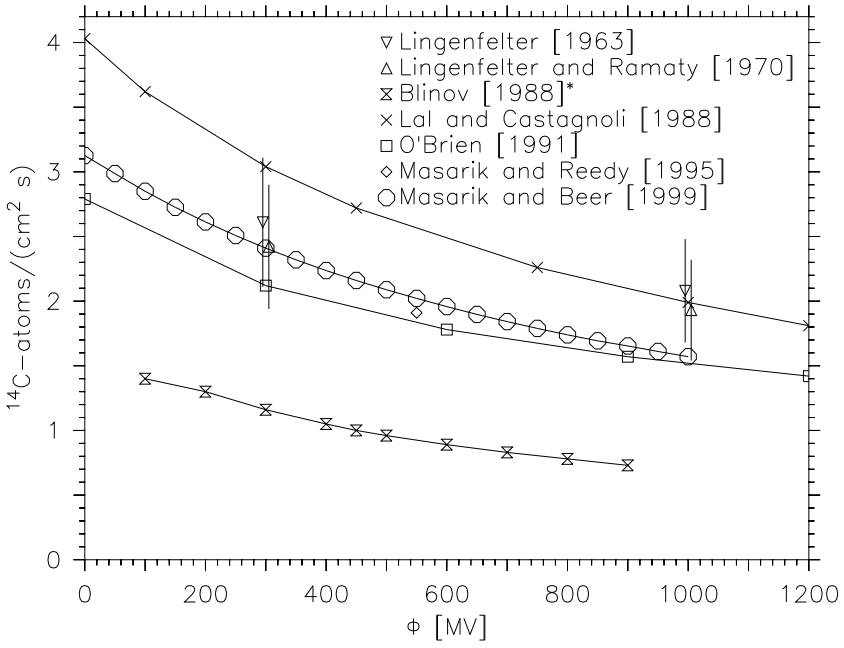

Figure 8.4: Dependence of the global average cosmogenic ^{14}C production rate on the solar activity taken from various publications. Φ denotes the shielding potential (in MV) that increases with increasing solar activity. The results of *Blinov* [1988] are normalized to a global average production rate of 1 atom cm^{-2} s^{-1} for a shielding potential of 450 MV (indicated by the *). Values calculated by *Lingenfelter* [1963] and *Lingenfelter and Ramaty* [1970] are included, assuming a shielding potential of 300 MV for solar minimum and 1000 MV for solar maximum respectively.

its effect on GCR related particle production in the atmosphere is shorter than the estimate of 9 to 12 months given by *Smart and Shea* [1985]; however, due to the high scatter it is still in the same range. Thus the parameterization of the global ^{14}CO source strength (Eq. (8.1)) can be approximately achieved with $x(t) = s(t + \Delta t)$, where s is the sunspot number and Δt is the average time lag of approximately -7 months.

8.2.3 The modulation potential Φ

In calculations of the global cosmogenic ^{14}C source strength [*O'Brien*, 1979; *Blinov*, 1988; *Lal*, 1988; *O'Brien et al.*, 1991; *Masarik and Reedy*, 1995; *Masarik and Beer*, 1999] the Ehmert potential [*Ehmert*, 1959],i.e., the heliospheric potential Φ or a modification of it has been used [*Smart and Shea*, 1985] (see section 5.2.1). Figure 8.4 depicts the relationship between the global average production rate of ^{14}C and the shielding potential Φ. Whereas the estimated absolute global source strength differs considerably between the various publications (see also Table 8.1), the relative variation with Φ is similar in all calculations. According to this, the

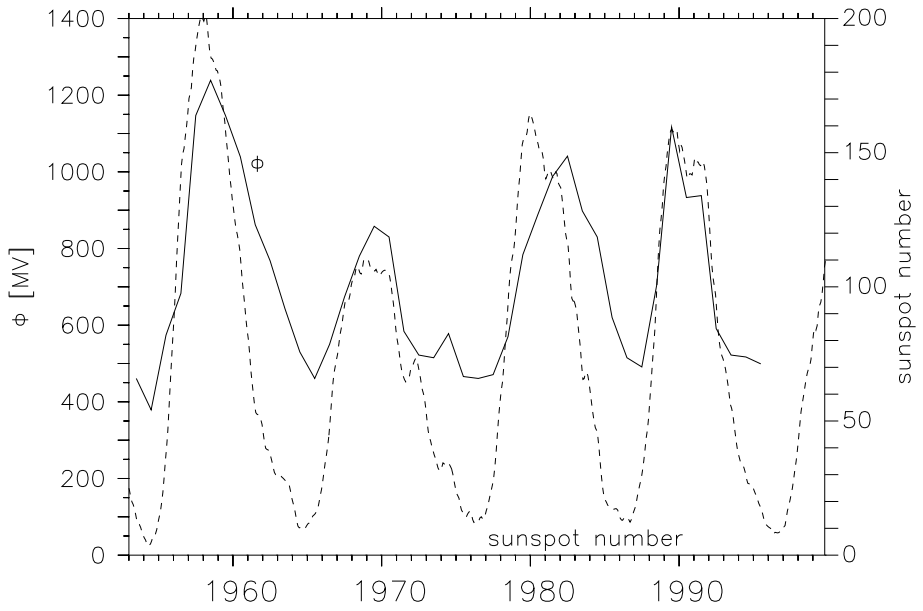

Figure 8.5: Shielding potential Φ calculated by *Masarik and Beer* [1999] (solid line), and smoothed sunspot number (dashed line).

global average production rate of ^{14}C is not linearly dependent on the modulation potential Φ. Furthermore, Φ is not directly measurable but rather a model parameter [e.g., *Smart and Shea*, 1985]. Values of Φ are not generally available on the time scale of 1 month [e.g., *Masarik and Beer*, 1999]. This restricts the direct application of the modulation potential Φ for "rescaling" ^{14}CO measurements and simulations to "standard" solar activity conditions.

However, *Masarik and Beer* [1999] recalculated the global average production rate of ^{14}C as a function of the modulation potential Φ (see Figure 8.4). Additionally, adjusting the potential Φ of the same model, in order to reproduce the measured neutron count rate at Deep River (46.10^{o}N, 77.50^{o}W), *Masarik and Beer* [1999] provided a time series of Φ (annual averages). The resulting Φ is depicted in Figure 8.5 together with the smoothed sunspot number. Combining the calculated modulation potential $\Phi(t)$ of *Masarik and Beer* [1999] with the estimated global average production rate $q(\Phi)$ derived from the same model, directly provides an estimate of the global average ^{14}C production rate as a function of time, in this case annual average values. To obtain the ^{14}C production rate as a function of time on a shorter time scale (1 month), the calculated Φ and the appropriate global average production q are compared with the annual mean sunspot number. The result is shown in Figure 8.6. Again monthly mean sunspot numbers and smoothed sunspot numbers are taken into account separately. An approximate linear relation between the modulation potential and the sunspot number is found. The global average ^{14}C production

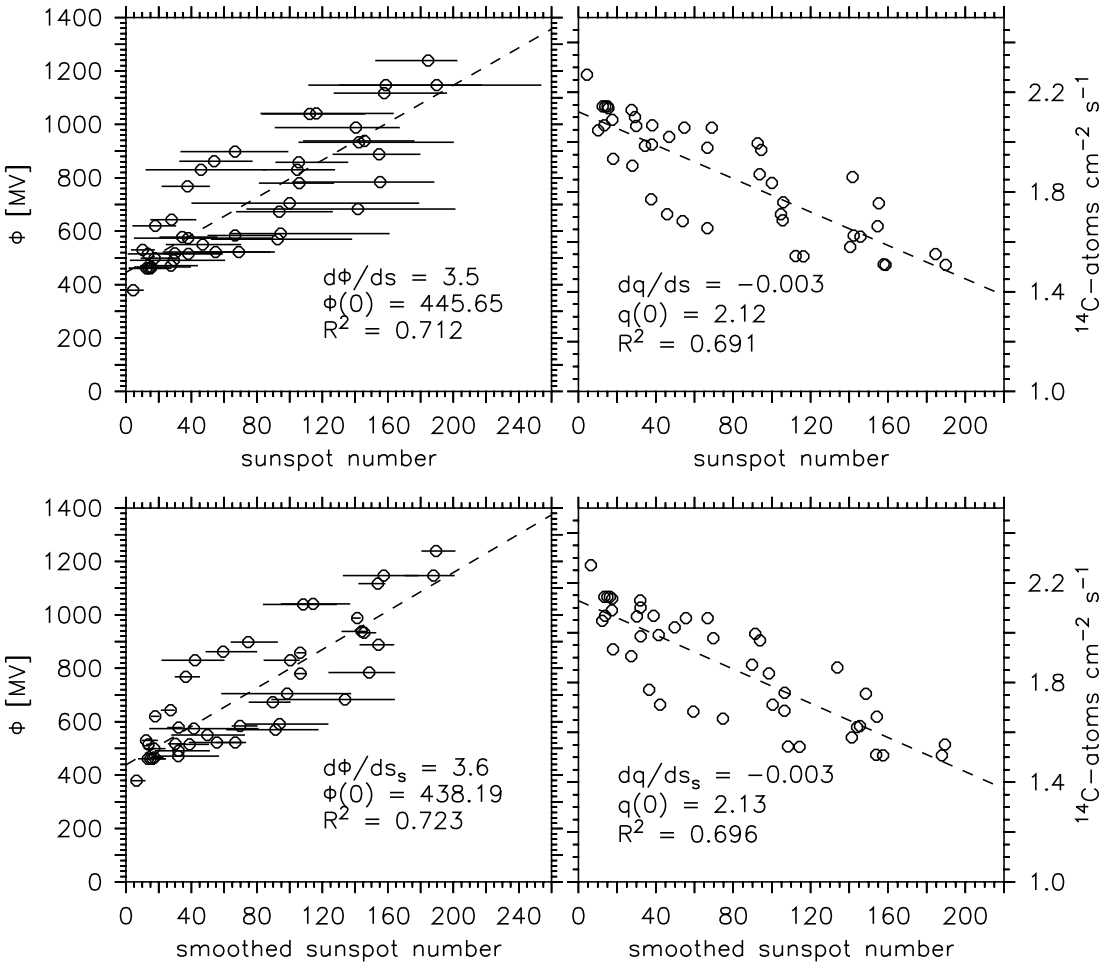

Figure 8.6: Correlation between sunspot number and shielding potential Φ (left column), and correlation between sunspot number and global average ^{14}CO production rate q (right column). $\Phi(t)$ (annual averages) and $q(\Phi)$ are taken from *Masarik and Beer* [1999]. The upper row shows the results calculated with the unsmoothed monthly mean sunspot numbers s, the lower row those calculated with the smoothed sunspot number s_s. The correlation coefficient R^2 is listed together with the parameters of the linear approximation. No time lag between sunspot number and Φ is assumed. The error bars show the range of sunspot numbers around the annual mean of each particular year.

rate [*Masarik and Beer*, 1999] also tends to be linearly correlated to the sunspot numbers. In both cases, the correlation is slightly better when the smoothed sunspot numbers are taken into account instead of the unsmoothed monthly averages.

As described above, *Masarik and Beer* [1999] estimated the modulation potential Φ by reproducing the neutron count rates at Deep River by means of a model. This implies that this calculated potential is valid at the time of the neutron measurements. As discussed above, the sunspot number and the modulation potential appropriate for the Earth's orbit are not necessarily in phase, since the solar wind

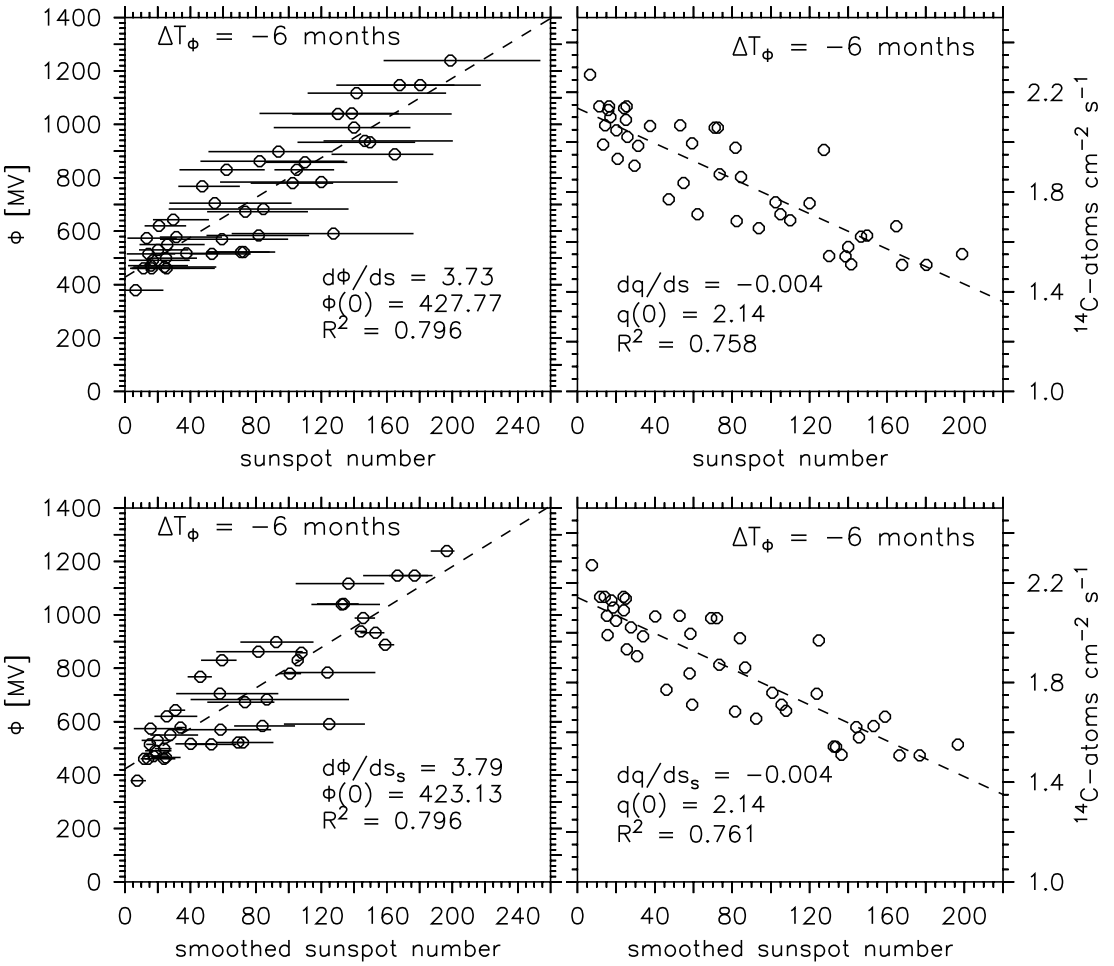

Figure 8.7: Same as Figure 8.6, however a time lag of 6 months between sunspot number and Φ is assumed. For this time lag the squared correlation coefficient R^2 is at its maximum.

plasma has to fill a certain volume in space first. Moreover, the sunspots are not directly responsible for variations of the solar wind plasma density, but rather are only an indication. As a consequence, a possible time lag between sunspot number change and the calculated Φ of *Masarik and Beer* [1999] has to be taken into account. Similar to the direct analysis of the sunspot number to neutron monitor count rate relation (section 8.2.2), the correlation between sunspot number and Φ can be optimized by variation of the assumed time lag. The result is shown in Figure 8.7. The time lag for the maximum correlation between the calculated Φ and the sunspot number is $\Delta T_\Phi = -6$ months, which is close to the time lag of $\Delta T = -7$ months between sunspot number and ^{14}C production rate derived from the neutron monitor count rates in section 8.2.3. Moreover, the time lag of 6 months between Φ and the sunspot number also optimizes the correlation between the sunspot number and the ^{14}C production rate that was calculated by *Masarik and Beer* [1999] consistently

with Φ. Consequently, the two approaches, i.e., the q to s relation (section 8.2.2) and the Φ to q relation (this section) are consistent with respect to the time lag between sunspot number change and its "effect" on the ^{14}C production.

Finally, the linear correlation between Φ and q can be used to interpolate the production rate estimates $q(\Phi(t))$ of *Masarik and Beer* [1999] to monthly average values by means of the monthly mean or smoothed sunspot number.

8.3 Variation of the global source strength of ^{14}C

As motivated in section 8.1, the short term variations (about 1 month) of the global source strength of ^{14}C(O) production are relevant for the ^{14}CO methodology, i.e., for using measurements of atmospheric ^{14}CO to constrain the distribution and seasonality of OH. Earlier estimates (see Table 8.1, Figure 8.4) of the global source strength and its variability with the solar cycle (and the geomagnetic field) focused mainly on an assessment of the global average ^{14}C production rate on much longer time scales than the atmospheric lifetime of ^{14}CO. These estimates are used for radiocarbon dating purposes and global carbon cycle reservoir estimates.

In section 8.2 above, observable or calculable quantities were introduced which are related to the solar activity. These variables can be used to parameterize the solar modulation of the global source strength as indicated in Eq. (8.1) with a time resolution of 1 month.

For an estimate three approximate scaling functions c_q related to the three approaches above are compared:

- The neutron count rate of the monitor at Climax (39.37^{o}N 106.18^{o}W), denoted as n_{clx}, is used as modulation parameter x in Eq. (8.1). The data is obtained from the World Data Center (WDC-C2). Further, the assumption is made that the relative amplitude of the global average ^{14}CO production rate is the same as that of the neutron count rate. This determines the ratio of solar maximum to solar minimum production rate to be $q_r = 0.69$.

- Following the approach of *Lingenfelter* [1963], the absolute global average production rate $q(t)$ is parameterized by linear interpolation using the smoothed sunspot number, modified by including a time lag between global source strength and sunspot number of $\Delta T = -7$ months, i.e., $x(t) = s_s(t + \Delta T)$ in Eq. (8.1). With the average production rate estimates of *Lingenfelter and Ramaty* [1970] (see Table 8.1) $q_r = \frac{q_{smax}}{q_{smin}}$ is calculated to be 0.8. In the analysis of *Lingenfelter* [1963] solar minimum is defined by a sunspot number of

9.1 (= x_{smin} in Eq. (8.1)), and solar maximum by a sunspot number of 187.5 (= x_{smax} in Eq. (8.1)) respectively.

- The result of *Masarik and Beer* [1999] ($q(\Phi(t))$) is interpolated to monthly average values by means of the smoothed sunspot number as described in section 8.2.3. The delay of 6 months between the sunspot number and the calculated modulation potential Φ is taken into account. This results in an absolute global average production rate of $q(t) = 2.14 - 0.0036 \cdot s_s(t + \Delta T_\Phi)$, with $\Delta T_\Phi = -6$ months. The global source strength scaling is then simply defined as $c_q = q(t)$ / 1 molec cm^{-2} s^{-1}. This definition sets the "standard" global source strength to 1 molec cm^{-2} s^{-1}, compared to the two previous approaches, where the "standard" is the solar minimum condition.

The above defined source strength scaling functions c_q are not directly comparable because the "standard" source strength is different in all three cases. Focusing only on the relative time dependence, the scaling functions are further "standardized" on the conditions averaged over the time interval 1955 to 1988 (three solar cycle periods) by

$$c'_q(t) = \frac{c_q(t)}{\frac{1}{L}\sum_{i=1}^{L} c_q(t_i)} \ , \tag{8.7}$$

where $L = 396$ is the number of months. The resulting c'_q are shown in Figure 8.8. The figure also includes the annual averages of the normalized scaling function c'_q based on the source strength estimate ($\Phi(t)$ and $q(\Phi)$) of *Masarik and Beer* [1999].

Although the three approaches presented above are not completely independent, differences are apparent. Especially the two scaling methods involving the sunspot number ($c'_q(\Phi_l(s_s))$ and $c'^{LF}_q(s_s)$) differ considerably at the local extrema. In contrast to that, the Climax neutron monitor count rate based scaling ($c'_q(n_{\mathrm{clx}})$) is very similar to the scaling based on the linear interpolation of *Lingenfelter* [1963] and *Lingenfelter and Ramaty* [1970] using the sunspot number ($c'^{LF}_q(s_s)$). The neutron count rate based scaling exhibits a large short term scatter compared to the other scaling functions, which are already smoother due to the use of the smoothed sunspot number for interpolation. The modulation potential based scaling implying the linear interpolation with sunspot numbers ($c'_q(\Phi_l(s_s))$) underestimates the maxima of the original relation $q(\Phi(t))$ of *Masarik and Beer* [1999]. This is due to the imperfect correlation between sunspot number and modulation potential (see Figure 8.7). Moreover, *Masarik and Beer* [1999] estimated the uncertainty in the calculated source strength $q(\Phi)$ to be $\pm 10\%$. The same uncertainty has to be attributed to the modulation potential Φ itself, because it was constrained by reproducing neutron count rates, whereby the simulated neutron count rates suffer in principle from the same uncertainties as the ^{14}C production rate. Taking these uncertainties into

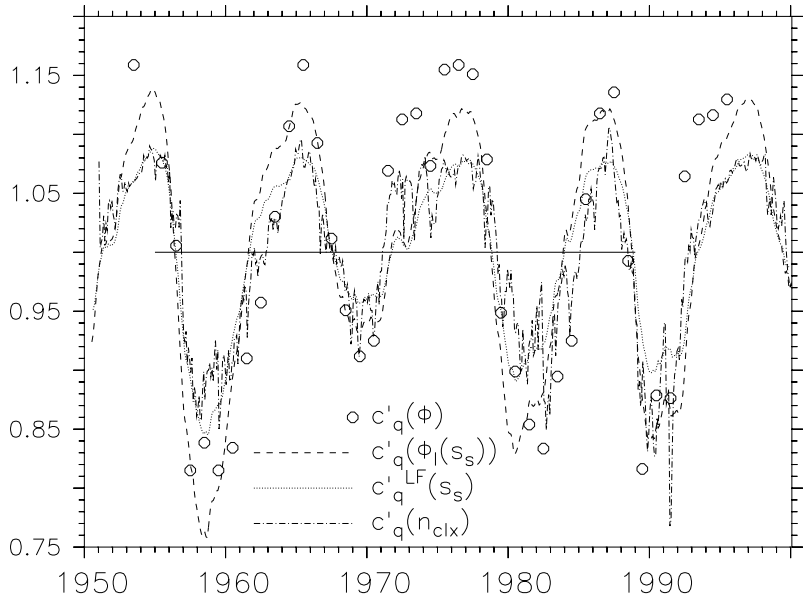

Figure 8.8: ^{14}CO production rate relative to the respective global average production rate during 1955 to 1988. $c'_q(\Phi)$ denotes the scaling based on the results of *Masarik and Beer* [1999]. $c'_q(\Phi_l(s_s))$ includes a linear interpolation of $c'_q(\Phi)$ by means of the smoothed sunspot number to obtain monthly averages. A time lag of 6 months between sunspots and modulation potential is assumed (see Figure 8.7). $c'^{\,\mathrm{LF}}_q(s_s)$ is the scaling function based on the results of *Lingenfelter* [1963] and *Lingenfelter and Ramaty* [1970], i.e., it is a linear interpolation of an absolute production rate estimate. A time lag of 7 months between sunspot number and production rate change is included (see section 8.2.2, Figure 8.2). $c'_q(n_{\mathrm{clx}})$ is the scaling function based on the neutron count rate observed at the Climax neutron monitor station.

account, all three approaches result in a consistent relative ^{14}C source strength scaling function $c'_q(t)$. The remaining differences provide an estimate of the minimum range of uncertainty of the method, and can be used to test the scaling.

8.4 Atmospheric ^{14}CO measurements and the solar cycle

With the estimate of the relative time dependence of the ^{14}C source strength ($c'_q(t)$), and the results of chapter 7 (atmospheric response), the time dependence of the atmospheric ^{14}CO mixing ratio ($c'_\chi(t)$) can be estimated. The uncertainty in the source strength scaling (c'_q) will cause an uncertainty in the resulting mixing ratio scaling (c'_χ). Moreover, the model results for the response time, needed to obtain the mixing ratio scaling from the source scaling (chapter 7), exhibit regional variations and differences between the different model configurations involved. This results in a further uncertainty in the mixing ratio scaling, arising from inaccuracies in the model transport. These uncertainties need to be estimated.

The result will provide a minimum uncertainty range of the rescaling method. The uncertainty may still be larger, because the involved response times are purely model based. Long time series of ^{14}CO measurements to check the results of the response time calculations are not yet available. A possible systematic error can therefore at this stage not be excluded.

In order to address the influence of uncertainties in the source scale and regional differences of the response time, the mixing ratio scaling c'_χ (Eq. 7.5) with $n = 12$ months is calculated from the source strength scaling estimates $c'_q(\Phi_l(s_s))$, $c'^{\,\mathrm{LF}}_q(s_s)$, and $c'_q(n_{\mathrm{clx}})$ (section 8.3). Three different response times are assumed, $\tau = 3.11$ months, which is the estimated global average response time (Table 7.2, 2.0-SPF not considered), $\tau = 2$ months, which is the fastest response predicted for the stratosphere (north pole, 1.2-SLT, see Figure 7.5), and $\tau = 5$ months, which is the response time of the SH high latitude local maximum predicted by the 2.0-SPF configuration (Figure 7.5). The appropriate weights of the current month's production rate scale are 0.163, 0.26, and 0.076 respectively. The result is shown in Figure 8.9.

The uncertainty in the source strength scaling (Figure 8.8) is basically mirrored in the mixing ratio scaling as is to be expected from the relationship between both (Eq. (7.5)). The convolution with the atmospheric response time filter function provides a smoothing which is best apparent in the neutron count rate based scaling (cf. Figures 8.8 and 8.9), where the scatter in the source strength scaling is notably large. Consequently, it is not critical whether monthly mean sunspot numbers or smoothed sunspot numbers are used for the parameterization. The sensitivity of the mixing ratio scaling c'_χ to the response time τ is small compared to the uncertainty arising from the source scaling uncertainty. Furthermore, since the response time is closely related to the atmospheric lifetime on a global scale (cf. chapter 7), a systematic error caused by the modeled response time is unlikely.

8.5 Conclusions

The aim was to assess the influence of variations in solar activity, i.e., the modulation of the primary GCR flux, on the atmospheric mixing ratio of ^{14}CO. This important process has to be considered before ^{14}CO measurements can be applied for tracing changes in OH and/or atmospheric dynamics. In chapter 5 it was shown that the spatial variability of the ^{14}C production rate distribution with the solar cycle plays a minor role for the relative distribution of ^{14}CO in the atmosphere, at least in the troposphere. Only the global source strength has to be considered for a first approximation. The time it takes to adjust the local mixing ratio of atmospheric ^{14}CO to variations in the global source strength was derived and discussed in

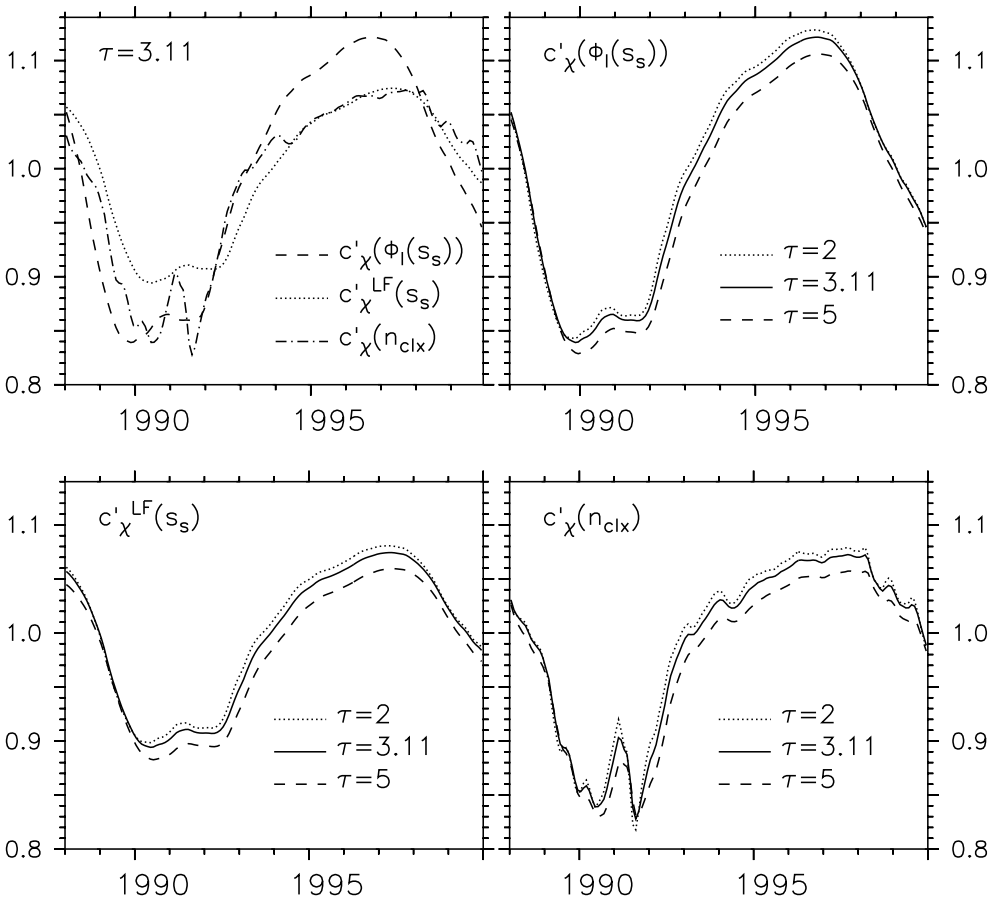

Figure 8.9: Atmospheric ^{14}CO mixing ratio normalized to the respective global average production rate during 1955 to 1988 calculated from various source scaling functions (see Figure 8.8) using different atmospheric response times (τ) of 2, 3.11, and 5 months with the appropriate weights of the current month's production rate scale (w_0) of 0.26, 0.163, and 0.076 respectively.

chapter 7. A functional relationship between the source strength (based on arbitrary standard conditions) and the resulting local mixing ratio of ^{14}CO was established. The uncertainty in the global average OH abundance, which is to be evaluated by ^{14}CO, is directly related to the uncertainty in the global average production rate of ^{14}C(O).

However, based on the previous findings, evaluation of the distribution and seasonality of OH can be "decoupled" from the issue of constraining the global OH abundance / average ^{14}C production rate. Such a ^{14}CO based evaluation of OH distribution and seasonality requires the knowledge of the relative temporal variation of the ^{14}C production rate with a temporal resolution of 1 month.

Quantification of the solar activity with regard to its effect on the global ^{14}C(O) production is, however, not straightforward, since no directly measurable global

parameter exists which describes the effect of the variable solar wind plasma characteristics onto the particle production in the atmosphere with sufficient accuracy. In general two different approaches are followed to resolve this issue. First, the source strength is simply parameterized by means of an observable that is related to solar activity, such as the sunspot number. The linear relationship found earlier [*Lingenfelter*, 1963; *O'Brien*, 1979; *Stuiver and Quay*, 1980] between the global average production rate of ^{14}C and the sunspot number is purely empirical and does not describe the physical processes. The second approach is to derive the required relationship by means of models that start from "first principles", i.e., incorporate all known relevant processes of GCR - solar wind interactions and particle interactions in the atmosphere. The model parameter Φ, i.e., the solar modulation potential, is then determined by reproducing observed GCR induced atmospheric particle fluxes, such as atmospheric neutrons, with the model.

In the analysis above, these two approaches are connected and compared with a third approach that relates the global average ^{14}C(O) production rate directly to the flux of atmospheric neutrons, i.e., the precursor of ^{14}C. This approach is also limited, mainly due to the "local character" of neutron measurements. It further assumes that the modulation of atmospheric neutrons has the same relative amplitude than that of the ^{14}C production rate.

Nevertheless, all three approaches lead to solar cycle dependencies of the global average ^{14}C production rate that are consistent within the uncertainties. Combining the so derived source strength scaling with the response of the atmospheric system (chapter 7) provides a scaling function for separating the solar modulation from measurements and simulations of ^{14}CO. The sensitivity to the local system response is small compared to the uncertainty arising from uncertainties in the timing of the global source strength.

As a consequence, measurements of atmospheric ^{14}CO sampled during different epochs with respect to the solar cycle can still be compared and analyzed for changes in the oxidation capacity and/or the dynamics of the atmosphere. Uncertainties in the rescaling of measurements to "standardized" solar activity conditions are mainly determined by the uncertainty in the time dependence of the source strength. Independent measurements of the global average ^{14}C production rate, especially its time dependence during the solar cycle, could help to minimize this uncertainty.

Further constraining the solar activity dependence of the atmospheric ^{14}CO mixing ratio from atmospheric measurements itself requires a test, i.e., the application of the derived rescaling method to a long time series of measurements. To date, only one dataset of atmospheric ^{14}CO measurements covering a whole solar cycle exists (Martin Manning, Dave Lowe, NIWA, personal communication, 2000). These

data observed at Baring Head, New Zealand, are, however, still unpublished and unfortunately have not been made available for use in this study.

9 Cross tropopause transport of solar proton induced atmospheric ^{14}CO: Modeling and observation of the 1989 proton events

Abstract. Solar proton events (SPEs) induce an additional ^{14}CO production in the high latitude middle stratosphere on timescales of hours to days. The total ^{14}CO produced by major SPEs can amount to the equivalent of several months of galactic cosmic ray (GCR) induced background ^{14}CO. This excess ^{14}CO is partially transported across the tropopause into the troposphere where it temporarily disturbs the background ^{14}CO mixing ratio. Using the 3-dimensional atmospheric model MATCH the SPE induced excess ^{14}CO at the Earth's surface is estimated. The modeled amount of excess ^{14}CO at the surface and the time lag of arrival depend on the numerical advection scheme used, and on the latitude and season. The time lag between the SPE and the maximum excess ^{14}CO at the surface gives valuable information on cross tropopause transport from the lower stratosphere into the troposphere. The model results are compared with ^{14}CO measurements from Baring Head, following SPE induced ^{14}CO production by three major SPEs that occurred in 1989. To extract the SPE signal from the time series, the measurements are first rescaled to comparable solar cycle conditions, to correct for the effect of the solar modulation of the GCR background ^{14}CO production. Three different rescaling techniques are applied. A quantitative agreement between model simulations and measurements exists for one of the two numerical advection schemes used. Additionally, the time lag derived from the measurements is comparable to stratospheric subsidence times which are independently derived from the European Centre for Medium-Range Weather Forecasts (ECMWF) reanalysis data.

9.1 Introduction

As already elucidated in section 5.2.1 the sun is responsible for temporal variations (11 year cycle) of the ^{14}C(O) production rate. Besides modulating the GCR flux, the sun itself occasionally produces low to medium energy protons (up to 10^{10}eV) during solar proton events (SPEs, earlier generically referred to as solar flares) [*Smart and Shea*, 1985]. Earlier it was believed that large SPEs occur mainly during periods of high solar activity, that is, at the same time as the GCR shielding is largest because of the modulation by the solar wind. However, *Feynman et al.* [1990] and *Freier and Webber* [1963] observed that the only periods when large SPEs are very rare are the 2 years on either side of solar minimum. During the other 7 years of a solar cycle, large SPEs have occurred.

The solar protons, once they reach the atmosphere, initiate particle cascades in much the same way as the GCR protons do, leading to atmospheric ^{14}CO formation, and accounting for 6 to 14% of the total ^{14}CO production averaged over a

solar cycle [*Lingenfelter and Ramaty*, 1970]. Whereas the GCR component is more continuous and mainly modulated on a time-scale of about 11 years, besides some short term variations (down to the order of one hour) with lower amplitude, SPEs are sporadic, of short duration (hours to days), irregular, and sometimes very intense. Only the few largest events during a solar cycle contribute significantly to the ^{14}CO production. This implies that during the major events the equivalent of up to several months of background GCR ^{14}CO is produced additionally within a few hours or days [*Lingenfelter and Ramaty*, 1970].

Due to their weaker energy spectrum solar protons on average cannot penetrate as deep into the atmosphere as galactic protons. Additionally, less energetic protons are much more efficiently shielded by the Earth's magnetic field (cf. section 5.2.1). Therefore the solar proton component of the atmospheric ^{14}CO production is much more confined to the polar middle stratosphere, whereas for the GCR background ^{14}CO as much as 36 to 49% of the production takes place in the troposphere (chapter 5), and reaches into the mid-latitudes. However, geomagnetic storms, which accompany major SPEs, can weaken the shielding of the Earth's magnetic field and reduce the cut-off rigidities (i.e. the charge-normalized momentum a particle needs to just be able to reach a certain point within the geomagnetic field) to as little as 20% of the normal cut-off rigidities depending on the geomagnetic latitude [*Lingenfelter and Ramaty*, 1970]. This results in a deeper penetration of the solar protons into the atmosphere and towards lower geomagnetic latitudes. Because of the higher energy of the GCR protons, this modulation, however, only weakly affects the GCR background ^{14}CO production.

SPE protons are the result of shock-wave acceleration [*Gaisser*, 1990] driven by fast coronal mass ejections (CMEs) [*Gosling*, 1997]. These occur often in conjunction with solar flares, i.e., with an increased solar short wave radiation flux. This may possibly affect the chemical composition of the stratosphere [*Crutzen*, 1975; *Heath et al.*, 1977; *Jackman et al.*, 1990], and because of radiative effects, also atmospheric transport. Such effects are not considered in the present study.

In this chapter the SPE induced ^{14}CO component is used as an atmospheric signal to derive information about the polar lower stratospheric transport and the cross tropopause transport from the high latitude middle and lowermost stratosphere into the troposphere. The focus is on three major SPEs that occurred in autumn 1989, for which a time series of atmospheric ^{14}CO measurements at Baring Head, New Zealand is available. These events and their potential impact on the atmospheric ^{14}CO mixing ratio have been mentioned in *Brenninkmeijer et al.* [1992].

First, a modeling study is performed in order to determine the anticipated general features of SPE signals in the atmospheric ^{14}CO mixing ratio at the surface

level. Subsequently, three methods of rescaling atmospheric ^{14}CO measurements to comparable solar cycle conditions are applied to the Baring Head dataset in order to detect the signal of the 1989 SPEs. The rescaling removes the variation in the atmospheric ^{14}CO mixing ratio caused by the solar modulation of the GCR based ^{14}C(O) production (see chapter 8). Finally, the model results and the results derived from the Baring Head dataset are compared with calculations from the European Centre for Medium-Range Weather Forecasts (ECMWF) reanalysis data to provide a third, independent derivation of the lower stratospheric and cross tropopause transport time scale.

9.2 A modeling study

9.2.1 Model setup

The GCR background source distribution of ^{14}C was taken from *Lingenfelter* [1963] for maximum solar activity (minimum ^{14}C production) and transformed from geomagnetic to geographic coordinates by use of the Altitude Adjusted Corrected Geomagnetic Coordinates (AACGM) algorithm of *Bhavnani and Hein* [1994] (Figure 5.3, LF). The source distribution is normalized to a global average ^{14}CO production rate of 1 molecule cm^{-2} s^{-1} in an idealized static atmosphere of constant depth (1033 g cm^{-2}). This normalization allows an independent parameterization of the "real" global average ^{14}CO production rate, which in this case is incorporated into the model (online). The global average GCR background ^{14}CO production rate was calculated with the results of *Lingenfelter* [1963], i.e. linearly interpolated between solar minimum and maximum, using the monthly mean sunspot number as the parameter for solar activity (Eq. (7.4)). For the 4 years from 1987 to 1990 this results in an annual global average ^{14}CO production rate of 2.42, 2.22, 2.06 and 2.10 molecules cm^{-2} s^{-1}. These values are most probably too high (chapter 8) for solar maximum, but this does not affect the results.

The SPE ^{14}CO production distribution parameterization is based on calculations of *Lingenfelter and Flamm* [1964]. In a $q - d$ plane, where q is the logarithm of the ^{14}C production rate in units of atoms g^{-1} s^{-1} and d is the atmospheric depth, the results for a given cut-off rigidity (or geomagnetic latitude) can approximately be represented by an 8 parameter continuous function, defined on 3 depth intervals: 3 parameters are used for a quadratic approximation of q from the top of the atmosphere ($d = 0$) to the depth of maximum production rate at d_{max}:

$$q_I(d) = a_1 + a_2 \cdot d + a_3 \cdot d^2 \text{ for } 0 \leq d \leq d_{max} \ . \tag{9.1}$$

Another 3 parameters in the same manner describe a quadratic approximation of q

	0^o	90^o
$q(0)$	$10^{-4.05}$ molec g^{-1} s^{-1}	$10^{-2.79}$ molec g^{-1} s^{-1}
d_{max}	39 g cm^{-2}	28 g cm^{-2}
$q(d_{max})$	$10^{-3.51}$ molec g^{-1} s^{-1}	$10^{-2.56}$ molec g^{-1} s^{-1}
d_1	140 g cm^{-2}	140 g cm^{-2}
$q(d_1)$	$10^{-4.22}$ molec g^{-1} s^{-1}	$10^{-3.58}$ molec g^{-1} s^{-1}

Table 9.1: Solar proton event induced ^{14}C(O) production rate at 0^o and 90^o geomagnetic latitude calculated by *Lingenfelter and Flamm* [1964] for various depths. $q(0)$ is the production rate at the "top of the atmosphere", d_{max} is the depth of maximum production rate. At depths $> d_1$ the production rate decreases exponentially. The geomagnetic equator is associated with 1000 MV cut-off rigidity, the geomagnetic poles with 0 MV cut-off rigidity respectively.

between d_{max} and d_1:

$$q_{II}(d) = a_4 + a_5 \cdot d + a_6 \cdot d^2 \text{ for } d_{max} \leq d \leq d_1 \ . \tag{9.2}$$

For depths larger than d_1 the logarithm of the production rate q over atmospheric depth d is almost linear, which is described by a linear approximation in the $q - d$-plane with the remaining 2 parameters:

$$q_{III}(d) = a_7 + a_8 \cdot d \text{ for } d_1 \leq d \ . \tag{9.3}$$

$q(0) = a_1$, d_{max}, $q(d_{max})$, d_1, and $q(d_1)$ can directly be taken from the results of *Lingenfelter and Flamm* [1964] and are listed in Table 9.1. In order to achieve a continuous and continuously differentiable approximation the first derivative of the approximation has to vanish in section one and two at d_{max}, where the logarithm of the production rate(q) is at its maximum

$$\frac{dq_I}{dd}(d_{max}) = a_2 + 2 \cdot a_3 \cdot d_{max} = 0 \tag{9.4}$$

$$\frac{dq_{II}}{dd}(d_{max}) = a_5 + 2 \cdot a_6 \cdot d_{max} = 0 \ . \tag{9.5}$$

Further the slope of section two and three at the intersection (i.e. at d_1, where q over d becomes linear) has to be continuous,

$$\frac{dq_{II}}{dd}(d_1) = \frac{qd_{III}}{dd}(d_1) \tag{9.6}$$

$$\Rightarrow \ a_5 + 2 \cdot a_6 \cdot d_1 = a_8 \ . \tag{9.7}$$

With these further requirements the 8 parameters $a_1 \ldots a_8$ are unambiguously defined.

The GCR background ^{14}C(O) production rate distribution in the model implicitly contains the information about the geomagnetic latitudes, because the production field was transformed from geomagnetic to geographic coordinates. For the latitude dependence of the SPE component of the ^{14}CO production the geomagnetic equator is therefore associated at a given longitude with the minimum GCR background production rate at approximately 100 g cm^{-2}. d_{max}, $q(0)$, $q(d_1)$ and $q(d_{max})$ are then linearly varied between the geomagnetic equator and the geomagnetic poles, associating the geomagnetic equator with 1000 MV and the geomagnetic poles with 0 MV cut-off rigidity, based on the results of *Lingenfelter and Flamm* [1964]. This determines the latitude dependent parameters $a_1 \ldots a_8$, that are calculated online.

So far, the parameterization, however, would result in a too high SPE induced ^{14}CO production rate at latitudes below 60^o, which is in contradiction to the results of *Lingenfelter and Flamm* [1964]. Therefore q is multiplied by a modulation function of the form

$$f_Y(x) = (1 + exp(\frac{x - x_c}{r}))^{-1} \tag{9.8}$$

where x varies between 0^o at 90^o geomagnetic latitude and 1 at the geomagnetic equator, x_c is chosen to be 0.4 and r, which is the slope parameter to be 0.03 The resulting distribution of the SPE ^{14}CO production rate component is also normalized to a global average production rate of 1 molecule cm^{-2} s^{-1}, leaving the total SPE ^{14}CO source strength as event-dependent parameter.

It is important to mention that the results of *Lingenfelter and Flamm* [1964] are valid for "medium" SPEs with a characteristic rigidity of 125 MV. The spectrum of the SPE protons can be described as an exponential function of the characteristic rigidity [*Freier and Webber*, 1963; *Lingenfelter and Ramaty*, 1970], i.e.,

$$J(P) = J_0 \cdot exp(-\frac{P}{P_0}) \ , \tag{9.9}$$

where P is the rigidity, P_0 the characteristic rigidity, and J the number spectrum in protons cm^{-2} s^{-1} ster^{-1}. The characteristic rigidity differs for each SPE and has typical values ranging from 50 MV to 325 MV [*Freier and Webber*, 1963; *Lingenfelter and Ramaty*, 1970]. Figure 9.1 shows the zonally averaged ^{14}CO production rate of both the GCR and the SPE component as they appear in the 3-D simulation.

Lingenfelter and Ramaty [1970] calculated the global ^{14}CO production resulting from SPEs as a function of their characteristic rigidity for a normal cut-off rigidity and for a cut-off rigidity reduced by 80% due to geomagnetic storms. They normalized their results to a proton flux of 1 proton cm^{-2} s^{-1} with energy larger than 30 MeV. With these results and the proton fluxes and characteristic rigidities provided by *Sauer et al.* [1990], the global ^{14}CO production during all SPEs that occurred in

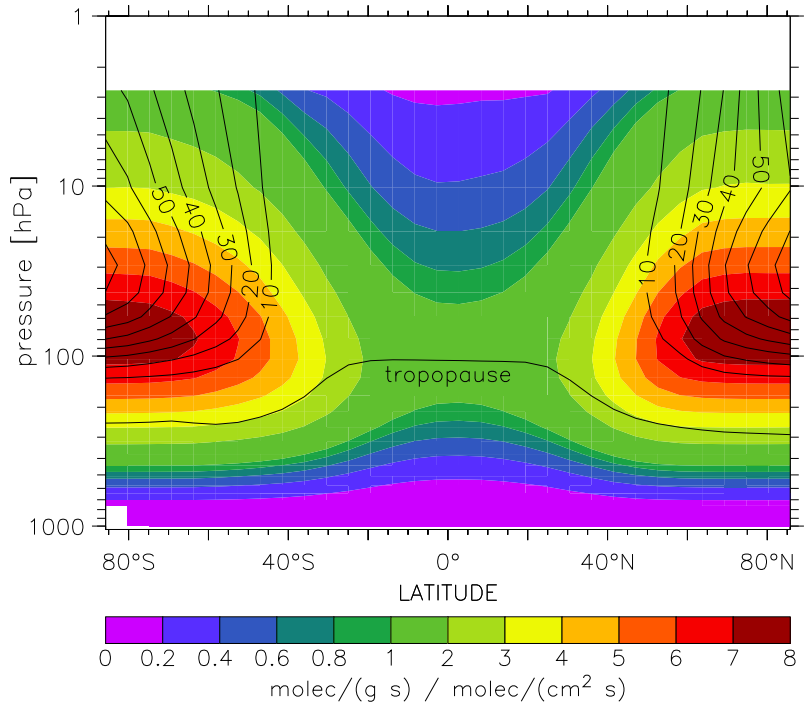

Figure 9.1: Annual zonal mean galactic cosmic ray induced ^{14}CO production rate (GCR, shaded) and annual zonal mean solar proton event induced ^{14}CO production rate (SPE, contour lines). The unit is molec g^{-1} s^{-1} normalized to a global average production rate of 1 molec cm^{-2} s^{-1}. The tropopause is the annual mean tropopause level from the NCEP reanalysis data for 1993.

1989 can be calculated. The results are listed in Table 9.2. The proton fluxes with energy larger than 30 MeV taken from *Sauer et al.* [1990] can also be found in *Shea and Smart* [1992], and are in reasonable agreement with fluxes derived by *Feynman et al.* [1993] from measurements with different instruments.

Only 3 of the 6 events that occurred in 1989 contributed significantly to the global ^{14}CO production. For the remaining events, the additional ^{14}CO production rates are at least one order of magnitude lower than that for the GCR background.

The time dependence of the 3 major SPE fluxes is derived from solar proton measurements of the GOES-7 satellite (geostationary operational environmental satellite No. 7), which are available from the National Geophysical Data Center - Space Physics Interactive Data Resource (NGDC-SPIDR). The total ^{14}CO production of each specific event is distributed on a daily averaged basis according to the flux of protons with energy above 30 MeV. The result is shown in Figure 9.2.

To study the fate of SPE induced atmospheric ^{14}CO, several model calculations are performed. All model simulations presented here are driven by the NCEP-meteorology of the year 1993 [*Kalnay et al.*, 1996]. The OH-1 distribution is pre-

	Date	P_0 [MV]	$I_{>30MeV}$ $[\frac{1}{cm^2}]$	$Q_{100\%}$ $[\frac{molec}{cm^2}]$	$q_{100\%}$ $[\frac{molec}{cm^2 s}]$	$Q_{20\%}$ $[\frac{molec}{cm^2}]$	$q_{20\%}$ $[\frac{molec}{cm^2 s}]$
1	Aug 12 - Sep 07	60.6	$1.53 \cdot 10^9$	$1.027 \cdot 10^6$	0.44	$2.433 \cdot 10^6$	1.04
2	Sep 12 - Sep 23	65.6	$3.37 \cdot 10^6$	$2.541 \cdot 10^3$	$3.68 \cdot 10^{-3}$	$6.133 \cdot 10^3$	$8.87 \cdot 10^{-3}$
3	Sep 29 - Oct 13	102.0	$1.42 \cdot 10^9$	$2.513 \cdot 10^6$	1.94	$6.210 \cdot 10^6$	4.79
4	Oct 19 - Nov 09	77.4	$4.25 \cdot 10^9$	$4.378 \cdot 10^6$	2.30	$1.079 \cdot 10^7$	5.68
5	Nov 15 - Nov 23	112.0	$6.43 \cdot 10^6$	$1.460 \cdot 10^4$	$1.88 \cdot 10^{-2}$	$3.742 \cdot 10^4$	$4.81 \cdot 10^{-2}$
6	Nov 26 - Dec 05	38.6	$1.33 \cdot 10^8$	$4.416 \cdot 10^4$	$5.11 \cdot 10^{-2}$	$1.003 \cdot 10^5$	$1.16 \cdot 10^{-1}$

Table 9.2: The solar proton events in 1989. Characteristic rigidity P_0 and flux $I_{>30MeV}$ of protons with energy greater than 30 MeV are taken from *Sauer et al.* [1990]. The total ^{14}CO production is calculated with the results of *Lingenfelter and Ramaty* [1970] for normal cut-off rigidity ($Q_{100\%}$) and an 80% reduced cut-off rigidity ($Q_{20\%}$). For comparison with the background cosmic ray production rate, the average production rate during the events is calculated for normal cut-off ($q_{100\%}$) and reduced cut-off ($q_{20\%}$).

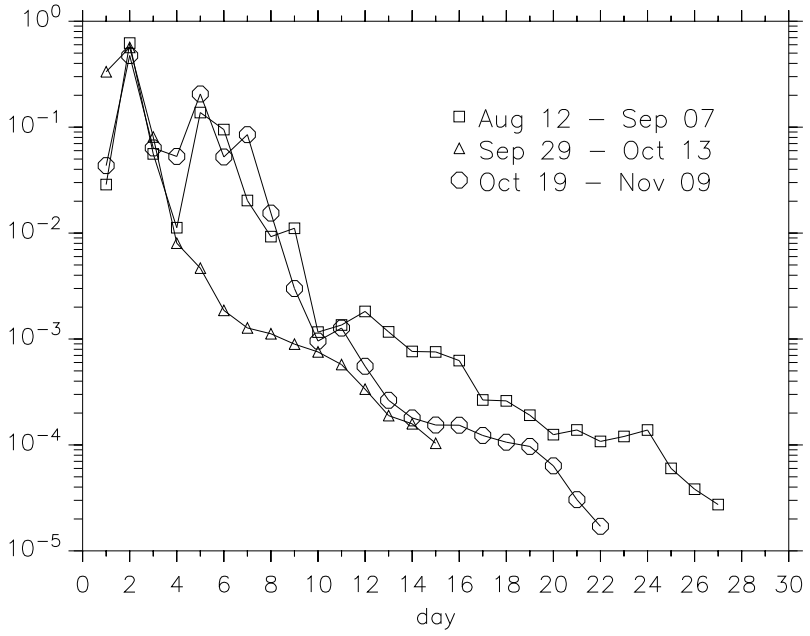

Figure 9.2: Relative distribution of the ^{14}CO production over time of the 3 major SPEs in 1989, based on GOES-7 solar proton flux measurements.

scribed for oxidation of ^{14}CO. The soil sink is parameterized as described in chapter 6. All model results are archived as 5 day averages. The global ^{14}CO background distribution arising only from the GCR source component is calculated by a simulation starting with zero mixing ratio of atmospheric ^{14}CO and integrating over two years (1987-1988). The result is used to initialize all subsequent model calculations.

The subsequent two year period (1989-1990) is first integrated without SPEs to account for the GCR background only. Then the same period (1989-1990) is integrated

including the 3 major SPEs, once for normal cut-off rigidity and next assuming only 20% of the normal cut-off rigidity. Variation of the cut-off rigidity, which in turn changes the total amount of SPE produced ^{14}CO, provides an estimate of the range of excess ^{14}CO expected at the surface level. The distribution of SPE induced ^{14}CO production is kept the same for both cut-off rigidities, although in reality it would probably shift in height as well.

The GCR-only simulation and the simulation including the SPEs (20% cut-off rigidity) are repeated using the OH-2 distribution, however explicitely extending throughout the stratosphere. This provides information about the influence of the oxidizing capacity (and its distribution) of the atmosphere on the SPE induced excess ^{14}CO signal. In a similar way, the GCR-only simulation and the simulation including the SPEs (20% cut-off rigidity) are repeated with the convection switched off in the model, in order to assess the influence of convective mixing in the troposphere.

Furthermore similar simulations (1989-1990) but with the SPEs assuming to have occurred 1/2 year earlier in time (i.e. in NH-spring 1989), still assuming normal cut-off rigidity, are performed in order to elucidate the effect of season, i.e., differences in transport. This is of importance for understanding future SPE ^{14}CO signals, because SPEs can occur in any season.

Each of the simulations described (including the initialization run) is performed with both the 2.0-SLT and the 2.0-SPF configuration. One further simulation with 2.0-SPF is performed in which only the strongest SPE (No. 4 in Table 9.2) is considered. And finally, one simulation with 2.0-SPFR (normal cut-off rigidity, 3 SPEs occurring in NH-autumn, OH-1) is performed to account for the effect of the mass mismatch rescaling.

All model simulations are summarized in Table 9.3.

9.2.2 Model results

The basic model results are depicted in Figure 9.3. Shown is the zonal mean ratio of the ^{14}CO mixing ratio in the lowest model layer simulated with the SPEs included to the respective mixing ratio in the GCR-only simulation. Both configurations (2.0-SLT and 2.0-SPF) predict a significant increase in the ^{14}CO mixing ratio at the surface some months after the SPEs. The latitudinal and temporal distribution of the excess ^{14}CO at the surface level, however, strongly depends on the advection scheme and the season in which the SPEs occur.

As a result of the SPEs, the zonal mean mixing ratio of ^{14}CO at the surface level exceeds the GCR background by up to 22%, for SPEs occurring in NH-autumn with a normal cut-off rigidity. Assuming the 80% reduced cut-off rigidity increases

	nr. of SPEs	season of SPE occurance	cut-off rigidity	OH distribution	
1	0			1,2	initialization
2	0			1,2	GCR background
3	3	NH-autumn	100%	1	1989-SPEs
4	3	NH-autumn	20%	1	range of excess ^{14}CO
5	3	NH-autumn	20%	2	sensitivity to OH distribution
6	3	NH-autumn	20%	1	sensitivity to convection
7	3	NH-spring (assumed)	100%	1	seasonality and interhemispheric difference of atmospheric transport
8	1	NH-autumn	100%	1	contribution of single events

Table 9.3: Summary of model simulations performed to study solar proton events. All model simulations are performed with the 2.0-SLT and the 2.0-SPF configuration, except the last one which is only performed with the 2.0-SPF configuration. Simulations one, two, and three are additionally performed with the 2.0-SPFR configuration (OH-1 only). All simulations are performed with the NCEP-reanalysis data of 1993 [*Kalnay et al.*, 1996].

the maximum to 55% (see Figure 9.7, upper row). The downward transport during NH-winter shows a very clear interhemispheric asymmetry when the 2.0-SPF configurations is used. At this time, the downward transport in the NH is about 2 times stronger than in the southern hemisphere (SH). In the 2.0-SLT configuration this feature is lacking; in fact, there is even a small but pronounced maximum of excess ^{14}CO at high southern latitudes less than two months after the SPE, so that the converse is observed.

The model runs with the SPEs shifted backwards by half a year into NH-spring provide information about the seasonality of the downward transport (Figure 9.3, right column). Now, both model configurations show a stronger downward transport in the SH, however in the 2.0-SLT configuration much more SPE induced ^{14}CO is transported downwards and reaches the surface much earlier. The maximum 2.0-SLT predicted excess is 32% compared to 18% for 2.0-SPF. Furthermore, the maximum excess predicted by the 2.0-SPF configuration is lower for NH-spring SPEs than for NH-autumn SPEs. This is reversed in the 2.0-SLT configuration.

The SPE signal at the surface level calculated with the 2.0-SPF configurations decays slower when the SPEs occur in NH-spring than when they occur in NH-autumn. The 2.0-SLT predicted decay is generally faster. This is consistent with results of the response time of atmospheric ^{14}CO to variations in the source strength (chapter 7). Moreover, the 2.0-SLT predicted decay of the signal is almost independent of the season.

The effect of a single SPE is estimated from the model simulation in which only

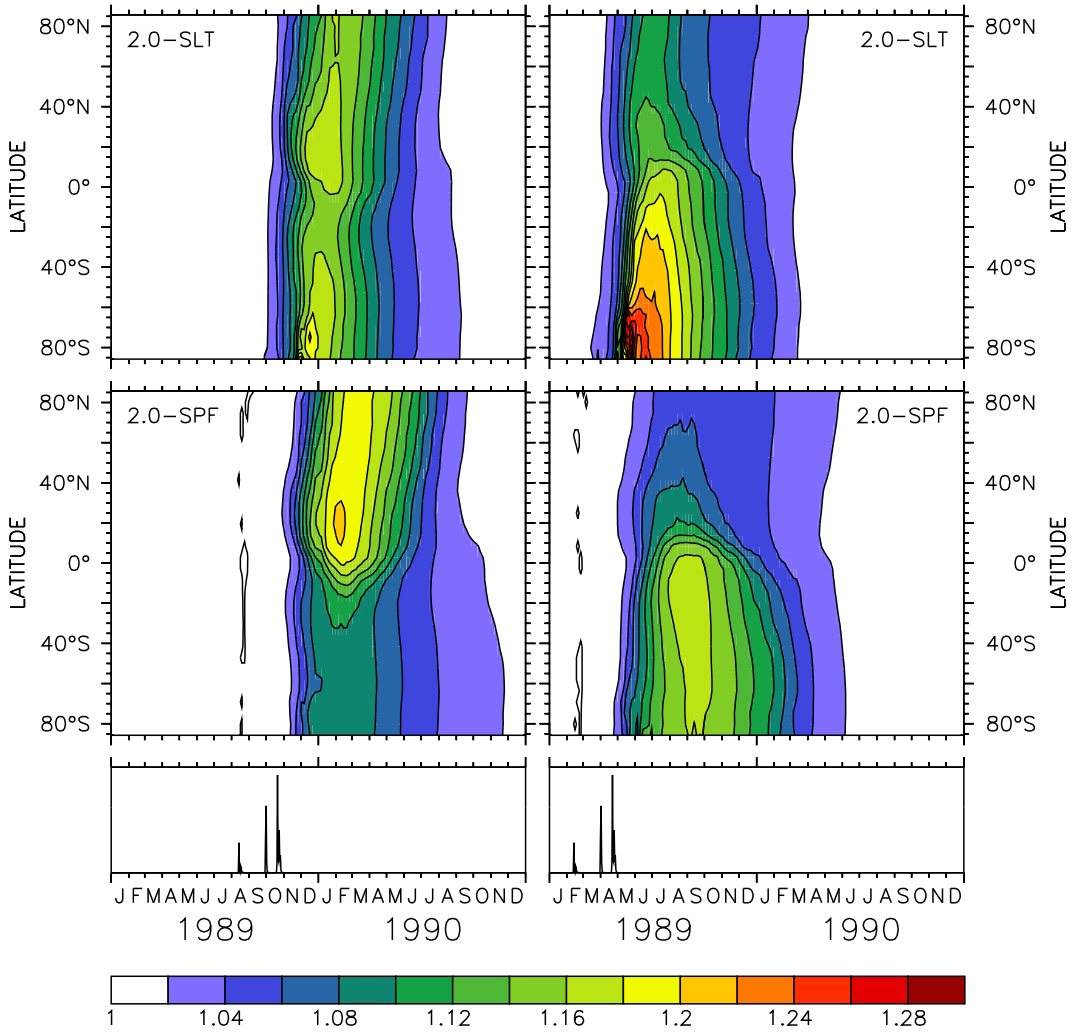

Figure 9.3: Zonal average enhancement of ^{14}CO in the lowest model layer after the 3 SPEs in 1989, calculated with the 2.0-SLT and 2.0-SPF configuration for normal cut-off rigidity. Plotted is the zonal mean ratio of the ^{14}CO mixing ratio calculated including SPEs to the ^{14}CO GCR background. The left column is for the SPEs occurring in autumn (as happened), the right column shows the corresponding results obtained with the three 1989 SPEs shifted half a year earlier in time. The peaks in the lowermost panel show the occurrence of the SPEs. The relative peak heights correspond to the total ^{14}CO production of the respective SPE.

the largest SPE is included (2.0-SPF, normal cut-off rigidity, SPE in NH-autumn). The result (not shown) looks very similar to Figure 9.3. However, the level of excess ^{14}CO after the SPE is only a bit more than one half of the excess with all 3 SPEs included. This corresponds to the fact that somewhat more than half of the total SPE ^{14}CO is produced by this event alone (Table 9.2).

Since the 3 individual SPEs are not distinguishable in the excess ^{14}CO signal induced

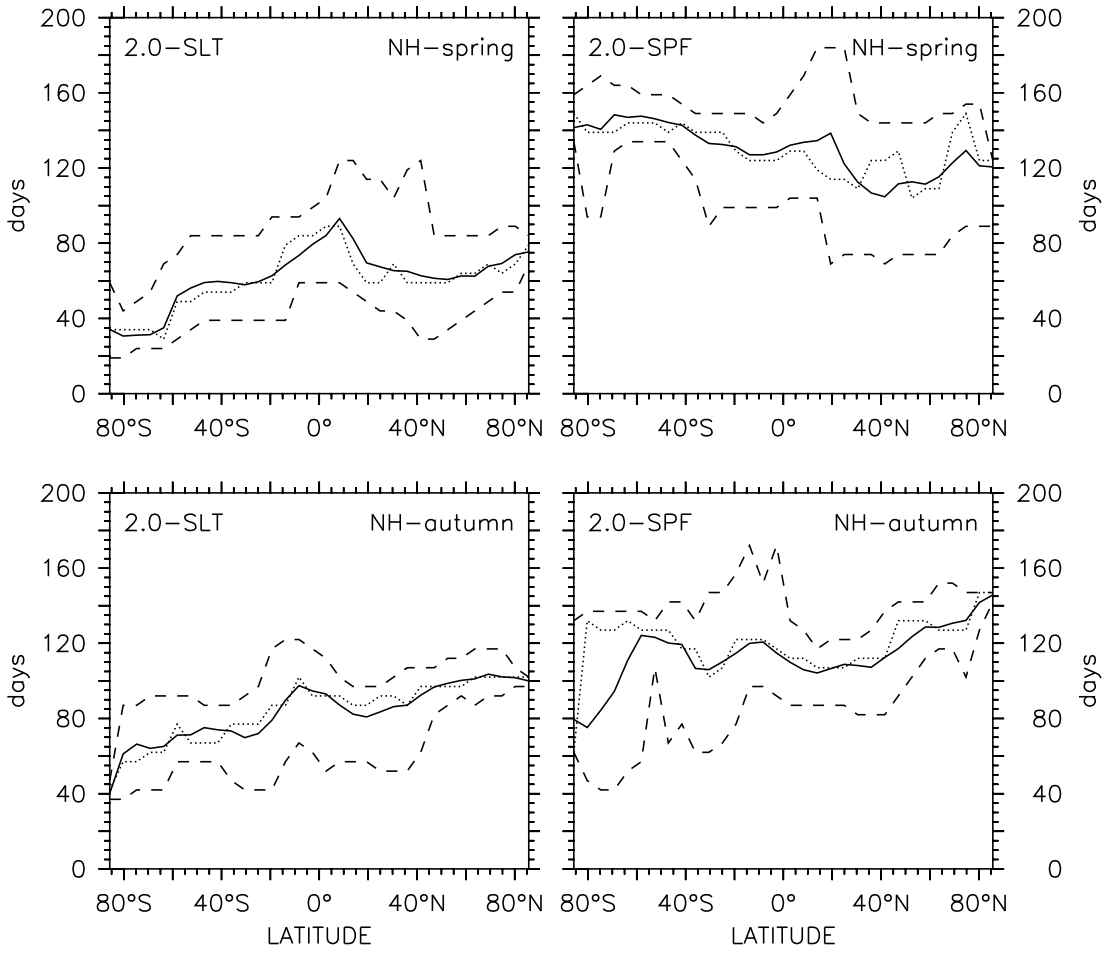

Figure 9.4: Zonal average time lag between the largest SPE and the maximum excess ^{14}CO in the lowest model layer (solid line) calculated with the 2.0-SLT and the 2.0-SPF configuration. The time lag is calculated for SPEs occurring in NH-spring (upper row) and in NH-autumn (lower row) respectively. The dashed lines indicate the maximum and the minimum predicted time lag at a given latitude, the dotted line is the time lag between the largest SPE and the maximum zonal mean excess ^{14}CO (see Figure 9.3).

at the surface level, the transport delay time is defined as the time lag between the maximum production rate of the largest SPE and the maximum increase of ^{14}CO in the model grid box. Zonally averaged results for the lowest model layer, i.e., the downward transport time are shown in Figure 9.4.

In general, the downward transport calculated by 2.0-SLT is faster than predicted by the 2.0-SPF configuration. Whereas in 2.0-SPF the maximum increase of the surface layer ^{14}CO mixing ratio is on average reached between 113 days (in the SH for the NH-autumn SPEs) and 136 days (SH, NH-spring) after the largest SPE, in 2.0-SLT it takes only 60 (SH, NH-spring) to 90 (NH, NH-autumn) days. In both cases the time lag varies with latitude and also shows large longitudinal variations, as indicated by

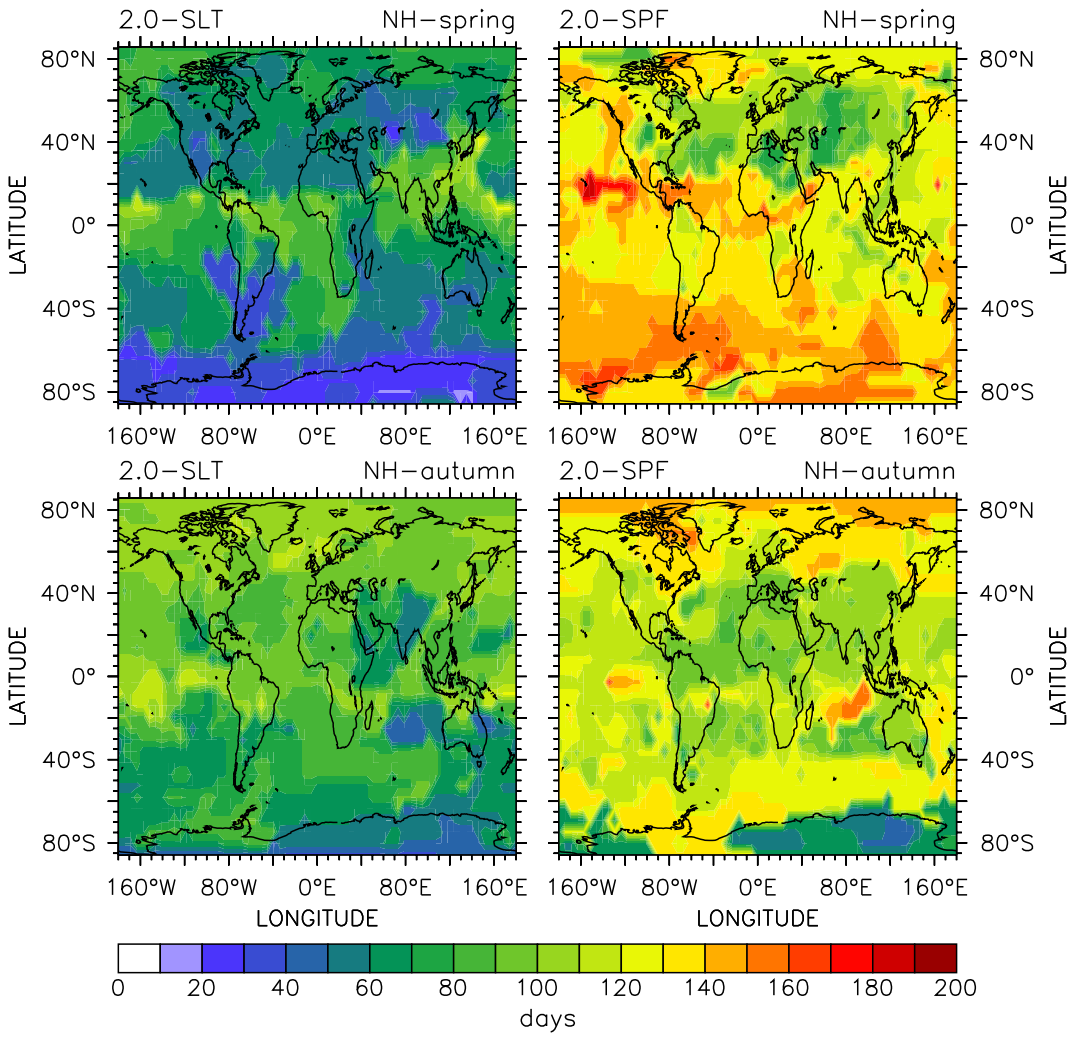

Figure 9.5: Time lag between occurrence of the largest SPE in 1989 and the subsequent maximum ^{14}CO enhancement in the lowest model layer calculated with different model configurations. The time lag was calculated for SPEs occurring in NH-spring (upper row) and in NH-autumn (lower row) respectively.

the maximum and minimum time lag at a given latitude (Figure 9.4). The local time lag between the largest SPE and maximum excess ^{14}CO at the surface is depicted in Figure 9.5. Local deviations of the time lag from the zonal average are clearly visible. Moreover, at a given latitude the deviation from the zonal average depends on the model configuration. For instance, the time lag after the NH-autumn SPEs over the southern Indian ocean is shorter than the zonal average when simulated with 2.0-SLT, while it is longer for the 2.0-SPF simulation. It can be expected that these small scale variations also depend on the meteorology driving the model, and may exhibit inter-annual variations.

Figure 9.6 shows the zonal average time lag between SPEs and the maximum ^{14}CO

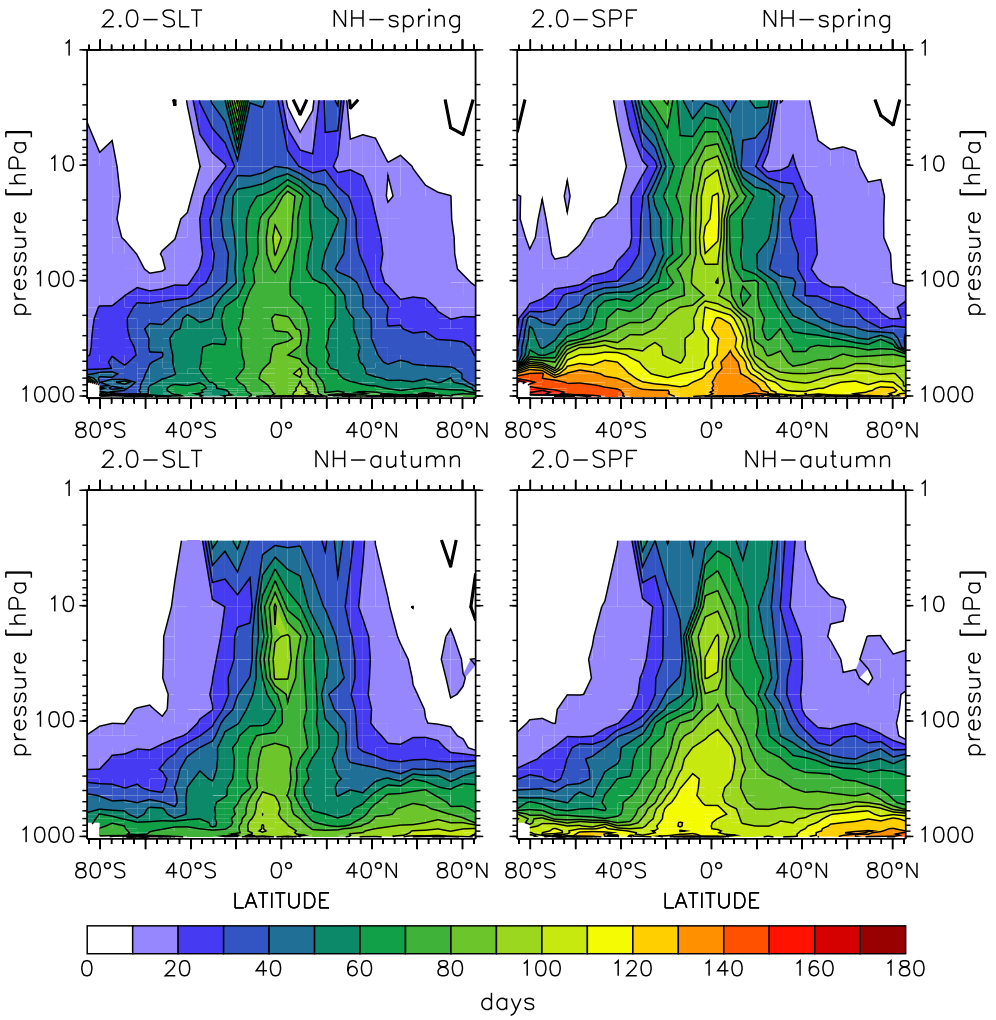

Figure 9.6: Zonal average time lag between occurrence of the largest SPE in 1989 and the subsequent maximum ^{14}CO enhancement calculated with different model configurations. The time lag was calculated for SPEs occurring in NH-spring (upper row) and in NH-autumn (lower row) respectively.

enhancement depending on the pressure level. Overall the time lag is longest in the tropical troposphere, increasing with pressure with one exception. A local maximum of the transport time is visible around 30 hPa in the tropics. The 2.0-SPF predicted time lag is generally longer than the time lag predicted by 2.0-SLT. There is a lower troposphere tropical maximum in the time lag in all of the simulation results, located in the summer hemisphere below 20^o latitude, which seems to follow the inter-tropical convergence zone (ITCZ). The tropospheric time lag exhibits a local minimum at the mid-latitudes, where the STE is expected to be most effective. Obviously, like the response time derived in chapter 7, the time lag is shorter for stronger STE rates. The results in Figure 9.6 then imply that the 2.0-SPF STE

in the SH is weaker than the NH STE, and the 2.0-SLT STE is stronger than the 2.0-SPF STE. This is consistent with the previously obtained indications (chapters 5 and 7).

An overview of the effect of the tropospheric OH distribution and of convection is presented in Figure 9.7. The relative ^{14}CO enhancement is reduced by 0.05 - 0.1, when OH-2 is used instead of OH-1. The 2.0-SLT predicted increase of ^{14}CO at the surface level after SPEs is more affected by the OH distribution than the 2.0-SPF simulations. However, the timing is hardly affected. Furthermore, the convection obviously has only a very small influence on the predicted surface level excess ^{14}CO due to SPEs.

For further quantification of these effects, Figure 9.8 shows the influence of the OH distribution and of convection on the SPE signal at the surface level, defined as the maximum zonal mean excess after SPEs. The upper row shows the change of the maximum predicted zonal average ratio (including SPEs to GCR-only) at the surface level when OH-2 is used instead of OH-1 and when the convection in the model is switched off respectively. Using OH-2 instead of OH-1 with the 2.0-SPF configuration, the maximum zonal mean excess ^{14}CO decreases by 0.03 - 0.04 in both hemispheres. At the surface level, the effect of the OH-2 distribution is somewhat larger on the 2.0-SLT predicted relative excess. In 2.0-SLT the maximum zonal mean excess decreases by 0.06 in the NH and 0.08 in the SH, with a maximum decrease of 0.11 at the south pole. These changes induced by the OH distribution (4%-8%) are a factor of 2.5 to 10 smaller than the maximum relative excess itself (20% to 40%). The effect of convection is smaller than the effect of exchanging the OH distribution. Excluding convective processes from the simulation, the SPE signal at the surface level decreases between 0 and 0.005, except around 20^{o}S, where it increases by up to 0.015.

The influence of OH and convection on the timing of the ^{14}CO excess signal at the surface level after the SPEs is shown in the lower row of Figure 9.8. Using OH-2 instead of OH-1, the time lag between largest SPE and maximum relative increase of ^{14}CO (zonal average) at the surface level increases by 0 - 14 days (7 days on average) in the 2.0-SPF simulation, and by 0 - 12 days (6 days on average) in the 2.0-SLT simulation. Excluding the convective tracer transport from the simulations increases the time lag on average by 1 day in both configurations; however, the changes depend on latitude with a range of -3 days to 6 days.

Finally, the effect of the mass mismatch rescaling correction on the SPE signal at the surface level is shown in Figure 9.9. The maximum relative zonal average excess of ^{14}CO at the surface level after the SPEs is reduced on average by 0.02 in the NH and 0.008 in the SH when the rescaling correction is included. At the same time,

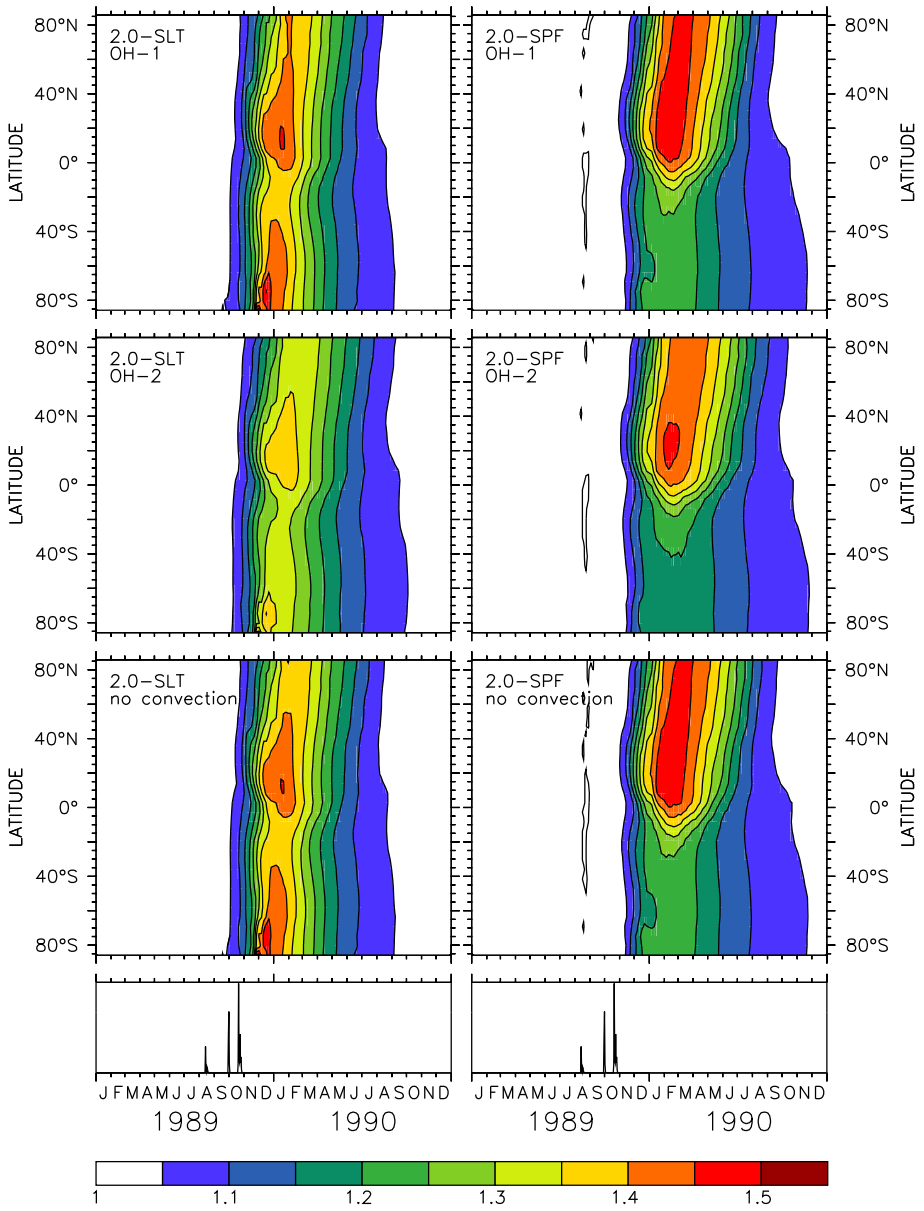

Figure 9.7: Zonal mean enhancement of ^{14}CO in the lowest model layer after the 3 SPEs in 1989, calculated with the 2.0-SLT (left column) and 2.0-SPF configuration (right column) for an 80% reduced cut-off rigidity. Plotted is the zonal mean ratio of the ^{14}CO mixing ratio calculated including SPEs to the ^{14}CO GCR background. Calculations are performed for the SPEs occurring in autumn (as happened). Results in the upper row are calculated with the OH-1 distribution, in the middle row with the OH-2 distribution. In the lower row convection is excluded (OH-1). The peaks in the lowermost panel show the occurrence of the SPEs. The relative peak heights correspond to the total ^{14}CO production of the respective SPE.

the time lag between largest SPE and maximum increase of ^{14}CO at the surface decreases on average by 7 days in the NH, and by 20 days in the SH. The decrease

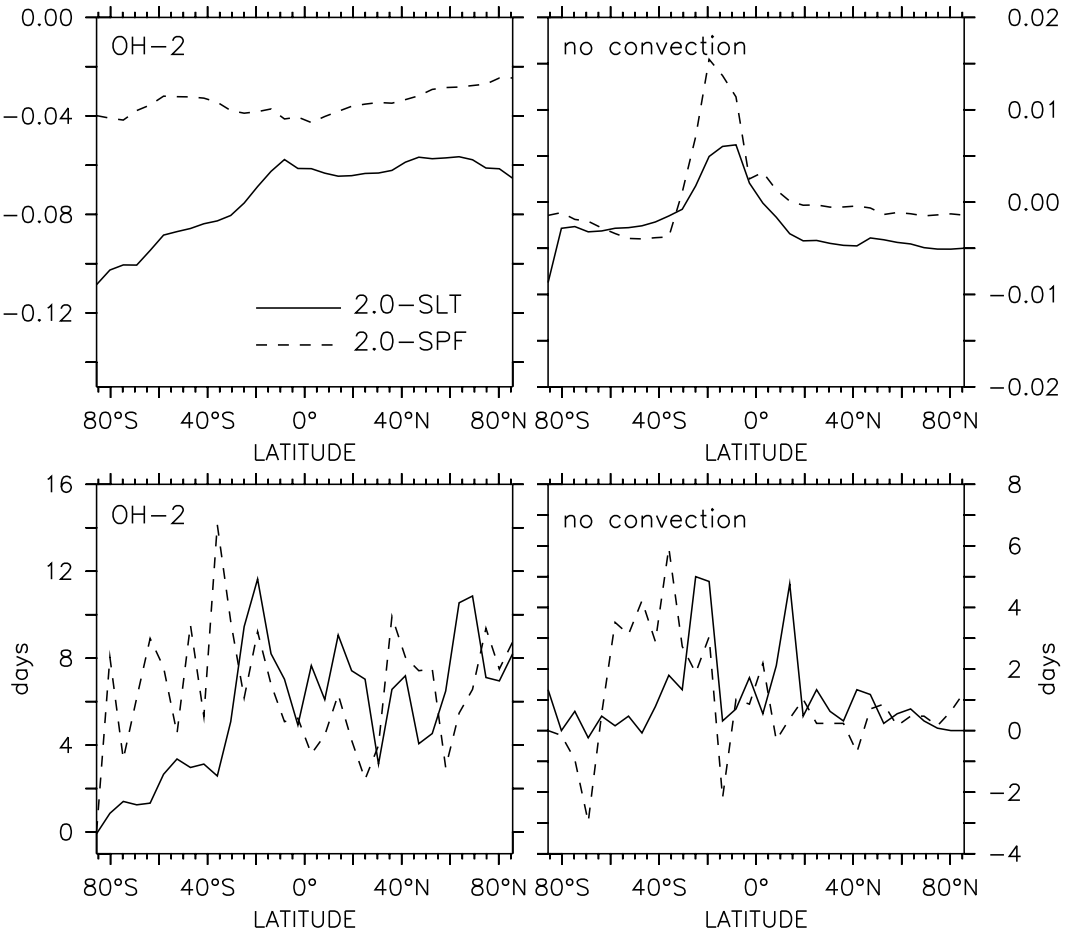

Figure 9.8: Sensitivity of maximum zonal average enhancement (upper) and zonal average time lag between occurrence of the largest SPE in 1989 and the subsequent maximum ^{14}CO enhancement in the lowest model layer (lower) to the OH distribution and convection. The left column shows the changes (differences) of relative excess and time lag for calculations with OH-2 (also in the stratosphere) compared to OH-1, the right column shows the respective changes (differences), when convective processes are excluded from the simulated transport. Calculations are for the SPEs in NH-autumn and 80% reduced cut-off rigidity.

of the time lag in the SH exhibits a peak of almost 40 days between 40^{o}S and 65^{o}S.

9.2.3 Discussion of the model results

The model runs predict a significant increase in tropospheric ^{14}CO after major SPEs. With only one SPE the cross tropopause downward transport time from the high latitude lowermost and middle stratosphere is well defined as the time elapsed between the maximum SPE ^{14}CO production rate and the maximum excess ^{14}CO at the surface. However if several SPEs occur in succession, as appeared in 1989, the situation can be generalized by an equivalent definition using the point in time of

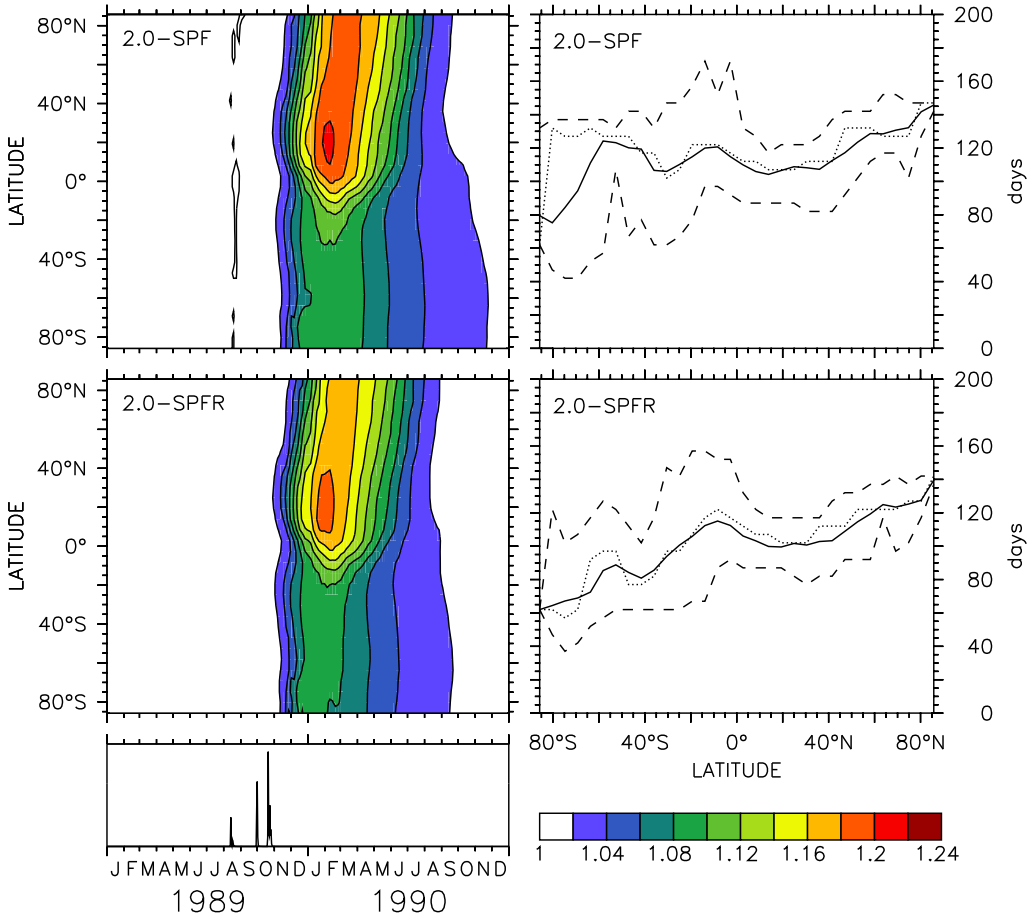

Figure 9.9: Effect of the global mass-mismatch rescaling (2.0-SPFR) on the simulated response to the 1989 SPEs compared to the uncorrected model configuration (2.0-SPF). The left column shows the zonal mean ratio of the ^{14}CO mixing ratio with SPEs versus the ^{14}CO GCR background (cf. Figure 9.3) in the lowest model layer. The right column shows the zonal mean time lag between largest SPE and maximum excess ^{14}CO in the lowest model layer (solid line). The time lag is calculated for SPEs occurring in NH-autumn. The dashed lines indicate the maximum and minimum time lag at a given latitude, the dotted line is the time lag between the largest SPE and the maximum zonal mean excess ^{14}CO (cf. Figure 9.4).

the center of mass with respect to the total ^{14}CO production of all SPEs involved. In case the single SPEs are not distinguishable in the excess ^{14}CO signal, the largest SPE can also be used instead.

The different configurations of the 3-D global atmospheric model predict different time lags between the occurrence of a SPE and the ensuing maximum excess ^{14}CO at the surface. The downward transport time predicted by the 2.0-SLT configuration is 2 to 3 months, and therefore considerably shorter than the 2.0-SPF predicted downward transport time of 4 to 5 months. For both configurations the downward

transport time is dependent on latitude and season. Furthermore the time lag shows large longitudinal variations. The mass mismatch rescaling correction included in the 2.0-SPFR configuration decreases the time lag between largest SPE and the maximum zonal average excess ^{14}CO at the surface level compared to the uncorrected configuration (2.0-SPF). This means that the simulated transport across the tropopause is faster in 2.0-SPFR than in 2.0-SPF.

The issue of the uncertainty in the GCR background ^{14}CO source distribution was discussed in detail in chapter 5. At this stage only relative changes are analyzed, which are less affected by this uncertainty.

The model configurations presented, although driven by the same offline wind data, calculate very different hemispheric and seasonal downward fluxes. The time lag at the surface level predicted by either model configuration, however, is hardly sensitive to the OH distribution used. The global average variation of the downward transport time scale at the surface, even if the OH distribution is changed drastically, is still within the range of uncertainty caused by the 5 day averaging of the model output. This insensitivity is mainly due to the fact that the GCR and the SPE component of the ^{14}CO source are both weighted towards the polar stratosphere and therefore share the same transport path towards the surface. As a consequence, both components are similarly affected by OH.

The sensitivity of the time lag to the convective transport is even smaller and therefore negligible. This implies that the simulated vertical mixing in the troposphere is not of relevance for the downward transport time, but the time scale is rather determined by the simulated large scale advective transport.

The level of the SPE induced excess ^{14}CO at the surface primarily depends on the proton flux and the characteristic rigidity of the respective SPE. Furthermore the cut-off rigidities of the Earth's magnetic field, which are heavily influenced by concurrent geomagnetic storms, are important parameters. All these factors determine the source strength and distribution of the SPE induced ^{14}CO. Because the SPE ^{14}CO source distribution is nearly hemispherically symmetric and located in the stratosphere, atmospheric transport, especially the cross tropopause downward transport from the polar stratosphere plays a key role for the amount and timing of SPE induced excess ^{14}CO that is observed at the surface level. Seasonality and interhemispheric differences in this atmospheric transport determine the surface level signal in the atmospheric ^{14}CO mixing ratio.

The excess signals at the surface level obtained with the different model configurations support the previous conclusions about the simulated STE (chapters 5 and 7). The STE rate predicted by 2.0-SLT is higher than that simulated by 2.0-SPF. The interhemispheric asymmetry of STE is more pronounced in the 2.0-SPF(R)

configuration than in the 2.0-SLT configuration (Figure 9.3 and 9.9). By means of the SPE signals, this differently simulated NH-SH asymmetry of STE becomes further resolved with respect to time. This can be achieved by comparison of the simulated SPE induced excess ^{14}CO signals at the surface level during different seasons. Whereas the 2.0-SPF(R) configuration exhibits a seasonal cycle of the STE in both hemispheres, the 2.0-SLT predicted STE is nearly hemispherically symmetric in spring.

Moreover, the analysis of the SPE produced excess ^{14}CO signal and its timing also provides information on the spatial distribution of STE fluxes on various scales. The zonal average time lag between the SPEs and the maximum ^{14}CO increase indirectly maps the flux of tracer out of the polar middle stratosphere. Imaginary lines perpendicular to the isochrones in Figure 9.6 indicate the direction of this flux. The zonal average excess ^{14}CO signal at the surface level provides an impression of the latitude dependence of the STE (Figure 9.3). And finally, the local time lag at the surface level indicates the role of STE for the ^{14}CO mixing ratio at a given location (Figure 9.5). On increasingly smaller scales, the particular results depend increasingly on the details of the tracer transport realization in the model, and on the underlying meteorology driving the advection.

Model calculations with meteorologies of years other than 1993 might give different results concerning the timing and amount of SPE induced excess ^{14}CO at the surface. From this, inter-annual variations of the large scale polar circulation and/or the stratosphere - troposphere exchange can potentially be derived.

As already mentioned above, the SPE ^{14}CO production rate distribution used was calculated by *Lingenfelter and Flamm* [1964] for a characteristic rigidity of 125 MV. This distribution shows a maximum ^{14}CO production rate at 30 hPa to 40 hPa, dependent on the geomagnetic latitude. With decreasing characteristic rigidity, this production rate maximum shifts to higher levels (lower pressure). The transport time scale in the above analysis is derived by identifying the maximum excess ^{14}CO at the surface level, and is therefore well defined as long as the production rate maximum is located below the upper model boundary, which is at roughly 2 hPa.

Furthermore, as shown by *Reeves et al.* [1992] not only the total proton flux, but also the characteristic rigidity of an SPE changes during the event. This will certainly affect the excess ^{14}CO signal shape. However, since the uncertainties in atmospheric transport of 3-D models are still quite high, it can be expected that such detailed information would be convoluted.

Finally it should not be concealed that current 3-D models appear to have difficulties with the stratospheric transport and the effect of the subtropical barrier [*Douglass et al.*, 1999; *Hall et al.*, 1999]. The models in general overestimate the stratospheric

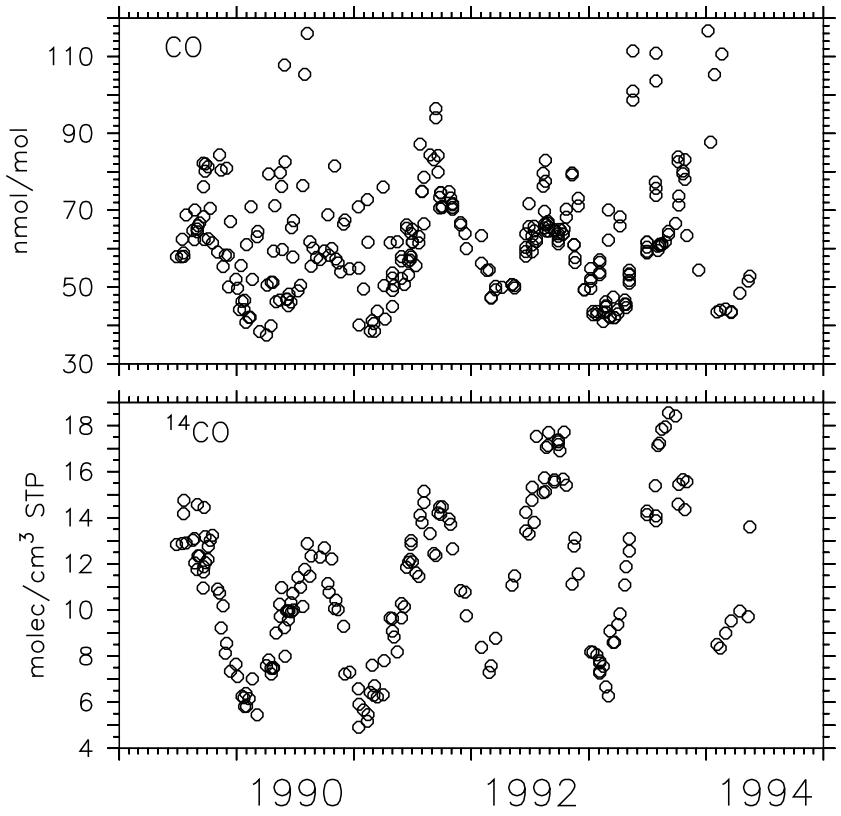

Figure 9.10: CO (upper) and ^{14}CO (lower) measurements at Baring Head (41.4^{o}S, 174.9^{o}E), New Zealand for the years 1989 to 1994 [*Brenninkmeijer et al.*, 1992; *Brenninkmeijer*, 1993, and unpublished results].

quasi horizontal transport across this barrier. In the case of ^{14}CO (GCR + SPE), however, the source is located primarily in the polar stratosphere. The tracer is transported downward at mid-latitudes, and therefore not affected significantly by the subtropical barrier. This implies that the time scales discussed in this analysis only describe the transport from the polar lowermost and middle stratosphere into the troposphere. For this atmospheric transport component, SPE induced ^{14}CO may be a helpful tracer for evaluating different numerical advection schemes in comparison with reality.

9.3 Measurements from Baring Head

At Baring Head (41.4^{o}S, 174.9^{o}E), New Zealand, atmospheric CO and its isotopic composition were measured during the period 1989 to 1994 [*Brenninkmeijer et al.*, 1992; *Brenninkmeijer*, 1993, and unpublished results]. The time series of CO and ^{14}CO are shown in Figure 9.10. The SPEs occurred in autumn 1989, i.e. during the first year of the time series. Therefore the analysis is focused on year one and two

Month	1989/90	1990/91
Oct	12.8 ± 0.45 (4)	11.71 ± 0.90 (4)
Nov	9.83 ± 1.16 (5)	9.95 ± 0.47 (4)
Dec	7.85 ± 0.63 (3)	7.26 ± 0.06 (2)
Jan	6.35 ± 0.48 (4)	5.77 ± 0.69 (4)
Feb	6.33 ± 0.61 (3)	6.16 ± 1.10 (4)

Table 9.4: Monthly mean atmospheric ^{14}CO mixing ratio at Baring Head, New Zealand, for spring to autumn 1989/90 and 1990/1991 in molecules cm^{-3} STP (standard temperature and pressure). Error intervals represent the 1 σ standard deviation, deduced from the measurements. The number of available measurements is given in parentheses.

of the dataset. Both years coincide with the maximum of solar cycle 22.

In Figure 9.10 it is visible that the SH late summer minimum of the atmospheric ^{14}CO mixing ratio of 1989/1990 is somewhat higher than that of 1990/1991. A quantitative comparison in Table 9.4 lists the monthly mean mixing ratios of ^{14}CO derived from the measurements for the SH spring and summer seasons. The uncertainties represent the standard deviation of the available measurements for the given month. Although Table 9.4 shows that the ^{14}CO mixing ratio in Dec/Jan 1989/90 was slightly higher than in Dec/Jan 1990/91, this result is hardly significant if the standard deviation is considered. Therefore a more accurate analysis is explored below.

Analyzing this dataset specifically for SPE signals requires taking into account all other processes that affect the local atmospheric ^{14}CO mixing ratio. A complication to be addressed first is that the measured atmospheric ^{14}CO not only contains the ^{14}CO of direct cosmogenic origin, as treated in the model, but also a smaller fraction of ^{14}CO from ^{14}C recycled through the biosphere. This "biogenic" ^{14}CO consists mainly of ^{14}CO contained in CO from biomass burning, and in CO from oxidation of methane and other natural volatile organic compounds. Every nmol mol^{-1} of atmospheric CO of biogenic origin contains about 0.038 ^{14}CO-molecules per cm^3 of air at standard temperature and pressure (STP) *Brenninkmeijer* [1993]. To subtract the biogenic ^{14}CO component from the measured values, one needs to know the fraction of CO that is of biogenic origin. Background CO at southern mid-latitudes, here measured at the remote station Baring Head, is 90 to 95% biogenic, as little CO is imported from the NH [*Manning et al.*, 1997] and even this small fraction from the NH contains mainly biogenic CO. Assuming that the background CO defined by the lower envelope (clear air, non polluted conditions at Baring Head) is 100% biogenic, then 1.52 ^{14}CO molecules cm^{-3} STP are estimated to be of biogenic origin in SH-autumn, when the CO mixing ratio is at its minimum (about 40 nmol mol^{-1}) and 2.47 molecules cm^{-3} STP of biogenic origin in SH-spring, when the background CO

mixing ratio reaches its maximum (about 65 nmol mol^{-1}). As a result the fraction of biogenic ^{14}CO fluctuates only between 18% and 25% throughout the year. The non-background values at Baring Head include excess CO from fossil fuel combustion which is free of ^{14}CO. Consequently, for comparing subsequent years the biogenic fraction of ^{14}CO can be neglected, provided that the background CO mixing ratio is nearly the same in the two years. In Feb/Mar/Apr 1991 the background CO mixing ratio at Baring Head was even slightly larger than in Feb/Mar/Apr 1990 (Figure 9.10). If this small surplus of CO was of biogenic origin, the ^{14}CO mixing ratio at the same time would also have a larger fraction of biogenic ^{14}CO, which would reduce the cosmogenic fraction of the ^{14}CO mixing ratio in Feb/Mar/Apr 1991 even further. Thus, neglecting the biogenic fraction means that the role of SPE induced excess ^{14}CO will likely be underestimated.

9.3.1 Analysis of the Baring Head dataset

For quantifying the inter-annual changes, the ^{14}CO measurements are smoothed with a low pass convolution filter of the form

$$f(t) = N \cdot exp(-(\frac{t}{\Delta T_F})^2) \tag{9.10}$$

in the frequency domain (by Fourier transformation) after linear interpolation of the data to daily values. N is a convenient normalization constant, t is time and ΔT_f the time window of the low pass filter. To critically assess the influence of the frequency domain, 3 cases with a time window width ΔT_f of 4 weeks, 2 weeks and 1 week respectively are considered.

The data are further normalized to equal conditions with respect to the solar activity, using the results from chapters 5, 7, and 8. Three approaches are applied to determine the relative modulation of the global source strength, similar to those discussed in chapter 8:

- The solar modulation potential Φ calculated by *Masarik and Beer* [1999] is used as modulation parameter for the source strength (interpolated as discussed in chapter 8). However, the normalization to average standard conditions is omitted. This results in an absolute source strength of

  $$q(t) = 2.14143 - 0.00359 \cdot s(t + \Delta T_\Phi) \tag{9.11}$$

  where $s(t)$ is the monthly mean sunspot number and $\Delta T_\Phi = -6$ months. The source scaling is simply $c_q^{(\Phi)} = q(t)$ / (molec cm^{-2} s^{-1}). The resulting normalization is then to a global average production rate of 1 molec cm^{-2} s^{-1}.

- Following the approach of *Lingenfelter* [1963], the monthly mean sunspot number is used as modulation parameter in Eq. (8.1), i.e. $x(t) = s(t + \Delta T)$ with $\Delta T = -7$ months. The ratio between solar maximum and solar minimum is estimated to be $q_r = 0.7$. The sunspot numbers at solar minimum and solar maximum are according to *Lingenfelter* [1963] $x_{smin} = s_{smin} = 9.1$ and $x_{smax} = s_{smax} = 187.4$ respectively.

- The neutron count rate (monthly averages) of the Mt. Wellington neutron monitor (42.92^{o}S, 147.25^{o}E, Tasmania, the closest one available to Baring Head) are used as modulation parameter in Eq. (8.1), i.e., $x(t) = n(t)$. The neutron data were obtained from the World Data Center (WDC-C2). It is further assumed that the relative amplitude of the neutron count rate and the ^{14}C(O) production rate during a solar cycle is the same. The resulting ratio of the ^{14}C(O) production rate between solar maximum and solar minimum calculated from the neutron count rates is then $q_r = 0.69$.

To obtain the rescaling function $c'_\chi(t)$ for the atmospheric ^{14}CO mixing ratio due to the solar cycle, the time dependence of the global ^{14}CO source strength $c_q(t)$ is convoluted with the atmospheric response filter (chapter 7) for each of the 3 approaches. The SH tropospheric response time is estimated to $\tau = 3.5$ months (average of all predictions, Table 7.2), and the appropriate weight of the current month's production rate scale to $w_0 = 0.14$. The uncertainty in the atmospheric response time hardly affects the results, since the time window used for smoothing is 4 weeks or less, which is at least a factor of 3 smaller than the atmospheric response time. The resulting rescaling functions ${c'_\chi}^{-1}(t)$ (cf. Eq. (7.2)) are presented in Figure 9.11. The long term series of the rescaling factor ${c'_\chi}^{-1}$ (Figure 9.11, left) exhibits large variations between subsequent solar cycles. Compared to these variations, the variations within the time interval of the observations (Figure 9.11, right) are small. In particular during the years of interest, i.e., in 1989 and 1990, the slope of the scaling function is flat. For comparison, also the "raw" scaling functions, not taking into account the atmospheric response time, i.e., $c'_\chi(t) = c_q(t)$ (formally obtained with the filter $w_0 = 1$) are included. The "memory-effect" of the atmosphere, i.e., the delayed response of the ^{14}CO mixing ratio to variations in the global source strength, results primarily in a smoothing of the scaling function. Finally, the different "standard" for the chosen normalizations is clearly visible in Figure 9.11. Whereas the rescaling based on sunspot number or neutron count rate provides only a relative normalization to solar minimum conditions, the modulation potential based rescaling performs an absolute normalization to a global average production rate of 1 molec cm^{-2} s^{-1}.

The impact of the 3 different data rescaling processes on the time series of measure-

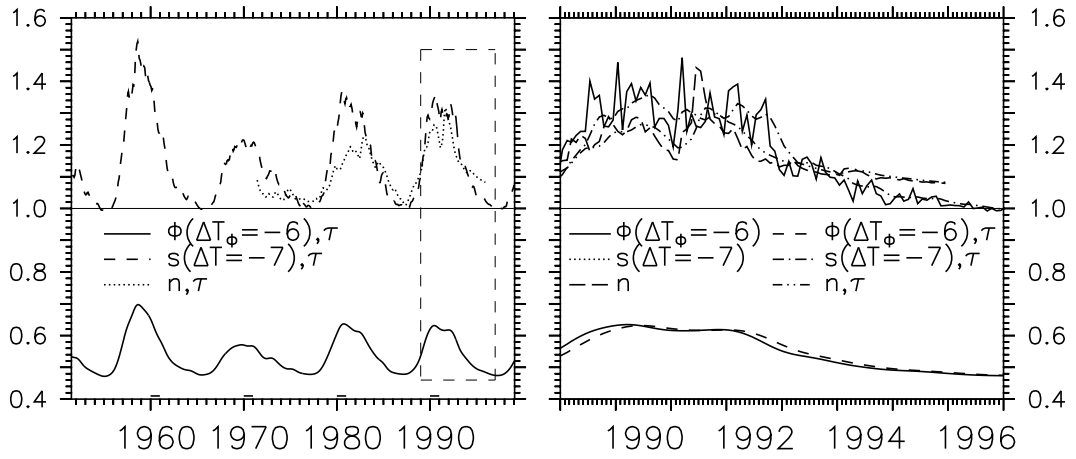

Figure 9.11: Scaling functions $c'_\chi{}^{-1}$ for normalizing ^{14}CO measurements due to the solar cycle. The left side shows the long term scaling factors based on the calculated modulation potential (Φ) of *Masarik and Beer* [1999], on the monthly mean sunspot number (s), and on the Mt. Wellington neutron monitor count rate (n) respectively. c'_χ is calculated from the respective source strength scaling by convolution with the atmospheric response filter (indicated by τ, see chapter 7), with $\tau = 3.5$ months and $w_0 = 0.14$. The dashed box indicates the time interval that is used for rescaling the Baring Head time series. This is shown enlarged on the right-hand side. Here also the scaling functions that do not consider the atmospheric response (i.e., $w_0 = 1$, denoted without τ) are included. The sunspot number based rescaling function implies a time lag of $\Delta T = -7$ months, the shielding potential based function a time lag of $\Delta T_\Phi = -6$ months.

ments and the unscaled data are shown in Figure 9.12 for a 4, 2 and 1 week time window of the smoothing convolution filter (Eq. (9.10)). If there were no inter-annual variations in atmospheric transport and in the OH concentration, the rescaled local ^{14}CO extrema (minimum in autumn, maximum in spring) would have the same value each year. In other words, under the assumption that the rescaling is perfect, i.e., that it indeed removes any variation due to the GCR ^{14}CO source strength modulation from the data, the remaining trends and inter-annual differences have to be caused by other effects (i.e., sinks, transport processes, or SPEs).

The rescaling is applied to the 5 year period of the dataset. However in the following, the focus is only on the first two years of the dataset, which are relevant for detecting the SPEs of 1989. For those two years, the maximum and likewise the minimum ^{14}CO mixing ratios are indeed on the same level respectively, after the rescaling is applied (Figure 9.12).

Shown in Figure 9.13 is the ratio of the rescaled ^{14}CO mixing ratio at time t versus the respective mixing ratio exactly one year later, again for the 3 rescaling methods plus the unscaled smoothed data and the 3 time windows used for data smoothing. This gives direct information about the inter-annual variation of the ^{14}CO mixing

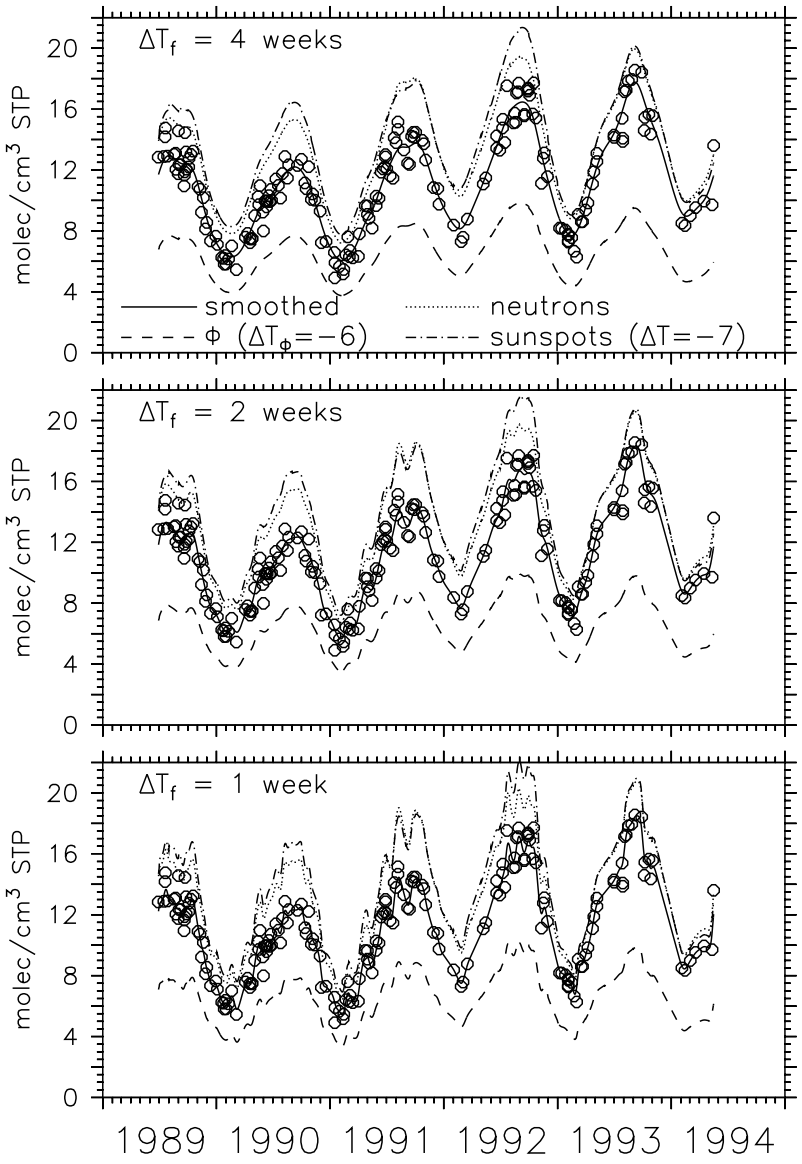

Figure 9.12: Results of the different ^{14}CO rescaling methods used to compensate for the solar cycle for the smoothed data obtained with a time window of the convolution filter ΔT_f (Eq. (9.10)) of 4 weeks (upper), 2 weeks (middle) and 1 week (lower).

ratio. The first observation is that the rescaling has a small effect on the overall shape and that the characteristic fluctuations are retained (Figure 9.13, upper). The reason for this rescaling to be moderate is that the solar activity is at its maximum in 1989/90; the global average ^{14}CO production rate did not change much between these years. For all rescaling methods applied, four local maxima can be identified (Figure 9.13, upper). The first and the second maximum can immediately be explained. At the beginning of the ^{14}CO time series, the scatter is high, which leads to a "double-maximum" in the smoothed curve (cf. Figure 9.12, upper) in the

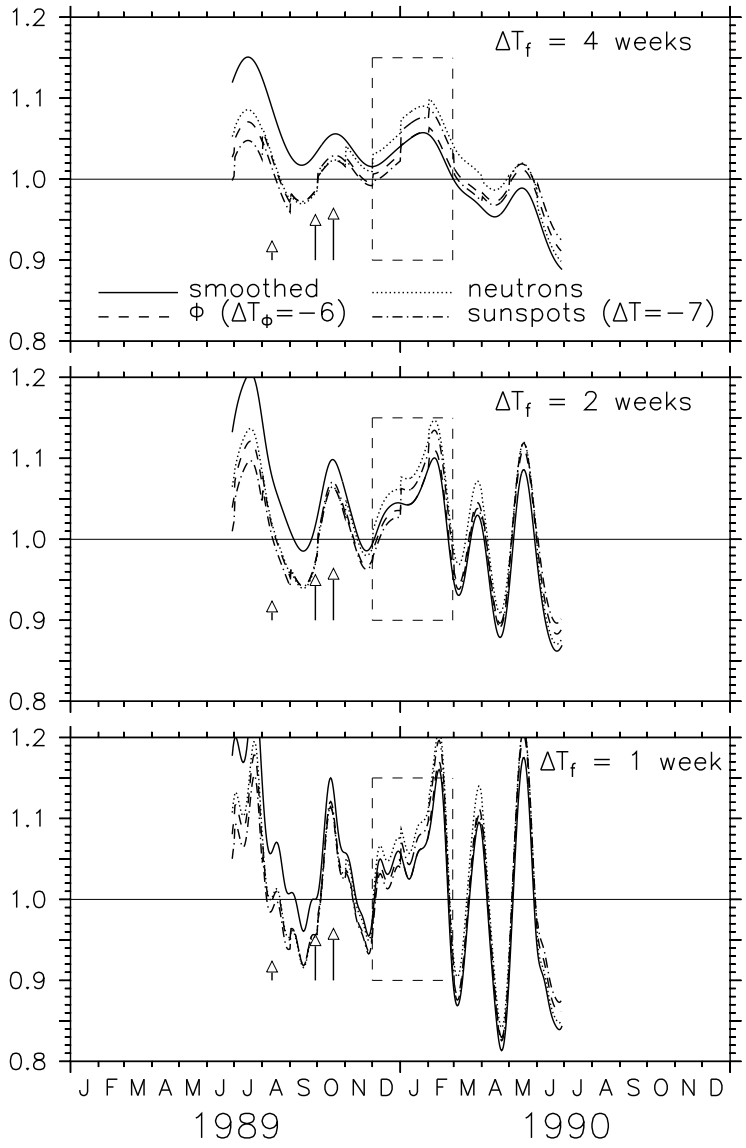

Figure 9.13: Ratio of the smoothed and rescaled ^{14}CO measurements at time t to the respective value one year later for three different convolution filter time windows ΔT_f (Eq. (9.10)) of 4 weeks (upper), 2 weeks (middle), and 1 week (lower). The arrows indicate the occurrence of the 3 major SPEs in 1989, the arrow length represents the total SPE induced ^{14}CO production.

middle of 1989. The third local maximum in Figure 9.13 (upper) indicates 7 - 10% excess ^{14}CO in Dec 1989 to Feb 1990 compared to the same period one year later. The plausible explanation of this enhanced atmospheric ^{14}CO level is the occurrence of the 3 major SPEs in August to October 1989, in agreement with the model results presented in section 9.2.2.

Smoothing the data with shorter time windows (Eq. (9.10)) leads to similar results,

as shown also in Figure 9.12 for a 2 week (middle) and a 1 week time window (lower). The corresponding excess ^{14}CO signals are shown in Figure 9.13 (middle and lower respectively). Passing increasingly higher frequencies through the low pass filter (Eq. (9.10)) leads to a more structured signal. The result obtained with the 1 week window (Figure 9.13, lower) suggests that the 3 SPEs are actually distinguishable in their excess ^{14}CO signal. This contention is supported by the fact that the relative height of the excess ^{14}CO signal resembles the relative SPE strengths (in terms of the total ^{14}CO production), which are represented by the length of the arrows in Figure 9.13 indicating the occurrence of the SPEs. Furthermore, the delay times of the maximum excess ^{14}CO after the respective SPEs (maximum proton flux, cf. Figure 9.2) are 117 days, 89 days and 114 days (all $\pm$ 2 days, derived from the smoothed data with $\Delta T_f = 1$ week) for the three events. These correspond closely to the characteristic rigidities of the proton spectra of the events (Table 9.2), which are 60.6 MV, 102.0 MV, and 77.4 MV respectively. With increasing characteristic rigidity, the penetration depth of the solar protons into the atmosphere increases. Consequently the SPE induced ^{14}CO production also occurs deeper into the atmosphere and it takes less time to transport the additional ^{14}CO into the troposphere.

The local maxima that occur in March and May 1990 in the 1 week filtered excess ^{14}CO plot (Figure 9.13, lower) and the corresponding peaks obtained with longer time windows (Figure 9.13 upper and middle) may possibly be caused by variations in the strength of stratosphere - troposphere exchange. The SPEs build up an additional stratospheric ^{14}CO reservoir that feeds ^{14}CO into the troposphere. However, the strength of stratosphere - troposphere exchange is not necessarily the same for a given calendar month from one year to the next. A tentative indication for this is given by the repeatedly occurring small peaks of the ^{14}CO mixing ratio in the SH autumn and winter between the minimum and maximum ^{14}CO mixing ratio of the years 1990 and 1991 (Figure 9.12, lower).

9.3.2 Comparison with the model results

The results of the various model simulations discussed in the first part of this chapter applied to Baring Head are shown in Figure 9.14, depicting the modeled excess ^{14}CO at Baring Head after the 1989 SPEs. In contrast to the measurement data smoothed with the 1 week time window (Figure 9.13, lower), the 3 different events are not distinguishable in the model results, even though the implicit filtering of the model results due to the 5-day averaging of the model output is shorter than the 1 week time window applied to the observations. A simulation with the 2.0-SPF configuration, taking only into account the largest SPE reproduces essentially the same curve shape (not shown) as the respective run with all 3 events included, but with the level of

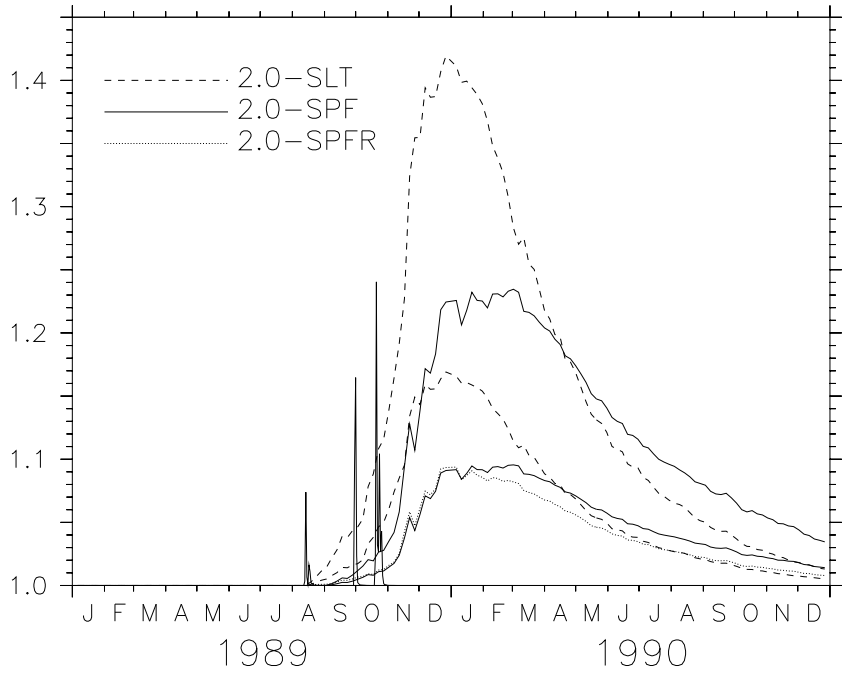

Figure 9.14: Simulated SPE induced excess ^{14}CO for Baring Head (41.4^{o}S, 174.9^{o}E), New Zealand, after the 3 major SPEs in 1989. The peaks indicate the SPEs, the height of the peaks represents the total ^{14}CO production induced by the corresponding event. Calculations are performed with different model configurations and the OH-1 distribution. The lower and upper limit for the 2.0-SLT and the 2.0-SPF configuration are obtained by assuming a normal cut-off rigidity and an 80% reduced cut-off rigidity, respectively. For 2.0-SPFR only the normal cut-off rigidity is considered.

excess ^{14}CO halved as discussed in section 9.2.2. This means that in the model the largest SPE determines the time dependence of the SPE induced excess ^{14}CO at the surface. The model therefore is too diffusive and not capable of describing the transport in detail. Furthermore, this means that for a time scale estimation of the cross tropopause transport of the SPE induced ^{14}CO in the model only the largest SPE can be used. Simulations with the 2.0-SLT configuration predict a time lag of 67 days between the largest SPE and the maximum excess ^{14}CO at Baring Head. The uncertainty is estimated to be $\pm$5 days, because the maximum is well defined. In contrast to that, the 2.0-SPF scheme predicts a delay of roughly 100 days with an uncertainty of at least $\pm$30 days because the maximum is very broad. Thus, the 2.0-SLT cross tropopause transport of the SPE induced ^{14}CO is too fast, the time lag being only 60% of the real. The 2.0-SPF time lag is close to the one observed; however the SPE induced ^{14}CO production signal is even more smeared out by this configuration. This is consistent with the slower response of the ^{14}CO mixing ratio to variations in the global source strength in 2.0-SPF compared to 2.0-SLT, as derived in chapter 7 (cf. Table 7.2). Furthermore, the mass mismatch inherent to the 2.0-

SPF configuration seems to have only a moderate effect for this particular location, as can be concluded from the comparison of the 2.0-SPF predicted excess signal with the respective signal obtained with 2.0-SPFR. This is understandable, since for the present analysis only relative changes are considered, and both ^{14}CO contributions (GCR background + SPE induced) are similarly affected by the rescaling procedure.

9.4 Independent estimate of the transport time scale

In order to verify the time-scale estimates of the SPE induced ^{14}CO downward motion, an independent estimate is provided for comparison. This estimate is derived from the dynamics of the downward motion of air in the high latitude lower stratosphere. "The downward motion of air parcels in the high latitude lower stratosphere can be regarded as a part of the global stratospheric Brewer-Dobson circulation. This circulation is forced by the dissipation in the winter hemispheric stratosphere of Rossby and gravity waves that originate from the troposphere. This dissipation causes a deceleration of the (mainly zonal) wind, which disturbs the geostrophic balance between the poleward-directed pressure gradient force and the equatorward-directed Coriolis force. The resulting net force drives stratospheric air parcels towards the winter pole; by continuity the air parcels move downward in the extra-tropical winter hemisphere, and are 'sucked up' in the tropics. When the stratospheric air parcels reach the tropopause, they are effectively mixed into the troposphere by synoptic weather systems within a few weeks" (Peter Siegmund, KNMI, personal communication, 1999).

To obtain an independent estimate of the transport time scale, the magnitude of the mean downward motion of air parcels in the lower stratosphere at high latitudes has been estimated by diagnosing the Transformed Eulerian Mean (TEM) vertical velocity ω^*, using the 15-year (1979-1993) ECMWF reanalysis (ERA) dataset [*Gibson et al.*, 1997]. "The TEM circulation is the Eulerian mean circulation in which the part forced by eddy heat transport is removed. For each of the 180 months of the ERA period, the ω^* in the lower stratosphere is diagnosed separately, with a latitudinal resolution of 2.5 degrees and (for the present study) at the levels of 10, 30, 50, 70, 100, 150, 250 and 300 hPa. The equation for ω^* is given, e.g., by *Peixoto and Oort* [1992]. The ω^* values applied in this study are 15-year August to November averages over the regions poleward of 60^oN and 60^oS, along with the respective averages for the year 1989.

The ERA data are produced by a frozen version of the ECMWF model. Therefore, the ERA data do not suffer from changes in the model during the period 1979-1993, as would be the case if 'normal' model analysis would be applied. This advantage is particularly large for the vertical velocity, because this quantity strongly depends on

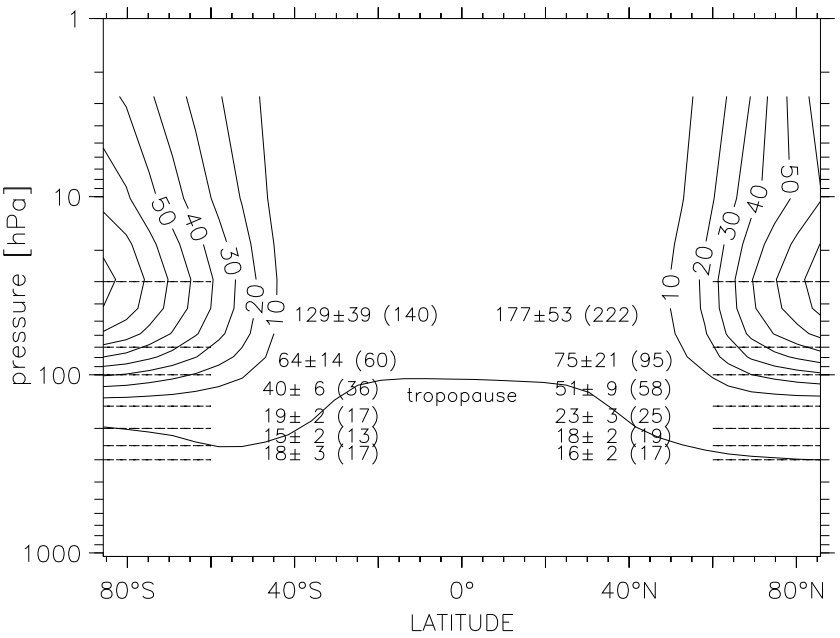

Figure 9.15: SPE induced ^{14}CO production rate distribution in units of 1 molecule g^{-1} s^{-1} normalized to a global average production rate of 1 molecule cm^{-2} s^{-1} in the model atmosphere. The tropopause is the average WMO-tropopause level (*WMO* [1992], see section 1.5) from August to November 1993 obtained from the NCEP-reanalysis data. The ECMWF reanalysis based subsidence durations between the indicated pressure levels (dotted lines) are given in days. These are averaged over 60^o to 90^o latitude, the months of August to November, and the years 1979 to 1993. The error is the standard deviation according to the year-to-year variation as described in the text. The value in parentheses is the respective subsidence time for the year 1989.

the formulation of the model. However, also in the ERA dataset ω^* still remains a rather uncertain quantity. This is particularly true for ω^* in the stratosphere, where the number of observations is small and where the modeled circulation is influenced by the imposed upper boundary (10 hPa) conditions of the model.

Computations for the two hemispheres of the extra-tropical average of ω^* (i.e. of the strength of the Brewer-Dobson circulation) using ERA data give generally somewhat larger (tens of %) values than found in similar studies [e.g., *Holton*, 1990; *Rosenlof*, 1995]. For averages over a smaller area the differences would likely be larger. For the ω^* as used in this study, averaged as described above, an educated guess of its accuracy is 50%. Despite this large uncertainty, there are at present no more accurate, useful vertical velocity data available" (Peter Siegmund, KNMI, personal communication, 1999).

The result of the subsidence velocity analysis is presented in Figure 9.15. Shown is the time it takes the air to subside between the indicated pressure levels. The

year-to-year variation of the subsidence time is computed as standard variation

$$\sigma_t = \frac{dp}{\omega^{*2}} \sigma_{\omega^*} \ , \tag{9.12}$$

where p is pressure, and σ_{ω^*} is the standard deviation of ω^* calculated according to Eq. (7.14). This variation (Figure 9.15) is smaller than the general uncertainty of the method as discussed above. Therefore in the discussion below the averaged values are used, but in addition the respective numbers for the year 1989 are provided in parentheses. Assuming a time lag of 14 days for the air that just crossed the tropopause to reach the surface (tropospheric mixing time), the maximum excess ^{14}CO at Baring Head induced by the three SPEs should then originate from a pressure level between 95 hPa and 120 hPa, not considering the uncertainty in the subsidence velocity. Assuming a 50% overestimation of the subsidence velocity, the respective levels are 55 hPa - 70 hPa. According to the results of *Lingenfelter and Flamm* [1964], the maximum of the SPE induced ^{14}C production rate is expected to be somewhat higher, at about 30 hPa. But these calculations also predict a significant production rate at 70 hPa to 100 hPa. A re-calculation of the SPE ^{14}CO source component with better knowledge of the solar proton spectrum and flux during SPEs and all relevant cross sections is therefore desirable. This could either be performed with particle production transport codes as used by *Masarik and Reedy* [1995] or *Masarik and Beer* [1999], or probably by an adaption of the method presented in *O'Brien and Sauer* [2000].

9.5 Discussion

Even though the temporal increase in ^{14}CO is relatively small, the good agreement that is obtained between the model predictions and the observations for the timing and the magnitude gives confidence in the quality of the experimental data and the theoretical interpretation. One issue that needs to be addressed is whether the signal extracted from the measurements at Baring Head is due to artifacts in the observations. The data have only a small measurement uncertainty of 2% *Brenninkmeijer* [1993], but there is a natural scatter well in excess of this. To test the robustness of the signal extracted from the data, the filtering is performed repeatedly, with random omission of about 10% of the data points. Some results are shown in Figure 9.16. These tests show that the signal may change somewhat in shape and magnitude, but remains essentially the same. This implies that it is unlikely that the signal extracted is coincidental.

Other causes for a signal in ^{14}CO may have been changes in sampling strategies, or in the synoptic conditions. For instance, sampling air solely during southerly

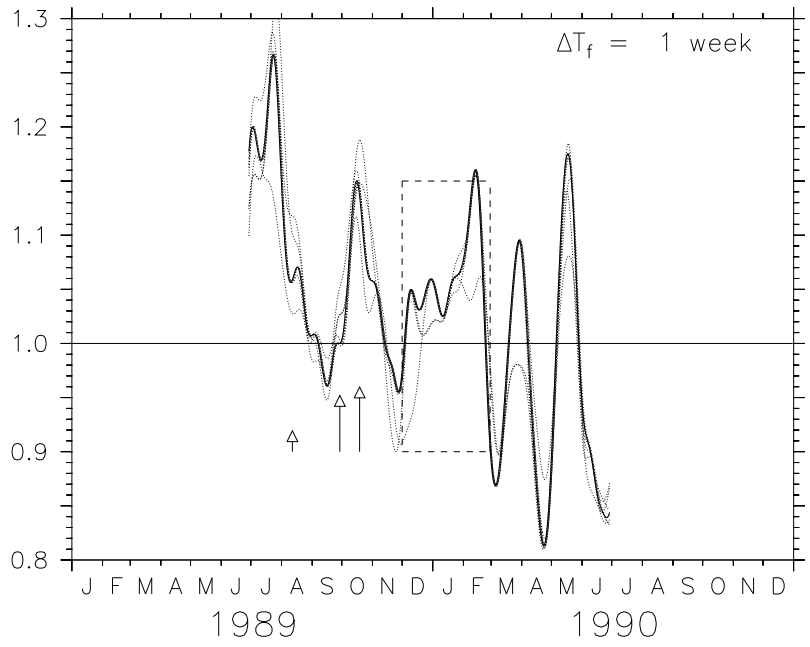

Figure 9.16: Ratio of the smoothed ^{14}CO measurements at time t to the respective value one year later for a convolution filter time window ΔT_f (Eq. (9.10)) of 1 week. The solid line shows the result for the full time-series (cf. Figure 9.13), the thin dotted lines show a set of results derived from time-series where 20 data-points have been omitted at random. The arrows indicate the occurrence of the 3 major SPEs in 1989, the arrow length represents the total ^{14}CO production.

wind conditions may lead to a bias. Southerly air reaching Baring Head contains more ^{14}CO and generally less CO, since the CO sources are smaller, but the ^{14}CO source strength increases with geomagnetic latitude. Such a bias is highly unlikely because not only southerly conditions were sampled, but also because there was no significant synoptic difference between the 2 years involved.

Further factors that affect the local ^{14}CO mixing ratio have to be considered. A major one is OH itself. If the elevated ^{14}CO values in early 1990 at Baring Head were solely explained by lower OH levels, then this would be in conflict with the CO measurements of the same period, which show actually slightly lower values compared to one year later.

Although it is difficult, if not impossible, to prove that only the SPEs are responsible for the difference in the observed ^{14}CO, there is no direct evidence for changes in OH. Records of methane and methylchloroform (CH_3CCl_3, MCF) have been inspected from Cape Grim (40.68^o S, 144.68^o E), Tasmania, for the years involved, and levels are tentatively somewhat lower in the 1990 seasonal minimum. This could point to a higher OH concentration. However, it is difficult to assign trend lines to these records to estimate changes. Methane values show important variations from 1990

onwards [*Dlugokencky et al.*, 1994]. Methylchloroform started to decrease rapidly in 1992 [*Prinn et al.*, 1992; *Spivakovsky et al.*, 2000]. Important factors affecting the mixing ratio of these gases are changes in source strength. For methylchloroform the movement of the inter-tropical convergence zone (ITCZ) also plays a role, since its main source is (was) in the northern hemisphere. Known reasons for inter-annual changes in OH, such as year-to-year changes in water vapor or stratospheric ozone are unlikely to produce exactly the kind of signal in ^{14}CO that can be expected from SPEs.

9.6 Conclusions

Major SPEs induce additional stratospheric ^{14}CO production on time scales of hours to days. The equivalent of up to several months of GCR background ^{14}CO can be produced, depending on the SPE's total proton flux and the characteristic rigidity of the SPE's energy spectrum. The latitude and time dependence of the SPE induced excess ^{14}CO at the surface level contains valuable information about the cross tropopause downward transport, because the source is almost exclusively in the polar stratosphere.

A transport time scale can be defined as the delay between the maximum (or center of mass) of the ^{14}CO production during the SPE and the maximum ^{14}CO increase at the surface. Different model configurations (in particular with different numerical advection schemes) yield a strongly different cross tropopause downward transport, i.e., a different transport time and a different amount of excess ^{14}CO at the surface. This especially concerns the strength and seasonality of the transport component from the polar lowermost and middle stratosphere into the troposphere and its differences between the two hemispheres. The measurable time lag and the amount of SPE induced excess ^{14}CO at the surface can therefore serve as a valuable test for the stratosphere - troposphere exchange by which 3-dimensional model transport and numerical advection schemes can be evaluated, in particular in terms of seasonal and hemispheric differences. This test is, according to the model results, almost independent of the distribution of the oxidizing capacity of the atmosphere, and the time lag is dominated by the large scale transport properties.

A time series of ^{14}CO measurements at Baring Head, New Zealand, indicates a temporal increase of ^{14}CO at the surface 3 to 4 months after 3 major SPEs in Aug/Sep/Oct 1989. The small signal could have been obscured by the solar modulation of the GCR induced background ^{14}CO production; however, 3 different techniques used to rescale the measurements show the same result. The relative height of the SPE induced ^{14}CO increase at the surface corresponds well with the total ^{14}CO production during each respective event. The time lag between each event

and the maximum increase of ^{14}CO at the surface decreases with increasing characteristic rigidity of the event, since the SPE induced ^{14}CO production then takes place deeper in the stratosphere. The peak relative increase of ^{14}CO above the background mixing ratio is about 10-20% which is also predicted by the model, however, with a wide range, depending on the advection scheme and the assumed cut-off rigidity. Because both the cut-off rigidity and the characteristic rigidity of the SPE determine the SPE ^{14}CO source distribution and strength, conclusions about the cut-off rigidity cannot be drawn.

The time lag between the SPE and the maximum excess ^{14}CO at the surface level, which is mainly determined by the stratospheric subsidence, is 3 to 4 months. This corresponds, within the uncertainties, to the subsidence time calculated independently from the ECMWF reanalysis data. The 2.0-SLT configuration underestimates this delay time; the cross tropopause transport takes only 2-3 months and therefore is too fast. The 2.0-SPF configuration predicts 4 to 5 months, which seems to be an overestimation of the time lag; however, it has to be taken into account that the center of mass of the SPE induced ^{14}CO source distribution that is used in the model, might be somewhat too high. In this case the 2.0-SPF configurations results would fit very well with the ECMWF based estimate, but the 2.0-SLT based prediction of the time lag would be even more significantly underestimated. Both model configurations fail to predict the fast decay of the excess ^{14}CO signal at the surface and are not able to resolve the three individual events.

The next solar maximum is expected in 2001. SPEs are likely to occur. This offers the chance to measure the SPE induced excess ^{14}CO again. Measurement sites in both hemispheres could provide very valuable information about the cross tropopause transport, especially about interhemispheric differences.

10 A ^{14}CO based model inter-comparison: Stratosphere - troposphere exchange in MATCH and TM3

Abstract. More than half of the cosmogenic ^{14}CO is produced in the stratosphere. Therefore, not only the tropospheric OH abundance determines the tropospheric ^{14}CO mixing ratio, but also the stratosphere - troposphere exchange (STE) of the tracer. Various model configurations of MATCH and TM3 are compared with regard to this aspect. Different numerical advection schemes are used in the two models. Furthermore, the underlying meteorological data driving the advection are different. As a consequence, differences in the simulated STE occur. The influence of the horizontal and vertical grid resolution on the simulated STE of ^{14}CO is assessed with TM3. Furthermore, the simulated STE is investigated with respect to the interhemispheric asymmetry of the downward flux across the tropopause and its localization. The seasonal variation in both hemispheres and the amplitude of the annual cycle is discussed. And finally, the phase lag between STE and OH seasonality in the troposphere and the stratosphere is compared in order to understand the influence of STE on the tropospheric ^{14}CO mixing ratio. It turns out that depending on the particular model configuration the most important aspects of STE according to the present knowledge are qualitatively represented by the models. Large uncertainties remain, however, concerning the absolute downward mass flux of ^{14}CO. Nevertheless, differences between the particular model configurations with respect to the interhemispheric asymmetry, the phase and the amplitude of STE can probably be used to further constrain the STE when simulated ^{14}CO mixing ratios are compared to measurements.

10.1 Introduction

Most of the model simulations performed so far, aiming at the understanding and assessment of the relevant processes and their uncertainties determining the atmospheric mixing ratio of ^{14}CO, have been performed with the MATCH model in various configurations. Thereby, the differences between the particular configurations focus mainly on the large scale advection determining the tracer transport. All configurations were driven offline by the same meteorological data, i.e., the NCEP reanalysis data [*Kalnay et al.*, 1996]. As indicated in chapter 2, the quality of the meteorological data is at least equally important for the usability of the model predictions as is the accuracy of the advection algorithm itself. In other words, the best advection algorithm will never deliver realistic results when the underlying meteorological data are deficient. This is of special importance when offline models are expected to reproduce particular measurements sampled in the real atmosphere.

Therefore, the analysis of the uncertainties in the simulated atmospheric ^{14}CO mix-

ing ratio arising from inaccuracies in the realization of the simulated tracer transport is further expanded in this chapter. For this purpose, model simulations of atmospheric ^{14}CO performed with the offline model TM3 (KNMI-Version) are analyzed under various aspects. The influence of the chosen model grid resolution (horizontal and vertical) on the simulated ^{14}CO mixing ratio is assessed. Furthermore, the TM3 simulations are compared to MATCH simulations that are obtained under the same initial and boundary conditions (e.g., source of ^{14}CO, OH distribution). This is especially of interest since different advection algorithms are implemented in MATCH and TM3, and, what may be even more important, the TM3 advection is driven by the ECMWF reanalysis data, whereas MATCH is driven by the NCEP reanalysis data (both 1993). All TM3 simulations were performed by KNMI (Ad Jeuken, personal communication 1998-2000). The special focus of this model inter-comparison is on the simulated stratosphere - troposphere exchange (STE), i.e., on its strength, its seasonality, and its localization. Differences between the various model configurations can be used to constrain the relevant effects which determine the atmospheric ^{14}CO mixing ratio. And finally, measurements of ^{14}CO in comparison to the model results can then be used to evaluate the models with respect to these effects.

10.2 Model setup

The two models are initialized with zero mass mixing ratio of atmospheric ^{14}CO and subsequently integrated (for up to two years) with the ^{14}C(O) source distribution of *Lingenfelter* [1963] (LF, see chapter 5) for solar minimum conditions. The source distribution is normalized to a global average production rate of 1 molec cm^{-2} s^{-1} in an idealized static atmosphere of constant depth (1033 g cm^{-2}). The interpolation of the ^{14}CO source on the TM3 grid is performed in the same way as described for the MATCH grid in chapter 5 (i.e., pre-calculation on horizontal coordinates, and online interpolation on the pressure levels). The MATCH advection is driven by the NCEP-reanalysis meteorology of 1993 [*Kalnay et al.*, 1996], the TM3 advection by the ECMWF reanalysis meteorology of the same year.

The OH-1 distribution is prescribed for the ^{14}CO oxidation. For this, the tropospheric OH distribution of MATCH is redistributed onto the various TM3 grid resolutions using a transformation algorithm, similar to that presented in section 2.4. First, the horizontal (latitude, longitude) overlap fraction for every pair of grid columns is calculated as

$$f_A = \frac{A_S \bigcap A_D}{A_D} \ , \tag{10.1}$$

where A_S is the base area of the source grid column (MATCH), A_D the base area of the destination grid column (TM3), and "$\bigcap$" indicates the intersection of both.

If this horizontal overlap fraction is non-zero, the overlap of the grid boxes in vertical direction are calculated for this particular pair of source and destination grid columns. To ensure a 100% vertical overlap, the vertical model coordinates are internally converted to pure sigma coordinates of the form

$$\sigma = \frac{p}{p_s} \ , \tag{10.2}$$

where p is the pressure level at the box interfaces (i.e. lower and upper boundary of a given grid box) and p_s is the surface pressure of the respective grid column. Furthermore, the upper grid boundary is set to $\sigma_{top} = 0$. As a consequence all valid sigma levels on both the source and the destination grid are in the range $0 \leq \sigma \leq 1$. The resulting vertical overlap fraction of a particular pair of grid boxes is then

$$f_\sigma = \frac{\Delta\sigma_S \bigcap \Delta\sigma_D}{\Delta\sigma_D} \ , \tag{10.3}$$

where $\Delta\sigma$ is the sigma-level interval covered by a given grid box on the source (S) and destination (D) grid respectively. Finally, the contribution δOH of OH in the destination grid box that resides in the source grid box is

$$\delta\mathrm{OH} = f_A(A_D, A_S) \cdot f_\sigma(\Delta\sigma_D, \Delta\sigma_A) \cdot \mathrm{OH}_S \ . \tag{10.4}$$

The resulting OH concentration in the destination grid box is then obtained by summation of δOH over all columns and vertical levels of both grids. The surface pressure of June 1993 is used as the reference surface pressure p_s for the transformation.

As in MATCH, OH-2D is used in TM3 above the climatological mean tropopause (Eq. (1.10)). The stratospheric OH-2D distribution is transformed to the TM3 grid in horizontal (latitudinal) direction by the same algorithm as the tropospheric OH distribution described above. The vertical interpolation on the TM3 pressure levels is performed online as in the MATCH configurations (see section 1.4).

The production rate q of ^{14}CO as it appears on the model grid and the loss rate l due to oxidation by OH are included in the model output for some model configurations. The MATCH configurations 2.0-SLT, 2.0-SPF, and 2.0-SPFR are used. For those and for the TM3-L-L31 configuration, the stratosphere - troposphere exchange (STE) is quantified by separately tracing ^{14}CO that is produced in the stratosphere and ^{14}CO that is produced in the troposphere. The resulting mass mixing ratios of these additional tracers are denoted as χ_{st} and χ_{tr} respectively. The tropopause pressure for distinction between stratospheric and tropospheric ^{14}CO production is prescribed offline by the NCEP reanalysis tropopause pressure (1993, daily averages) in MATCH, and diagnosed online according to the WMO definition [*WMO*, 1992]

	1st year				2nd year			
	χ	χ_{tr},χ_{st}	q	l	χ	χ_{tr},χ_{st}	q	l
2.0-SLT	X	X	X	X	X	X	X	X
2.0-SPF	X	X	X	X	X	X	X	X
2.0-SPFR	X	X	X	X	X	X	X	X
TM3-L-L19	X		X	X	X		X	X
TM3-L-L31					X	X	X	X
TM3-H-L19	X		X	X				

Table 10.1: Overview of model output available for the MATCH - TM3 inter-comparison. χ, χ_{tr}, and χ_{st}, are the mixing ratios of ^{14}CO, ^{14}CO produced in the troposphere, and ^{14}CO produced in the stratosphere, respectively. The tropopause is diagnosed online according to the WMO definition [*WMO*, 1992] in TM3 and prescribed by the NCEP reanalysis tropopause of 1993 (daily averages) [*Kalnay et al.*, 1996] in MATCH. q is the production rate and l the loss rate of ^{14}CO in the model atmosphere.

in TM3. In order to force linearity, χ_{st} and χ_{tr} are adjusted to match the total ^{14}CO mixing ratio χ at every time step, i.e.,

$$\chi_{st} \leftarrow \chi \cdot \frac{\chi_{st}}{\chi_{tr} + \chi_{st}} \tag{10.5}$$

$$\chi_{tr} \leftarrow \chi \cdot \frac{\chi_{tr}}{\chi_{tr} + \chi_{st}} \ . \tag{10.6}$$

This adjustment is, however, only included in the MATCH simulations.

All model output is archived as 5-day averages, except for February 26 - 28, where the TM3 output is a three day average. The TM3 simulations were all performed at KNMI (Ad Jeuken, KNMI, personal communication, 1998-2000). Table 10.1 gives an overview of the various model simulations and the model output that is available for further analysis.

10.3 Model results

The overall model results listed in Table 10.2 are renormalized to a global average ^{14}CO production rate of 1 molec cm^{-2} s^{-1} in the respective model atmospheres. The resulting annual ^{14}CO production is 7.94 ± 0.5 kg for all model configurations. The annual global loss of ^{14}CO through oxidation by OH is of similar magnitude. The deviation from the long term equilibrium between production and loss of ^{14}CO is less than 0.4% in MATCH (except 2.0-SPF) and less than 1.3% in TM3. For 2.0-SPF the annual global loss is 21% larger than the annual global production, indicating the additional artificial source contribution due to the grid mismatch discussed in chapter 2. The equilibrium state and the mismatch in the 2.0-SPF configuration

	$\bar{l}$	$\bar{m}$	$\sigma_m \bar{m}^{-1}$	$\dot{m}_q$	$\dot{m}_l$	$\tau_l = \frac{\bar{m}}{\dot{m}_l}$
	molec cm^{-2} s^{-1}	kg	%	kg yr^{-1}	kg yr^{-1}	months
2.0-SLT	0.996	2.361	1.4	7.893	7.863	3.60
2.0-SPF	1.208	2.980	1.3	7.893	9.535	3.75
2.0-SPFR	0.997	2.475	0.5	7.893	7.867	3.78
TM3-L-L19	1.006	2.130	1.0	7.982	8.030	3.18
TM3-L-L31	1.011	2.158	1.4	7.982	8.072	3.21
TM3-H-L19				7.974		

Table 10.2: Annual global mean loss rate ($\bar{l}$), annual mean global burden ($\bar{m}$), global production ($\dot{m}_q$), and global loss ($\dot{m}_l$) of ^{14}CO in the model atmosphere of various model configurations. σ_m is the standard deviation of the average burden with respect to time (5-day averages versus annual average). τ_l is the global average atmospheric lifetime of ^{14}CO due to oxidation by OH. All values are normalized to a global annual average ^{14}CO production rate of 1 molec cm^{-2} s^{-1} in the respective model atmosphere. Missing data is not available.

is also mirrored in the average loss rate of ^{14}CO in the model atmosphere; for all model configurations this is within $\pm$1.1% of the renormalized global average ^{14}CO production rate of 1 molec cm^{-2} s^{-1}, except for 2.0-SPF, where the loss rate is 21% larger than the "physical" contribution to the ^{14}CO production.

The resulting global atmospheric burden of ^{14}CO is, except for the 2.0-SPF configuration, between 2.1 and 2.5 kg for the given source strength. The standard deviation of the global atmospheric ^{14}CO burden with respect to time is small ($< 1.5\%$ of the burden). The reason for this is the constant source strength throughout the year. And finally, as already found in chapter 7, the global atmospheric lifetime τ_l of ^{14}CO predicted by TM3 is on average about 14% shorter than predicted by the MATCH 2.0 configurations; the full range of all configurations considered is 3.18 to 3.78 months (Table 10.2).

For further investigation of the differences between the particular configurations, various aspects are addressed separately in the following sections.

10.3.1 Horizontal resolution

The influence of the horizontal model grid resolution of TM3 on the resulting ^{14}CO mixing ratio is analyzed from the results of the first year simulation (initialized with zero mass mixing ratio). The development of the global atmospheric burden towards equilibrium is depicted in Figure 10.1. A slight mismatch between global burden and cumulative production minus loss occurs. This mismatch is about 0.05 kg after one year, i.e, less than 3% of the global burden. Whereas the global ^{14}CO growth rate is almost independent of the horizontal resolution during the first 2 months, it

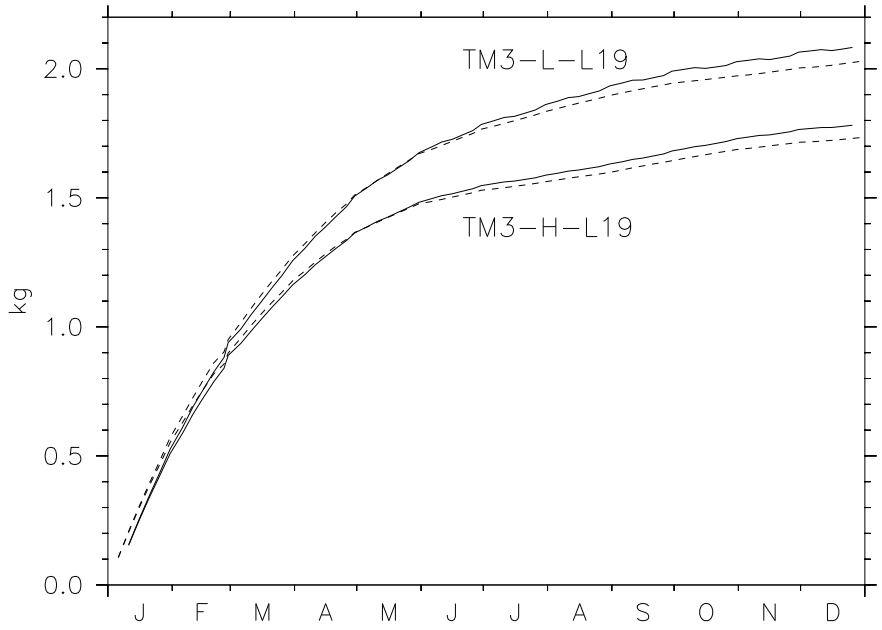

Figure 10.1: Global atmospheric burden of ^{14}CO (solid lines) and time integrated production minus loss (dashed lines) calculated by TM3 with different horizontal resolutions. The initial ^{14}CO mass mixing ratio is set to zero. The values are normalized to an annual global average ^{14}CO production rate of 1 molec cm^{-2} s^{-1} in the respective model atmosphere.

starts to diverge after two to three months, with a smaller growth rate for the higher horizontal resolution. The equilibrium global burden, approximately reached after one year, is 1.8 kg in TM3-H-L19 and 2.1 kg in TM3-L-L19, i.e., 14% lower on the TM3-H-L19 grid than on the TM3-L-L19 grid. This has to be taken into account in comparing the global distribution of ^{14}CO.

The ^{14}CO mixing ratio during the first year simulated with TM3-L-L19 and TM3-H-L19 is normalized to a global average ^{14}CO production rate of 1 molec cm^{-2} s^{-1} in the respective model atmospheres for comparison. The result is shown in Figure 10.2. The zonally averaged annual cycle of ^{14}CO at the surface level is similar in both resolutions, because the OH distribution and seasonality is the same. However, for a given global atmospheric ^{14}CO production rate, the amount of ^{14}CO at the surface level is up to 15% higher for the higher resolution compared to the lower resolution. Two exceptions are the first month, and the SH tropics and mid-latitudes in the second half of the year, where the surface level ^{14}CO predicted with TM3-H-L19 is lower than the TM3-L-L19 predicted mixing ratio, but not by more than 5%. Therefore, the higher horizontal resolution tends to predict a higher ^{14}CO mixing ratio at the surface level compared to the lower horizontal resolution.

Taking into account the differences in the simulated global atmospheric burden, this effect is even more pronounced. The simulated global atmospheric burden on the

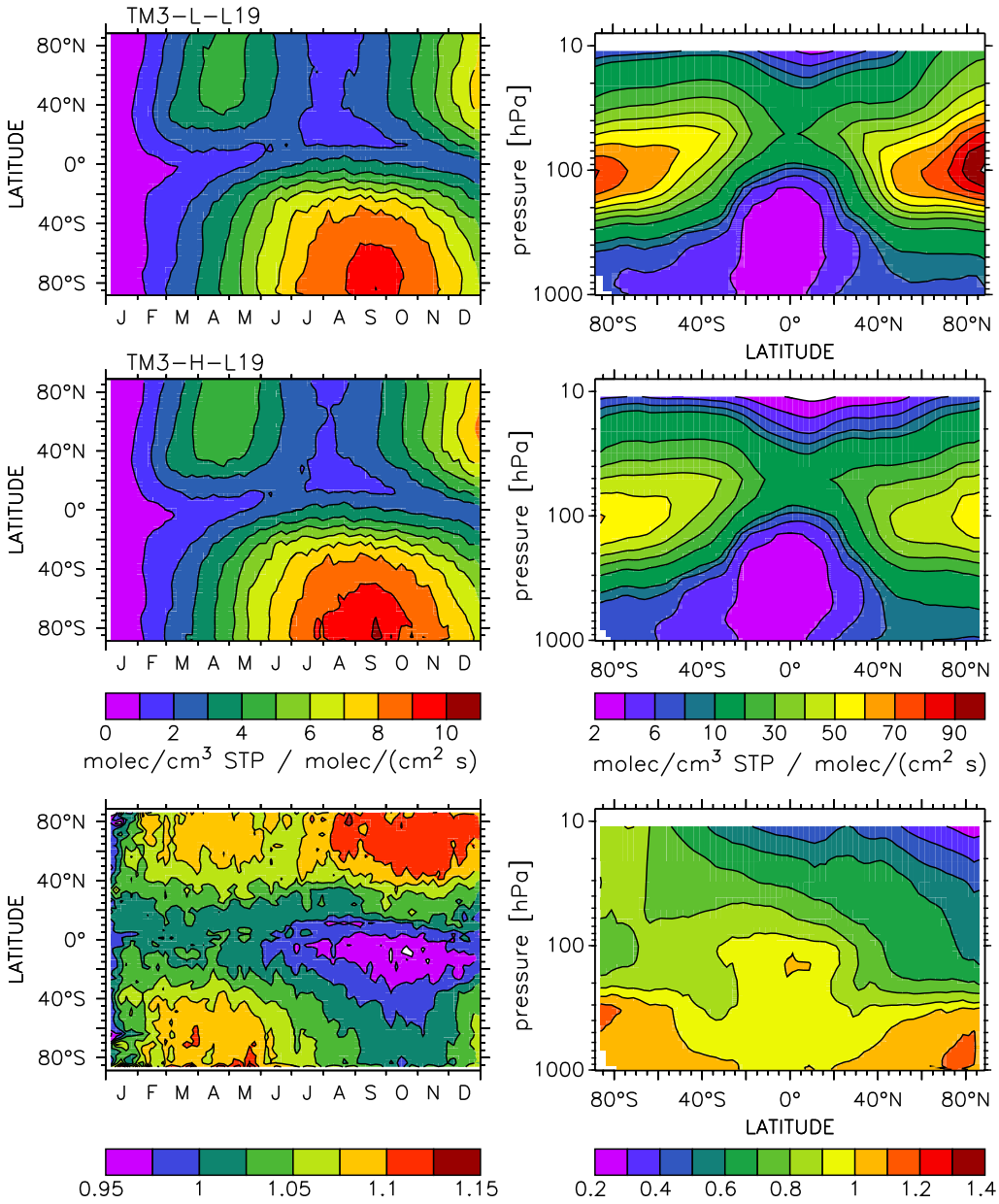

Figure 10.2: Zonal mean surface mass mixing ratio of ^{14}CO (left column) and zonal mean vertical distribution after one year (Dec. 27 - Dec. 31 average, right column) calculated with TM3 using different horizontal resolutions. The initial mass mixing ratio (Jan. 1) is set to zero. All values are normalized to an annual global average ^{14}CO production rate of 1 molec cm^{-2} s^{-1} in the respective model atmospheres. The lower row shows the zonal average ratio of the TM3-H-L19 to the TM3-L-L19 results.

higher resolution grid is 13% to 15% lower in the second half of the year than on the low resolution grid (Figure 10.1). As a consequence, a renormalization of the simulated ^{14}CO mixing ratio to the same global average burden would result in an

enhanced discrepancy in the surface layer mixing ratio between TM3-H-L19 and TM3-L-L19. For a given global atmospheric burden the ^{14}CO mixing ratio at the surface level simulated with the higher horizontal resolution is then overall higher (by 9% to 35%) than the respective mixing ratio on the lower resolution grid.

The vertical distribution of ^{14}CO is likewise affected by the choice of the horizontal resolution. This can be seen in the right column of Figure 10.2. After one year integration time, the lowermost stratospheric levels of ^{14}CO are 20% to 40% lower on the higher resolution grid compared to the lower resolution grid. This discrepancy is smaller but still significant when the different global atmospheric burden is taken into account (10% - 30%). The tropospheric ^{14}CO levels, in contrast, are generally enhanced when the higher horizontal resolution is used. Taking into account the differences in the global atmospheric burden, this holds throughout the troposphere, though if only the global average production rate is considered, in the tropics the mixing ratio is lower than on the lower resolution grid.

10.3.2 Vertical resolution

The influence of the vertical grid resolution on the simulated ^{14}CO mixing ratio is shown in Figure 10.3. The simulations are performed with the TM3-L-L19 and the TM3-L-L31 configurations. The second year of integration after initialization with zero mixing ratio is analyzed. The predicted global atmospheric burden (in equilibrium) differs only by about 1.3% (Table 10.2) between simulations on the lower vertical resolution grid (TM3-L-L19) and the higher vertical resolution grid (TM3-L-L31). A renormalization to the same global average production rate of ^{14}CO in the model atmosphere is therefore sufficient for comparison.

The overall seasonal cycle of ^{14}CO at the surface level is very similar for both vertical resolutions; the common OH distribution and seasonality is the dominating factor. However, changing the vertical resolution affects the absolute level of the ^{14}CO mixing ratio at the surface level. On the annual average, the surface level ^{14}CO mixing ratio is reduced when the vertical resolution is increased. On a smaller time scale the situation is more complicated, however. Increasing the vertical resolution, the ^{14}CO mixing ratio at the surface level tends to decrease by 5% to 10% during the second half of the year. During the first half of the year, it decreases by up to 20% in the SH, whereas it increases by up to 10% in the NH. As a consequence, when the higher vertical resolution is used, the spring maximum is stronger in the NH than in the SH, when the higher vertical resolution is used, whereas the spring maxima predicted by the lower vertical resolution simulations are almost the same in both hemispheres.

The annual average vertical distribution of ^{14}CO (Figure 10.3) exhibits 5% to 10%

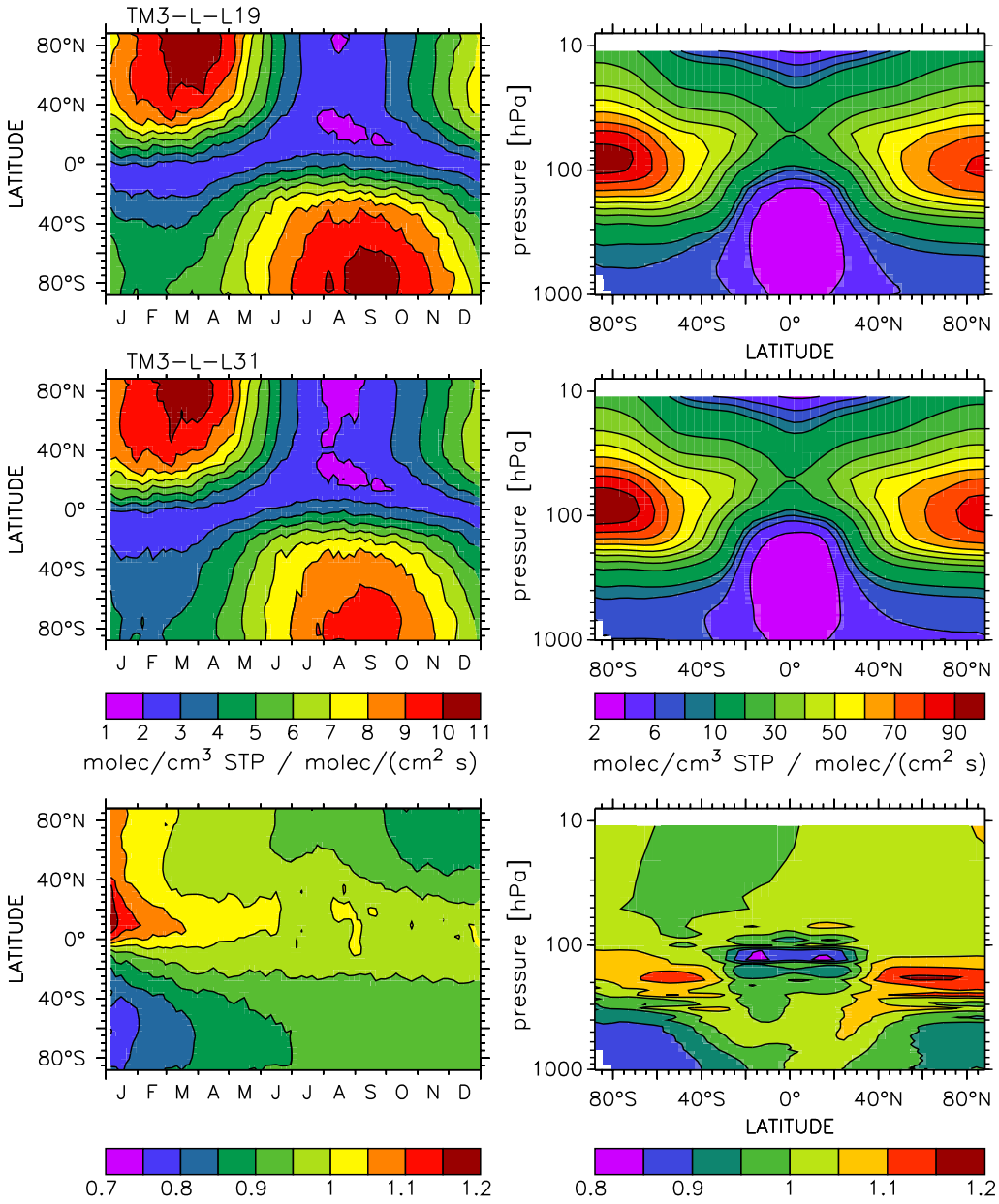

Figure 10.3: Zonal mean surface mass mixing ratio of ^{14}CO (left column) and annual zonal mean vertical distribution (right column) calculated with TM3 using different vertical resolutions. All values are normalized to an annual global average ^{14}CO production rate of 1 molec cm^{-2} s^{-1} in the respective model atmosphere. The lower row shows the ratio of the TM3-L-L31 to the TM3-L-L19 results.

lower values in the troposphere when the vertical resolution is increased, except in the NH tropics and the upper tropical troposphere, where the mixing ratio increases by less than 5% (Figure 10.3, lower right). At the same time, the ^{14}CO mixing ratio in the tropical stratosphere is reduced by 5% to 10%, with a maximum reduction

of 20% at 15^o to 20^o in both hemispheres below 100 hPa. In contrast to that, at latitudes higher than 40^o the stratospheric (above 300 hPa) ^{14}CO mixing ratio increases by 10% to 15%, with the maximum of up to 20% in the NH, when the vertical resolution is increased.

10.3.3 MATCH versus TM3

For the following comparison of the simulated ^{14}CO mixing ratio obtained with various configurations of MATCH and TM3, the results are all normalized to a global average ^{14}CO production rate of 1 molec cm^{-2} s^{-1} in the respective model atmospheres. The differently simulated global atmospheric burden of ^{14}CO in equilibrium is not taken into account, since it is not a free model parameter. It is fully determined by the global source strength of ^{14}CO, the global OH distribution, and the model characteristics. The simulations of 2.0-SLT, 2.0-SPFR, TM3-L-L19, and TM3-L-L31 for the second year after initialization with zero mixing ratio are used for the analysis.

10.3.3.1 Seasonal cycle of ^{14}CO at the surface level The zonally averaged simulated annual cycle of ^{14}CO at the surface level is compared in Figure 10.4. The general characteristics of the ^{14}CO seasonal cycle at the surface level are the same for all configurations, with ^{14}CO mixing ratios highest in spring and lowest in autumn. The annual amplitude increases with latitude. Differences are also present with respect to the asymmetry between NH and SH, and the absolute level of the ^{14}CO mixing ratio.

For all configurations the predicted NH minimum (July to September) at high latitudes is lower than the respective SH minimum (January to March). Likewise, SH maximum (August to October) predicted by MATCH at high latitudes is larger than the NH maximum (February to April). In contrast to that, TM3-L-L19 predicts approximately equal high latitude maxima in both hemispheres, and TM3-L-L31 predicts a stronger maximum in the NH.

The zonally averaged latitudinal gradient of ^{14}CO during the periods of extreme ^{14}CO mixing ratios at the surface level is shown in more detail in Figure 10.5. During both periods the minimum ^{14}CO mixing ratio is predicted to be located in the tropics, at 5^oS in March/April, and at 15^oN in September/October. The latitudinal gradient in the spring hemisphere is steeper from 0^o to 30^o than north/south of 30^o. During SH autumn the ^{14}CO mixing ratio increases almost linearly from the equator towards the south pole. In contrast to that, in NH autumn, the maximum ^{14}CO mixing ratio is reached around 35^oN. North of this latitude the mixing ratio is

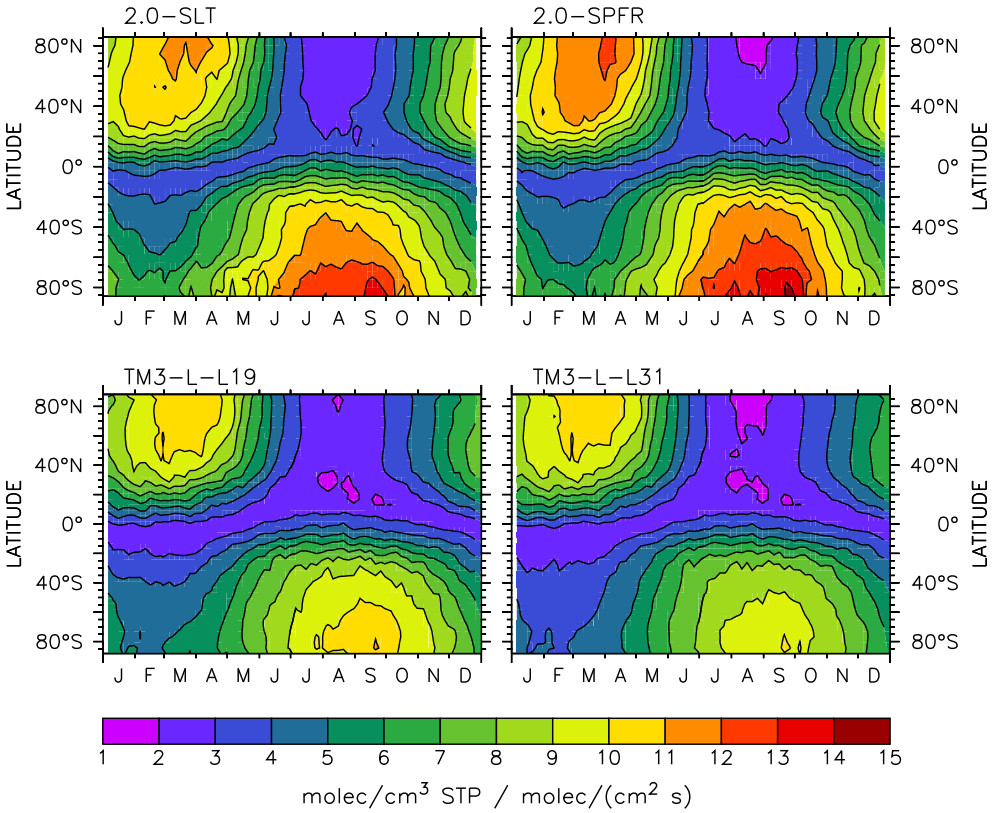

Figure 10.4: Zonal mean ^{14}CO mass mixing ratio at the surface level calculated with different configurations of MATCH and TM3. The mass mixing ratios are normalized to an annual global average ^{14}CO production rate of 1 molec cm^{-2} s^{-1} in the respective model atmospheres.

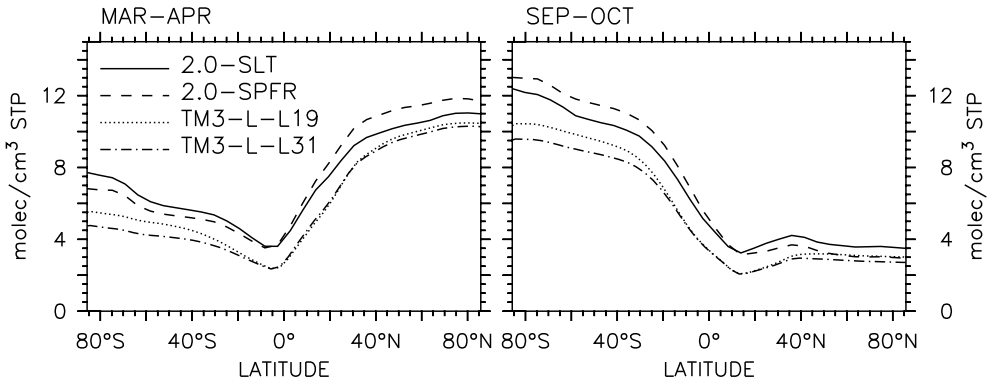

Figure 10.5: Zonal mean ^{14}CO mass mixing ratio at the surface level averaged over the periods March/April (left) and September/October (right) calculated with various model configurations of MATCH and TM3. The mass mixing ratios are normalized to an annual global average ^{14}CO production rate of 1 molec cm^{-2} s^{-1} in the respective model atmospheres.

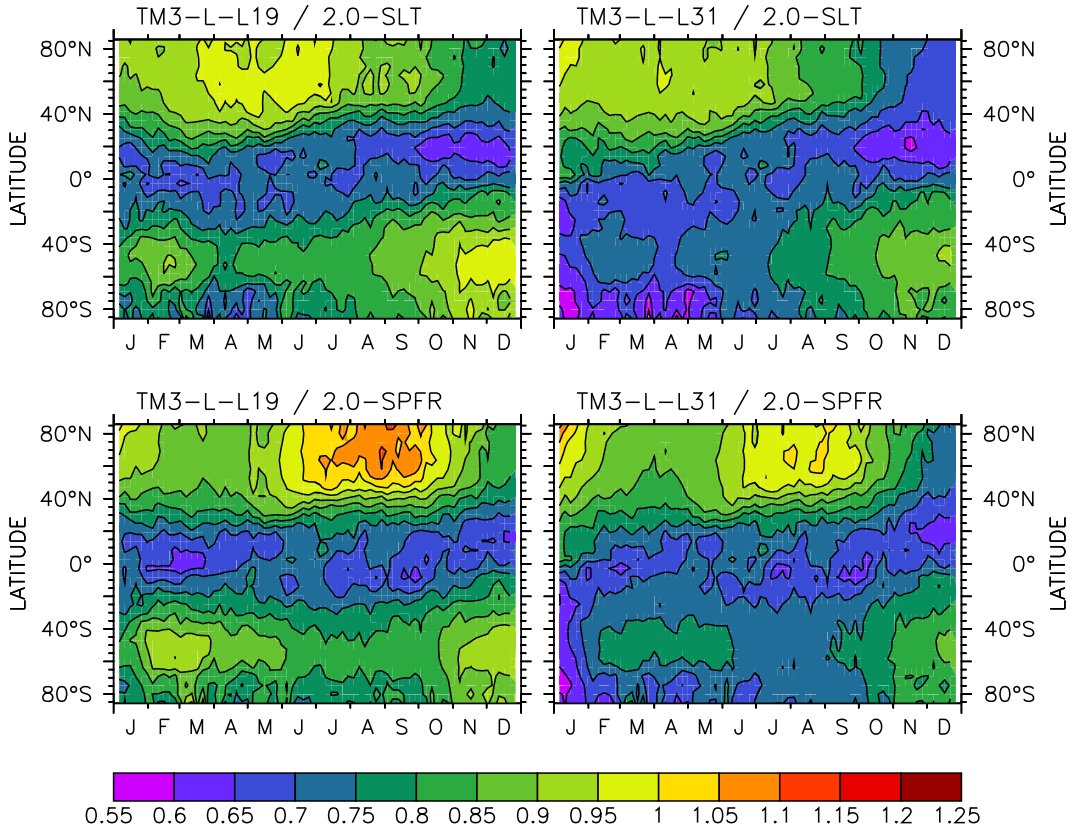

Figure 10.6: Zonal mean ratio of ^{14}CO mass mixing ratio at the surface level between results calculated with various model configurations of MATCH and TM3. The mass mixing ratios are normalized to an annual global average ^{14}CO production rate of 1 molec cm^{-2} s^{-1} in the respective model atmosphere.

almost constant, and rather tends to decrease towards the north pole. The level of the ^{14}CO mixing ratio during March/April and September/October predicted by the two MATCH configurations is higher than predicted by the two TM3 configurations, except at high northern latitudes during NH autumn, where the results of 2.0-SPFR and TM3-L-L19 are almost identical. Moreover, the difference between the TM3 configurations with respect to the latitudinal gradient of ^{14}CO in spring and autumn is most pronounced at high SH latitudes.

To further investigate the surface level ^{14}CO mixing ratio and its seasonality, Figure 10.6 shows a comparison of the simulated results. Compared to the 2.0-SLT configuration of MATCH, TM3 predicts generally lower ^{14}CO mixing ratios at the surface level (Figure 10.6, upper). The discrepancy between 2.0-SLT and TM3, however, further depends on the latitude, the season, and the vertical resolution of TM3.

The difference between the simulated ^{14}CO mixing ratio at the surface level in 2.0-

SLT and TM3-L-L19 is largest in the tropics, where TM3-L-L19 predicts 25% to 35% lower mixing ratios than 2.0-SLT, almost independent of the season. At higher latitudes the TM3-L-L19 predicted ^{14}CO mixing ratio at the surface level is lower than the 2.0-SLT result by 5% to 35% depending on the hemisphere and the season. In the NH, the smallest discrepancy of 5% between TM3-L-L19 and 2.0-SLT occurs between April and July, the largest discrepancy of 25% in winter. In the SH, the TM3-L-L19 mixing ratio is lower than the 2.0-SLT mixing ratio by 5% in December around 50^{o}S, up to 35% at high latitudes between March and May, the latter being comparable to the situation in the tropics.

With increasing vertical resolution of TM3, the discrepancy between MATCH and TM3 also increases, i.e., TM3-L-L31 predicts lower surface level ^{14}CO mixing ratios than TM3-L-L19. This can be seen for instance in the NH north of 40^{o}N. There, the TM3-L-L19 predicts 0% to 25% lower mixing ratios, TM3-L-L31 however, 5% to 35% lower mixing ratios than 2.0-SLT. In the SH during the second half of the year, this effect of the vertical resolution is similar. The TM3-L-L19 predicted mixing ratio south of 40^{o}S is 0% to 25% lower than the 2.0-SLT predicted mixing ratio, whereas the TM3-L-L31 results are 10% to 30% lower than the 2.0-SLT results. During the first half of the year, however, the effect of the vertical resolution on the SH ^{14}CO mixing ratio at the surface level is even larger. The mixing ratio simulated with TM3-L-L19 is 5% to 25% lower than the 2.0-SLT result, whereas the TM3-L-L31 result is at least 25% lower than the 2.0-SLT result.

Comparison of the TM3 results with the 2.0-SPFR results generally shows a similar picture concerning the latitudinal and seasonal differences between the MATCH and TM3 simulated ^{14}CO mixing ratio at the surface level (Figure 10.6, lower). The TM3 predicted ^{14}CO mixing ratio at the surface level tends to be overall lower than the 2.0-SPFR result, however with one exception. At latitudes north of 40^{o}N between July and September, the TM3 predicted mixing ratio is higher than the 2.0-SPFR predicted. This is more pronounced for the lower vertical resolution (TM3-L-L19) compared to TM3-L-L31.

10.3.3.2 Vertical distribution of ^{14}CO To assess the differences in the simulated vertical distribution of ^{14}CO and its seasonality from the various model configurations, Figure 10.7 shows the zonally averaged ^{14}CO mixing ratio in March/April, and Figure 10.8 shows the simulated mixing ratio for the period September/October.

The general characteristics of the vertical ^{14}CO distribution are independent of the model configuration and the season (cf. chapter 5). The maximum mixing ratio in a particular hemisphere is located in the lowermost stratosphere, where the main

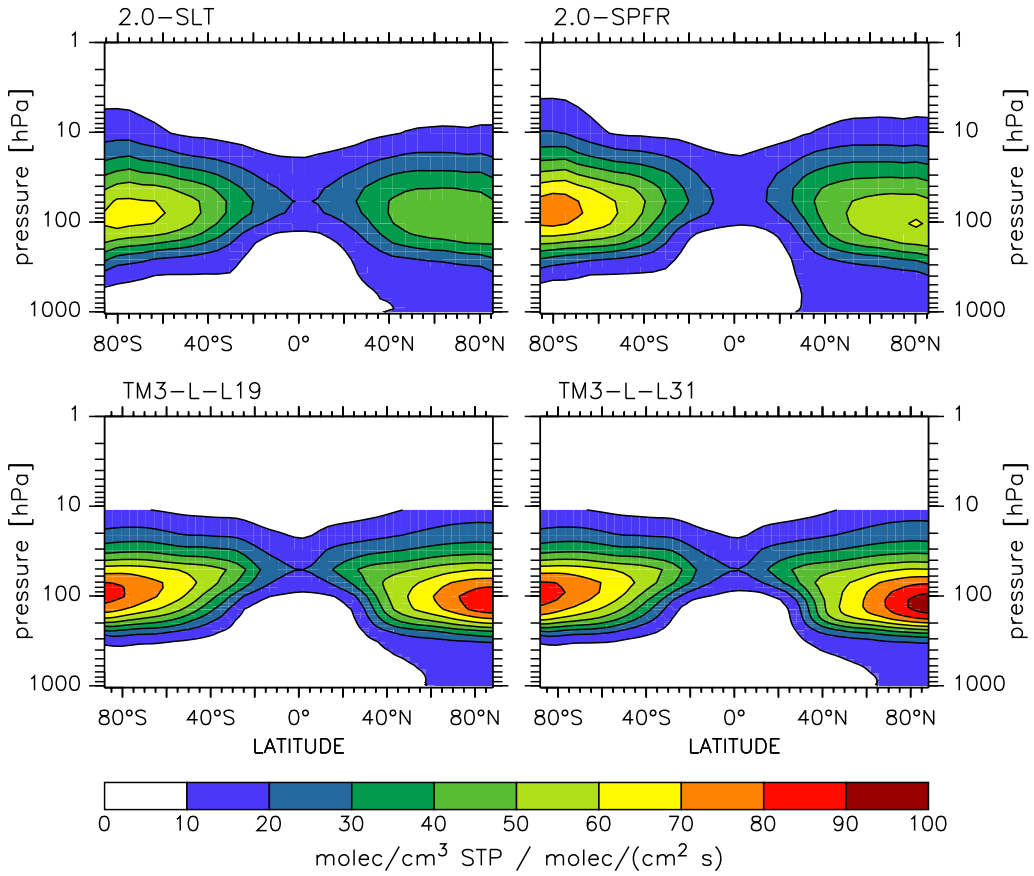

Figure 10.7: Zonal mean ^{14}CO mass mixing ratio averaged over the period March/April calculated with various model configurations of MATCH and TM3. The mass mixing ratios are normalized to an annual global average ^{14}CO production rate of 1 molec cm^{-2} s^{-1} in the respective model atmospheres.

source of ^{14}CO is located. The absolute value of this maximum exhibits a seasonal cycle. The mixing ratio in the troposphere is a factor of 5 to 10 lower than the lowermost stratospheric maximum.

The most distinctive indicator of differences between the particular configurations is the maximum of the simulated ^{14}CO mixing ratio in the lowermost stratosphere, its seasonality, and its interhemispheric difference. For the period March/April (Figure 10.7) the MATCH configurations predict a stronger stratospheric maximum of ^{14}CO in the SH compared to the NH maximum. This interhemispheric difference is more pronounced in 2.0-SLT than in 2.0-SPFR. In contrast to that, TM3 predicts no significant interhemispheric difference (TM3-L-L19) or, with the higher vertical resolution, a reversed difference with a larger maximum in the NH than in the SH. Furthermore, the TM3 predicted stratospheric maxima are larger than the MATCH predicted maxima in both hemispheres.

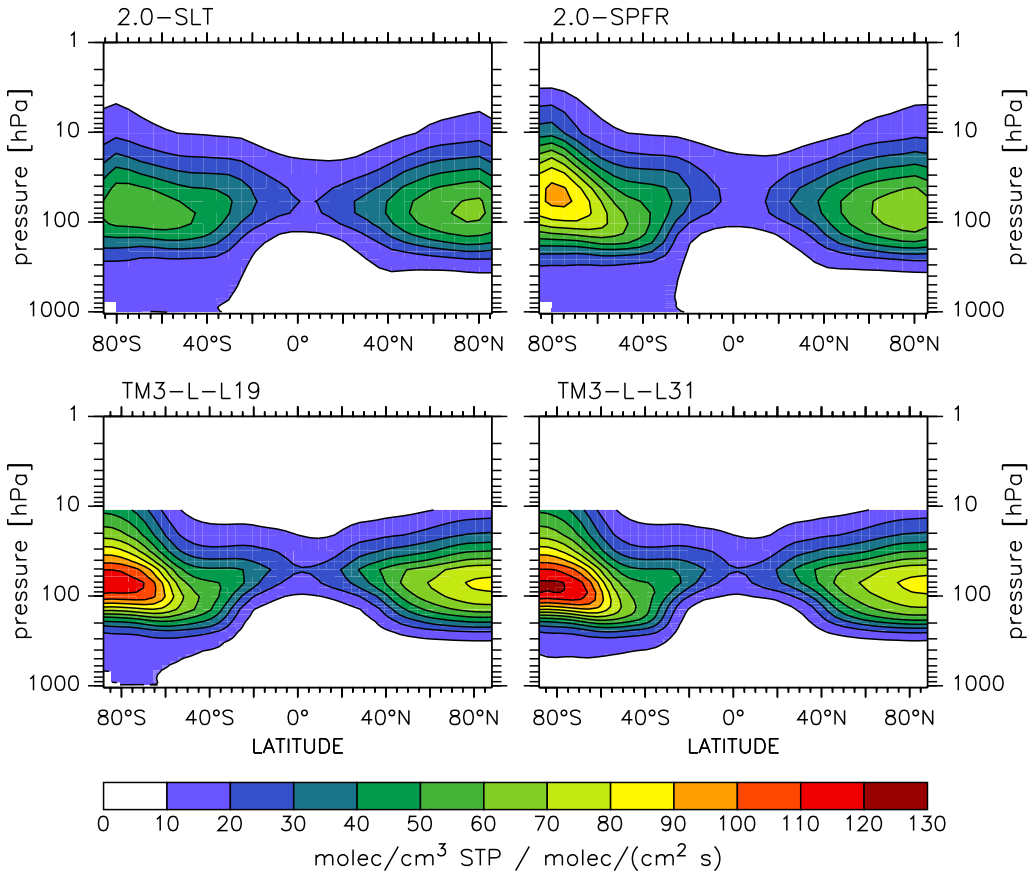

Figure 10.8: Same as Figure 10.7, except for the period September/October.

In September/October (Figure 10.8) the situation is different. All model configurations, except 2.0-SLT, predict a larger stratospheric maximum of ^{14}CO in the SH. This interhemispheric difference is most pronounced in TM3-L-L31, followed by TM3-L-L19, i.e., with the lower vertical resolution, and by 2.0-SPFR. The 2.0-SLT configuration simulates a reversed interhemispheric difference for this period with a larger maximum in the NH stratosphere, compared to the SH maximum. As for the period March/April, the stratospheric maxima in both hemispheres are larger when simulated with TM3 compared to the MATCH results.

The complete simulated annual cycle of the zonally averaged maximum ^{14}CO mixing ratio is shown in Figure 10.9. The vertical maximum in the tropics is almost constant throughout the year and of similar magnitude in all configurations, except for 2.0-SPFR, where the equatorial vertical maximum is about 30% lower compared to the other configurations. The latitudinal gradient of the vertical maximum is weakest in 2.0-SLT compared to the other configurations.

North and south of 40^o distinctive differences between the simulated vertical maximum ^{14}CO mixing ratios of the particular configurations are present. At these

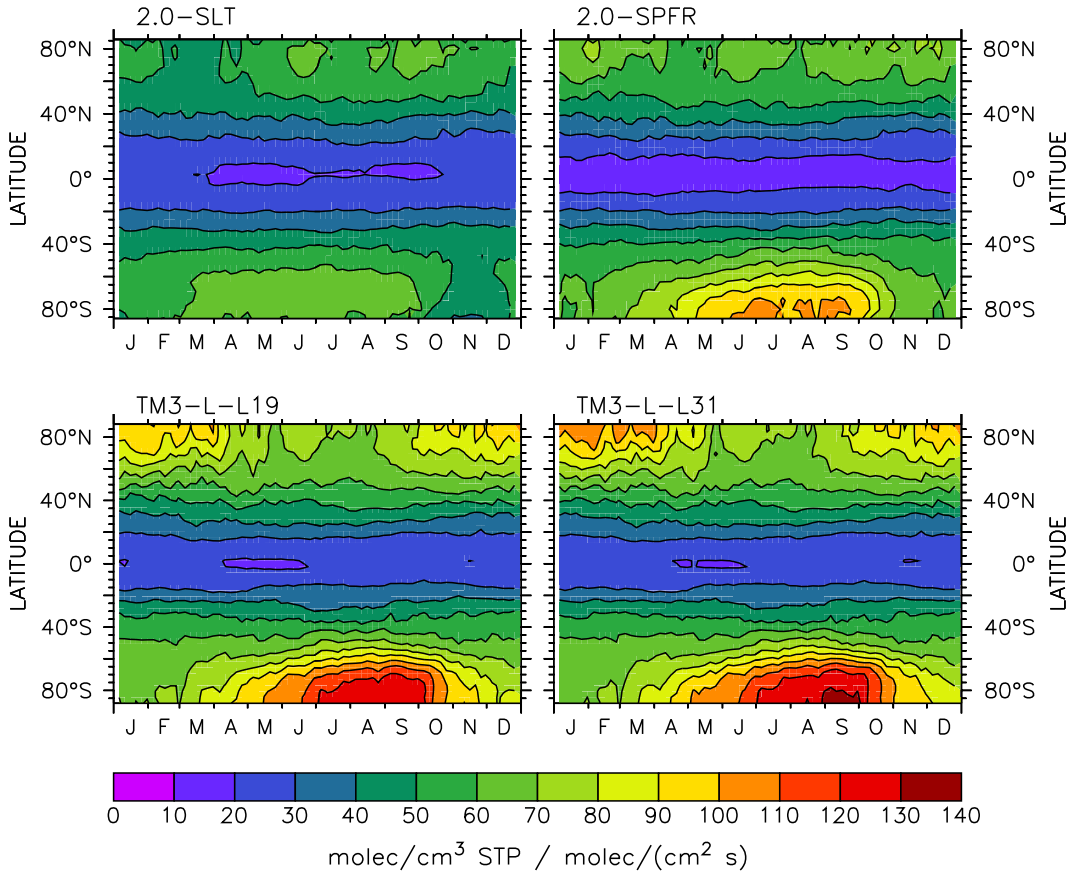

Figure 10.9: Vertical maximum of the zonally averaged ^{14}CO mass mixing ratio calculated with various model configurations of MATCH and TM3. The mass mixing ratios are normalized to an annual global average ^{14}CO production rate of 1 molec cm^{-2} s^{-1} in the respective model atmospheres.

latitudes and a given time, the TM3 predicted vertical maximum tends to be larger than the MATCH predicted vertical maximum of ^{14}CO. Moreover, TM3 predicts an annual oscillation of the absolute vertical maximum between NH and SH, with the absolute maximum in the SH between June and September, and the lower NH maximum between December and May. This characteristic is most pronounced in TM3-L-L31. The 2.0-SPFR configuration predicts a similar annual cycle in the SH; however it is less distinct, and there is almost no discernible annual cycle in the NH. Furthermore, the SH vertical maximum of ^{14}CO is larger than or equal to the NH maximum throughout the year when simulated with 2.0-SPFR. The annual cycle of the vertical maximum ^{14}CO mixing ratio at high latitudes predicted by 2.0-SLT is very weak (within ±20%). In addition, in the NH there is no distinct maximum between December and May, because the vertical maximum ^{14}CO mixing ratio is of similar magnitude in June/July and September/October.

10.3.3.3 The simulated stratosphere - troposphere exchange The analysis so far provides several indications that the simulated downward transport of ^{14}CO from the main source region to the surface level, i.e., the stratosphere - troposphere exchange (STE), substantially differs between the various model configurations. This is investigated further in this section.

The first issue to be addressed is the simulated tropopause pressure. In the MATCH simulations the tropopause pressure of the NCEP reanalysis meteorology 1993 [*Kalnay et al.*, 1996] is used offline. This tropopause pressure is, however, in good agreement with the online diagnosed tropopause pressure according to the WMO definition [*WMO*, 1992] (cf. section 1.5). In the TM3 simulation the tropopause pressure is diagnosed online according to the WMO definition [*WMO*, 1992], based on the driving meteorological ECMWF data. Therefore, differences between the MATCH and the TM3 simulated tropopause pressure can be expected. Figure 10.10 shows a comparison of the tropopause pressure diagnosed with TM3-L-L31 and the NCEP-reanalysis pressure, both for the year 1993. At first sight, the annual cycle of the zonal averaged tropopause pressure simulated by TM3 and the respective NCEP reanalysis data are very similar, especially in the NH (Figure 10.10, upper row). The most striking difference between TM3 and NCEP occurs in the tropics between June and September, where the NCEP tropopause exhibits more variability and tends to be lower (at higher pressure) than the TM3 diagnosed tropopause. During the same period, TM3 diagnoses the tropopause at lower pressure levels compared to NCEP, also at higher SH latitudes. In both cases, the tropopause pressure at high SH latitudes exhibits a strong seasonal cycle. Between July and October, the tropopause level near the south pole is temporarily comparable to the tropical tropopause level. This characteristic is most probably not realistic. Since it occurs in both models, however, either the tropopause is not well defined, or the NCEP and ECMWF reanalysis data share similar shortcomings concerning the tropopause, i.e., errors in the vertical temperature gradient.

The regression analysis of the tropopause pressure shows that TM3 generally tends to predict a higher tropopause pressure than NCEP, with one exception. At high tropopause pressures, i.e., at high latitudes, the situation is reversed, and the NCEP tropopause is below (at higher pressure) the TM3 tropopause. The correlation coefficient R^2 between the NCEP tropopause pressure and the TM3 diagnosed tropopause pressure is on average about 0.8, and larger than 0.7 with four exceptions, three of which occur during June to August, when the NCEP tropopause exhibits a large short term variability compared to the TM3 tropopause.

As already discussed in chapter 5, the relative distribution of the simulated global atmospheric burden of ^{14}CO and especially the differences between different models reveal information about the simulated STE rate (cf. Figures 5.7 and 5.8). Fig-

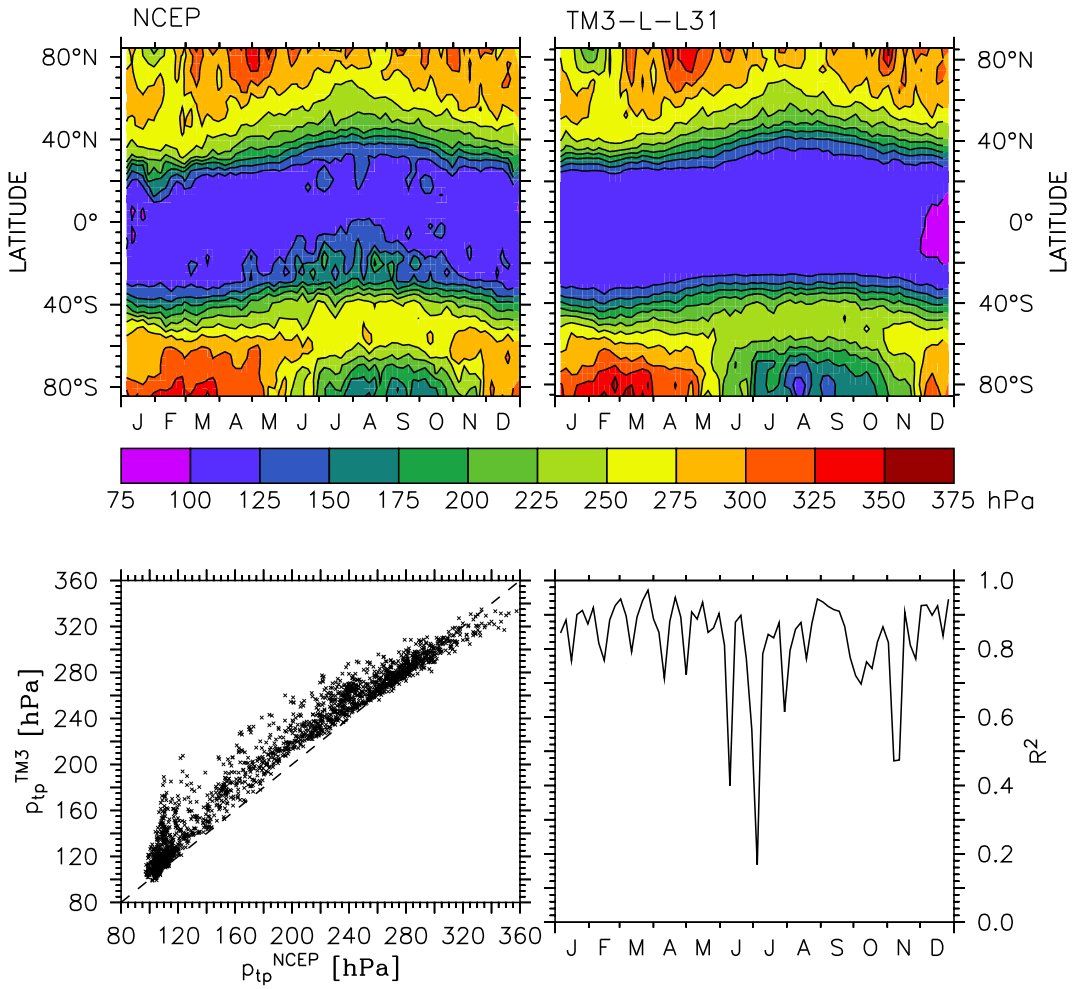

Figure 10.10: Zonal mean tropopause pressure diagnosed by the TM3-L-L31 configuration (upper right) compared to the NCEP-reanalysis tropopause pressure (upper left). The TM3 result is re-gridded on the MATCH-grid and directly compared for all model columns (5-day averages) by a linear regression analysis (lower left). R^2 is the square of Pearson's correlation coefficient (lower right, cf. Eq. (8.2)).

ure 10.11 shows the relative atmospheric burden distribution simulated with various model configurations. As already found for the MATCH simulations (cf. chapter 5), the global atmospheric burden predicted by TM3 also does not vary more than 3% around the annual average.

The increased vertical resolution of TM3-L-L31 hardly affects the burden distribution compared to TM3-L-L19. Similarly, the mass mismatch rescaling implemented in 2.0-SPFR does not significantly alter the distribution of the simulated global ^{14}CO burden compared to the uncorrected configuration (2.0-SPF). However, the differences in the global ^{14}CO mass distribution between MATCH and TM3 are considerable, and larger than the respective differences between the semi-Lagrangian

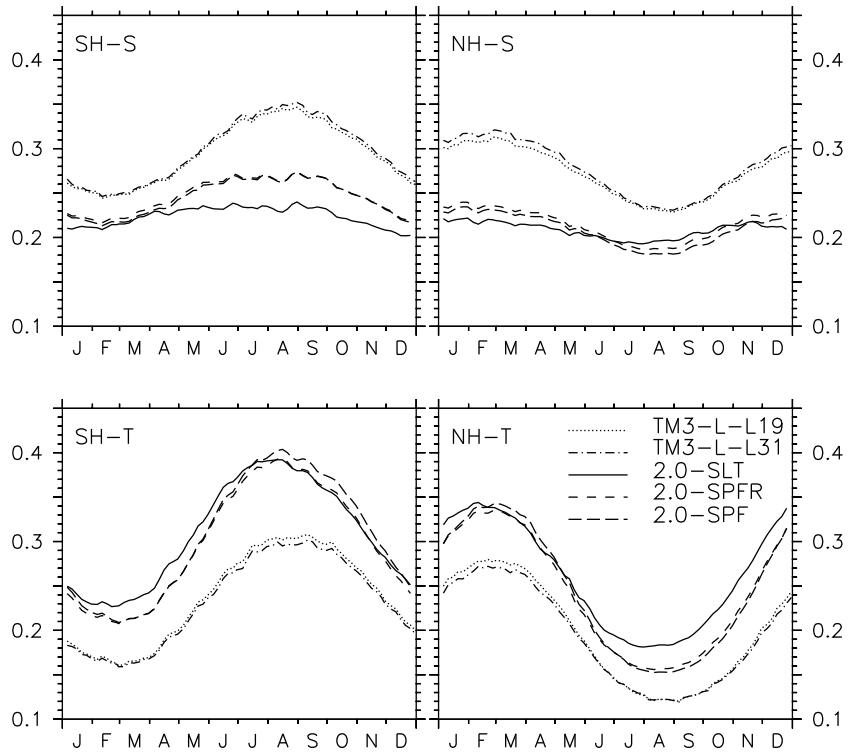

Figure 10.11: Annual cycle of the atmospheric ^{14}CO burden fraction in the southern hemisphere stratosphere (SH-S), the northern hemisphere stratosphere (NH-S), the southern hemisphere troposphere (SH-T), and the northern hemisphere troposphere (NH-T), calculated with various configuration and the ^{14}CO source distribution from *Lingenfelter* [1963] (LF) for solar minimum conditions. The tropopause in TM3-L-L31 is online diagnosed according to the WMO definition [*WMO*, 1992]. For TM3-L-L19, the diagnosed tropopause of TM3-L-L31 is assumed. Simulations with the MATCH configurations employ the NCEP reanalysis [*Kalnay et al.*, 1996] tropopause pressure for the year 1993 (daily averages, offline). The annual variability of the total atmospheric burden in all cases is less than ±3% around the annual average.

and SPITFIRE configurations of MATCH.

Generally, TM3 predicts a larger stratospheric fraction of the ^{14}CO burden than MATCH. The annual cycle of the tropospheric burden fraction in both hemispheres is, apart from the different level, similar in both models and clearly related to the OH seasonality. In the stratosphere the seasonal cycle of the ^{14}CO burden fraction is in phase with the tropospheric cycle of the respective hemisphere. This is likewise to be attributed to the stratospheric OH seasonality. However, in contrast to the phase, the amplitude of the stratospheric burden fraction and the shape of the curve differ between MATCH and TM3. The stratospheric seasonal cycle amplitude predicted by MATCH is smaller than the amplitude predicted by TM3, with the smallest amplitude being predicted by 2.0-SLT. Moreover, the TM3 simulated

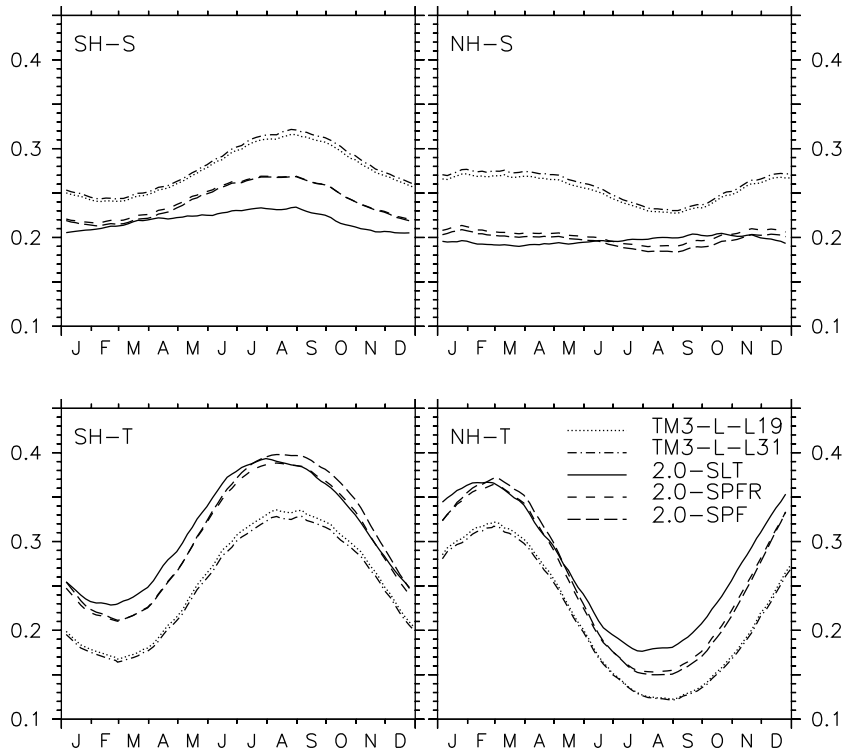

Figure 10.12: Same as Figure 10.11, except using the climatological mean tropopause ($(300 - 215 \cdot cos^2(\phi))$ hPa, where ϕ is latitude, see section 1.5).

stratospheric burden fraction is almost sinusoidal, whereas the MATCH simulated fraction exhibits a broad maximum in both hemispheres (cf. chapter 5, Figures 5.7 and 5.8).

In order to estimate the influence of differences in the tropopause diagnostic on these results, the analysis is repeated, however with the climatological mean tropopause (Eq. (1.10)) dividing the stratosphere and the troposphere. The result is shown in Figure 10.12. The results are qualitatively the same as discussed for Figure 10.11. However, using the climatological tropopause reduces the stratospheric burden in TM3 and thus increases the tropospheric burden, bringing it into closer agreement with the MATCH results. The SH fraction of the global atmospheric ^{14}CO burden simulated by MATCH hardly changes when the climatological tropopause is used instead of the NCEP tropopause. In the NH, the stratospheric fraction is mainly reduced during the time of the maximum (between November and May), in favor of an enhanced tropospheric fraction. Therefore, the NH stratospheric amplitude becomes smaller, this fraction simulated by MATCH is almost constant throughout the year when the climatological tropopause is assumed. This effect occurs for the TM3 results in both hemispheres. The stratospheric fraction during the time of the maximum (NH: November to May, SH: June to October) is reduced, the respective

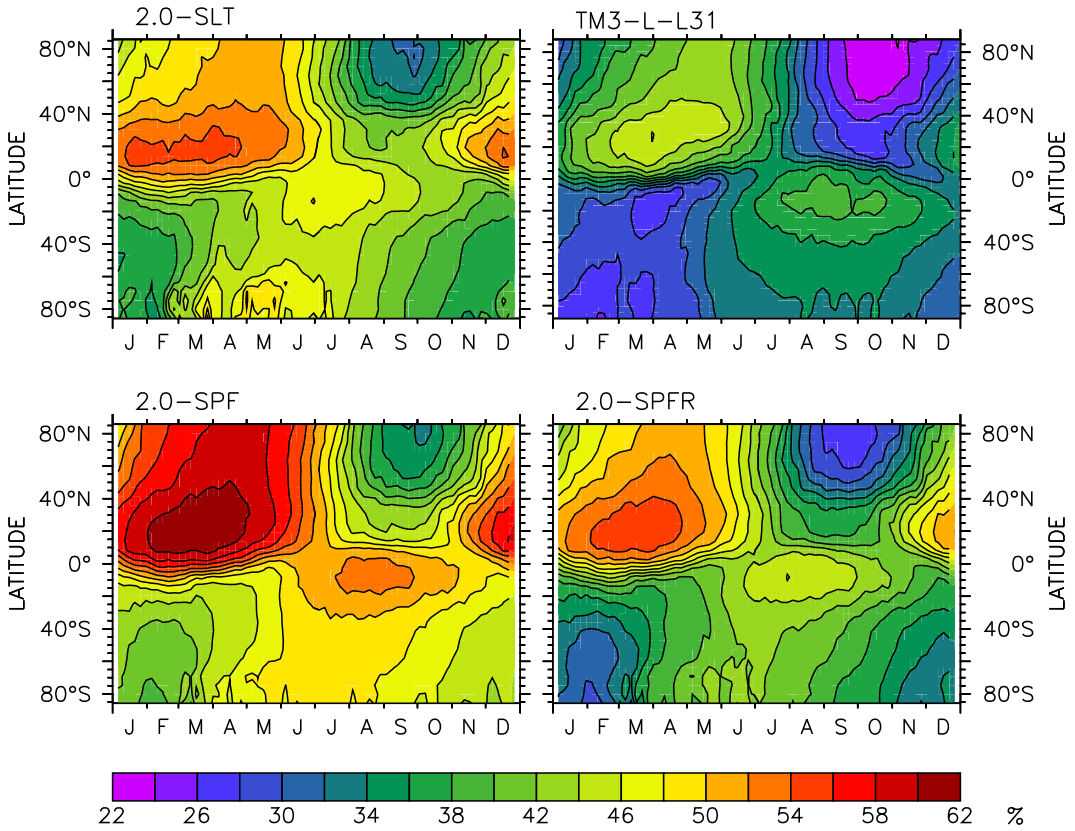

Figure 10.13: Zonal average fraction of stratospheric ^{14}CO at the surface level calculated with various model configurations. The tropopause is diagnosed online according to the WMO definition [*WMO*, 1992] (TM3-L-L31), and prescribed by the NCEP reanalysis tropopause pressure of the year 1993 [*Kalnay et al.*, 1996] (2.0-SLT, 2.0-SPF, 2.0-SPFR, see section 1.5).

tropospheric maximum is increased. As a consequence the TM3 simulated amplitude of the stratospheric fraction is reduced, and the tropospheric amplitude becomes enlarged. In this case, also the TM3 simulated NH stratospheric burden fraction exhibits a broad maximum.

Finally, the seasonal cycle and the strength of the STE is estimated by the results of tracing ^{14}CO that is produced in the stratosphere (χ_{st}) separately from ^{14}CO that is produced in the troposphere (χ_{tr}). A measure of the influence of the STE on the ^{14}CO mixing ratio at a given time and location in the troposphere is the fraction of stratospheric ^{14}CO, i.e.,

$$f_s = \frac{\chi_{st}}{\chi_{st} + \chi_{tr}} \ . \tag{10.7}$$

The zonal average of this fraction at the surface level is shown in Figure 10.13 for various model configurations. The fraction of ^{14}CO at the surface level originating from the stratosphere exhibits a distinct seasonal cycle and is dependent on latitude for

all model configurations. At a given time and location, the fraction of stratospheric ^{14}CO at the surface level is lower when simulated with TM3-L-L31 in comparison to MATCH. The TM3-L-L31 simulated fraction ranges from 22% at high northern latitudes in autumn, when the surface level mixing ratio of ^{14}CO is at its minimum, to 46% in the NH lower latitudes during the spring maximum (cf. Figure 10.4). In the MATCH simulations these extrema of stratospheric ^{14}CO at the surface level occur at the same time and latitude as in TM3, but are different in magnitude. The highest stratospheric fraction of surface level ^{14}CO is predicted by 2.0-SPF, ranging from 32% to 62%. The ranges predicted by 2.0-SLT and 2.0-SPFR are 30% to 56%, and 26% to 56%, respectively, and therefore lower than that of 2.0-SPF.

The overall seasonality and latitude dependence of the stratospheric fraction of ^{14}CO at the surface level is similar in all of the MATCH configurations tested. This also holds for the TM3-L-L31 simulation in the NH. In the SH, in contrast, the TM3-L-L31 simulation exhibits an additional characteristic. In TM3-L-L31, the SH seasonal cycle of the stratospheric fraction of surface level ^{14}CO is quasi the NH cycle mirrored along the equator and phase shifted by half a year. Furthermore, the maximum stratospheric fraction is somewhat reduced, and the minimum stratospheric fraction somewhat enhanced in the SH. This implies another local maximum of the stratospheric fraction in the SH lower latitudes in SH spring, and likewise another local minimum in the SH tropics in SH autumn. This effect is also present, but less pronounced, in the SPITFIRE based simulations of MATCH, and almost invisible in the 2.0-SLT simulations. Furthermore, the MATCH simulations do not show the local autumn minimum in the tropics of both hemispheres, but rather a minimum at high latitudes.

10.4 Discussion: The simulated STE

Sharing the same ^{14}CO production rate distribution, global source strength and OH distribution, differences in the simulated ^{14}CO mixing ratio between different model configurations can only arise from differences in the tracer transport realization, such as the advection algorithm, the meteorological data, and the grid resolution.

Since the prescribed source strength is constant in time, production and loss of ^{14}CO in the model atmosphere tend towards equilibrium. As a consequence, the temporal variation of the global atmospheric burden of ^{14}CO is rather low, below 3% around the annual average. The absolute value of the simulated atmospheric burden of ^{14}CO for a given source strength of ^{14}CO is unambiguously determined by the OH abundance and distribution, and by the tracer transport.

This effect is particularly distinctive in TM3 when the horizontal grid resolution is

changed. Doubling the grid points in the latitudinal and the longitudinal direction (from TM3-L-L19 to TM3-H-L19), different ^{14}CO mixing ratios are predicted at the surface level (Figure 10.2). At the same time, the lowermost stratospheric minimum in both hemispheres decreases (Figure 10.2). Moreover, the equilibrium global atmospheric burden of ^{14}CO is reduced (Figure 10.1) Thus, at the higher horizontal resolution ^{14}CO is more effectively transported from the main source region in the lowermost stratosphere towards the main sink region in the troposphere.

This explanation is in agreement with the results of *van Velthoven and Kelder* [1996], who found that "the evaluated total amount of air transferred from the stratosphere to the troposphere per month is sensitive to the chosen horizontal resolution." *van Velthoven and Kelder* [1996] estimated with TM3 a 10% larger STE downward mass flux of air on the finer grid, compared to the coarser grid. They attributed this to a better representation of small scale processes that contribute significantly to the STE on the finer grid, which are, however, not resolved on the coarser grid. Furthermore, this enhancement of the downward flux of air was found to be almost constant throughout the year, i.e., the seasonality of the global air mass flux across the tropopause is hardly affected by the horizontal model resolution. In contrast to that, the effect of the on average enhanced downward flux calculated with the higher horizontal resolution on the atmospheric ^{14}CO mixing ratio at the surface level exhibits a seasonal (and latitudinal) variation. The change of the surface level ^{14}CO mixing ratio with increasing horizontal resolution ranges from -5% to 15% (Figure 10.2, lower left), not taking into account the differently simulated global atmospheric burden. Although ^{14}CO is a reactive tracer compared to air itself, which can be regarded as an inert tracer, the relative change of the surface level ^{14}CO when the STE is changed is independent of the tropospheric OH concentration. The reason is that the reaction of ^{14}CO with OH is of first order. In other words, feeding 10% more ^{14}CO from the stratosphere into the troposphere results in a 10% increase in the stratospheric contribution to the mixing ratio at the surface level. The tropospheric source, however, is not changed and therefore the tropospheric contribution to the simulated surface level ^{14}CO mixing ratio (χ_{tr}) remains the same. As a consequence, the relative change of the simulated ^{14}CO mixing ratio at the surface level provides a measure of the influence of changed STE at a particular latitude and time (Figure 10.2, lower left). The ratio of ^{14}CO mixing ratios is related to the stratospheric fraction of ^{14}CO at a given time and location (Eq. (10.7)) by

$$\frac{\chi'}{\chi} = \frac{1 - f_s}{1 - f'_s} \,, \tag{10.8}$$

where the prime denotes the changed grid.

For further interpretation of the results obtained by variation of the horizontal grid

resolution, however, two limitations have to be considered. First, the results obtained are not representative for the equilibrium state of the model atmosphere with respect to the atmospheric burden, since only the first year after initialization with zero ^{14}CO mixing ratio is available. And second, the simulated atmospheric burden of ^{14}CO in equilibrium differs significantly between the two resolutions. The latter issue can be resolved by renormalization of the results obtained on different grids to the same global atmospheric burden. This leads to an overall higher STE on the grid with higher horizontal resolution compared to the lower horizontal resolution. Ignoring the first issue, the influence of the horizontal grid resolution on the simulated ^{14}CO mixing ratio at the surface level reveals the following characteristics of the simulated STE. Increasing the horizontal resolution in TM3 increases the STE similarly in both hemispheres during the first half of the year. The ratio in the lower left part of Figure 10.2 is almost mirrored with respect to the equator. This is completely different during the second half of the year. At this time, the NH STE is much more enhanced than the SH STE (renormalized to the same global atmospheric burden). According to *van Velthoven and Kelder* [1996] this then implies that small scale processes are much more important for the NH STE than for the SH STE, at least during the second half of the year.

The effect of the vertical grid resolution can be investigated in the same way (Figure 10.3). For these simulations the model is in equilibrium state with respect to the global atmospheric burden of ^{14}CO, since the second year after initialization is analyzed. Furthermore, the simulated equilibrium burden is almost independent of the vertical resolution (Table 10.2). The change in the TM3 predicted surface level ^{14}CO with increasing vertical resolution is in the range of -20% to +10% depending on latitude and season. As discussed above, this can be directly interpreted in terms of an altered STE rate. The simulated SH ^{14}CO mixing ratio at the surface level tends to decrease more than the respective NH mixing ratio when the vertical resolution is increased, implying that the SH STE is more weakened than the NH STE. This is hardly visible in the simulated vertical distribution of ^{14}CO; however, it is sufficient to generate an interhemispheric asymmetry in the spring maximum ^{14}CO mixing ratio at the surface level, with higher values in the NH than in the SH (Figures 10.3 and 10.5). This characteristic is not obtained by any of the MATCH configurations which were examined (see also Figure 10.4).

The simulated annual cycle of the vertical ^{14}CO mixing ratio distribution and the differences between the particular model configurations reveal further information about the simulated tracer transport. TM3 generally predicts higher ^{14}CO mixing ratios in the lowermost stratosphere than MATCH, especially at high latitudes (Figures 10.7, 10.8 and 10.9). At the same time, TM3 tends to predict lower ^{14}CO mixing ratios at the surface level (Figure 10.6), especially in the tropics. Since the

simulations with both models share the same ^{14}CO source distribution and OH distribution, only a difference in the simulated transport can account for this effect. Therefore, the transport of ^{14}CO from the lowermost stratospheric source regions into the tropical tropospheric sink region is less effective in TM3 than in MATCH. Three transport components are to be considered for this effect, namely the STE and further the latitudinal transport in the stratosphere and in the troposphere.

The analysis of the tropospheric response time to variations in the global source strength (chapter 7) unveiled a small detail that differs between MATCH and TM3. The local minima of the tropospheric response times at low latitudes occur between 30^o and 40^o latitude in MATCH, while they are closer to the equator, around 20^o or less in TM3 (Figure 7.5). One of the important conclusions in chapter 7 is that the tropospheric response time is a semi-quantitative measure of the STE rate. A larger STE rate decreases the tropospheric response time to variations in the global source strength. Furthermore, the local response time minimum coincides with the maximum downward flux. This implies that the maximum downward transport of ^{14}CO from the stratosphere into the troposphere in TM3 is located closer to the equator than in MATCH. With decreasing latitude, however, the annual average OH concentration in the simulations increases. As a consequence, in TM3 compared to MATCH, more ^{14}CO is oxidized by OH on its way down in the tropical lower stratosphere and upper troposphere. This is consistent with the shorter global atmospheric lifetime of ^{14}CO, the shorter stratospheric lifetime of ^{14}CO (see Table 7.1), and the lower global atmospheric burden in equilibrium predicted by TM3 compared to MATCH (see Table 10.2). In contrast to this, the STE simulated by MATCH occurs at higher latitudes where the average OH concentration is lower. Moreover the cross tropopause flux is stronger compared to TM3. Less ^{14}CO reaches the tropical stratosphere but is rather transported down into the troposphere. As a consequence, in MATCH more ^{14}CO reaches the tropical troposphere than in TM3 (cf. Figure 10.6). For the TM3 model these results further imply an effective, possibly overestimated, stratospheric horizontal transport of ^{14}CO across the subtropical barrier, from the polar stratosphere to the tropical stratosphere (cf. chapter 9).

The stronger STE in MATCH compared to TM3 results in a higher tropospheric fraction of the global ^{14}CO burden, and likewise in a lower stratospheric fraction (Figures 10.11 and 10.12). The stratospheric fraction of the simulated global atmospheric ^{14}CO burden exhibits a seasonal cycle that differs between the particular model configurations and between the two hemispheres. The annual cycle of the stratospheric OH concentration in both hemispheres is quasi sinusoidal and phase shifted by half a year (Figure 1.6). The prescribed stratospheric OH distribution is common to all model simulations. As a consequence, differences of the stratospheric burden fraction between the hemispheres, apart from the phase shift, and between

different model configurations can only arise from differences in transport, especially STE. All model configurations predict a larger seasonality, i.e., a larger amplitude of the stratospheric burden fraction in the SH compared to the NH (Figure 10.12). Furthermore, the SH cycle is quasi sinusoidal, whereas the NH cycle is disturbed. In the SH, the relative amplitude of the stratospheric fraction predicted by MATCH (except 2.0-SLT) is comparable to that of TM3. In contrast to that, in the NH the seasonality of the stratospheric burden fraction is more pronounced in TM3 than in MATCH. The 2.0-SLT configuration predicts the smallest seasonality in both hemispheres with an almost constant fraction in the NH. These characteristics are directly mirrored in the vertical maximum ^{14}CO mixing ratio at high latitudes (Figure 10.9).

Thus, in the SH stratosphere, the simulated burden fraction and maximum ^{14}CO mixing ratio is driven by the OH seasonality, in much the same way as in the troposphere. The downward transport hardly affects this annual cycle, apart from the amplitude. This holds for TM3 and the SPITFIRE configurations of MATCH; however, in 2.0-SLT the simulated STE of ^{14}CO is much stronger and therefore significantly disturbs the annual cycle of the SH stratospheric burden fraction. For instance, in August/September about one or two months after the OH minimum (Figure 1.6), the stratospheric burden fraction (Figure 10.12) and the stratospheric ^{14}CO mixing ratio (Figure 10.9) are at their maximum, after ^{14}CO accumulated in the SH stratosphere during the months before, due to the decreasing OH concentration. This effect is pronounced in TM3 and 2.0-SPF(R). In 2.0-SLT, in contrast, the ^{14}CO produced in the stratosphere where it is less effectively oxidized due to the decreasing OH concentration, is transported down into the troposphere. This explains the higher fraction of stratospheric ^{14}CO at the surface level predicted by 2.0-SLT compared to TM3 and 2.0-SPFR (Figure 10.13) between April and August, and the lower SH tropospheric burden fraction predicted by 2.0-SLT compared to 2.0-SPFR (Figure 10.12). In TM3 the simulated downward transport of ^{14}CO is rather weak, resulting in a comparably low fraction of stratospheric ^{14}CO at the surface level in the SH (Figure 10.13).

The same mechanism occurs in the NH. Here, in all model configurations the NH seasonal cycle of ^{14}CO is determined by the OH seasonality, overlayed to differing degrees by the STE seasonality. In March/April, the fraction of stratospheric ^{14}CO at the surface level in the NH mid-latitude is at its absolute maximum. Two to three months before that, the NH stratospheric OH concentration was at its minimum, implying that ^{14}CO produced in the stratosphere during NH winter has a temporarily increased lifetime before oxidation. However, the ^{14}CO is not accumulated in the NH stratosphere, as can be seen from the NH stratospheric burden fraction (Figure 10.12), but rather transported down into the troposphere. In August/September

one to two months after the NH stratospheric OH maximum, the NH stratospheric burden reaches its minimum. Less ^{14}CO is available to be transported into the troposphere. As a consequence, the fraction of ^{14}CO of stratospheric origin at the surface level is at its minimum in September/October.

Not only the simulated STE strength, but also the timing differs between the particular configurations. In 2.0-SLT the downward transport of ^{14}CO is stronger and shifted in time. For instance, the extrema of the predicted tropospheric burden (Figure 10.12) in both hemispheres occur about 0.5 to 1 month earlier in the 2.0-SLT simulations compared to the 2.0-SPF(R) and TM3 simulations. Similarly, the maximum of the stratospheric fraction of ^{14}CO at the surface level in both hemispheres occurs earlier in the 2.0-SLT simulations than in the TM3 and 2.0-SPF(R) simulations. Obviously the 2.0-SLT simulated STE is "faster" than that of other configurations. This is fully in agreement with the results obtained in chapter 9, where the downward transport of solar proton event (SPE) induced ^{14}CO was investigated.

The analysis of the response time of atmospheric ^{14}CO to variations in the global source strength (chapter 7) already revealed an interhemispheric asymmetry in the simulated STE, with a stronger STE in the NH. For the model configurations involved in the present analysis, this asymmetry is most pronounced in the 2.0-SPFR configuration, less pronounced in TM3, and least pronounced in 2.0-SLT. These characteristics are mirrored in the distribution of the simulated global atmospheric burden of ^{14}CO (Figure 10.12). Likewise, the fraction of ^{14}CO originating from the stratosphere at the surface level is on average higher in the NH than in the SH (Figure 10.13) for all configurations. Furthermore, the ratio between the NH maximum and the SH maximum of the stratospheric fraction at the surface level also corresponds to the ranking among the model configurations with respect to the interhemispheric asymmetry of the simulated STE.

The above analysis, however, additionally reveals information about the amplitude of the simulated STE seasonal cycle in both hemispheres. Although sharing the same stratospheric OH distribution and seasonality, the particular model configurations predict different amplitudes of the stratospheric burden fraction in both hemispheres (Figure 10.12). Furthermore, the stratospheric OH seasonality is very similar in both hemispheres (cf. Figure 1.6). Since the burden fraction is determined by OH and the STE, the relative amplitude of the stratospheric burden fraction is inversely related to the relative amplitude of STE. Hence, the relative NH seasonal amplitude of the ^{14}CO STE is larger than the relative SH STE amplitude in all configurations. Moreover, the SH seasonal amplitude of STE is predicted to be smallest in TM3, larger in 2.0-SPFR, and largest in 2.0-SLT. In the NH the seasonal amplitude of ^{14}CO STE predicted by MATCH is high enough to compensate the OH driven

seasonality of the stratospheric burden of ^{14}CO, resulting in an almost constant NH stratospheric burden fraction throughout the year (Figure 10.12). This is also simulated in the SH by the 2.0-SLT configuration. As a further consequence, the vertical maximum ^{14}CO concentration is predicted by 2.0-SLT to be almost constant throughout the year in both hemispheres (Figure 10.9). This characteristic is also present in the NH when simulated with 2.0-SPFR, although less distinct.

The issue to be considered is how well the particular model configurations represent the "real" STE. An extensive overview of all relevant aspects with respect to STE is provided by *Holton et al.* [1995]. Still large uncertainties exist. However, the NH STE is generally found to be stronger than the SH STE [*Holton*, 1990; *Holton et al.*, 1995]. *Grewe and Dameris* [1996] and *Holton* [1990] estimated a 50% weaker STE in the SH compared to the NH. Furthermore, *Holton* [1990] found a stronger seasonal variation of the downward mass flux across the 100 hPa level in the NH compared to the SH, "with a three times larger value in winter than in summer, and intermediate values in the equinoctial seasons" [*Holton*, 1990]. *Appenzeller et al.* [1996] also found that the seasonal STE cycle is generally weaker, i.e., with a lower relative amplitude in the SH than in the NH. Furthermore, the seasonality of the mass flux across the 100 hPa level is basically confirmed by *Appenzeller et al.* [1996]. The resulting mass transport across the tropopause in the NH exhibits a maximum in late spring, a secondary maximum in mid winter, and a distinct minimum in autumn. The weaker SH seasonal STE cycle exhibits the maximum downward mass flux across the tropopause in mid winter [*Appenzeller et al.*, 1996]. This is the result of two components contributing to the STE: Whereas the SH annual variation of the downward mass flux across the tropopause in the SH is dominated by the mass flux across the upper boundary of the lowermost stratosphere, in the NH a substantial contribution to the downward mass flux is provided by the tropopause height variation [*Appenzeller et al.*, 1996]. And finally, *Grewe and Dameris* [1996] showed that the downward mass flux from the stratosphere into the troposphere occurs primarily between 25^oN and 40^oN, and 30^oS and 50^oS respectively, with a small inter-annual variability of the exchange pattern.

More exact estimates of the STE (e.g., the absolute mass flux) are hampered for several reasons. Estimates of the absolute mass flux are considerably dependent on the tropopause definition [*Holton et al.*, 1995; *Grewe and Dameris*, 1996] (see also Figures 10.11 and 10.12). Furthermore, the contribution of particular meteorological processes (see e.g., *Shapiro* [1980]; *Ebel et al.* [1996]) on different scales to the global STE is not yet fully understood [*Holton et al.*, 1995]. Moreover, the exchange of chemical constituents is not necessarily directly related to the air mass exchange, because it further depends on correlations between the tracer mixing ratios and the air mass flow, caused for instance by seasonal variations in the source and/or sink

distribution of the tracer [*Holton*, 1990; *Appenzeller et al.*, 1996; *Holton et al.*, 1995]. As a consequence, the influence of stratospheric ozone to tropospheric ozone levels is still an issue of research [*Roelofs and Lelieveld*, 1997].

Nevertheless, the STE rate calculated by *van Velthoven and Kelder* [1996] with the TM3 model driven by the ECMWF reanalysis meteorology exhibits the main characteristics of STE, i.e., the interhemispheric asymmetry of the downward flux, its relative annual amplitude, and the seasonality of STE are in considerable qualitative agreement with the present understanding of STE. The discussion above indicates that the main downward flux in TM3 probably occurs too close to the equator. The simulated maximum downward transport of ^{14}CO occurs around 20^o in both hemispheres. Since the main source of ^{14}CO is located in the lower stratosphere at high latitudes, the downward flux of air (with no latitudinal gradient) in TM3 can be expected even at lower latitudes.

The inter-comparison of TM3 and MATCH in different configurations shows that the MATCH model driven by the NCEP reanalysis meteorology also exhibits the main characteristics of STE. The intensity of these characteristics, however, depends on the particular model configuration. Differences between the configurations can be used to estimate the influence of STE on the simulated tropospheric ^{14}CO mixing ratio. Comparison with measurements of ^{14}CO can then be used to rule out certain aspects of STE.

The seasonality of ^{14}CO in the troposphere is primarily driven by the tropospheric OH seasonality, but disturbed by the seasonally varying input of ^{14}CO from the stratosphere. This input in turn is determined by the seasonality of the downward flux (i.e., the strength of STE) and the seasonality of stratospheric OH. Figure 10.14 shows the seasonality of the STE as calculated by *Appenzeller et al.* [1996], in comparison with the seasonality of the stratospheric and tropospheric OH abundance in the simulations (OH-1). Both amplitude and phase lag of the downward mass flux relative to the OH abundance substantially differ between the two hemispheres. In the SH the STE flux is largest when OH is at its minimum, i.e., shortly before ^{14}CO reaches its maximum. Therefore the SH stratospheric burden is reduced in favor of an enhanced tropospheric burden. In SH summer, when OH is at its maximum, the SH STE rate is at its minimum. The phase lag of almost exactly half a year between STE rate and tropospheric and stratospheric OH explains the quasi sinusoidal signal of the stratospheric ^{14}CO and tropospheric burden fraction in the SH (Figure 10.12) with a generally lower stratospheric burden fraction. In the NH the situation is more complicated. Here the phase lag between STE and OH is about 3 to 4 months. Again the superposition of the OH seasonality and the STE seasonality determines the stratospheric burden fraction. This explains the broad maximum of the stratospheric burden fraction, which is, however, smaller than in

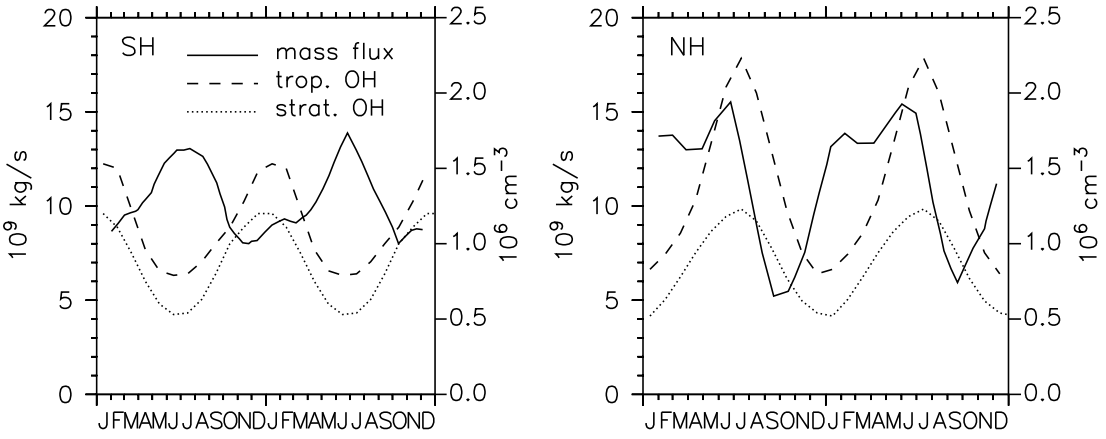

Figure 10.14: Seasonal cycle of STE (downward mass flux of air in 10^9 kg s^{-1}) calculated by *Appenzeller et al.* [1996] for the years 1992/1993, and seasonal cycle of stratospheric and tropospheric OH (in 10^6 cm^{-3}) as used in the simulations (OH-1), for the southern hemisphere (SH) and the northern hemisphere (NH).

the SH (Figure 10.12). In the troposphere compared to the stratosphere, the effect of the STE seasonality on the burden fraction is less visible, since the tropospheric OH is dominating the seasonal cycle.

In this context two more characteristics are interesting to be noted. First, the tropospheric minimum of ^{14}CO at the surface level seems to follow the simulated ITCZ (cf. Figures 10.4 and 10.5). The seasonally varying location of this minimum may therefore be used to define the simulated ITCZ in the model. And second, the simulated seasonal cycle of ^{14}CO at the surface level in the SH is not exactly phase shifted by half a year compared to the NH annual cycle (Figure 10.4). The NH maximum is reached in March/April, the SH minimum one to two months earlier in February. Similarly, the NH minimum is reached in August, one to two months earlier than the SH maximum in September/October. This furthermore implies that in both hemispheres the time interval between maximum and minimum is about two months shorter (5 months) than the time interval between minimum and maximum (7 months). This may easily be verified by measurements of ^{14}CO.

Finally, it should be noted that the fraction of stratospheric ^{14}CO at the surface level simulated by the 2.0-SPF configuration (Figure 10.13, lower left) suffers from the artificial source component (mass mismatch, see chapter 2), because according to Eq. (10.5) the stratospheric fraction is renormalized to the total ^{14}CO mixing ratio in every time step. Since the mass mismatch in 2.0-SPF is, however, dependent on the vertical tracer gradient, the ^{14}CO produced in the stratosphere (χ_{st}) is may be differently affected than the ^{14}CO produced in the troposphere (χ_{tr}). Nevertheless, the overall pattern of the zonally averaged fraction of stratospheric ^{14}CO at the surface

level is, apart from the level, similarly simulated by all MATCH configurations tested here.It differs, however, considerably compared to the TM3 result (Figure 10.13). This is possibly an indication that the simulated STE is more dependent on the offline data driving the advection in the model than on the advection algorithm itself. At this stage, however, this can only be taken as an indication, since TM3 also uses a different advection algorithm than MATCH. Future model simulations with MATCH using ECMWF data and the semi-Lagrangian and the SPITFIRE advection scheme could help to clarify this. At the time of the present analysis, the ECMWF data were unfortunately not available for the MATCH simulations.

10.5 Conclusions

Various configurations of MATCH and TM3 were tested with particular attention to the simulated stratosphere - troposphere exchange (STE) of ^{14}CO. All model configurations more or less represent the basic characteristics of STE according to the present knowledge. The interhemispheric asymmetry of STE with a higher exchange rate in the NH is most pronounced in the 2.0-SPFR configuration, least pronounced in 2.0-SLT, and intermediate in TM3. Furthermore, the seasonal amplitude of STE in all tested model configurations is larger in the NH than in the SH. Overall, MATCH predicts a stronger STE flux of ^{14}CO than TM3. These results basically confirm the results obtained from the analysis of the response time of the atmospheric ^{14}CO mixing ratio to variations in the global source strength (chapter 7). The model results further indicate that the simulated STE depends not only on the chosen advection algorithm, but also on the offline meteorological data driving the advection, the latter apparently being the dominant factor. This needs to be investigated in more detail in the future.

The response time analysis (chapter 7) indicated that the downward transport in TM3 is located closer to the equator (around 20^o) compared to MATCH (30^o to 40^o). This is consistent with a reduced stratospheric and global lifetime of ^{14}CO simulated by TM3, and also with the simulated ^{14}CO mixing ratio at the surface level, which is generally lower in the tropics than predicted by the MATCH configurations. It implies, however, that TM3 simulates an enhanced horizontal transport of ^{14}CO in the stratosphere from the polar region to the tropics, i.e., across the subtropical barrier.

Increasing the horizontal grid resolution in TM3 results in an enhanced STE, because with an increasing grid resolution more processes on smaller scales which contribute to the STE are resolved by the model. The results indicate that these small scale processes are more important in the NH compared to the SH. In contrast to that,

increasing the vertical grid resolution tends to decrease the STE, with a larger effect in the SH than in the NH.

The seasonal cycle of atmospheric ^{14}CO at the surface level is primarily determined by the OH seasonality, however superposed by the seasonal variation of the downward flux of ^{14}CO from the stratosphere into the troposphere. The model simulations predict a weaker influence of the STE on the tropospheric ^{14}CO mixing ratio in the SH compared to the NH. This results from the weaker downward transport in the SH in general, but also from the phase lag of almost exactly half a year between the OH seasonality and the SH STE seasonality. In the SH, the STE flux is highest when OH is at its minimum, i.e., when ^{14}CO levels are rather high in both the stratosphere and the troposphere. In the NH, this phase lag between OH and STE is shorter, and the influence of the STE seasonality on tropospheric ^{14}CO is larger.

Generally, the influence of STE is much more pronounced in the stratosphere. The simulated stratospheric burden fraction driven by OH is much more disturbed by the STE in the NH stratosphere than in the NH troposphere. Furthermore, the annual amplitude of the simulated vertical maximum ^{14}CO in the lowermost stratosphere is larger than the ^{14}CO variation at the surface level. According to the simulations, the overall largest atmospheric ^{14}CO mixing ratio is found in the SH lower stratosphere, most probably in September. The level of this absolute maximum of the atmospheric ^{14}CO mixing ratio for a given global source strength depends very much on the model configuration. The simulations range roughly from 60 to 140 molec cm^{-3} STP for a global average source strength of 1 molec cm^{-2} s^{-1}. As a consequence, measurements of the lowermost stratospheric ^{14}CO mixing ratio in combination with measurements at the surface level are the key to further constraining the STE, the stratospheric OH abundance, and possibly the global source strength of ^{14}CO.

The differences between the particular model configurations with respect to the simulated STE flux of ^{14}CO can be used to assess the uncertainties in the simulated ^{14}CO mixing ratio arising from uncertainties in the simulated STE. Comparison of the model results with measurements of ^{14}CO can then be used to evaluate the simulated STE provided that the OH distribution and seasonality are known. In contrast to that, the simulated tropospheric OH distribution and seasonality can still be evaluated by ^{14}CO measurements, because in the troposphere OH is the dominating factor determining the seasonal variability.

11 The application of atmospheric ^{14}CO measurements: Implications for assessing OH and stratosphere - troposphere exchange

Abstract. For the first time ^{14}CO observations are used to evaluate the simulated atmospheric transport and oxidation capacity in a 3-D atmospheric model on the global scale. It is shown that the ^{14}CO methodology provides a unique quantitative test and at the same time a great challenge for three dimensional chemical tracer models (CTMs) and general circulation models (GCMs) with respect to the simulated stratosphere - troposphere exchange and the OH distribution. A large number of ^{14}CO measurements is used for constructing a zonal average annual cycle of cosmogenic ^{14}CO at the surface level. For this the contribution of secondary ^{14}CO of biogenic origin is estimated and subtracted from the observations. The resulting observed seasonal cycle of ^{14}CO and the latitudinal gradients at the surface level are quantitatively compared to results obtained with various model configurations of MATCH and TM3. Uncertainties in the approach are estimated and discussed. From the known differences between the particular model configurations a consistent explanation of the discrepancies between model simulations and observations is derived. The implications for stratosphere - troposphere exchange, and the OH distribution and seasonality are discussed. In particular the role of both in determining the observed interhemispheric asymmetry of ^{14}CO is resolved. Finally, ^{14}CO measurements, sampled during a number of aircraft campaigns are compared to the model simulations of the vertical ^{14}CO gradient. Especially samples of air from the lowermost stratosphere provide useful information on the way to further constrain remaining uncertainties in the ^{14}CO methodology.

11.1 Introduction

In the previous chapters several aspects of the ^{14}CO methodology were assessed theoretically. The simulated tropospheric transport of the 3-D atmospheric model MATCH, especially in meridional direction, was evaluated using the tracer SF_6 (chapter 3), and the global OH abundance was constrained by methylchloroform (MCF) simulations (chapter 4). Furthermore, the influence of uncertainties in the source distribution of ^{14}CO and its variation with the solar cycle were discussed (chapter 5), the influence of CO destruction in soil on atmospheric ^{14}CO was estimated (chapter 6), and the varying global source strength of $^{14}C(O)$ and its implication for the atmospheric ^{14}CO mixing ratio was investigated (chapter 7). Finally, chapter 9 comprises a discussion of the possible effect of occasional solar proton events on atmospheric ^{14}CO levels. In all these modeling studies the uncertainties arising from shortcomings with respect to the model realization were carefully tracked, mostly by the quantitative comparison of results from differing model con-

figurations.

A first application of atmospheric ^{14}CO is presented in chapter 10. This still purely theoretical study focuses on differences between various model configurations with respect to the simulated stratosphere - troposphere exchange. In contrast to any artificial tracer used for testing 3-D atmospheric models, ^{14}CO is a real, measurable species and several measurements of atmospheric ^{14}CO mixing ratios have been made during the last years, mostly at the surface level. Therefore, the overall remaining question of how the model simulations compare to the observations is addressed in this chapter. For this, all currently available ^{14}CO observations (partly still unpublished) are collected. From the observations at the surface level an average zonal mean seasonal cycle (i.e., a 2-D climatology) is constructed using several results of the previous chapters. This 2-D climatology is quantitatively compared to the model simulations. Moreover, the smaller number of ^{14}CO observations measured on board of aircrafts are used to further constrain the remaining uncertainties. Deviations between model simulations and observations provide valuable information on model deficiencies and / or possibly indicate atmospheric processes (chemistry and dynamics) that are either unknown or not yet fully understood. ^{14}CO observations offer a high potential to track changes of atmospheric chemistry and dynamics in future applications.

11.2 Contribution of non-cosmogenic ^{14}CO

Before the model simulations can be compared to observations the amount of ^{14}CO originating from recycled ^{14}C, i.e., the secondary source of ^{14}CO that is not included in the model simulations has to be assessed. This "biogenic" source contribution comprises ^{14}CO from biomass burning, methane and NMHC (non-methane hydrocarbon) oxidation, and ocean emissions (see section 1.1.4). *Bergamaschi et al.* [2000b,a] constrained the global estimates of different CO sources by an inversion technique and calculated the contribution of the different CO sources determining the observed CO mixing ratio (monthly averages) at 31 globally distributed locations of the NOAA-CMDL (National Oceanic and Atmospheric Administration Climate Monitoring and Diagnostics Laboratory) network. From these results the fraction of CO that contains ^{14}C is calculated at the 31 locations according to

$$f_{14} = \frac{\chi_{\mathrm{CO}(*)}}{\chi_{\mathrm{CO}}} \ , \tag{11.1}$$

where χ_{CO} denotes the total CO mixing ratio, i.e., including contributions of the ^{14}C free technological CO emissions and anthropogenic NMHC emissions. In contrast to that, $\chi_{\mathrm{CO}(*)}$ only comprises the contribution of oceanic emissions, forest burning, savanna burning, methane oxidation and oxidation of natural NMHCs.

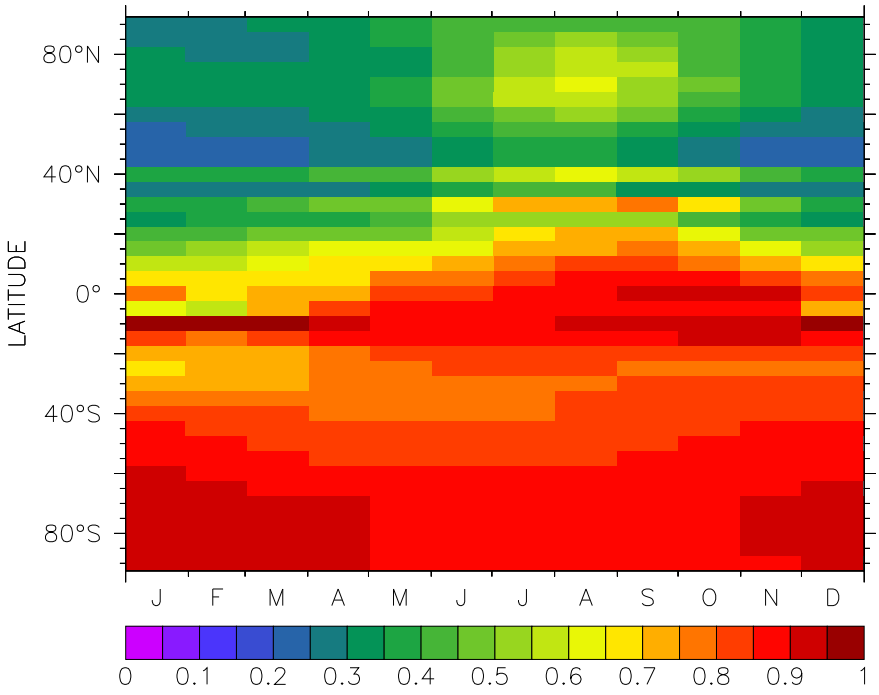

Figure 11.1: Fraction f_{14} of CO that contains ^{14}C. The monthly average estimates of *Bergamaschi et al.* [2000b,a] at 31 NOAA-CMDL locations are interpolated to a 5^o latitude grid, assuming that each particular location is representative for the entire latitude belt it resides in.

The results of *Bergamaschi et al.* [2000b,a] for the 31 NOAA-CMDL stations are interpolated assuming that each particular station is representative for the entire latitude belt. This assumption is justified, since the atmospheric lifetime of CO is long compared to the zonal mixing time. Furthermore the NOAA-CMDL measurements are filtered to represent the remote atmosphere. And finally, remaining uncertainties in the 3-D model and the inversion technique used by *Bergamaschi et al.* [2000b,a] are possibly of similar magnitude to zonal variations and do not justify an evaluation on a smaller scale. The result of the analysis averaged on 5^o latitude intervals is shown in Figure 11.1. In the NH, the anthropogenic sources (e.g., burning of ^{14}C free fossil fuel) clearly reduce the fraction of CO that contains ^{14}CO. As a consequence, the NH ^{14}C fraction exhibits a maximum of up to 80% in summer when fossil fuel consumption is reduced compared to the main heating period in winter, when the ^{14}C fraction is less than 30%. In the SH the annual cycle of the ^{14}C fraction is small, and more than 70% of all CO contains ^{14}C during the whole year.

In order to estimate the absolute contribution of the secondary source (recycled ^{14}C) to the observed atmospheric ^{14}CO mixing ratio, the CO mixing ratio has to be known along with the $^{14}C/^{12}C$ ratio, i.e., how much ^{14}C is contained in biogenic

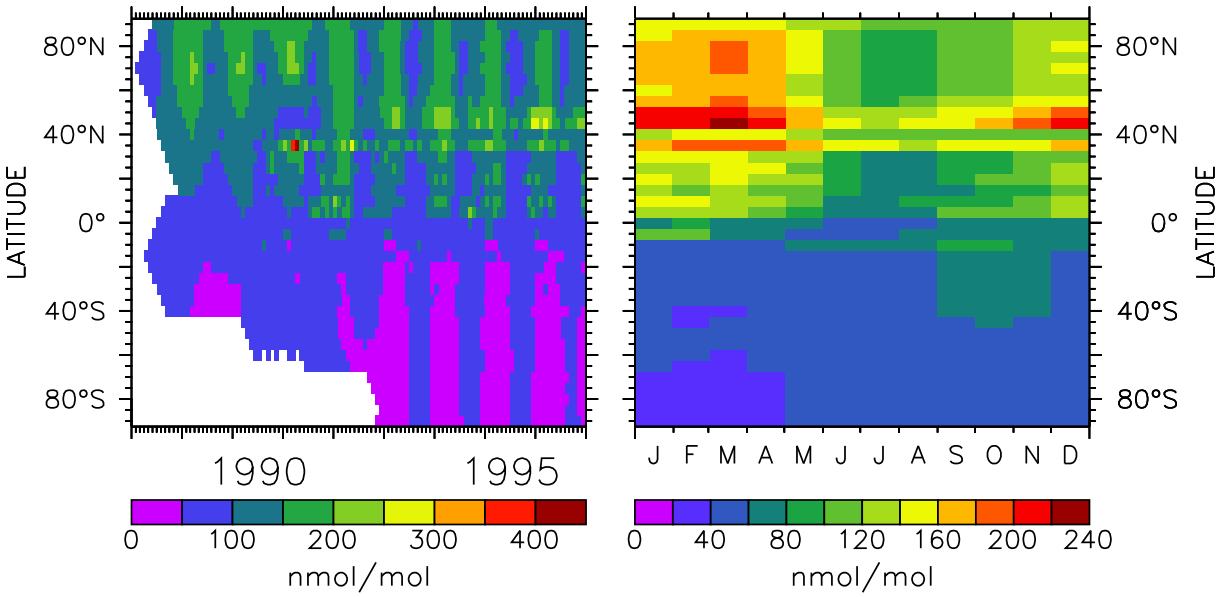

Figure 11.2: Observations of tropospheric CO from the NOAA-CMDL Cooperative Air Sampling Network from 1988 to 1996 (left). The observed monthly average mixing ratio is interpolated on a 5^o latitude grid. White spaces indicate insufficient data coverage. The right side shows the monthly CO mixing ratio averaged from 1993 to 1996.

CO. The "biogenic" contribution (in mol mol^{-1}) to the atmospheric ^{14}CO is then

$$\chi_{\text{bio}} = f_{14} \cdot \chi_{\text{CO}} \cdot \frac{^{14}C}{^{12}C} \cdot \tag{11.2}$$

Since the "biogenic" CO is with respect to the ^{14}C content in equilibrium with the biomass, the average contribution of biogenic ^{14}CO can be estimated with the natural ^{14}C/^{12}C ratio (120 pMC, δ^{13}C = -25$^o/_{oo}$, Eq. (1.6)) [*Brenninkmeijer*, 1993]. The result is (Eq. (1.7)) 0.038 molec cm^{-3} STP per nmol mol^{-1} CO, or equivalently 0.037 molec cm^{-3} STP per kg kg^{-1} CO.

The measurements of atmospheric CO from the NOAA-CMDL Cooperative Air Sampling Network provide a global view of the CO distribution and seasonality [*Novelli et al.*, 1992, 1998]. The monthly mean mixing ratios of CO are interpolated on a 5^o latitude grid, assuming that each particular observation is representative for the zonal average. The result for the data covering the period 1988 to 1996 is shown in Figure 11.2.

The right side of Figure 11.2 shows the monthly mean CO mixing ratio averaged from 1993 to 1996, i.e., the period during which enough observations are available to cover the entire globe. Inter-annual variations of the CO mixing ratio are thus averaged out in order to obtain a monthly CO climatology.

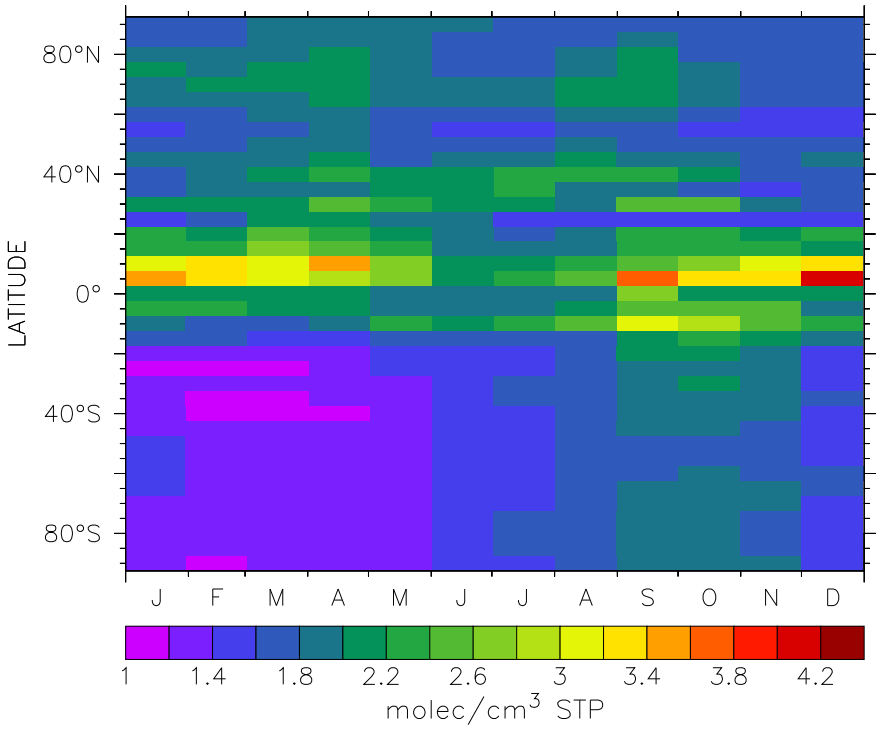

Figure 11.3: Monthly zonal average tropospheric ^{14}CO of biogenic origin (Eq. (11.2)).

With this CO climatology, the fraction f_{14} of CO that contains ^{14}CO (Figure 11.1), and the average ^{14}C/^{12}C ratio of CO, the average biogenic contribution $\chi_{\rm bio}$ can be estimated using Eq. (11.2) (monthly zonal averages). The result is depicted in Figure 11.3. The highest contribution of secondary ^{14}CO occurs in the NH tropics, where the abundance and oxidation rate of natural methane and NMHCs is largest. The lowest contribution of "biogenic" ^{14}CO is in the SH between December and May, when the CO mixing ratio is generally lowest (cf. Figure 11.2). Except in the tropics the secondary ^{14}CO contribution exhibits only a moderate seasonal cycle.

11.3 Observations of ^{14}CO at the surface level: A 2-D climatology

Knowing the secondary contribution of ^{14}CO ($\chi_{\rm bio}$, Eq. (11.2)), the cosmogenic part of atmospheric ^{14}CO measurements is readily determined:

$$\tilde{\chi} = \tilde{\chi}_{\rm cosmo+bio} - \chi_{\rm bio} \ . \tag{11.3}$$

The tilde denotes observational data, χ without index denotes the cosmogenic part of the ^{14}CO mixing ratio, consistent with previous chapters. The biogenic contribution $\chi_{\rm bio}$ is based on CO observations (NOAA-CMDL) and model results (f_{14}).

For the evaluation of model simulated ^{14}CO mixing ratios at the surface level several observations are taken into account. Table 11.1 lists locations where ^{14}CO has been sampled (and partly is still being sampled). The time interval of the data and the number of observations used for the present study are also listed. References are included in case the observations or parts of them are already published. Additionally, the ^{14}CO observations at the surface level obtained during various campaigns are included in the following analysis. Those are listed in Table 11.2 with the same information provided as in Table 11.1. Further unpublished ^{14}CO observations at locations in the SH and from several trans-equatorial ship cruises exist (Martin Manning, Dave Lowe, personal communication, 2000). These were, however, not made available for this study.

The observed ^{14}CO mixing ratios and the estimated primary cosmogenic contribution are shown in Figures 11.4, 11.5, 11.6, and 11.7.

In order to compare the observed ^{14}CO mixing ratios with the model simulations on a global scale, the ^{14}CO observations (the primary cosmogenic contribution $\tilde{\chi}$) are combined in a 2-D climatology, i.e., a zonally averaged seasonal cycle of ^{14}CO at the surface level is constructed from the observations, after the observations were rescaled to standard conditions with respect to the solar activity (see below). The assumption is made that each particular observation is representative for the day of the year the air was sampled and for the entire latitude belt of the sampling location. This averages out inter-annual variations; however, it allows the discussion of simulated OH and stratosphere - troposphere exchange in a "climatological" approximation. Nevertheless, inter-annual variations can be estimated by model simulations based on meteorologies of particular years. The simulated ^{14}CO mixing ratios can then directly be compared to the observations at a given time and location.

Rescaling of the observations to well defined conditions with respect to solar activity is required, since the measured ^{14}CO mixing ratios are obtained during different periods. Therefore the three solar cycle rescaling procedures c'_χ discussed in chapter 8 are applied. These are based on

1. the shielding potential Φ and the production rate calculated by *Masarik and Beer* [1999], linearly interpolated using the smoothed sunspot number, and taking into account a delay time of ΔT_Φ = -6 months between shielding potential and sunspot number variation ($c'_\chi(\Phi(s_s(t + \Delta T_\Phi)))$),

2. a linear interpolation using the smoothed sunspot number according to *Lingenfelter* [1963] and *Lingenfelter and Ramaty* [1970], however including a delay time of ΔT = -7 months between sunspot number and ^{14}C production rate variation ($c'_\chi(s_s(t + \Delta T))$),

Station	Latitude	Longitude	#	Reference
	Date			
Alert	82.45^{o}N	62.52^{o}W	45	*Brenninkmeijer et al.* [1999]
	1996/07/19	1998/01/02		
Ny Ålesund	78.90^{o}N	11.88^{o}E	93	*Brenninkmeijer et al.* [1999]
	1996/04/03	1999/06/16		(*)
Point Barrow	71.32^{o}N	156.60^{o}W	16	*Quay et al.* [2000]
	1994/03/23	1995/07/28		
Kollumerwaard	53.30^{o}N	6.30^{o}E	19	(*)
	1997/10/16	1998/11/24		
Mainz	49.98^{o}N	8.23^{o}E	24	(*)
	1996/02/14	2000/03/08		
Olympic	48.08^{o}N	123.10^{o}W	93	*Quay et al.* [2000]
Peninsula	1991/07/21	1997/03/22		
Schauinsland	47.92^{o}N	7.92^{o}E	63	(*)
	1995/02/21	2000/03/13		
Sonnblick	47.03^{o}N	12.95^{o}E	65	*Rom et al.* [1999a]
	1996/09/20	1999/11/25		*Gros et al.* [2000]
Happo	36.68^{o}N	137.80^{o}E	48	*Kato et al.* [2000]
	1997/02/10	1998/11/02		
Izaña	28.30^{o}N	16.48^{o}W	61	*Kato et al.* [2000]
	1996/05/23	1999/10/20		(*)
Barbados	13.17^{o}N	59.43^{o}W	96	*Mak and Southon* [1998]
	1996/07/10	1998/11/29		
Maledives	4.97^{o}N	73.47^{o}E	22	(*)
	1998/08/13	1999/03/20		
Kenya	1.53^{o}N	27.27^{o}E	12	(*)
	1996/07/29	1997/09/10		
Baring Head	41.40^{o}S	174.90^{o}E	197	*Brenninkmeijer* [1993]
	1989/06/28	1994/05/17		*Brenninkmeijer et al.* [1992], (*)
Scott Base	77.85^{o}S	166.78^{o}E	78	*Brenninkmeijer* [1993]
	1991/06/30	1994/01/11		*Brenninkmeijer et al.* [1992]

Table 11.1: Locations of ^{14}CO observational sites, time interval of measurements, and number of samples (#) used in the present analysis. The references for published data are included; (*) denotes unpublished data from Brenninkmeijer et al.

3. the neutron count rate at the Climax neutron monitor station ($c'_\chi(n_{\rm clx})$).

The resulting ^{14}CO mixing ratios are consequently standardized to the global average production rate between 1955 and 1988. All three approaches include the response of atmospheric ^{14}CO to variations in the global source strength with an estimated

Campaign	Latitude	Longitude	#	Reference
	Date			
ALASKA	32.80^{o}N-58.50^{o}N		13	*Mak et al.* [1992]
	1992/07/31	1992/08/11		*Mak et al.* [1994]
TROICA-02	43.45^{o}N-58.40^{o}N	50.30^{o}E-134.24^{o}E	12	*Bergamaschi et al.* [1998]
	1996/07/25	1996/08/11		
TROICA-03	48.66^{o}N-58.34^{o}N	46.61^{o}E-133.30^{o}E	20	*Röckmann et al.* [1999]
	1997/04/02	1997/04/13		
TROICA-05	51.81^{o}N-61.22^{o}N	56.75^{o}E-121.56^{o}E	16	(*)
	1999/06/27	1999/07/23		
PACIFIC	22.00^{o}N-56.00^{o}N	130^{o}W - 155^{o}W	7	*Quay et al.* [2000]
	1991/03/10	1991/03/31		
VICKERS	11.00^{o}S-53.00^{o}N	168^{o}E - 164^{o}E	9	*Quay et al.* [2000]
	1992/08/08	1992/10/16		
RITS93A	67.50^{o}S-49.20^{o}N	140^{o}W - 148^{o}W	24	*Quay et al.* [2000]
	1993/01/04	1993/05/03		
RITS93B	67.30^{o}S-54.90^{o}N	140^{o}W	25	*Quay et al.* [2000]
	1993/11/23	1993/12/27		
RITS95	54.50^{o}S-44.80^{o}N	160^{o}W	16	*Quay et al.* [2000]
	1995/10/13	1995/11/18		
INDOEX	33.67^{o}S-18.43^{o}N	27.33^{o}E- 85.17^{o}E	14	(*)
	1999/02/13	1999/03/29		

Table 11.2: Various campaigns with observations of ^{14}CO at the surface level. The number (#) of observations has been collected during the listed time interval within the geographical range. The references for published data is included; (*) denotes unpublished data from Brenninkmeijer et al.

global average response time of $\tau = 3.11$ months and the weight of the current month's production rate scale of $w_0 = 0.163$ (cf. chapter 8). As shown in chapter 8 the sensitivity of the scaling function to the response time is small compared to the uncertainties arising from uncertainties in the source strength scaling.

The resulting seasonal cycle of observed atmospheric ^{14}CO at the surface level on a 5^o latitude grid is shown in Figure 11.8. Because the observational data is not filtered in any way, the variability is rather high. This implies that all specific events and conditions of each particular sampling site are mirrored in this climatology. For comparison with model results this variability has to be compared to uncertainties in the model simulations. Since these uncertainties are large, for a first evaluation of the simulated ^{14}CO seasonal cycle at the surface level on a global scale the climatology is therefore sufficient.

The effect of rescaling the observations to standard solar activity conditions is partic-

ularly visible at high southern latitudes. The differences between the three applied solar cycle rescaling functions are small compared to the short term variations in the data and uncertainties in the model simulations. Therefore the unweighted average of the three rescaling functions is used to obtain one single standardized cosmogenic ^{14}CO climatology to be compared with the model simulations in the further analysis, i.e.,

$$\tilde{\chi} = \frac{1}{3}(c'_\chi(\Phi(s_s(t+\Delta T_\Phi))) + c'_\chi(s_s(t+\Delta T)) + c'_\chi(n_{\mathrm{clx}}))(\tilde{\chi}_{\mathrm{cosmo+bio}} - \chi_{\mathrm{bio}}) \ . \quad (11.4)$$

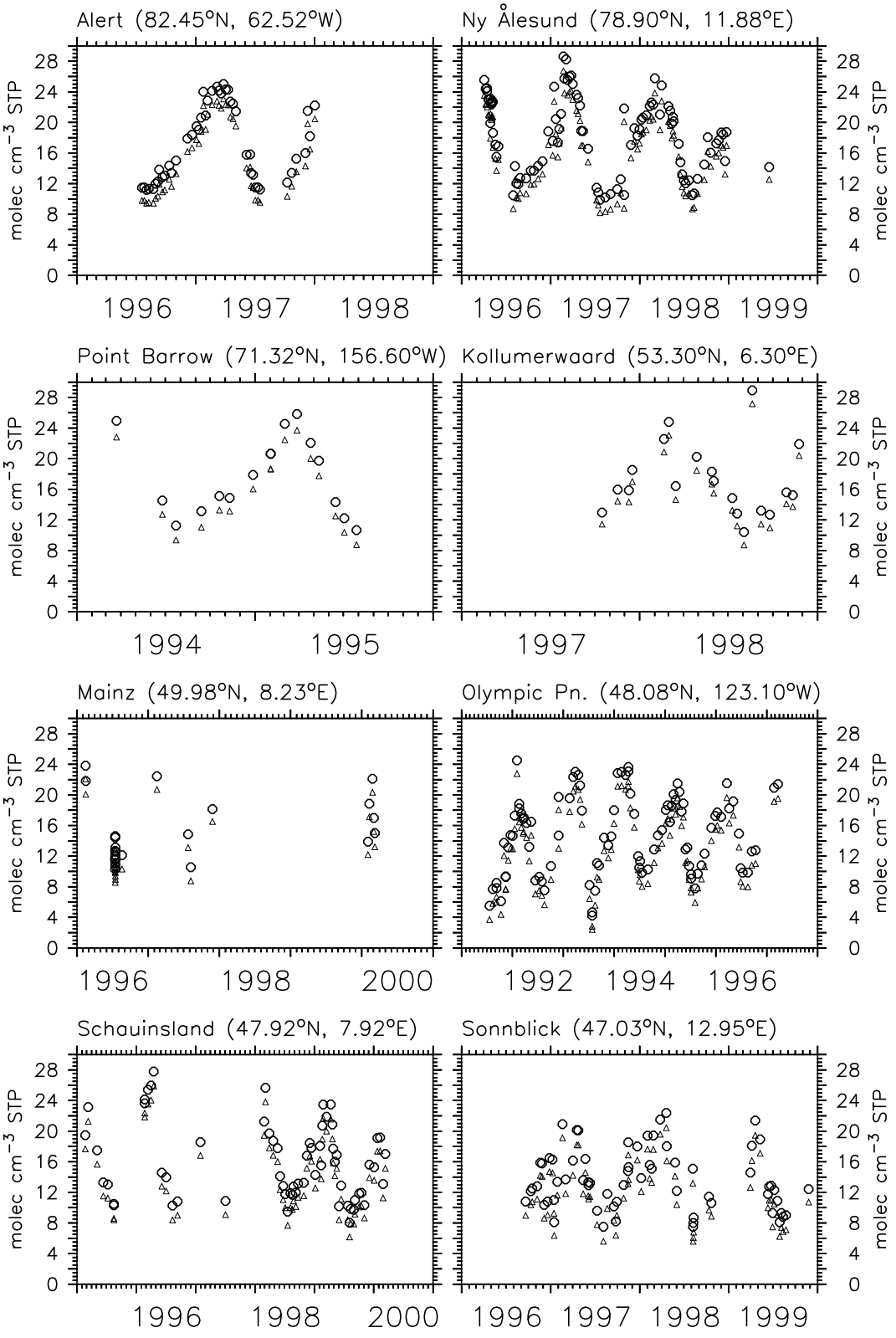

Figure 11.4: Observed ^{14}CO mixing ratios at the surface level (circles) and estimated primary cosmogenic contribution (triangles)

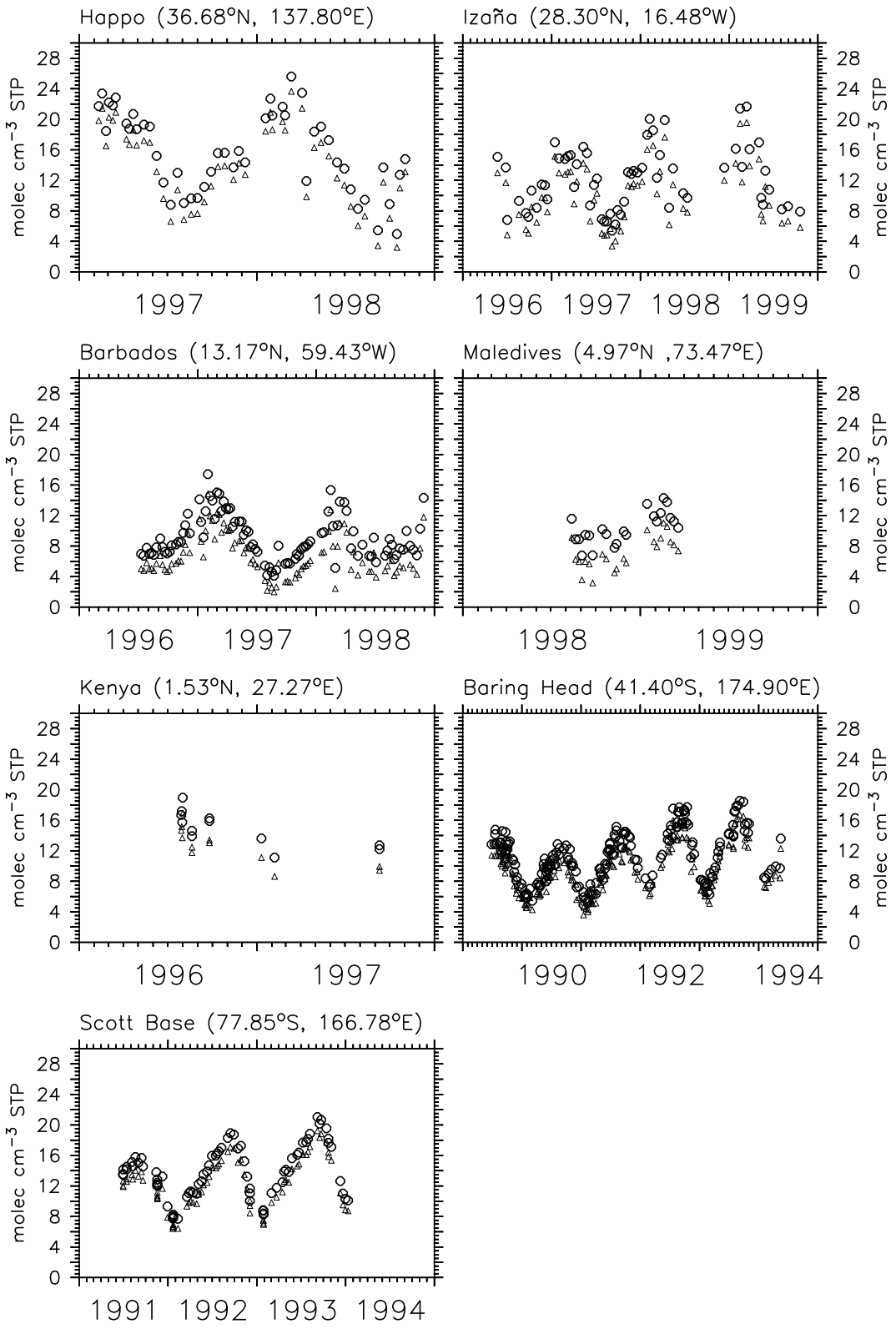

Figure 11.5: Observed ^{14}CO mixing ratios at the surface level (circles) and estimated primary cosmogenic contribution (triangles)

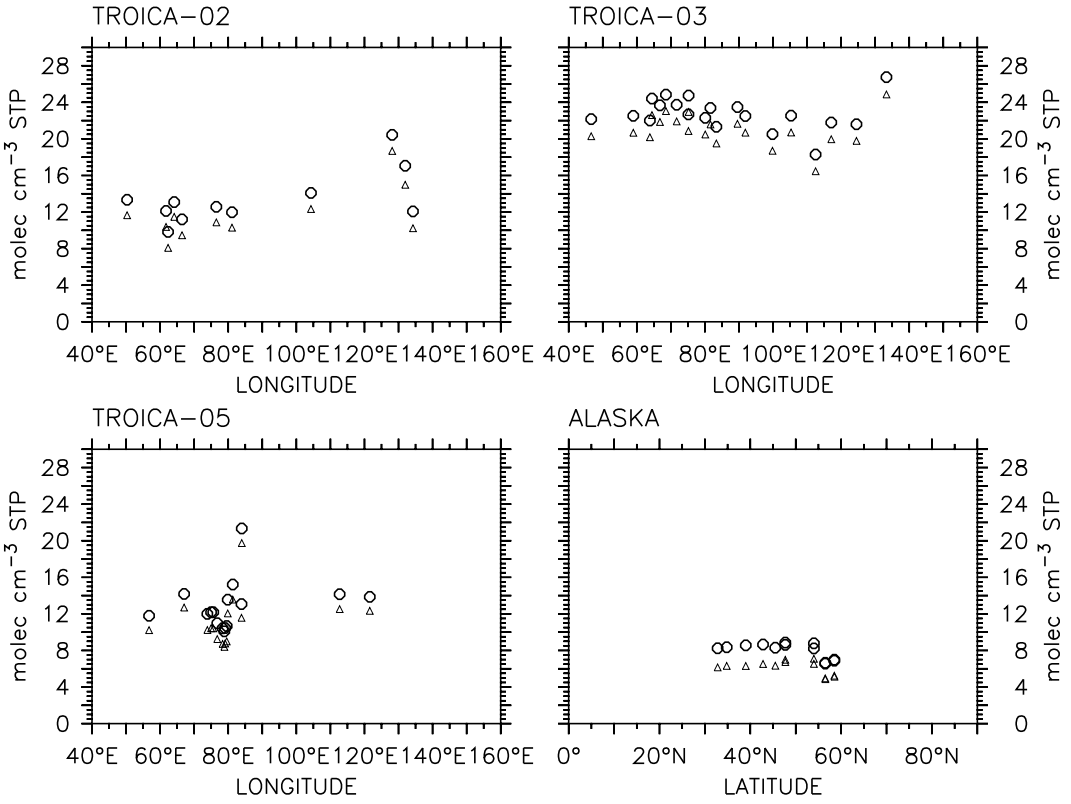

Figure 11.6: Observed ^{14}CO mixing ratios at the surface level (circles) and estimated primary cosmogenic contribution (triangles). The TROICA campaigns were on board the Trans-Siberian railroad.

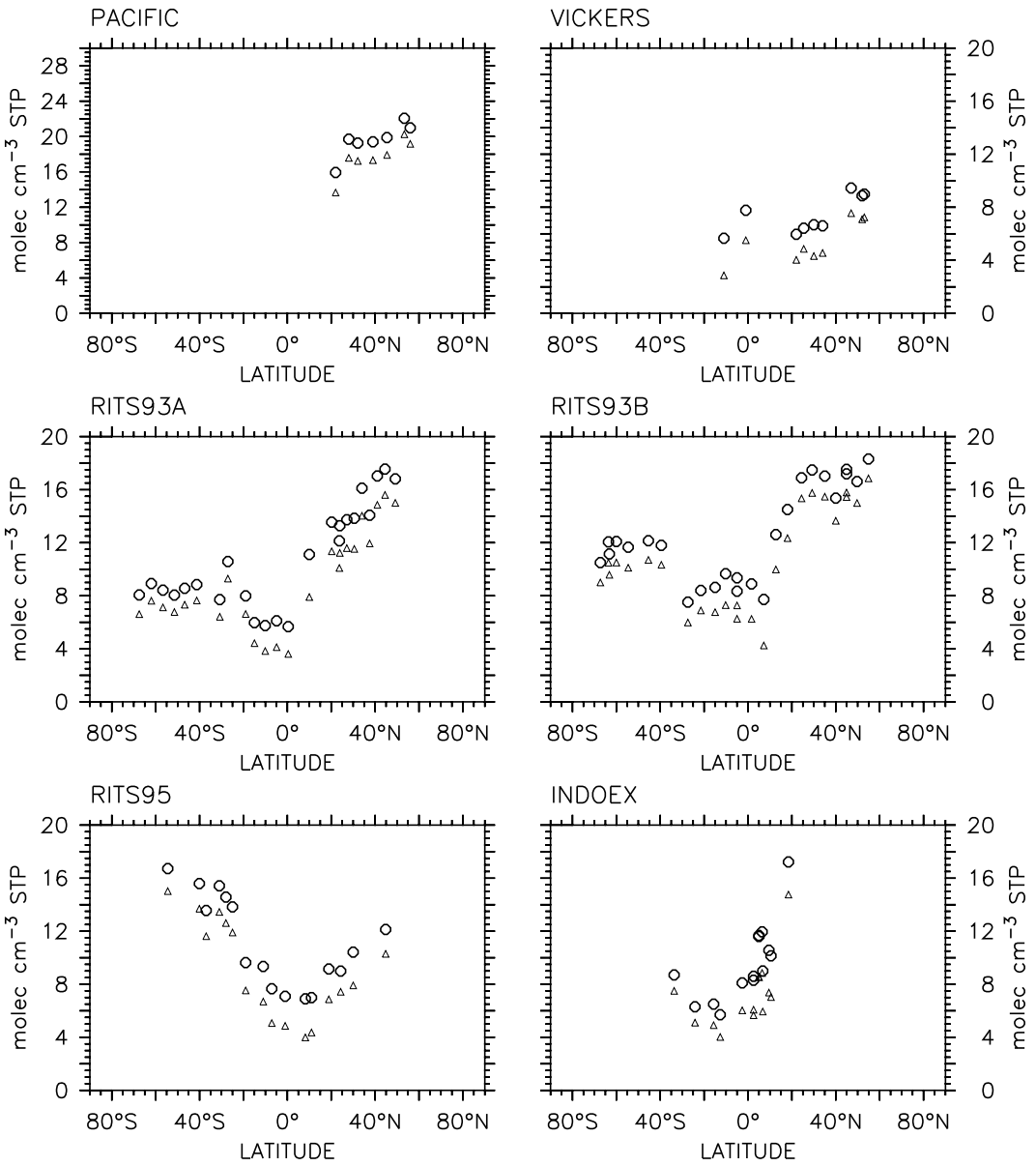

Figure 11.7: Observed ^{14}CO mixing ratios at the surface level obtained during various ship cruises (circles) and estimated primary cosmogenic contribution (triangles).

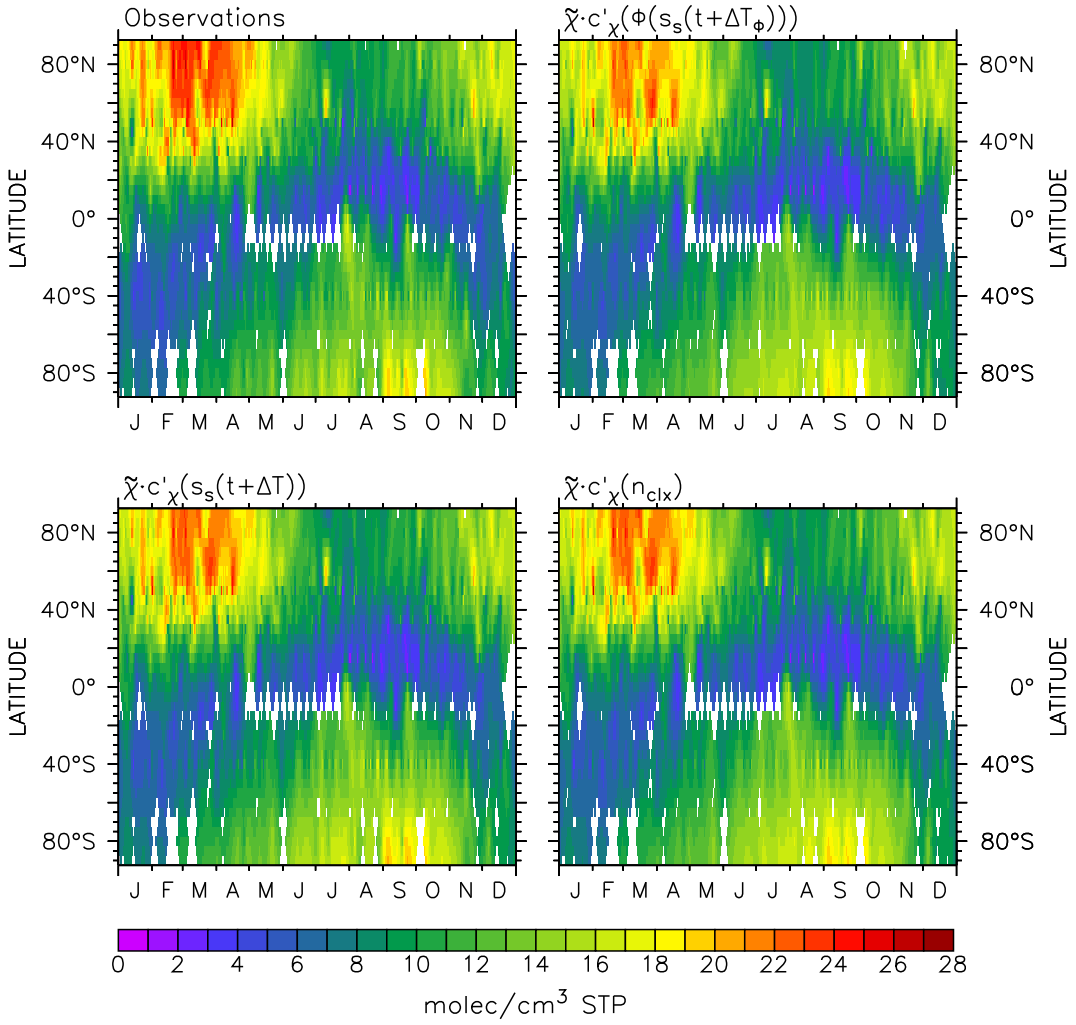

Figure 11.8: Zonal average climatology of cosmogenic ^{14}CO observations at the surface level. The estimated biogenic contribution has been subtracted from the originally observed ^{14}CO mixing ratios. The upper left panel shows the unscaled cosmogenic contribution in molec cm^{-3} STP. The other panels show the mixing ratios standardized to the average conditions during the period 1955 to 1988 with respect to the solar cycle using the approaches described in chapter 8. White spaces indicate insufficient data coverage for adequate interpolation.

11.4 Model simulations

11.4.1 Model setup

For comparison with the ^{14}CO observations model simulations with various model configurations are performed. An integration initialized with zero mass mixing ratio on January 1, 1993 is performed with 2.0-SLT driven by the NCEP-reanalysis meteorologies [*Kalnay et al.*, 1996] of the years 1993 to June 1999. The OH-1 distribution is prescribed (monthly averages) for the ^{14}CO oxidation. The ^{14}CO source distribution of *Lingenfelter* [1963] (LF, cf. chapter 5) for intermediate solar cycle conditions normalized to a global average production rate of 1 molec cm^{-2} s^{-1} in an idealized static atmosphere of constant depth (1033 g cm^{-2}) is used. This intermediate distribution is obtained by locally (at given geomagnetic latitude and depth) averaging the source distributions for solar minimum and solar maximum conditions. The model simulation with 2.0-SLT is repeated with the OH-S distribution. Furthermore, these two simulations are repeated with the ^{14}CO source distribution of *Masarik and Beer* [1999] for a shielding potential Φ of 650 MV, also normalized to a global average production rate of 1 molec cm^{-2} s^{-1} in an idealized static atmosphere of constant depth (1033 g cm^{-2}).

The resulting tracer distribution of the first simulation (2.0-SLT, LF, OH-1) on December 31, 1996 (i.e., after a four year integration) is used to initialize further a set of simulations for the period January 1, 1997 to December 31, 1998, all driven by the NCEP-reanalysis meteorology of the years 1997 and 1998. These include a simulation with the 2.0-SPFR configuration using the OH-1 distribution and the normalized intermediate LF source distribution, and simulations with 2.0-SLT and 2.0-SPFR using the same source distribution, but with the OH-2 distribution. Furthermore, the 2 year integrations with 2.0-SLT and 2.0-SPFR are each repeated twice, once with the stratospheric OH abundance (OH-2D) reduced by a factor of two in the NH, and once with the stratospheric OH abundance halved in the SH. The latter simulations are performed in order to estimate the influence of the stratospheric OH abundance on the simulated the surface level ^{14}CO.

And finally, a TM3-L-L31 simulation initialized with zero mass mixing ratio from January 1, 1996 to June 31, 1998 is included in the analysis. The TM3-L-L31 model is driven by the ECMWF reanalysis meteorology of the years 1996 to 1998. The OH-1 distribution is prescribed for the ^{14}CO oxidation, and the source distribution of *Lingenfelter* [1963] (LF) for intermediate solar cycle conditions normalized to a global average production rate of 1 molec cm^{-2} s^{-1} in an idealized static atmosphere of constant depth (1033 g cm^{-2}) is used. The TM3-L-L31 model simulation was performed at KNMI (Ad Jeuken, personal communication, 1998-2000).

In all model simulations three tracer distributions are calculated separately, namely ^{14}CO, ^{14}CO that is produced in the stratosphere, and ^{14}CO that is produced in the troposphere. The resulting mixing ratios are denoted by χ, χ_{st}, and χ_{tr} respectively (cf. chapter 10). The tropopause is diagnosed online according to the WMO definition [*WMO*, 1992]. All model output is archived as 5-day averages, except in February, where the TM3-L-L31 output is a 3-day average between February, 26 and February, 28.

11.4.2 Estimate of various uncertainties

Before the model simulations can be compared to the derived ^{14}CO climatology at the surface level, further aspects concerning uncertainties of the method have to be assessed. These are discussed in this section.

11.4.2.1 Soil activity and the deviation from the zonal average The first issue pertains mainly the model simulations. As discussed in chapter 6, the soil activity (which is not included in the model simulations described above) may potentially significantly affect the ^{14}CO mixing ratio at the surface level. Since the strength of this additional sink and its variations with time and under varying conditions such as soil temperature and moisture are still uncertain, the soil sink is maximally estimated in chapter 6. The ^{14}CO observations, in contrast, implicitly include the effect of the real soil activity. As already indicated above, the constructed ^{14}CO climatology at the surface level contains all characteristics of the particular sampling sites, including local effects of the soil sink. Therefore the uncertainty in the ^{14}CO climatology with respect to local effects of the soil activity has to be estimated. A maximum estimate can be obtained from the model results in chapter 6. For each particular observation of ^{14}CO shown in Figures 11.4, 11.5, 11.6, and 11.7 the effect of the soil sink is calculated as the ratio of the simulated ^{14}CO mixing ratio at the surface level including the soil sink to the respective mixing ratio at the particular location without soil activity. The results of all observational locations are interpolated on the climatology grid, i.e., on 1-day $\times$ 5^o latitude intervals.

The second uncertainty arises from the reduction to two dimensions. Any observation included in the climatology is assumed to be representative for the zonal average. This assumption can likewise be evaluated and the corresponding uncertainty can be estimated by model simulations. For each particular observation the deviation from the zonal average is calculated from the 2.0-SLT (OH-1, LF) simulation of the year 1997. The ratios of the simulated ^{14}CO mixing ratios at the particular locations to the respective zonal average are averaged on the climatology grid. The results are depicted in Figure 11.9.

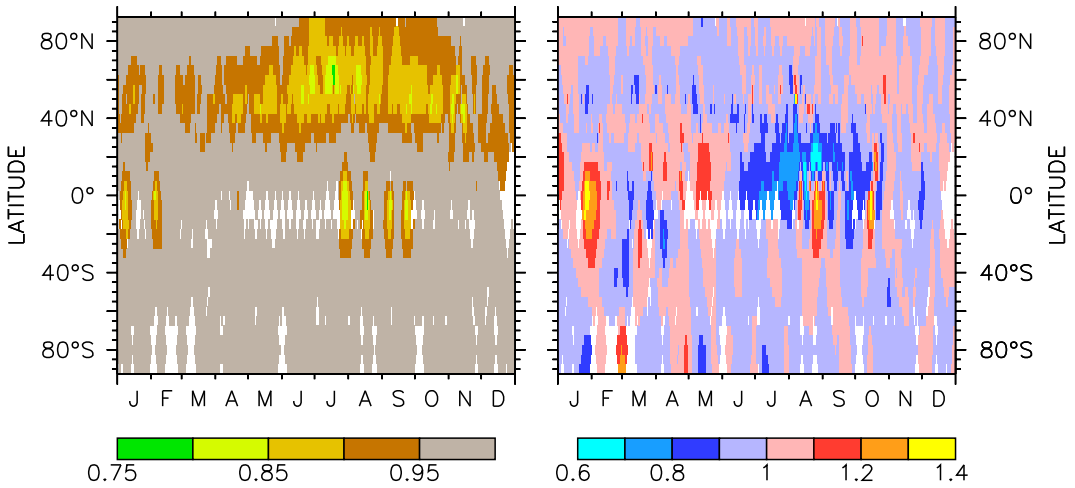

Figure 11.9: Estimated influence of soil sink (left) and deviation from zonal average (right). The left panel shows the ratio of the model simulated ^{14}CO mixing ratio at the surface level with active soil versus the respective mixing ratio without soil activity. This ratio is evaluated for each particular ^{14}CO observation included in the ^{14}CO climatology (Figure 11.8) and interpolated onto the same 1-day $\times$ 5^o latitude grid. The right panel shows the ratio of the simulated ^{14}CO mixing ratio at the observational sites (surface level) to the respective simulated zonal average, also averaged on the 1-day $\times$ 5^o latitude grid. For the soil sink estimate model simulations with the 2.0-SLT and 2.0-SPFR configurations for the year 1994 are averaged (see chapter 6). The deviation from the zonal average is calculated with 2.0-SLT (OH-1, LF) for the year 1997. White spaces indicate insufficient data coverage.

As to be expected the soil sink has only a moderate effect (less than 5% reduction) in the SH, except in the tropics and at mid latitudes between July and September and in January/February. These deviations in the tropics can however be traced back to the observations in Kenya (cf. Figure 11.5), where the simulated effect of the soil sink is large (cf. Figure 6.1). In the NH, north of 30^{o}N the uncertainty arising from the soil activity is larger than in the SH, especially in summer, when the reduction of the simulated mixing ratio of ^{14}CO by soil activity at the observational locations can exceed 15%. The maximum reduction can be traced back to the TROICA-5 observations with a simulated soil effect of 21%.

The simulated ^{14}CO mixing ratio at the observational locations (surface) is representative for the respective zonal average to within $\pm$10% at most times and latitudes (Figure 11.9, right). Larger deviations, up to $\pm$20% from the zonal average, occur mainly for the ALASKA, BARBADOS, MALEDIVES, TROICA-2, VICKERS, RITS93A, RITS93, and KENYA observations. The largest deviations are simulated for BARBADOS in August (-37%) and VICKERS (+40%).

11.4.2.2 Inter-annual variability of ^{14}CO at the surface level The measurements of ^{14}CO at the surface level used for the construction of the climatology (Figure 11.8) have been performed in different years, but only the day of the year is taken into account for the climatology (with the exception of rescaling to "standard" solar cycle conditions). The meteorological conditions at a given location and time of the year, however, vary between subsequent years. Disregarding these inter-annual variations introduces a further uncertainty in the climatology. This has to be assessed before model simulations can be quantitatively compared to the climatology.

Inter-annual variations in the atmospheric ^{14}CO mixing ratio arising solely from variations in the meteorological conditions can be estimated by model simulations based on meteorologies of different years, provided that all other boundary conditions, such as the OH distribution and seasonality, and the ^{14}CO source distribution and global strength do not change between the years. Since the inter-annual variation is implied in the meteorological fields driving the model advection, estimates of the inter-annual variation pattern should be similar for different advection algorithms, although they would likely differ in the absolute magnitude.

From the model simulations with the 2.0-SLT configuration (OH-1, LF) a five year (1994-1998) climatology of the seasonal cycle of ^{14}CO at the surface level is averaged. A measure of the inter-annual variation is then the deviation of the simulated mixing ratio at a particular time from this climatological average. The result is shown in Figure 11.10. At most latitudes this deviation is $\pm 5\%$ or less. Deviations larger than $\pm 10\%$ occasionally occur at high southern latitudes and around the equator in April 1998.

Consequently the inter-annual variation of the zonally averaged ^{14}CO mixing ratio at the surface level is small, and a comparison of observations with model simulations for different years is justified, at least with respect to the varying meteorological conditions.

11.4.2.3 Influence of the ground effect *O'Brien et al.* [1978] calculated a significantly enhanced atmospheric neutron flux directly above the Earth's surface in the lower 20 g cm^{-2}, caused by the discontinuity in neutron production and scattering properties near the air / seawater and air / ground interface. *Mak et al.* [1999] measured the ^{14}CO production rate near the surface and found a roughly doubled production rate at the surface level compared to the production rate at 150 m altitude and above. This enhanced production rate, however, does not bias the atmospheric ^{14}CO measurements at surface level, since the ^{14}C production from surface level up to 0.9 times the surface pressure contributes only less than 0.5% to the total

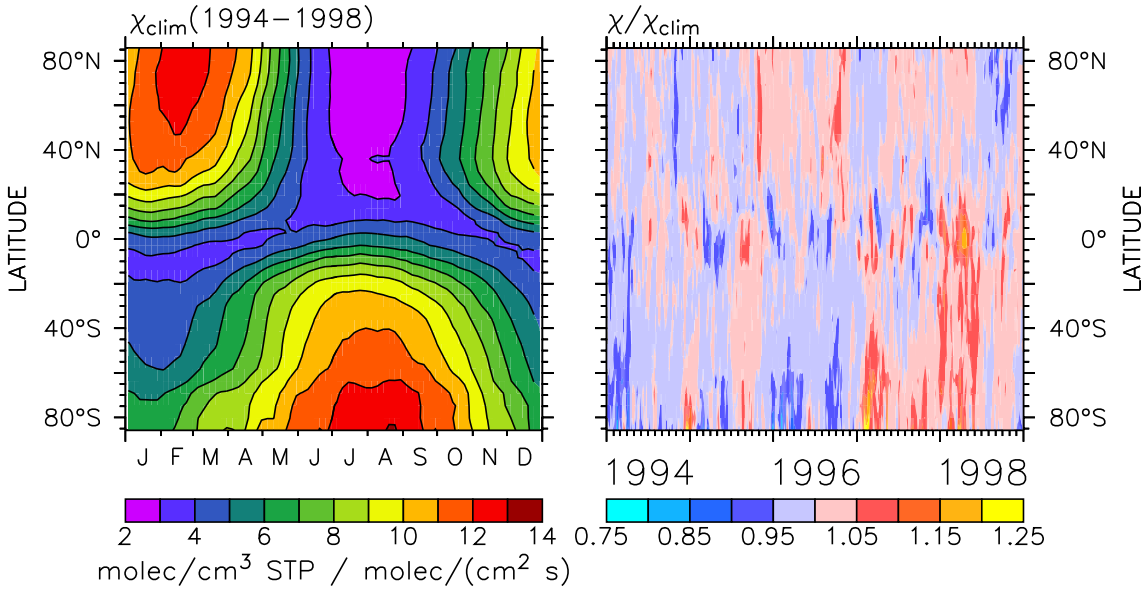

Figure 11.10: Simulated 5-year climatology of zonal average atmospheric ^{14}CO mixing ratio χ_{clim} at the surface level obtained with the 2.0-SLT (OH-1, intermediate LF) configuration (left), and inter-annual variation of the simulated the surface zonal average ^{14}CO mixing ratio plotted as ratio of the particular year to the simulated 5 year climatology (right). The ^{14}CO mass mixing ratios are renormalized to a global average production rate of 1 molec cm^{-2} s^{-1} in the model atmosphere.

^{14}C production. This estimate is based on the LF source distribution [*Lingenfelter*, 1963] for solar minimum conditions, i.e., the ^{14}C source distribution with the largest production rate near the surface compared to others [*O'Brien et al.*, 1991; *Masarik and Beer*, 1999] (see chapter 5). The ^{14}CO mixing ratio is not determined by the local production rate, because the troposphere is well mixed (cf. chapter 5). For instance, the contribution of ^{14}CO originating from the stratosphere to the ^{14}CO at the surface level was estimated to 30%-55% depending on latitude and season (cf. Figure 10.13). Compared to this the local cosmogenic production is negligible.

11.4.2.4 The influence of the stratospheric OH abundance The last issue to be addressed before the comparison between model simulations and observations can be discussed, is the influence of the stratospheric OH abundance on the simulated ^{14}CO at the surface level. This influence is estimated by the model simulations (2.0-SLT and 2.0-SPFR) with a stratospheric OH abundance reduced by 50% in the NH and in the SH separately. The result is shown in Figure 11.11. Reducing the stratospheric OH abundance in one hemisphere by a factor of two throughout the year results in an increase of up to 9% in the zonal average ^{14}CO mixing ratio at the surface level in the same hemisphere for the 2.0-SPFR simulations and up

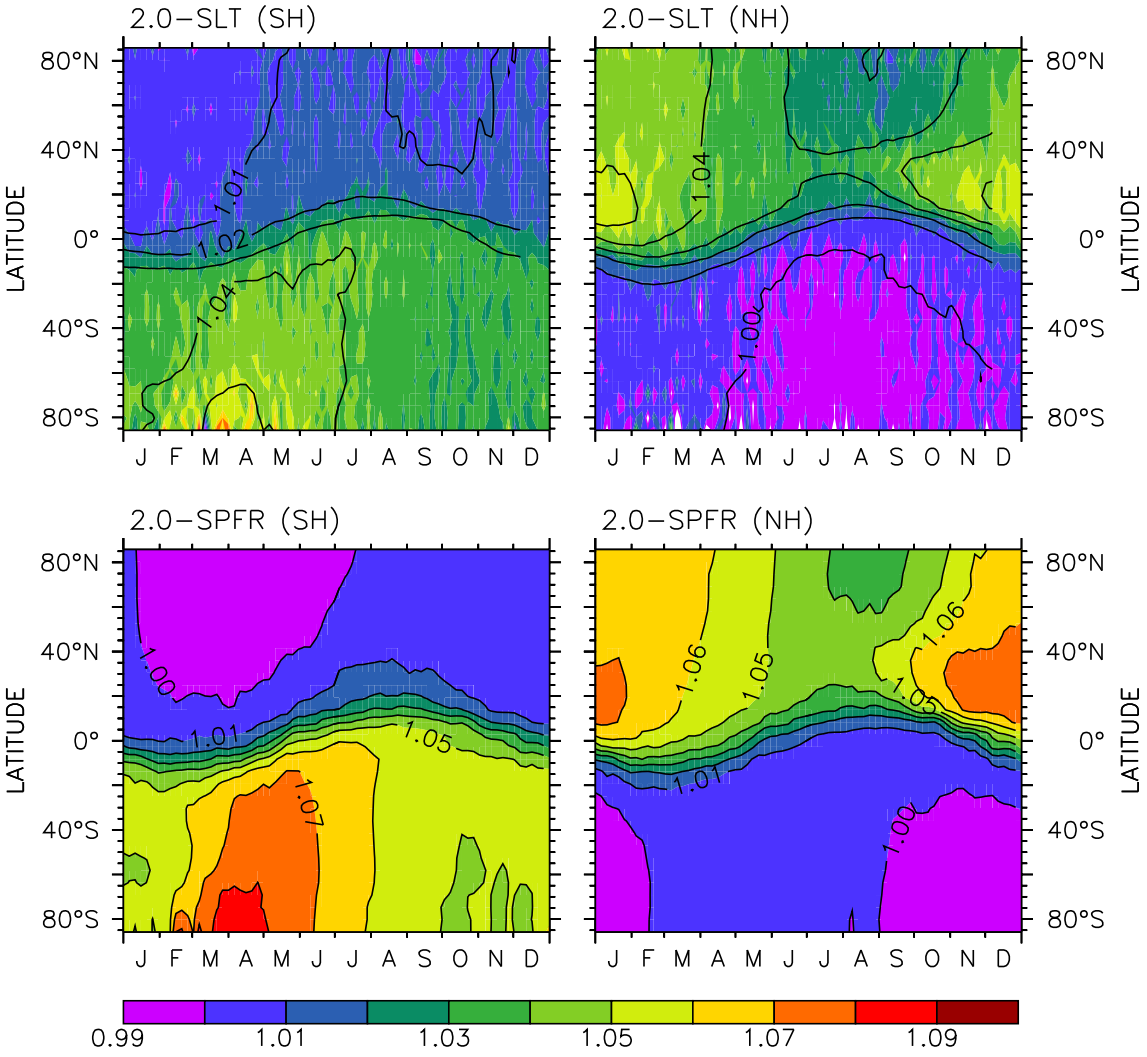

Figure 11.11: Effect of a reduced stratospheric OH abundance on the simulated ^{14}CO mixing ratio at the surface level. The figure shows the zonal average ratio of the simulated ^{14}CO mixing ratio at the surface level calculated with the stratospheric OH abundance reduced by 50% in the NH / SH versus the respective ^{14}CO mixing ratio obtained with 100% stratospheric OH (OH-2D). The simulations are performed with the 2.0-SLT and 2.0-SPFR configuration respectively, using the OH-1 distribution and seasonality and the intermediate LF source distribution of ^{14}CO.

to 6% for the 2.0-SLT simulations. The 2.0-SPFR simulations predict a slightly higher sensitivity of the SH compared to the NH, which is not seen in the 2.0-SLT simulations.

Although in the model simulations the stratospheric OH is scaled separately in the geographical hemispheres, the resulting increased ^{14}CO mixing ratio at the surface level temporarily reaches beyond the equator. Since the tropospheric OH abundance is not changed, this is primarily related to the moving inter-tropical convergence zone

(ITCZ) which defines the climatological hemispheres at a given time of the year. In addition, reducing the stratospheric OH in one hemisphere causes a reduction of up to 1% in the ^{14}CO mixing ratios at the surface level in the opposite hemisphere. This cross-ITCZ transport is, however, not realistic, but rather can be attributed to the algorithms used to force the global tracer mass conservation. These algorithms (such as the global rescaling in 2.0-SPFR, and the "mass-fixer" in 2.0-SLT) imply a non-physical far-reaching transport of tracer mass as discussed in chapter 2.

11.5 ^{14}CO at the surface level: Model versus observations

11.5.1 The global average production rate of ^{14}CO

So far the model simulations of atmospheric ^{14}CO were performed in a normalized mode, i.e., the resulting mass mixing ratios were standardized to a particular global source strength, usually 1 molec cm^{-2} s^{-1}. The ^{14}CO climatology at the surface level discussed above was obtained by rescaling the observations relative to the average conditions between 1955 and 1988 with respect to solar activity, i.e., it was normalized to the global average production rate of ^{14}CO during this period. This has to be taken into account for a comparison of model simulations with the observational data and therefore requires a scaling of the model simulations by the global average production rate between 1955 and 1988.

However, the absolute average production rate of ^{14}CO has a considerable uncertainty (cf. Table 8.1 and Figure 8.4). Therefore as a first test the optimal global average production rate $q_{\rm opt}$ which would be needed in the model atmosphere to minimize the deviation of the model results from the observations is determined by minimizing the RMS - deviation

$$\Delta_{\rm RMS} = \left(\frac{1}{2 \cdot 1{\rm yr}} \int_{T=0}^{T=1{\rm yr}} \int_{\phi=-90^o}^{\phi=90^o} (\tilde{\chi}(\phi,T) - q_{\rm opt} \cdot \chi(\phi,T))^2 cos(\phi) d\phi dT\right)^{\frac{1}{2}} \qquad (11.5)$$

between the observed ^{14}CO mixing ratio $\tilde{\chi}$ (the climatology at the surface level) and the simulated ^{14}CO mixing ratio standardized to 1 molec cm^{-2} s^{-1} in the respective model atmospheres. The integration is performed over latitude ϕ and time T (in years). The resulting $q_{\rm opt}$ calculated with various model configurations is listed in Table 11.3. The table also lists the respective global average RMS - deviation (Eq. (11.5)) and the respective RMS deviations in the NH and SH. The optimal global average ^{14}CO production rate for the period 1955 to 1988 derived in this manner can be compared to independent production rate estimates. From the results of *Masarik and Beer* [1999] (i.e., the global average production rate of ^{14}C as a function of the shielding potential Φ ($q_{^{14}C}(\Phi)$) and the shielding potential as a

	OH	source	time	$\bar{q}_{\rm opt}$	$\Delta_{\rm RMS}$			$\Delta_{\rm RMS}(\bar{q})$		
					global	SH	NH	global	SH	NH
2.0-SLT	OH-1	LF	1994-1998	1.45	2.94	2.02	3.61	3.81	4.22	3.36
2.0-SLT	OH-S	LF	1994-1998	1.39	2.47	1.87	2.94	3.95	4.07	3.82
2.0-SLT	OH-1	MA	1994-1998	1.70	3.00	1.92	3.76	3.02	2.21	3.64
2.0-SLT	OH-S	MA	1994-1998	1.61	2.57	1.83	3.11	2.77	2.32	3.14
TM3-L-L31	OH-1	LF	1997	2.07	2.62	2.09	3.04	3.12	1.52	4.11
2.0-SLT	OH-1	LF	1997	1.43	3.01	2.08	3.68	3.95	4.52	3.29
2.0-SPFR	OH-1	LF	1998	1.38	3.26	2.14	4.06	4.52	5.15	3.81
2.0-SLT	OH-1	LF	1998	1.42	3.03	2.10	3.72	4.06	4.58	3.48
2.0-SLT	OH-2	LF	1998	1.05	3.02	2.34	3.55	8.26	10.08	6.00
2.0-SPFR	OH-2	LF	1998	1.04	3.19	2.33	3.84	8.44	10.49	5.83

Table 11.3: Optimal global average production rate $\bar{q}_{\rm opt}$ of ^{14}CO (in molec cm^{-2} s^{-1}) for the period 1955-1988 and resulting RMS-deviation ($\Delta_{\rm RMS}$ in molec cm^{-2} s^{-1}) of model simulations from observations of ^{14}CO at the surface level (global, SH, NH). The observations are corrected for the estimated biogenic contribution and standardized to average conditions (1955-1988) with respect to solar activity. The best estimate of the global average ^{14}CO production rate in the period 1955-1988 is $\bar{q}$ = 1.76 molec cm^{-2} s^{-1} [*Masarik and Beer*, 1999]. The resulting RMS deviation from the observations for the scaled model simulations using this production rate is also listed ($\Delta_{\rm RMS}(\bar{q})$). LF denotes the source distribution of *Lingenfelter* [1963] intermediate between solar minimum and solar maximum conditions (linearly interpolated at given latitude and depth), MA the source distribution calculated by *Masarik and Beer* [1999] for a shielding potential Φ = 650 MV.

function of time (annual averages, $\Phi(t)$), cf. chapter 8) the global average production rate $\bar{q}$ of ^{14}CO of the period 1955 to 1988 is calculated to be 1.76 molec cm^{-2} s^{-1}, implying a ^{14}C to ^{14}CO reaction efficiency of 0.95 [*MacKay et al.*, 1963; *Pandow et al.*, 1960]. As can be seen from Figure 8.4 the ^{14}C production rate estimated by *Masarik and Beer* [1999] is intermediate compared to other estimates. For this estimated average production rate $\bar{q}$ the resulting RMS deviations between model simulations and observations (Eq. (11.5)) are also listed in Table 11.3.

11.5.1.1 The optimal global source strength of ^{14}CO Scaling the model simulated ^{14}CO with the respective optimal global average production rate (Table 11.3), the remaining discrepancy between model results and observations is larger in the NH compared to the SH for all model configurations. The optimal global average production rate for the 2.0-SLT configuration (LF, OH-1) hardly depends on the particular year of the underlying meteorological data. This is consistent with the small inter-annual variability of the simulated surface level ^{14}CO as derived above (Figure 11.10). Using the MA source distribution instead of the LF source distribution requires a larger global average ^{14}CO production rate in the model atmosphere

for reproducing the observations at the surface level, since a larger fraction of ^{14}CO in the MA source is located in the stratosphere compared to the LF source (cf. chapter 5). The corresponding minimum RMS deviation is (for a given OH distribution) smaller for the LF source distribution compared to the MA distribution.

For the same OH distribution (OH-1) the optimal global average production rate of ^{14}CO in the model atmosphere is largest in TM3-L-L31, and smallest in 2.0-SPFR, the latter, however, being only slightly lower than in 2.0-SLT. The ranking of the corresponding minimum RMS deviations is reversed. Furthermore, the remaining discrepancy in the SH hardly differs between those three configurations, in contrast to the discrepancy in the NH.

Comparing different OH distributions, the best agreement between model simulations (2.0-SLT) and ^{14}CO observations at the surface level, i.e., the smallest RMS deviation, is obtained with the OH-S distribution, followed by OH-1, and is largest for OH-2. At the same time, the required ^{14}CO source strength is largest for OH-1, slightly smaller for OH-S, but significantly smaller for OH-2.

The overall largest global average production rate is required in the TM3-L-L31 atmosphere, while the smallest discrepancy is achieved with the 2.0-SLT configuration using the OH-S distribution and the LF source. Finally, the required global source strength of ^{14}CO is closest to the estimated of 1.76 molec cm^{-2} s^{-1} for the 2.0-SLT configuration using OH-1 and the MA source distribution.

11.5.1.2 The estimated global source strength of ^{14}CO Using a global ^{14}CO source strength of 1.76 molec cm^{-2} s^{-1}, the OH-1 distribution and the LF production rate distribution, the TM3-L-L31 configuration simulates ^{14}CO mixing ratios at the surface level that are closest to the observations, especially in the SH, followed by 2.0-SLT and 2.0-SPFR (Table 11.3). With those boundary conditions the remaining RMS-deviation between simulations and observations is larger in the SH than in the NH in the MATCH configurations and vice versa in the TM3-L-L31 configuration. Using the OH-2 distribution, the deviation from the observations is smaller in the 2.0-SLT simulations compared to the 2.0-SPFR simulations, and in both cases larger in the SH compared to the NH. Furthermore, with the OH-S distribution the deviation between model (2.0-SLT) results and observations is smaller than with OH-1. And finally, using the MA source distribution results in a smaller discrepancy between the model simulations and the observations at the surface level than using the LF source distribution.

11.5.1.3 Discussion Calculating the ^{14}CO source strength q_{opt} that is required in the model atmosphere in order to optimally reproduce the ^{14}CO observations

at the surface level and the corresponding minimum RMS - deviation provide a quantitative estimate of the model performance with respect to the simulated ^{14}CO mixing ratio on a global or hemispheric scale. In the discussions in chapters 5, 7, and 10 it was shown that the simulated ^{14}CO mixing ratios scale with the annual global average source strength of ^{14}CO on the one hand, and with the air mass weighted annual global average OH abundance on the other, i.e.,

$$\chi^* = \chi(\mathrm{OH}, q_0)\frac{f_q}{f_{\mathrm{OH}}} \tag{11.6}$$

where χ is the simulated mixing ratio (in molec cm^{-3} STP) standardized to a global average ^{14}CO production rate q_0 (usually 1 molec cm^{-2} s^{-1}), f_q is the source strength scaling (e.g., $= \bar{q}/q_0$) and f_{OH} the scaling of the global average OH abundance. As a consequence the optimal source strength q_{opt} can be interpreted as the ratio of these two scaling parameters:

$$q_{\mathrm{opt}} = q_0\frac{f_q}{f_{\mathrm{OH}}} \ . \tag{11.7}$$

If one parameter (f_q or f_{OH}) were known exactly, the other could readily be computed from the model simulations and the observations (q_{opt}), under the assumption that the source strength and the global OH abundance solely determine the simulated mixing ratio, disregarding other important mechanisms such as the stratosphere - troposphere exchange. Likewise, if both parameters on the right hand side are fully constrained, the model performance can be tested.

Using the source strength scaling $f_q = 1.76$ for the estimated global average source strength, the required scaling of the global average OH abundance is determined (Eq. 11.7) by the values of q_{opt} listed in Table 11.3. For instance, the OH-1 distribution in the 2.0-SLT configuration using the LF source distribution has to be globally scaled by a factor of 1.21 in order to minimize the RMS deviation between simulated (5 year average) and observed ^{14}CO mixing ratios at the surface level for a global source strength of 1.76 molec cm^{-2} s^{-1} in the model atmosphere. The respective scaling of the global average OH-1 concentration required to minimize the RMS-deviation for the 2.0-SPFR configuration is $f_{\mathrm{OH}} = 1.28$.

The OH-2 distribution (with a 30% lower global average OH concentration, cf. Table 1.1) requires a scaling of 1.68 in the 2.0-SLT atmosphere, and 1.69 in the 2.0-SPFR atmosphere, respectively. In contrast to that, only a factor of 1.43 is needed in order to scale OH-2 to the same global air mass weighted average OH concentration as OH-1. The respective scaling for OH-S (2.0-SLT, LF) is 1.27, whereby the global average OH abundance in OH-1 is about 10% larger than in OH-S.

An increase in the annual global average OH concentration, for instance by 21% in the 2.0-SLT configuration using the LF source distribution would, however, likewise

shorten the simulated methylchloroform (MCF) lifetime in the model atmosphere, which is estimated with the OH-1 distribution to 4.4 ± 0.1 years, in agreement with previous estimates (see chapter 4). Moreover, most model simulations (depending on the configuration) using OH-1 represented the MCF mixing ratio at the ALE/GAGE stations within $\pm 10\%$ (cf. Table 4.7). Consequently, a 20% or more increase in global average OH abundance is rather unlikely.

This conclusion has an important implication. If, on the global scale, the OH abundance in the model is not deficient, either another boundary condition is inadequate, or a process additionally determining the ^{14}CO mixing ratio at the surface level is simulated deficiently by the model. The effects of the two remaining possibilities are closely related. The boundary condition in question is the source distribution of ^{14}CO, especially in the vertical, and the process affecting the ^{14}CO mixing ratio at the surface level is the simulated stratosphere - troposphere exchange (STE). Using the MA source distribution instead of the LF source distribution in 2.0-SLT, the resulting OH scaling factor f_{OH} is only 1.04 for OH-1 and 1.09 for OH-S. An increase of the annual global average OH concentration by 4% (OH-1) or 9% (OH-S) is, however, still consistent with the results obtained from the MCF simulations (cf. chapter 4), i.e., the model is still expected to reproduce the MCF observations within the same range of uncertainty. As discussed in chapter 5, the MA source distribution exhibits a higher fraction of the global ^{14}CO production in the stratosphere (62-66%) than the LF distribution (51-53%, cf. Table 5.1). The same effect, i.e., reduced simulated ^{14}CO mixing ratios at the surface level can thus be achieved by either increasing the global OH abundance (which can be excluded by the MCF simulations) or by shifting the ^{14}CO production to higher levels. As a consequence, a weaker STE would also provide the same result. This can be seen from the TM3-L-L31 simulations. In chapters 7 and 10 it was shown that the STE is weaker in TM3-L-L31 compared to MATCH. As a consequence the optimal source strength in the TM3-L-L31 model atmosphere (q_{opt}, Table 11.3) is larger compared to MATCH, and estimated to 2.07 molec cm^{-2} s^{-1}. This implies a required OH scaling f_{OH} of 0.85, when a global average production rate $\bar{q} = 1.76$ molec cm^{-2} s^{-1} is assumed (Eq. (11.7)), indicating that the STE might be too weak.

At the same time, however, the remaining global RMS deviation between model simulations and observations at the surface level for a given global source strength of 1.76 molec cm^{-2} s^{-1} is smallest for TM3-L-L31 among all model configurations using the LF source distribution. It is only smaller for the 2.0-SLT configuration using OH-S and the MA source distribution. On the hemispheric scale the situation is not that clear. In the SH, again the TM3-L-L31 configuration exhibits the smallest deviation for the estimated global source strength, in contrast to the NH, where the 2.0-SLT simulations are on average closer to the observations.

The differences between the hemispheres and the presumably too weak STE in TM3-L-L19 indicate that for further discussion the analysis so far might be oversimplified. And indeed, horizontal and seasonal effects have not yet taken into account, which can provide additional valuable information. This information is derived and discussed next.

11.5.2 OH or stratosphere - troposphere exchange ?

Two approaches are considered for the comparison between the observations (the 2-D climatology $\tilde{\chi}$ (Figure 11.8) of cosmogenic ^{14}CO at the surface level defined in Eq. (11.4)) and the model simulations. These two approaches imply the extreme assumptions that either the OH distribution and seasonality or the stratosphere - troposphere exchange (STE) in the model is solely responsible for deviations between model simulations and observations at a given time T and location (latitude ϕ). For the first approach (OH) the adequate measure is simply the ratio between model simulations of the ^{14}CO mixing ratio at the surface level (zonal average) and the respective observations, i.e.,

$$r_{\mathrm{OH}}(\phi, T) = \frac{\bar{q} \cdot \chi(\phi, T)}{\tilde{\chi}(\phi, T)} \ , \tag{11.8}$$

whereby the model results have to be scaled to the estimated global average production rate $\bar{q}$ between 1955 and 1988. This is chosen to be 1.76 molec cm^{-2} s^{-1} as discussed above.

The second approach (STE) requires likewise an appropriate measure. For ^{14}CO, information about the role of STE at a given time and location can be achieved by separately tracing ^{14}CO of stratospheric (χ_{st}) and tropospheric (χ_{tr}) origin in the model atmosphere (cf. chapter 10). With this information the hypothetical question how the stratospheric contribution of ^{14}CO at the surface level has to be changed (i.e., scaled by a factor of r_{STE}) in the model results in order to reproduce the observations, i.e.,

$$\bar{q} \cdot (\chi_{tr} + r_{\mathrm{STE}} \cdot \chi_{st}) = \tilde{\chi} \tag{11.9}$$

can be answered. Solving for r_{STE} results in

$$r_{\mathrm{STE}} = \frac{\tilde{\chi}}{\bar{q} \cdot \chi_{st}} - \frac{\chi_{tr}}{\chi_{st}} \ . \tag{11.10}$$

Values of r_{STE} between 0 and 1 indicate that the STE is probably too strong, values larger than 1 suggest that the STE is too weak and more ^{14}CO from the model stratosphere is required to explain the observed ^{14}CO mixing ratios at the surface level. For negative values of r_{STE} the contribution of ^{14}CO of tropospheric origin

simulated at a given time and latitude is already too large compared to the observations without any ^{14}CO from the stratosphere.

The results for various model configurations are shown in Figures 11.12, 11.13, 11.14, and 11.15. The left columns show the ratio r_{OH} (Eq. (11.8)) between scaled model results and observations, the right column the required scaling r_{STE} of the ^{14}CO contribution originating from the stratosphere (Eq. (11.10)).

11.5.2.1 Seasonal cycle of simulated and observed ^{14}CO at the surface level in the SH One striking characteristic common to all model simulations is the overestimation of the observed ^{14}CO mixing ratio at the surface level in the SH with only one exception. The TM3-L-L31 configuration (using OH-1 and the LF source) tends to underestimate the SH ^{14}CO mixing ratio at the surface level on average (SH, annual) by 3-4% (Figure 11.14). The smallest positive deviation in the SH is simulated by 2.0-SLT using the MA source and the OH-S distribution (13% on average, Figure 11.13). Using the OH-1 distribution instead results in a 15% overestimate of the observations in the SH on an annual hemispheric average (Figure 11.13). Using the LF source distribution (with relatively more ^{14}CO production in the troposphere compared to MA, see chapter 5) the model simulations exceed the observations in the SH on average by 34% (2.0-SLT, OH-S), 38% (2.0-SLT, OH-1), and 46% (2.0-SPFR, OH-1) respectively (Figures 11.12 and 11.14). The largest discrepancy between model simulations and observations in the SH is obtained when the OH-2 distribution is used. The measurements are then overestimated by 102% and 106% by the 2.0-SLT and 2.0-SPFR configuration using the LF source, respectively (Figure 11.15).

The discrepancy between model simulations (2.0-SLT and 2.0-SPFR) and observations in the SH is, however, not constant throughout the year, but rather exhibits a seasonal variation with a higher ratio r_{OH} in SH autumn and winter (April to August) compared to the rest of the year. This characteristic is common to the OH-1 and OH-S distribution and also independent of the source distribution employed. In 2.0-SPFR (Figure 11.14) this tends to be less pronounced than in 2.0-SLT (Figure 11.12). In TM3-L-L31 (Figure 11.14) this characteristic is least pronounced.

Taking into account all uncertainties discussed above and in previous chapters this implies that the TM3-L-L31 simulations (OH-1, LF) at least in the SH do not significantly deviate from the observations. And indeed, for a given global ^{14}CO source strength of 1.76 molec cm^{-2} s^{-1} the RMS deviation of the simulations from the observations in the SH is smallest for TM3-L-L31 using OH-1 and the LF source distribution (Table 11.3). Among the MATCH simulations performed, the smallest RMS deviation of the simulations from the SH observations is achieved with the

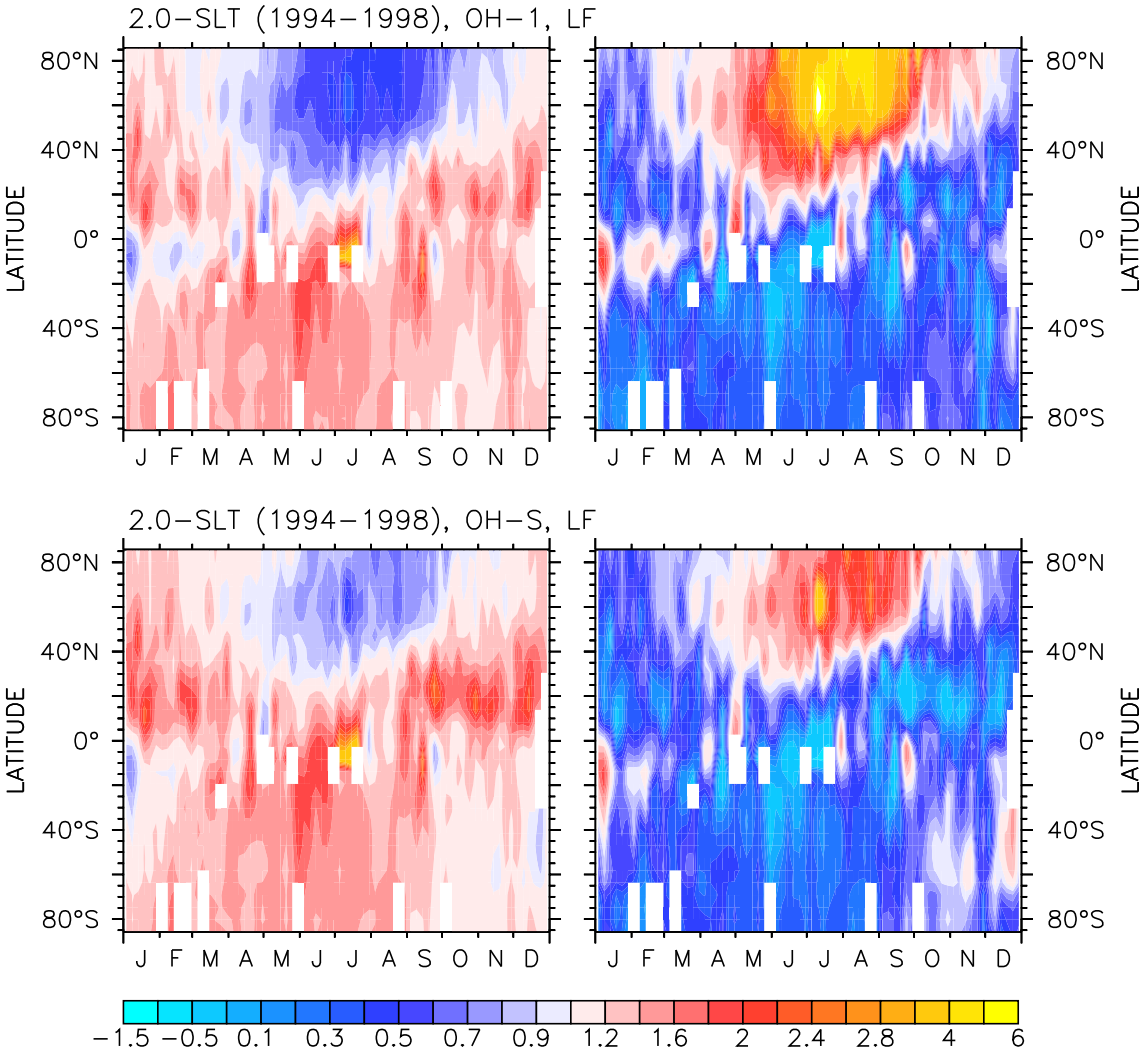

Figure 11.12: Ratio of simulated to observed cosmogenic ^{14}CO at the surface level (r_{OH}, Eq (11.8), left column) and required scaling of ^{14}CO of stratospheric origin (r_{STE}, Eq. (11.10), right). The latter scaling is required if the deviation between simulations and observations is solely attributed to STE processes. Observations of cosmogenic ^{14}CO at the surface level are defined by the 2-D climatology (Figure 11.8, Eq. (11.4)). White boxes indicate insufficient data coverage of observations. All simulated ^{14}CO mixing ratios are rescaled to a global average ^{14}CO production rate of $\bar{q} = 1.76$ molec cm^{-2} s^{-1} in the respective model atmosphere. The upper row shows the results of the 2.0-SLT simulations (average of 1994 to 1998) using the LF source distribution intermediate between solar minimum and solar maximum and the OH-1 distribution. The lower row shows the same for the OH-S distribution.

2.0-SLT configuration using the OH-S distribution and the MA source.

If the discrepancy between model simulations and observations is solely attributed to deficiencies of the simulated STE, in all MATCH configurations the SH STE has to

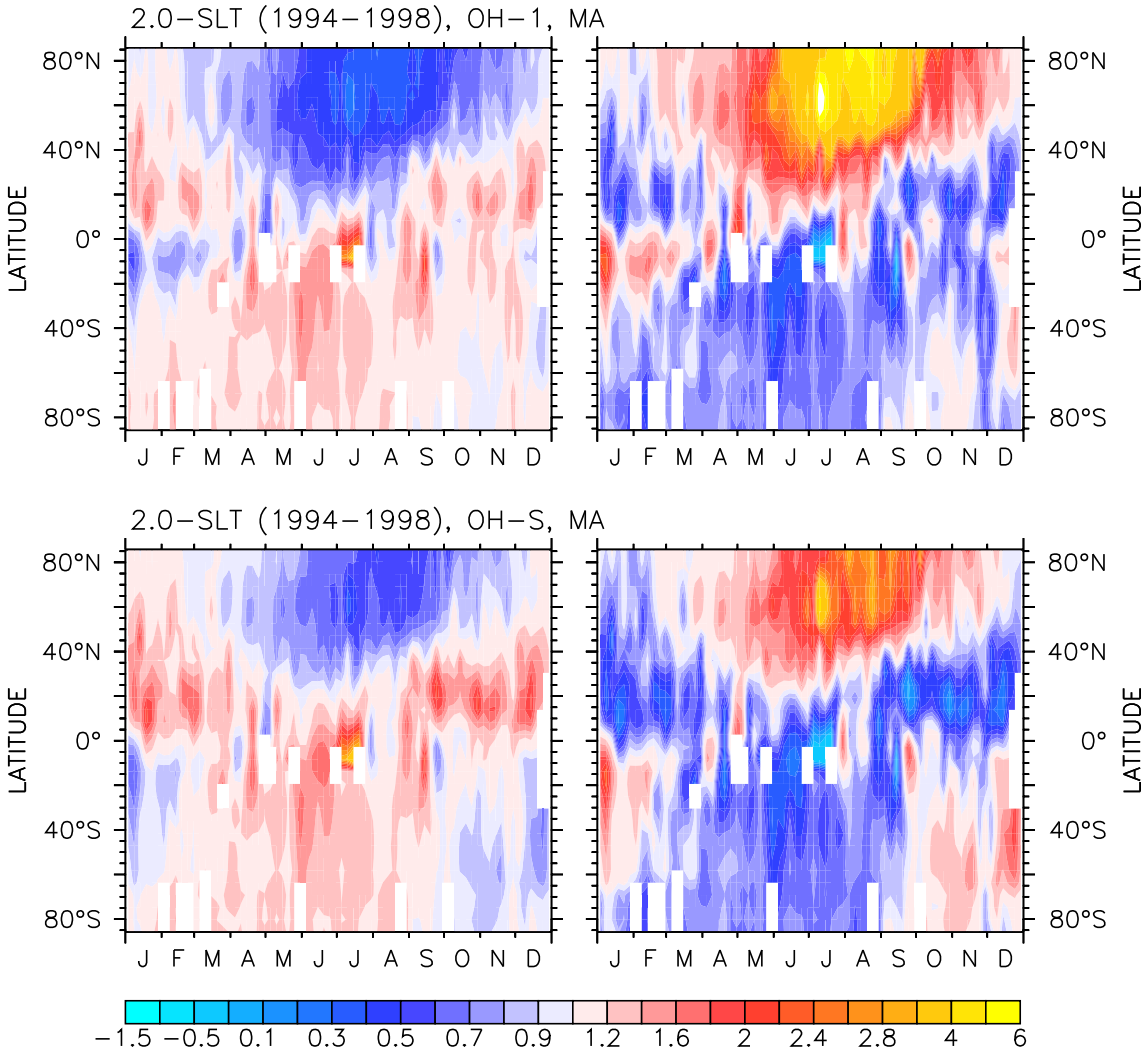

Figure 11.13: As Figure 11.12, but for 2.0-SLT (average of 1994 to 1998), the MA source distribution for $\Phi = 650$ MV, and OH-1 (upper row), and OH-S (lower row) respectively.

be reduced in order to reproduce the observations in the SH. On average, the ^{14}CO contribution originating from the stratosphere at the surface level has to be reduced to 86% (2.0-SLT, OH-S, MA), 80% (2.0-SLT, OH-1, MA), 48% (2.0-SLT, OH-S, LF), 40% (2.0-SLT, OH-1, LF), and 27% (2.0-SPFR, OH-1, LF) of the simulated level, respectively. To compensate for the small deviation of the TM3-L-L31 simulations in the SH at the surface level, the amount of ^{14}CO originating from the stratosphere has to be increased on average by 26%. For the MATCH simulations using the OH-2 distribution even the amount of ^{14}CO produced in the troposphere results in too high ^{14}CO mixing ratios at the SH surface level (Figure 11.15). The required scaling factor r_{STE} for χ_{st} is therefore negative, averaged over the SH and the whole year -0.15 (2.0-SLT, LF) and -0.23 (2.0-SPFR, LF), respectively.

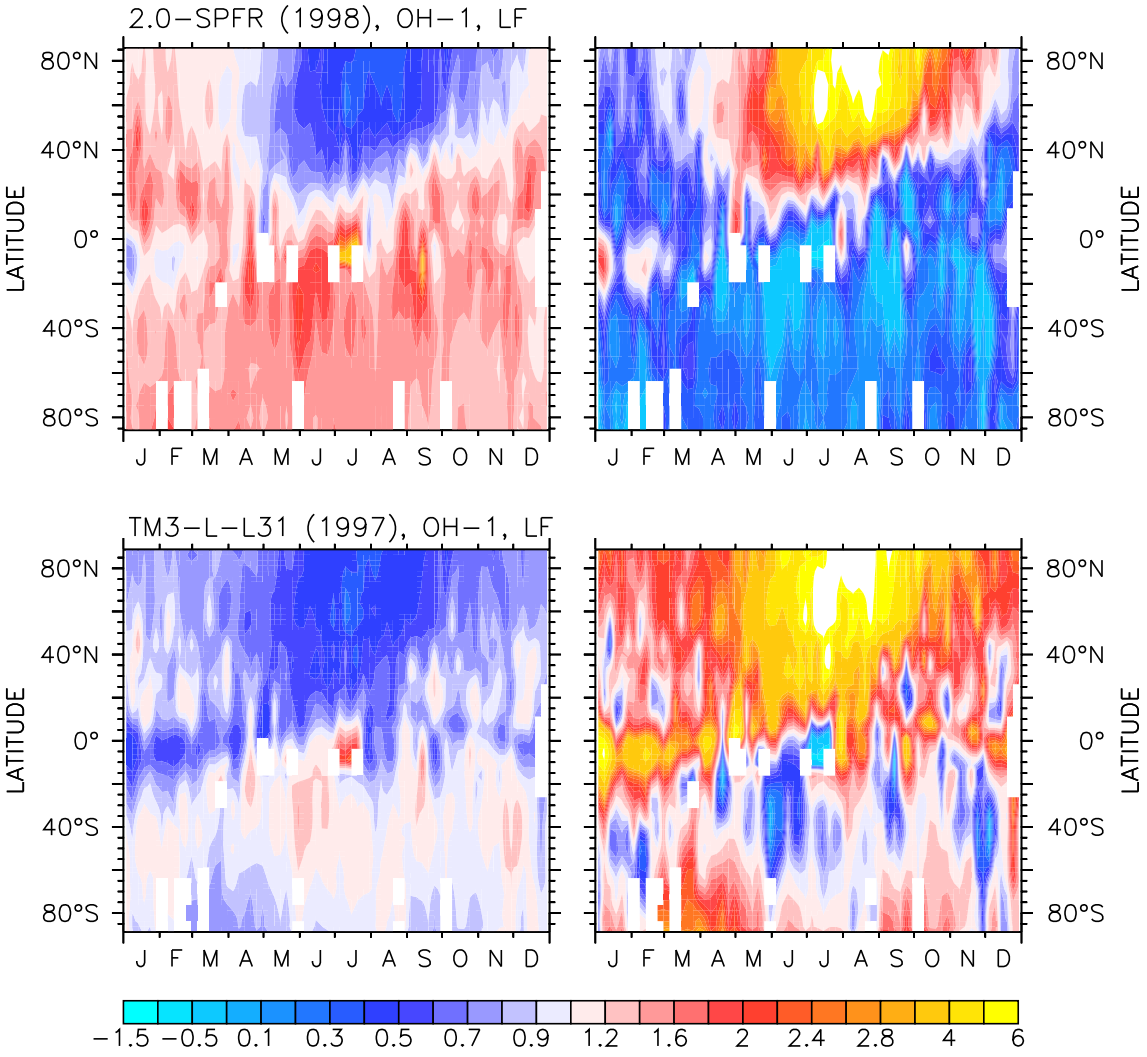

Figure 11.14: As Figure 11.12, but for 2.0-SPFR (upper row) and TM3-L-L31 (lower row). In both model simulations the intermediate LF source distribution is used and the OH-1 distribution is prescribed. The meteorological year is 1997 for TM3-L-L31 and 1998 for 2.0-SPFR.

11.5.2.2 Seasonal cycle of simulated and observed ^{14}CO at the surface level in the NH The second important characteristic of the model simulations is the deviation from the ^{14}CO observations in the NH at the surface level, which exhibits a very distinct seasonal cycle north of 40^{o}N in all model configurations. All model simulations, regardless of which source distribution or OH-distribution is used, significantly underestimate the ^{14}CO mixing ratio at the surface level north of 40^{o}N between June and September. In 2.0-SLT the simulated ^{14}CO mixing ratio during this period and within this latitude belt is on average only 44% (OH-1, MA), 56% (OH-1, LF), 63% (OH-S, MA), and 78% (OH-S, LF) of the observed mixing ratio, respectively (Figures 11.12 and 11.13). The 2.0-SPFR configuration predicts

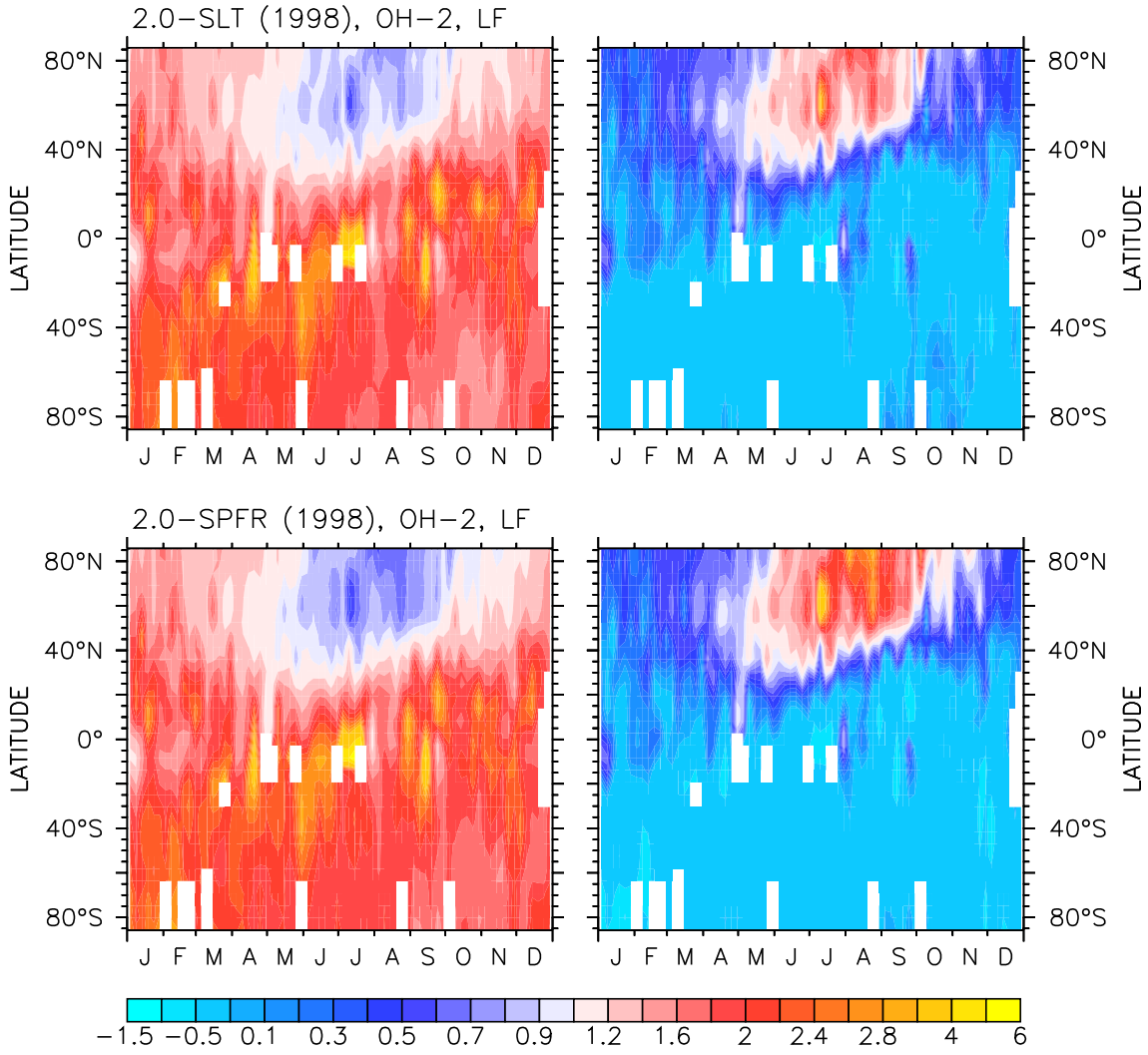

Figure 11.15: As Figure 11.12, but for 2.0-SLT (upper row) and 2.0-SPFR (lower row) using the intermediate LF source distribution and the OH-2 distribution. The meteorological year in both cases is 1998.

on average only 48% (OH-1, LF), and the TM3-L-L31 configuration only 47% (OH-1, LF) of the observed ^{14}CO mixing ratio at the surface level north of 40^{o}N between June and September (Figure 11.14). Even when the OH-2 distribution is used (Figure 11.15), which during the time in question has an average OH concentration in the NH which is 28% to 34% lower than OH-1 (cf. Table 1.1), the 2.0-SLT and 2.0-SPFR configurations using the LF source underestimate the observations still by 10% and 19%, respectively.

If this lack of ^{14}CO is to be compensated by a higher import of stratospheric ^{14}CO, the amount of ^{14}CO at the surface level originating from the stratosphere (χ_{st}) has to be increased north of 40^{o}N between June and September on average by a factor

of 3.63 (OH-1, MA), 3.19 (OH-1, LF), 2.15 (OH-S, MA), and 1.74 (OH-S, LF) in the 2.0-SLT simulations, by 4.55 in the 2.0-SPFR (OH-1, LF) simulation, and by 5.18 in the TM3-L-L31 simulation (OH-1, LF), respectively. With OH-2 and the LF source distribution, the required increase in the stratospheric contribution at the surface level is on average 1.33 (2.0-SLT) and 1.71 (2.0-SPFR) during the period and within the latitude belt in question.

During NH winter, the model configurations tend to overestimate the observed ^{14}CO mixing ratio at the surface level in the NH, except TM3-L-L31 using OH-1 and the LF source distribution (Figure 11.14), which underestimates the NH ^{14}CO mixing ratio throughout the year. Therefore, a decreased stratospheric contribution to the surface level ^{14}CO is required in NH winter in the MATCH configurations, whereas the TM3-L-L31 simulation requires an increased STE, provided that the deviation of the simulations from the observations is to be compensated solely by a changed downward flux of ^{14}CO from the stratosphere into the troposphere.

In the NH south of 40^oN the situation is similar to the SH, though with a different phase. The model configurations tend to overestimate the observed ^{14}CO mixing ratio at the surface level with a maximum in winter and to underestimate it between 20^oN and 40^oN in summer.

Averaged over the NH and the whole year, the ratio between model results and observations is 0.87 (OH-1, MA), 1.02 (OH-1, LF), 1.04 (OH-S, MA), and 1.21 (OH-S, LF) for the 2.0-SLT configuration (Figures 11.12 and 11.13), and 1.00 (LF, OH-1) for the 2.0-SPFR configuration, respectively (Figure 11.14). The TM3-L-L31 (OH-1, LF) configuration predicts on average 0.71 times lower ^{14}CO mixing ratios at the surface level than observed (Figure 11.14). Using OH-2, 2.0-SLT overestimates the ^{14}CO mixing ratio at the surface level by a factor of 1.46, and 2.0-SPFR by 1.41, respectively (Figure 11.15). For a hypothetical compensation through a stronger STE, on average the part of ^{14}CO originating from the stratosphere then has to be scaled by a factor of 1.64 (OH-1, MA), 1.32 (OH-1, LF), 1.13 (OH-S, MA), and 0.81 (OH-S, LF) in the 2.0-SLT atmosphere, and by 1.62 in the 2.0-SPFR (OH-1, LF) atmosphere. In TM3-L-L31 (OH-1, LF), the required factor is 2.71 on average. Using the OH-2 distribution, ^{14}CO from the stratosphere at the surface level has to be scaled down by a factor of 0.51 (2.0-SLT) and 0.60 (2.0-SPFR), respectively.

11.5.2.3 Discussion The deviation of the model simulations from the observations of ^{14}CO at the surface level exhibits a seasonal cycle in both hemispheres. This implies that agreement between model simulations and observations cannot be achieved by scaling either the annual average OH concentration, the global source strength, or the annual average strength of STE downward transport. Rather the

seasonal variation of at least one of these parameters is deficiently simulated by the models. The weakest seasonal variation of the deviation is predicted by TM3-L-L31 in the SH.

The observed seasonal cycle of ^{14}CO at the surface level in the SH (cf. Figures 11.5 and 11.8) exhibits a maximum between August (30^{o}S-60^{o}S) and September (60^{o}S-90^{o}S), and a minimum in February. Both the times of minimum and maximum ^{14}CO are reproduced within 0.5 months by the 2.0-SPFR and the TM3-L-L31 configuration (cf. Figure 10.4). The 2.0-SLT configuration also reproduces the time of the minimum in February, although on average, the maximum tends to be reached almost one month earlier in July/August (cf. Figure 11.10), with a considerable interannual variation. This earlier minimum is consistent with the small phase shift of 0.5 to 1 month between the SH tropospheric burden fraction predicted by TM3-L-L31 and 2.0-SPFR on the one side and by 2.0-SLT on the other (cf. Figure 10.12). In chapter 10 it was concluded that the 2.0-SLT STE is "faster" compared to the STE in 2.0-SPFR and TM3-L-L31, i.e., the annual cycle of the downward flux in 2.0-SLT is phase shifted by at least 0.5 to 1 month earlier compared to TM3-L-L31 and 2.0-SPFR. Two resulting effects are the faster downward transport of SPE induced ^{14}CO in 2.0-SLT compared to 2.0-SPFR (chapter 9, Figures 9.3 and 9.9), and the earlier occurrence of the maximum fraction of stratospheric ^{14}CO at the surface level in the 2.0-SLT simulations compared to the 2.0-SPFR and TM3-L-L31 simulations (Figure 10.13). The latter indicates further that differences between the particular model configurations with respect to this phase shift are more pronounced in the SH than in the NH. Furthermore the annual average strength of the simulated STE is lower in TM3-L-L31 than in the MATCH configurations (see chapters 7 and 10). In conclusion, in the SH the simulated STE of TM3-L-L31 is better qualified for reproducing the ^{14}CO observations at the surface level than the MATCH simulated STE. This concerns the absolute strength and seasonality of the STE. It is indicated by the lower deviation of the TM3-L-L31 simulations with a smaller amplitude of r_{OH} in the SH compared to the 2.0-SLT simulations. This is moreover consistent with the estimated global source strength of ^{14}CO and the OH (OH-1) distribution and seasonality in the SH. In other words, at least in the SH the TM3-L-L31 STE seems to be more realistic than the MATCH STE, because it reproduces the observed ^{14}CO levels at the surface without requiring any changes in the estimated OH distribution or source strength of ^{14}CO. However, this conclusion implies that the OH distribution employed (OH-1), and the global ^{14}CO source strength are also realistic, at least for the SH.

As a further consequence the MATCH simulated STE in the SH is too strong, and the ^{14}CO of stratospheric origin at the SH surface level in MATCH has to be reduced on annual average to 40% (2.0-SLT, Figure 11.12) and 27% (2.0-SPFR, Figure 11.14) of

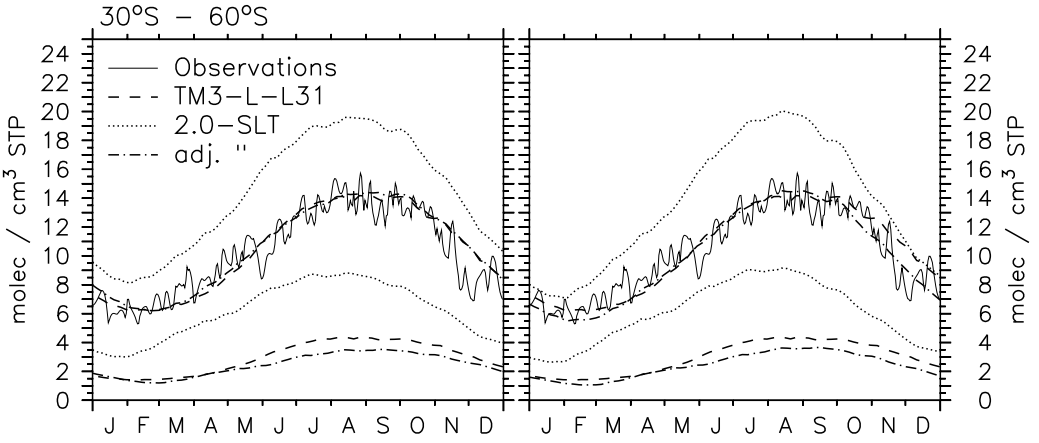

Figure 11.16: Effect of phase shifted and reduced stratospheric ^{14}CO contribution to ^{14}CO at the surface level. The solid line shows the observation (2-D climatology of primary ^{14}CO at the surface level standardized to the global average production rate between 1955 and 1988, Figure 11.8, Eq. (11.4)) averaged between 30^{o}S and 60^{o}S. The dashed lines show the model simulation (averaged over the same range) obtained with TM3-L-L31, the OH-1 distribution, and the intermediate LF source distribution, whereby a global average production rate of 1.76 molec cm^{-2} s^{-1} in the model atmosphere is assumed. The upper line is the total ^{14}CO mixing ratio (χ) and the lower line the ^{14}CO mixing ratio of ^{14}CO originating from the stratosphere (χ_{st}), respectively. The results for 2.0-SLT are shown by the dotted lines. The dashed-dotted line (adjusted 2.0-SLT) is obtained by scaling the simulated stratospheric ^{14}CO at the surface level (2.0-SLT) by 0.4 and shifting it by one month to later times. The right panel shows the same, but using the OH-S distribution in 2.0-SLT instead of OH-1. The meteorological year in all cases is 1997.

its simulated level, respectively, under the same boundary conditions used in TM3-L-L31, i.e., using the OH-1 distribution and the LF source. Using the MA source distribution instead (with the maximum estimated production in the stratosphere), the ^{14}CO of stratospheric origin is still too high and has to be reduced to 80% of its simulated level on annual average (Figure 11.13).

The effect of the required changes in the stratospheric ^{14}CO contribution in 2.0-SLT (LF) in the SH mid-latitudes is summarized in Figure 11.16 in comparison to the TM3-L-L31 simulations and the observations. Scaling down the 2.0-SLT simulated stratospheric ^{14}CO at the surface level (χ_{st}, Eq. (11.9)) by $r_{\mathrm{STE}} = 0.4$ and shifting its contribution by one month, i.e.,

$$\chi'(t) = \bar{q} \cdot (\chi_{tr}(t) + r_{\mathrm{STE}} \cdot \chi_{st}(t - 1 \text{ month})) \ , \tag{11.11}$$

the differences between the 2.0-SLT and the TM3-L-L31 predicted ^{14}CO mixing ratio at the surface level vanish on average between 30^{o}S and 60^{o}S. Moreover, the model results agree with the observations within the range of uncertainty. The remaining small difference between the mixing ratio of stratospheric ^{14}CO at the surface level

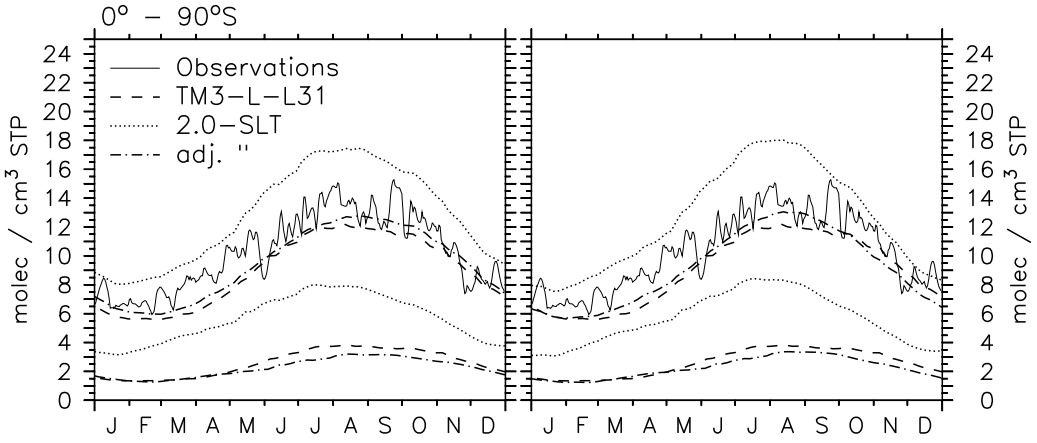

Figure 11.17: As Figure 11.16, but for the entire SH.

(χ_{st}, lower lines) between 2.0-SLT (adjusted) and TM3-L-L31 can be attributed to deviations in the online diagnosed tropopause pressure which is used to distinguish the production of ^{14}CO in the stratosphere from the tropospheric production (cf. Figure 10.10). Using the OH-S distribution in 2.0-SLT and following the same procedure, the result is very similar (Figure 11.16, right), since the SH seasonality and average abundance of OH-1 and OH-S are similar (cf. Figure 1.6). The largest deviation from the TM3-L-L31 (OH-1) results occur between October and December, when the average SH concentration of OH-S differs from the respective OH-1 concentration (cf. Figure 1.6).

The overall agreement between model simulations (TM3-L-L31 and 2.0-SLT) and observations of ^{14}CO in the SH can consequently be achieved solely by adjusting the simulated stratospheric contribution to the ^{14}CO at the surface level without changing the tropospheric OH distribution. This also holds for the entire SH, as shown in Figure 11.17. Both the TM3-L-L31 simulations and the adjusted 2.0-SLT simulations agree with the observations within the uncertainties. In particular, the range of the estimated production rate $\bar{q}$ and the uncertainty in the global average OH abundance have to be taken into account. For instance, a 10% increased production rate would shift the model simulated annual cycle by 10% to higher ^{14}CO mixing ratios.

The resulting annual average contribution of ^{14}CO originating from the stratosphere at the surface level (χ_{st}) is estimated to 2.43 molec cm^{-3} STP with a minimum of 1.29 cm^{-3} STP in February and a maximum of 3.59 cm^{-3} STP in August (Figure 11.17). The peak to mean amplitude is therefore 48% around the annual average.

If, in contrast, the deviations of the MATCH simulations from the observations in the SH are rather attributed to deficiencies in the OH distribution and seasonality, an increased OH concentration in the SH, especially in winter is required. From the

analysis of r_{OH} it can be concluded that the annual average OH concentration in the SH has to be increased by at least 13% (OH-S, MA, Figure 11.13) and up to 38% (OH-1, LF, Figure 11.12) in the 2.0-SLT SH, and 46% in the 2.0-SPFR SH (Figure 11.14). Moreover, the seasonality has to be modulated, i.e., in autumn/winter the OH concentration in the SH has to be increased more than in summer/spring, implying a smaller annual amplitude of the SH OH concentration (cf. Figure 1.6). These changes are even required when the ^{14}CO production is maximally shifted into the stratosphere, i.e., when the MA source distribution is used (Figure 11.13).

An increase in SH OH on average, however, would decrease the simulated global average lifetime of methylchloroform (MCF, see chapter 4), unless the OH concentration is decreased by the same amount elsewhere for compensation, i.e., in order to preserve the global average concentration that determines the simulated lifetime of MCF. In this case the NH average OH concentration has to be decreased. Increasing the SH OH and decreasing the NH OH concentration results in a lower or even reversed interhemispheric asymmetry in the OH abundance with higher average OH concentrations in the SH. This has been suggested earlier by *Brenninkmeijer et al.* [1992]; however, it would not be in favor of a better agreement between model simulations and observations of MCF within the limitations of this method (cf. chapter 4). Moreover, the reasons for a higher SH OH abundance and the additionally required seasonal modulation would still be unresolved, whereas the overestimated STE in MATCH is a known problem [*Lawrence et al.*, 1999a]. Thus a higher SH and reduced NH OH abundance than predicted cannot be fully excluded at this stage, although a reduced contribution of stratospheric ^{14}CO to the ^{14}CO mixing ratio at the surface level, and a changed seasonality seems to be more likely.

In the NH the situation is much more complicated. The observed seasonal cycle of ^{14}CO at the surface level exhibits a maximum between February and March and a minimum between July and August (Figures 11.4, 11.5, and 11.8). This characteristic is reproduced within 0.5 months by all involved model configurations (cf. Figures 10.4 and 11.10). It is further consistent with the extrema of the simulated tropospheric burden fraction in the NH (Figure 10.12). The absolute level of the observed ^{14}CO mixing ratio at the surface level is, however, significantly underestimated north of 40^{o}N between June and September by all model configurations, independent of the source distribution and the OH distribution. Even with the OH-2 distribution this characteristic is present (Figure 11.15). In contrast to that, during the rest of the year the observed ^{14}CO mixing ratio north of 40^{o}N tends to be overestimated, except by TM3-L-L31, which predicts lower ^{14}CO levels than observed throughout the year.

As in the SH, also in the NH the 2.0-SLT simulated STE seasonality is phase shifted compared to the 2.0-SPFR and TM3-L-L31 STE seasonality, with the maximum

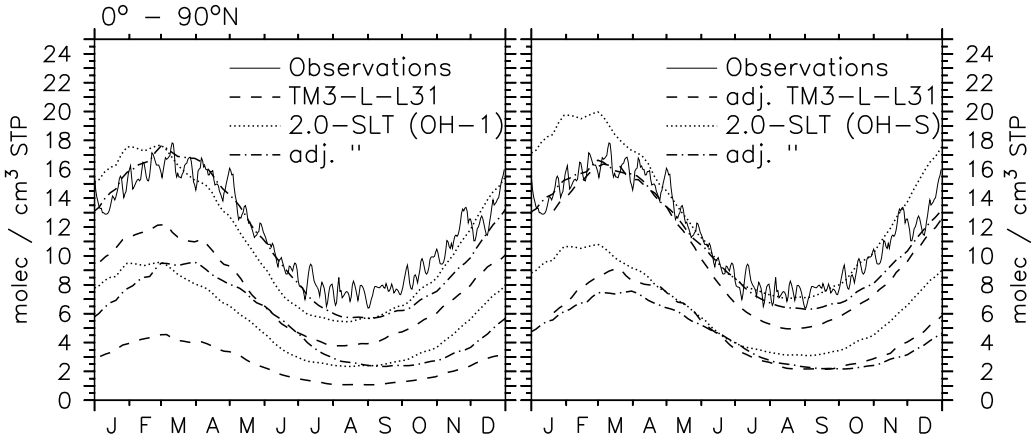

Figure 11.18: As Figure 11.16, except for 0^o-90^oN. The dashed-dotted line (adjusted 2.0-SLT) is obtained by shifting the stratospheric ^{14}CO seasonal cycle at the surface level by one month to later times (left panel). In the right panel, the TM3-L-L31 stratospheric contribution of ^{14}CO at the surface level (χ_{st}) is doubled and shifted by half a month to later times. The 2.0-SLT simulations are performed using OH-S instead of OH-1. The adjustment of the 2.0-SLT (OH-S) simulations include a shift of 1 month to later times, and a scaling of χ_{st} by 0.7. The meteorological year in all cases is 1997.

downward transport occuring earlier in 2.0-SLT. This is indicated by the earlier extrema (about 0.5 months) of the simulated tropospheric burden fraction in 2.0-SLT in the NH compared to the 2.0-SPFR and TM3-L-L31 simulations (cf. Figure 10.12). Furthermore, similar to the situation in the SH, in the NH the occasionally SPE induced ^{14}CO is also transported faster into the troposphere in 2.0-SLT compared to 2.0-SPFR (chapter 9, Figures 9.3 and 9.9). Finally, the NH maximum of stratospheric ^{14}CO at the surface level is reached earlier in 2.0-SLT compared to 2.0-SPFR and TM3-L-L31 (cf. Figure 10.13).

One might conclude that a reduction of the stratospheric OH concentration could increase the amount of ^{14}CO that is transported downward, since less of the ^{14}CO becomes oxidized in the stratosphere. The estimates above, however, show that the sensitivity of the simulated ^{14}CO mixing ratio at the surface level to the stratospheric OH abundance in either hemisphere is rather small (Figure 11.11). A reduction of the stratospheric OH abundance by 50% results in a maximum ^{14}CO increase of 9% at the surface level. Between June and September, north of 40^oN, where the most additional ^{14}CO from the stratosphere would be needed, the effect is smallest, and the ^{14}CO mixing ratio increases by less than 5%.

Following the same approach as in the SH, the deviation of the model simulations from the observations can hypothetically be attributed to deficiencies in the simulated STE. Figure 11.18 shows the required changes in the simulated ^{14}CO originating from the stratosphere at the surface level. In order to obtain consistent results

between TM3-L-L31 and 2.0-SLT (both OH-1, LF) a doubling of the amount of ^{14}CO from the stratosphere at the surface level is on average required in TM3-L-L31. Then the model simulations and observations agree within the range of uncertainties, without a change of the stratospheric contribution χ_{st} in 2.0-SLT. This agreement is further improved by shifting χ_{st} by 0.5 months and 1 month to later times in TM3-L-L31 and 2.0-SLT, respectively (cf. Eq. (11.11)). The resulting stratospheric contribution χ_{st} at the surface level varies then (average of adjusted TM3-L-L31 and adjusted 2.0-SLT, both OH-1) from 2.25 molec cm^{-3} STP in September / October to 9.34 molec cm^{-3} STP in March (Figure 11.18). The annual average is 5.19 molec cm^{-3} STP, and therefore the peak to mean amplitude is +80% / -57%.

The 2.0-SLT simulations with OH-S instead of OH-1 require a reduction of the stratospheric ^{14}CO contribution at the surface level to 70% of the predicted value on average. Assuming that the effect of exchanging OH-1 by OH-S is similar in TM3-L-L31, the required scaling of the TM3-L-L31 simulated stratospheric ^{14}CO at the surface would then decrease to 1.4. The average NH seasonal cycle of stratospheric ^{14}CO at the surface level exhibits then a minimum of 2.17 molec cm^{-2} s^{-1} in September / October, a maximum of 7.56 molec cm^{-2} s^{-1} in March, and an annual average of 4.49 molec cm^{-2} s^{-1}. The peak to mean amplitude is therefore +68% / -52%.

As a consequence, in the NH the average deviation of the model simulated ^{14}CO at the surface level from the observations can be explained partly by deficiencies in the simulated stratospheric contribution to ^{14}CO at the surface level, and partly by effects of the chosen OH distribution. The observations of ^{14}CO at the surface level in the NH can consistently be reproduced by a 2.0-SLT setup, using the OH-S distribution and the LF source distribution, but with the stratospheric contribution reduced by roughly one third. In the TM3-L-L31 configuration using the same boundary conditions, the NH STE is underestimated and has to be increased by approximately 40%. In both configurations the agreement between model simulations and observations at the surface level is improved by shifting the STE seasonality between 0.5 and 1 month to later times.

On smaller scales than hemispheric, however, larger deviations between model simulations and observations are apparent. Especially the distinct seasonal cycle of the deviation north of 40^{o}N (Figure 11.19), where all model configurations significantly underestimate the observations at the surface level between June and September (Figures 11.12, 11.13, 11.14, and 11.15) is not yet resolved. Simulations with the OH-1 distribution similarly underestimate the NH autumn minimum of ^{14}CO at the surface level in TM3-L-L31 and 2.0-SLT, after the STE rate of TM3-L-L31 is hypothetically adjusted to that of 2.0-SLT. Calculations with 2.0-SLT and the OH-S distribution agree likewise better with the observations when the stratospheric con-

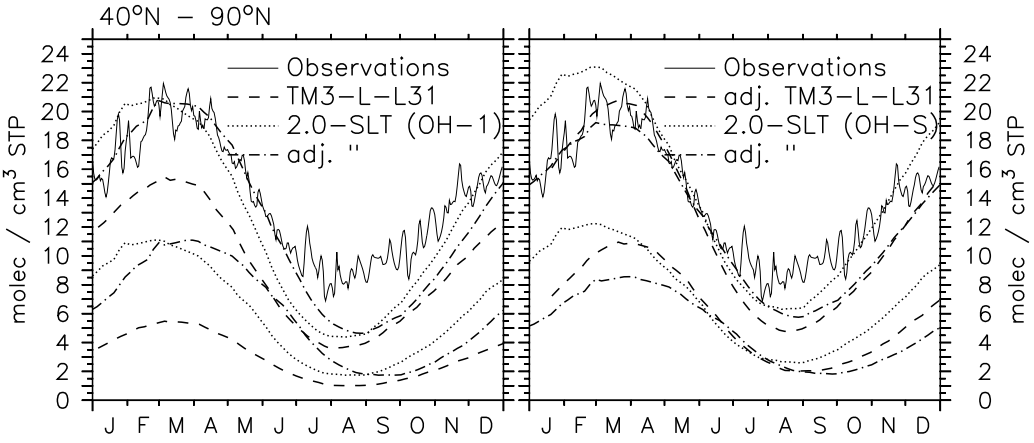

Figure 11.19: As Figure 11.18, but averaged over 40^{o}N to 90^{o}N.

tribution to ^{14}CO at the surface is down-scaled to 2/3. But also calculations with OH-S still tend to underestimate the observed ^{14}CO mixing ratio at the surface level north of 40^{o}N in autumn, and to overestimate it in spring. This remaining discrepancy between simulations and observations has then to be compensated by either a lower OH concentration in summer and autumn, and a higher OH concentration in spring, implying a reduction of the seasonal OH amplitude, or by an additional modulation of the stratospheric fraction of ^{14}CO. The second solution, i.e, an additional modulation of the contribution of stratospheric ^{14}CO at the surface level requires an increased NH STE rate in summer / autumn, when the STE rate is claimed to be at its minimum (cf. Figure 10.14). This would therefore decrease the seasonal amplitude of the NH STE. The first solution, i.e., a lower annual OH amplitude north of 40^{o}N, is, however, consistent with the MCF simulations (see chapter 4), as long as the annual average OH concentration is not changed, or the excess OH is redistributed, e.g, to the tropics. Finally, the possibility that the underestimated ^{14}CO minimum at high northern latitudes in autumn in the model is caused by a too strong transport component from the polar region into the tropics can be excluded, since an overestimated transport in the meridional direction is not in agreement with the simulated SF_6 and F11 latitudinal gradients, which are well reproduced by the model (cf. chapters 3 and 4).

So far, mainly two of the three model configurations have been discussed and compared, namely TM3-L-L31 and 2.0-SLT. The 2.0-SPFR simulations can also be consistently arranged in the framework developed above. Figure 11.20 shows the effect of changing the ^{14}CO contribution from the stratosphere to ^{14}CO at the surface level in both hemispheres in comparison to the observations. The resulting scaling in the NH and SH is consistent with the numbers from the discussion above. Moreover the phase shift of 1 month in the NH, whereas no phase shift is required in the SH,

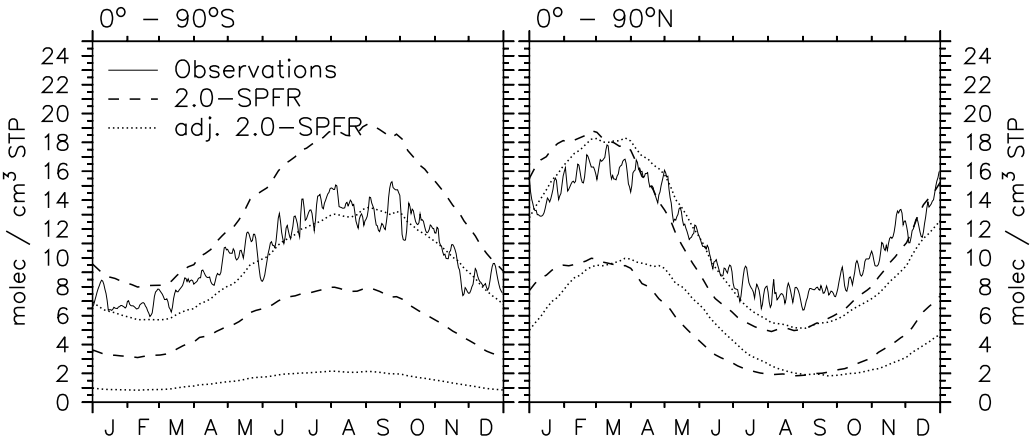

Figure 11.20: As Figure 11.16, except for 2.0-SPFR. The dashed lines show the model simulations (^{14}CO mixing ratio at the surface level averaged over the respective hemisphere, upper line) and the stratospheric contribution χ_{st} (lower line). The dotted lines show the respective adjusted results. In the SH (left) the stratospheric contribution χ_{st} of ^{14}CO to ^{14}CO at the surface level is scaled down by a factor of 0.27 without a phase shift. In the NH (right) χ_{st} is not scaled, however shifted by one months to later times. The meteorological year for the simulations is 1998.

confirms the results discussed in chapter 10 concerning the differences of the STE timing between the particular model configurations.

In summary, the ^{14}CO observations at the surface level can consistently be reproduced by the models and implications with respect to the STE strength and seasonality and the OH distribution and seasonality in both hemispheres become apparent. Other approaches cannot be excluded at this stage; however, they would require extensive assumptions beyond the present knowledge. For instance, adjusting the TM3-L-L31 simulated ^{14}CO mixing ratio at the surface level in the NH on average to the observations requires a 43% increased global average ^{14}CO source strength (1955-1988), i.e., 2.51 molec cm^{-2} s^{-1}. This however, does not resolve the seasonal variation of the deviations. Furthermore, the SH observations would then be overestimated by the model, implying either a too strong simulated STE in the TM3-L-L31 SH compared to the NH, or a much too low OH abundance in the SH. Similarly, the NH deviation between the TM3-L-L31 simulations and observations can be adjusted by increasing the stratospheric contribution to the surface level ^{14}CO on average by a factor of 2.71, or alternatively by decreasing the average NH OH abundance by 30% on average. To resolve the seasonality, the OH seasonality has to be changed in addition.

Moreover, it is important to note that the overall consistency in the above discussion is achieved by using the intermediate LF distribution [*Lingenfelter*, 1963] and an estimated global average source strength of 1.76 molec cm^{-2} s^{-1} [*Masarik and Beer*,

1999] between 1955 and 1988. Among the estimated source distributions, the LF source distributions exhibits the weakest vertical gradient, i.e., the highest fraction of ^{14}CO production in the troposphere (cf. chapter 5). Using the MA or the OB source distribution instead (chapter 5) results in lower simulated ^{14}CO mixing ratios at the surface level, since relatively more ^{14}CO is produced in the stratosphere (chapter 5). Obtaining an agreement between model simulations and observations using one of these other distributions would therefore require an enhanced STE in the model, a larger global average production rate of ^{14}CO than assumed, or a reduced OH abundance.

The remaining issue to be discussed is the relationship between the simulated stratospheric ^{14}CO contribution χ_{st} and the STE rate. As already discussed in chapter 10, χ_{st} at a given time and location scales with the amount of ^{14}CO that is introduced at the tropopause from the stratosphere into the troposphere. The reason is that the reaction with OH is of first order, and therefore a relative reduction of the ^{14}CO input at the top of the troposphere results in the same relative reduction of the mixing ratio (stratospheric fraction) at the surface, independent of the OH distribution in between. Thus, relative changes of χ_{st} directly render the relative change of the STE rate of ^{14}CO, whereas the absolute level of χ_{st} arriving at the surface level further depends on the OH abundance, i.e., on how much of the stratospheric ^{14}CO is oxidized on its way down. This implies that for a given OH distribution and seasonality, and a given ^{14}CO source distribution the STE rate of different model configurations at a given time can directly be compared in terms of χ_{st}. This is, however, not applicable for a quantitative estimate of the interhemispheric asymmetry of the STE, since the tropospheric OH also exhibits an interhemispheric asymmetry, and the absolute level of χ_{st} depends on the tropospheric OH abundance and seasonality as well. For the same reason χ_{st} is further not necessarily suited to directly measure the seasonal amplitude of STE. For such purposes the ratio of stratospheric to tropospheric ^{14}CO at the surface level may be more appropriate, since the χ_{tr} seasonality and distribution also contains the information about the tropospheric OH. At this stage however, this is speculative and has to be further investigated and tested in future. It potentially provides a means to estimate quantitatively the model simulated STE rate (especially the seasonality and the interhemispheric differences) in comparison to measurements. Currently, it only implies that quantitative conclusions about the STE rate from the discussion of the stratospheric ^{14}CO (χ_{st}) at the surface level beyond differences between particular model configurations under the same boundary conditions have to be drawn with caution. Nevertheless, the relationship between the STE rate and χ_{st} is well established, for instance, from the tracer characteristics it is obvious that a reduced χ_{st} can be achieved by a decreased mass flux from the stratosphere into the troposphere.

One final detail that is important in the context of the advection algorithm / meteorological data issue is also indicated in the above analysis. The timing of the STE is obviously not solely dependent on the meteorological data driving the offline advection, but additionally on the chosen advection algorithm. For instance, 2.0-SPFR exhibits the SH maximum of STE later than 2.0-SLT, although both use the same meteorological dataset.

The resulting adjusted model simulations in comparison to the original observations of ^{14}CO at the surface level are shown in Figures 11.21, 11.22, 11.23, and 11.24. The adjusted TM3-L-L31 (OH-1, LF) simulations are

$$\chi' = (\chi_{tr}(t) + 2 \cdot \chi_{st}(t - 0.5)) \cdot \bar{q} \cdot \bar{c}_\chi(T) + \chi_{\text{bio}}(\phi, t) \text{ in the NH} \quad (11.12)$$

$$\chi' = (\chi_{tr}(t) + \chi_{st}(t)) \cdot \bar{q} \cdot \bar{c}_\chi(T) + \chi_{\text{bio}}(\phi, t) \text{ in the SH} , \quad (11.13)$$

and the adjusted 2.0-SLT (OH-S, LF) simulations are

$$\chi' = (\chi_{tr}(t) + 0.7 \cdot \chi_{st}(t - 1)) \cdot \bar{q} \cdot \bar{c}_\chi(T) + \chi_{\text{bio}}(\phi, t) \text{ in the NH} \quad (11.14)$$

$$\chi' = (\chi_{tr}(t) + 0.4 \cdot \chi_{st}(t - 1)) \cdot \bar{q} \cdot \bar{c}_\chi(T) + \chi_{\text{bio}}(\phi, t) \text{ in the SH} \quad (11.15)$$

respectively. The time t (in months) and the latitude ϕ indicate the use of monthly zonal average values of the biogenic contribution χ_{bio} (Eq. (11.2)), and $\bar{c}_\chi(T)$ is the scaling due to the long term (T) changing solar activity, more precisely the average of the three approaches discussed in chapter 8, i.e.,

$$\bar{c}_\chi = \frac{1}{3}(c'_\chi(\Phi(s_s(t + \Delta T_\Phi))) + c'_\chi(s_s(t + \Delta T)) + c'_\chi(n_{\text{clx}})) . \quad (11.16)$$

The global average ^{14}CO production between 1955 and 1988 is estimated to $\bar{q} = 1.76$ molec cm^{-2} s^{-1}. For the sampling stations (Table 11.1) the meteorological year of the observations and the model simulations (offline data) is identical and indicated on the horizontal axis. This implies that inter-annual variations of the ^{14}CO mixing ratio caused by inter-annual variations of the meteorological conditions are included in the model results, at least those that are resolved in the offline data. Furthermore, the variability on shorter time scales (down to 5 day intervals) of model predicted and observed ^{14}CO mixing ratios can be directly compared. For instance, at Izaña (Figure 11.23) the models both tend to reproduce the observed variability during the period of the spring maximum.

In summary, with the changes discussed above, the models reproduce the observations nearly at all sites, within the remaining range of uncertainty mainly arising from model deficiencies and the climatological approach. The seasonal cycle of ^{14}CO at all sites is captured, as well as the time dependent latitudinal gradient and the equatorial minimum.

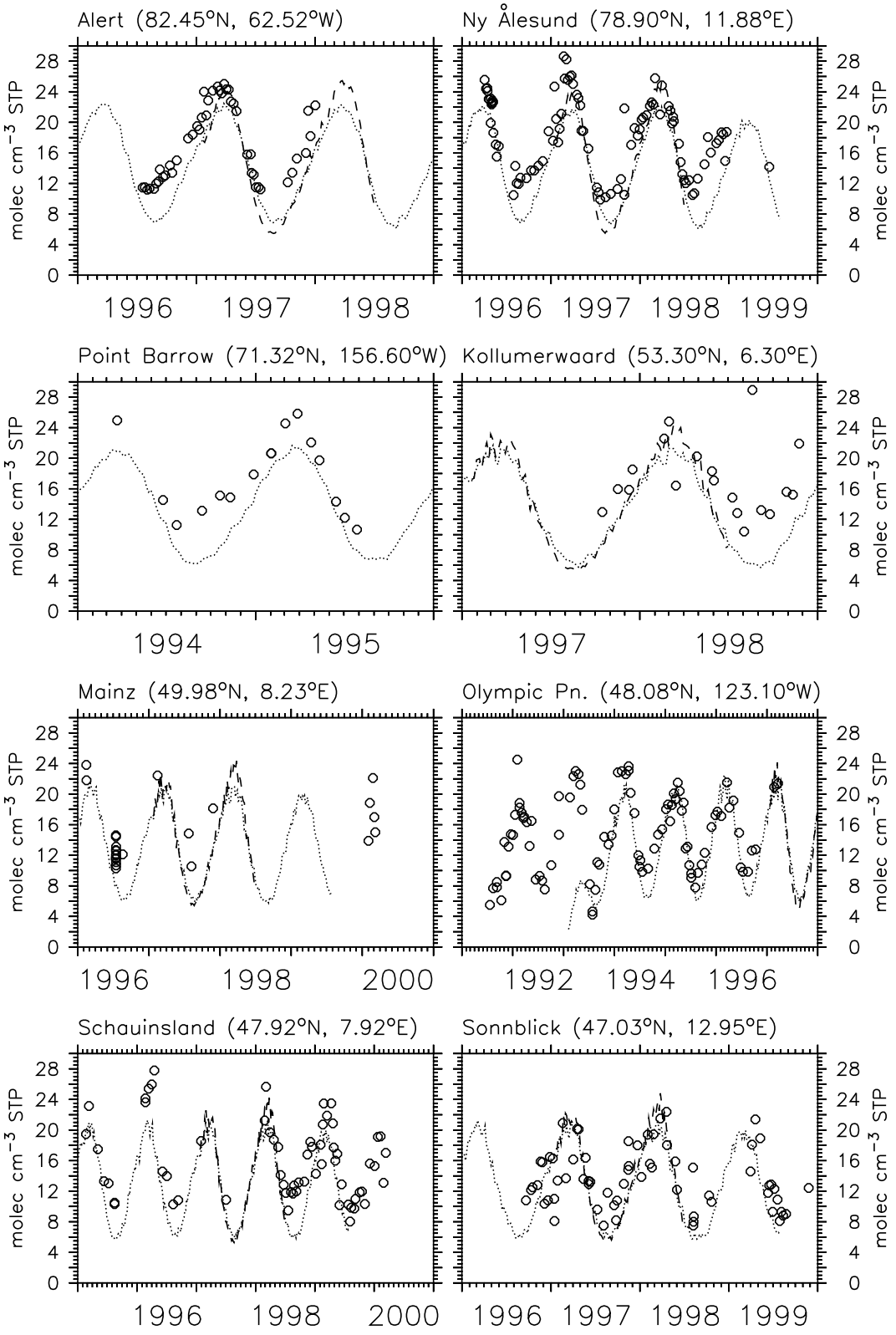

Figure 11.21: Observed ^{14}CO mixing ratios at the surface level (circles), adjusted model simulations of TM3-L-L31 using OH-1 and LF (dashed line), and adjusted model simulations of 2.0-SLT using OH-S and LF (dotted line). 2.0-SLT results for 1993 suffer from spin-up from zero initialization.

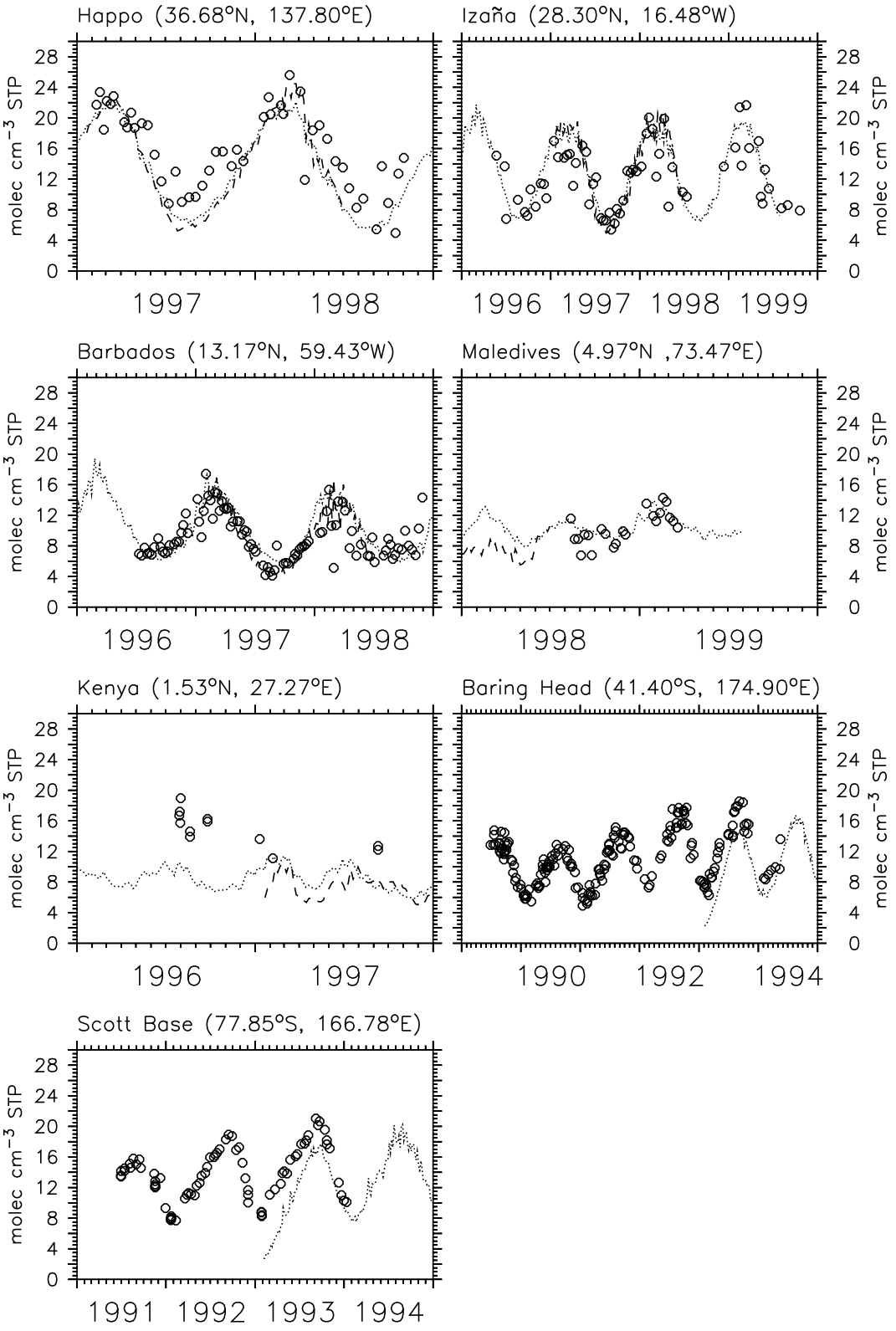

Figure 11.22: Observed ^{14}CO mixing ratios at the surface level (circles), adjusted model simulations of TM3-L-L31 using OH-1 and LF (dashed line), and adjusted model simulations of 2.0-SLT using OH-S and LF (dotted line). 2.0-SLT results for 1993 suffer from spin-up from zero initialization.

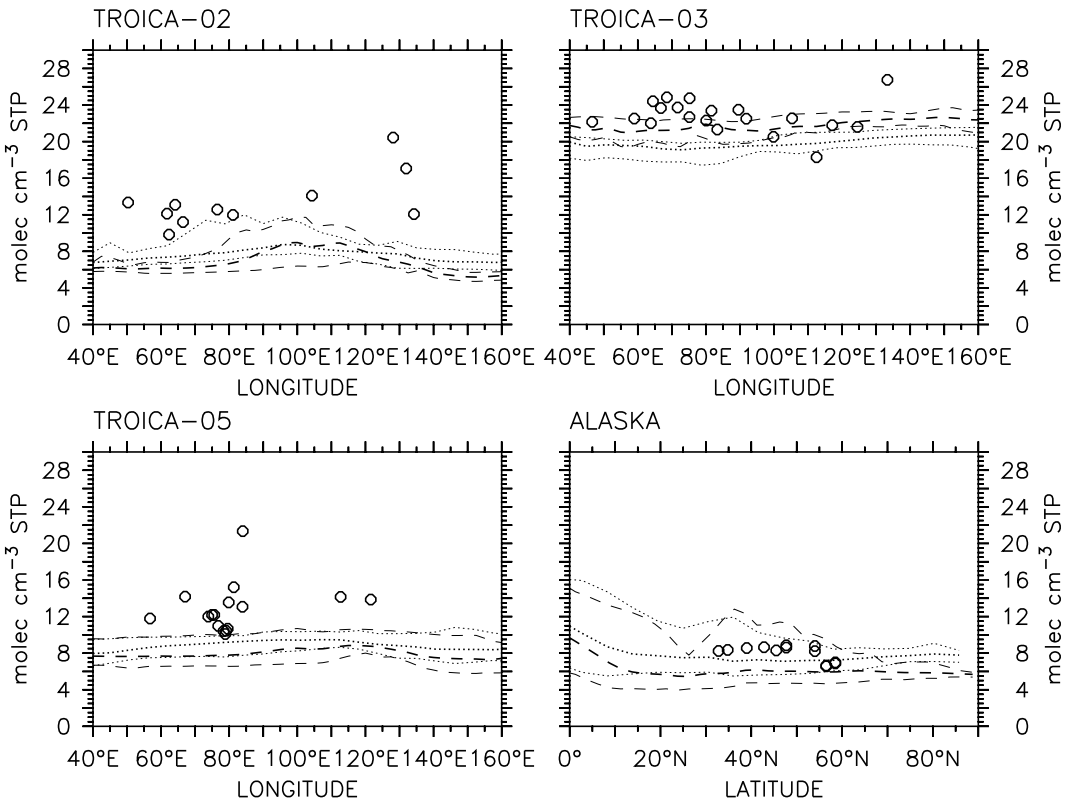

Figure 11.23: Observed ^{14}CO mixing ratios at the surface level (circles), adjusted model simulations of TM3-L-L31 using OH-1 and LF (dashed lines), and adjusted model simulations of 2.0-SLT using OH-S and LF (dotted lines). The thin lines indicate the full range of the model simulations within the time and latitude interval listed in Table 11.2 (TROICA). The thick lines represent the respective averages. For ALASKA, model output for the longitude interval 140^{o}W to 160^{o}W is used. The 2.0-SLT simulations are for the meteorological year of the observations (Table 11.2), except for ALASKA, where the 1997 simulations are plotted. The adjusted TM3-L-L31 results are for 1997 in all cases.

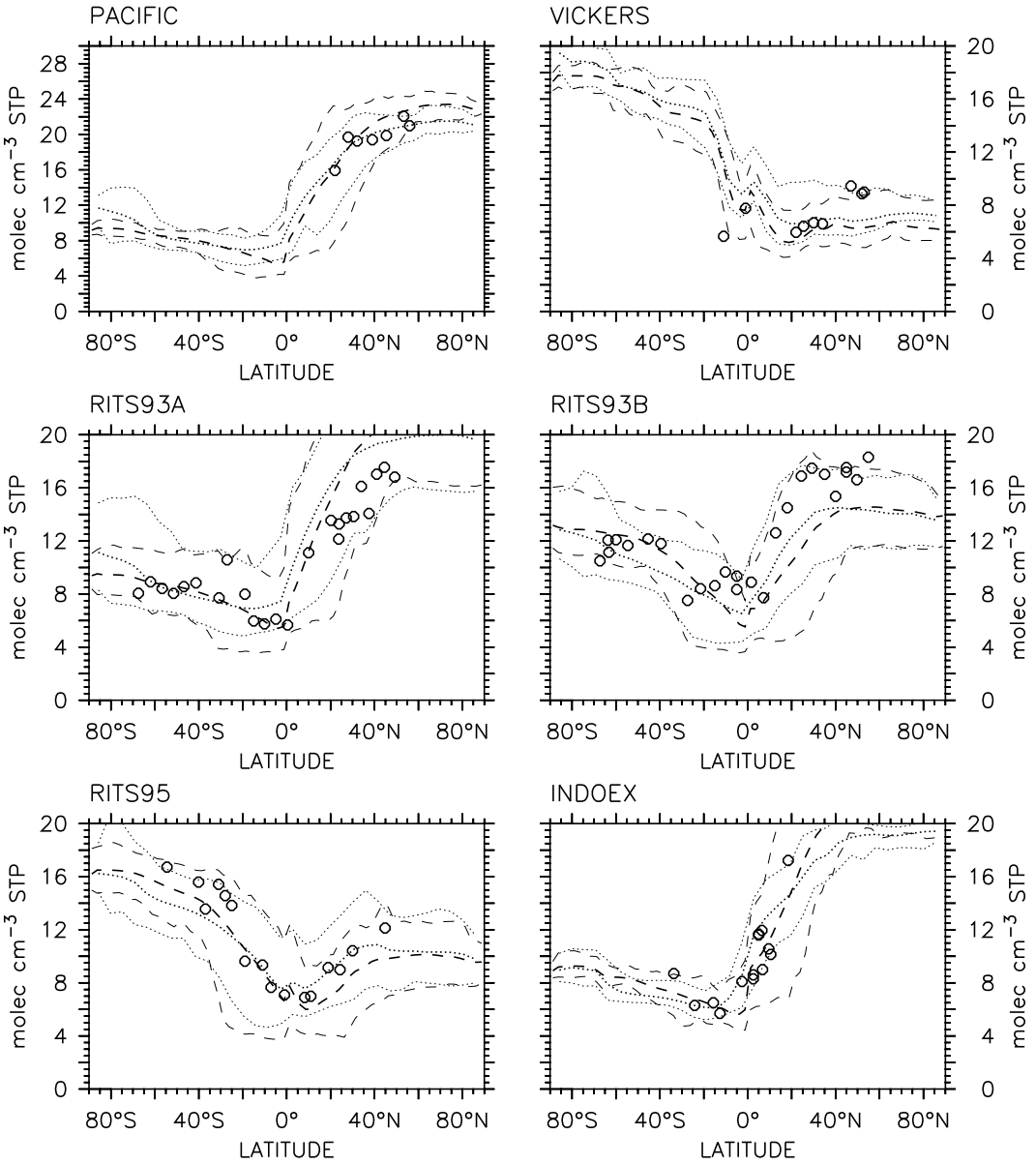

Figure 11.24: Observed ^{14}CO mixing ratios at the surface level (circles), adjusted model simulations of TM3-L-L31 using OH-1 and LF (dashed lines), and adjusted model simulations of 2.0-SLT using OH-S and LF (dotted lines). The thin lines indicate the full range of the model simulations within the time and longitude interval listed in Table 11.2. For RITS93A and RITS93B a longitude belt of $\pm 5^o$ around the average listed in Table 11.2 is chosen. The thick lines represent the respective averages. The meteorological year of the model simulations is 1997, except for the 2.0-SLT simulations in case of RITS95 and INDOEX, for which the year of the observations is used (Table 11.2).

Campaign	Latitude	Longitude	#	Reference
	Time			
ANTARCTIC-01	49.00^{o}S-90.00^{o}S	172.00^{o}E-166.30^{o}E	13	*Mak et al.* [1992]
	1990/11/16	1990/12/13		
ANTARCTIC-02	45.00^{o}S-66.00^{o}S	172.00^{o}E-169.00^{o}E	9	*Mak et al.* [1992]
	1991/01/10	1991/01/23		
TRANSPAC-01	39.53^{o}S-32.50^{o}N	177.30^{o}E-130.70^{o}E	12	*Mak et al.* [1992]
	1991/02/22	1991/02/26		
TRANSPAC-02	32.00^{o}N-16.00^{o}S	123.00^{o}E-171.35^{o}E	16	*Mak et al.* [1992]
	1991/08/19	1991/08/20		
TRANSPAC-03	39.50^{o}S-32.00^{o}N	175.49^{o}E-145.55^{o}E	9	*Mak et al.* [1992]
	1991/08/29	1991/08/30		
WINFLY90	47.08^{o}S-76.93^{o}S	165.38^{o}E-171.51^{o}E	10	*Mak et al.* [1992]
	1990/08/24	1990/08/27		
WINFLY91	41.92^{o}S-76.23^{o}S	171.50^{o}E-166.38^{o}E	7	*Mak et al.* [1992]
	1991/08/25			
FLIGHTS93	74.87^{o}S-46.50^{o}S	160.00^{o}E-170.00^{o}E	26	*Brenninkmeijer et al.* [1996]
	1993/10/21	1993/10/25		
CARIBIC	15.81^{o}S-49.37^{o}N	6.70^{o}E-75.48^{o}E	135	(*)
	1997/26/11	2000/03/26		

Table 11.4: Various aircraft campaigns with ^{14}CO observations. The number (#) of observations has been performed during the listed time interval within the geographical range. The references for published data are included, (*) denotes unpublished data from Brenninkmeijer et al.

11.6 Aircraft measurements of atmospheric ^{14}CO

So far, only ^{14}CO observations at the surface level have been compared with the model simulations. In chapter 10 it was shown how the various model configurations predict the vertical gradient, the lowermost stratospheric maximum, and the seasonality of ^{14}CO in the upper troposphere and lower stratosphere. These predictions can be compared to measurements of ^{14}CO sampled during aircraft campaigns. This is discussed next.

11.6.1 The data

Aircraft campaigns with available ^{14}CO observations are listed in Table 11.4. The flight paths except for the CARIBIC flights (Civil Aircraft for Regular Investigation of the Atmosphere Based on an Instrument Container) are depicted in Figure 11.25.

Especially in the SH, by far not enough data is available yet to construct a 2-D

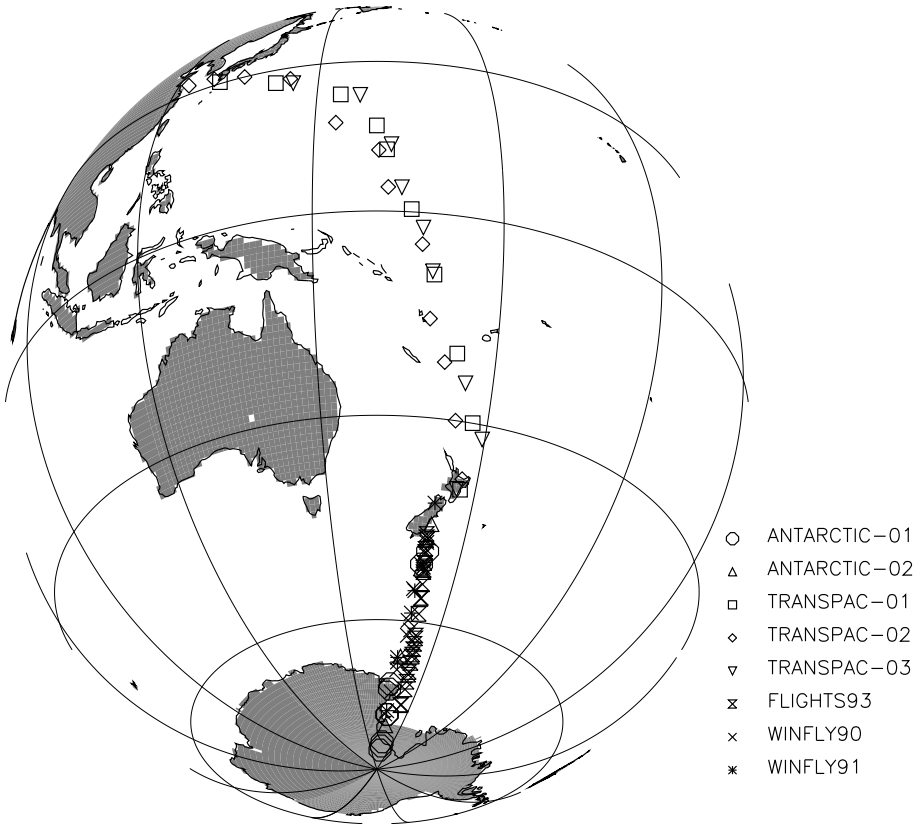

Figure 11.25: Locations of ^{14}CO observations during various aircraft campaigns

climatology in the same way as for the observations at the surface level. Such an approach is further complicated, since the aircraft measurements are not necessarily sampled at the same pressure level. In the NH, thanks to the large number of CARIBIC samples of ^{14}CO, the situation is better; however, the data coverage is still not sufficient. In particular, observations north of 50^{o}N, where the highest NH ^{14}CO levels in the upper troposphere and lower stratosphere are to be expected, do not exist. Therefore a quantitative analysis on the global scale is limited. Nevertheless, the ^{14}CO observations from aircraft campaigns can be used to test the consistency of the model simulations and the validity of the discussion so far for the simulated ^{14}CO above the surface level.

For this the ^{14}CO observations are rescaled with respect to solar activity in the same way as the observations from the surface level, i.e., the measurements are standardized to the global average production rate of the period 1955 to 1988 (Eq. (11.4)). The biogenic contribution, however, is neglected (i.e., $\chi_{\text{bio}} \approx 0$) since this correction is small and not well constrained in the free troposphere and stratosphere. It can be expected that with increasing altitude the contribution of the secondary source of ^{14}CO decreases and the primary source becomes more important.

11.6.2 Model versus observations

The ^{14}CO observations from the aircraft campaigns, the effect of the rescaling with respect to solar activity, and the model results are shown in Figures 11.26, 11.27, and 11.28 for the 2.0-SLT simulations using OH-S and the intermediate LF source distribution with a global average production rate of 1.76 molec cm^{-2} s^{-1} in the model atmosphere. The model predictions obtained with TM3-L-L31 (OH-1, LF) together with the observations are depicted in Figures 11.29, 11.30, and 11.31.

The model simulations reproduce the observed weak vertical gradient in the troposphere below 300 hPa to 400 hPa, in particular the TM3-L-L31 (OH-1, LF) simulations, whereas 2.0-SLT (OH-S, LF) predicts increasing ^{14}CO mixing ratios in the upper troposphere.

The TM3-L-L31 (OH-1, LF) predicted ^{14}CO mixing ratios are generally lower than the respective 2.0-SLT simulations, and therefore are closer to the observations. The 2.0-SLT (OH-S, LF) calculations tend to overestimate the observed ^{14}CO mixing ratios in the troposphere, consistent with the situation at the surface level (cf. Figure 11.12). All observations from aircraft are sampled south of 50^{o}N, therefore underestimated ^{14}CO levels in the troposphere as at the surface north of 40^{o}N between June and September are not present.

Some observations clearly show a stratospheric influence, in particular observations of FLIGHTS93 in the SH and CARIBIC in the NH. The highest observed ^{14}CO mixing ratio was measured in the SH during FLIGHTS93 where the flight path was located in the lower stratosphere [*Brenninkmeijer et al.*, 1996, 1995]. In the NH, the CARIBIC observations with higher ^{14}CO levels most probably result from air samples taken fully or partly at times when the aircraft passed a tropopause fold and therefore stratospheric air was sampled.

The maximum of ^{14}CO in the lower stratosphere predicted by 2.0-SLT in the SH is lower than the maximum observed mixing ratio sampled at lower altitudes (FLIGHTS93, Figure 11.27). The respective stratospheric ^{14}CO maximum predicted by TM3-L-L31 is significantly larger in contrast to that (Figure 11.30). Finally the vertical gradient above 400 hPa is much steeper predicted by TM3-L-L31 than by 2.0-SLT.

11.6.3 Discussion

The observed weak vertical gradient in the troposphere is reproduced by the model simulations, especially by TM3-L-L31, whereas the 2.0-SLT predicted gradient is steeper with higher ^{14}CO levels in the tropopause region. As a consequence, the situation at the surface level is basically mirrored in the free troposphere. The best

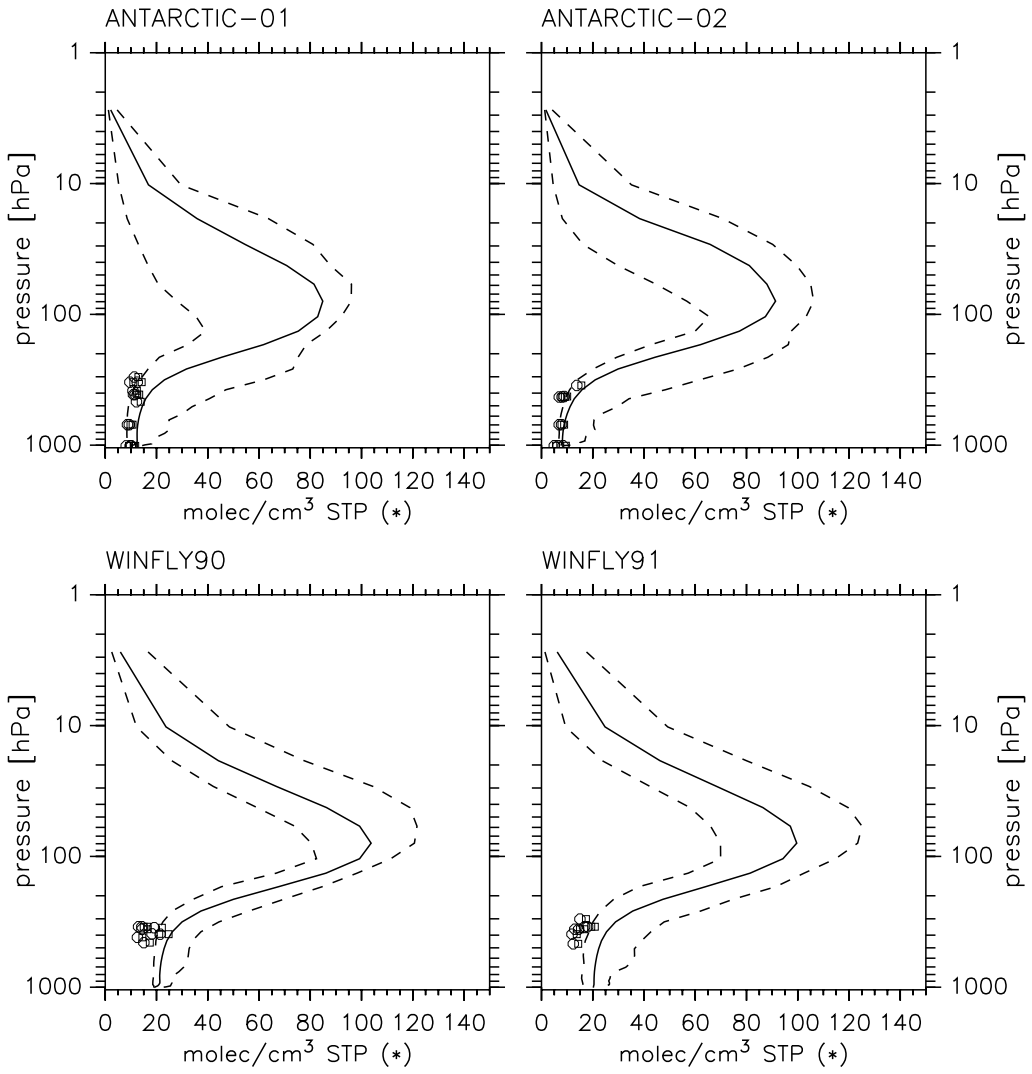

Figure 11.26: Original ^{14}CO observations (circles) and rescaled with respect to solar activity to the global average production rate between 1955 and 1988 (squares). The model simulations are obtained with the 2.0-SLT configuration using OH-S and the intermediate LF distribution. The global average ^{14}CO production rate (1955 - 1988) is assumed to be $\bar{q} = 1.76$ molec cm^{-2} s^{-1} in the model atmosphere. The solid line shows the average model predicted ^{14}CO mixing ratio in the latitude, longitude and time interval listed in Table 11.4, whereby the model results for the meteorological years 1994 to 1998 are averaged. The extreme values predicted by the model in the latitude, longitude and time interval in question, including the inter-annual variations are indicated by the dashed lines.

agreement between simulations and observations is achieved with the TM3-L-L31 model configuration using OH-1 and the LF source distribution. From the ^{14}CO observations at the surface level it was concluded that the SH STE in 2.0-SLT is too strong. This is consistent with the aircraft observations. The ^{14}CO mixing ratio in the free troposphere tends to be overestimated by 2.0-SLT, whereas the

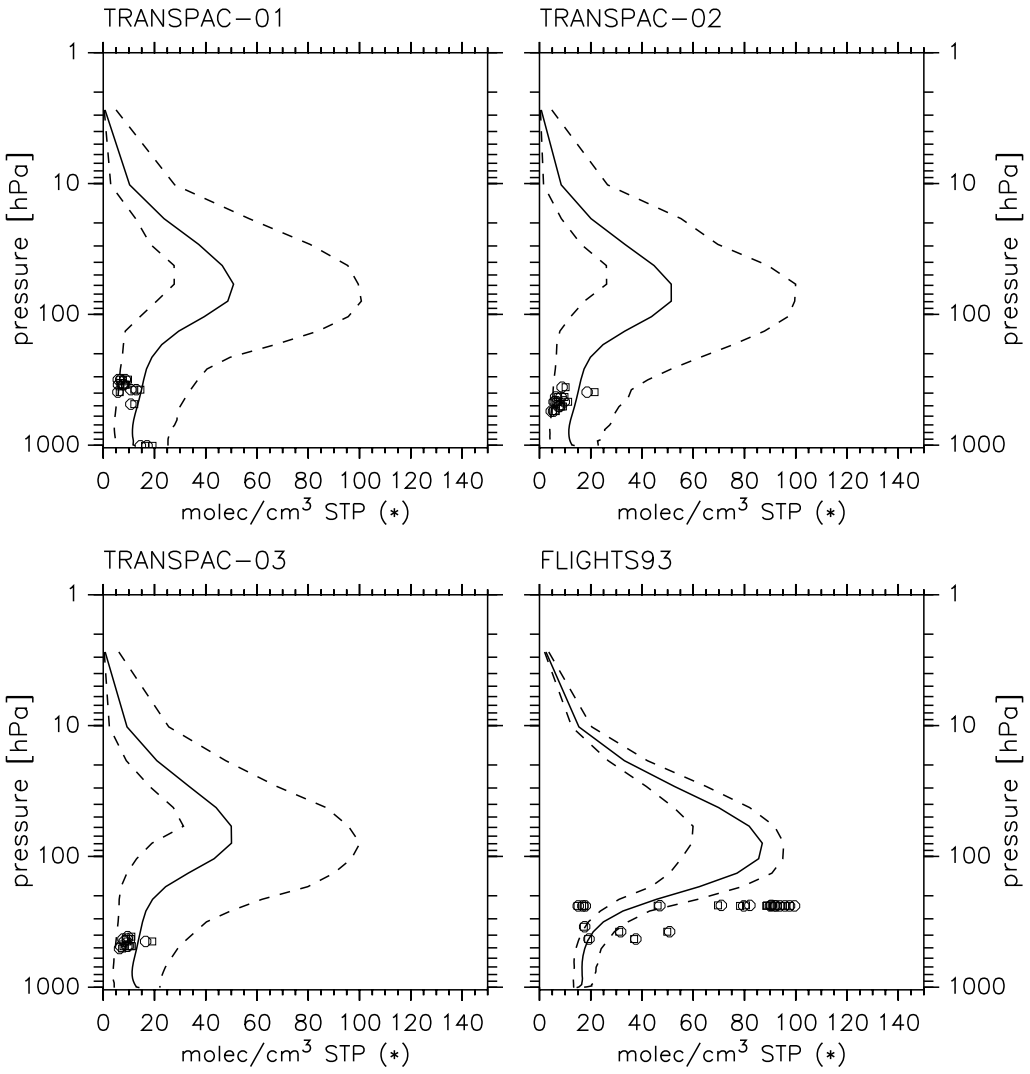

Figure 11.27: see Figure 11.26

lower stratosphere observations exhibit higher ^{14}CO mixing ratios than predicted by 2.0-SLT. The lower STE rate in the SH of TM3-L-L31 causes the steeper vertical gradient of ^{14}CO in the tropopause region and lower stratosphere compared to the 2.0-SLT SH. Furthermore, the weaker STE in TM3-L-L31 compared to 2.0-SLT explains the difference in the simulated vertical gradients in the troposphere.

As a consequence, in the NH the CARIBIC observations of high ^{14}CO mixing ratios are reproduced by TM3-L-L31, whereby the indicated range (Figure 11.31) covers the whole time and latitude interval. This is not achieved by the 2.0-SLT simulations, although in this case the range of simulated ^{14}CO vertical profiles additionally includes the inter-annual variation of 5 years (Figure 11.28).

The maximum observed ^{14}CO levels have been sampled in the SH in October

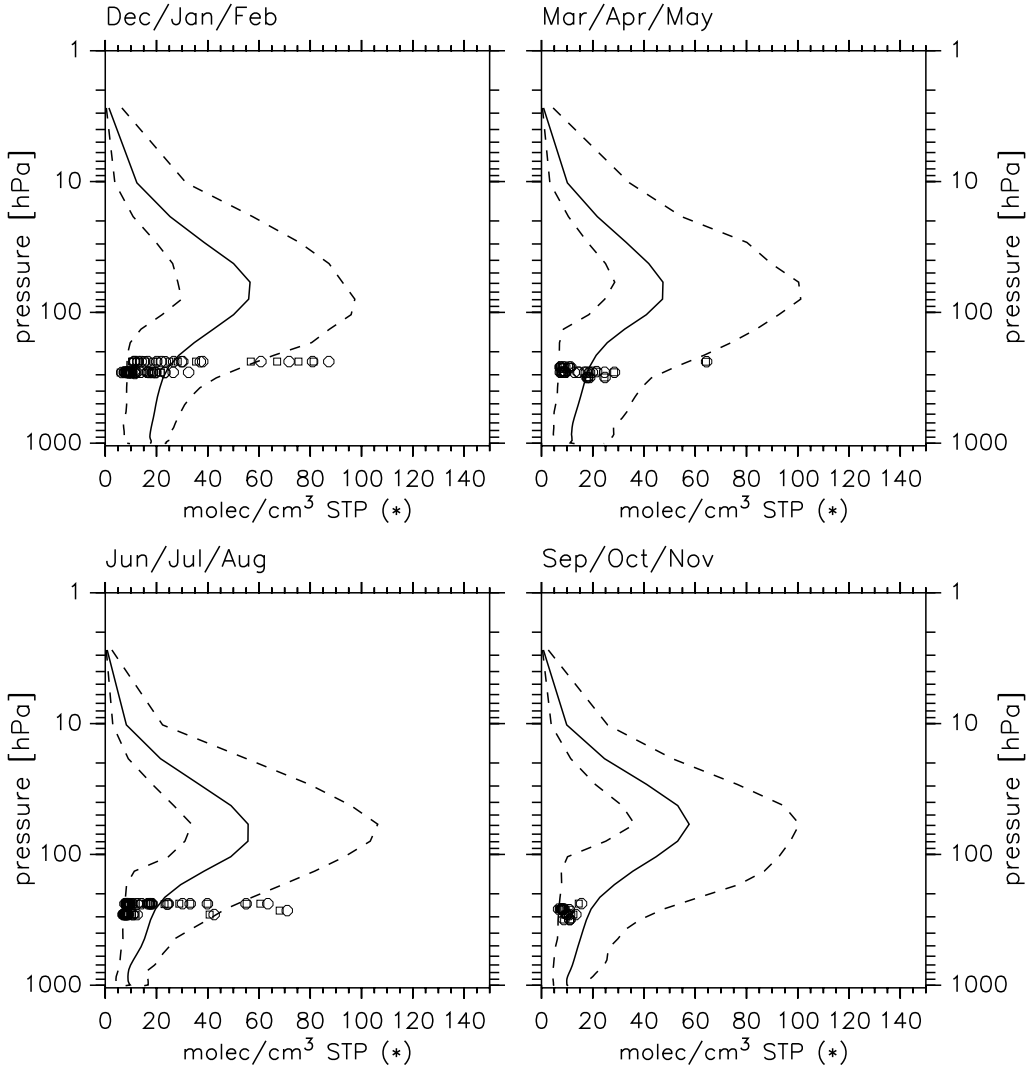

Figure 11.28: As Figure 11.26, except for CARIBIC observations. The observations and simulations are plotted separately for different seasons.

(FLIGHTS93, Table 11.4, Figures 11.27 and 11.30). In chapter 10 it was indicated that from the model simulations the maximum ^{14}CO in the lower SH stratosphere is to be expected somewhen between June and September (cf. Figure 10.9), however with still high ^{14}CO mixing ratios in October. More measurements during different seasons in this region could therefore provide valuable information about the timing and seasonal amplitude of the SH STE. Similar measurements at high northern latitudes could provide this information for the NH.

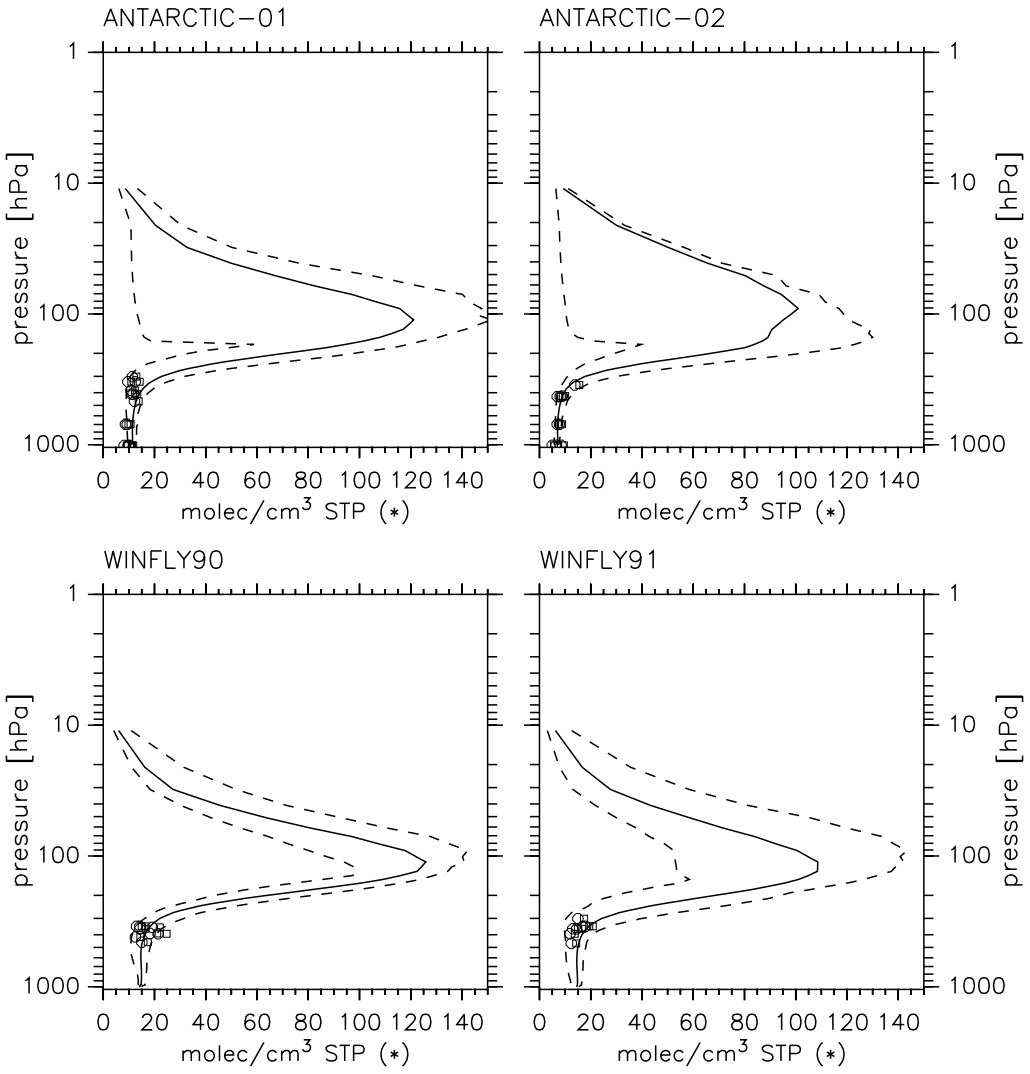

Figure 11.29: Original ^{14}CO observations (circles) and rescaled with respect to solar activity to the global average production rate between 1955 and 1988 (squares). The model simulations are obtained with the TM3-L-L31 configuration using OH-1 and the intermediate LF distribution. The global average ^{14}CO production rate (1955 - 1988) is assumed to be $\bar{q} = 1.76$ molec cm^{-2} s^{-1} in the model atmosphere. The solid line shows the average model predicted ^{14}CO mixing ratio in the latitude, longitude and time interval listed in Table 11.4 for the meteorological year 1997. The extreme values predicted by the model in the latitude, longitude and time interval in question, are indicated by the dashed lines.

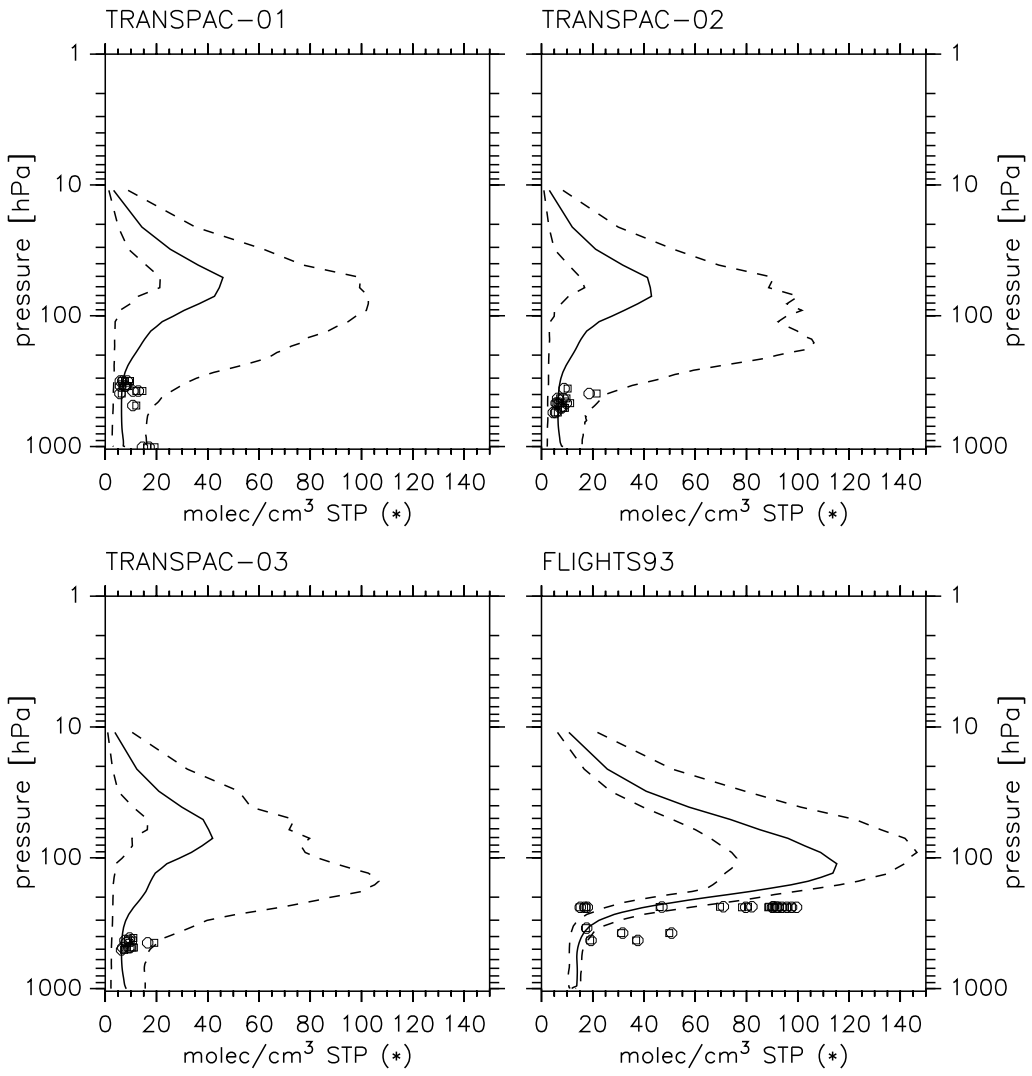

Figure 11.30: see Figure 11.29

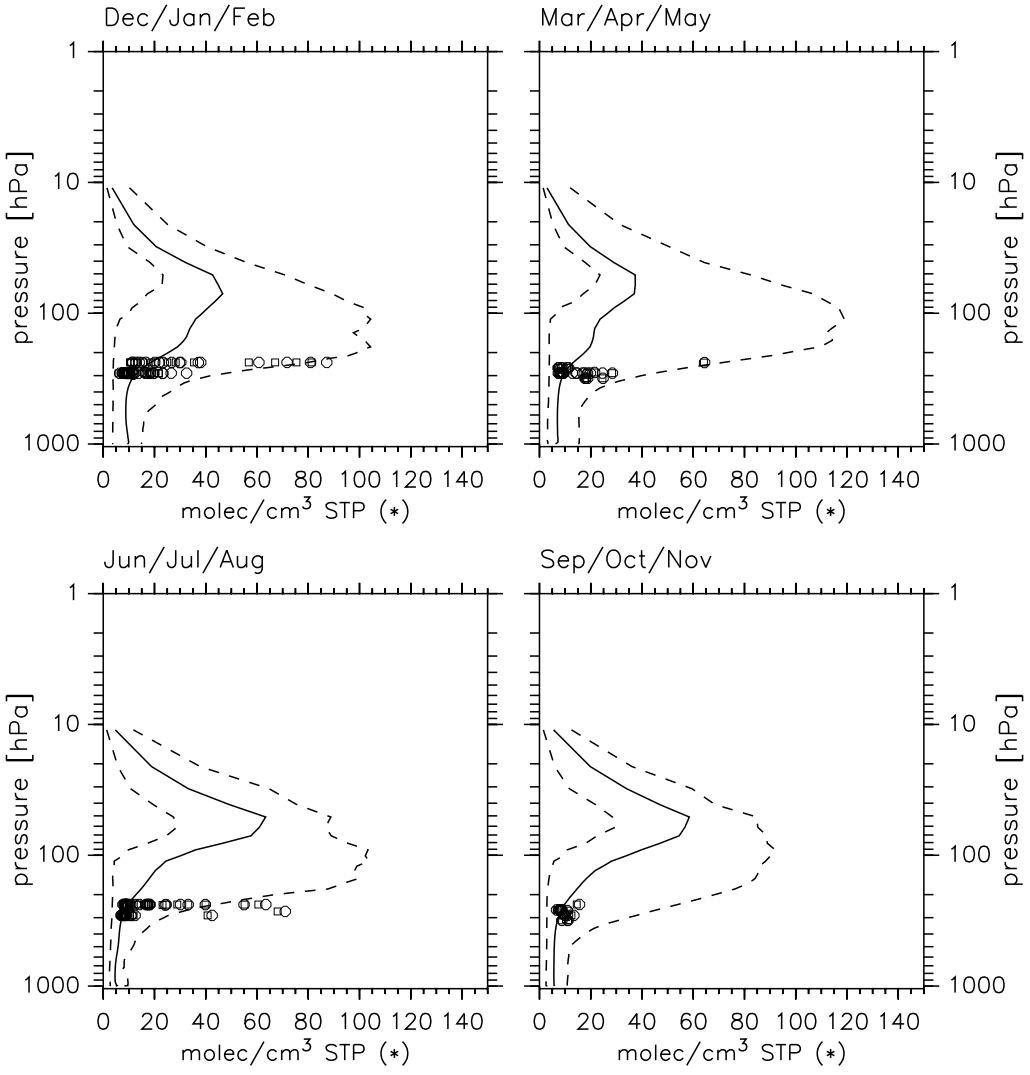

Figure 11.31: As Figure 11.29, except for CARIBIC observations. The observations and simulations are plotted separately for different seasons.

11.7 Conclusions

From the available ^{14}CO observations at the surface level a climatological zonal average seasonal cycle of cosmogenic ^{14}CO was constructed. For this ^{14}CO from secondary sources, mainly oceanic emissions of CO, and CO from methane and NMHC oxidation, was estimated and subtracted from the observations. The contribution of secondary ^{14}CO is largest in the tropics. In the NH mid and high latitudes it is small due to the large amount of ^{14}C free CO from fossil fuel combustion. In the SH, the CO is almost entirely of biogenic origin, however the CO abundance is generally small. Since the observations are not all for the same period, the varying global source strength of ^{14}CO with the changing solar activity was also taken into account by standardizing the data to the average conditions for the period 1955 to 1988 using the results of chapters 7 and 8.

From the comparison of the model simulated seasonal cycle of cosmogenic ^{14}CO at the surface level with the climatological averaged observations of cosmogenic ^{14}CO a consistent explanation for the model deviations from the observations is constructed for all the model configurations considered. 2.0-SLT most probably overestimates the STE by a factor of 2.5 in the SH and by 1.4 in the NH. For TM3-L-L31, it is estimated that the NH STE is underestimated by a factor of 0.7, whereas the simulated STE in the SH is suited to reproduce the observed ^{14}CO observations. In the 2.0-SLT configuration of MATCH, the STE seasonality is phase shifted by at least 1 month in both hemispheres, i.e., the maximum of the downward flux occurs 1 month too early. In TM3-L-L31, a phase shift of 0.5 months in the same direction is only observed in the NH. The 2.0-SPFR configuration in the same way overestimates the SH STE by a factor of 3.7, however no phase shift of the STE seasonality can be derived. In contrast to that, in the NH the results are comparable to those of the 2.0-SLT configuration.

Moreover, several indications suggest that the OH-S distribution and seasonality is better suited to reproduce the observed ^{14}CO observations at the surface level in both hemispheres. Whereas in the SH the differences between OH-1 and OH-S are rather small, in the NH OH-1 exhibits a larger seasonal amplitude, especially at high latitudes. But even with OH-S the ^{14}CO mixing ratio north of 40^{o}N between June and September is underestimated, indicating that also in OH-S the seasonal OH amplitude at the NH mid and high latitudes is overestimated. Alternatively, a reduced STE amplitude with a much higher exchange rate in summer, i.e., when the STE rate is claimed to be at its minimum would be required in the models. The influence of the stratospheric OH abundance on the simulated ^{14}CO mixing ratio at the surface level is small and stratospheric OH cannot explain the deviations between model simulations and observations at the surface level. A reduction of

stratospheric OH by 50% throughout the year results in a maximum increase of ^{14}CO of 9% at the surface level.

The conclusions are consistent with the ^{14}CO source distribution estimate of *Lingenfelter* [1963] (LF) and the source strength estimate from *Masarik and Beer* [1999]. This implies a global average ^{14}CO production rate of 1.76 molec cm^{-2} s^{-1} during the period 1955 to 1988, and further that 51%-53% of the global ^{14}CO is produced in the stratosphere. The source distribution estimates of *Masarik and Beer* [1999] (MA) or *O'Brien et al.* [1991] (OB), which exhibit a higher fraction of ^{14}CO production in the stratosphere, explain the observed ^{14}CO at the surface level only under further modifications: Either a higher global average ^{14}CO production rate is required, or a stronger STE rate in the model simulations, or a reduced global OH abundance.

The results are also consistent with ^{14}CO observations in the free troposphere and lower stratosphere. ^{14}CO hardly exhibits a vertical gradient in the troposphere, whereas the gradient across the tropopause and in the lower stratosphere is very steep. These characteristics are consistently reproduced by the models when the above model deficiencies are taken into account. This further indicates the high potential of ^{14}CO observations in the lower stratosphere and upper troposphere for further model evaluation, since the simulated vertical profile of ^{14}CO is critically dependent on the STE rate. Furthermore, the time of the maximum ^{14}CO mixing ratio in the lower stratosphere provides useful information about the STE seasonality.

Deficiencies in the simulated horizontal transport could be responsible for the model deviations from the observations, especially in meridional direction as discussed in *Quay et al.* [2000] with a 2-D modeling approach. However, this can be excluded for the 3-D approach presented above, since the models reproduce the latitudinal gradients of SF_6 (cf. chapter 3) and F11 (cf. chapter 4).

The results so far imply an important conclusion, which is related to the as yet unresolved interhemispheric asymmetry of ^{14}CO [*Brenninkmeijer et al.*, 1992] with higher ^{14}CO mixing ratios observed in the NH compared to the SH. *Brenninkmeijer et al.* [1992] suggested a higher OH abundance in the SH compared to the NH, based on 2-D simulations. This is also claimed in *Montzka et al.* [2000] based on MCF observations. However, in chapter 4 the limitation of this method, i.e., of the usability of MCF measurements for constraining the hemispheric OH abundance was discussed. The interhemispheric exchange time is the dominating factor for the interhemispheric gradient of MCF, since it is a factor of 5 shorter than the estimated lifetime of the tracer. Therefore these results are highly questionable. The 3-D simulations above indicate that the interhemispheric ^{14}CO asymmetry can also be explained solely by a weaker STE in the SH compared to the NH. As a consequence,

evidence for higher OH abundance in the SH from ^{14}CO observations is not longer supported. This does not imply that a higher OH abundance in the SH compared to the NH can be fully excluded at this stage. A possible reason for higher SH OH levels is, however, still unresolved and no quantitative indications from chemical species determining OH exist. In this context, it has to be further noted that the best estimate of the OH distribution and seasonality, i.e. OH-S, exhibits on annual average an insignificant interhemispheric asymmetry (cf. Table 1.1, Figure 1.6).

In summary, it is shown that the ^{14}CO methodology is a highly useful test for 3-D atmospheric models. It provides a standard test for the simulated STE and OH distribution and seasonality and is therefore a great challenge for most "state-of-the-art" 3-D models. Furthermore, in combination with artificial tracers it may be used in 3-D models for quantitative estimates of the model simulated STE rate, especially with respect to the inter-hemispheric asymmetry and the seasonality of the downward mass flux across any desired control surface in the model.

Overall Conclusions

In this study the fate of atmospheric ^{14}CO has been examined using two different 3-D atmospheric transport models. The main objectives were (1) to develop a methodology for using ^{14}CO measurements to evaluate the model simulated OH distribution and/or stratosphere - troposphere exchange, and (2) to improve the knowledge about the processes determining ^{14}CO in the atmosphere. The route towards these objectives has been subdivided into several separate studies following systematic steps.

A quantitative comparison of 3-D model simulations with observations requires global tracer mass conservation in simulated transport. This requirement, although being self-evident, is not straightforward to fulfill. Even for mass-flux-form advection schemes, which are inherently tracer mass conserving, a mass mismatch occurs if the implementation into a 3-D model does not ensure full consistency between the air mass and the wind velocities in each particular box of the model grid. Enforcing global tracer mass conservation after the simulated transport step is in principle possible, however, it implies either the violation of the standard monotonicity requirement, or it leads to non-physical additional tracer transport components.

The tropospheric transport properties of the model of atmospheric chemistry and transport (MATCH) in various configurations were tested by simulations of SF_6. The model reproduces observed latitudinal and longitudinal gradients of the tracer. The estimated interhemispheric exchange time is about 1.1 ± 0.2 years, dependent on the particular configuration. Compared to other "state-of-the-art" 3-D atmospheric chemistry models, the vertical mixing within the troposphere in MATCH is rather weak, and the interhemispheric exchange time is rather long.

MATCH simulations with emissions estimates of MCF and F11 reproduce long term observations (15 years) of these tracers within reasonable ($\pm 15\%$) uncertainties. With this method, the global average OH abundance in the model atmosphere can be constrained. The estimated global average atmospheric lifetime of MCF is 4-5 years. This is long compared to the interhemispheric exchange time. Investigations with respect to OH on smaller spatial scales, such as for instance the evaluation of average hemispheric abundances of OH in the model atmosphere with MCF, are therefore limited. The same limitation holds on time scales shorter than one year, since the seasonal cycle of MCF is very weak, due to its long lifetime.

As a promising alternative, the ^{14}CO methodology for evaluation of the model simulated OH distribution and seasonality has been systematically developed. The 3-D source distribution of ^{14}CO was successfully implemented into two different 3-D atmospheric (offline) transport models. The source distribution of ^{14}CO exhibits a

small interhemispheric asymmetry with a 5-6% higher production in the SH than in the NH. This asymmetry is caused by the asymmetric shape of the geomagnetic field. Moreover, 51-66% of the global ^{14}CO production occurs in the stratosphere. The maximum production rate is located in the lowermost stratosphere.

The global source strength of ^{14}CO is almost constant throughout one year. Since a normalized constant source strength was implemented in the models, the global atmospheric burden of ^{14}CO tends towards equilibrium in the model atmosphere. The partitioning of the global atmospheric ^{14}CO burden oscillates with a period of one year between the two hemispheres and the stratosphere and the troposphere. This oscillation is mainly driven by the OH seasonality in the respective domain, but it is superposed by the seasonal cycle of the stratosphere - troposphere exchange rate.

The source strength of ^{14}CO is not constant during longer time periods, but rather varies periodically with the solar activity with a nominal period of 11 years and an amplitude of 15-25% (dependent on the particular cycle) around the long term average. At the same time, the spatial distribution pattern of ^{14}CO varies with solar activity, mainly in horizontal direction. However, variations of the relative source distribution in the meridional direction are attenuated by meridional tropospheric mixing. As a consequence, the effect of the varying source distribution on the relative atmospheric ^{14}CO distribution is small, at least in the troposphere. In the model, the effect of solar activity on horizontal gradients of tropospheric ^{14}CO mixing ratios is small compared to uncertainties arising from inaccuracies in the model transport realization. Therefore, the variable source distribution can be ignored to a first approximation, and the solar cycle modulation can be reduced to a global scaling of the global average production rate of ^{14}CO. Model simulations can be performed with a standard source distribution and strength; the solar cycle variation can be separated from model simulations. The resulting atmospheric ^{14}CO mixing ratio can be scaled to the actual production rate.

However, the local atmospheric ^{14}CO mixing ratio does not respond instantaneously to the global source strength variations, since the global atmospheric lifetime of ^{14}CO is about 3 months. On scales smaller than the global scale, the response time of atmospheric ^{14}CO to the time dependent global scaling of the source strength of ^{14}CO is, however, not determined by the local lifetime of atmospheric ^{14}CO before oxidation with OH. Instead, it strongly depends on the atmospheric transport properties, especially the stratosphere - troposphere exchange rate and its localization. This response time was estimated from 3-D model simulations. It turned out that the latitude dependence is completely different from that of the lifetime and provides valuable information about the stratosphere - troposphere exchange in the model atmosphere. The general mathematical concept can be applied similarly to other

atmospheric parameters which depend on a global scaling.

The spatial variation of the response time of atmospheric ^{14}CO to the variation of the global source strength and its effect on the atmospheric ^{14}CO mixing ratio timing is small compared to the uncertainty, which is still inherent in the global source strength of ^{14}CO itself and its variation with solar activity on the time scale of a solar cycle. These uncertainties arise mainly from the lack of a global, measurable parameter that quantitatively describes the physical effect of the changing solar activity on the global atmospheric ^{14}CO production rate. The uncertainty in the relative variation was estimated by three, not fully independent, empirical approaches based on neutron count rates, sunspot numbers, and model predicted shielding potentials of the solar wind plasma. With this, at least the relative variation of the source strength is further constrained. As a consequence, ^{14}CO observations from different periods can be standardized to a given period with respect to the solar cycle. Time series of ^{14}CO observations can be investigated with respect to relative changes of atmospheric transport and/or OH.

Major solar proton events occasionally induce a significant additional stratospheric ^{14}CO production lasting hours to days. Simulations with a 3-D atmospheric transport model predicted a measurable increase of ^{14}CO in the troposphere and at surface level, depending on the strength of the particular event. The delay time between the solar proton event and the maximum increase of ^{14}CO at surface level is critically dependent on the transport time of the tracer from the stratosphere into the troposphere. From observations of atmospheric ^{14}CO several indications were derived that this effect is indeed measurable.

A model inter-comparison study based on ^{14}CO simulations involving two different 3-D models in various configurations showed the applicability of the ^{14}CO methodology focusing on the simulated stratosphere - troposphere exchange. The richness of details derivable from ^{14}CO simulations is rather unique in comparison to more complex tracers. The same details for the real atmosphere can in principle be provided by observations of this purely natural tracer.

A large number of ^{14}CO observations have already become available, most of them at the surface level. From the available observations and with the results concerning the solar activity, a climatological zonally averaged seasonal cycle of cosmogenic ^{14}CO at surface level was constructed. For this, the small contribution of secondary ^{14}CO (mainly from biomass burning, and methane and NMHC oxidation) was estimated and subtracted from the observations. This database was quantitatively compared to 3-D model simulations of primary cosmogenic ^{14}CO, which has been regarded as an independent tracer in the model simulations.

Agreement between model simulations and observations at surface level could be

achieved by various approaches. However, only one combination of ^{14}CO source distribution, OH distribution, and stratosphere - troposphere exchange is consistent with all model configurations, and furthermore with other constraints, such as the MCF simulations (OH), and the present knowledge about the source strength and distribution of ^{14}CO, and the stratosphere - troposphere exchange. The latter is probably the least known parameter in the list, especially with respect to its seasonal cycle and its interhemispheric asymmetry. As a consequence the solution for overall agreement between model simulations and observation based climatology of ^{14}CO has considerable implications for the simulated stratosphere - troposphere exchange in the model. The simulated stratosphere - troposphere exchange can be readily evaluated.

The implications for the simulated stratosphere - troposphere exchange (average STE rate, seasonality, interhemispheric asymmetry) derived from ^{14}CO observations at surface level are further consistent with observations of ^{14}CO in the free troposphere and the lower stratosphere. The ^{14}CO mixing ratio in the troposphere hardly exhibits a vertical gradient. In contrast to that, the vertical gradient of ^{14}CO in the tropopause region and lower stratosphere is very steep. Furthermore, model simulations suggest that the stratospheric OH abundance only has a minor influence on tropospheric ^{14}CO levels.

Although a higher annual average OH abundance in the SH compared to the NH causing the observed interhemispheric asymmetry of ^{14}CO with higher levels in the NH cannot be excluded at this stage, evidence for it is no longer supported. The interhemispheric asymmetry is more likely caused by a weaker stratosphere - troposphere exchange rate in the SH compared to the NH.

In summary, the applicability of the ^{14}CO methodology for evaluation of stratosphere - troposphere exchange rates and OH distributions and seasonalities in 3-D atmospheric models has been shown. Every serious atmospheric transport and chemistry model should be able to reproduce the ^{14}CO observations. Or, in other words, deviations between simulated and observed ^{14}CO mixing ratios will manifest model deficiencies concerning transport and/or chemistry. This further implies as a consequence that ^{14}CO is a valuable, natural tracer very well suited to track changes in the real atmosphere which are related to either parameter. The rather expensive measurements are therefore quite worthwhile in order to follow the fate of the air that we breathe.

Outlook

As indicated in previous discussions, two important issues related to the source of ^{14}CO are still to be resolved. The most important issue is the uncertainty in the global average production rate of ^{14}CO, which after all is needed to constrain the global average OH abundance independent of other methods. *Mak et al.* [1999] have undertaken a first attempt to further constrain the global average ^{14}CO production rate by direct measurements, however, the measurements were taken at surface level where the production rate of ^{14}CO is lowest. Moreover, near surface exposure experiments suffer from the ground effect [*O'Brien et al.*, 1978]. As a consequence other approaches are required. The MPICH ^{14}CO exposure experiment in collaboration with Lufthansa airline looks promising. Cylinders containing pressurized air of known composition are going to be exposed to the natural cosmic radiation on board a passenger aircraft. Carbon-14 accumulates in the cylinder where no photochemistry takes place. Knowing the flight path, the resulting ^{14}CO production can directly be compared to the calculated production rate estimates. The second issue, the vertical gradient of the ^{14}CO production, can potentially be constrained in combination with similar experiments at high altitudes (e.g., on mountains). This will further help to reduce uncertainties in determining model calculated OH and/or stratosphere - troposphere exchange rates by ^{14}CO observations.

In the same way, measurements of ^{14}CO in the tropopause region, especially in the lower stratosphere, provide valuable information to further constrain the remaining uncertainties, independent of the production rate issues. Especially observations as obtained in the CARIBIC project, but with flight paths at higher latitudes, would be extremely valuable. Optimal, although difficult to obtain would be vertical profiles of ^{14}CO at high latitudes. Techniques for high altitude sampling and AMS techniques for even smaller samples are worthwhile to develop.

The regular sampling at remote surface locations provides unique information about inter-annual variations of the OH seasonality and/or the stratosphere - troposphere exchange. Especially the accurate determination of the seasonal extrema is critical for comparison with model simulations. Therefore an increased sampling rate in spring and autumn would be desirable. Moreover, the sampling rate wherever possible should be increased after the rare major solar proton events.

For atmospheric transport and chemistry modeling the newly developed ^{14}CO methodology can be used for detailed model inter-comparison studies, particularly with regard to the ability of different advection algorithms to reproduce the observed ^{14}CO climatology. In the same way, model simulated OH distributions can be studied, even offline and independent of the model the OH was originally calculated with. Moreover, ongoing ^{14}CO observations provide the basis of testing meteorolog-

ical reanalysis data with respect to the implied inter-annual variations. For example the effect of the El Niño - Southern Oscillation phenomenon (ENSO) and the Quasi-Biennial Oscillation (QBO) on the ^{14}CO mixing ratio has yet to be investigated. In the same way, general circulation models can be tested.

And finally, by means of the ^{14}CO methodology, a quantitative stratosphere - troposphere diagnostic tool for 3-D atmospheric models can be developed. For this, artificial tracers for assessing the air mass flux can be included in the simulations. From this, the seasonality and interhemispheric differences of the downward air mass flux across any desired control surface is readily accessible.

List of Acronyms and Abbreviations

2-D	two-dimensional
3-D	three-dimensional
1.2-SLT	MATCH Version 1.2 with semi-Lagrangian advection scheme
2.0-SLT	MATCH Version 2.0 with semi-Lagrangian advection scheme
2.0-SPF	MATCH Version 2.0 with SPITFIRE advection scheme
2.0-SPFR	MATCH Version 2.0 with SPITFIRE advection scheme, tracer mass conservation forced by global rescaling
AACGM	altitude adjusted corrected geomagnetic coordinates
ALE/GAGE	atmospheric lifetime experiment / global atmospheric gases experiment
AMS	accelerator mass spectrometry
CARIBIC	civil aircraft for regular investigation of the atmosphere based on an instrument container
CCM2	NCAR community climate model 2
$CFCl_3$	tri-chloro-fluoro-methane, fluoro-chloroform
CH_3CCl_3	methylchloroform, 1,1,1-trichloroethane
CH_4	methane
CME	coronal mass ejection
CO	carbon monoxide
^{14}CO	radiocarbon monoxide
$^{14}C(O)$	referring to ^{14}C and to ^{14}CO
CTM	chemical transport model
DKRZ	Deutsches Klimarechenzentrum (Hamburg), German Climate Computing Centre
ECHAM3	European community Hamburg climate model version 3
ECMWF	European Centre for Medium-range Weather Forecasts
ENSO	El Niño - Southern Oscillation
ERA	ECMWF re-analysis
EU	Europe
F11	$CFCl_3$
FE	Far East
GCM	general circulation model

GCR	galactic cosmic ray
GEIA	global emission inventory activity
GOES-7	geostationary operational environmental satellite No. 7
HCFC	hydrochlorofluorocarbon
IGOSS	integrated global ocean series system
IMAU	Institute for Marine and Atmospheric Research Utrecht, The Netherlands
INDOEX	Indian ocean experiment
IPCC	Intergovernmental Panel on Climate Change
ITCZ	inter-tropical convergence zone
KNMI	Koninklijk Nederlands Meteorologisch Instituut, Royal Netherlands Meteorological Institute
LF	atmospheric ^{14}CO source distribution of *Lingenfelter* [1963]
MA	atmospheric ^{14}CO source distribution of *Masarik and Beer* [1999]
MATCH	model of atmospheric transport and chemistry
MBL	marine boundary layer
MCF	CH_3CCl_3, methylchloroform
MPICH	Max-Planck-Institute for Chemistry, Mainz, Germany
msl	mean sea level
MV	Mega-Volt
NA	North America
NCAR	National Center for Atmospheric Research, Boulder, U.S.A.
NCEP	National Centers for Environmental Prediction, U.S.A.
NetCDF	network common data form
NGDC-SPIDR	National Geophysical Data Center - Space Physics Interactive Data Resource, U.S.A
NH	northern hemisphere
NIWA	National Institute of Water and Atmospheric Research Ltd., New Zealand
NM	northern mid-latitudes
NMHC	non-methane-hydrocarbon
NOAA-CMDL	National Oceanic and Atmospheric Administration Climate Monitoring and Diagnostics Laboratory, U.S.A.
NOAA-PMEL	National Oceanic and Atmospheric Administration -

	Pacific Marine Environmental Laboratory, U.S.A.
NT	northern tropics
OB	atmospheric ^{14}CO source distribution of *O'Brien et al.* [1991]
OH	hydroxyl-radical
RMS	root-mean-square
SF_6	sulphur-hexafluoride
SH	southern hemisphere
SPE	solar proton event
SPITFIRE	split implementation of tracer transport using flux-integral representations
STE	stratosphere - troposphere exchange
STP	standard temperature and pressure (273.15K, 1013.25hPa)
TEM	transformed Eulerian mean
TM3	tracer transport model 3
TROICA	Trans-Siberian observations into the chemistry of the atmosphere
WDC-C2	World Data Center C2, Japan
WMO	World Meteorological Organization
pMC	per-cent modern carbon
QBO	Quasi-Biennial Oscillation

List of Figures

List of Tables

References

Appenzeller, C., J. R. Holton, and K. H. Rosenlof. Seasonal variation of mass transport across the tropopause. *J. Geophys. Res.*, *101*(D10), 15 071–15 078, 1996.

Armstrong, T. W., K. C. Chandler, and J. Barish. Calculations of neutron flux spectra induced in the Earth's atmosphere by galactic cosmic rays. *J. Geophys. Res.*, *16*, 2715–2726, 1973.

Bates, T. S., K. C. Kelly, J. E. Johnson, and R. H. Gammon. Regional and seasonal variations in the flux of oceanic carbon monoxide to the atmosphere. *J. Geophys. Res.*, *100*(D11), 23 093–23 101, 1995.

Bergamaschi, P., C. A. M. Brenninkmeijer, M. Hahn, T. Röckmann, D. H. Scharffe, P. J. Crutzen, N. F. Elansky, I. B. Belikov, N. B. A. Trivett, and D. E. J. Worthy. Isotope analysis based source identification for atmospheric CH_4 and CO sampled across Russia using the Trans-Siberian railroad. *J. Geophys. Res.*, *103*(D7), 8227–8235, 1998.

Bergamaschi, P., R. Hein, C. A. M. Brenninkmeijer, and P. J. Crutzen. Inverse modeling of the global CO cycle: 2. Inversion of $^{13}C/^{12}C$ and $^{18}O/^{16}O$ isotope ratios. *J. Geophys. Res.*, *105*(D2), 1929–1945, 2000a.

Bergamaschi, P., R. Hein, M. Heimann, and P. J. Crutzen. Inverse modeling of the global CO cycle: 1. Inversion of CO mixing ratios. *J. Geophys. Res.*, *105*(D2), 1909–1927, 2000b.

Bhavnani, K. H. and C. A. Hein. An improved algorithm for computing altitude dependent corrected geomagnetic coordinates. Scientific Report No.7, PL-TR-94-2310, Phillips Laboratory, Directorate of Geophysics, Air Force Material Command, Hanscom Air Force Base, Bedford, MA 01731-3010, 1994.

Blinov, A. The dependence of cosmogenic isotope production rate on solar activity and geomagnetic field variations. In F. Stephenson and A. Wolfendale, editors, *Secular Solar and Geomagnetic Variations in the last 10000 Years*, pages 329–340. Kluwer Academic Publishers, 1988.

Bott, A. A positive definite advection scheme obtained by non-linear renormalization of the advective fluxes. *Mon. Weather Rev.*, *117*, 1006–1015, 1989.

Bott, A. Monotone flux limitation in the area-preserving flux-form advection algorithm. *Mon. Weather Rev.*, *120*, 2592–2602, 1992.

Brasseur, G. P., D. A. Hauglustaine, S. Walters, P. J. Rasch, J. F. Muller, C. Granier, and X. X. Tie. MOZART, a global chemical transport model for ozone and related chemical tracers: 1. Model description. *J. Geophys. Res.*, *103*(D21), 28 265–28 289, 1998.

Brenninkmeijer, C. A. M. Measurement of the abundance of ^{14}CO in the atmosphere and the $^{13}C/^{12}C$ and $^{18}O/^{16}O$ ratio of atmospheric CO with applications in New Zealand and Antarctica. *J. Geophys. Res.*, *98*(D6), 10 595–10 614, 1993.

Brenninkmeijer, C. A. M., D. C. Lowe, M. R. Manning, R. J. Sparks, and P. F. J. v. Velthoven. The ^{13}C, ^{14}C, and ^{18}O isotopic composition of CO, CH_4, and CO_2 in the higher southern latitudes lower stratosphere. *J. Geophys. Res.*, *100*(D12), 26 163–26 172, 1995.

Brenninkmeijer, C. A. M., M. R. Manning, D. C. Lowe, G. Wallace, R. J. Sparks, and A. Volz-Thomas. Interhemispheric asymmetry in OH abundance inferred from measurements of atmospheric ^{14}CO. *Nature*, *356*, 50–52, 1992.

Brenninkmeijer, C. A. M., R. Müller, P. J. Crutzen, D. C. Lowe, M. R. Manning, R. J. Sparks, and P. F. J. v. Velthofen. A large ^{13}CO deficit in the lower Antarctic stratosphere due to "ozone hole" chemistry: Part I, observations. *Geophys. Res. Lett.*, *23*(16), 2125–2128, 1996.

Brenninkmeijer, C. A. M. and P. A. Roberts. An air-driven pressure booster pump for aircraft-based sampling. *J. Atm. Oc. Tech.*, *11*(6), 1664–1671, 1994.

Brenninkmeijer, C. A. M., T. Röckmann, M. Bräunlich, P. Jöckel, and P. Bergamaschi. Review of progress in isotope studies of atmospheric carbon monoxide. *Chemosphere Glob. Change Sci.*, *1*, 33–52, 1999.

Butler, J. H., J. W. Elkins, T. M. Thompson, B. D. Hall, T. H. Swanson, and V. Koropalov. Oceanic consumption of CH_3CCl_3: Implications for tropospheric OH. *J. Geophys. Res.*, *96*(D12), 22 347–22 355, 1991.

Conrad, R. and W. Seiler. Influence of temperature, moisture, and organic carbon on the flux of H2 and CO between soil and atmosphere: Field studies in subtropical regions. *J. Geophys. Res.*, *90*(D3), 5699–5709, 1985.

Crutzen, P. J. Solar proton events: Stratospheric sources of nitric oxide. *Science*, *189*, 457–459, 1975.

Crutzen, P. J. Ozone in the troposphere. In H. B. Singh, editor, *Composition, chemistry, and climate of the atmosphere*, pages 349–393. Van Nostrand Reinold, 1995a.

Crutzen, P. J. The role of methane in atmospheric chemistry and climate. In W. v. Engelhardt, editor, *Ruminant physiology: Digestion, metabolism, growth, and reproduction: Proceedings of the Eight International Symposium on Ruminant Physiology*, pages 291–315. Ferdinand Enke Verlag, Germany, 1995b.

Crutzen, P. J., M. Hahn, G. S. Golitsyn, C. A. M. Brenninkmeier, D. H. Scharffe, I. B. Berlikov, M. Maiss, P. Bergamaschi, T. Röckmann, A. M. Grisenko, and V. M. Sevostyanov. Trace gas measurements between Moscow and Vladivostok using the Trans-Siberian Railroad. *J. Atmos. Chem.*, *29*, 179–194, 1998.

Crutzen, P. J. and P. H. Zimmermann. The changing photochemistry of the troposphere. *Tellus*, *43AB*(4), 136–151, 1991.

Cunnold, D. Emission distribution of CCl_3F (CFC-11), GEIA Document: cfc.txt 17 Apr 95. 1995.

Cunnold, D. M., P. J. Fraser, R. F. Weiss, R. G. Prinn, P. G. Simmonds, F. N. Alyea, and A. J. Crawford. Global trends and annual releases of CCl_3F and CCl_2F_2 estimated from ALE/GAGE and other measurements from July 1978 to June 1991. *J. Geophys. Res.*, *99*(D1), 1107–1126, 1994.

Cunnold, D. M. and R. G. Prinn. Comment on "Tropospheric OH in a three-dimensional chemical tracer model: An assessment based on observations of CH_3CCl_3" by C. M. Spivakovsky et al. *J. Geophys. Res.*, *96*(D9), 17 391–17 393, 1991.

Cunnold, D. M., R. G. Prinn, R. A. Rasmussen, P. G. Simmonds, F. N. Alyea, C. A. Cardelino, A. J. Crawford, P. J. Fraser, and R. D. Rosen. The atmospheric lifetime experiment 3. Lifetime methodology and application to three years of $CFCl_3$ Data. *J. Geophys. Res.*, *88*(C13), 8379–8400, 1983.

Dameris, M., D. Nodorp, and R. Sausen. Correlation between tropopause height pressure and TOMS-data for the EASOE-Winter 1991/1992. *Beitr. Phys. Atmos.*, *68*, 227–232, 1995.

Damon, P. E., J. C. Lerman, and A. Long. Temporal fluctuations of atmospheric ^{14}C: Causal factors and implications. *Ann. Rev. Earth Planet. Sci.*, *6*, 457–494, 1978.

Damon, P. E. and C. P. Sonett. Solar and terrestrial components of the atmospheric ^{14}C variation spectrum. In C. P. Sonett, M. S. Giampapa, and M. S. Matthews, editors, *The sun in time*, pages 360–388. The University of Arizona Press, Tucson, Arizona, 1991.

DeMore, W. B., S. P. Sander, D. M. Golden, R. F. Hampson, M. J. Kurylo, C. J. Howard, A. R. Ravishankara, C. E. Kolb, and M. J. Molina. Chemical kinetics and photochemical data for use in stratospheric modeling. Evaluation number 12. JPL Publication 97-4, Jet Propulsion Laboratory, Pasadena, CA, 1997.

Denning, A. S., M. Holzer, K. R. Gurney, M. Heimann, R. M. Law, P. J. Rayner, I. Y. Fung, S.-M. Fan, S. Taguchi, P. Friedlingstein, I. Balkanski, J. Taylor, M. Maiss, and I. Levin. Three-dimensional transport and concentration of SF_6: A model intercomparison study (TransCom 2). *Tellus*, *51B*, 266–297, 1999.

Dentener, F., J. Feichter, and A. Jeuken. Simulation of the transport of Radon^{222} using on-line and off-line global models at different horizontal resolutions: A detailed comparison with measurements. *Tellus*, *51B*, 573–602, 1999.

DKRZ. The ECHAM3 atmospheric general circulation model (Revision 2). 1992. Edited by Model User Support Group.

Dlugokencky, E. J., K. A. Masaire, P. M. Lang, P. P. Tans, L. P. Steele, and E. G. Nisbet. A dramatic decrease in the growth rate of atmospheric methane in the northern hemisphere during 1992. *Geophys. Res. Lett.*, *21*(1), 45–48, 1994.

Douglass, A. R., M. J. Prather, T. M. Hall, S. E. Strahan, P. J. Rasch, L. C. Sparling, L. Coy, and J. M. Rodriguez. Choosing meteorological input for the global modeling initiative assessment of high-speed aircraft. *J. Geophys. Res.*, *104*(D22), 27 545–27 564, 1999.

Ebel, A., H. Elbern, J. Hendricks, and R. Meyer. Stratosphere - troposphere exchange and its impact on the structure of the lower stratosphere. *J. Geomag. Geoelectr.*, *48*, 135–144, 1996.

Ehmert, A. On the modulation of the primary cosmic ray spectrum by solar activity. Technical report, Institut für Stratosphärenphysik im Max-Planck-Institut für Aeronomie, Lindau b. Göttingen, 1959.

Feynman, J., T. P. Armstrong, L. Dao-Gibner, and S. Silverman. New interplanetary proton fluence model. *J. Spacecraft Rockets*, *27*, 403–410, 1990.

Feynman, J., G. Spitale, J. Wang, and S. Gabriel. Interplanetary proton fluence model: JPL 1991. *J. Geophys. Res.*, *98*(A8), 13 281–13 294, 1993.

Fisher, D. A., T. Duafala, P. M. Midgley, C. Niemi, A. Makhijani, and S. Seidel. Report on concentrations, lifetimes, and trends of CFCs, halons, and related species; Chapter 2: Production and emission of CFCs, halons, and related molecules. Technical Report NASA-RP-1339, NASA, 1994.

Freier, P. S. and W. R. Webber. Exponential rigidity spectrums for solar-flare cosmic rays. *J. Geophys. Res.*, *68*(6), 1605–1629, 1963.

Fung, I., J. J. Lerner, E. Matthews, M. Prather, L. P. Steele, and P. J. Fraser. Three-dimensional model synthesis of the global methane cycle. *J. Geophys. Res.*, *96*(D7), 13 003–13 065, 1991.

Gaisser, T. K. *Cosmic rays and particle physics*. Cambridge University Press, 1990.

Galanter, M., H. Levy II, and G. R. Carmichael. Impacts of biomass burning on tropospheric CO, NO_x, and O_3. *J. Geophys. Res.*, *105*(D5), 6633–6653, 2000.

Gerkens, R. R. and J. A. Franklin. The rate of degradation of 1,1,1 trichloroethane in water by hydrolysis and dechlorination. *Chemosphere*, *19*, 1929–1937, 1989.

Gibson, J. K., P. Kallberg, S. Uppala, A. Hernandez, A. Nomura, and E. Serrano. ERA description. Technical Report 1, ECMWF Re-Analysis Project Report Series, 1997.

Gosling, J. T. Coronal mass ejections: An overview. In N. Crooker, J. A. Joselyn, and J. Feynman, editors, *Coronal mass ejections*, Geophysical Monograph 99. American Geophysical Union, 1997.

Grewe, V. and M. Dameris. Calculating the global mass exchange between stratosphere and troposphere. *Ann. Geoph.*, *14*, 431–442, 1996.

Gros, V., M. Bräunlich., T. Röckmann, P. Jöckel, P. Bergamaschi, C. A. M. Brenninkmeijer, W. Rom, W. Kutschera, A. Kaiser, H. E. Scheel, M. Mandl, J. van der Plicht, and G. Possnert. Detailed analysis of the isotopic composition of CO and characterization of the air masses arriving at Mt. Sonnblick (Austrian Alps). *J. Geophys. Res.*, *in press*, 2000.

Hack, J. J. Parameterization of the moist convection in the national center for atmospheric research community climate model (CCM2). *J. Geophys. Res.*, *99*(D3), 5551–5568, 1994.

Hack, J. J., B. A. Boville, B. P. Briegleb, J. T. Kiehl, P. J. Rasch, and D. L. Williamson. Description of the NCAR Community Clinate Model (CCM2). Technical Report NCAR/TN-382+STR, National Center for Atmosperic Research, Boulder, Colorado, 1993.

Hall, T. M., D. W. Waugh, K. A. Boering, and R. A. Plumb. Evaluation of transport in stratospheric models. *J. Geophys. Res.*, *104*(D15), 18 815–18 839, 1999.

Hartley, D. and R. Prinn. Comment on "Tropospheric OH in a three-dimensional chemical tracer model: An assessment based on observations of CH_3CCl_3" by C. M. Spivakovsky et al. *J. Geophys. Res.*, *96*(D9), 17 383–17 387, 1991.

Heath, D. F., A. J. Krueger, and P. J. Crutzen. Solar proton event: Influence on stratospheric ozone. *Science*, *197*, 886–889, 1977.

Heimann, M. The Global Atmospheric Tracer Model TM2. Technical Report No. 10, DKRZ-Hamburg, 1995.

Heimann, M. and C. D. Keeling. A three-dimensional model of atmospheric CO_2 transport based on observed winds: 2. Model description and simulated tracer experiments. In D. H. Peterson, editor, *Aspects of climate variability in the Pacific and the western Americas*, Geophysical Monograph 55, pages 237–275. American Geophysical Union, 1989.

Hess, W. N., E. H. Canfield, and R. E. Lingenfelter. Cosmic-ray neutron demography. *J. Geophys. Res.*, *66*, 665–677, 1961.

Hess, W. N., H. W. Patterson, R. Wallace, and E. L. Chupp. Cosmic-ray neutron energy spectrum. *Phys. Rev.*, *116*, 445–457, 1959.

Heymann, M. Perceptions of uncertainty: A problem in atmospheric modelling? In *TRAP annual report*, pages 12–18. 1998.

Holton, J. R. On the global exchange of mass between the stratosphere and troposphere. *J. Atm. Sci.*, *47*, 392–395, 1990.

Holton, J. R., P. H. Haynes, M. E. McIntyre, A. R. Douglass, R. B. Rood, and L. Pfister. Stratosphere-troposphere exchange. *Rev. Geophys.*, *33*(4), 403–439, 1995.

Holtslag, A. A. M. and B. A. Boville. Local versus nonlocal boundary-layer diffusion in a global climate model. *J. Climate*, *6*, 1825–1842, 1993.

Hourdin, F. and A. Armengaud. The use of finite-volume methods for atmospheric advection of trace species. Part I: Test of various formulations in a general circulation model. *Mon. Weather Rev.*, *127*, 822–837, 1999.

IPCC. Climate Change 1994. 1994.

Jackman, C. H., A. R. Douglass, R. B. Rood, R. D. McPeters, and P. E. Maede. Effect of solar proton events on the middle atmosphere during the past two solar cycles as computed using a two-dimensional model. *J. Geophys. Res.*, *95*(D6), 7417–7428, 1990.

Jeuken, A. B. M. *Evaluation of chemistry and climate models using measurements and data assimilation*. Phd, Technical University Eindhoven, 2000.

Jokipii, J. R. Variations of the cosmic-ray flux with time. In C. P. Sonett, M. S. Giampapa, and M. S. Matthews, editors, *The sun in time*, pages 205–220. The University of Arizona Press, Tucson, Arizona, 1991.

Junge, C., W. Seiler, and P. Warneck. The atmospheric ^{12}CO and ^{14}CO budget. *J. Geophys. Res.*, *76*(12), 2866–2879, 1971.

Kalnay, E., M. Kanamitsu, R. Kistler, W. Collins, D. Deaven, L. Gandin, M. Iredell, S. Saha, G. White, J. Woollen, Y. Zhu, M. Chelliah, W. Ebisuzaki, W. Higgins, J. Janowiak, K. C. Mo, C. Ropelewski, J. Wang, A. Leetmaa, R. Reynolds, R. Jenne, and D. Joseph. The NCEP/NCAR 40-Year Reanalysis Project. *Bul. Am. Met. Soc.*, *77*(3), 437–471, 1996.

Kanakidou, M. and P. Crutzen. The photochemical source of carbon monoxide: Importance, uncertainties and feedback. *Chemosphere Glob. Change Sci.*, *1*, 91–109, 1999.

Kanakidou, M., F. J. Dentener, and P. J. Crutzen. A global three-dimensional study of the fate of HCFCs and HFC-134a in the troposphere. *J. Geophys. Res.*, *100*(D9), 18 781–18 801, 1995.

Kato, S., Y. Kajii, H. Akimoto, M. Bräunlich, T. Röckmann, and C. A. M. Brenninkmeijer. Observed and modeled seasonal variation of ^{13}C, ^{18}O, and ^{14}C of atmospheric CO at Happo, a remote site in Japan, and a comparison with other records. *J. Geophys. Res.*, *105*(D7), 8891–8900, 2000.

Krol, M., P. J. van Leeuwen, and J. Lelieveld. Global OH trend inferred from methylchloroform measurements. *J. Geophys. Res.*, *103*(D9), 10 697–10 711, 1998.

Lal, D. Theoretically expected variations in the terrestrial cosmic-ray production rates of isotopes. In G. C. Castagnoli, editor, *Solar terrestrial relationships and the Earth environment in the last Millenia*, pages 215–233. North-Holland, Amsterdam, 1988.

Lal, D. and B. Peters. Cosmic ray produced radioactivity on the Earth. In S. Flügge, editor, *Handbuch der Physik*, volume 46, pages 551–612. Springer, 1967.

Lawrence, M. G. *Photochemistry in the tropical troposphere: Studies with a global 3D chemistry-meteorology model*. Phd, Georgia Institute of Technology, 1996.

Lawrence, M. G., P. J. Crutzen, P. J. Rasch, B. E. Eaton, and N. M. Mahowald. A model for studies of tropospheric photochemistry: Description, global distributions, and evaluation. *J. Geophys. Res.*, *104*(D21), 26 245–26 278, 1999a.

Lawrence, M. G., J. Landgraf, and P. Jöckel. Artifacts in global modelling: Two recent examples. *EOS*, *80*, 1999b.

Lelieveld, J. and R. v. Dorland. Ozone chemistry changes in the troposphere and consequent radiative forcing of climate. In W. C. Wang and I. S. A. Isaksen, editors, *Atmospheric ozone as a climate gas*, pages 227–258. Springer Verlag, Berlin, 1995.

Levin, I. and V. Hesshaimer. Refining of atmospheric transport model entries by the globally observed passive tracer distributions of ^{85}Kr and sulfur hexafluoride (SF_6). *J. Geophys. Res.*, *101*(D11), 16 745–16 755, 1996.

Levy, H. Normal atmosphere: Large radical and formaldehyde concentrations predicted. *Science*, *173*, 141–143, 1971.

Libby, W. F. Atmospheric helium three and radiocarbon from cosmic radiation. *Phys. Rev.*, *69*(2), 671–672, 1946.

Light, E. S., M. Merker, H. J. Verschell, R. B. Mendell, and S. A. Korff. Time dependent worldwide distribution of atmospheric neutrons and of their products, 2. Calculation. *J. Geophys. Res.*, *78*, 2741–2762, 1973.

Lin, S.-J. and R. Rood. Multi-dimensional flux-form semi-Lagrangian transport schemes. *Mon. Weather Rev.*, *124*, 2046–2070, 1996.

Lingenfelter, R. E. Production of carbon 14 by cosmic-ray neutrons. *Rev. Geophys.*, *1*, 35–55, 1963.

Lingenfelter, R. E. and E. J. Flamm. Production of carbon 14 by solar protons. *J. Atm. Sci.*, *21*, 134–140, 1964.

Lingenfelter, R. E. and R. Ramaty. Astrophysical and geophysical variations in C14 production. In I. Olsson, editor, *Radiocarbon variations and absolute chronology*, pages 513–537. Wiley, New York, 1970.

Logan, J. A., M. J. Prather, S. C. Wofsy, and M. B. McElroy. Tropospheric chemistry: A global perspective. *J. Geophys. Res.*, *86*(C8), 7210–7254, 1981.

Louis, J. F. A parametric model of vertical eddy fluxes in the atmosphere. *Bound. Lay. Met.*, *17*, 187–202, 1979.

Machenhauer, B., J. Feichter, A. Chlond, M. Olk, A. Bott, E. V. Holm, B. P. Leonard, S.-J. Lin, P. J. Rasch, S. Brinkop, R. Sausen, P. Braesicke, and U. Langematz. MPI Workshop on conservative tracer transport schemes. Technical Report 265, Max-Planck-Institute for Meteorology, 1998.

MacKay, C., M. Pandow, and R. Wolfgang. On the chemistry of natural radiocarbon. *J. Geophys. Res.*, *68*, 3929–3931, 1963.

Maiss, M. and C. A. M. Brenninkmeijer. Atmospheric SF_6: Trends, sources, and prospects. *Environ. Sci. Technol.*, *32*, 3077–3086, 1998.

Mak, J. E. and C. A. M. Brenninkmeijer. Compressed air sample technology for isotopic analysis of atmospheric carbon monoxide. *J. Atm. Oc. Tech.*, *11*(2), 1994.

Mak, J. E., C. A. M. Brenninkmeijer, and M. R. Manning. Evidence for a missing carbon monoxide sink based on tropospheric measurements of ^{14}CO. *J. Geophys. Res.*, *19*(14), 1467–1470, 1992.

Mak, J. E., C. A. M. Brenninkmeijer, and J. R. Southon. Direct measurement of the production rate of ^{14}C near Earth's surface. *Geophys. Res. Lett.*, *26*(22), 3381–3384, 1999.

Mak, J. E., C. A. M. Brenninkmeijer, and J. Tamaresis. Atmospheric ^{14}CO observations and their use for estimating carbon monoxide removal rates. *J. Geophys. Res.*, *99*(D11), 22 915–22 922, 1994.

Mak, J. E. and J. R. Southon. Assessment of tropical OH seasonality using atmospheric ^{14}CO measurements from Barbados. *Geophys. Res. Lett.*, *25*(15), 2801–2804, 1998.

Manning, M. R. Characteristic modes of isotopic variations in atmospheric chemistry. *Geophys. Res. Lett.*, *26*(9), 1263–1266, 1999.

Manning, M. R., C. A. M. Brenninkmeijer, and W. Allan. Atmospheric carbon monoxide budget of the southern hemisphere: Implications of ^{13}C/^{12}C measurements. *J. Geophys. Res.*, *102*(D9), 10 673–10 682, 1997.

Masarik, J. and J. Beer. Simulation of particle fluxes and cosmogenic nuclide production in the Earth's atmosphere. *J. Geophys. Res.*, *104*(D10), 12 099–12 111, 1999.

Masarik, J. and R. C. Reedy. Terrestrial cosmogenic-nuclide production systematics calculated from numerical simulations. *Earth Plan. Sci. Lett.*, *136*, 381–395, 1995.

McCulloch, A., P. M. Midgley, and D. A. Fisher. Distribution of emissions of chlorofluorocarbons (CFCs) 11, 12, 113, 114 and 115 among reporting and non-reporting countries in 1986. *Atmos. Environ.*, *28*(16), 2567–2582, 1994.

McLinden, M. O. Physical properties of alternatives of the fully halogenated chlorofluorocarbons. In *Scientific assessment of stratospheric ozone*, volume WMO Report No.20, pages 11–41. World Meteorol. Organ., Geneva, 1989.

Merker, M., E. S. Light, H. J. Verschell, R. B. Mendell, and S. A. Korff. Time dependent worldwide distribution of atmospheric neutrons and of their products, 1. Fast neutron observations. *J. Geophys. Res.*, *78*, 2727–2740, 1973.

Midgley, P. M. The production and release to the atmosphere of 1,1,1-trichloroethane (methyl chloroform). *Atmos. Environ.*, *23*(12), 2663–2665, 1989.

Midgley, P. M. and A. McCulloch. The production and global distribution of emissions to the atmosphere of 1,1,1-trichloroethane (methyl chloroform). *Atmos. Environ.*, *29*(14), 1601–1608, 1995.

Miles, R. F. Density of cosmic-ray neutrons in the atmosphere. *J. Geophys. Res.*, *69*, 1277–1284, 1964.

Miller, B. R., J. Huang, R. F. Weiss, R. G. Prinn, and P. J. Fraser. Atmospheric trend and lifetime of chlorodifluoromethane (HCFC-22) and the global tropospheric OH concentration. *J. Geophys. Res.*, *103*(D11), 13 237–13 248, 1998.

Montzka, S. A., C. M. Spivakovsky, J. H. Butler, J. W. Elkins, L. T. Lock, and D. J. Mondeel. New observational constraints for atmospheric hydroxyl on global and hemispheric scales. *Science*, *288*, 500–503, 2000.

Novelli, P. C., K. A. Masarie, and P. M. Lang. Distributions and recent changes in carbon monoxide in the lower troposphere. *J. Geophys. Res.*, *103*(D15), 19 015–19 033, 1998.

Novelli, P. C., L. P. Steele, and P. P. Tans. Mixing ratios of carbon monoxide in the troposphere. *J. Geophys. Res.*, *97*(D18), 20 731–20 750, 1992.

O'Brien, K. Cosmic-Ray propagation in the atmosphere. *Nuovo Cimento*, *3A*(3), 521–547, 1971.

O'Brien, K. Secular variations in the production of cosmogenic isotopes in the Earth's atmosphere. *J. Geophys. Res.*, *84*(A2), 423–431, 1979.

O'Brien, K., A. de la Zerda Lerner, M. A. Shea, and D. F. Smart. The production of cosmogenic isotopes in the earth's atmosphere and their inventories. In C. P. Sonett, M. S. Giampapa, and M. S. Matthews, editors, *The sun in time*, pages 317–342. The University of Arizona Press, Tucson, Arizona, 1991.

O'Brien, K. and G. de P. Burke. Calculated cosmic ray neutron monitor response to solar modulation of galactic cosmic rays. *J. Geophys. Res.*, *78*(16), 3013–3019, 1973.

O'Brien, K., H. A. Sandmeier, G. E. Hansen, and J. E. Campbell. Cosmic ray induced neutron background sources and fluxes for geometries of air over water, ground, iron, and aluminium. *J. Geophys. Res.*, *83*(A1), 114–120, 1978.

O'Brien, K. and H. H. Sauer. On the atmospheric response to solar-particle-events. *submitted to Intern. J. Geomag. Aeronom.*, 2000.

Pan, H.-L. and W.-S. Wu. Implementing a mass flux convection parameterization package for the NMC medium-range forecast model. Technical report, NMC, 1995. Office Note, No. 409.

Pandow, M., C. MacKay, and R. Wolfgang. The reaction of atomic carbon with oxygen: Significance for the natural radio-carbon cycle. *J. Inorg. Nucl. Chem.*, *14*, 153–158, 1960.

Peixoto, J. P. and A. H. Oort. Physics of climate. Technical report, American Institute of Physics, 1992.

Prather, M. J. Numerical advection by conservation of second order moments. *J. Geophys. Res.*, *91*(D6), 6671–6681, 1986.

Prather, M. J. Timescales in atmospheric chemistry: Theory, GWPs for CH_4 and CO, and runaway growth. *Geophys. Res. Lett.*, *23*(19), 2597–2600, 1996.

Prinn, R., D. Cunnold, R. Rasmussen, P. Simmonds, F. Alyea, A. Crawford, P. Fraser, and R. Rosen. Atmospheric trends in methylchloroform and the global average for hydroxyl radical. *Science*, *238*, 945–950, 1987.

Prinn, R., D. Cunnold, P. Simmonds, F. Alyea, R. Boldi, A. Crawford, P. Fraser, D. Gutzler, D. Hartley, R. Rosen, and R. Rasmussen. Global average concentration and trend for hydroxyl radicals deduced from ALE/GAGE trichloroethane (methyl chloroform) data 1978-1990. *J. Geophys. Res.*, *97*(D2), 2445–2461, 1992.

Prinn, R. G., R. A. Rasmussen, P. G. Simmonds, F. N. Alyea, D. M. Cunnold, B. C. Lane, C. A. Cardelino, and A. J. Crawford. The atmospheric lifetime experiment

5. Results for CH_3CCl_3 based on three years of data. *J. Geophys. Res.*, *88*(C13), 8415–8426, 1983a.

Prinn, R. G., P. G. Simmonds, R. A. Rasmussen, R. D. Rosen, F. N. Alyea, C. A. Cardelino, A. J. Crawford, D. M. Cunnold, P. J. Fraser, and J. E. Lovelock. The atmospheric lifetime experiment 1. Introduction, instrumentation, and overview. *J. Geophys. Res.*, *88*(C13), 8353–8367, 1983b.

Prinn, R. G., R. F. Weiss, B. R. Miller, J. Huang, F. N. Alyea, D. M. Cunnold, P. J. Fraser, D. E. Hartley, and P. G. Simmonds. Atmospheric trends and lifetime of CH_3CCl_3 and global OH concentrations. *Science*, *269*, 187–192, 1995.

Quay, P., S. King, D. White, M. Brockington, B. Plotkin, R. Gammon, S. Gerst, and J. Stutsman. Atmospheric ^{14}CO: A tracer of OH concentration and mixing rates. *J. Geophys. Res.*, *105*(D12), 15 147–15 166, 2000.

Rasch, P. J., B. A. Boville, and G. P. Brasseur. A three-dimensional general circulation model with coupled chemistry for the middle atmosphere. *J. Geophys. Res.*, *100*(D5), 9041–9071, 1995.

Rasch, P. J. and M. G. Lawrence. Recent developments in transport methods at NCAR. In B. Machenhauer, editor, *MPI-Hamburg Report No. 265*, pages 65–75. MPI-Hamburg, 1998.

Rasch, P. J., N. M. Mahowald, and B. E. Eaton. Representations of transport, convection, and the hydrologic cycle in chemical transport models: Implications for the modeling of short-lived and soluble species. *J. Geophys. Res.*, *102*(D23), 28 127–28 138, 1997.

Rasch, P. J. and D. L. Williamson. Computational aspects of moisture transport in global models of the atmosphere. *Q. J. R. Meteorol. Soc.*, *116*, 1071–1090, 1990.

Ravishankara, A. R., S. Solomon, A. A. Turnispeed, and R. F. Warren. Atmospheric lifetimes of long lived halogenated species. *Science*, *259*, 194–199, 1993.

Reedy, R. C., J. R. Arnold, and D. Lal. Cosmic-ray record in solar system matter. *Ann. Rev. Nucl. Part. Sci.*, *33*, 505–537, 1983.

Reeves, G. D., T. E. Cayton, S. P. Gary, and R. D. Belian. The great solar energetic particle events of 1989 observed from geosynchronous orbit. *J. Geophys. Res.*, *97*(A5), 6219–6226, 1992.

Reichler, T. *Eine globale Klimatologie der Tropopausenhöhe auf der Basis von ECMWF-Analysen*. Diplomarbeit, Universität Augsburg, 1995.

Reynolds, R. W. and T. M. Smith. Improved global sea surface temperature analyses. *J. Climate*, *7*, 929–948, 1994.

Röckmann, T. and C. A. Brenninkmeijer. CO and CO_2 isotopic composition in Spitsbergen during the 1995 ARCTOC campaign. *Tellus*, *49B*, 445–465, 1997.

Röckmann, T., C. A. M. Brenninkmeijer, M. Hahn, and N. F. Elansky. CO mixing and isotope ratios across Russia; trans-Siberian railroad expedition TROICA 3, April 1997. *Chemosphere Glob. Change Sci.*, *1*, 219–231, 1999.

Roelofs, G.-J. and J. Lelieveld. Model study of the influence of cross-tropopause O_3 transports on tropospheric O_3 levels. *Tellus*, *49B*, 38–55, 1997.

Rom, W., C. Brenninkmeijer, M. Bräunlich, G. R., M. Mandl, A. Kaiser, W. Kutschera, A. Priller, S. Puchegger, T. Röckmann, and P. Steier. A detailed 2-year record of atmospheric ^{14}CO in the temperate northern hemisphere. *Nucl. Instr. Meth. B*, *161*, 780–785, 2000.

Rom, W., C. A. M. Brenninkmeijer, M. Bräunlich, R. Golser, M. Mandl, A. Kaiser, W. Kutschera, A. Priller, S. Puchegger, T. Röckmann, and P. Steier. The "CO-OH-Europe" project and measurements of ^{14}C monoxide concentrations in air from the high-altitude observatory Sonnblick (3106 m) in the Austrian Alps. In *Proceedings of the International Workshop on Frontiers in Accelerator Mass Spectrometry, Tsukuba/Japan and Sakura/Japan*, pages 228–243. 1999a.

Rom, W., C. A. M. Brenninkmeijer, C. B. Ramsey, W. Kutschera, A. Priller, S. Puchegger, T. Röckmann, and P. Steier. Methodological aspects of atmospheric ^{14}CO measurements with AMS. *Nucl. Instr. Meth. B, (Proceedings of the Eighth International Conference on Accelerator Mass Spectrometry, Vienna, Austria, September 6-10, 1999)*, *in press*, 1999b.

Rood, R. B. Numerical advection algorithms and their role in atmospheric transport and chemistry models. *Rev. Geophys.*, *25*(1), 71–100, 1987.

Rosenlof, K. H. Seasonal cycle of the residual mean circulation in the stratosphere. *J. Geophys. Res.*, *100*(D3), 5173–5191, 1995.

Rosinski, J. M. and D. L. Williamson. The accumulation of rounding errors and port validation for global atmospheric models. *SIAM J. SCI. Comput.*, *18*(2), 552–564, 1997.

Russell, G. L. and A. Lerner. A finite difference scheme for the tracer transport equation. *J. Appl. Met.*, *20*, 1483–1498, 1981.

Sanhueza, E., Y. Dong, D. Scharffe, J. M. Lobert, and P. J. Crutzen. Carbon monoxide uptake by temperature forest soils: the effects of leaves and humus layers. *Tellus*, *50B*, 51–58, 1998.

Sauer, H. H., R. D. Zwickl, and M. J. Ness. Summary data for the solar energetic particle events of August through December 1989. Technical report, Space Environment Laboratory, NOAA, 1990.

Seinfeld, J. H. and S. N. Pandis. *Atmospheric Chemistry and Physics*. John Wiley, New York, 1997.

Shapiro, M. A. Turbulent mixing within tropopause folds as a mechanism for the exchange of chemical constituents between the stratosphere and troposphere. *J. Atm. Sci.*, *37*, 994–1004, 1980.

Shea, M. A. and D. F. Smart. Recent and historical solar proton events. *Radiocarbon*, *34*(2), 255–262, 1992.

Singh, H. B. Atmospheric halocarbons: Evidence in favour of reduced average hydroxyl radical concentration in the troposphere. *Geophys. Res. Lett.*, *4*(3), 101–104, 1977.

Smart, D. F. and M. A. Shea. Galactic cosmic radiation and solar energetic particles. In A. S. Jursa, editor, *Handbook of Geophysics and the Space Environment*, pages 6–1 – 6–29. Air Force Geophysics Laboratory, Hanscom Air Force Base, MA, 1985.

Spivakovsky, C. M. Reply on comment on "Tropospheric OH in a three-dimensional chemical tracer model: An assessment based on observations of CH_3CCl_3" by C. M. Spivakovsky et al. *J. Geophys. Res.*, *96*(D9), 17 395–17 398, 1991.

Spivakovsky, C. M., J. A. Logan, S. A. Montzka, Y. J. Balkanski, M. Foreman-Fowler, D. B. A. Jones, L. W. Horowitz, A. C. Fusco, C. A. M. Brenninkmeijer, M. J. Prather, S. C. Wofsy, and M. B. McElroy. Three-dimensional climatological distribution of tropospheric OH: Update and evaluation. *J. Geophys. Res.*, *105*(D7), 8931–8980, 2000.

Spivakovsky, C. M., R. Yevich, J. A. Logan, S. C. Wofsy, M. B. McElroy, and M. J. Prather. Tropospheric OH in a three-dimensional chemical tracer model: An assessment based on observations of CH_3CCl_3. *J. Geophys. Res.*, *95*(D11), 18 441–18 471, 1990.

Spivakovsky, C. M., R. Yevich, J. A. Logan, S. C. Wofsy, M. B. McElroy, and M. J. Prather. Reply on comment on "Tropospheric OH in a three-dimensional

chemical tracer model: An assessment based on observations of CH_3CCl_3" by C. M. Spivakovsky et al. *J. Geophys. Res.*, *96*(D9), 17 389–17 390, 1991.

Steil, B., C. Brühl, P. J. Crutzen, and E. Manzini. A MA-GCM with interactive chemistry (MAECHAM4-CHEM), simulations for present, past and future. In *Proceedings of the XIX. Quadrennial Ozone Symposium*. Sapporo, Japan, 2000.

Stuiver, M. and H. A. Polach. Discussion of reporting ^{14}C data. *Radiocarbon*, *19*(3), 355–363, 1977.

Stuiver, M. and P. D. Quay. Changes in atmospheric carbon-14 attributed to a variable sun. *Science*, *207*(4426), 11–19, 1980.

Tans, P. P. A note on isotopic ratios and the global atmospheric methane budget. *Glob. Biogeochem. Cycles*, *11*(1), 77–81, 1997.

Tiedtke, M. A. A comprehensive mass flux scheme for cumulus parameterization in large scale models. *Mon. Weather Rev.*, *117*, 1641, 1989.

Tobler, W. Population database of the Consortium for Internal Earth Science Information Network (CIESIN) and the Environmental Systems Research Institute, Inc. (ESRI). Technical Report NCGIA-TR-95-6, National Center for Geographic Information and Analysis, Dept. of Geography, University of California, Santa Barbara, CA., 1995.

Tyler, S. C., G. A. Klouda, G. W. Brailsford, A. C. Manning, J. M. Conny, and A. J. T. Jull. Seasonal snapshots of the isotopic (^{14}C, ^{13}C) composition of tropospheric carbon monoxide at Niwot Ridge, Colorado. *Chemosphere Glob. Change Sci.*, *1*, 185–203, 1999.

United Nations. *1992 Energy Statistics Yearbook*. United Nations Publication Sales No. E/F.94.XVII.9. Departement for economic and social information and policy analysis, Statistical Division, New York, 1994.

van Velthoven, P. F. J. and H. Kelder. Estimates of stratosphere-troposphere exchange: Sensitivity to model formulation and horizontal resolution. *J. Geophys. Res.*, *101*(D1), 1429 – 1434, 1996.

Volz, A., D. H. Ehhalt, and R. G. Derwent. Seasonal and latitudinal variation of ^{14}CO and the tropospheric concentration of OH radicals. *J. Geophys. Res.*, *86*(NC6), 5163–5171, 1981.

Weinstock, B. Carbon monoxide: Residence time in the atmosphere. *Science*, *166*, 224–225, 1969.

Williamson, D. L. and P. J. Rasch. Two-dimensional semi-Lagrangian transport with shape-preserving interpolation. *Mon. Weather Rev.*, *117*, 102–129, 1989.

WMO. International meteorological vocabulary. 1992.

Young, P., G. Hale, and M. Chadwick. ENDF/B-VI Data file for N14, ENDF/B-VI Neutron data library, Revision 3. 1994.

Zhang, G. J. and N. A. McFarlane. Sensitivity of climate simulations to the parameterization of cumulus convection in the Canadian Climate Center general circulation model. *Atmos. Ocean*, *33*, 407–446, 1995.

Acknowledgements

Many, many thanks

- to my parents for supporting my education and making possible the study of physics, furthermore, for their continuous support and encouragement
- to my wife Anikó for her great patience, for keeping me grounded during stressy times, especially during the last phase of writing this thesis, for her continuous moral support, and for the life beyond science
- to my supervisor Dr. Carl A. M. Brenninkmeijer for employing me in his working group, for involving me into this interesting field, for his patience, his always open ear to my problems, for innumerable valuable discussions, for his unrivaled advancement and never ending support, for providing the excellent work environment, for being uncomplicated, for taking the risks of a modeling-study, for making possible to visit several conferences, workshops, summer-schools, for the Spitsbergen trip, and last but not least for proofreading this thesis
- to his wife Cathy for standing by his side and for her charming pleasantness
- to Dr. Mark G. Lawrence for the inauguration into the secrets of 3-dimensional global atmospheric modeling, for the intense cooperation, for many, many fruitful discussions, for his immediate help on problems, for all his suggestions, and finally, for his tremendous effort in proofreading this thesis in all details
- to Prof. Dr. Ulrich Platt and Prof. Dr. Paul Crutzen for their continuous interest in my work, for valuable and interesting discussions, for always helpful comments, and for the assessment of this thesis
- to Dr. Ad Jeuken (KNMI) for the fruitful cooperation, especially for performing the TM3 model simulations at KNMI, which turned out to be an integral part of this thesis and the basis of important conclusions
- to Dr. Peter F. J. van Velthoven for his invitation to visit KNMI, and for mediating the cooperation with people from KNMI
- to Dr. Peter Siegmund from KNMI for several salutary discussions, for his cooperation in investigating the solar proton event effect, and for providing the subsidence estimates
- to my room mates and colleagues Dr. Eva Oberlander and Dr. Thomas Röckmann for their pleasant company, for the communication whenever needed, also beyond the work, for their advice, their steady support, and for proofreading this thesis

- to the modeling colleagues Rolf von Kuhlmann, Dr. Benedikt Steil, and Dr. Mark G. Lawrence for the discussions on the mass conservation issue

- to the modeling colleagues Rolf von Kuhlmann, Dr. Rolf Sander, Dr. Benedikt Steil, Dr. Christoph Brühl, Roland von Glasow, Dr. Ahmad Zand, Dr. Olivier Boucher, Dr. Jochen Landgraf, Dr. Ulrich Pöschl, Dr. Thomas Trautmann, Dr. Stefanie Meilinger, Dr. Beiping Luo and Jörg Trentmann for the joined lunch-breaks, the Wednesday tea-time, the interesting discussions about almost everything, the steady help on computer and software related issues, the comfortable working environment, and especially to Jörg Trentmann for proofreading this thesis, and also for the "Cappuccino-discussions" after lunch

- to Dr. Ingeborg Levin and Dr. Vago Hesshaimer for numerous valuable discussions about cosmic ray isotope production, for the joint effort in understanding the secrets of cosmic rays, for the invitation to join a seminar on this subject, and for the continuous interest in my work

- to Prof. Dr. Paul Quay and Dr. John E. Mak for providing their ^{14}CO data, the latter also for interesting discussions

- to Dr. Clarissa M. Spivakovsky for providing the OH distribution

- to Dr. Maarten Krol from IMAU for the discussions and his advice for the methylchloroform study, and also for providing the data

- to Dr. Phil J. Rasch and Dr. Brian Eaton from NCAR for the continuous development of MATCH, and the cooperation on the mass conservation issue

- to Prof. Dr. Martin Heimann for his valuable comments on the mass conservation issue, and for providing information and data required for the SF_6 study

- to Dr. Keran O'Brien and Dr. Jozef Masarik for providing their ^{14}C production rate data

- to Dr. Robert Reedy and Dr. Keran O'Brien for intensively reading the draft of the solar proton event study and their numerous and constructive comments, which are exclusively incorporated in the present version

- to all present and former members of the Brenninkmeijer-group for their nice cooperation and valuable discussions (Dr. Sergey Assonov, Dr. Peter Bergamaschi, Dr. Maya Bräunlich, Jörg Dunker, Dr. Valérie Gros, Dr. Denis Haan, Michael Hahn, Wolfgang Hahnewacker, Rolf Hofmann, Dr. Jeff Johnston, Jan Kaiser, Dr. Shungo Kato, Claus Koeppel, Dr. Manfred Maiss, Jens Mühle, Dr. Eva Oberlander, Dr. Tae Siek Rhee, Dr. Thomas Röckmann, Dr. Andreas Zahn, Harald Schäfer, Dieter Scharffe, Reinhold Schmunk)

- to Klaus Egenolf, Martin Körfer and Heinz Gimm from the MPICH computing center for their support
- to the DKRZ user consulting group for their support
- to all colleagues from MPICH for making this Institute what it is, especially to Bettina Krüger and Anja Wienhold (secretary of air chemistry department), Gerhild Feyerherd and Iris Bambach (Zeichenbüro), and further to all people from the administration for being unbureaucratic
- to all people involved in the valuable measurements of the CO isotopic signature at several locations all over the world
- all the people behind the data-bases used in this thesis, such as ECMWF, IGOSS, GEIA, NCEP, NGDC-SPIDR, NOAA-CMDL, WDC-C2
- to the European Commission for the financial support (DG XII, "CO-OH-Europe" project, EC "SINDICATE" project for super computer usage)
- to the developers of Ferret, GrADS and the NetCDF library for their efforts to build such valuable software-tools and sharing them for free
- to all scientists who are free of vain, who are able to enjoy scientific progress and results, even if the results are not their own, whom I met during various conferences, workshops, summer-schools and other visits